Crunching data to stop crime before it happens *p. 1484*

Receptor binds toxic α-synuclein fibrils *pp. 1498 & 1513*

Positive emotional states in bumblebees *pp. 1499 & 1529*

Science

$15
30 SEPTEMBER 2016
sciencemag.org

AAAS

GENETIC GEOGRAPHY

Global maps of animal diversity *pp. 1494 & 1532*

CONTENTS

30 SEPTEMBER 2016 • VOLUME 353 • ISSUE 6307

1484 Predicting crime hot spots

1483

NEWS

IN BRIEF

1474 News at a glance

IN DEPTH

1477 DEEP SPACE NETWORK GLITCHES WORRY SCIENTISTS
NASA's aging radio antennas have faced years of budget cuts *By P. Voosen*

1478 WILL NOBEL PRIZE OVERLOOK LIGO'S MASTER BUILDER?
Barry Barish assembled the gravitational wave detectors *By A. Cho*

1480 CANADA AIMS TO REWRITE ENVIRONMENTAL LAW
Scientists urge government to tighten project reviews *By L. Evans Ogden*

1481 A LIFELINE FOR GREEK SCIENCE—OR LIVING ON BORROWED TIME?
New foundation will fund peer-reviewed grants, but crisis persists *By E. Stokstad*

1482 ROSETTA ENDS 2-YEAR COMET MISSION WITH FINAL DESCENT
Fluffy particles indicate that 67P/Churyumov-Gerasimenko was born gently from flocks of pebbles *By D. Clery*

1483 FOSSIL FISHES CHALLENGE 'URBAN LEGEND' OF EVOLUTION
Genome duplications, thought to power evolutionary radiations, can't explain explosion of fishes *By E. Pennisi*

FEATURES

1484 CRIME FORECASTERS
Police are turning to big data and algorithms to stop crime before it happens. But how biased is predictive policing—and does it even work? *By M. Hvistendahl*

1488 THE BIGGEST EAR
It will take one more burst of ingenuity to get China's massive radio telescope to live up to its promise *By D. Normile*
▸ VIDEO

INSIGHTS

PERSPECTIVES

1492 DETECTING STRUCTURE IN A PROTOSTELLAR DISK
Spiral structure may provide clues about the early stages of star and planet formation *By K. Rice*
▸ REPORT P. 1519

1494 A LATITUDINAL GRADIENT FOR GENETIC DIVERSITY
Within-species diversity of amphibians and terrestrial mammals is highest in the tropics *By H. M. Pereira*
▸ REPORT P. 1532

1495 CONSTRAINING LITHOSPHERIC FLOW
Geophysical data help to determine the viscosity of Earth's crust and upper mantle *By B. J. P. Kaus*
▸ REPORT P. 1515

1496 SOCIAL MEMORY GOES VIRAL
A precisely mapped brain network discriminates and remembers friends and strangers *By K. Saxena and R. G. M. Morris*
▸ REPORT P. 1536

1498 IMMUNE RECEPTOR FOR PATHOGENIC α-SYNUCLEIN
An immune protein facilitates neuronal uptake of a Parkinson's disease–associated protein *By M. Jucker and M. Heikenwalder*
▸ RESEARCH ARTICLE P. 1513

1499 BEE HAPPY
Bumblebees show decision-making that reflects emotion-like states *By M. T. Mendl and E. S. Paul*
▸ REPORT P. 1529

1501 JAMES W. CRONIN (1931–2016)
A Nobel laureate raised the profile of physics worldwide *By A. A. Watson*

POLICY FORUM

1502 GROWING PAINS FOR GLOBAL MONITORING OF SOCIETAL EVENTS
Automated event coding raises promise and concerns *By W. Wang* et al.
▸ PODCAST

BOOKS *ET AL.*

1504 RETHINKING THE ARROW OF TIME
Citing shortcomings in Eddington's theory, a physicist proposes a new explanation for the existence of "now" *By L. Jardine-Wright*

1505 LEVELING UP
Advocates aim to stimulate renewed interest in a hierarchical theory of evolution *By B. Autzen*

LETTERS

1506 SCIENTISTS STAND WITH STANDING ROCK
By S. R. Januchowski-Hartley et al.

1506 BUILD HABITATS, NOT FENCES, FOR CARIBOU
By G. Proulx and R. A. Powell

1507 ILLEGAL WILDLIFE TRADE: LOOK TO THE ELEPHANTS
By G. Wittemyer

1507 ERRATA

Downloaded from http://science.sciencemag.org/ on October 7, 2016

Published by AAAS

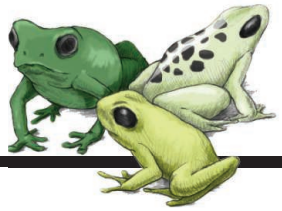

1494 & 1532
Mapping genetic diversity

1514
Tumor epigenetics

RESEARCH

IN BRIEF

1509 From *Science* and other journals

REVIEW

1512 **ADDITIVE MANUFACTURE**
Multiprocess 3D printing for increasing component functionality
E. MacDonald and R. Wicker
REVIEW SUMMARY; FOR FULL TEXT:
dx.doi.org/10.1126/science.aaf2093

RESEARCH ARTICLES

1513 **NEURODEGENERATION**
Pathological α-synuclein transmission initiated by binding lymphocyte-activation gene 3 *X. Mao* et al.
RESEARCH ARTICLE SUMMARY; FOR FULL TEXT:
dx.doi.org/10.1126/science.aah3374
▸ PERSPECTIVE P. 1498

1514 **CANCER**
The linker histone H1.0 generates epigenetic and functional intratumor heterogeneity *C. Morales Torres* et al.
RESEARCH ARTICLE SUMMARY; FOR FULL TEXT:
dx.doi.org/10.1126/science.aaf1644

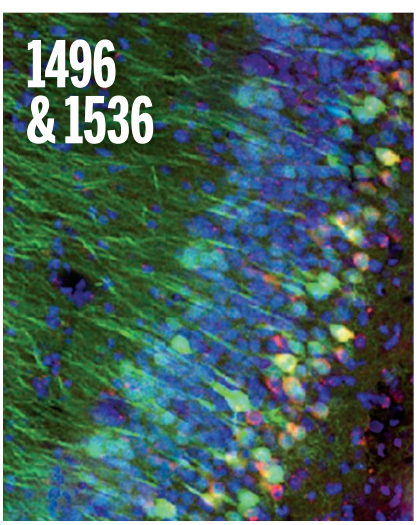

REPORTS

1515 **GEOPHYSICS**
High-resolution lithosphere viscosity and dynamics revealed by magnetotelluric imaging *L. Liu and D. Hasterok*
▸ PERSPECTIVE P. 1495

1519 **PROTOPLANETARY DISKS**
Spiral density waves in a young protoplanetary disk *L. M. Pérez* et al.
▸ PERSPECTIVE P. 1492

GRAPHENE

1522 Electron optics with p-n junctions in ballistic graphene *S. Chen* et al.

1526 Ballistic miniband conduction in a graphene superlattice *M. Lee* et al.

1529 **COGNITION**
Unexpected rewards induce dopamine-dependent positive emotion–like state changes in bumblebees *C. J. Perry* et al.
▸ PERSPECTIVE P. 1499

1532 **BIODIVERSITY**
An Anthropocene map of genetic diversity *A. Miraldo* et al.
▸ PERSPECTIVE P. 1494

1536 **SOCIAL MEMORY**
Ventral CA1 neurons store social memory *T. Okuyama* et al.
▸ PERSPECTIVE P. 1496

1541 **VIROLOGY**
MAVS-dependent host species range and pathogenicity of human hepatitis A virus *A. Hirai-Yuki* et al.

1545 **ENHANCER FUNCTION**
High-resolution interrogation of functional elements in the noncoding genome *N. E. Sanjana* et al.
▸ REPORT BY C. P. FULCO *ET AL.*
10.1126/science.aag2445

1549 **GENE REGULATION**
Cyclin A2 is an RNA binding protein that controls *Mre11* mRNA translation *A. Kanakkanthara* et al.

1553 **SIGNALING**
Drosophila insulin release is triggered by adipose Stunted ligand to brain Methuselah receptor *R. Delanoue* et al.

1557 **HIV-1 VACCINES**
Priming HIV-1 broadly neutralizing antibody precursors in human Ig loci transgenic mice *D. Sok* et al.

DEPARTMENTS

1473 **EDITORIAL**
The boldness of philanthropists
By David Baltimore

1586 **WORKING LIFE**
Doing science while black
By Edward J. Smith

ON THE COVER

A juvenile Iberian lynx (*Lynx pardinus*). This species, native to the southern Iberian Peninsula, is the most threatened felid in the world. Many other animals have also suffered the loss of populations and genetic diversity due to past and recent habitat destruction, introduction of disease, or competition with invasive species. See pages 1494 and 1532.
Photo: © Roland Seitre/Minden Pictures

Science Staff 1470
AAAS News & Notes 1508
New Products 1561
Science Careers 1562

SCIENCE (ISSN 0036-8075) is published weekly on Friday, except the last week in December, by the American Association for the Advancement of Science, 1200 New York Avenue, NW, Washington, DC 20005. Periodicals mail postage (publication No. 484460) paid at Washington, DC, and additional mailing offices. Copyright © 2016 by the American Association for the Advancement of Science. The title SCIENCE is a registered trademark of the AAAS. Domestic individual membership and subscription (51 issues): $165 ($74 allocated to subscription). Domestic institutional subscription (51 issues): $1522; Foreign postage extra: Mexico, Caribbean (surface mail) $55; other countries (air assist delivery) $89. First class, airmail, student, and emeritus rates on request. Canadian rates with GST available upon request, GST #1254 88122. Publications Mail Agreement Number 1069624. **Printed in the U.S.A.**
Change of address: Allow 4 weeks, giving old and new addresses and 8-digit account number. **Postmaster:** Send change of address to AAAS, P.O. Box 96178, Washington, DC 20090–6178. **Single-copy sales:** $15.00 current issue, $20.00 back issue prepaid includes surface postage; bulk rates on request. **Authorization to photocopy** material for internal or personal use under circumstances not falling within the fair use provisions of the Copyright Act is granted by AAAS to libraries and other users registered with the Copyright Clearance Center (CCC) Transactional Reporting Service, provided that $35.00 per article is paid directly to CCC, 222 Rosewood Drive, Danvers, MA 01923. The identification code for *Science* is 0036-8075. *Science* is indexed in the *Reader's Guide to Periodical Literature* and in several specialized indexes.

Published by AAAS

Downloaded from http://science.sciencemag.org/ on October 7, 2016

Science
AAAS
1200 New York Avenue, NW, Washington, DC 20005
Clarendon House, Clarendon Road, Cambridge, UK CB2 8FH

Editor-in-Chief Jeremy Berg
Executive Editor Monica M. Bradford **News Editor** Tim Appenzeller
Deputy Editors Lisa D. Chong, Andrew M. Sugden(UK), Valda J. Vinson, Jake S. Yeston

Research and Insights

DEPUTY EDITOR, EMERITUS Barbara R. Jasny **SR. EDITORS** Caroline Ash(UK), Gilbert J. Chin, Julia Fahrenkamp-Uppenbrink(UK), Pamela J. Hines, Stella M. Hurtley(UK), Paula A. Kiberstis, Marc S. Lavine(Canada), Kristen L. Mueller, Ian S. Osborne(UK), Beverly A. Purnell, L. Bryan Ray, Guy Riddihough, H. Jesse Smith, Jelena Stajic, Peter Stern(UK), Phillip D. Szuromi, Sacha Vignieri, Brad Wible, Nicholas S. Wigginton, Laura M. Zahn **ASSOCIATE EDITORS** Brent Grocholski, Keith T. Smith **ASSOCIATE BOOK REVIEW EDITOR** Valerie B. Thompson **LETTERS EDITOR** Jennifer Sills **LEAD CONTENT PRODUCTION EDITORS** Harry Jach, Lauren Kmec **CONTENT PRODUCTION EDITORS** Jeffrey E. Cook, Chris Filiatreau, Cynthia Howe, Barbara P. Ordway, Catherine Wolner **SR. EDITORIAL COORDINATORS** Carolyn Kyle, Beverly Shields **EDITORIAL COORDINATORS** Aneera Dobbins, Joi S. Granger, Jeffrey Hearn, Lisa Johnson, Maryrose Madrid, Anita Wynn **PUBLICATIONS ASSISTANTS** Nida Masiulis, Dona Mathieu, Le-Toya Mayne Flood, Shannon McMahon, Scott Miller, Jerry Richardson, Alice Whaley(UK), Gwen Grant(UK), Brian White **EXECUTIVE ASSISTANT** Anna Bashkirova **ADMINISTRATIVE SUPPORT** Janet Clements(UK), Lizanne Newton(UK)

News

NEWS MANAGING EDITOR John Travis **INTERNATIONAL EDITOR** Richard Stone **DEPUTY NEWS EDITORS** Elizabeth Culotta, David Grimm, Eric Hand David Malakoff, Leslie Roberts **CONTRIBUING EDITOR** Martin Enserink(Europe) **SR. CORRESPONDENTS** Daniel Clery(UK), Jeffrey Mervis, Elizabeth Pennisi **NEWS WRITERS** Adrian Cho, Jon Cohen, Jennifer Couzin-Frankel, Carolyn Gramling, Jocelyn Kaiser, Catherine Matacic, Kelly Servick, Robert F. Service, Erik Stokstad(Cambridge, UK), Paul Voosen, Meredith Wadman **INTERNS** Jessica Boddy, Ben Panko **CONTRIBUTING CORRESPONDENTS** John Bohannon, Warren Cornwall, Ann Gibbons, Mara Hvistendahl, Sam Kean, Eli Kintisch, Kai Kupferschmidt(Berlin), Andrew Lawler, Mitch Leslie, Charles C. Mann, Eliot Marshall, Virginia Morell, Dennis Normile(Shanghai), Heather Pringle, Tania Rabesandratana(London), Emily Underwood, Gretchen Vogel(Berlin), Lizzie Wade(Mexico City) **CAREERS** Donisha Adams, Rachel Bernstein(Editor), Maggie Kuo **COPY EDITORS** Julia Cole, Dorie Chevlen, Jennifer Levin (Chief) **ADMINISTRATIVE SUPPORT** Jessica Adams

Executive Publisher Rush D. Holt
Publisher Bill Moran **Chief Digital Media Officer** Rob Covey

BUSINESS OPERATIONS AND PORTFOLIO MANAGEMENT DIRECTOR Sarah Whalen **PRODUCT DEVELOPMENT DIRECTOR** Will Schweitzer **PRODUCT DEVELOPMENT ASSOCIATE** Hannah Heckner **BUSINESS SYSTEMS AND FINANCIAL ANALYSIS DIRECTOR** Randy Yi **SENIOR SYSTEMS ANALYST** Nicole Mehmedovich **DIRECTOR, BUSINESS OPERATIONS & ANALYSIS** Eric Knott **MANAGER, BUSINESS OPERATIONS** Jessica Tierney **SENIOR BUSINESS ANALYST** Cory Lipman **BUSINESS ANALYSTS** David Garrison, Michael Hardesty Meron Kebede, Sandy Kim **FINANCIAL ANALYST** Drew Sher **DIRECTOR, COPYRIGHTS LICENSING SPECIAL PROJECTS** Emilie David **PERMISSIONS ASSOCIATE** Elizabeth Sandler **RIGHTS, CONTRACTS, AND LICENSING ASSOCIATE** Lili Kiser **RIGHTS & PERMISSIONS ASSISTANT** Alexander Lee

MARKETING DIRECTOR Elise Swinehart **ASSOCIATE MARKETING DIRECTOR** Stacey Burke Bowers **MARKETING ASSOCIATE** Steven Goodman **CREATIVE DIRECTOR** Scott Rodgerson **SENIOR ART ASSOCIATES** Paula Fry **ART ASSOCIATE** Kim Huynh

FULFILLMENT SYSTEMS AND OPERATIONS membership@aaas.org **MANAGER, MEMBER SERVICES** Pat Butler **SPECIALISTS** Terrance Morrison, Latasha Russell **MANAGER, DATA ENTRY** Mickie Napoleoni **DATA ENTRY SPECIALISTS** Brenden Aquilino, Fiona Giblin **MARKETING ASSOCIATE** Isa Sesay-Bah

PUBLISHER RELATIONS, EASTERN REGION Keith Layson **PUBLISHER RELATIONS, WESTERN REGION** Ryan Rexroth **SALES RESEARCH COORDINATOR** Aiesha Marshall **ASSOCIATE DIRECTOR, INSTITUTIONAL LICENSING OPERATIONS** Iquo Edim **SENIOR OPERATIONS ANALYST** Lana Guz **MANAGER, AGENT RELATIONS & CUSTOMER SUCCESS** Judy Lillibridge

WEB TECHNOLOGIES PORTFOLIO MANAGER Trista Smith **TECHNICAL MANAGER** Chris Coleman **PROJECT MANAGER** Nick Fletcher **DEVELOPERS** Ryan Jensen, Jimmy Marks, Brandon Morrison **BUSINESS ANALYST** Christina Wofford

DIGITAL MEDIA DIRECTOR OF ANALYTICS Enrique Gonzales **DIGITAL REPORTING ANALYST** Eric Hossinger **SR. MULTIMEDIA PRODUCER** Sarah Crespi **MANAGING DIGITAL PRODUCER** Alison Crawford **PRODUCER** Liana Birke **VIDEO PRODUCER** Chris Burns, Nguyên Khôi Nguyễn **DIGITAL SOCIAL MEDIA PRODUCER** Brice Russ

DIRECTOR OF OPERATIONS PRINT AND ONLINE Lizabeth Harman **DIGITAL/PRINT STRATEGY MANAGER** Jason Hillman **QUALITY TECHNICAL MANAGER** Marcus Spiegler **PROJECT ACCOUNT MANAGER** Tara Kelly **DIGITAL PRODUCTION MANAGER** Lisa Stanford **ASSISTANT MANAGER DIGITAL/PRINT** Rebecca Doshi **SENIOR CONTENT SPECIALISTS** Steve Forrester, Antoinette Hodal, Lori Murphy, Anthony Rosen **CONTENT SPECIALISTS** Jacob Hedrick, Kimberley Oster **ADVERTISING OPERATIONS SPECIALIST** Ashley Jeter

DESIGN DIRECTOR Beth Rakouskas **DESIGN EDITOR** Marcy Atarod **SENIOR DESIGNER** Chrystal Smith **GRAPHICS MANAGING EDITOR** Alberto Cuadra **GRAPHICS EDITOR** Garvin Grullón **SENIOR SCIENTIFIC ILLUSTRATORS** Chris Bickel, Katharine Sutliff **SCIENTIFIC ILLUSTRATOR** Valerie Altounian **INTERACTIVE GRAPHICS EDITOR** Jia You **SENIOR GRAPHICS SPECIALISTS** Holly Bishop, Nathalie Cary **PHOTOGRAPHY MANAGING EDITOR** William Douthitt **SENIOR PHOTO EDITOR** Christy Steele **PHOTO EDITOR** Emily Petersen

DIRECTOR, GLOBAL COLLABORATION, CUSTOM PUBLICATIONS, ADVERTISING Bill Moran **EDITOR, CUSTOM PUBLISHING** Sean Sanders: 202-326-6430 **ADVERTISING MARKETING MANAGER** Justin Sawyers: 202-326-7061 science_advertising@aaas.org **ADVERTISING SUPPORT MANAGER** Karen Foote: 202-326-6740 **ADVERTISING PRODUCTION OPERATIONS MANAGER** Deborah Tompkins **SR. PRODUCTION SPECIALIST/GRAPHIC DESIGNER** Amy Hardcastle **SR. TRAFFIC ASSOCIATE** Christine Hall **SALES COORDINATOR** Shirley Young **ASSOCIATE DIRECTOR, COLLABORATION, CUSTOM PUBLICATIONS/CHINA/TAIWAN/KOREA/SINGAPORE** Ruolei Wu: +86-186 0082 9345, rwu@aaas.org **COLLABORATION/CUSTOM PUBLICATIONS/JAPAN** Adarsh Sandhu + 81532-81-5142 asandhu@aaas.org **EAST COAST/E. CANADA** Laurie Faraday: 508-747-9395, FAX 617-507-8189 **WEST COAST/W. CANADA** Lynne Stickrod: 415-931-9782, FAX 415-520-6940 **MIDWEST** Jeffrey Dembksi: 847-498-4520 x3005, Steven Loerch: 847-498-4520 x3006 **UK EUROPE/ASIA** Roger Goncalves: TEL/FAX +41 43 243 1358 **JAPAN** Katsuyoshi Fukamizu(Tokyo): +81-3-3219-5777 kfukamizu@aaas.org **CHINA/TAIWAN** Ruolei Wu: +86-186 0082 9345, rwu@aaas.org

WORLDWIDE ASSOCIATE DIRECTOR OF SCIENCE CAREERS Tracy Holmes: +44 (0) 1223 326525, FAX +44 (0) 1223 326532 tholmes@science-int.co.uk **CLASSIFIED** advertise@sciencecareers.org **U.S. SALES** Tina Burks: 202-326-6577, Nancy Toema: 202-326-6578 **EUROPE/ROW SALES** Sarah Lelarge **SALES ASSISTANT** Kelly Grace **JAPAN** Hiroyuki Mashiki(Kyoto): +81-75-823-1109 hmashiki@aaas.org **CHINA/TAIWAN** Ruolei Wu: +86-186 0082 9345 rwu@aaas.org **MARKETING MANAGER** Allison Pritchard **MARKETING ASSOCIATE** Aimee Aponte

AAAS BOARD OF DIRECTORS, CHAIR Geraldine L. Richmond **PRESIDENT** Barbara A. Schaal **PRESIDENT-ELECT** Susan Hockfield **TREASURER** David Evans Shaw **CHIEF EXECUTIVE OFFICER** Rush D. Holt **BOARD** Cynthia M. Beall, May R. Berenbaum, Carlos J. Bustamante, Stephen P.A. Fodor, Claire M. Fraser, Michael S. Gazzaniga, Laura H. Greene, Elizabeth Loftus, Mercedes Pascual

SUBSCRIPTION SERVICES For change of address, missing issues, new orders and renewals, and payment questions: 866-434-AAAS (2227) or 202-326-6417, FAX 202-842-1065. Mailing addresses: AAAS, P.O. Box 96178, Washington, DC 20090-6178 or AAAS Member Services, 1200 New York Avenue, NW, Washington, DC 20005

INSTITUTIONAL SITE LICENSES 202-326-6730 **REPRINTS:** Author Inquiries 800-635-7181 **COMMERCIAL INQUIRIES** 803-359-4578 **PERMISSIONS** 202-326-6765, permissions@aaas.org **AAAS Member Services** 202-326-6417 or http://membercentral.aaas.org/discounts

Science serves as a forum for discussion of important issues related to the advancement of science by publishing material on which a consensus has been reached as well as including the presentation of minority of conflicting points of view. Accordingly, all articles published in *Science*—including editorials, news and comment, and book reviews—are signed and reflect the individual views of the authors and not official points of view adopted by AAAS or the institutions with which the authors are affiliated.

INFORMATION FOR AUTHORS See pages 624 and 625 of the 5 February 2016 issue or access www.sciencemag.org/authors/science-information-authors

SENIOR EDITORIAL BOARD
Gary King, *Harvard University,* **Susan M. Rosenberg,** *Baylor College of Medicine,*
Ali Shilatifard, *Northwestern University Feinberg School of Medicine*

BOARD OF REVIEWING EDITORS (Statistics board members indicated with **(S)**)

Adriano Aguzzi, *U. Hospital Zürich*
Takuzo Aida, *U. of Tokyo*
Leslie Aiello, *Wenner-Gren Foundation*
Judith Allen, *U. of Edinburgh*
Sonia Altizer, *U. of Georgia*
Sebastian Amigorena, *Institut Curie*
Kathryn Anderson, *Memorial Sloan-Kettering Cancer Center*
Meinrat O. Andreae, *Max-Planck Inst. Mainz*
Paola Arlotta, *Harvard U.*
Johan Auwerx, *EPFL*
David Awschalom, *U. of Chicago*
Clare Baker, *University of Cambridge*
Nenad Ban, *ETH Zurich*
Franz Bauer, *Pontificia Universidad Católica de Chile*
Ray H. Baughman, *U. of Texas, Dallas*
David Baum, *U. of Wisconsin*
Carlo Beenakker, *Leiden U.*
Kamran Behnia, *ESPCI-ParisTech*
Yasmine Belkaid, *NIAID, NIH*
Philip Benfey, *Duke U.*
May Berenbaum, *U. of Illinois*
Gabriele Bergers, *U. of California, San Francisco*
Bradley Bernstein, *Massachusettes General Hospital*
Peer Bork, *EMBL*
Bernard Bourdon, *Ecole Normale Supérieure de Lyon*
Chris Bowler, *École Normale Supérieure*
Ian Boyd, *U. of St. Andrews*
Emily Brodsky, *U. of California, Santa Cruz*
Ron Brookmeyer, *U. of California Los Angeles* **(S)**
Christian Büchel, *U. Hamburg-Eppendorf*
Joseph A. Burns, *Cornell U.*
Carter Tribley Butts, *U. of California, Irvine*
Gyorgy Buzsaki, *New York U. School of Medicine*
Blanche Capel, *Duke U.*
Mats Carlsson, *U. of Oslo*
Ib Chorkendorff, *U. of Denmark*
David Clapham, *Children's Hospital Boston*
Joel Cohen, *Rockefeller U., Columbia U.*
James J. Collins, *MIT*
Robert Cook-Deegan, *Duke U.*
Lisa Coussens, *Oregon Health & Science U.*
Alan Cowman, *Walter & Eliza Hall Inst.*
Robert H. Crabtree, *Yale U.*
Roberta Croce, *Vrije Universiteit*
Janet Currie, *Princeton U.*
Jeff L. Dangl, *U. of North Carolina*
Tom Daniel, *U. of Washington*
Frans de Waal, *Emory U.*
Stanislas Dehaene, *Collège de France*
Robert Desimone, *MIT*
Claude Desplan, *New York U.*
Dennis Discher, *U. of Pennsylvania*
Gerald W. Dorn II, *Washington U. School of Medicine*
Jennifer A. Doudna, *U. of California, Berkeley*
Bruce Dunn, *U. of California, Los Angeles*
William Dunphy, *Caltech*
Christopher Dye, *WHO*
Todd Ehlers, *U. of Tuebingen*
David Ehrhardt, *Carnegie Inst. of Washington*
Tim Elston, *U. of North Carolina at Chapel Hill*
Jennifer Elisseeff, *Johns Hopkins U.*
Gerhard Ertl, *Fritz-Haber-Institut, Berlin*
Barry Everitt, *U. of Cambridge*
Ernst Fehr, *Johns Hopkins U.*
Anne C. Ferguson-Smith, *U. of Cambridge*
Michael Feuer, *The George Washington U.*
Toren Finkel, *NHLBI, NIH*
Kate Fitzgerald, *U. of Massachusetts*
Peter Fratzl, *Max-Planck Inst.*
Elaine Fuchs, *Rockefeller U.*
Daniel Geschwind, *UCLA*
Karl-Heinz Glassmeier, *TU Braunschweig*
Ramon Gonzalez, *Rice U.*
Elizabeth Grove, *U. of Chicago*
Nicolas Gruber, *ETH Zurich*
Kip Guy, *St. Jude's Children's Research Hospital*
Taekjip Ha, *U. of Illinois at Urbana-Champaign*
Wolf-Dietrich Hardt, *ETH Zurich*
Christian Haass, *Ludwig Maximilians U.*
Sharon Hammes-Schiffer, *U. of Illinois at Urbana–Champaign*
Michael Hasselmo, *Boston U.*
Martin Heimann, *Max-Planck Inst. Jena*
Yka Helariutta, *U. of Cambridge*
James A. Hendler, *Rensselaer Polytechnic Inst.*
Janet G. Hering, *Swiss Fed. Inst. of Aquatic Science & Technology*
Kai-Uwe Hinrichs, *U. of Bremen*
David Hodell, *U. of Cambridge*
Lora Hooper, *UT Southwestern Medical Ctr. at Dallas*
Tamas Horvath, *Yale University*
Raymond Huey, *U. of Washington*
Fred Hughson, *Princeton U.*
Auke Ijspeert, *EPFL Lausanne*
Stephen Jackson, *USGS and U. of Arizona*
Steven Jacobsen, *U. of California, Los Angeles*
Seema Jayachandra, *Northwestern U.*
Kai Johnsson, *EPFL Lausanne*
Peter Jonas, *Inst. of Science & Technology (IST) Austria*
Matt Kaeberlein, *U. of Washington*
William Kaelin Jr., *Dana-Farber Cancer Inst.*
Daniel Kahne, *Harvard U.*
Daniel Kammen, *U. of California, Berkeley*
Abby Kavner, *U. of California, Los Angeles*
Hitoshi Kawakatsu, *U. of Tokyo*
Masashi Kawasaki, *U. of Tokyo*
V. Narry Kim, *Seoul National U.*
Robert Kingston, *Harvard Medical School*
Etienne Koechlin, *Ecole Normale Suprieure*
Alexander Kolodkin, *Johns Hopkins U.*
Thomas Langer, *U. of Cologne*
Mitchell A. Lazar, *U. of Pennsylvania*
David Lazer, *Harvard U.*
Thomas Lecuit, *IBDM*
Virginia Lee, *U. of Pennsylvania*
Stanley Lemon, *U. of North Carolina at Chapel Hill*
Ottoline Leyser, *Cambridge U.*
Wendell Lim, *U.C. San Francisco*
Marcia C. Linn, *U. of California, Berkeley*
Jianguo Liu, *Michigan State U.*
Luis Liz-Marzan, *CIC biomaGUNE*
Jonathan Losos, *Harvard U.*
Ke Lu, *Chinese Acad. of Sciences*
Christian Lüscher, *U. of Geneva*
Laura Machesky, *CRUK Beatson Inst. for Cancer Research*
Anne Magurran, *U. of St. Andrews*
Oscar Marin, *CSIC & U. Miguel Hernández*
Charles Marshall, *U. of California, Berkeley*
C. Robertson McClung, *Dartmouth College*
Rodrigo Medellin, *U. of Mexico*
Graham Medley, *U. of Warwick*
Tom Misteli, *NCI*
Yasushi Miyashita, *U. of Tokyo*
Mary Ann Moran, *U. of Georgia*
Richard Morris, *U. of Edinburgh*
Alison Motsinger-Reif, *NC State U.* **(S)**
Thomas Murray, *The Hastings Center*
Daniel Neumark, *U. of California, Berkeley*
Kitty Nijmeijer, *U. of Twente*
Helga Nowotny, *European Research Advisory Board*
Ben Olken, *MIT*
Rachel O'Reilly, *Warwick U.*
Joe Orenstein, *U. of California Berkeley & Lawrence Berkeley National Lab*
Harry Orr, *U. of Minnesota*
Pilar Ossorio, *U. of Wisconsin*
Andrew Oswald, *U. of Warwick*
Isabella Pagano, *Istituto Nazionale di Astrofisica*
Margaret Palmer, *U. of Maryland*
Steve Palumbi, *Stanford U.*
Jane Parker, *Max-Planck Inst. of Plant Breeding Research*
Giovanni Parmigiani, *Dana-Farber Cancer Inst.* **(S)**
John H. J. Petrini, *Memorial Sloan-Kettering Cancer Center*
Samuel Pfaff, *Salk Institute for Biological Studies*
Joshua Plotkin, *U. of Pennsylvania*
Albert Polman, *FOM Institute AMOLF*
Philippe Poulin, *CNRS*
Jonathan Pritchard, *Stanford U.*
Wim van der Putten, *Netherlands Institute of Ecology*
David Randall, *Colorado State U.*
Felix Rey, *Institut Pasteur*
Trevor Robbins, *U. of Cambridge*
Jim Roberts, *Fred Hutchinson Cancer Research Ctr.*
Amy Rosenzweig, *Northwestern University*
Mike Ryan, *U. of Texas, Austin*
Mitinori Saitou, *Kyoto U.*
Shimon Sakaguchi, *Kyoto U.*
Miquel Salmeron, *Lawrence Berkeley National Lab*
Jürgen Sandkühler, *Medical U. of Vienna*
Alexander Schier, *Harvard U.*
Vladimir Shalaev, *Purdue U.*
Robert Siliciano, *Johns Hopkins School of Medicine*
Denis Simon, *Arizona State U.*
Uri Simonsohn, *U. of Pennsylvania*
Alison Smith, *John Innes Centre*
Richard Smith, *U. of North Carolina* **(S)**
John Speakman, *U. of Aberdeen*
Allan C. Spradling, *Carnegie Institution of Washington*
Jonathan Sprent, *Garvan Inst. of Medical Research*
Eric Steig, *U. of Washington*
Paula Stephan, *Georgia State U. and National Bureau of Economic Research*
Molly Stevens, *Imperial College London*
V. S. Subrahmanian, *U. of Maryland*
Ira Tabas, *Columbia U.*
Sarah Teichmann, *Cambridge U.*
John Thomas, *North Carolina State U.*
Shubha Tole, *Tata Institute of Fundamental Research*
Christopher Tyler-Smith, *The Wellcome Trust Sanger Inst.*
Herbert Virgin, *Washington U.*
Bert Vogelstein, *Johns Hopkins U.*
David Wallach, *Weizmann Inst. of Science*
Ian Walmsley, *U. of Oxford*
Jane-Ling Wang, *U. of California, Davis* **(S)**
David Waxman, *Fudan U.*
Jonathan Weissman, *U. of California, San Francisco*
Chris Wikle, *U. of Missouri* **(S)**
Ian A. Wilson, *The Scripps Res. Inst.* **(S)**
Timothy D. Wilson, *U. of Virginia*
Rosemary Wyse, *Johns Hopkins U.*
Jan Zaanen, *Leiden U.*
Kenneth Zaret, *U. of Pennsylvania School of Medicine*
Jonathan Zehr, *U. of California, Santa Cruz*
Len Zon, *Children's Hospital Boston*
Maria Zuber, *MIT*

BOOK REVIEW BOARD
David Bloom, *Harvard U.*, **Samuel Bowring,** *MIT,* **Angela Creager,** *Princeton U.,*
Richard Shweder, *U. of Chicago,* **Ed Wasserman,** *DuPont*

Published by AAAS

EDITORIAL

The boldness of philanthropists

Last week, Priscilla Chan and Mark Zuckerberg announced their new philanthropic initiative with the goal of "curing, preventing, and managing all diseases by the end of the century." This may raise some eyebrows, but this effort—part of the $45 billion Chan Zuckerberg Initiative—joins forces with other philanthropists to push the envelope and support audacious ideas, with long-term commitments, to solve some of our greatest challenges.

Philanthropists have long supported academic science, from endowing faculty positions to establishing new research centers. During the 20th century, their financing complemented the steady federal support that U.S. research and development (R&D) enjoyed, particularly in basic science. Regrettably, such government funding turned stagnant in the 21st century. Federal support of R&D at higher education institutions has fallen over 11% since 2011, the longest multiyear decline in federal funding for academic R&D since data collection began in 1972. What does this mean for achieving breakthrough discoveries in science?

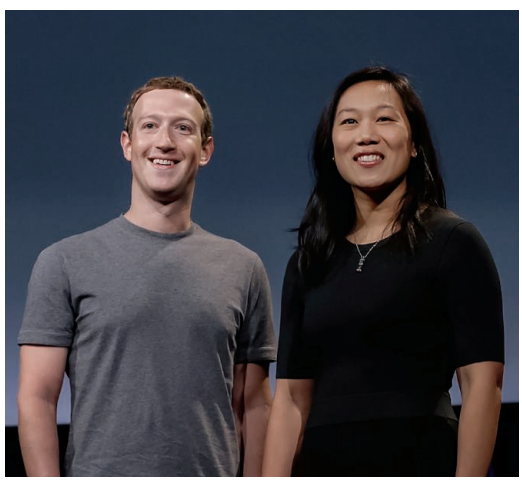

"...philanthropists...push the envelope...to solve some of our greatest challenges."

To solve some of our greatest societal problems, we not only need to focus on basic science research—we also need sufficient resources and new approaches. Basic research allows innovative thinkers in science and engineering to work toward ambitious and important goals, including in biomedicine. This was certainly the case in cancer research, where substantial progress was made once scientists had gained sufficient understanding of gene structure and function to support translational thinking and convert basic findings into cures. However, without adequate resources, great visions cannot be fulfilled. Although private funding cannot match the scale of government funding (the U.S. National Institutes of Health alone is allocated $30 billion per year), it can help fill gaps. Most importantly, it can initiate research thrusts into unproven directions, which generally do not draw government funding.

New approaches are also required. Chan and Zuckerberg will direct their first science-focused investment to establish a "Biohub" that marries engineering and life sciences research from multiple institutions. Based in San Francisco's Mission Bay, this hub will draw on the talented scientists and engineers from the University of California at Berkeley and at San Francisco, and Stanford University. Its proximity to the technologists of Silicon Valley is an asset as well. Future scientific advances likely will be at the interface of different disciplines—a "convergence" that requires breaking down barriers between fields. This is exactly what Biohub is planning. Such cross-disciplinary, open, and collaborative research also has been envisioned by other philanthropists, including Eli and Edythe Broad when the Broad Institute was organized in 2004.

In 2012, the Science Philanthropy Alliance was launched (for which I am an advisor) to shepherd private giving for basic research. Drawing on the expertise of foundations, philanthropists, and scientists across fields of basic research, the Alliance helps philanthropists make forays into supporting creative basic research. Indeed, Chan and Zuckerberg spoke with a wide range of scientists (including me) and philanthropists from around the world, through the Alliance network, to better understand where their intervention could make important things happen that otherwise would languish. They have dared to think big, and I encourage philanthropists to engage with the scientific community for advice.

This year has already seen billions of philanthropic dollars go to science, including from Paul Allen to support bioscience, Sean Parker to advance cancer immunotherapy research, Sandy and Joan Weill for brain research, and Yuri Milner for the study of our universe. These dollars will play an important role in scientific progress. Big-profile gifts raise concerns for some, such as downplaying the need to increase federal dollars for basic research. But these gifts are certainly broadcasting a common message—philanthropists recognize that a long view of progress is worth investing in.

–David Baltimore

David Baltimore is a Nobel Prize winner (1975, Physiology or Medicine), president emeritus of and professor at the California Institute of Technology, a member of the Board of Directors of the Broad Institute, and a consultant for the Science Philanthropy Alliance.
Email: baltimo@caltech.edu

Published online 21 September 2016; 10.1126/science.aak9610

PHOTOS: (INSET) AP PHOTO/JEFF CHIU. FILE; (TOP RIGHT) BOB PAZ

Downloaded from http://science.sciencemag.org/ on October 7, 2016

Published by AAAS

> “If this is always going to be a zoo animal, then stop. The goals have to be … ecological restoration and function.”
>
> **Ecologist Ben Novak** of Revive & Restore in San Francisco, California, on “reviving” extinct species; he says good candidates have a unique ecosystem role, like the forest-altering passenger pigeon. **http://bit.ly/deextinction**

IN BRIEF

A view of the Arctic in high relief

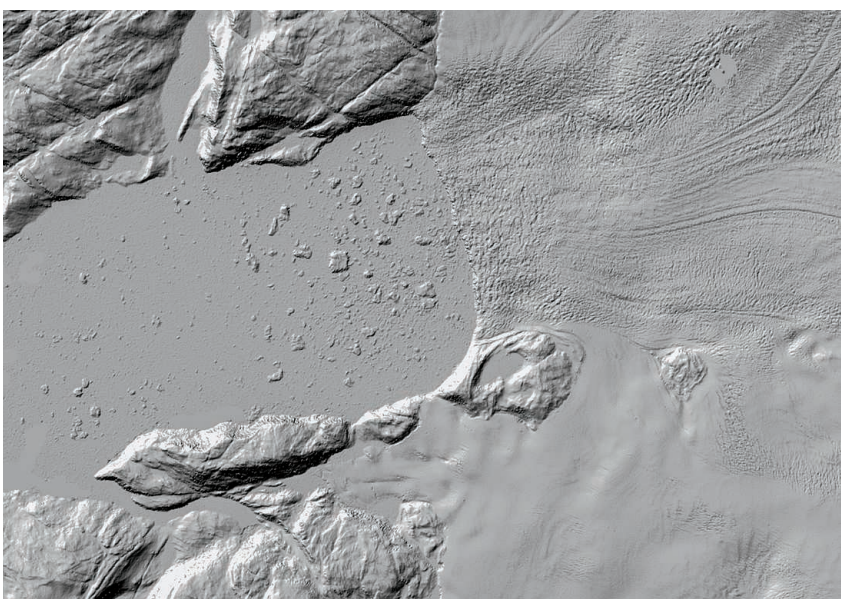

The thawing surface of the Arctic is coming into finer focus. On 29 September, U.S. officials released new high-resolution digital elevation models (DEMs) for 94% of the Arctic. The maps can help track thawing glaciers, count sinkholes in thawing permafrost, and calculate the release of carbon from clear-cut forests. Here, a DEM with an 8-meter resolution shows western Greenland’s Illullip Glacier as it plunges into the ocean. The project relies on stereo satellite images; combined, they create a DEM that is vertically accurate within 50 centimeters. Even higher 2-meter-resolution models for Alaska and parts of Russia have now been released, and models for the rest of the Arctic at that resolution should be finished by next year, says Paul Morin, who leads the ArcticDEM project at the Polar Geospatial Center at the University of Minnesota, Twin Cities. The maps were released at a meeting of science ministers and other high-level officials held this week in Washington, D.C., part of a White House effort to advance international science collaboration in the Arctic. Airborne LIDAR (light detection and ranging), a radarlike approach that uses lasers, has mapped smaller areas in fine detail—but those efforts are expensive and spotty. Next up, Morin says, is a new DEM for Antarctica.

PHOTO: PAUL MORIN, POLAR GEOSPATIAL CENTER

AROUND THE WORLD

China’s space clock is ticking

JIUQUAN SATELLITE LAUNCH CENTER, IN CHINA | China’s Cold Atom Clock in Space (CACS) experiment, the first of its kind in orbit, was confirmed to be operating smoothly last week after being launched aboard the Tiangong-2 space station on 15 September. Freed from gravitational effects, the CACS promises to be more accurate than its Earth-bound counterparts, expected to lose only a second over 30 million years. To keep time, the clock counts signals emitted by the supercooled rubidium atoms as they oscillate between energy states. Such clocks might find applications in navigation systems and measuring fundamental constants such as the gravitational redshift. The CACS is one of 14 scientific instruments aboard Tiangong-2 and an example of how “space science experiments have been becoming more and more important,” says Liu Liang, a physicist at the Chinese Academy of Sciences’s Shanghai Institute of Optics and Fine Mechanics who led the work on the clock. Tiangong-2 is a step toward China’s goal of a permanent orbiting space station.

U.N. declares war on superbugs

NEW YORK CITY | The United Nations General Assembly last week unanimously approved a political declaration committing nations to a more active battle against the growing global threat of microbial resistance to existing drugs. “Antimicrobial resistance is a global crisis—a slow motion tsunami,” Margaret Chan, director-general of the World Health Organization (WHO) in Geneva, Switzerland, told the assembly. The document, which pledges nations to follow a blueprint laid out last year by WHO, calls for sustained research and development on new antimicrobials and diagnostics, and for incentives to attract pharmaceutical company investment. It also calls for appropriate use of existing medicines and vaccines in humans, animals, and agriculture. Misuse of once-effective drugs has led to rapidly evolving resistance in many microbial species; for example, WHO estimates that in 2014, 480,000 people developed

Downloaded from http://science.sciencemag.org/ on October 7, 2016

Published by AAAS

Thomas Thwaites's commitment to living as a goat earned him an Ig Nobel Prize.

Ig Nobels honor goat man, mirror scratching

London technologist Thomas Thwaites wanted a break from being human. So, after designing custom prosthetic limbs and undergoing intense physical training, he lived like a goat in the Swiss Alps for a few days, chewing grass and just trying to fit in with the herd. It's crucial to have friends in the goats' intensely hierarchical world, Thwaites says; luckily, he adds, he found a goat "buddy." And last week, at a ceremony at Harvard University, his hard work also earned him an Ig Nobel Prize in biology. He shared the prize with Oxford, U.K.–based ethicist and veterinarian Charles Foster, who, independently, lived for days at a time as a badger to better understand the nonhuman "worldview." In fact, many of the winning studies in this 26th year of the Ig Nobel contest—which celebrates scientific studies that "make you laugh, and then think"—focused on perception and deception, from surveys asking liars how often they lie (and pondering whether to believe their answers) to studies of itch relief via scratching the wrong arm in a mirror. Each Ig Nobel winner received a $10 trillion prize—a Zimbabwean banknote with little value as a result of hyperinflation.

multidrug-resistant tuberculosis (TB), linked to incorrect use of TB therapies and to poor quality medicines.

Human embryo DNA edited

STOCKHOLM | As the ethics of gene editing in human embryos continues to spark intense debate, Swedish developmental biologist Fredrik Lanner of the Karolinska Institute in Stockholm is now the first researcher to begin trying to edit healthy human embryos, NPR reported last week. (Chinese scientists in April reported using gene editing on flawed embryos not viable for fertility treatments.) Using the gene-editing technology CRISPR-Cas9, Lanner aims to deactivate genes in the embryos to see what roles they play in early development, and to find new treatments for infertility and miscarriage. U.K. scientists were given the go-ahead for similar research in February. Many researchers worry that gene editing will lead to "designer babies" and new hereditary diseases, but Lanner has defended his efforts, saying that basic research like his is necessary to avoid those situations.

A human embryo at the eight-cell stage, very early in its development.

Experimental reactor's end nigh?

TOKYO | Japan may finally pull the plug on Monju, an experimental reactor plagued by accidents, cover-ups, cost overruns, and other problems that have kept it idle for all but a few months since it came online in 1994. On 21 September, Japanese media reported that the nation's cabinet had decided to set up a committee to explore decommissioning Monju. A "breeder" reactor, it was intended to burn plutonium that had accumulated in the spent fuel of conventional reactors; the plutonium would be blended with natural or reprocessed uranium to ultimately produce more fissile fuel that it consumed. But in December 1994, just months after achieving a self-sustained nuclear reaction, it suffered a massive coolant leak and resultant fire. Continuing accidents and safety issues have kept it mostly offline ever since, and Japan's utilities and citizens' groups have long since soured on the project. However, a final decision won't be reached until the end of this year. **http://bit.ly/Monju**

FINDINGS

U.S. off track for climate goal

Nearly a year after the Paris climate change summit, the United States must close a significant gap to meet the commitments it made to cut greenhouse gases, according to a new analysis in *Nature Climate Change* this week. Even if the United States implements all current and proposed policies, it would miss a 2025 target by as much as 1.5 billion metric tons of carbon dioxide per year—roughly 20% of the nation's total emissions. The 2025 pledge is to cut greenhouse gas emissions by 26% to 28% below 2005 levels—down to between 4.5 billion and 5.5 billion metric tons. The study, by scientists at the federal Lawrence Berkeley National Laboratory in Berkeley, California, found that the United States would only reach the goal in the most optimistic scenario: if the Obama administration's power plant regulations survive a current

PHOTOS: (TOP TO BOTTOM) TIM BOWDITCH; YORGOS NIKAS/SCIENCE SOURCE

Downloaded from http://science.sciencemag.org/ on October 7, 2016

Published by AAAS

court challenge; if policymakers take additional steps, including more electricity regulations and stopping methane leaks from oil and gas drilling; and if all of those measures produce the biggest emission reductions possible. http://bit.ly/ClimateGoal

NEWSMAKERS

Head of fusion lab exits

Stewart Prager has stepped down as director of the Princeton Plasma Physics Laboratory (PPPL) in New Jersey, after a malfunction this summer knocked the lab's main facility out of action, perhaps for a year. PPPL physicists aim to study the fusion of deuterium nuclei trapped in magnetic fields within the lab's National Spherical Torus Experiment, which had undergone a $94 million upgrade from 2012 until last year. However, in August a magnetic coil failed, rendering the machine inoperable. Researchers are working to figure out what happened and redesign the machine, says PPPL spokesperson Larry Bernard. Prager said in a statement that after 8 years as director he was already thinking of stepping down. "It is best for new, continuing leadership to shepherd the rebuilding of the facility and the engineering changes that will be needed over the next year," Prager says. PPPL's Terry Brog will serve as acting director until a new director is chosen.

Three Qs

Facebook Co-Founder Mark Zuckerberg and his wife, pediatrician Priscilla Chan, plan to devote $3 billion over 10 years to bring together scientists and engineers "to help cure, prevent, or manage all diseases by the end of the century" (*Science*, 23 September, p. 1346). The Chan Zuckerberg Initiative's science venture will be led by neurobiologist **Cornelia Bargmann** of The Rockefeller University in New York City, who was also co-chair of the advisory group to the federal government's Brain Research through Advancing Innovative Neurotechnologies (BRAIN) Initiative. http://bit.ly/BargmannQA

Q: Why did you want to leave full-time research for this job?
A: This initiative is a spectacular opportunity to do something unique and forward looking and effective for science. When something like that comes your way, you just have to say yes.

Q: Did working on the BRAIN Initiative get you interested in leading a big science project?
A: I've seen that you can work with scientists from different backgrounds and sensibilities and come up with something better than anyone can do alone. I think that prepared me ... for what it would take to do something like this.

Q: The goal of curing or managing all diseases by 2100 is ambitious. Is it doable?
A: Do you know how much medicine has advanced in the past 80 years? Even in our lifetime, in terms of heart disease and cancer and AIDS. Why should that stop now? Part of the genius of this [initiative] is that long-term time frame. There are a lot of problems that will take decades. But if you know they're important, you keep working on them.

Fertility specialist John Zhang holds the newborn baby (face blurred for privacy).

PHOTO: NEW HOPE FERTILITY CENTER

New method makes 'three-parent' baby

Five months ago, a little boy was born with cells containing DNA from three parents—the first baby to be created through a new genetic technique in order to avoid mitochondrial disease, *New Scientist* revealed this week. The method aims to prevent a rare class of conditions in which the DNA of the mother's mitochondria, the energy-generating organelles in all human cells including eggs, is defective. Inheriting such mutations can produce life-threatening disease in the baby. The new method, previously tried on monkeys, was performed in Mexico by New York City fertility specialist John Zhang and his colleagues; U.S. officials haven't yet given it the green light. The mother was a 36-year-old woman who had lost two children to a mitochondrial disease. By removing the DNA-containing nucleus from one of her eggs and inserting it into the nucleus-free egg of a donor, which was then fertilized with the father's sperm, researchers avoided passing along the defective mitochondrial DNA—but left the baby with three genetic parents. The baby was still healthy at 3 months, the team notes in an abstract for an October meeting. http://bit.ly/3parentbaby

Six contenders for WHO head

The World Health Organization (WHO) in Geneva, Switzerland, on 23 September unveiled the names of the six candidates vying to succeed Margaret Chan as director-general. They include: Ethiopian Minister of Foreign Affairs and former Minister of Health **Tedros Adhanom Ghebreyesus**; Italian physician and WHO Assistant Director-General for Family, Women's and Children's Health **Flavia Bustreo**; French cardiologist and former Minister of Health **Philippe Douste-Blazy**; U.K. physician **David Nabarro**, who is leading the United Nations's response to the Haiti cholera outbreak; Pakistani cardiologist and former science and technology minister **Sania Nishtar**; and Hungarian physician and former health minister **Miklós Szócska**. The elections, which will be held in May 2017, come at a critical point for WHO, which was widely criticized for its slow response to the Ebola outbreak in West Africa and is in the middle of implementing reforms. http://bit.ly/WHOhead

Downloaded from http://science.sciencemag.org/ on October 7, 2016

Published by AAAS

way, NASA asked the DSN to cut its budget by $100 million over 7 years. In late 2015, the DSN was asked to find further cuts. "If you look at NASA's budget for the DSN it tends to go down in time, rather than up," said Leslie Deutsch, deputy director of JPL's interplanetary network directorate, in an August presentation to a NASA working group.

These cuts do not hit day-to-day operations, Vrotsos says. "Our first, second, and third job is to return all the science data possible." But they have delayed the start of new antennas and transmitters in Madrid and California, and they could complicate repairs to cracking, degraded concrete in the pedestals of two Madrid dishes. Last year, a report from NASA's Office of Inspector General warned that these postponements could jeopardize the network's reliability, especially for older missions, like Voyager 1 and 2, that depend on congested radio bands only supported by some of the network's older dishes.

If there's hope for further investment in deep-space communication, it might be international: In 2013, the European Space Agency (ESA) finished its own 120° network of 35-meter antennas in Spain, Australia, and Argentina, which now communicates with ESA missions like Rosetta, Gaia, and Mars Express, and also backs up the NASA network. India and Japan have individual antennas to communicate with their missions, and NASA has been in talks with South Korea and the United Arab Emirates as potential DSN partners.

Further on, JPL plans to save money by operating the antennas remotely rather than staffing each location continuously. It also plans to move to an internet-inspired scheme for transmitting data packets that is more tolerant of faults.

Meanwhile, NASA has begun testing laser-based systems as possible successors to radio transmissions. Optical signals, with wavelengths 10,000 times shorter than radio waves, allow far higher rates of data transmission and aren't subject to interference from Earth's cacophonous radio bands. As a result, the transmitters can be small, light, and energy efficient. (However, clouds can easily block the signals, which means that low-Earth-orbit relay satellites may be needed for an "interplanetary internet.")

For now, scientists want to be certain the DSN has the support it needs to stay in the background, says Clive Neal, a lunar scientist at the University of Notre Dame in South Bend, Indiana. "It's worked so well for so many years that people do take it for granted," he says. "Are proper investments being made so we can continue to?" ■

PHYSICS

Will Nobel Prize overlook LIGO's master builder?

Barry Barish assembled the gravitational wave detectors but hasn't shared the glory

By **Adrian Cho**

Next week, the 2016 Nobel Prize in Physics will be announced, and many scientists expect it to honor the detection of ripples in space called gravitational waves, reported in February. If other prizes are a guide, the Nobel will go to the troika of physicists who 32 years ago conceived of LIGO, the duo of giant detectors responsible for the discovery: Rainer Weiss of the Massachusetts Institute of Technology (MIT) in Cambridge, and Ronald Drever and Kip Thorne of the California Institute of Technology (Caltech) in Pasadena. But some influential physicists, including previous Nobel laureates, say the prize, which can be split three ways at most, should include somebody else: Barry Barish.

Barish, a particle physicist at Caltech, didn't invent LIGO, the Laser Interferometer Gravitational-Wave Observatory. But he made it happen. The hardware at LIGO's two observatories in Hanford, Washington, and Livingston, Louisiana; the structure of the collaboration; even the big-science character of gravitational wave research—all were molded by Barish, who is now 80. "Without him there would have been no discovery," says Sheldon Glashow, a Nobel Prize–winning theorist at Boston University, who has written to some members of the Nobel Committee arguing the case for Barish. "It would be an enormous injustice" if he didn't share in the Nobel, Glashow says.

When Barish took over as the second director of LIGO in 1994, he inherited a project that was "dead in the water," says Richard Isaacson, the National Science Foundation's (NSF's) program director for gravitational physics from 1973 to 2002. LIGO had hatched a decade earlier, when NSF began funding Weiss and Drever to marry their work on using interferometers—L-shaped

PHOTO: MAXIMILIEN BRICE/CERN

assemblages of lasers and mirrors—to detect the stretching of space set off by, say, two massive black holes spiraling together. But with Weiss, Drever, and Thorne, a theorist, tripping over one another, the project remained larval. By 1987, NSF wanted a single director for the project, and Caltech appointed Rochus "Robbie" Vogt.

Decisive but volatile, Vogt pulled the team together to write a coherent proposal for twin interferometers with 4-kilometer-long arms. He won crucial support in Washington, D.C., says Stanley Whitcomb, a LIGO physicist at Caltech. "Robbie was very effective in conveying to members of Congress the excitement of LIGO's science," he says. In 1990, the National Science Board (NSB), which sets policy for NSF, approved construction of the observatory, priced at $250 million—the biggest thing NSF had ever attempted.

But Vogt disdained bureaucratic oversight and vexed NSF officials. He kept the LIGO team unworkably small and refused to supply a detailed work plan or document researchers' progress, Isaacson says. Things got so bad that in 1993 NSF asked Congress to hold back $43 million that the agency had requested for LIGO the following year. By the end of the year, Caltech eased Vogt out of leadership.

Barish brought swift and sweeping changes. Lanky, soft-spoken, and even-tempered, he was born in Omaha, Nebraska, and raised in Los Angeles, California, where he attended public schools. He already had experience with big collaborations, having worked in a group of 140 physicists search-

Downloaded from http://science.sciencemag.org/ on October 7, 2016

Published by AAAS

In February, Barry Barish presented LIGO's discovery to physicists, while other leaders spoke to the press.

ing for particles called magnetic monopoles at Italy's underground Gran Sasso National Laboratory. He had also worked on the biggest of big-science projects, the $10 billion Superconducting Super Collider in Waxahachie, Texas, which Congress canceled mid-construction in 1993.

First off, Barish reorganized LIGO management, expanding the team and delegating authority. Within months, he developed the detailed work plan that NSF wanted. Whereas Vogt stressed unfettered innovation, Barish likened LIGO to building a bridge—one that would be very long, complicated, and expensive. He revised the project to improve infrastructure, such as the vacuum chambers that hold the interferometers. He also established permanent scientific staff at the two LIGO outposts and a steady R&D program for future upgrades. These changes required a budget boost to $292 million, Isaacson says, which NSB approved.

Barish and his deputy, Caltech's Gary Sanders, also shook up the culture of the collaboration. Caltech physicists had a prototype interferometer and relied on experienced individuals to restart it daily. Barish and Sanders prodded them to run it steadily 24 hours a day and to study it methodically, eliminating what Sanders calls the "guru mentality." The factorylike approach galled many of LIGO's leading lights, who felt devalued and quit.

Meanwhile, Barish expanded LIGO beyond the bounds of Caltech and MIT. In 1997, he brought in new expertise by establishing the independent LIGO Scientific Collaboration (LSC), the group of external scientists who would use LIGO. "I don't think we would have made the discovery in the time we did without that massive accumulation of intellect," says David Berley, NSF's project manager for LIGO from 1992 to 2000. Sanders says the decision to create LSC was initially unpopular among physicists who feared that big science was taking over their field. (It was.)

Key technical aspects of the LIGO interferometers reflect Barish's touch, too. He decided to change the lasers that pump light into the instruments from ones that squeeze light from argon gas to more powerful and reliable solid-state lasers, then just coming to market. He also pushed to switch from analog to digital controls.

> ***"Without him there would have been no discovery."***
>
> **Sheldon Glashow**, Boston University

Construction of LIGO finished in 1999, and it began taking data 3 years later. Barish stepped down in 2005 to head up design of the International Linear Collider, a proposed 30-kilometer, straight-shot accelerator that some particle physicists say is the future of their field. But before giving up the reins, he ushered through plans for a crucial upgrade to the interferometers that ensured LIGO's almost immediate success in detecting gravitational waves when the machines turned on a year ago. LIGO collaborators say Barish set a high standard for fairness and integrity. "I always felt appreciated and respected by him," says Gabriela González of Louisiana State University, Baton Rouge, spokesperson for the 1100-member LSC.

Ironically, Barish recently tarnished his own sterling reputation. In May, at a meeting in Pittsburgh, Pennsylvania, he began an after-dinner talk with a slide showing a man writing on a woman's bare back and, next to her, a stage prop in the form of a cartoonish racial caricature. The incident ignited a Twitterstorm, and in a statement LSC disavowed the image as "inherently very offensive." Barish says he found the photograph, from an early 20th century Broadway playbill, on the internet and was trying to make a play on the term "back story." He says he hadn't noticed the sexist and racist content. "I made a mistake, I should have been more careful," he says.

Barish apologized to the entire LIGO collaboration by email. But Elizabeth Simmons, a theorist from Michigan State University in East Lansing, says she questioned Barish about the image at the dinner and that he dismissed her objection, saying, "This [slide] is not my talk." Tova Holmes, a graduate student at the University of California, Berkeley, who also attended the dinner, says, "Anybody who had ever thought about what it is like not to be a white man in physics would never have chosen that image."

Other prizes suggest Barish is a long shot for the Nobel. Several awards have already honored LIGO's discovery, including the Gruber Cosmology Prize, the Kavli Prize in Astrophysics, the Shaw Prize in Astronomy, and the Special Breakthrough Prize in Fundamental Physics. All lauded Weiss, Drever, and Thorne, but not Barish.

The situation highlights a problem for prizes: They favor ideas over execution. "There isn't a way to recognize good management," González says. Whitcomb says that the U.S. National Medal of Science, honoring science in service to the nation, would be "well, well deserved" for Barish.

Of the Nobel, Barish says, "I think there's a bit of truth that LIGO wouldn't be here if I didn't do it, so I don't think I'm undeserving." He's hoping that the Nobel Committee takes the time to learn LIGO's history. "If they wait a year and give it to these three guys, at least I'll feel that they thought about it," he says. "If they decide [to give it to them] this October, I'll have more bad feelings because they won't have done their homework." ■

Downloaded from http://science.sciencemag.org/ on October 7, 2016

Published by AAAS

ENVIRONMENTAL POLICY

Canada aims to rewrite environmental law

Scientists urge Trudeau government to adopt stronger rules for project reviews

By **Lesley Evans Ogden**

After Canadian officials approved construction of a massive dam on British Columbia's Peace River in 2014, many of the nation's environmental scientists were dismayed. The dam would drown key wildlife habitat and First Nations lands, they argued, and the decision highlighted how the nation's Conservative government had weakened the rules for assessing the environmental impacts of projects such as mines, dams, and pipelines. The 2012 rewrite of the Canadian Environmental Assessment Act (CEAA) had cut the number of reviews from thousands to a handful, reduced input from independent experts and the public, and shifted some oversight from national to provincial officials. To researchers, the changes snubbed science in the name of promoting economic growth.

Now, under new Liberal Prime Minister Justin Trudeau, researchers are getting a chance to help rewrite the rules again. This month, an expert panel appointed by Trudeau's government launched a 3-month-long, nationwide listening tour to collect ideas for revising the CEAA. Its goal is to issue recommendations on how Trudeau can fulfill his promises to "restore confidence" in Canada's environmental reviews and "ensure that decisions on major projects are based on science, facts, and evidence."

The effort—part of Trudeau's broader push to revamp Canada's environmental policies—is likely to fuel fierce debate. Industry groups say they welcome the discussion, but some have signaled that they see little need for major reforms. In contrast, calls for wholesale change are coming from some scientists and First Nations groups, which argue they have too little voice in decisions affecting their livelihoods. "We need to re-engineer environmental assessment from the ground floor up," says Chris Tollefson, a law professor at the University of Victoria in Canada and executive director of the Pacific Centre for Environmental Law and Litigation. But that "is not going to be an easy thing to do," he predicts.

Academic researchers who have joined the fray say one of their major goals is to increase the transparency of data used in assessing projects. Now, companies seeking permits for proposed projects hire consultants to collect many of the data required by government regulators. But that material is often inaccessible to the public, native governments, and independent scientists, notes ecologist Jon Moore of Simon Fraser University, Burnaby, in Canada. Such secrecy has "undesirable consequences," Moore argued in comments filed earlier this year on issues the government should consider in its CEAA review. It is "financially inefficient; each project must be assessed without fully benefiting from previous environmental assessments." It also "does not contribute to scientific progress in Canada," because outside researchers can't draw on the data. And it obscures how decisions were reached. "Science and evidence can be torqued," Moore concluded, "when it is under such strong conflicts of interest."

Such issues highlight the "need to figure out a way, within the [environmental assessment] process, to fund and support truly independent science," wrote Tollefson, who also submitted comments. But he noted that budget cuts at federal agencies that are supposed to provide expertise for assessments mean other groups—including conservation and First Nations groups—may have to find ways to fill the information gaps.

Critics say Canada's environmental assessment law, which was rewritten in 2012, doesn't provide for proper oversight of major projects such as oil sands mines.

PHOTO: BEN NELMS/BLOOMBERG VIA GETTY IMAGES

Industry groups have downplayed concerns about transparency and conflicts of interest. The "scientific requirements associated with [assessments] are comprehensive and well established," wrote Patrick McDonald, manager of oil sands at the Canadian Association for Petroleum Producers in Calgary, in comments. And he says industry hires consultants that meet "the utmost professional standards."

Researchers also want officials to put assessments in a broader context. Some, including mining officials, argue the current process does a poor job of evaluating "cumulative impacts"—how multiple mines may affect a single river, for example. And it ignores how a project may affect Canada's ability to meet commitments made under international pacts on climate, sustainable development, or biodiversity protection. Too often, says political scientist Robert Gibson of the University of Waterloo in Canada, the CEAA accepts degradation instead of encouraging improvement. "We want things to get better, so why should your … process be aiming for 'less bad'?"

Others warn against making the law so broad that regulators once again must assess thousands of projects. The government has reviewed just 14 projects under the 2012 rewrite, they note, rejecting two. "What needs to happen in this third iteration is to find a middle ground between assessing every project, versus only focusing on these big projects," argues Martin Olszynski, a law professor at the University of Calgary.

The expert panel that will weigh such arguments includes legal, aboriginal, and industry experts, but no research scientists. That is a "glaring omission," argues Alana Westwood, a Halifax-based ecologist with Evidence for Democracy, a science advocacy group in Ottawa. Researchers won't know whether their ideas have gained traction until the end of January 2017, when the panel is scheduled to present its recommendations to government officials. ■

Lesley Evans Ogden is a writer in Vancouver, Canada.

Downloaded from http://science.sciencemag.org/ on October 7, 2016

Published by AAAS

PHOTO: MINISTRY OF EDUCATION, RESEARCH AND RELIGIOUS AFFAIRS

Researchers in Greece developed a novel laser system to clean ancient sculptures. A new foundation hopes to rejuvenate the cash-starved scientific community.

SCIENCE POLICY

A lifeline for Greek science—or living on borrowed time?

New foundation will fund peer-reviewed grants, but scientists fear that it won't bail them out of crisis

By **Erik Stokstad**

When the global financial crisis hit Europe in 2008, no country's scientists were hit harder than those in Greece. Funding for stipends and salaries plummeted and talent began to flee. Now, the Greek government is trying to stop the nationwide brain drain—and perhaps reverse it. In the most visible step, this week the Greek parliament was expected to take up legislation to create the Hellenic Foundation for Research and Innovation (HFRI). Intended to cut bureaucracy and political interference as well as bolster funding, it is modeled after the German Research Foundation and the U.S. National Science Foundation. Politicians are expected to greenlight it by mid-October.

Over the next 3 years, HFRI will distribute about €225 million in peer-reviewed grants. The science ministry plans to spend €18 million of the funds immediately on graduate and postdoctoral research projects. "It's a good start," says Sotirios Harissopulos, director of the Institute of Nuclear and Particle Physics of the National Centre of Scientific Research Demokritos near Athens. "These are measures that will at least decelerate the brain drain." But although many Greek researchers welcome the new foundation, they say that much more funding is required to revitalize science in their country. "It is enough only for scientific survival," says environmental chemist Euripides Stephanou, former rector of the University of Crete, who left last year to become research vice president at The Cyprus Institute in Athalassa, Greece.

Between 2008 and 2010, total R&D spending in Greece fell 15%, and it hasn't recovered to its precrisis peak. Austerity measures imposed since 2011 forced institutes and universities to cut salaries by up to 30%. As staff left or retired, hiring freezes withered departments. At the Bioacademy, a major biomedical center in Athens, the number of graduate students and postdocs has fallen from 220 to fewer than 100 in the last year. "We're growing old as a research community," says Georgia Gregoriou, a neuroscientist at the University of Crete, Heraklion, in Greece. "This is terrible."

Total grant funding has held relatively steady thanks to the European Union's Horizon 2020 science program and the EU structural funds for regional development, 8% of which Greece gives to science. The trouble is that the ministry's calls for proposals have been sporadic, funding decisions not always transparent, and money comes with what researchers describe as rigid terms and copious paperwork. Costas Fotakis, the research minister since 2015, says he has tried to simplify rules and speed up delivery. But the latest tranche of EU funds, €1.2 billion for Greek R&D from 2014 to 2020, poses a new dilemma: EU regulations now specify that the funds must be spent mainly in poorer provinces, which is not where most researchers in Greece are located. Fotakis hopes to find a solution by next year.

HFRI won't have that geographic constraint in distributing grants, nor have to earmark money for applied science. In addition, it will regularly solicit proposals—a longstanding wish of Greek scientists. According to the draft law, universities and research centers will elect a board to oversee the foundation. "The state will not interfere in scientific choices or prioritization," Fotakis says. (Stephanou worries that the board might fall victim to academic politics, though.) The call for Ph.D. project funding will be released in the coming days, followed by a call for postdoctoral research grants, and the ministry hopes to put money in the pockets of successful applicants by January 2017.

"All of this is peanuts compared to the needs of the research sector," says Achilleas Mitsos of the University of the Aegean, Mytilíni, in Greece. Overall Greek investment in science and innovation was 0.8% of gross domestic product in 2014. The government hopes to raise that to 1%—still just half the EU average. Greece's ambitions could be undermined by the short-term nature of HFRI's funding, three-quarters of which is a loan from the European Investment Bank. Fotakis says the government plans to continue its contribution to HFRI—€20 million a year—after 2018.

In other steps, the science ministry raised the budget for government-funded research institutes by 60% for 2016, nearly to precrisis levels. It also approved 100 hires for these research centers and 500 hires for university positions for this year, and another 500 for universities next year. "Things are definitely better," says Ioannis Georgantopoulos, an x-ray astronomer at the National Observatory of Athens, who plans in the coming months to advertise new staff positions—for the first time in 6 years.

Some scientists remain skeptical that the government can truly deliver, but Nektarios Tavernarakis, director of the Institute of Molecular Biology and Biotechnology in Heraklion, says morale at his center is up. "People feel that the worst has passed, and that there are reasons to be optimistic." ■

Published by AAAS

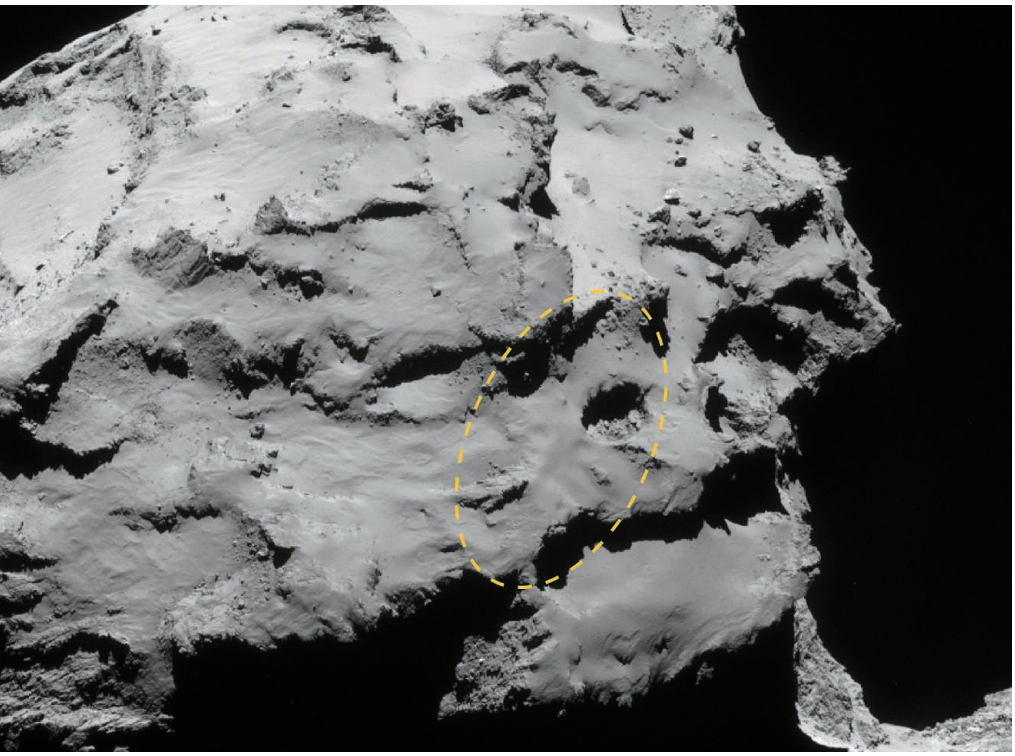

Rosetta will land near a pit containing 3-meter-sized "goosebumps." Some think they are the comet's building blocks; others say they are too big.

PLANETARY SCIENCE

Rosetta ends 2-year comet mission with final descent

Fluffy particles indicate that 67P/Churyumov-Gerasimenko was born gently from flocks of pebbles

By **Daniel Clery**

All good things must come to an end, and so it will be on 30 September when the Rosetta spacecraft makes its planned soft landing onto the surface of comet 67P/Churyumov-Gerasimenko, the culmination of 2 years of close-up studies. Solar power has waned as 67P's orbit takes it and the orbiting Rosetta farther from the sun, and so the mission team decided to go on a last data-gathering descent before the lights go out. Contact with Rosetta will almost certainly be lost after it lands, as its communication dish is unlikely to be pointed toward Earth.

This last data grab—including detailed imaging of the comet's surface—is a bonus after a mission that is already changing theorists' views about how comets and planets arose early in the solar system. Several Rosetta observations suggest that comets form not from jolting mergers of larger cometesimals, meters to kilometers across, but rather from the gentle coalescence of clouds of pebbles. And the detection of a single, feather-light, millimeter-sized particle, announced on 29 September at a European Space Agency (ESA) press briefing, should further the view of a quiet birth. It appears to be a fragile dust mote that has survived, cradled in the comet, since the birth of the solar system. "This really is the seed at the starting point of everything," says Marco Fulle, a mission scientist at the Trieste Astronomical Observatory in Italy.

As the mission winds down, Rosetta scientists are finally in a position to answer one of their earliest questions about 67P: the origin of its two-lobed "rubber duck" shape. Were two small comets glommed together at some point in the past, or is one body being eroded by the sun into a dumbbell shape? A consensus is beginning to emerge. Rosetta's camera found onionlike layers created during formation but exposed on 67P's surface by erosion. The layers are oriented differently in the two lobes, suggesting separate formation and a later meld. But the union must have been gentle, because the comet lacks areas of high-density material that would have been created by a heavyweight crunch.

Rosetta scientists are also killing off the age-old notion that comets are "dirty snowballs," mostly ice with some dust mixed in. As earlier studies of other comets had suggested, the comet "is more like an icy dirtball," says Anders Johansen, an astronomer at Lund University in Sweden who is not involved in the mission—an idea backed up by Rosetta's observation of a high ratio of dust to water vapor in the material lofted into space by the sun's heat. This "dirt" is unlike anything found on Earth, Fulle says: a low-density mineral sponge, like pumice but extremely fragile. Some 70% of its volume is made up of voids, some of which are filled with organic molecules.

On its surface, 67P looks like a miniplanet. "It has a wide variety of terrains, almost like Earth," says Eberhard Gruen, a mission scientist at the Max Planck Institute for Nuclear Physics in Heidelberg, Germany: apparently smooth plains, cliffs, and mountains. But unlike Earth, its surface is being eroded as the sun's heat turns on jets of sublimating ices, kicking up dust. Rosetta analyzed many of these particles as they launched off the surface, and most were made of compact, dense minerals that require the heat of the inner solar system to form. They probably drifted outward to cooler parts of the solar system, where they were swept up into the comet—suggesting they are not so primordial, says Alessandra Rotundi, principal investigator of Rosetta's dust-analyzing instrument at the Parthenope University of Naples in Italy.

But Rotundi's team also detected particles that entered the instrument while registering no mass. "We thought something was wrong with the instrument," she says. These "fluffy particles," also picked up by other sensors, turned out to have a density less than air on Earth. Researchers now estimate that 15% of 67P's volume is made up of fluffy particles, which are 99.95% empty space.

One of these delicate beasts found its way into an instrument that contains an atomic force microscope, capable of studying structures as small as a few nanometers. It showed that the fluffy particle has a fractal structure, like the branches of a tree or an indented coastline, with the same level of intricacy at scales both large and small, says Thurid Mannel, a scientist on the microscope instrument team at the Institute of Space Research in Graz, Austria, who presented preliminary results at the ESA briefing. The pattern is just what theorists would predict if it had been built up

PHOTO: ESA/ROSETTA/NAVCAM, CC-BY-SA IGO 3.0

Downloaded from http://science.sciencemag.org/ on October 7, 2016

Published by AAAS

gently by nanometer-sized particles sticking together in the nebula that formed the solar system, gradually growing in size as more and more particles were added. Not everyone is convinced about fluffy particles, Gruen says. "The final word is not out yet."

But if they are as ancient and delicate as they appear, their survival on 67P suggests that the comet was not exposed to high temperatures or violent impacts. This runs counter to the traditional theory of comet (and planet) formation: that particles cling together into pebbles, which form boulders, which coalesce into kilometer-scale "cometesimals"—with collisions getting more violent at each stage. That scenario already faced challenges: Whereas small particles can stick electrostatically, it's harder to explain the formation of meter-sized objects, which don't exert much gravity.

A rival theory holds that pebbles tend to gather in bunches because of aerodynamic drag in the primordial gas cloud; eventually, giant flocks of pebbles collapse under their own collective gravity to form comet-sized objects directly. Several strands of evidence suggest 67P was formed from pebbles: The size distribution of material blown off the surface shows much is centimeter-sized; radio scans of 67P's internal structure found few of the large voids expected to form around boulders; and before the short-lived Philae lander ran out of battery power it sent close-up images revealing a wealth of pebbles. "What we thought about the outer solar system may be wrong," Fulle says. "Now, we have to fight to persuade people the comet formed in this way."

Not all evidence supports this view. Images of pits in the comet's surface show numerous lumps 3 meters across on the pits' sides—"like oranges in a box," says Holger Sierks of the Max Planck Institute for Solar System Research in Göttingen, Germany, chief of Rosetta's main camera. Although these lumps may have formed as ices sublimated out of the pit, some team scientists believe that these outsized "goosebumps" are 67P's primordial building blocks. They are a prime target for imaging during today's descent to the surface.

A slew of instruments will keep gathering data as Rosetta approaches the surface at the speed of a gentle stroll. For team members whose instruments have already been turned off to conserve power, the ending is bittersweet—but their work is far from over. Most instrument teams have only examined their own data, and are just now thinking about combining data sets. "We've just started collaborating with other teams," Sierks says. "This is the beginning of the story, not the end." ■

PHOTO: BLICKWINKEL/ALAMY STOCK PHOTO

EVOLUTIONARY BIOLOGY

Fossil fishes challenge 'urban legend' of evolution

Genome duplications, thought to power evolutionary radiations, can't explain explosion of fishes

By **Elizabeth Pennisi**

Imagine a half-ton tuna laid out on a dock next to a seahorse, a minnow, and a moray eel. That's just a snapshot of the astonishing diversity found in the group of fishes called teleosts, or ray-finned fish, which today have 30,000 species—more than all living mammals, birds, reptiles, and amphibians combined. For more than a decade, many researchers have assumed that teleosts' dizzying array of body types evolved because their immediate ancestor somehow duplicated its entire genome, leaving whole sets of genes free to take on other functions.

Now, an examination of the fish fossil record challenges that view. Despite duplicating their genome about 160 million years ago, teleost fish hewed to a few conventional body types for their first 150 million years. Meanwhile, the holostean fishes, a related group with genomes that never underwent a doubling, evolved a stunning diversity of body plans. The work "demonstrates beautifully how necessary it is to look at the fossil record when testing hypotheses about … large-scale evolutionary changes," says Robert Sansom, a paleontologist at the University of Manchester in the United Kingdom.

Researchers puzzle over precisely how teleost fishes, such as this spotted sailfin sucker catfish, evolved a dazzling array of forms.

The link between genome duplication and diversification has seemed so intuitive that it's "almost become an urban legend," says Michael Lynch, an evolutionary biologist at Indiana University, Bloomington. The textbook case was the contrast between teleosts, with their spectacular diversity, and holosteans, which today have a mere eight species in just two body types (bowfins and gars). Flowering plants, too, are rife with duplications and are champions of diversity among plants. In both cases, biologists assumed that a DNA replication quirk doubled the genome. Then, while the preexisting genes kept the species viable, the extra gene copies could evolve new functions, thus speeding evolutionary change.

John Clarke, now a paleontologist at the University of Pennsylvania, decided to test this "legend" by comparing the diversity of teleosts and holosteans in the fossil record. He visited 15 museums around the world, measuring and photographing specimens from 250 million to 100 million years ago, then compared their rates of diversification. "Teleosts weren't always special," Clarke concludes. As he and his colleagues report this week in the *Proceedings of the National Academy of Sciences*, teleosts got off to a slow start in their first 150 million years. Meanwhile, the holosteans evolved diverse shapes and sizes, most of which have since gone extinct. "[Fish] without the duplicated genome are diversifying just fine," as fast or even faster than teleosts, notes Michael Alfaro, an evolutionary ichthyologist at the University of California, Los Angeles.

Some evidence suggests that genome duplications may actually promote diversity, but not right away. In several groups of flowering plants, diversity seems to have exploded perhaps as many as 50 million years after the genomes doubled. "More and more examples from the plant field [show] a time lag," says Ingo Braasch, an evolutionary developmental geneticist at Michigan State University in East Lansing. Such a lag might also be at play in the teleost story.

Others, however, think it's time for evolutionary biologists to move on. "Genome duplication was such a nice, tidy explanation" for this rich diversity, Sansom says. "Now, we need to look for other explanations." ■

Downloaded from http://science.sciencemag.org/ on October 7, 2016

Published by AAAS

Downloaded from http://science.sciencemag.org/

CRIME FORECASTERS

Police are turning to big data to stop crime before it happens. But is predictive policing biased—and does it even work?

By **Mara Hvistendahl**, *in Pittsburgh, Pennsylvania; Photography by* **Stephanie Strasberg**

Riding high in their squad car, officers Jamie Pascucci and Joe Kania are cruising the neighborhood of Homewood, scanning the streets for trouble. Pittsburgh, Pennsylvania, has one of the highest murder rates among large U.S. cities, and violent crime is particularly severe in Homewood, a 98% black pocket of aging, pock-marked Victorians on the east side. Young, white officers from outside the neighborhood, Pascucci and Kania patrol using a mixture of police radio, calls to their department's communications center, and instinct. They get occasional help from ShotSpotter, a network of sensors that detects gunshots and relays the information to a laptop mounted between the front seats.

But starting next month, Pascucci and Kania may get a new type of guidance. Homewood is set to become the initial pilot zone for Pittsburgh's "predictive policing" program. Police car laptops will display maps showing locations where crime is likely to occur, based on data-crunching algorithms developed by scientists at Carnegie Mellon University here. In theory, the

Corrected 6 October 2016. See full text.

Published by AAAS

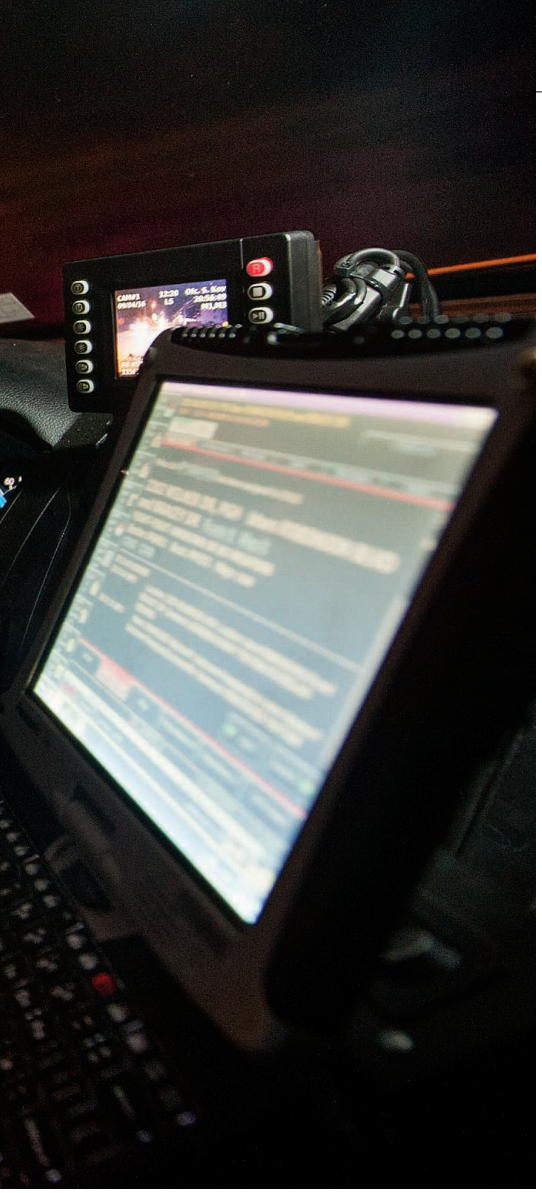

Officer Shane Kovach patrols Homewood, a Pittsburgh, Pennsylvania, neighborhood where predictive policing will soon be introduced.

maps could help cops do a better job of preventing crime.

Many other cities have already adopted similar systems, which incorporate everything from minor crime reports to criminals' Facebook profiles. They're catching on outside the United States as well. Drawing on approaches from fields as diverse as seismology and epidemiology, the algorithms can help bring down crime rates while also reducing bias in policing, their creators say. They replace more basic trendspotting and gut feelings about where crimes will happen and who will commit them with ostensibly objective analysis.

That's a strategy worth trying at a time when relations between U.S. police and minorities are at an all-time low, says Pittsburgh Police Chief Cameron McLay, who acknowledges that policing has a long way to go to fix bias. (Last year, McLay showed up at a New Year's Eve celebration holding a sign that read, "I resolve to end racism @ work.") McLay sees the use of big data—combined with more community-focused strategies—as part of a palliative for policing's ills.

But civil liberties groups and racial justice organizations are wary. They argue that predictive policing perpetuates racial prejudice in a dangerous new way, by shrouding it in the legitimacy accorded by science. Crime prediction models rely on flawed statistics that reflect the inherent bias in the criminal justice system, they contend—the same type of bias that makes black men more likely to get shot dead by the police than white men. Privacy is another key concern. In Chicago, Illinois, one scientist has helped the police department generate a list of individuals deemed likely to perpetrate or be victims of violent crime in the near future; those people are then told they're considered at risk, even if they have done nothing wrong.

> ***"They're not predicting the future. What they're actually predicting is where the next recorded police observations are going to occur."***
>
> **William Isaac**, the Human Rights Data Analysis Group

To what degree predictive policing actually prevents crime, meanwhile, is up for debate. Proponents point to quick reductions in crime rates. But John Hollywood, an analyst for RAND Corporation in Arlington, Virginia, who co-authored a report on the issue, says the advantage over other best-practice techniques is "incremental at best."

THE NOTION OF CRIME FORECASTING dates back to 1931, when sociologist Clifford R. Shaw of the University of Chicago and criminologist Henry D. McKay of Chicago's Institute for Juvenile Research wrote a book exploring the persistence of juvenile crime in specific neighborhoods. Scientists have experimented with using statistical and geospatial analyses to determine crime risk levels ever since. In the 1990s, the National Institute of Justice (NIJ) and others embraced geographic information system tools for mapping crime data, and researchers began using everything from basic regression analysis to cutting-edge mathematical models to forecast when and where the next outbreak might occur. But until recently, the limits of computing power and storage prevented them from using large data sets.

In 2006, researchers at the University of California, Los Angeles (UCLA), and UC Irvine teamed up with the Los Angeles Police Department (LAPD). By then, police departments were catching up in data collection, making crime forecasting "a real possibility rather than just a theoretical novelty," says UCLA anthropologist Jeffrey Brantingham. LAPD was using hot spot maps of past crimes to determine where to send patrols—a strategy the department called "cops on the dot." Brantingham's team believed they could make the maps predictive rather than merely descriptive.

Postdoctoral scholar George Mohler, now a mathematician at Indiana University-Purdue University, Indianapolis, suggested that borrowing models from seismology might be useful. Earthquakes take place at a relatively fixed rate along existing fault lines, but quakes can also occur in clusters, when an initial quake is followed by aftershocks occurring near in time and space, Brantingham explains. "Crime is actually very similar," he says. Some crimes are caused by built-in features of the environment, like a bar that closes at 2 a.m. every night, unleashing rowdy drunks onto a neighborhood. Others, such as a series of gang murders or a rash of neighborhood burglaries, happen because criminals' success invites more crimes or incites retaliation. Criminologists call this "repeat victimization"—the criminal equivalent of aftershocks.

Brantingham and Mohler developed an algorithm—now a proprietary software package called PredPol—that predicts what will happen within a given police shift. The software, used by 60 police departments around the country, incorporates a narrow set of closely related crime events from both the immediate and longer-term past, with more recent crimes given heavier weight. The software strips personal details and looks at "only what, where, and when," Brantingham says. At the beginning of a shift, officers are shown maps with 150-by-150-meter boxes indicating where crime is likely to flare up. Fighting crime, the company says in promotional slides, is about "getting in the box."

Here in Pittsburgh, Carnegie Mellon data scientists Wil Gorr and Daniel Neill developed a similar program for Chief McLay not long after he arrived in 2014. A fit, genial man who looks like Mr. Clean, McLay previously held what he calls a "retirement job" as a leadership development consultant; he decided to get back into active policing just days after Michael Brown, an unarmed black man, was killed in Ferguson, Missouri, triggering nationwide protests. McLay was convinced that improving the use of data in

Downloaded from http://science.sciencemag.org/ on October 7, 2016

Corrected 6 October 2016. See full text.

Published by AAAS

Crimes of the future

One commonly used approach in predictive policing seeks to forecast where and when crime will happen; another focuses on who will commit crime or become a victim.

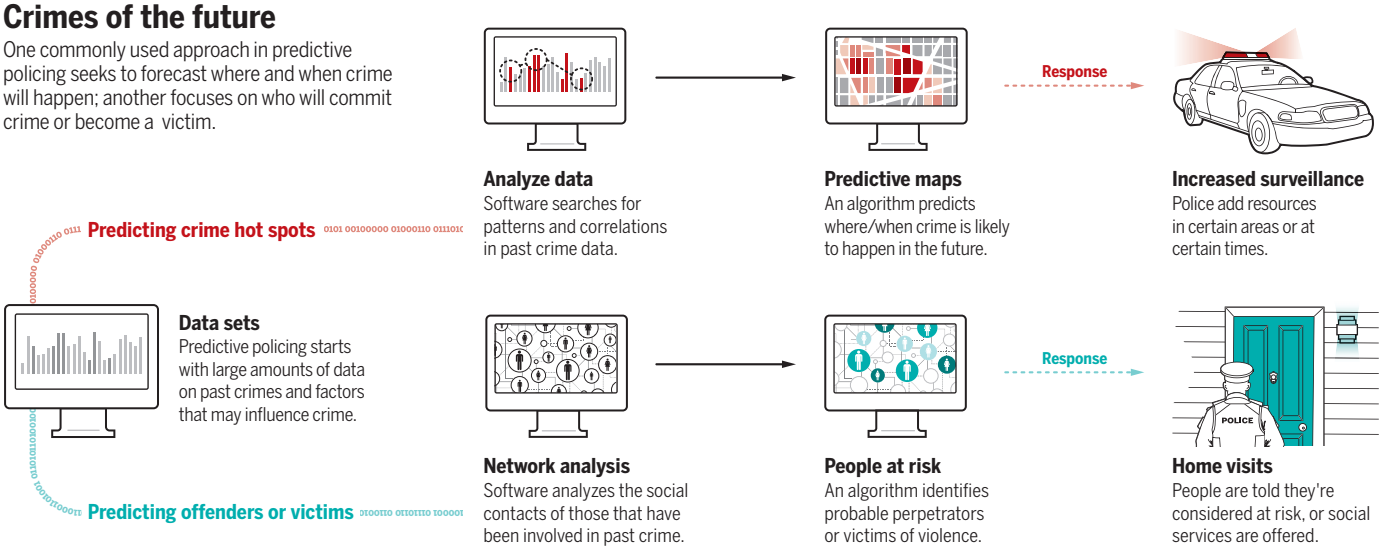

policing would lead to better outcomes.

Like PredPol, Pittsburgh's CrimeScan program has a geographic focus, but it draws on a broader variety of indicators. Gorr and Neill took their inspiration from criminology research showing that criminals tend to be generalists, and they tend to progress from minor to more serious crimes. As a result, the duo hypothesized, reports of minor crimes could help predict potential flare-ups of violent crime. In a gang confrontation, Neill says, "maybe it starts out with harsh words and offensive graffiti, and turns into fist fights, which turn into shootings, which turn into lots of shootings." Along with observations from the recent past, CrimeScan incorporates scores of minor crime offenses and 911 calls—about things like disorderly conduct, narcotics, and loitering—to spit out predictions about city blocks likely to see upsurges in violent crime in the next few days or weeks.

> ***"There are some cities where they have done a great job on hot spot policing, and they have terrible relationships with their communities of color."***
>
> **Cameron McLay**, Pittsburgh Bureau of Police

THE CHICAGO POLICE DEPARTMENT (CPD), meanwhile, has taken predictive policing one step further—and made it personal. The department is using network analysis to generate a highly controversial Strategic Subject List of people deemed at risk of becoming either victims or perpetrators of violent crimes. Officers and community members then pay visits to people on the list to inform them that they are considered high-risk.

The Custom Notification program, as it's called, was inspired in part by studies done by Andrew Papachristos, a sociologist at Yale University. Papachristos grew up in Chicago's Rogers Park neighborhood in the 1980s and '90s, at the height of the crack era. Being white insulated him from some of the violence, he says: "The color of my skin meant I never had to join a gang." But one night, Papachristos watched as a gang burned his parents' diner to the ground because they refused to pay extortion money.

Decades later, when he started studying crime, Papachristos wanted to understand the networks behind it. For a 2014 paper, he and Christopher Wildeman of Cornell University studied a high-crime neighborhood on Chicago's West Side. They found that 41% of all gun homicide victims in the community of 82,000 belonged to a network of people who had been arrested together, and who comprised a mere 4% of the population—suggesting, with other studies, that much can be learned about crime by examining the company people keep, Papachristos says.

Intrigued by these ideas, the Chicago police teamed up with Miles Wernick, a medical imaging researcher at the Illinois Institute of Technology in Chicago, to develop the Custom Notification program. Because gang violence was distributed across the city, hot spot policing wasn't as effective in Chicago, says Commander Jonathan Lewin, head of technology for the department. "The geography of the map isn't as helpful as looking at people and how risky a person is," he says.

The list has invited allegations that CPD is veering dangerously close to the flawed "precrime" unit in the sci-fi film *Minority Report*, which taps the premonitions of a trio of mutated humans to stop potential murderers before they act. And in bringing bad press, the program has contributed to the problems of the beleaguered CPD, which a mayoral task force described last April as having "systemic institutional failures going back decades that can no longer be ignored."

Papachristos—who is not involved with the Strategic Subject List himself—cautions that the program overemphasizes both an individual's potential to offend and the use of policing, rather than other services, to fight crime. That "reinforces the way in which America devalues the lives of young people of color," he wrote in the *Chicago Tribune* on 1 August.

What's more, the police data that this and other predictive policing programs rely on are skewed toward crimes committed by people of color, says William Isaac, an analyst with the Human Rights Data Analysis Group and a Ph.D. candidate at Michigan State University in East Lansing. That renders any predictions suspect, he says: "They're not predicting the future. What they're actually predicting is where the next recorded police observations are going to occur." Predictions, indeed, can become self-fulfilling prophecies, says Jennifer Lynch of the Electronic Frontier Foundation in San Francisco, California. "We know from past examples that when police are expecting violence, they often respond with violence."

Brantingham, the architect of PredPol, agrees that civil liberties concerns "are really important questions." But he says that predictive policing can be more

DIAGRAM: G. GRULLÓN/*SCIENCE*

Downloaded from http://science.sciencemag.org/ on October 7, 2016

Corrected 6 October 2016. See full text.

Published by AAAS

fair than the status quo: "What's often forgotten is that any time you put an officer in the field there's a risk of civil liberties violations."

Other critics, meanwhile, raise a more fundamental question about predictive policing: Does it even work?

IN A 2012 IBM SMARTER PLANET commercial, a police officer glances at the screen of his squad car, then speeds to a convenience store. He arrives as a clerk is counting money, and moments before a would-be robber shows up. That's science fiction, says RAND's Hollywood—and likely to stay that way. To predict specific crimes, he says, "we would need to improve the precision of our predictions by a factor of 1000."

As to whether existing methods of predictive policing work as advertised, by forecasting the likelihood of crime, the evidence is scarce, and the few data points are not encouraging. For instance, an assessment of Chicago's Strategic Subject List program published by Hollywood and fellow RAND researchers last month found that individuals singled out in the pilot phase were no more likely to become victims of homicides than a comparison group. They were, however, more likely to be arrested for a shooting—possibly because, the researchers write, "some officers may have used the list as leads to closing shooting cases." (The program's "scores are not used for probable cause, and individuals cannot be arrested because of a high score," a spokesperson for CPD says.)

Some scholars have tested models' predictive power against historical crime rates, with encouraging results. But evaluating a program once in use can be more complicated. A randomized, controlled study—a design borrowed from medicine—is the gold standard, but few departments are willing to designate a control area or group, where they won't try to predict crime. "The average police chief lasts 3 years," McLay says. "I don't have time for controls." Hollywood adds that with programs like Chicago's, which single out individuals, "no one wants to say, 'I'm not going to perform interventions with the 10 people who are most at risk.'"

The issue is complicated by the fact that algorithms like PredPol's are proprietary, making it difficult for outside scholars or the general public to evaluate their effectiveness. "For the sake of transparency and for policymakers, we need to have some insight into what's going on so that it can be validated by outside groups," Isaac says. But Brantingham says researchers can evaluate the outcome without knowing all the underlying research.

One notable randomized, controlled experiment was conducted by the Shreveport, Louisiana, police department in 2012 with NIJ funding. The study found that the difference in crime reduction between the control and experimental districts was statistically insignificant. But the experiment, which focused on property crimes, also revealed the challenges of such studies. Take-up of predictive hot spot policing among the three experimental districts was high at first, but dropped off after 4 months as enthusiasm waned, likely skewing the results. Commanders in one of the control districts, meanwhile, grew excited by the experimental districts' success at reducing crime and decided to pursue their own targeted operations in known hot spots.

The most extensive independent evaluation of predictive policing so far, the RAND report, is lukewarm about even the most sophisticated predictive methods, stating that "increases in predictive power have tended to show diminishing returns." Hollywood adds that "the places where really sophisticated data mining algorithms shine" are those where "there are very complex nonlinear relationships between input data and output data." (One example is optical character recognition, which is used for digitizing printed texts.) With crime, he adds, "It's much more simple—the more risk, the more crime. There aren't really complicated relationships going on."

PERCHED AT A CONFERENCE TABLE overlooking the blighted Allegheny-West neighborhood, Chief McLay says he is keenly aware that rolling out CrimeScan will not solve all the Pittsburgh department's problems. "There are some cities where they have done a great job on hot spot policing, and they have terrible relationships with their communities of color," he says.

The key, some experts say, is not to rely only on statistical methods, but to combine them with other approaches. For example, Papachristos is now working with the Chicago Violence Reduction Strategy, a program that identifies individuals at risk of becoming either violent offenders or victims, then gets them access to social services and employment assistance. A few appear on the Strategic Subject List, says Chris Mallette, the program's executive director, but most are selected through old-fashioned observation.

McLay seems to lean toward a similar approach. As CrimeScan launches, he also aims to build relationships with high-crime communities and ensure that big data are used to solve problems rather than simply focus police work. "Therein lies the key: Who finds that sweet spot?" he says. "Who uses just enough data to be really good, and has the relationships that are just robust enough? That's the challenge that policing in this country is facing right now." ■

Crime often clusters in hot spots like those on the map behind Pittsburgh, Pennsylvania, Police Chief Cameron McLay. He hopes that algorithms capable of predicting future hot spots will help make police work less biased.

PHOTO: STEPHANIE STRASBERG

Downloaded from http://science.sciencemag.org/ on October 7, 2016

Corrected 6 October 2016. See full text.

Published by AAAS

THE BIGGEST EAR

It will take one more burst of ingenuity to get China's massive radio telescope to live up to its promise

By **Dennis Normile**, *in Dawodang, China*

Downloaded from http://science.sciencemag.org/ on October 7, 2016

PHOTOS: (LEFT TO RIGHT) XINHUA/ALAMY STOCK PHOTO; VCG/CONTRIBUTOR/GETTY IMAGES

In a stunning landscape of jagged limestone hills in southwestern China, engineers are putting the finishing touches on a grand astronomy facility: a half-kilometer-wide dish nestled in a natural depression that will gather radio signals from the cosmos. The world's largest radio telescope will catalog pulsars; probe gravitational waves, dark matter, and fast radio bursts; and listen for transmissions from alien civilizations.

Yet the architect of the tour de force is blasé about what his telescope might capture. "I'm really not very interested in science, I'm sorry to say," says Nan Rendong, chief scientist and chief engineer of the Five-hundred-meter Aperture Spherical radio Telescope (FAST) here. Colleagues insist he is joking, but there is no question that what has consumed 2 decades of his life—and is now wowing other astronomers—is engineering. "As a civil engineering feat, FAST is obviously amazing," says Fred Lo, former director of the U.S. National Radio Astronomy Observatory (NRAO) in Charlottesville, Virginia.

It is not just FAST's sheer size—it has more than twice the collecting area of the runner-up, the 305-meter dish in Arecibo, Puerto Rico. FAST is also breaking new ground in radio astronomy with a design that pulls a section of the spherical dish into a gradually moving paraboloid to aim at and track cosmic objects as Earth rotates, bringing the benefits of a tilting, turning antenna to a fixed dish. This innovation "is absolutely unique, nobody has ever done this before," says Dick Manchester, a radio astronomer at Australia's Commonwealth Scientific and Industrial Research Organisation (CSIRO) in Sydney.

There's another reason that Nan isn't worrying about science just yet. Although dignitaries celebrated FAST's completion at a 25 September ceremony here in Guizhou province, the telescope isn't yet working as planned. Nan is focused on solving a recently uncovered technical glitch that's hindering the dish-shaping capability and limiting the early science. To get FAST to live up to its scientific promise, he says, "we have a lot to do."

"There is no question, Nan is the main driving force for FAST, from beginning to end," Lo says. Nan's engineering bent dates from his undergraduate days studying ultrahigh-frequency electronics at Tsinghua University in Beijing in the mid-1960s; during China's tumultuous Cultural Revolution he spent a decade working at an electronics factory. He then returned to academia, earning a Ph.D. in astronomy and astro-

Published by AAAS

An otherworldly karst landscape made getting materials and equipment to the site fiendishly difficult. Far left, a worker on the giant truss encircling the dish.

physics from the University of Science and Technology of China in Hefei.

FAST's long gestation began in the 1990s, when Nan served on China's delegation to the international working group that eventually proposed the Square Kilometre Array (SKA) as a next-generation radio telescope. Astronomers were counting on advances in interferometry to combine radio waves from dozens or even hundreds of dishes, thereby creating a collecting area far bigger than any existing telescope. In the early days of planning, China vied to host the SKA, proposing to build several large dishes in the limestone depressions that dimple its southwestern provinces. Chinese astronomers even did preliminary work on FAST as a prototype.

Instead, the SKA's backers opted for a design featuring thousands of small dishes. China was dropped from the list of candidate sites in 2006; construction of the first phase of the SKA, in South Africa and Australia, is expected to begin in 2018. Swallowing their disappointment, Nan and his colleagues pushed China to build FAST anyway (*Science*, 19 June 2009, p. 1508).

Single dishes excel at observing point sources like neutron stars and at scanning a multitude of frequencies in the search for extraterrestrial intelligence, says astronomer Li Di, a FAST project scientist, who previously worked at NASA's Jet Propulsion Laboratory in Pasadena, California. Another advantage is that, compared with the multiple dishes in an array, single dishes are "relatively cheap and relatively straightforward to upgrade," says George Hobbs, an astronomer at CSIRO. "You just keep building better receivers."

After an international review panel endorsed FAST, China's National Development and Reform Commission in 2007 provided $90 million to launch the project; additional support from several agencies topped up the funding to $180 million. Nan had led much of the preliminary work on FAST, and in 2008 he was anointed chief scientist and chief engineer. "Traditionally, that's two jobs," Li says, but Nan's practical experience and scientific training, he says, allowed him to speak to funding agencies "with both his engineering and science hats on."

Nan already knew where to build the dish—and he knew it wouldn't be easy. In the 1990s, satellite surveys had identified 400 candidate depressions in China's southwest provinces. That number was winnowed down until Nan personally inspected a few of them. He recalls hiking into the Dawodang depression and looking up to see a nearly circular view of the sky that "was like being at the bottom of a well."

Published by AAAS

Downloaded from http://science.sciencemag.org/ on October 7, 2016

Radio astronomy writ large

The world's largest radio telescope, China's new Five-hundred-meter Aperture Spherical radio Telescope (FAST), will gather radio signals from the cosmos to catalog pulsars; probe gravitational waves, dark matter, and fast radio bursts; and listen for transmissions from alien civilizations.

A "bowl within a wok"

FAST's signature innovation is a system that pulls a section of the dish as much as 300 meters across into a parabola to focus cosmic radio waves on receivers. Provided a glitch is resolved, the parabola's position can be shifted in real time to keep it trained on an astronomical object as Earth rotates.

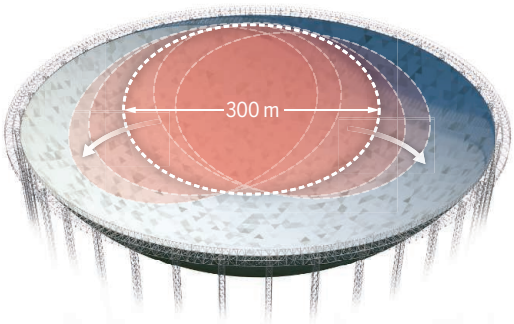

Bigger *is* better

FAST has more than twice the collecting area of the world's second largest radio telescope, the Arecibo Observatory in Puerto Rico, enabling it to study fainter and more distant objects.

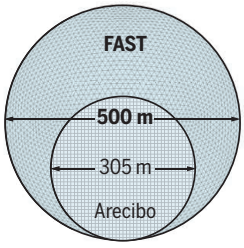

Snug fit

FAST planners studied some 400 karst depressions in southwestern China before deciding Dawodang was just right for cradling the telescope's massive dish.

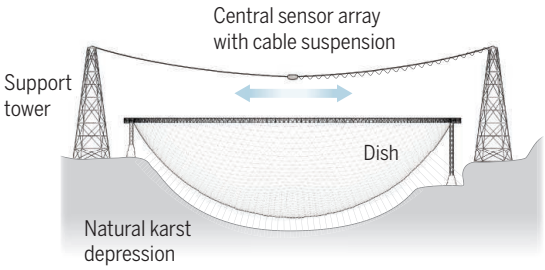

Tuning the radio dial

To deform the reflector and create the bowl-within-a-wok effect, 2225 actuators, essentially high-tech winches, are anchored into rock beneath the dish's 4450 triangular reflector panels. A 300-meter-diameter deformed section can be trained on objects 26° from the zenith; smaller sections can view the skies up to 40° from the zenith.

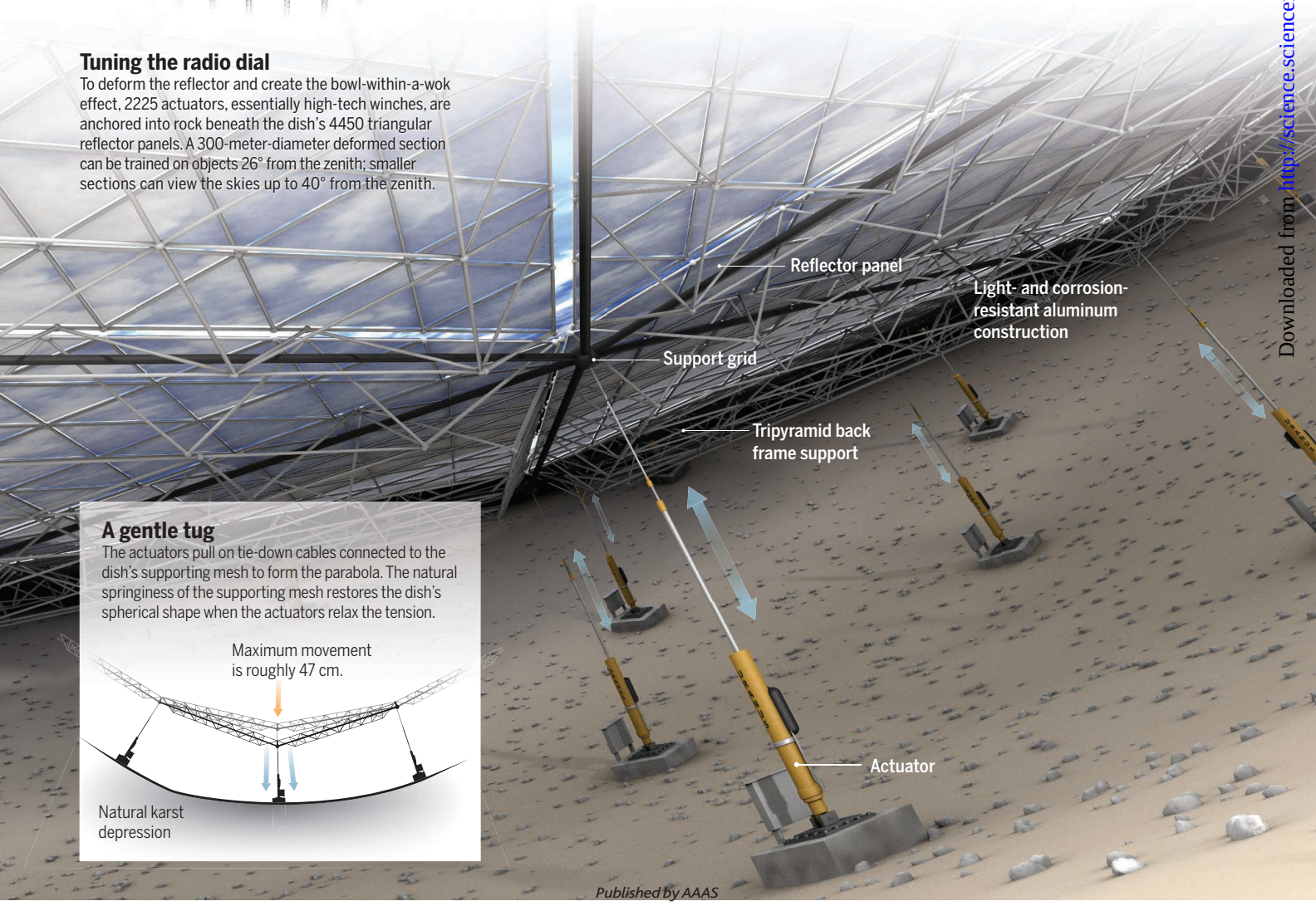

A gentle tug

The actuators pull on tie-down cables connected to the dish's supporting mesh to form the parabola. The natural springiness of the supporting mesh restores the dish's spherical shape when the actuators relax the tension.

Downloaded from http://science.sciencemag.org/ on October 7, 2016

Published by AAAS

"The site is the best for FAST, [but is] the worst for construction," Nan says. It is hours from the nearest highway, down bone-jarring, narrow roads that wind through towering pinnacles and tiny villages. The FAST team built a 7-kilometer road linking the depression to the nearest town. The difficult access curtailed use of heavy equipment. "Almost everything had to be done manually," Nan says. "Very devoted laborers," he says, shouldered 100-kilogram loads in temperatures topping 40°C. By comparison, he says, "Building a bridge in Beijing or Shanghai is a piece of cake."

The team modeled FAST after the Arecibo telescope. Both are built in karst depressions and supported on steel cable meshes slung like hammocks from supports fixed to the limestone pinnacles. And like the Arecibo Observatory, FAST takes an unusual approach to focusing incoming radio waves.

Radio telescope dishes are typically parabolic because that shape focuses waves from astronomical objects in line with the parabola's axis to a point above the dish. The telescope's receivers—or a subreflector—are positioned at that point. But a parabolic telescope must be steerable and able to point at astronomical objects and track them as Earth rotates, because parabolic reflectors distort waves from off-axis targets.

It's impossible to steer Arecibo and FAST because their enormous dishes are anchored to the ground. So both have a spherical shape, allowing them to collect and concentrate waves from off-axis sources without focusing on a point. Arecibo aims at cosmic objects by shifting the position of the receiver platform to catch the reflected waves. Within the platform, a complex mirror system brings them into focus. But that limits the slice of observable sky to about 20° from zenith; farther from the zenith, the distortion is too great. The correction system also results in a platform weighing about 900 tons. "That mirror system and the whole platform are very big for Arecibo, and it would have been huge for FAST—and heavy," Manchester says.

Instead, Nan and his team designed a system that pulls a roughly 300-meter-diameter section of FAST's spherical reflector into a subtle parabola, while positioning receivers along the parabola's axis (see graphic, opposite page). "It's like forming a smaller bowl within a big wok," Li says. The position of the parabola can be shifted in real time, so that the parabolic axis always aims at a cosmic object of interest as Earth rotates, just as a steerable radio telescope does. FAST can observe up to 40° from zenith. And because it does not need a complex corrective mechanism, its receiver platform can host more instruments than Arecibo's.

Making an active surface reflector "was a bold move," Manchester says. To deform the reflector, FAST has 2225 actuators, essentially high-tech winches, anchored into rock beneath the dish. The actuators tug the dish into a parabola by pulling on tie-down cables connected to the dish's supporting mesh. The mesh's natural springiness restores the dish's spherical shape when the actuators relax the tension. Lasers mounted on small posts protruding through the dish check the coordinates of 1000 points on its surface, allowing fine-tuning of the shape.

To make this system work, the engineers solved a host of challenges. For starters, the actuators emit radio interference that is "many times stronger than the signal from the sky," Nan says. There was no suitable commercially available shielding, so they developed their own.

Another problem was caught during the final design review before construction, when engineers belatedly realized that repeatedly stressing and relaxing ordinary steel cables could lead to fatigue failure, the phenomenon familiar to anyone who has bent a paper clip back and forth until it snaps. The FAST team solved this problem by turning to a Chinese-developed cable that's fatigue-resistant for up to 2 million stress cycles, far more than the 300,000 cycles the FAST cables will endure over the telescope's 30-year design life.

An astronomer with an engineering bent, Nan Rendong led much of the early work on the radio telescope and is its chief scientist and chief engineer.

IN JANUARY, with most of the dish's 4450 triangular reflector panels in place but none of its receivers available, Nan had his crew rig up something resembling a spindly fishbone TV antenna and suspend it over the dish. As radio receivers go it was primitive, but FAST's enormous collecting area enabled it to pick up signals from the Crab Pulsar, a radio source at the heart of the Crab Nebula. "It was amazing that they could do this with a simple antenna," CSIRO's Hobbs says.

For Nan, the test was FAST's first light, the initial scientific observation that marks the start of a telescope's working life. In focusing on the Crab Nebula, Nan turned one of China's earliest astronomical observations into one of its latest: A millennium ago, Song dynasty observers noted a transitory "guest star," later pegged as the supernova that created the nebula.

But as the dish's construction entered the home stretch, another glitch cropped up. "The actuators are breaking down at a higher rate than anticipated," Li says. The team is investigating the cause and possible fixes.

Getting big telescopes working at full potential is always a challenge, says John Ford, formerly in charge of electronics at NRAO's Green Bank observatory in West Virginia. On Green Bank's 100-meter steerable dish, actuators used to counter gravitational effects were "failing on us way more than we thought they would," he says, because water was leaking in and freezing. Waterproofing the actuators was a headache because they are 100 meters in the air. FAST engineers should have an easier time because their actuators are accessible from the ground, Ford says.

For now, Li says FAST operators will use their working actuators to hold part of the reflector in a parabola, point it at the sky, and simply catch whatever signals they can as Earth rotates. It will take 200 days of such drift scan observations to survey the full northern sky, and he expects they will discover as many as 1000 pulsars, adding to the roughly 2500 now known. Astronomers use these radio beacons, powered by spinning neutron stars, to study the interstellar medium and detect gravitational waves. "We will conduct the world's best survey for pulsars," Li says.

"Eventually we will get the telescope working perfectly," vows Zhu Ming, a FAST project astronomer. Manchester agrees: "They're very close to achieving an absolutely remarkable feat." ■

CREDITS: (PHOTO) NATIONAL ASTRONOMICAL OBSERVATORIES, CHINESE ACADEMY OF SCIENCES; (GRAPHIC, OPPOSITE PAGE) C. BICKEL/*SCIENCE*

Downloaded from http://science.sciencemag.org/ on October 7, 2016

Published by AAAS

Downloaded from http://science.sciencemag.org/ on October 7, 2016

ASTROPHYSICS

Detecting structure in a protostellar disk

Spiral structure may provide clues about the early stages of star and planet formation

By **Ken Rice**

It is now well accepted that stars form from clouds of gas and dust that collapse under their own gravity (*1*). However, if all the material fell directly onto the young protostar, it would spin up so much that it would ultimately tear itself apart. Instead, most of the material will initially form a thin, rotationally supported, protostellar disk. On page 1519 of this issue, Pérez *et al.* (*2*) present a high-resolution image of such a disk, using the Atacama Millimeter/submillimeter Array (ALMA). It is this disk that provides mechanisms for transporting angular momentum outward—allowing mass to accrete onto the central protostar—and is the site of planet formation (see the illustration).

How angular momentum is transported outward, allowing mass to flow in, is still not quite clear. However, we would expect the disk mass at very early times to be large, relative to that of the central protostar. If so, the disk becomes susceptible to the growth of a gravitational instability (*3*). This instability manifests itself through the growth of spiral density waves, much like those observed in many disk galaxies (see the figure).

To date, there have been a number of examples of protostellar systems that show evidence of spiral density waves in their circumstellar disks (*4*, *5*). However, in almost all cases the properties of the disk, such as its mass and accretion rate, suggest that these are not self-gravitating spiral waves and are more likely due to embedded planets or some other process.

The self-gravitating phase, if it occurs, happens when the protostellar system is very young, the disk is still massive, the accretion rate is still high (*6*), and the system is

Institute for Astronomy, University of Edinburgh, Edinburgh EH9 3HJ, UK. Email: wkmr@roe.ac.uk

ILLUSTRATION: RGB VENTURES/SUPERSTOCK/ALAMY STOCK PHOTO

Published by AAAS

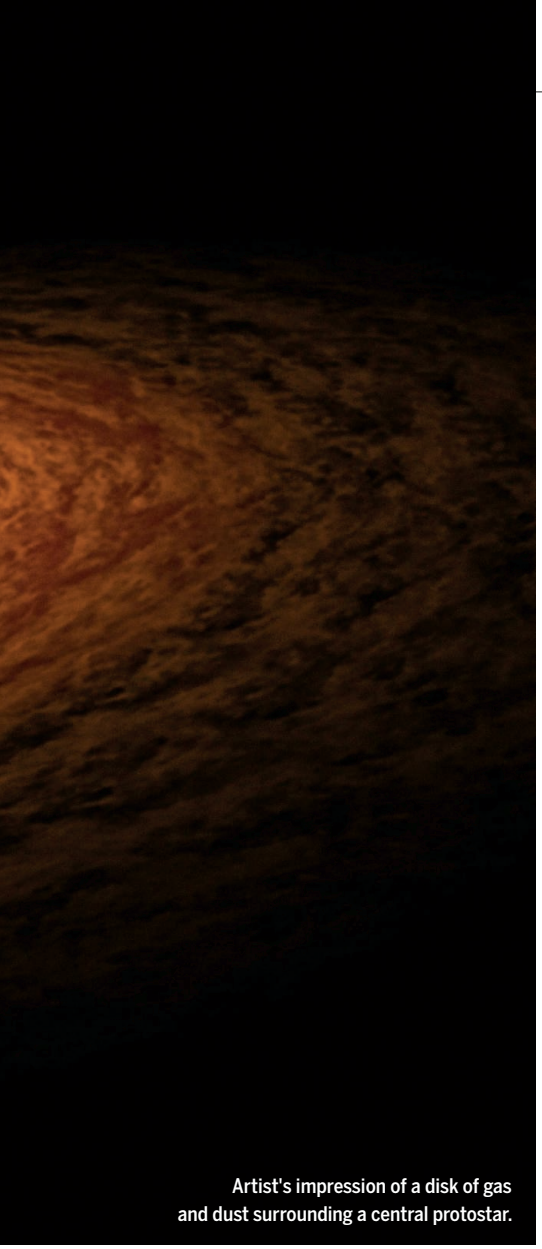

Artist's impression of a disk of gas and dust surrounding a central protostar.

GRAPHIC: KEN RICE

still probably embedded within its nascent gas cloud. Consequently, directly observing these self-gravitating structures is very difficult (*7*). However, with the advent of ALMA, direct observation has become much easier because ALMA not only has improved resolution and sensitivity but also observes at the wavelengths at which we might expect such structures to be detectable.

It is this direct observation capability that makes the result presented by Pérez *et al*. so intriguing. The high-resolution image suggests the presence of spiral density waves in this very young protostellar system, Elias 2-27. The disk may have a mass close to one-quarter that of the central star, and the mass accretion rate is close to 10^{-7} solar masses per year, which places it in the region of parameter space where we might expect the disk to be susceptible to the gravitational instability. Therefore, this direct observation of self-gravitating spiral waves may be the first in a disk around a young protostar.

On the other hand, the two-armed spirals seen in the disk of Elias 2-27 are only expected in disks with masses close to half that of the central star (*8*), and the disk radius is such that it only becomes marginally gravitationally unstable if the opacity is reduced relative to what might be expected. So, even though this is very suggestive, it is not yet conclusive that the spirals are indeed driven by the gravitational instability.

However, even if the spiral density waves in Elias 2-27 are not being driven by disk self-gravity, this result is still indicating that we are starting to be able to probe structures in disks around very young stars. This ability is clearly important because this phase is when most of the mass is accreted onto the central protostar, and such observations will help us to understand the processes involved in driving mass accretion.

It is also possible that this phase of protostellar disk evolution will play a key role in the growth of planet-building material. It is still unclear how micrometer-sized dust grains grow to form kilometer-sized planetesimals that then coagulate to form either the cores of gas- or ice-giant planets or smaller rocky planets. One possible mechanism is that grains become concentrated in these spiral density waves, and this then acts to promote their growth (*9*). In fact, the enhancement of dust grains in these spiral density waves can appreciably influence our likelihood of observing these structures (*10*, *11*), and observations such as those presented by Pérez *et al*. will allow us to study whether these structures are indeed promoting grain growth.

There is also still some uncertainty about the overall planet-formation process. It is generally accepted that the dominant process is the growth of solid cores that (if they become sufficiently massive) may then collect a gaseous envelope to become a Jupiter-like gas giant (*12*, *13*). However, we now have direct images of some exoplanets (*14*) that tend to be young, massive, and on very wide orbits. These exoplanets provide a challenge to this standard mechanism, and it is possible that they form via gravitational collapse when the system is very young and the disk is self-gravitating. Therefore, observations such as those presented by Pérez *et al*. may allow us to investigate this possibility in more detail.

It has even been suggested that big gas-giant planets that may form via direct gravitational collapse in the outer parts of young protostellar disks may spiral inward and lose mass via tidal interactions with their host star (*15*), potentially becoming rocky, terrestrial planets. Having the ability to directly observe disks around very young protostars may therefore provide constraints on this mechanism and whether or not it can actually operate.

Not only is the result presented by Pérez *et al*. possibly the first direct evidence for self-gravitating spiral density waves in a protostellar disk, it is also a very welcome step toward being able to probe the earliest stages of star formation. It is likely that this stage will be important for both the formation of the star itself and the subsequent formation of a planetary system. These observations will therefore play a crucial role in improving our understanding of both star and planet formation. ■

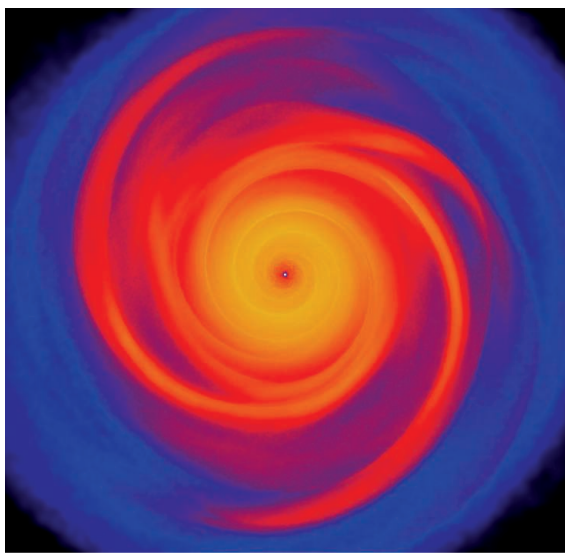

A snapshot from a numerical simulation of a massive disk around a young protostar showing the presence of spiral density waves being driven by the gravitational instability.

REFERENCES

1. S. Terebey, F. H. Shu, P. Cassen, *Astrophys. J.* **286**, 529 (1984).
2. L. M. Pérez *et al.*, *Science* **353**, 1519 (2016).
3. A. Toomre, *Astrophys. J.* **139**, 1217 (1964).
4. C. A. Grady *et al.*, *Astrophys. J.* **762**, 48 (2013).
5. T. Muto *et al.*, *Astrophys. J.* **748**, L22 (2012).
6. C. J. Clarke, *Mon. Not. Royal Astron. Soc.* **396**, 1066 (2009).
7. M. M. Dunham *et al.*, in *Protostars and Planets VI*, H. Beuther *et al.*, Eds. (Univ. Arizona Press, Tucson), pp. 195–218.
8. G. Lodato, W. K. M. Rice, *Mon. Not. R. Astron. Soc.* **358**, 1489 (2005).
9. W. K. M. Rice *et al.*, *Mon. Not. R. Astron. Soc.* **355**, 543 (2004).
10. G. Dipierro *et al.*, *Mon. Not. R. Astron. Soc.* **451**, 974 (2015).
11. C. Hall *et al.*, *Mon. Not. R. Astron. Soc.* **458**, 306 (2016).
12. J. B. Pollack *et al.*, *Icarus* **124**, 62 (1996).
13. S. Ida, D. N. C. Lin, *Astrophys. J.* **604**, 388 (2004).
14. C. Marois *et al.*, *Science* **322**, 1348 (2008).
15. S. Nayakshin, *Mon. Not. R. Astron. Soc.* **408**, L36 (2010).

10.1126/science.aag2855

Downloaded from http://science.sciencemag.org/ on October 7, 2016

Published by AAAS

ECOLOGY

A latitudinal gradient for genetic diversity

Within-species diversity of amphibians and terrestrial mammals is highest in the tropics

By **Henrique M. Pereira**[1,2,3]

The tropics have by far the highest species diversity on Earth. Over two-thirds of terrestrial vertebrates occur in tropical moist forests (*1*). The species diversity is also highest in the tropics for several other taxa, such as vascular plants and arthropods, and in other realms, including freshwater and marine ecosystems. These latitudinal gradients were described decades ago (*2*), but recent work has yielded detailed knowledge of species-richness patterns. For example, Hurlbert and Jetz suggest that global maps of terrestrial vertebrate species richness are now accurate at resolutions of 100 to 200 km (*3*). Yet, little is known about the global patterns of genetic diversity. On page 1532 of this issue, Miraldo *et al.* help to fill this gap by presenting a global map of intraspecific (within-species) genetic diversity of amphibians and terrestrial mammals (*4*).

Many journals have required for years that authors submit sequence data to public databases. Miraldo *et al.* tapped into this resource to obtain more than 318,000 mitochondrial DNA sequences. However, not all these sequences could be used for a spatial analysis. Only 13% were georeferenced with explicit spatial coordinates. Another 30% had locality names. For the latter, Miraldo *et al.* assigned spatial coordinates to the locality names. Next, they grouped all usable sequences of a given species into ~400-km grid cells, ecosystems with different levels of human influence, and 10° latitudinal bands. They estimated intraspecific genetic diversity as the average number of variable nucleotide sites in the cytochrome B gene in pairwise sequence comparisons. Finally, they averaged the intraspecific genetic diversities across species.

[1]German Centre for Integrative Biodiversity Research (iDiv), Halle-Jena-Leipzig, Deutscher Platz 5e, 04103 Leipzig, Germany. [2]Institute of Biology, Martin Luther University Halle-Wittenberg, Germany. [3]CIBIO/InBIO, Universidade do Porto, Portugal. Email: hpereira@idiv.de

The results suggest that for the two taxa analyzed, levels of intraspecific diversity are high in the tropics. However, whereas species richness declines almost monotonically away from the equator (*1*), genetic diversity seems to plateau around the equator (see the figure). This difference was not analyzed by Miraldo *et al.* and therefore will require further confirmation.

A possible limitation of the current analysis is the spatial heterogeneity in the data; in many tropical areas, the proportion of species sampled or the number of sequences are low. Furthermore, the authors gridded available point sequence data to estimate genetic diversity, in contrast to some species richness maps, where individual species ranges are stacked to estimate species richness. In the former case, sampling effort can vary dramatically in neighboring spatial units. Addressing this problem will require harmonized efforts to sample genetic diversity in gap regions.

There is still a vibrant debate over what drives the latitudinal pattern in species richness (*5*, *6*). Several explanations have been proposed for the higher diversity of the tropics. For example, higher climatic stability in the tropics may lead to lower extinction rates; higher evolutionary speed may result in higher speciation rates; and a larger surface area of tropical biomes over geological time may have led to a higher number of individuals on average and thus higher speciation and lower extinction rates. According to another hypothesis, greater energy availability in the tropics leads to larger populations. Biotic interactions can further cause positive feedbacks and reinforce the gradient. These mechanisms are not mutually exclusive and may all interact over time.

The high intraspecific genetic diversity in the tropics found by Miraldo *et al.* and other recent studies (*7*, *8*) supports the evolutionary speed hypothesis, which is based on the idea that higher temperatures in the tropics lead to higher mutation rates. However, high numbers of mutations may also accumulate in large or stable population sizes over time (*5*). The influence of other drivers on the latitudinal gradient cannot, therefore, be excluded. Furthermore, intraspecific and interspecies diversity may interact in complex ways. For example, high species richness can increase intraspecific diversity as a result of increased competition for similar resources (*9*).

The total biodiversity at the genetic level of a region can be obtained by multiplying the number of species with the intraspecific diversity (see the figure). The resulting latitudinal gradient for total biodiversity is much more

Latitudinal gradients of biodiversity

Miraldo *et al.* show that latitudinal gradients are similar for within-species diversity and for species richness. Multiplying the two components to obtain the total biodiversity curve produces a more pronounced gradient.

Species diversity

Species diversity is highest in the tropics and declines with increasing latitude, reaching very low levels at the poles.

Within-species diversity

The genetic diversity within species is also highest in the tropics but plateaus around the equator before falling off sharply with latitude.

Total genetic diversity

The total genetic biodiversity is calculated by multiplying the species diversity and the within-species diversity. It peaks sharply in the tropics.

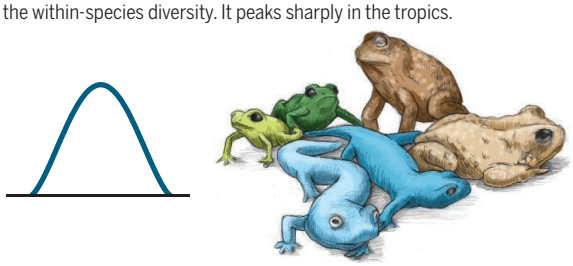

GRAPHIC: V. ALTOUNIAN/*SCIENCE*

Downloaded from http://science.sciencemag.org/ on October 7, 2016

Published by AAAS

pronounced than for any of its components in isolation. The idea of total biodiversity as a multiplication of two components is also important for understanding the impacts of humans on biodiversity. A reduction of local species richness has been reported in several human-dominated habitats, although responses may differ across taxa (*10*, *11*). Miraldo *et al*. found similar impacts at the intraspecific level, with amphibians showing lower genetic diversity in human-dominated ecosystems than in more natural ecosystems, although the response for mammals was not as clear. Therefore, reductions in species richness and genetic diversity caused by human activities have a negative synergistic effect on total biodiversity.

The study by Miraldo *et al*. has important implications for conservation. Protected areas have arguably been one of the most important tools for conserving the world's biodiversity. It remains unclear whether areas prioritized for conservation based on species diversity or even phylogenetic diversity (*12*) also capture intraspecific diversity. But perhaps the key question is how intraspecific diversity is changing over time in response to human drivers. This is an important societal question because Target 13 of the Convention on Biological Diversity for 2020 aims for the maintenance of genetic diversity. Moving from a single snapshot of the global distribution of genetic diversity to a dynamic map over time would allow major progress in answering this question. Such temporal studies will require advanced analyses, such as that by Miraldo *et al*., but also improved geographical annotation of sequence data (*13*) and an increased effort to monitor global genetic diversity. ■

REFERENCES

1. G. M. Mace *et al.*, in *Ecosystems and Human Well-Being: Current State and Trends: Findings of the Condition and Trends Working Group of the Millennium Ecosystem Assessment*, vol. 1 of *The Millennium Ecosystem Assessment Series*, R. Hassan, R. Scholes, N. Ash, Eds. (Island Press, Washington, DC, 2005), pp. 77–126.
2. E. R. Pianka, *Am. Nat.* **100**, 33 (1966).
3. A. H. Hurlbert, W. Jetz, *Proc. Natl. Acad. U.S.A.* **104**, 13384 (2007).
4. A. Miraldo *et al.*, *Science* **353**, 1532 (2016).
5. P. V. A. Fine, *Annu. Rev. Ecol. Evol. Syst.* **46**, 369 (2015).
6. G. G. Mittelbach *et al.*, *Ecol. Lett.* **10**, 315 (2007).
7. L. N. Gillman, D. J. Keeling, H. A. Ross, S. D. Wright, *Proc. R. Soc. B* **276**, 3353 (2009).
8. L. N. Gillman, D. J. Keeling, R. C. Gardner, S. D. Wright, *J. Evol. Biol.* **23**, 1327 (2010).
9. A. Jousset, N. Eisenhauer, M. Merker, N. Mouquet, S. Scheu, *Sci. Adv.* **2**, e1600124 (2016).
10. H. M. Pereira, L. M. Navarro, I. S. Martins, *Annu. Rev. Environ. Resour.* **37**, 25 (2012).
11. T. Newbold *et al.*, *Nature* **520**, 45 (2015).
12. S. Sarkar *et al.*, *Annu. Rev. Environ. Resour.* **31**, 123 (2006).
13. P. Gratton *et al.*, *J. Biogeogr.* 10.1111/jbi.12786 (2016).

10.1126/science.aah6730

PHOTO: BRIAN JANNSEN/ALAMY STOCK PHOTO

Liu *et al*. use electrical resistivity data as a first-order proxy for the viscosity of the lithosphere beneath the Colorado Plateau. A two-dimensional model based on these results matches GPS and topography data.

GEOPHYSICS

Constraining lithospheric flow

Geophysical data help to determine the viscosity of Earth's crust and upper mantle

By **Boris J. P. Kaus**

The motion of Earth's tectonic plates—the lithosphere—is driven by the subduction of relatively cold and dense oceanic plates into the mantle. The resulting forces drive the motions of continental plates, but the manner in which this happens depends on the effective viscosities of the lithosphere and mantle. On page 1515 of this issue, Liu and Hasterok (*1*) discuss a novel method of constraining viscosities of the lithosphere from geophysical data.

Laboratory experiments on rock samples deformed under high pressures and temperatures show that viscosity is sensitive to many parameters, including temperature, stress, fluid content, and composition (*2*). Such experiments are necessarily performed at deformation rates much faster than actual geological processes. To apply the laboratory-derived viscosity laws to nature, they must be extrapolated over 10 orders of magnitude, introducing uncertainty. Moreover, it is unclear to what extent experiments on centimeter-scale samples are representative of the crust and lithosphere (*3*). As a result, the viscosity distribution of the lithosphere is one of the least certain parameters in geodynamics.

Alternative ways to determine viscosity on geological time scales are thus needed. A number of geophysical methods have been proposed, including postglacial rebound (*4*), geoid modeling (*5*), fitting global mantle-flow models to observed plate velocities (*6*), and postseismic relaxation studies (*7*). However, most of these techniques are sensitive to the larger-scale viscosity structure of the mantle and not all that much to the viscosity structure of the lithosphere. In some areas, well-understood geological structures occur, such as in Hawaii, where the load of the volcano bends the Pacific plate, or in the Zagros Mountains, where the crust is folded in a regular manner. In those cases, comparison of computer model results with observations can help to determine the material properties of the crust and lithosphere in a more direct manner (*8*, *9*). But these methods rely on having a good physical understanding of the underlying processes that formed these structures, which is only rarely the case.

Liu and Hasterok now propose a method that combines the results of magnetotelluric (MT) inversions with geodynamic models. MT inversions map out the lithosphere's electrical resistivity, which is sensitive to both fluid content and temperature. Making use of the fact that electrical resistivity and viscosity have a similar sensitivity to temperature, the authors propose a simple conversion factor to translate variations in electrical resistivity into variations in viscosity. Modeling of the Colorado Plateau (see the figure) shows that models with MT-derived lateral viscosity variations produce a much better fit to the GPS observations and topographies than do models without such variations.

This promising result suggests that MT inversion results give a first-order image of the variation of effective viscosities in the lithosphere, even though the magnitude of these variations needs to be calibrated with geodynamic flow models. Liu and Hasterok show that the use of nonlinear and brittle viscous-creep laws does not alter their basic conclusions. It remains unclear why electrical resistivity correlates so well with viscosity, but this relationship suggests that mechanically weaker zones in the lithosphere, which

Institute of Geosciences, Johannes Gutenberg University, D-55128 Mainz, Germany. Email: kaus@uni-mainz.de

Downloaded from http://science.sciencemag.org/ on October 7, 2016

Published by AAAS

have smaller effective viscosities, are preferred fluid pathways.

However, the results have only been obtained with two-dimensional models in a single location. It is unclear how uncertainties in the MT inversion affect the results. Other data such as gravity anomalies, stresses, and seismicity have not been taken into account. Moreover, the models have been fitted to the data by manually adjusting the input parameters. Thus, it remains to be seen whether the viscosity structure derived in this manner is uniquely constrained and to what extent the models satisfy other geophysical data.

Recently, geodynamic inversion approaches have been proposed that change input parameters automatically to minimize the misfit between models and observations (*10*, *11*). These approaches give uncertainty bounds on the rheological parameters of the lithosphere. In a recent study, Baumann and I have applied such a method to the India-Asia collision zone, using gravity anomalies, GPS velocities, and topography as data (*11*). The results show that the rheological creep law parameters obtained in this manner are consistent with, but often better constrained than, laboratory-based values. Yet there is often not a single unique model that fits the observations; instead, several sets of models fit the data nearly equally well, each with its own particular lithospheric viscosity structure (*12*). Incorporating more data in such inversions is likely to reduce the ambiguities of the inversion. The study of Liu and Hasterok suggests that MT data are a promising candidate.

Many questions remain about how tectonic processes work on geological time scales. Recent results, including those reported by Liu and Hasterok, show that much can be learned by comparing physically consistent models of lithospheric deformation with geophysical data sets. Coupling two- and three-dimensional models of the lithosphere with available geophysical data will help to constrain the effective viscosity of the present-day lithosphere. This will bring us a bit closer to understanding how the lithosphere deforms on geological time scales. ■

REFERENCES AND NOTES

1. L. Liu, D. Hasterok, *Science* **353**, 1515 (2016).
2. D. L. Kohlstedt, B. Evans, S. J. Mackwell, *J. Geophys. Res.* **100**, 17587 (1995).
3. E. B. Burov, in *Treatise on Geophysics, Volume 6—Crust and Lithosphere Dynamics*, G. Schubert, A. B. Watts, Eds. (Elsevier Science, 2007), pp. 99–151.
4. J. X. Mitrovica, A. M. Forte, *J. Geophys. Res.* **102**, 2751 (1997).
5. M. A. Richards, B. H. Hager, *J. Geophys. Res.* **89**, 5987 (1984).
6. T. W. Becker, *Geophys. J. Int.* **167**, 943 (2006).
7. A. M. Freed, T. Herring, R. Bürgmann, *Earth Planet. Sci. Lett.* **300**, 1 (2010).
8. P. Yamato, B. J. P. Kaus, F. Mouthereau, S. Castelltort, *Geology* **39**, 815 (2011).
9. S. Zhong, A. B. Watts, *J. Geophys. Res.* **118**, 6025 (2013).
10. V. Ratnaswamy, G. Stadler, M. Gurnis, *Geophys. J. Int.* **202**, 768 (2015).
11. T. S. Baumann, B. J. P. Kaus, *Geophys. J. Int.* **202**, 1289 (2015).
12. T. S. Baumann, *Geophys. J. Int.* 10.1093/gji/ggw279 (2016).

ACKNOWLEDGMENTS

Supported by European Research Council Starting Grant 258830.

10.1126/science.aai8442

Lithosphere dynamics

In this block diagram, the topography of the Colorado Plateau has been exaggerated by a factor of 10. Liu and Hasterok combine electrical resistivity, topography, and GPS velocities with geodynamic models to constrain flow velocities and lithospheric viscosity variations beneath the plateau.

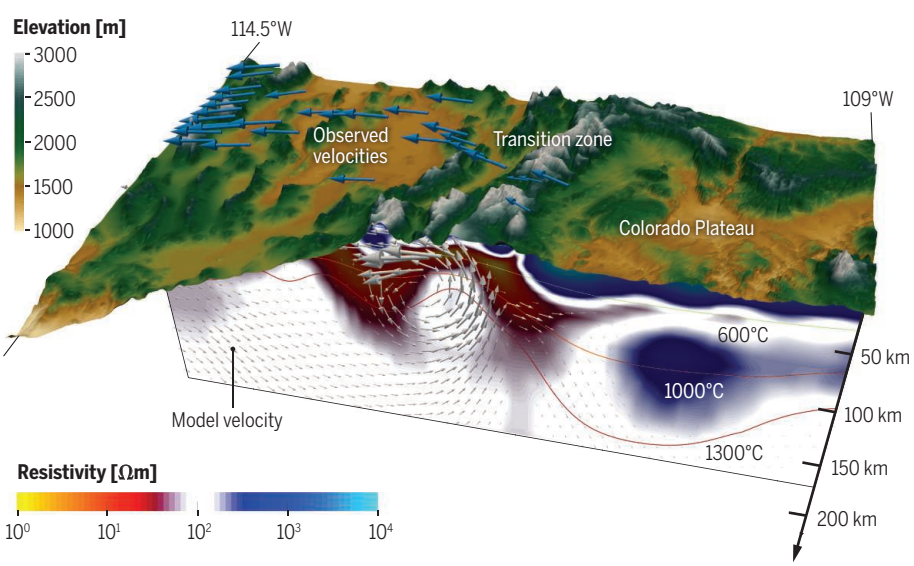

SOCIAL NEUROSCIENCE

Social memory goes viral

A precisely mapped brain network discriminates and remembers friends and strangers

By **Kapil Saxena**[1,2] *and* **Richard G. M. Morris**[1,2]

It is a curious feature of studies of recognition memory that the experimental subjects are almost always tested alone. They may be asked to scan a set of landscape pictures and later recognize having seen them before or to study a set of words or faces. For a social species such as ourselves—and mammals in general—being tested alone is a curious state of affairs. Social memory, social comparisons, and reciprocity have been a major driving force in brain evolution (*1*), and the effect of social interactions on memory deserves more attention. This experimental lacuna is now being put right, not only in social and evolutionary psychology and in work on "joint attention" by infants and their mothers, but also in animal studies that seek to identify the areas of the brain and the mechanisms mediating recognition of a familiar conspecific. On page 1536 of this issue, Okuyama *et al.* supplement behavioral analysis with an arsenal of modern viral vector–based, optogenetic, and imaging techniques to examine social memory (*2*). They identify the ventral hippocampus in the brain as critical for storing a social memory, or engram, with connectivity to the nucleus accumbens as key to the expression of such a memory (see the figure).

In this project, the RIKEN team waded into a long-standing controversy fueled by experiments using older techniques (e.g., brain lesions) about whether and how the hippocampal formation is involved in recognition memory. One prominent view is that the hippocampus is always involved in this type of memory (*3*); another is that it only becomes involved in recognition memory when the particular associations or relationships of a stimulus must be processed to achieve later recall (*4*, *5*). In this latter view, the ostensibly

[1]*Centre for Brain Development and Repair, INSTEM, Bangalore 560065, India.* [2]*Patrick Wilde Centre and Centre for Cognitive and Neural Systems, University of Edinburgh, Edinburgh, EH8 9JZ, UK. Email: r.g.m.morris@ed.ac.uk*

CREDIT: ADAPTED BY C. BICKEL/*SCIENCE* FROM A FIGURE BY T. S. BAUMANN, JOHANNES GUTENBERG UNIVERSITY

Downloaded from http://science.sciencemag.org/ on October 7, 2016

Published by AAAS

simpler identification of stimulus familiarity may be successfully realized in another part of the brain—the neocortex—at earlier stages of perceptual processing. Is social memory any different? Judging that someone is "familiar" is much simpler than full recall of the time or context of any preceding encounter. A further issue is whether all of the hippocampus, or just parts of it, might be involved in recognition memory (*6*, *7*).

Okuyama *et al.* used two behavioral techniques to look at social memory in mice. One involved social discrimination, the other a resident-intruder test, and both tested whether a second mouse involved in the test was familiar or novel. Arguably, the resident-intruder test involves a context association. Using ingenious viral-based techniques, which allowed selective inhibition of neurons in specific subregions of the hippocampus or their axonal terminals in brain regions to which they project, the RIKEN team enabled the neural activity of specific cells to be selectively silenced (e.g., through viral-mediated expression of light-sensitive archaerhodopsin). Turning neurons off is clearly a step forward from permanently damaging them with a lesion. It enables more exacting analyses of the specific neurons involved, even if physically intermingled with others. Repeated "on-off" testing also allows the use of a smaller number of animals for a larger number of observations. The clear result was that shutting down the ventral but not the dorsal hippocampus impaired both tests of social recognition memory.

Anatomical projection studies revealed connectivity from the ventral hippocampus to other brain regions—the basolateral amygdala, olfactory bulb, and nucleus accumbens—but it turned out that only shutting down afferents within the nucleus accumbens was essential for social memory. The development of an engineered line of mice, called Trpc4 mice, also enabled a particular layer of pyramidal cells within the ventral hippocampus to be assayed, as well as the shell region of the nucleus accumbens to which it projects. Optogenetic excitation of this pathway had the specific effect of making the test mouse perceive a novel mouse as if it were familiar. Careful timing of excitation and inhibition during interactions between two mice enabled activation of the hippocampal nucleus accumbens pathway to be identified as a signature of familiarity.

Tests of necessity such as these are not the same as seeing the neurons involved in a memory change their activity in response to familiarity or novelty. A further array of viral-based techniques was deployed to do this, including the use of a genetic marker of calcium signaling (the calcium sensor protein GCaMP6) coupled to the use of miniature endoscopes mounted on the heads of the test animals. An increase in the number of active cells was observed in the ventral but not the dorsal hippocampus as one mouse became familiar with another. Endoscopic imaging was supplemented by a further viral-based trick that enabled the labeling and manipulation of memory engram cells, by means of a fluorescent marker whose color changed over time as it was expressed. In this way, the proportion of coactivated cells was measured when a mouse was exposed to a familiar or unfamiliar "stranger" mouse. Coactivation increased with additional familiarization. Last, using a *c-fos* labeling technique to help identify the neurons activated by social memory, the team examined whether a social memory was truly forgotten over time or had just become quiescent. Strikingly, selective optogenetic activation of the engram cells at a time when the mice behaved as if they had forgotten which animals were familiar and which were novel revealed a reawakening of the memory. A bit like working on that vague sense of familiarity we have of someone we may have met long ago, reactivation of the network ensemble brought memory back to mind for the mouse, just as a retrieval cue may do for us.

This analysis of social memory through inhibition, excitation, connectional analyses, and direct brain-cell monitoring is remarkable. Still, a puzzling feature of the work is that the social memories of the mice were apparently quite short-lasting—generally present for a few hours but gone within a day or two. However, rodent societies are complex (*8*), and social memories clearly must last. It is hard to imagine that a mouse would forget a friend, a fellow burrow-mate, or even the mouse that yesterday stole its morsel of cheese. The use of these new techniques may yet unlock the puzzle of what makes social memories fade or last.

Innovation is everywhere in neuroscience just now. Mainly, we hear about new technologies, often inspired by genetics; these certainly are game changers. But conceptual changes are important as well, especially in relation to the development of animal models that allow interventional and translational studies. The long-standing assumption about any difference between a human and an animal study is that it is due to differences between the two species. However, this assumes that we are testing things in the same way. With the development of new analytically powerful approaches to social behavior, the style of behavioral neuroscience with animal models is changing rapidly. These new approaches could prove enormously valuable in finding treatments for autism spectrum disorder for which we still have little understanding of its associated abnormalities of social interaction. Social memory, not just social media, has gone viral. ■

Remembering friends and strangers

A diagram of the mouse brain shows how the ventral hippocampus mediates social memory. Cells in the ventral hippocampus (red), but not the dorsal hippocampus, project to several brain areas. Only the circuit to the shell region of the nucleus accumbens is found to influence social memory.

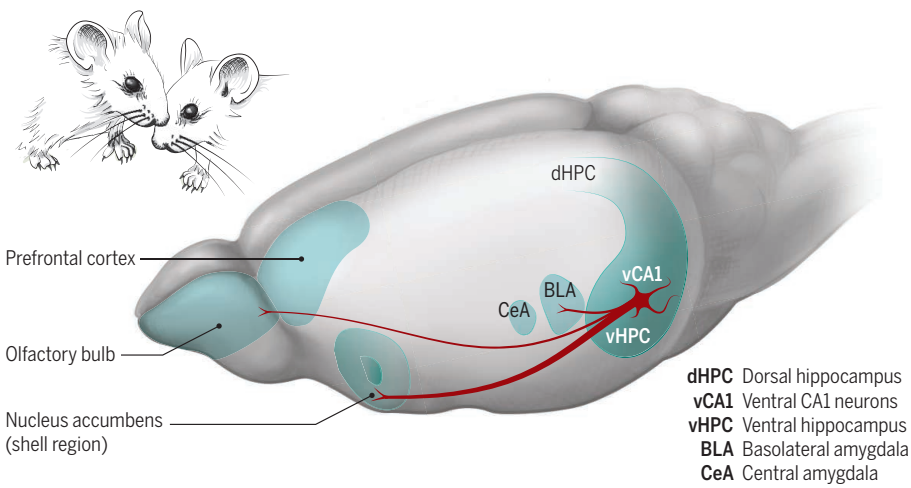

GRAPHIC: K. SUTLIFF/*SCIENCE*

REFERENCES

1. R. M. Whitaker *et al.*, *Sci. Rep.* **6**, 31459 (2016).
2. T. Okuyama *et al.*, *Science* **353**, 1536 (2016).
3. L. R. Squire, *Psych. Rev.* **99**, 195 (1992).
4. J. P. Aggleton, M. W. Brown, *Behav. Brain Sci.* **22**, 425 (1999).
5. H. Eichenbaum, A. P. Yonelinas, C. Ranganath, *Annu. Rev. Neurosci.* **30**, 123 (2007).
6. F. L. Hitti, S. A. Siegelbaum, *Nature* **508**, 88 (2014).
7. D. A. Caruana, G. M. Alexander, S. M. Dudek, *Learn. Mem.* **19**, 391 (2012).
8. R. Lore, K. Flannelly, *Sci. Am.* **236**, 106 (1977).

10.1126/science.aai7788

Downloaded from http://science.sciencemag.org/ on October 7, 2016

Published by AAAS

NEURODEGENERATIVE DISEASE

Immune receptor for pathogenic α-synuclein

An immune protein facilitates neuronal uptake of a Parkinson's disease–associated protein

By **Mathias Jucker**[1] *and* **Mathias Heikenwalder**[2]

In neurodegenerative diseases such as Parkinson's disease and Alzheimer's disease, specific proteins misfold into β sheet–rich conformations that aggregate. For Parkinson's disease and Lewy body dementia, the hallmark pathology is neuronal inclusions of aggregated α-synuclein called Lewy bodies and Lewy neurites. The spreading of these lesions in the brain is at least partly the result of prion-like self-propagation and cell-to-cell transfer of pathogenic α-synuclein assemblies (*1*). Inoculation of brain extracts containing aggregated α-synuclein and also synthetic α-synuclein fibrils into mice and nonhuman primates induces aggregation at the injection site, followed by the formation of lesions in neuronally connected brain regions, and ultimately neurodegeneration (*2*, *3*). The appearance of α-synuclein lesions in fetal brain grafts in Parkinson's disease suggests that cell-to-cell spreading of lesions also occurs in humans. There is also in vitro evidence for cell-to-cell transfer of α-synuclein assemblies (*2*). However, the mechanism of intercellular transmission of α-synuclein aggregates—as well as of other pathogenic protein assemblies, such as those consisting of Aβ and tau in Alzheimer's disease—is poorly understood (*1*). On page 1513 of this issue, Mao *et al.* (*4*) report that the cell-surface lymphocyte activation gene 3 protein (LAG3/CD233) is a neuronal receptor mediating the endocytosis of aggregated α-synuclein, enabling the spread and toxicity of α-synuclein assemblies.

Mao *et al.* screened a library of transmembrane proteins for potential binding to recombinant α-synuclein fibrils, but not monomeric α-synuclein. The binding proteins identified included amyloid precursor–like protein 1 (APLP1) and neurexins, but the strongest binding partner for α-synuclein fibrils was LAG3. The screening approach was virtually identical to a previous endeavor that identified the cellular prion protein as a receptor for oligomeric assemblies of Aβ (*5*). Interestingly, APLP1 was also found in the oligomeric Aβ screen and thus may be a general binding protein for amyloid structures. By contrast, LAG3 binding appeared to be specific for aggregated α-synuclein, which was confirmed in subsequent cellular assays using fibrillar Aβ and tau (*4*).

Upon binding to LAG3, α-synuclein is endocytosed via a clathrin-dependent mechanism. LAG3-dependent endocytosis was also observed with brain extracts containing α-synuclein aggregates. Subsequent cell-to-cell movement of α-synuclein was observed in a three-chamber cell system using mixtures of wild-type cells and cells lacking LAG3 (*Lag3*$^{-/-}$). Inoculation of α-synuclein fibrils into wild-type mice induced α-synuclein lesions, neuron loss, and behavioral deficits; these effects were diminished in *Lag3*$^{-/-}$ mice. APLP1, neurexins, or other known α-synuclein–binding partners such as heparin sulfate proteoglycans or sodium-potassium adenosine triphosphatase (*6*, *7*) may be responsible for the residual toxicity in *Lag3*$^{-/-}$ mice.

LAG3 (*8*) has so far been linked mainly to immunological functions. It is strongly expressed on activated T, natural killer, and B cells, where it dampens several autoimmune diseases (*9*). Moreover, LAG3 coordinates plasmacytoid dendritic cell homeostasis and contributes to humoral immune responses (*10*). Suppression of LAG3 function reduces T cell exhaustion, boosting cellular immunological antitumor or antigenic functions (*9*). No or little expression of LAG3 has been reported in the brain, although LAG3 expression may be induced under certain neurodegenerative or neuroinflammatory conditions. Mao *et al.* now report LAG3 expression in neuronal cultures from wild-type mice.

LAG3 contains four extracellular immunoglobulin superfamily domains. The main α-synuclein binding site resides in domain 1 (D1), with additional weak binding in D2 and D3, but not D4. Notably, D1 of LAG3 is also crucial for binding major histocompatibility complex (MHC) class II molecules (*11*) (see the figure). Differences in the amino acid sequence or the three-dimensional domain structure of D1 might mediate preferential binding to α-synuclein. Interestingly, other immunoglobulin superfamily domain–containing proteins such as CD4, which also contains a MHC class II–binding D1, do not bind α-synuclein. Immunoglobulin domains are common biological modules in several different protein classes, facilitating interactions with each other. The presence of abundant β sheets in these domains also enables binding to other proteins. Increased β sheets in misfolded α-synuclein may thus be important for its binding to LAG3. Notably, alternative splicing or proteolytic cleavage can generate soluble LAG3 (including the D1 to D4 domains) (*9*, *12*), which may also mediate binding to misfolded α-synuclein.

Cell-to-cell transmission of pathogenic protein assemblies is a poorly understood multistep process involving cellular uptake, propagation, and escape from the cell. It is unclear which stage (or stages) of this cycle mediate neurotoxicity, and neurotoxic

[1]*Hertie Institute for Clinical Brain Research, University of Tübingen, and German Center for Neurodegenerative Diseases (DZNE), 72076 Tübingen, Germany.* [2]*Division of Chronic Inflammation and Cancer, German Cancer Research Center (DKFZ), Heidelberg, Germany. Email: mathias.jucker@uni-tuebingen.de*

Intercellular transmission

LAG3 functions in neurons to facilitate the spread of pathogenic α-synuclein.

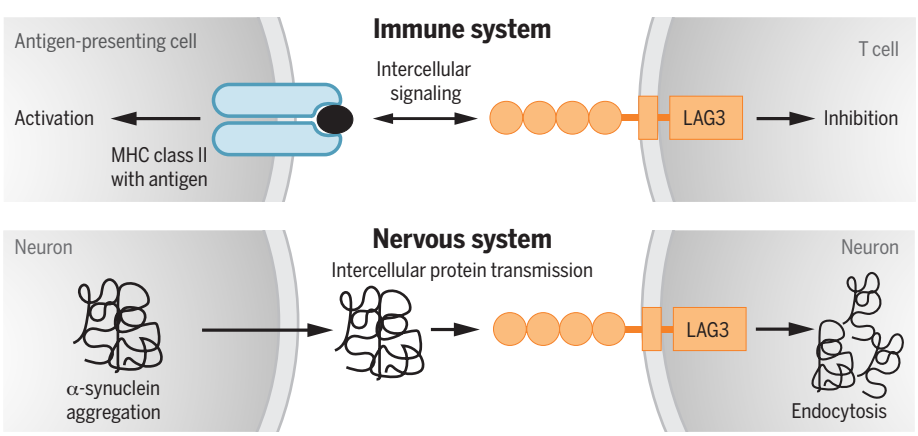

GRAPHIC: N. CARY/*SCIENCE*

Downloaded from http://science.sciencemag.org/ on October 7, 2016

Published by AAAS

mechanisms may vary between pathogenic proteins or even between cells (*13*). However, interfering with any stage has the potential to block the spreading and neurotoxicity of proteopathic lesions (*1*, *13*). It will be important to determine whether LAG3 is simply a cell-surface binding protein that mediates the uptake of pathogenic α-synuclein, or whether LAG3 might mediate further intracellular trafficking or signaling or propagation of aggregates. Another crucial step in transmission is the exit of pathogenic α-synuclein from cells. Strikingly, an unconventional deubiquitylase USP19-dependent secretion pathway for misfolded cytoplasmic proteins, including misfolded α-synuclein but not tau (*14*), suggests that the mechanisms for uptake and release may be very specific for given proteopathic aggregates.

In Parkinson's disease, α-synuclein aggregation in the brain begins many years before the onset of symptoms (*15*). Thus, interfering with the α-synuclein cascade is likely to be most effective when initiated at an early preclinical stage. LAG3-blocking antibodies were used by Mao *et al.*, and anticancer agents that block LAG3 have been developed to overcome immunosuppressive mechanisms within the tumor microenvironment (*9*). However, to minimize the risk of autoimmune or hyperimmune activation phenotypes, very specific suppression of LAG3 in the brain is needed if this protein is to be safely targeted in the treatment of brain diseases.

If LAG3 is confirmed to be a receptor for pathogenic α-synuclein, it will be important to define the structural requirements for binding and the nature of the pathogenic α-synuclein species that binds LAG3. Although many important issues remain to be resolved, the remarkable interaction of LAG3 and aggregated α-synuclein calls for additional research to determine the physiological function of LAG3 in the brain and to evaluate the potential of LAG3 as a therapeutic target for modifying the course of Lewy body dementia and Parkinson's disease. ■

REFERENCES

1. M. Jucker, L. C. Walker, *Nature* **501**, 45 (2013).
2. J. L. Guo, V. M. Lee, *Nat. Med.* **20**, 130 (2014).
3. A. Recasens *et al.*, *Ann. Neurol.* **75**, 351 (2014).
4. X. Mao *et al.*, *Science* **353**, aah3374 (2016).
5. J. Lauren, D. A. Gimbel, H. B. Nygaard, J. W. Gilbert, S. M. Strittmatter, *Nature* **457**, 1128 (2009).
6. B. B. Holmes *et al.*, *Proc. Natl. Acad. Sci. U.S.A.* **110**, E3138 (2013).
7. A. N. Shrivastava *et al.*, *EMBO J.* **34**, 2408 (2015).
8. F. Triebel *et al.*, *J. Exp. Med.* **171**, 1393 (1990).
9. L. T. Nguyen, P. S. Ohashi, *Nat. Rev. Immunol.* **15**, 45 (2015).
10. T. Okamura *et al.*, *Nat. Commun.* **6**, 6329 (2015).
11. B. Huard *et al.*, *Proc. Natl. Acad. Sci. U.S.A.* **94**, 5744 (1997).
12. N. Li *et al.*, *EMBO J.* **26**, 494 (2007).
13. D. W. Sanders, S. K. Kaufman, B. B. Holmes, M. I. Diamond, *Neuron* **89**, 433 (2016).
14. J. G. Lee, S. Takahama, G. Zhang, S. I. Tomarev, Y. Ye, *Nat. Cell. Biol.* **18**, 765 (2016).
15. K. Del Tredici, H. Braak, *Mov. Disord.* **27**, 597 (2012).

10.1126/science.aai9377

Decision-making behavior in bumblebees appears analogous to optimism in humans.

PHOTO: SMUDGE 9000/FLICKR

BEHAVIOR

Bee happy

Bumblebees show decision-making that reflects emotion-like states

By **Michael T. Mendl** *and* **Elizabeth S. Paul**

In his book, *The Expression of the Emotions in Man and Animals*, Charles Darwin noted that "Even insects express anger, terror, jealousy, and love by their stridulation." Almost 150 years later, spurred by an interest in the evolutionary roots of emotional (affective) processes and their underlying mechanisms, there has been a sudden upsurge of research into the question of whether insects and other invertebrates may indeed have emotion-like states (*1*–*4*). Recent work has focused on negative affect, but on page 1529 of this issue, Perry *et al.* (*5*) broaden the scope to consider positive emotions. The authors report decision-making behavior in bumblebees that is analogous to optimism in humans and may reflect positive affect in both humans and other species (*6*–*8*). Moreover, the behavior appears to depend on the activity of dopamine, a neurotransmitter involved in the processing of reward in humans.

Emotions are quintessentially subjective experiences—positive or negative feelings such as happiness or anger—so how can such private states be studied in nonhuman animals? One way is to provide an operational definition of emotion that allows researchers to identify what state an animal is in and hence to search for associated underlying mechanisms, and physiological, behavioral and cognitive markers that, unlike feelings, can be measured objectively. A recent suggestion is to use general properties of human emotion, including valence [positivity or negativity; a key defining characteristic of human emotion (*7, 9*)], arousal or scalability, persistence after a stimulus or event, and generalization across situations—so-called "emotion primitives" (*1*)–to identify affective states in other species.

Another operational definition is that emotions are states elicited by rewards and punishers, where a reward is something for which an animal will work and a punisher is something that it will work to avoid (*7, 9, 10*). On this basis, an animal exposed to a punisher is in a negative affective state. Even if researchers disagree, such definitions lay out assumptions that can be argued and improved, and make clear exactly why a particular method for inducing an emotion, or a particular measure of emotion, is being studied. Many scientists are agnostic about whether these operationally defined states are consciously experienced in animals, and it is possible that some species subjectively

Centre for Behavioural Biology, School of Veterinary Science, University of Bristol, BS40 5DU, UK. E-mail: mike.mendl@bris.ac.uk

Downloaded from http://science.sciencemag.org/ on October 7, 2016

Published by AAAS

experience emotion whereas others exhibit behavioral and physiological indicators of emotion ("emotion-like") without any accompanying feeling (*11*).

Perry *et al.* used a rewarding sweet sucrose solution to induce a positive emotional state in bumblebees, in line with the rewards-punishers operational definition. They then confirmed this state with a cognitive bias test that is based on the finding that human emotions can bias decision-making under ambiguous conditions (*6*). Thus, happy people are more likely than unhappy people to make optimistic judgments about ambiguous situations (*7*). This cognitive bias test is now used widely in animal emotion research (*8*). Bumblebees were trained such that in any trial, a cylinder was placed either on one side of a foraging arena next to a green card or on the other side next to a blue card. One of the location-color combinations indicated that the cylinder contained a 30% sucrose solution reward, whereas the other location-color combination indicated that the cylinder contained just water. The bees learned to fly faster to the cylinder on trials with the sucrose reward configuration (see the figure). Occasional trials were then used to test their responses to ambiguity by presenting the cylinder between the two trained locations and next to an intermediately colored (blue-green) card. The prediction was that bees in a positive affective state would fly faster to intermediate cues, analogous with an optimistic judgment of ambiguity (*6*). Indeed, Perry *et al.* found that bees given an unexpected 60% sucrose reward to induce a positive affective state prior to an ambiguity trial, flew faster to the cylinder than non-rewarded bees.

Perry *et al.* then tested the idea that emotional states generalize across contexts (*1*), observing that the 60% sucrose solution also improved the speed of recovery (resumption of foraging) from a subsequent predator attack simulated by brief restraint. The effect of sucrose disappeared when a dopamine antagonist (fluphenazine) was topically applied before the predation test. Fluphenazine also prevented sucrose-induced optimistic-like responses to ambiguity in the cognitive bias test.

The findings of Perry *et al.* suggest that a sucrose reward induces a putatively positive state in an insect that persists for at least a short time, has effects across both positive (foraging) and negative (simulated predation) contexts, alters behavior as predicted in a cognitive bias test specifically designed to assess the valence of affective states, and is mediated by dopaminergic circuitry. Such a state satisfies a number of the criteria identified by the operational definitions of emotion (*1, 10*).

It is possible that the induced behavioral state of the bees, rather than having affective properties, was simply one of general increased activity resulting from the energizing effects of sucrose. However, Perry *et al.* showed that the sucrose-induced faster flight in the ambiguity test was not observed in other foraging contexts, and did not occur in response to novel stimuli, indicating that it was unlikely to be an effect of a general activity increase. In the absence of a specific control in the simulated predation context, it remains possible that sucrose may have exerted its effects via a general energizing effect on the speed of recovery after restraint.

The finding that a dopamine antagonist blocked the effects of sucrose in the foraging and predator tests indicates that the same underlying state was at work in both contexts. For example, increased activity of reward-sensitive dopaminergic neurons, which could be likened to a primitive positively valenced state, may bias action selection in favor of active or approach behavior in response to relevant stimuli (*12*). On its own, however, this mechanism would not explain the specificity of such a response to ambiguous as opposed to novel stimuli. Moreover, given that dopamine is also involved in punishment processing (*12, 13*), fluphenazine would have been expected to interfere with dopamine-mediated suppression of action in response to simulated predation in the absence of a sucrose reward, but this was not observed.

The study of Perry *et al.* extends recent work on invertebrate emotion, in particular by focusing on positive states and their impact across contexts. It also supports the hypothesis that one function of affective states is to act as a predictor of decision outcome probabilities that guides decision-making, particularly under ambiguity in which current information on outcomes is lacking (*9*). Given the likely adaptive value of such emotion-cognition interactions, it is not surprising that insects, like other taxa, possess emotion-like systems to implement them.

Many questions remain to be answered, including whether cross-context effects are indeed the result of an internal state that is mediated by the same underlying neural mechanisms. Likewise, do induced negative states also show cross-context effects and are these mediated by the same or different neural processes? The extent to which such states exhibit other operationally defined properties of emotion and hence warrant the label, is also unclear. Finally, whether "emotion-like" states in insects are accompanied by emotional feelings remains unanswered, but the possibility of insect consciousness is now the topic of exciting new theories and vigorous debate (*14, 15*). ■

Testing emotion-like states

A cognitive bias test examines affect-induced changes in decision-making under ambiguity. Bees are trained to associate one set of cues with a sucrose reward and another set of cues with no reward.

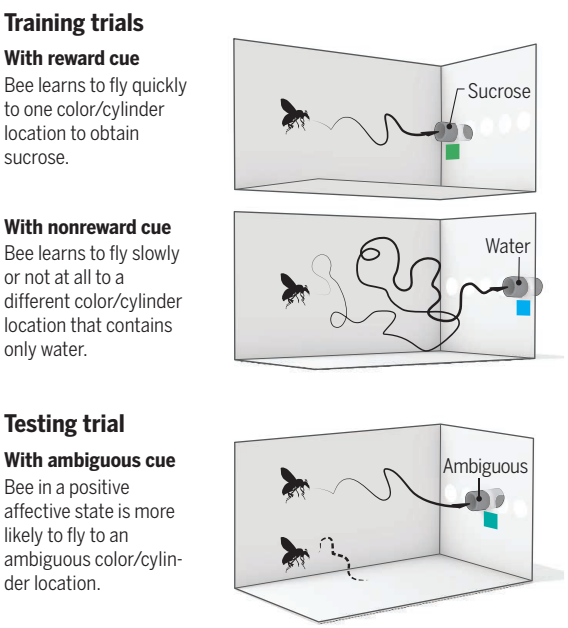

REFERENCES AND NOTES

1. D. J. Anderson, R. Adolphs, *Cell* **157**, 187 (2014).
2. M. Bateson, S. Desire, S. E. Gartside, G. A. Wright, *Curr. Biol.* **21**, 1070 (2011).
3. P. Fossat, J. Bacqué-Cazenave, P. De Deurwaerdère, J.-P. Delbecque, D. Cattaert, *Science* **344**, 1293 (2014).
4. W. T. Gibson *et al.*, *Curr. Biol.* **25**, 1401 (2015).
5. C. J. Perry, L. Baciadonna, L. Chittka, *Science* **353**, 1529 (2016).
6. E. J. Harding, E. S. Paul, M. Mendl, *Nature* **427**, 312 (2004).
7. E. S. Paul, E. J. Harding, M. Mendl, *Neurosci. Biobehav. Rev.* **29**, 469 (2005).
8. L. Gygax, *Anim. Behav.* **95**, 59 (2014).
9. M. Mendl, O. H. P. Burman, E. S. Paul, *Proc. R. Soc. B Biol. Sci.* **277**, 2895 (2010).
10. E. T. Rolls, *Emotion Explained* (Oxford Univ. Press, 2005).
11. K. C. Berridge, P. Winkielman, *Cogn. Emotion* **17**, 181 (2003).
12. Y. Aso *et al.*, *eLife* **3**, e04580 (2014).
13. S. Waddell, *Curr. Opin. Neurobiol.* **23**, 324 (2013).
14. A. B. Barron, C. Klein, *Proc. Natl. Acad. Sci. U.S.A.* **11**, 4900 (2016).
15. C. Klein, A. B. Barron, *Anim. Sentience* 2016.100 (2016).

ACKNOWLEDGMENTS

E.S.P. was supported by grants from the U.K. National Centre for the Replacement, Refinement & Reduction of Animals in Research (NC3Rs) research council (grant K/00008X/1 to M.T.M.) and the U.K. Biotechnology and Biological Sciences Research Council (grant BB/K00042X/1 to C. J. Nicol).

10.1126/science.aai9375

GRAPHIC: V. ALTOUNIAN/*SCIENCE*

Downloaded from http://science.sciencemag.org/ on October 7, 2016

Published by AAAS

RETROSPECTIVE

James W. Cronin (1931–2016)

A Nobel laureate raised the profile of physics worldwide

By **Alan A. Watson**

James W. Cronin, who shared the Nobel Prize for Physics in 1980 with Val L. Fitch for the discovery of an unexpected breakdown in the symmetries of charge (C) and parity (P), died on 25 August 2016. Their work helps explain the conundrum as to why there is more matter than antimatter in the universe. An outstanding experimentalist and gifted data analyst, Cronin's talents led to major discoveries in the fields of particle and cosmic-ray physics.

Jim Cronin was born in 1931 in Chicago, Illinois, and raised in Dallas, Texas, where his father was a classics professor at Southern Methodist University. In 1953, he started graduate work at the University of Chicago under Samuel K. Allison, studying energy levels in the carbon nucleus. He moved to the Brookhaven National Laboratory in New York, and then to Princeton University, where he honed the spark-chamber technique to a fine art. These devices were used on many projects, including the CP violation work and the Brookhaven experiment that established the existence of two types of neutrinos. In 1971, Jim returned to the University of Chicago because of its proximity to the Fermi National Accelerator Laboratory (FNAL) and because of the location of his wife's family.

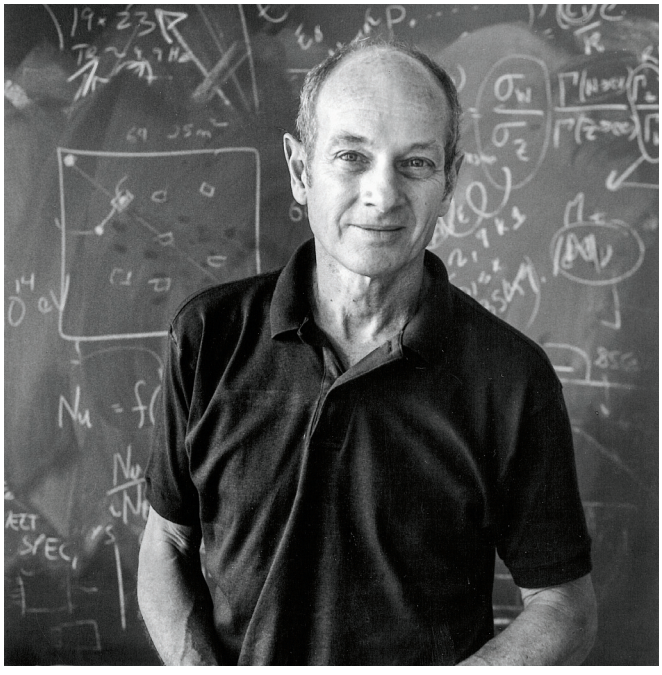

In 1977, Jim was appointed head the FNAL Colliding Beams division but resigned soon after. A largely administrative role did not suit him: He was a man who liked a very active part in whatever experiment interested him. A golden age of particle physics was ending, and experiments that required teams of more than 100 people did not appeal to him. But he had one last hurrah: In 1982, while on sabbatical leave in Geneva, Switzerland at CERN (the European Organization for Nuclear Research), he made, with 10 others, what remains the best direct measurement of the lifetime of the neutral pion.

I first saw Jim at a Rencontres de Moriond physics conference in France in March 1981, shortly after he had won the Nobel Prize. A group of skiers assembled at the top of a slope, each carrying a flaming torch marking out Jim's initials; they then skied down together. This dramatic display was a striking indication of how he was revered by his colleagues. In 1986, Jim decided to study cosmic rays and, with a tenacity and care that I later came to know well, he visited cosmic-ray strongholds to discuss his design for an instrument to search for gamma rays from a binary stellar system. We first met in Leeds, U.K., in November 1986. A firm friendship, fueled by a mutual interest in malt whisky, quickly developed. In 1991, we decided to build a collaboration and raise the money needed to construct an instrument of unprecedented size to study cosmic rays with energies up to 10^{20} electronvolts. Flux estimates of such events, about one per square kilometer per century, demanded a huge detector. Thirteen years later, the Pierre Auger Observatory, covering 3000 km^2 of Western Argentina (the size of Rhode Island), started taking data and continues to do so with a team of over 400 hundred scientists from 16 countries. The route to this achievement was strewn with difficulties, and it was a privilege to be at Jim's side as we overcame them, largely through his formidable drive and the discrete use of his status. For example, although the United States was not a member of the United Nations Educational, Scientific and Cultural Organization (UNESCO), he extracted $100,000 for scientists from developing countries to work on a 6-month design study at FNAL, got support for us to tour the Far East to raise interest, and prised $1 million from the University of Chicago to build a stunning center at the site. We visited Hanoi and, although the United States then had no diplomatic relations with Vietnam, met the vice president of the Communist Party, a former theoretical particle physicist.

Evaluation of our plans by an international body proved impossible, so Jim invited a panel of experts, including a Nobel laureate, to assess us. Their report helped raise $50 million, an unprecedented sum for cosmic-ray work, although one agency commented, "Of course it is a favorable report: You chose the committee." Jim also formed a remarkable relationship with Argentina's President Carlos Menem, who gave 11 million pesos. They met three times, Menem appearing to believe that being photographed with a Nobel laureate might help to have the constitution changed to allow him to run for a third term.

The success of the Auger Observatory, coupled with Jim's many visits, has greatly enhanced the profile of fundamental physics in Argentina, Brazil, Mexico, and Vietnam. Although the Vietnamese group is no longer a member, a thriving astrophysics school has evolved there. The small town of Malargüe, Argentina, which hosts the observatory, now has the James Cronin School, financed by Jim and by private donors. A U.K. engineer, who developed the communications system, founded his own company, with his first contract, to make the single-track rail-lines in Scotland safer and more reliable, using Auger technology. Neither of us had realized that the Auger Collaboration would become so large, but Jim thrived in the environment, stimulating young people greatly, while carrying out his own analysis using the FORTRAN programming language and an ancient graphics package hosted on a dedicated Chicago computer.

Jim will be sorely missed by all who knew him. Without his strong sense of direction and his persuasive skills, the Pierre Auger Observatory, and many other projects, would never have succeeded. ■

School of Physics and Astronomy, University of Leeds, UK. Email: a.a.watson@leeds.ac.uk

10.1126/science.aaj2021

PHOTO: UNIVERSITY OF CHICAGO NEWS OFFICE

Downloaded from http://science.sciencemag.org/ on October 7, 2016

Published by AAAS

POLICY FORUM

POLITICAL SCIENCE

Growing pains for global monitoring of societal events

Automated event coding raises promise and concerns

By Wei Wang,[1] Ryan Kennedy,[2] David Lazer,[3,4] Naren Ramakrishnan[1]

There have been serious efforts over the past 40 years to use newspaper articles to create global-scale databases of events occurring in every corner of the world, to help understand and shape responses to global problems. Although most have been limited by the technology of the time (*1*) [see supplementary materials (SM)], two recent groundbreaking projects to provide global, real-time "event data" that take advantage of automated coding from news media have gained widespread recognition: International Crisis Early Warning System (ICEWS), maintained by Lockheed Martin, and Global Data on Events Language and Tone (GDELT), developed and maintained by Kalev Leetaru at Georgetown University (*2*, *3*). The scale of these programs is unprecedented, and their promise has been reflected in the attention they have received from scholars, media, and governments. However, they suffer from major issues with respect to reliability and validity. Opportunities exist to use new methods and to develop an infrastructure that will yield robust and reliable "big data" to study global events—from conflict to ecological change (*3*).

Automated event coding parses individual sentences into SUBJECT VERB OBJECT format and categorizes the action using a framework like CAMEO (Conflict and Mediation Event Observations). So a statement like "Secretary of State John Kerry complained about Russia's support of Syria's Bashar al-Assad" would be coded as US GOVERNMENT/DISAPPROVE/RUSSIAN GOVERNMENT. This can be refined into a numeric level of hostility or cooperation by using scales like the Goldstein Score. Whereas CAMEO focuses on categories for international and domestic conflict, similar frameworks could be developed for almost any kind of interaction in news media (e.g., transactions between businesses or debates over scientific findings).

Uses for the resulting data have been manifold. Hand-coded and automated event data have been used to anticipate conflict escalation (*2*). When combined with statistical and agent-based models, ICEWS claims a forecasting accuracy of 80%. GDELT has been used to track, e.g., wildlife crime and the rise of hate speech following the U.K. Brexit vote.

There are several challenges in the current approach. First, the focus on sentences removes a great deal of context. Event occurrences do not neatly partition into sentences. This lack of context, for example, often fails to distinguish rereporting of historic events, and this results in high rates of duplication.

> ***"Event data can provide insights into...global problems, from...security to the spread of diseases."***

Second, event data programs can have inconsistent corpuses over time. For instance, GDELT has expanded the number and variety of its sources. Although expansions are positive—incorporating, for example, more non-Western news sources—there is difficulty interpreting what a spike in GDELT data at a particular time means; the project has not been entirely transparent on how these expansions have taken place. ICEWS has been more consistent about maintaining a common set of sources across nearly 25 years.

Third, the text-processing systems used in event coding are still similar to ones developed more than 20 years ago. Although ICEWS has recently begun leveraging a machine-learning approach, GDELT still relies on dictionary-based pattern matching that leads to overly simplified or misclassified coding instances. The field of text processing has developed a range of tools to address these issues (*4*, *5*). Finally, although there are a few large event-coding programs, the academic groups working on these problems are surprisingly diffuse and isolated (see SM).

RELIABILITY

Our first set of experiments deals with the reliability of event data—whether programs ostensibly using similar coding rules produce similar data. We used four sources of event data [ICEWS, GDELT, Gold Standard Report (GSR), and Social, Political, and Economic Event Database (SPEED)], all designed to detect protest events. GDELT and ICEWS are fully automated and are the best attempts so far at real-time global event data. The GSR data set, generated by the nonprofit MITRE Corporation, is hand-coded from local and international newswires in Latin America since 2011 (*6*). SPEED is a semiautomated global event data system by the University of Illinois that uses a combination of human and automated techniques for identifying events. It touts the high validity of its event coding (*7*). GSR and SPEED were developed to provide a "ground truth," but their methods would be difficult and expensive to scale. Despite these systems' different origins (e.g., ICEWS was meant to encode strategic interactions, often among nation-states, and GSR was meant to focus on tactical, local issues) (see SM), we anticipate that overall there should be a high correlation between the time series of events generated by these projects, even if the event counts are not comparable.

We find a weak correlation between event data collections [correlation coefficient (r) < 0.3]. The average correlation between GDELT and the GSR across Latin America is 0.222, and the correlation between ICEWS and the GSR is 0.229. SPEED and GDELT records match (i.e., both data sets recorded a protest happening on the same day) 17.2% of the time. SPEED and ICEWS agree on 10.3% of events. ICEWS and GDELT rarely agree with each other, with an average correlation across Latin America of 0.317 (see SM). Correlations between countries improve when there are large upticks in event counts. For example, the increase in protests in Venezuela in January 2014 is well captured by both ICEWS and GDELT (see the chart). They also improve when the time scales are rougher (from daily to weekly or monthly) (see SM). Reliance on English-language news coverage results in stronger correlations for states more often in the Western press (e.g., Brazil) (*8*) (see SM).

VALIDITY

To assess the the degree to which event-coding projects reflect unique real-world events, we leveraged a special characteristic of the GDELT data set. Since its launch in April 2013, GDELT has provided URLs for most of its coded events. We looked at pro-

[1]Discovery Analytics Center, Virginia Tech, Arlington, VA 22203, USA. [2]Center for International and Comparative Studies, University of Houston, Houston, TX 77204, USA. [3]Lazer Lab, Northeastern University, Boston, MA 02115, USA. [4]Institute for Quantitative Social Science, Harvard University, Cambridge, MA 02138, USA. Email: rkennedy@uh.edu

Downloaded from http://science.sciencemag.org/ on October 7, 2016

Published by AAAS

test events up to 2 July 2014 (431,549 records); extracted content for records with a valid URL (344,481 records); and filtered them to assess the validity of their classification as protest events. This yielded 113,932 unique, nonduplicated events that are highly probable to be about protests at the time reported. Even for these filtered records, only 49.5% are classified as referring to actual protests, roughly in line with what we found in 1000 human-coded records (see SM). After keyword and temporal filtering, de-duplication of events, and machine-learning classification of real events from nonevents or planned events, only 21% of GDELT's valid URLs indicate a true protest event.

The ICEWS system was more robust (about 80% of keyword-filtered events were classified as protest events) but still vulnerable to duplicate events (<20% of the recorded events). Thus, computer-automated event data often duplicate and misclassify events, and tools, including the ones used here, deal with many of these issues (*4*, *5*). Similar tests for the other 19 event categories in GDELT and ICEWS found similar problems (see SM).

Weekly count of protest events in Venezuela

Event data from GDELT, Global Data on Events Language and Tone; ICEWS, International Crisis Early Warning System; and GSR, Gold Standard Report (see suppl. materials).

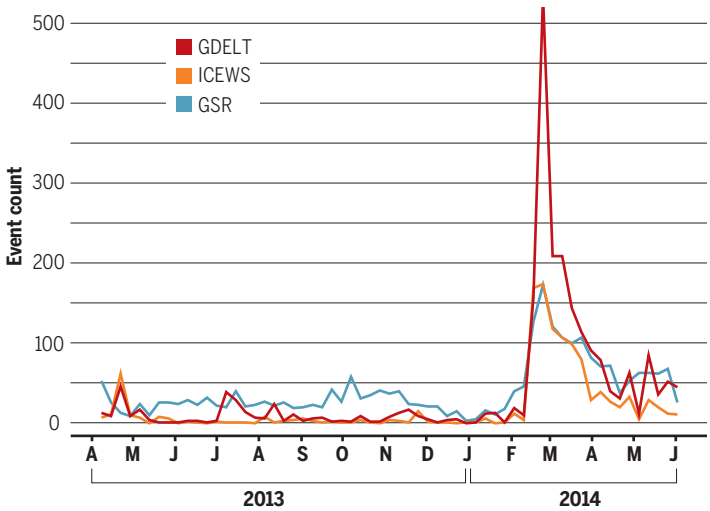

GRAPHIC: N. CARY/SCIENCE

POLICY IMPLICATIONS

Coding of interactions in news media is complex, as it involves actor recognition and normalization, time-frame detection, geocoding, event encoding, classification, multilingual support, and other issues. Yet the history of event data has been one of small teams and underfunded research. It has not helped that much of the development has taken place in political science, a discipline under constant threat of having its National Science Foundation (NSF) funding cut by Congress.

As scholars and government agencies create the next generation of large-scale event data, two goals should shape their efforts. First, new efforts must develop a multidisciplinary community of scholars, including computational linguists, data analytics professionals, information extraction practitioners, and domain experts. Although there have been improvements in the natural language processing used for ICEWS (*9*), innovation in the event data field has been slow, especially in handling contextual features and temporal and geographic information. Neither ICEWS nor GDELT were designed to de-duplicate events; multiple occurrences have sometimes been used to denote event significance and to support improved modeling. The one-sentence-per-event model is not sufficient for predictive, diagnostic, or abductive reasoning. Research on probabilistic databases can help one reason about inconsistency issues in information extraction and how best to integrate imprecise information into event coding (*10*, *11*). It is time to develop a strong community of teams competing to create the best possible event data, and event-coding software should be released publicly to encourage community engagement.

Second, the corpus used to create event data must be made explicit, and, to the extent possible, shared between teams. As demonstrated by legal issues faced by GDELT [a dispute over use of source materials resulted in scholars abandoning the project and obstacles to using the data for publication (see SM)], the current system, where corpus development can only be done by well-funded individual teams with exclusive rights to material, is problematic and encourages atomization of the field. Such a corpus should include more non-English sources to avoid some of the issues observed above (see SM).

We recommend developing open test beds of event data against which different approaches can be tested. These test beds should be composed of a representative set of textual data, with some portion hand-coded. Such test beds can be used in contests, like those sponsored by DARPA (Defense Advanced Research Projects Agency) or TREC (Text Retrieval Conference), where different approaches to text analysis compete to produce the best automated coding for event data. This would allow scholars to test tools already developed for text analysis in other areas and to produce tools that deal with tracking interactions from media reports.

A consortium should be developed to provide real-time controlled access to a comprehensive array of copyrighted material, to protect the business interests of news agencies, and to elicit broader social interest in event data. The UN Global Pulse initiative and Flowminder in Sweden, which address similar issues regarding cell phone data, could provide a model.

Programs like those proposed here have been tried in other areas, such as social media analysis and search-engine technology, with strong results (*12*). Such an effort can go a long way toward settling the debate over the extent to which fully automated approaches, like those of GDELT and ICEWS, can compete with semiautomated approaches like that of SPEED. Event data can provide insights into a range of global problems, from national security to the spread of diseases. Our ability to reason about world affairs would be improved by the availability of high-quality event data. ■

REFERENCES AND NOTES

1. P. A. Schrodt, D. J. Gerner, *Am. J. Pol. Sci.* **38**, 825 (1994).
2. S. P. O'Brien, *Int. Stud. Rev.* **12**, 87 (2010).
3. K. Leetaru, P. A. Schrodt, paper presented at the International Studies Association Annual Convention, San Francisco, CA, 3 to 6 April 2013 (ISA, Storrs, CT, 2013); http://data.gdeltproject.org/documentation/ISA.2013.GDELT.pdf.
4. R. Huang, E. Riloff, in *Proceedings of the 26th Conference of the Association for the Advancement of Artificial Intelligence*, Toronto, Ontario, Canada, 22 to 26 July 2012 (AAII, 2012), pp. 1664–1670.
5. D. McClosky *et al.*, in *Proceedings of the 49th Annual Meeting of the Association for Computational Linguistics: Human Language Technologies (HLT 11)*, Portland, OR, 19 to 24 June 2011 (Association for Computational Linguistics, Stroudsburg, PA, 2011), pp. 1626–1635.
6. N. Ramakrishnan *et al.*, in *Proceedings of the 20th ACM SIGKDD International Conference on Knowledge Discovery and Data Mining*, New York, NY, 24 to 27 August 2014 (ACM, 2014), pp. 1799–1808.
7. P. F. Nardulli *et al.*, *Sociol. Methodol.* **45**, 148 (2015).
8. N. B, Weidmann. *J. Conflict Resolut.* **59**, 1129 (2015),
9. E. Boschee *et al.*, in *Handbook of Computational Approaches to Counterterrorism* (Springer, New York, 2013), pp. 51–67.
10. R. Gupta, S. Sarawagi, in *Proceedings VLDB '06,* Seoul, Korea, 12 to 15 September 2006 (Very Large Database Endowment, 2006), pp. 965–976.
11. J. Pujara *et al.*, *AI Mag.* **36**, 65 (2015).
12. See, for example, Intelligence Advanced Research Projects Activity's (IARPA's) Open Source Indicators program, https://www.iarpa.gov/.

ACKNOWLEDGMENTS

Research was supported in part by IARPA via Department of the Interior, National Business Center (DoI/NBC, D12PC000337), and NSF (grant 1125095). Views and conclusions contained herein are those of the authors and should not be interpreted as representing official policies or endorsements, either expressed or implied, of IARPA, DoI/NBC, NSF, or U.S. government.

SUPPLEMENTARY MATERIALS

www.sciencemag.org/content/353/6307/1502/suppl/DC1

10.1126/science.aaf6758

Downloaded from http://science.sciencemag.org/ on October 7, 2016

Published by AAAS

BOOKS *et al.*

PHYSICS

Rethinking the arrow of time

Citing shortcomings in Eddington's theory, a physicist proposes a new explanation for the existence of "now"

By **Lisa Jardine-Wright**

As an astrophysicist and lecturer of relativity and quantum mechanics, I frequently discuss the fundamental principles of Einstein's theories and the interpretations of counterintuitive quantum mechanical properties. However, rarely have I considered the importance or significance of the concept of "now." It is an everyday reality that I simply take for granted. Richard Muller, on the other hand, has given the concept considerable thought. In *Now: The Physics of Time,* Muller successfully introduces and describes most, if not all, of the key elements in an undergraduate physics course, masterfully connecting them with the conceptual thread of "the arrow of time."

When I was a child, I had many questions relating to time: Is it discrete or continuous? What is the smallest measurement of time that we can make? And, as I get older: Is time actually passing faster, or is it just my perception? You may consider such questions to be metaphysical or philosophical, but Muller discusses these and others through the lens of a number of major 20th-century physics discoveries.

With major discoveries come major players. Muller touches on the work and theories of Albert Einstein, Georges Lemaître, Erwin Schrödinger, and Arthur Eddington, to name just a few.

Now
The Physics of Time
Richard A. Muller
Norton, 2016. 364 pp.

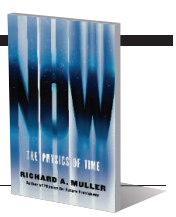

There are five parts to the book, and as they progress, Muller's discussion evolves from physics to metaphysics and philosophy. Throughout, he continually reminds the reader that we must not accept theories unless they are testable or falsifiable.

I also infer a second evolution in the book's progression: a gradual transition from accepted theory to speculation. Consider the question, why is it that we remember the past and not the future? I have long considered Eddington's explanation—that the direction of time can be understood through the second law of thermodynamics—to be perfectly acceptable. However, in Muller's view, this explanation is inadequate.

Muller believes that Eddington's entropy explanation of the arrow of time is "deeply flawed" because his theory and subsequent related theories make no predictions but only explain the phenomenon. Muller suggests alternatives such as the "decreasing-entropy" arrow—the theory that we evolve to order rather than disorder on a local level—and the radiation arrow, suggested by the eminent Swiss physicist Walther Ritz, in which radiation drives time forward. He also discusses the possibility that time is an emergent property of our own consciousness (the psychological arrow) and the idea that the parameters of our universe are somehow special, as evidenced by the presence of intelligent life (the anthropic arrow). It is in these sections where Muller touches on aspects of metaphysics and philosophy: the nature of existence, the fact that we are able to ask questions about the universe, and the reason that time must move forward. As yet, there is no definite answer as to why we remember the past and not the future, but Muller suggests that quantum theory or a four-dimensional Big Bang may hold the key.

"Suppose time stopped. Would you notice? How? Suppose it moved forward in fits and spurts, or at a totally different rate. Could you detect the difference?" asks Richard Muller.

Along the way, the reader is treated to excellent descriptions of key fundamental concepts in physics, including apparent paradoxes in special relativity, $E = mc^2$, the principle of equivalence, black holes, quantum entanglement, statistical physics, the Big Bang, inflation, and the cosmic microwave background.

The strength of this book lies in Muller's experience as a lecturer and teacher, which has enabled him to describe and explain difficult concepts with simplicity. An example can be found in chapter 3 when he discusses length contraction. To measure a moving bus, he explains, we must measure the front and the back simultaneously. But that, according to Muller, is the catch: "That concept is relative. Simultaneous in one reference frame is not simultaneous in another reference frame. A direct consequence is the fact that the length will be different in different frames."

In his introduction, Muller states that his goal is "to bring together the essential physics, assembling pieces like a jigsaw puzzle until a clear picture of *now* emerges." Has he achieved this goal? The book definitely pre-sents a clear picture of essential physics. The significance of "now" and how time, as well as space, might have been created by the Big Bang is more suggestive than emphatic, in my opinion.

Maybe Muller's theories are right about time. Maybe Eddington's reliance on entropy to understand time is misguided. But one thing is certainly true about *Now*: It provides a concise master class in understanding the essentials of physics. I would recommend it to early-year undergraduate physics majors, who will likely find that it will help to crystallize and catalyze their own conceptual understanding of such fundamental principles. ■

10.1126/science.aah6871

The reviewer is at the Cavendish Laboratory, University of Cambridge, Cambridge CB3 0HE, UK. Email: ljw21@cam.ac.uk

PHOTO: BLOOMBERG/GETTY IMAGES

Downloaded from http://science.sciencemag.org/ on October 7, 2016

Published by AAAS

EVOLUTIONARY BIOLOGY

Leveling up

Advocates aim to stimulate renewed interest in a hierarchical theory of evolution

By **Bengt Autzen**

"I am hungry for change—for developments in hierarchy theory from the younger generation," writes Niles Eldredge in the opening pages of *Evolutionary Theory*. The edited volume provides a contemporary selection of historical, conceptual, and empirical essays on the hierarchy theory of evolution that Eldredge and his collaborators hope will bring about renewed enthusiasm for the theory in evolutionary biology circles.

The hierarchy theory of evolution has two central pillars, neither of which is uncontroversial. First, the theory maintains that biological nature is organized into genealogical and economic hierarchies. The genealogical hierarchy results from the way biological information is transmitted over generations, whereas the economic hierarchy results from the interaction of biological entities with the environment. Explaining biological evolution requires elaborating on the interaction between these two hierarchies. Second, advocates of the theory posit that—like a sloshing bucket—large-scale environmental disruptions cause mass extinctions with proportionally large associated evolutionary reactions, whereas smaller environmental disruptions have lesser associated evolutionary effects.

The book consists of 16 essays that are organized into three parts. The first part focuses on conceptual and terminological issues related to hierarchy theory. This section includes an insightful essay by the paleontologist and evolutionary biologist Bruce Lieberman that makes the case that evolutionary biology is both a historical science and a science that discovers laws.

The reviewer is at the Department of Philosophy, University of Bristol, Bristol BS8 1TH, UK. Email: b.autzen@bristol.ac.uk

The second part of the book is dedicated to the dynamic relationships between entities at different levels of biological hierarchies. The essay contributed by evolutionary ecologist Mihaela Pavličev and collaborators—which develops an abstract theory of the behavior of emergent systems by examining structural similarities between biological systems at the molecular level and in human cultural evolution—was particularly illuminating.

The third and final part of the book turns to the notion of macroevolution, where hierarchy theory originated. In one of the essays in this section, paleoecologist Warren Allmon offers a detailed analysis of the role that tempo and mode play in macroevolutionary theory. Allmon's proposed usage of these terms promises to clarify a sometimes ambiguous discourse invoking these concepts.

All three parts of the book begin with introductory sections written by the editors. To me, these sections have the character of additional essays rather than introductory comments. As such, they constitute a missed opportunity for making the volume accessible to a wider audience.

A more substantive concern relates to the different connotations of hierarchy theory at play in the volume. In its strict reading, hierarchy theory refers to the evolutionary theory developed by Eldredge and most comprehensively outlined in his monograph *Unfinished Synthesis* (*1*). Crucial features of this account are the interplay between economic and genealogical hierarchies and a thesis regarding the causes of macroevolution. Understood more liberally, hierarchy theory refers to the idea that the biological world is organized hierarchically and that this structural feature is relevant for understanding evolution. Both interpretations are at play in the volume, but the distinction is not always clear.

"Community-level feedback" may have played a role in species extinction and diversification in the Karoo Basin of South Africa, argue Peter Roopnarine and Kenneth Angielczyk.

Evolutionary Theory
A Hierarchical Perspective
Niles Eldredge, Telmo Pievani, Emanuele Serrelli, Ilya Tëmkin, Eds.
University of Chicago Press, 2016. 393 pp.

For instance, in chapter 6, evolutionary biologist T. Ryan Gregory and collaborators convincingly make the case for a multilevel approach to explain the evolution of transposable elements (TEs) in the human genome. Drawing an analogy to the "gene's-eye view" of evolution, their account opposes organism-centric evolution. By doing so, the essay fits well into the framework of multilevel selection theory. Does this amount to providing a hierarchical theory of evolution of TEs? Surely it does, if one applies the liberal reading of hierarchy theory. Matters are less clear, however, when it comes to the strict reading of hierarchy theory.

This contrast becomes apparent in chapter 8, when philosophers of biology Telmo Pievani and Andrea Parravicini discuss the gap between standard multilevel selection theory and the hierarchical theory of evolution, and in the conclusion of the book, when Pievani asserts that "the mainstream of evolutionary biologists still retains an antihierarchical attitude." This may be true if the strict reading of hierarchy theory is adopted but not if hierarchy theory is understood more liberally, given the prevalence of multilevel selection theory in contemporary evolutionary biology.

Despite these issues, both the range of topics covered in this volume and the diversity of contributors are impressive. As such, it serves an important need at a time when highly specialized journals rarely provide the opportunity for biologists and philosophers to jointly engage with conceptual issues in biology. ■

REFERENCES

1. N. Eldredge, *Unfinished Synthesis: Biological Hierarchies and Modern Evolutionary Thought* (Oxford Univ. Press, Oxford, 1985).

10.1126/science.aah6873

PHOTO: GABBRO/ALAMY STOCK PHOTO

Downloaded from http://science.sciencemag.org/ on October 7, 2016

Published by AAAS

LETTERS

Edited by **Jennifer Sills**

Scientists stand with Standing Rock

THE DAKOTA ACCESS Pipeline (DAPL) is a proposed 0.76-m-diameter pipeline spanning approximately 1850 km to transport crude oil (*1*). The Standing Rock Sioux Tribe of Fort Yates, North Dakota recently filed a lawsuit against the United States Army Corps of Engineers (*2*), who approved construction of DAPL segments in North Dakota. The Tribe argues that the environmental assessment conducted for DAPL (*1*) did not reflect important negative ecological, cultural, socioeconomic, and public health impacts on the Tribe and region (*2*). The DAPL project is just one of many haphazard approaches to natural resource extraction that overlook broader consequences of oil development (*3*). Such practices do not comply with recent Paris Agreement commitments to cut fossil fuel emissions by 2030 (*4*).

To date, more than 90 scientists have signed a resolution (*5*) in support of halting all construction of the DAPL until revised environmental and cultural assessments are carried out as requested by Standing Rock Sioux Tribe. In light of recent Paris Agreement commitments, the resolution calls for the U.S. Federal Government to give explicit consideration to how this and any other proposed national energy strategies affect public health, environmental justice, and biodiversity conservation.

Stephanie R. Januchowski-Hartley,[1]* Anne Hilborn,[2] Katherine C. Crocker,[3] Asia Murphy[4]

[1]Laboratoire Evolution et Diversité Biologique Université Paul Sabatier, Toulouse, 31062, France. [2]Department of Fish and Wildlife Conservation, Virginia Tech, Blacksburg, VA 24061, USA. [3]Department of Ecology and Evolutionary Biology, University of Michigan, Ann Arbor, MI 48109, USA. [4]Pennsylvania State University, University Park, PA 16802, USA.

*Corresponding author. Email: stephierenee@gmail.com

REFERENCES

1. Dakota Access Pipeline Project, United States Fish and Wildlife Service Environmental Assessment, Grassland and Wetland Easement Crossings (www.fws.gov/uploadedFiles/DAPL%20EA.pdf).
2. *Standing Rock Sioux Tribe* v. *U.S. Army Corps of Engineers*, Case 1:16-cv-01534 (http://earthjustice.org/sites/default/files/files/3154%201%20Complaint.pdf).
3. W. J. Palen *et al.*, *Nature* **510**, 465 (2014).
4. UNFCC, "Synthesis report on the aggregate effect of the intended nationally determined contributions" (United Nations Framework Convention on Climate Change, Paris, 2015); https://unfccc.int/resource/docs/2015/cop21/eng/l09r01.pdf.
5. S. Januchowski-Hartley *et al.*, "Dakota Access Pipeline Statement" (2016); https://srjanuchowski-hartley.com/dakota-access-pipeline-sign-on-letter.

10.1126/science.aaj2057

Supporters of the Standing Rock Sioux Tribe rally in opposition of the Dakota Access oil pipeline.

PHOTO: JACQUELYN MARTIN/ASSOCIATED PRESS

Build habitats, not fences, for caribou

IN HIS NEWS In Depth story "To save caribou, Alberta wants to fence them in" (22 July, p. 333), W. Cornwall reported on a proposed 50-year-long project to create a predator-free, fenced, 100-square-kilometer landscape to farm caribou in the Little Smoky range. The program intends to kill wolves, black bears, threatened grizzly bears, cougars, and all large prey such as moose, deer, and elk. Naïve farmed caribou calves will be released in areas where predators have been killed. Oil and gas and forestry activities will be allowed within the enclosure (*1*), and habitat loss and fragmentation will continue as usual.

Fencing wildlife is known to have substantial impacts on biodiversity (*2*), and removing large predators causes cascading ecological consequences (*3*). Releasing naïve caribou that are less sensitive to natural danger cues (*4*) will not address habitat loss and fragmentation, which are the ultimate reasons for the decline of the Little Smoky population (*5*). After the demonstrated failure of a highly unethical wolf-culling program from 2005 to 2012 (*6*), the creation of a predator-free enclosure may be the government's desperate last-ditch attempt to stimulate caribou recovery without jeopardizing industrial activities. The carrying capacity of the Little Smoky caribou range is very low (*7*), and culling wolves or creating artificial landscapes will not increase caribou numbers. The recovery of Little Smoky caribou depends on maintaining or increasing supplies of food and protective cover, which is best done by conserving high-quality priority zones that encompass and connect muskegs and pine-dominated habitats that are used by caribou (*6*). Breeding and raising naïve caribou should be done in zoos, not in the wild. Habitat conservation should be immediately implemented in the Little Smoky caribou range.

Gilbert Proulx[1]* and Roger A. Powell[2]

[1]Alpha Wildlife Research & Management, Sherwood Park AB T8H 1W3, Canada. [2]Department of Applied Ecology, North Carolina State University, Raleigh, NC 27695-7617, USA.

*Corresponding author. Email: gproulx@alphawildlife.ca

REFERENCES

1. Alberta Government, Little Smoky and A La Peche Caribou Range Plan (2016); http://aep.alberta.ca/fish-wildlife/wildlife-management/caribou-management/caribou-action-range-planning/documents/LittleSmokeyAlaPecheRangePlan-Draft-Jun2-2016.pdf.
2. R. Woodroffe *et al.*, *Science* **344**, 46 (2014).
3. W. J. Ripple *et al.*, *Science* **343**, 1241484 (2014).

Downloaded from http://science.sciencemag.org/ on October 7, 2016

Published by AAAS

4. J. Berger *et al.*, *Science* **291**, 1036 (2001).
5. Environment Canada, "Recovery strategy for the woodland caribou (*Rangifer tarandus caribou*), boreal population, in Canada" (Species at Risk Act Recovery Strategy Series, Environment Canada, Ottawa, Ont. Catalogue No. En3-4/140-2012E-PDF, 2012); http://publications.gc.ca/collections/collection_2012/ec/En3-4-140-2012-eng.pdf.
6. R. K. Brook *et al.*, *Can. Wildl. Biol. Manage.* **4**, 72 (2015).
7. G. Proulx, *Can. Wildl. Biol. Manage.* **4**, 81 (2015).

10.1126/science.aai9328

Illegal wildlife trade: Look to the elephants

THE EXPANSION OF global illegal trafficking and its cooption by sophisticated criminal syndicates have accelerated the overharvesting of species (*1*). Although we lack understanding of the illegal trade of most species, we have gained insight into elephant ivory trafficking through a variety of monitoring approaches. Assessing the strengths and weaknesses of these strategies can help us both improve them and apply them to research on other species imperiled by trafficking.

Approaches to monitor ivory trafficking are diverse. The Monitoring of the Illegal Killing of Elephants (MIKE) program (*2*, *3*) provides the most current metrics of illegal harvest. Analysis of illegal ivory seizures can identify international trafficking routes and key trade ports (*4*). Genetic assignment of seized ivory identifies source populations and intra-continental trade routes (*5*). Isotopic sourcing provides parallel insight to genetic data and can age seized contraband (*6*). Surveys provide fundamental data on population status and trends (*7*, *8*).

In aggregate, these approaches provide comprehensive information on the ivory supply chain and scale of illegal harvest. Within range states, this has raised awareness, directed anti-poaching efforts, and led to diplomatic pressures to stop poaching. On the trafficking side, identification of key destination markets, namely China but also the United States, Vietnam, and Thailand (*4*, *9*), and transit ports have focused demand reduction campaigns and threats of sanction from the Convention on International Trade in Endangered Species of Wild Fauna and Flora (CITES). Illegal trade in other species could greatly benefit from investment in similar data collection and collation efforts.

Strategies to control the crucial demand-side stimulants of ivory trafficking still need improvement. Focused demand reduction campaigns and domestic trade bans may serve to undermine the foundations driving illegal ivory trafficking. Overtures to end domestic trade in the primary ivory market of China, as recently implemented in the United States (*10*), have the potential to reduce avenues for laundering black market ivory, particularly if coupled with strict enforcement of border flows that stymy commerce of ivory from neighboring countries. Such actions should be supported and encouraged by the global community. The adoption of the International Union for Conservation of Nature (IUCN) resolution calling for the closure of domestic markets for elephant ivory sets a good precedent (*11*).

George Wittemyer

Save The Elephants, Nairobi, Kenya and Department of Fish Wildlife and Conservation Biology, Colorado State University, Fort Collins, CO 80523, USA.
Email: G.Wittemyer@colostate.edu

REFERENCES

1. U.N. Office on Drugs and Crime, "The globalization of crime: A transnational organized crime threat assessment" (2010); www.unodc.org/documents/data-and-analysis/tocta/TOCTA_Report_2010_low_res.pdf.
2. R. W. Burn, F. M. Underwood, J. Blanc, *PLOS ONE* **6**, e24165 (2011).
3. G. Wittemyer *et al.*, *Proc. Natl. Acad. Sci. U.S.A.* **111**, 13117 (2014).
4. F. M. Underwood, R. W. Burn, T. Milliken, *PLOS ONE* **8**, e76539 (2013).
5. S. K. Wasser *et al.*, *Science* **349**, 84 (2015).
6. K. T. Uno *et al.*, *Proc. Natl. Acad. Sci. U.S.A.* **110**, 11736 (2013).
7. M. J. Chase *et al.*, *PeerJ.* **4**, e2354 (2016).
8. F. Maisels *et al.*, *PLOS ONE* **8**, e59469 (2013).
9. CITES, "Monitoring the illegal killing of elephants" (2013); www.cites.org/eng/cop/16/doc/E-CoP16-53-01.pdf.
10. U.S. Federal Register Doc. 2016-13173 (2016); www.federalregister.gov/documents/2016/06/06/2016-13173/endangered-and-threatened-wildlife-and-plants-revision-of-the-section-4d-rule-for-the-african.
11. IUCN Resolution 007 (2016); https://portals.iucn.org/congress/motion/007.

10.1126/science.aai7807

ERRATA

Erratum for the Report "ESCRT III repairs nuclear envelope ruptures during cell migration to limit DNA damage and cell death" by M. Raab *et al.*, *Science* **353**, aah6167 (2016). Published online 29 July 2016; 10.1126/science.aah6167

Erratum for the Report "Enantioselective synthesis of an ophiobolin sesterterpene via a programmed radical cascade" by Z. G. Brill *et al.*, *Science* **353**, aah5232 (2016). Published online 29 July 2016; 10.1126/science.aah5232

Erratum for the Research Article "Asymmetric division of clonal muscle stem cells coordinates muscle regeneration in vivo" by D. B. Gurevich *et al.*, *Science* **353**, aah4673 (2016). Published online 8 July 2016; 10.1126/science.aah4673

Erratum for the Research Article "De novo design of protein homo-oligomers with modular hydrogen-bond network–mediated specificity" by S. E. Boyken *et al.*, *Science* **352**, aag1318 (2016). Published online 20 May 2016; 10.1126/science.aag1318

Published by AAAS

Downloaded from http://science.sciencemag.org/ on October 7, 2016

AAAS Leshner Fellows help confront climate impacts

By **Michaela Jarvis**

Climate scientists participating in the AAAS Leshner Leadership Institute are engaging communities across the United States in a way that could skirt—and possibly defuse—ideological opposition to acknowledging that the climate is changing.

On the front lines of a trend and drawing on training they received after being selected as the 2016 AAAS Leshner Fellows, the scientists are convening community leaders and policy-makers—in fields such as city planning, agriculture, disaster planning, and natural resource management—and asking them directly what kinds of scientific information they need to protect against ongoing changes in the climate, such as record flooding and heat waves.

"For me, public engagement is about working from the bottom up—one audience at a time—building relationships and trust, sharing knowledge, and figuring out how to address the needs of stakeholders," said fellow Benjamin Preston, senior research scientist at Oak Ridge National Laboratory and deputy director of the laboratory's 130-person Climate Change Science Institute. Preston is at work on an institution-wide plan to mobilize scientists to find out from city and county leaders "how our science, data, and tools can inform some of their challenging decisions."

Melissa Kenney (center) on the shore of the Chesapeake Bay

A March 2016 Gallup poll showed a sharp ideological divide in the acknowledgment of climate change, with just 40% of Republicans worried "a great deal" or "a fair amount" about global warming, as opposed to 84% of Democrats. According to research on the phenomenon, climate scientists presenting their data to the public has had little effect on public opinion.

"More information or more basic knowledge doesn't seem to overcome polarized differences on issues such as climate change," Matthew Nisbet, associate professor of communication studies and affiliate associate professor of public policy and urban affairs at Northeastern University, told the fellows at a training session.

"The whole concept of public engagement," said Tiffany Lohwater, AAAS deputy chief communications officer, who helps run the Leshner Leadership Institute program, "is recognizing that audiences have something to contribute to the conversation, that this can and should be a two-way dialogue. Particularly on issues that are politically polarized, this becomes even more important."

Earlier this month, fellow Kirstin Dow helped organize the 2016 Carolinas Climate Resilience Conference to bring together representatives of local communities, nongovernmental organizations, state and federal agencies, and researchers. With more than 250 participants, the conference was designed to promote scientific study that is responsive to people's needs, said Dow, professor of geography at the University of South Carolina and principal investigator of the NOAA-supported Carolinas Integrated Sciences and Assessments research team. In a region where lawmakers have suppressed reports of climate-change effects, Dow said her team's strategy is to "engage and support those responsible for public planning."

Soliciting information from communities regarding exactly what kinds of measurements they need from scientists to deal with climate impacts is not always a straightforward process. "It has to be a conversation," said fellow Jeffrey Dukes, "and it isn't an easy one."

In a meeting Dukes helped convene in northwest Indiana, he said community officials expressed a keen desire for information about flooding and record rains, but they were unclear whether they needed to know, for instance, how much rain fell in a half-hour or over two days in order to facilitate their planning. Dukes, who is director of the Purdue Climate Change Research Center, said a sort of interface had to be built between the scientists he works with and the community representatives, "to build foundational thinking on both sides in order to meet in the middle."

Fellow Melissa Kenney, assistant research professor in environmental decision support science at the University of Maryland, worked with students this summer to synthesize the challenges of community representatives in the Chesapeake Bay by reviewing existing reports and other documents. "We wanted to do our homework so we didn't ask a lot of questions that were already answered," Kenney said. She and her team are looking for "research gaps and science translation opportunities" to approach community leaders with processes and tools that will "facilitate evidence-based decision-making."

"In a densely populated watershed, climate is amplifying existing impacts on our region," added Kenney. "So we don't have a choice; we have to make decisions to consider current and future climate consequences."

As the director of the University of Minnesota's Institute on the Environment and the head of the university's Department of Ecology, Evolution and Behavior, fellow Jessica Hellmann works with natural resource agencies and land managers to help them confront climate impacts in their conservation planning. At the same time, she and her colleagues are reaching out to sustainability directors at corporations, who she said are "constantly seeking ways to make the sustainability case to corporate leadership."

Dukes, for one, is hopeful that his team's efforts will contribute to moving the public at large toward acknowledging and responding to climate change. "Climate impacts are happening, and it would be stupid not to consider them as we're spending all kinds of money constructing infrastructure," Dukes said. "We're going to save Hoosiers money and strengthen our state, and hopefully that will encourage people to take climate change into account."

The AAAS Leshner Leadership Institute is now accepting applications for 2017 from mid-career scientists working in infectious disease research. The application deadline is November 1. For more information, visit http://leshnerfellows.aaas.org.

PHOTO: ARIANA SUTTON-GRIER

Downloaded from http://science.sciencemag.org/ on October 7, 2016

Published by AAAS

RESEARCH

Brain sites and circuits to recognize friends

Okuyama et al., *p. 1536*

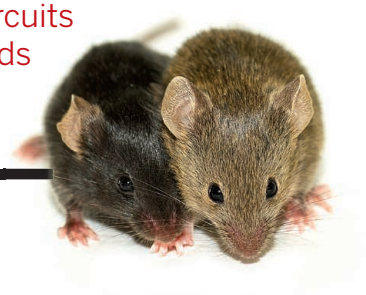

IN *SCIENCE* JOURNALS

Edited by **Nick Wigginton**

Detailed imaging of the local Milky Way suggests that it may resemble far-away spiral galaxies.

GALACTIC STRUCTURE

Mapping the local Milky Way

The spiral structures of far-away galaxies are among the most familiar celestial features. Viewed from within, the structure of our own Milky Way galaxy is harder to appreciate. Interstellar dust also makes it difficult to measure distances between stars in our galaxy with optical astronomy. Using radio astronomy, Xu *et al.* mapped the nearest spiral arm of the Milky Way in unprecedented detail. This approach helps constrain its size and orientation, as well as the rate of star formation within our galaxy. —KVH

Sci. Adv. 10.1126.sciadv.1600878 (2016).

SIGNALING

Organ cross-talk for insulin secretion

Organisms must adapt their growth to changing environmental conditions, such as variations in nutrient access. In *Drosophila*, dietary amino acids promote the release of insulin-like peptides from the brain, which activate organismic growth. Delanoue *et al*. show that the peptide Stunted (Sun) is produced by fat cells upon amino acid and TOR signaling. Sun binds to the G protein–coupled receptor Methuselah (Mth) to promote the release of insulin from cells in the brain in response to dietary amino acids. This work demonstrates that cross-talk between organs can modulate insulin levels and ultimately control body size. —BAP

Science, this issue p. 1553

HIV-1 VACCINES

On the path toward a vaccine

A major goal in combating HIV-1 is the development of a vaccine that can elicit broadly neutralizing antibodies (bNAbs). As bNAbs develop, however, they acquire many somatic mutations, so that they differ substantially in sequence and antigen-binding capability from their germline precursors. To circumvent this challenge, Sok *et al*. used mice engineered to express the human immunoglobulin locus. Despite the extremely rare frequency of germline precursor antibodies (less than one per mouse), nearly 30% of mice immunized with their germline-targeting immunogen developed a bNAb precursor response. This suggests feasibility in humans, where precursor frequencies are higher. —KLM

Science, this issue p. 1557

GRAPHENE

Recreating optics in graphene

Light usually takes the shortest path to propagate between two points. In contrast, electrons in solids experience collisions. To get into a regime that resembles the propagation of light, researchers need very clean materials. Having achieved this regime in graphene, Chen *et al*. used the bending of electron trajectories in magnetic fields to show that, at a boundary between regions of different carrier densities, electrons "refract" in analogy to the refraction of light. In a related experiment, Lee *et al*. probed the transport of these ballistic electrons in a superlattice band structure. —JS

Science, this issue pp. 1522 and 1526

GENE REGULATION

Repairing the breaks you make

Cyclin A2 is a mammalian cell cycle protein that plays a critical role in DNA replication and mitotic entry. It has been associated with poor clinical outcomes in human tumors. Kanakkanthara *et al*. show that cyclin A2 binds to the 3′ end of a specific mRNA molecule that codes for the critical DNA repair enzyme Mre11. This binding stimulates the expression of the Mre11 mRNA, thereby coordinating the replication of DNA with the presence of the machinery that

PHOTOS: (TOP TO BOTTOM) FASLOOFF/ISTOCKPHOTO; NASA/ESA/THE HUBBLE HERITAGE TEAM (STSCI/AURA)

Published by AAAS

repairs DNA lesions caused by replication errors. —GR

Science, this issue p. 1549

GEOPHYSICS

Rock deformation goes magnetic

The topography in regions such as the western United States depends on the strength of the crust and lithosphere. To better understand regional tectonic–scale topographic evolution, Liu *et al*. incorporated magnetotelluric imaging, which relies on electromagnetic fields to investigate subsurface properties, into lithospheric evolution models (see the Perspective by Kaus). This approach constrains the strength and viscosity of Earth's near-surface layer, highlighting how a new data source can shed light on the response of subsurface rock to stress. —BG

Science, this issue p. 1515; see also p. 1495

ADDITIVE MANUFACTURE

More function with 3D printing

The creation of parts by the guided layer-by-layer deposition of materials, better known as three-dimensional (3D) printing, is often confined to a single material. This can limit the functionality of the fabricated structures. MacDonald and Wicker review methods in 3D printing for integrating dissimilar materials and also for interconnecting active components, such as adding wires to power embedded sensors and motors. Multifunctional capabilities can be enhanced with electronic, mechanical, electromagnetic, and biological components. —PDS

Science, this issue p. 1512

3D periodic spiral antenna produced through hybrid manufacturing

ENHANCER FUNCTION

CRISPR editing illuminates function

The noncoding regions around a gene tend to control the transcription of protein-coding genes, but the specific elements involved are difficult to determine. Leveraging the editing ability of the CRISPR-Cas9 system, Sanjana *et al*. tiled guide RNAs across three genes associated with vemurafenib-resistant cancers. This allowed for the coverage of both coding and noncoding sequences in order to identify functional noncoding regions. CRISPR-Cas9 mutagenesis can therefore functionally evaluate noncoding mutations in an unbiased way. —LMZ

Science, this issue p. 1545

CANCER IMMUNOLOGY

Engineering antitumor activity

Dendritic cells present antigens, including those from tumor cells, to T cells to stimulate immune responses. Antitumor vaccines based on injecting dendritic cells, however, have not been effective. Li *et al*. found that melanoma cells released cytokines that activated a transcriptional pathway that suppressed the antitumor responses of dendritic cells infiltrating the tumors. Vaccination experiments in tumor-bearing mice suggested that injecting dendritic cells engineered to overcome or prevent the response to tumor-derived cytokines might prove to be an effective immunotherapy strategy in cancer patients. —LKF

Sci. Signal. **9**, ra94 (2016).

IN OTHER JOURNALS

Edited by **Kristen Mueller** *and* **Jesse Smith**

ANTIMICROBIAL RESISTANCE

Beware of the dust

Antimicrobial chemicals are used in many soaps and other personal-care products. They are found in household dust at concentrations comparable to those in wastewater. Laboratory studies have shown that these chemicals can promote antimicrobial resistance in aqueous environments. Hartmann *et al*. explore whether they are also associated with antimicrobial resistance in indoor dust. They report a positive association between antimicrobial concentration and the abundance of multiple antibiotic-resistant genes in indoor dust at a mixed-use athletic and educational facility. Antimicrobials may thus have a strong influence on the promotion and retention of antibiotic-resistant genes in indoor environments. —JFU

Environ. Sci. Technol. 10.1021/acs.est.6b00262 (2016).

CANCER THERAPY

Drugging an undruggable target

Transcription factors have long been viewed as "undruggable" targets for therapy; however, this concept may now need some tweaking. Cho *et al*. found that a small-molecule drug (PT2399) that inhibits the activity of the transcription factor HIF2α (hypoxia-inducible factor 2α) has promising antitumor effects in mouse models of kidney cancer. HIF2α controls the expression of genes that help tumors cope with low amounts of oxygen. In mice, PT2399 suppressed the growth of metastatic kidney tumors and improved the animals' survival. Not all tumors responded to the drug, suggesting that in a clinical setting, doctors may need to rely on yet-to-be-discovered biomarkers to match the drug with the patients most likely to benefit. —PAK

Nature 10.1038/nature19795 (2016).

PHOTOS: (LEFT TO RIGHT) DRAPER LABS/MACDONALD *ET AL.*; DON FAULKNER/FLICKR

Published by AAAS

ALSO IN *SCIENCE* JOURNALS

Edited by **Nick Wigginton**

NEURODEGENERATION

Receptor propagates protein aggregation

The protein α-synuclein, which is abundant in brain neurons, functions as a soluble monomer. Abnormal oligomerization of this protein into insoluble aggregates correlates with Parkinson's disease (PD). The progression of PD may depend on the spread of aggregation from neuron to neuron. Mao *et al.* show that the neuronal surface protein LAG3 (encoded by *lymphocyte-activation gene 3*) binds preferentially to multimeric rather than monomeric α-synuclein (see the Perspective by Jucker). Subsequent endocytosis internalizes the multimeric α-synuclein, seeding the aggregation phenomenon in new cells. —PJH

Science, this issue p. 1513; see also p. 1498

CANCER

A histone brake on tumor growth

Individual tumors consist of a diverse collection of cells with different propensities to grow uncontrollably. This heterogeneity is often associated with the degree of differentiation of the subpopulations of tumor cells. Morales Torres *et al*. show that the level of a chromatin protein, linker histone H1.0, underlies the variable differentiation and therefore the growth potential of cancer cell populations. Silencing the H1.0-encoding gene allows tumor cells to self-renew, whereas inducing its high expression promotes differentiation and limits tumor maintenance. These findings suggest how modulating epigenetic states might control tumor growth. —GR

Science, this issue p. 1514

PROTOPLANETARY DISKS

Spiral arms in a disk around a young star

A disk of gas and dust orbits around young stars as they form. Eventually, planets can form in such disks. Perez *et al.* used submillimeter interferometry to observe the protoplanetary disk around the young star Elias 2-27 (see the Perspective by Rice). Emission from the dust shows a spiral pattern within the body of the disk. Studying the structure of protoplanetary disks will help astronomers understand how young stars accrete material and how planets form. —KTS

Science, this issue p. 1519; see also p. 1492

BIODIVERSITY

Patterns of global genetic diversity

Mapping of global biodiversity has been focused mainly at the species level; the distribution of underlying genetic diversity is less well documented. Miraldo *et al*. attach geographic coordinates to publicly available mitochondrial DNA sequence data for 4500 species of mammals and amphibians (see the Perspective by Pereira). Genetic diversity is generally higher in the tropics than at higher latitudes and also shows patterns relating to the intensity of human activity. Specifically, amphibians have decreased genetic diversity in heavily affected regions, and mammals have the highest genetic diversity in regions with intermediate human impact. These findings pave the way for a deeper understanding of the impacts of humans on underlying patterns of fundamental biotic diversity. —AMS

Science, this issue p. 1532; see also p. 1494

HIV-1 INFECTION

Progression at a standstill

Although most people that become infected with HIV-1 develop AIDS, rare individuals maintain immune function in the presence of virus. This phenomenon is also seen in natural hosts of the closely related simian immunodeficiency virus (SIV). Muenchhoff *et al.* describe a cohort of pediatric HIV-1 patients that have normal CD4 T cell counts, despite high viremia and lack of antiviral treatment. These children have low immune activation, including lower expression of chemokine receptor CCR5 on central memory CD4 T cells, similar to sooty mangabeys infected with SIV. The immune mechanisms described in these patients shed light on HIV pathogenesis, which may help in developing treatments. —LP

Sci. Transl. Med. **8**, 358ra125 (2016).

VIROLOGY

Modeling hepatitis A in mice

Although viral hepatitis is a major cause of morbidity worldwide, scientists lack good small-animal models for studying it, especially models that recapitulate virus-caused liver pathology. Hirai-Yuki *et al*. report a mouse model for infection with hepatitis A virus (HAV). HAV-infected mice lacked type I interferon signaling, causing many symptoms similar to those of acute HAV in humans, including low-grade viremia and cell death and inflammation in the liver. Liver pathology depended on the innate immune signaling protein MAVS and interferon response factors 3 and 7. The use of these mice may provide important insights into the causes of viral hepatitis–dependent pathology in humans. —KLM

Science, this issue p. 1541

SOCIAL MEMORY

Sites and circuits to recognize friends

The ability to recognize and memorize familiar conspecifics is crucial for all social animals. Okuyama *et al.* found that the ventral hippocampus and its projections to a brain region called the nucleus accumbens are necessary and sufficient for a specific social memory (see the Perspective by Saxena and Morris). Both the number of activated ventral hippocampal neurons and the strength and stability of the responding cells were greater in response to a familiar than to a novel animal. Engram cell identification and manipulation technologies provided strong evidence that a specific population of pyramidal neurons in the ventral hippocampus holds the memory of a familiar animal. —PRS

Science, this issue p.1536; see also p. 1496

COGNITION

Bees have good moods, too

Mood can influence our impression of ambiguous stimuli. Perry *et al*. show that such emotional-state biases are present in bumblebees, a finding that greatly increases the breadth of taxa in which such emotional influences are found (see the Perspective by Mendl and Paul). Specifically, bees that were given a reward of sugar water before a choice between two neutral cues responded as though the cues were positive stimuli. Further, bees given sugar water were more resilient in the face of a simulated predator attack. The application of a dopamine antagonist eliminated these positive predispositions, suggesting that the mechanism is similar to that found in vertebrates. —SNV

Science, this issue p. 1529; see also p. 1499

Published by AAAS

Magellanic penguins in Punto Tombo, Argentina

EVOLUTION

The importance of variation

The environment exerts powerful selective forces on species, shaping their morphology. Despite this, individuals within a species can be quite variable, suggesting that selection may not always operate in expected ways. Koehn *et al*. measured selection in Magellanic penguins at Punta Tombo, Argentina, over nearly 30 years. Though this extreme environment would seem to impose powerful selective forces, they found evidence of selection at a suite of traits in only 7 of those years. When selection was detected, primarily for body size, it favored larger individuals. Such inconsistency in the strength and shape of selection over time likely maintains important variation within the population overall and suggests that there is no clear best-adapted morphology in this dynamic habitat. —SNV

Auk 10.1642/AUK-16-50.1 (2016).

VACCINATION

Mapping the barriers to vaccination

Common infectious diseases are in decline thanks to increasing vaccination coverage, but this is a vulnerable triumph: UNICEF reports that nearly 22 million children remained unvaccinated in 2013. A study by de Figueiredo *et al*. shows two broad indicators at work: one, a suite of socioeconomic factors, and the other, attitudinal beliefs. Their vaccine performance index calls out the countries that are least likely, based on a series of indicators, to meet the Global Vaccine Action Plan target. These countries are largely in sub-Saharan Africa and Southeast Asia, where poor vaccination coverage correlates with a lack of access to water, health care, and education. Active refusal to vaccinate is more likely to occur in European countries. —CA

Lancet Global Health **4**, e726 (2016).

PHOTO: JEROME DELAY/AP PHOTO

Socioeconomic factors and attitudinal beliefs shape worldwide vaccination rates.

HEMATOPOIESIS

Transforming blood cell development

Although the transplantation of hematopoietic stem cells (HSCs) enables many life-saving procedures, their limited availability prevents wider use. A better understanding of how they develop may assist in expanding the supply. During embryonic development, HSCs arise from a subset of endothelial cells in the dorsal aorta. Using zebrafish as a model, Monteiro *et al*. find that signaling pathways dependent on the protein TGFβ (transforming growth factor β) drive the endothelial-to-hematopoietic transition that leads to HSC development. First, TGFβ produced by the endothelial cells themselves programs the endothelium, and then its production by the notochord orchestrates the transition. —BAP

Dev. Cell **38**, 358 (2016).

INTERSTELLAR MEDIUM

Reflected starlight traces dust structure

The diffuse interstellar medium (ISM) is structured on many scales. Studies of gas absorption lines have shown that structure persists all the way down to solar-system scales, contrary to theoretical expectations, but it has been unclear whether the solid dust particles share this behavior. Miville-Deschênes *et al*. studied the cirrus-like pattern of starlight reflecting off of dust grains in a nearby region of the ISM. They find that the dust is structured with a single power law on all the scales that they can probe, a sign of turbulent motion within the ISM driven by galactic feedback processes. —KTS

Astron. Astrophys. **593**, A4 (2016).

CHEMICAL PHYSICS

Tracking triplets in pentacene polymers

Singlet fission is like a two-for-one sale in a solar cell: Light absorption populates a singlet state that splits into two triplet carriers. Key questions for efficient implementation of this phenomenon are how to optimize the formation of the triplets and then how to keep them apart afterward. Sanders *et al*. systematically studied singlet fission in oligomers and polymers of pentacene, a compound explored extensively for this purpose already as a monomer and dimer. They found that the fission rate gets faster as the pentacene chains get longer, though the consistently short lifetime of the triplet pair afterward is length-independent. —JSY

Chem **1**, 505 (2016).

Published by AAAS

REVIEW SUMMARY

ADDITIVE MANUFACTURE

Multiprocess 3D printing for increasing component functionality

Eric MacDonald* **and Ryan Wicker***

BACKGROUND: Three-dimensional (3D) printing, known more formally as additive manufacturing, has become the focus of media and public attention in recent years as the decades-old technology has at last approached the performance necessary for direct production of end-use devices. The most popular forms of standard 3D printing include vat photopolymerization, powder bed fusion, material extrusion, sheet lamination, directed energy deposition, material jetting, and binder jetting, each creating parts layer by layer and offering different options in terms of cost, feature detail, and materials. Whereas traditional manufacturing technologies, such as casting, forging, machining, and injection molding, are well suited for mass production of identical commodity items, 3D printing allows for the creation of complex geometric shapes that can be mass-customized, because no die or mold is required and design concepts are translated into products through direct digital manufacturing. Furthermore, the additively layered approach enables the merging of multiple components into a single piece, which removes the requirement for subsequent assembly operations. Recently, the patents for the original 3D printing processes have begun to expire, which is resulting in a burgeoning number of low-cost desktop systems that provide increased accessibility to society at large. Industry has recognized the manufacturing advantages of these technologies and is investing in production systems to make complex components for jet engines, customized bodies for cars, and even pharmaceuticals. Although standard 3D printing technologies have advanced so that it is now possible to print in a wide range of materials including metals, ceramics, and polymers, the resulting structures are generally limited to a single material, or, at best, a limited number of compatible materials.

ON OUR WEBSITE

Read the full article at http://dx.doi.org/10.1126/science.aaf2093

ADVANCES: For the technology to become more widely adopted in mainstream manufacturing, 3D printing must provide end-use products by fabricating more than just simple structures with sufficient mechanical strength to retain shape. Recently, research has resulted in the capability to use new materials with commercial 3D printers, and customized printers have been enhanced with complementary traditional manufacturing processes, an approach known as multiprocess or hybrid 3D printing. Collectively, these advancements are leading to fabrications that are not only geometrically complex, but functionally complex as well. By introducing the robotic placement of components, micromachining for intricate detail, embedding of wires, and dispensing of functional inks, complex structures can be constructed with additional electronic, electromagnetic, optical, thermodynamic, chemical, and electromechanical content.

OUTLOOK: Multiprocess 3D printing is a nascent area of research in which basic 3D printing is augmented to fabricate structures with multifunctionality. Progress will lead to local manufacturing with customized 3D spatial control of material, geometry, and placement of subcomponents. This next generation of printers will allow for the fabrication of arbitrarily shaped end-use devices, leading to direct and distributed manufacturing of products ranging from human organs to satellites. The ramifications are substantial, given that 3D printing will enable the fabrication of customer-specific products locally and on demand, improving personalization and reducing shipping costs and delays. Examples could include replacement components for grain-milling equipment in a remote village in the developing world, biomedical devices created specifically for a patient in a hospital before surgery, and satellite components printed in orbit, thus avoiding the delays and costs associated with launch operations. The automotive, aerospace, defense, pharmaceutical, biomedical, and consumer industries, among others, will benefit from the new design and manufacturing freedom made possible by multiprocess 3D printing. ■

The list of author affiliations is available in the full article online.
*Corresponding author. Email: ewmacdonald@ysu.edu (E.M.); rwicker@utep.edu (R.W.)
Cite this article as E. MacDonald and R. Wicker, *Science* 353, aaf2093 (2016). DOI: 10.1126/science.aaf2093

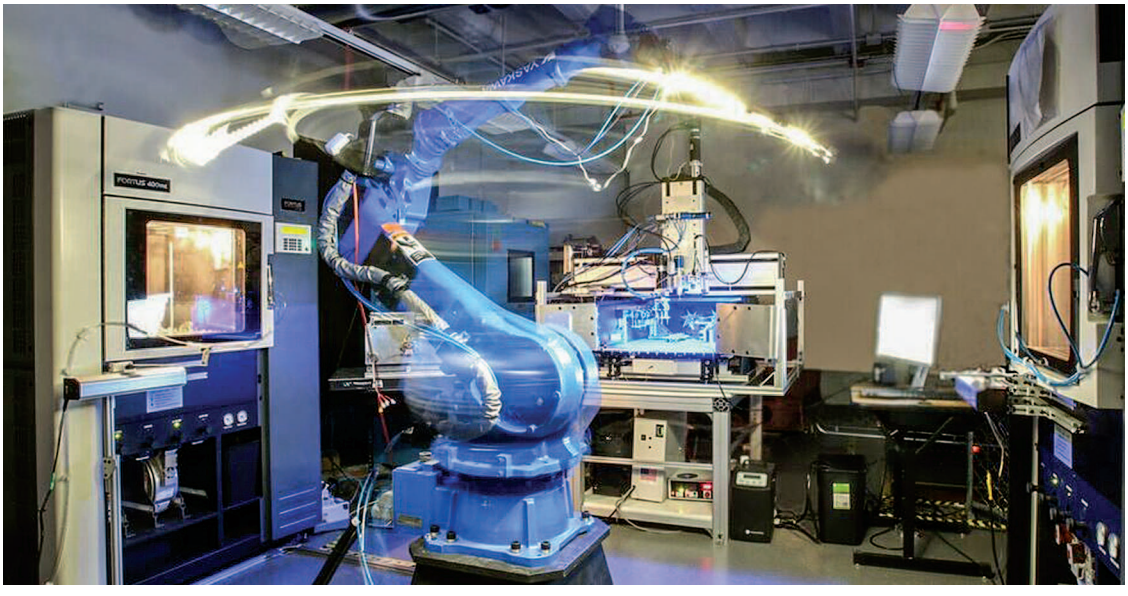

A long-exposure photo of the Multi3D Manufacturing system for multiprocess 3D printing. Two production 3D printers are shown collaboratively printing, with a six-axis robot for conveyance and post-process assembly. A central gantry in the background incorporates other complementary manufacturing processes (machining, component placement, wire and foil embedding, and direct write) to provide geometrically complex structures combining polymers, metals, and active components.

Downloaded from http://science.sciencemag.org/ on October 7, 2016

REVIEW

ADDITIVE MANUFACTURE

Multiprocess 3D printing for increasing component functionality

Eric MacDonald* **and Ryan Wicker***

Layer-by-layer deposition of materials to manufacture parts—better known as three-dimensional (3D) printing or additive manufacturing—has been flourishing as a fabrication process in the past several years and now can create complex geometries for use as models, assembly fixtures, and production molds. Increasing interest has focused on the use of this technology for direct manufacturing of production parts; however, it remains generally limited to single-material fabrication, which can limit the end-use functionality of the fabricated structures. The next generation of 3D printing will entail not only the integration of dissimilar materials but the embedding of active components in order to deliver functionality that was not possible previously. Examples could include arbitrarily shaped electronics with integrated microfluidic thermal management and intelligent prostheses custom-fit to the anatomy of a specific patient. We review the state of the art in multiprocess (or hybrid) 3D printing, in which complementary processes, both novel and traditional, are combined to advance the future of manufacturing.

Traditional manufacturing is well optimized for mass production of identical parts but can involve complex assembly steps, result in material waste, and incur substantial expense for low-volume production. Three-dimensional (3D) printing, a technology receiving considerable attention recently for direct part production, allows the creation of complex geometric shapes that can be mass-customized without a need for part-specific tooling such as dies or molds. Originally referred to by terms such as rapid prototyping, solid freeform fabrication, and others, this layer-by-layer fabrication methodology converts a precursor material in a spatially controlled manner to create a complex shape. As the technology has developed over the past three decades, both the spatial resolution and the diversity of usable materials have improved. These advancements have led to an increase in end-use production of consumer, aerospace, and biomedical devices as industry has recognized the potential opportunities offered by 3D printing for improving designs, reducing assembly requirements through part consolidation, and optimizing the manufacturing supply chain through point-of-use manufacturing. General Electric's chief executive officer, Jeff Immelt, has recently stated that by 2020, the corporation plans to produce over 100,000 3D-printed parts for jet engines, and to meet these goals, General Electric plans a $3.5 billion investment in 3D printing (*1*). Simultaneously, as 3D printing patents are expiring, the costs of these systems are decreasing dramatically, and they now are becoming accessible to the general public. Collectively, these trends are leading to a democratization of manufacturing (*2*). 3D printing, now often referred to as additive manufacturing to emphasize production rather than prototyping (*3*), is evolving. Figure 1 illustrates the potential for fabricating end-use structures with embedded fluidic control printed from a traditional single-material 3D printer (powder bed fusion of electron beam–melted titanium) (*4*).

One potentially disruptive step in the evolution of 3D printing will be to increase the functionality of the manufactured components. The 3D printing process can be started and stopped to incorporate complementary fabrication processes or embed subcomponents manufactured using traditional methods; however, until recently, 3D printing has been generally relegated to the prototyping of single-material structures for form and fit evaluation (*5*). The next generation of 3D printers will enable products with multifunctional capabilities, including combinations of features not possible with a single print material, produced within a unified, tooling-free, multiprocess printing environment. In this context, multiprocess (or hybrid) 3D printing is defined as additive manufacturing enhanced with complementary processes. These complementary processes can include traditional manufacturing such as machining, cutting, dispensing, robotic placement, and more. This new approach represents a paradigm shift in which the goal is to fabricate, in a nonassembly process, multifunctional end-use devices, potentially combining electronic, electromagnetic, optical, fluidic, actuation, chemical, and thermal features simultaneously—all with the inherent geometric benefits of 3D printing. Moreover, without tooling requirements, these advanced 3D printing technologies continue to leverage mass customization (*6*), through which, for instance, sophisticated biomedical devices can now be fabricated for the specific anatomy of a patient. Figure 2 illustrates two examples of multifunctional devices that highlight the possibilities of using multiprocess 3D printing systems: (i) a gaming die that includes a processor, an accelerometer, and light-emitting diodes (LEDs) to enhance the outcome of a roll by illuminating the top surface (*7*) (Fig. 2A) and (ii) a periodic spiral antenna that allows for physical patterns of conductors and dielectrics with unprecedented geometries, which will inevitably provide new levels of performance in next-generation antennas (Fig. 2B).

In this Review, we provide an overview of current 3D printing technologies, discuss advances and limitations in multiprocess 3D printing specifically with respect to multifunctionality, and describe a number of functionalities that have been investigated and enabled by 3D printing. Limited only by the readers' imaginations, the innumerable design opportunities provided by this manufacturing technology cannot effectively be covered in this Review for all applications of multifunctional printing (such as organ printing), and the included examples only serve to highlight the potential and motivate further advances.

Fig. 1. Example of 3D-printed multifunctionality achieved with commercially available 3D printing technology. Shown is a pneumatically controlled prosthetic hand fabricated in titanium by using a powder bed fusion 3D printing technology known as electron beam melting (*4*). [Photo courtesy of Oak Ridge National Laboratory]

The W. M. Keck Center for 3D Innovation, University of Texas at El Paso, El Paso, TX 79968, USA.
***Corresponding author. Email: ewmacdonald@ysu.edu (E.M.); rwicker@utep.edu (R.W.)**

Downloaded from http://science.sciencemag.org/ on October 7, 2016

Multifunctional fabrication processes

The cornerstone of 3D printing is the layer-by-layer fabrication methodology, which allows manufacturing flexibility with the provision of interrupting the process to leverage complementary processes. The ASTM (American Society for Testing and Materials) F42 subcommittee was established in 2009 (*8*) to provide standards for common terminology, testing methods, and file formats, among other concepts for additive manufacturing, and has identified a taxonomy of seven basic 3D printing processes.

1) Vat photopolymerization is a process involving a vat of liquid photo-curable polymer that is selectively cured with an energy source such as a laser beam or a lamp with a projection system. The fabricated part is typically created layer by layer on a platform that descends after selectively curing each layer.

2) Material extrusion is a process in which material is selectively dispensed through an extrusion nozzle. The most common materials used are thermoplastics requiring heated extrusion. The process generally includes layer-by-layer fabrication with a movable platform and/or extruder.

3) Powder bed fusion involves selectively fusing regions of powder in a bed using a thermal energy source such as a laser or electron beam. A platform supporting the bed descends by a layer thickness, and a rake or roller dispenses additional powder to create the next layer.

4) Binder jetting selectively dispenses a binder to join powder feedstock in a bed supported by a platform. As in powder bed fusion, the platform descends by a layer thickness, and a rake or roller dispenses additional powder. Most parts require postprocessing with an infiltrant and a furnace cycle.

5) Material jetting selectively deposits droplets of the build material, which are typically photo-cured. Deposition and curing are repeated for all layers.

6) Sheet lamination is a process in which individual sheets of material are bonded together to form a structure, typically requiring machining or cutting between layers to accurately form the 2D shape for each particular layer.

7) Directed energy deposition directs both a material deposition (typically wire or powder) and an energy source (typically a laser or an electron beam) at the surface being built.

Each of these processes stands to benefit from enhancements enabling the printing of structures with increased functionality. The earliest reported research in the 1990s leveraged the layered technique of 3D printing by interrupting the process to integrate functional components and conductive traces within a structure (*9*). Kataria and Rosen enhanced vat photopolymerization with inserts (*10*), and Lopes *et al.* dispensed conductive inks to manufacture electronics with antennas built directly into solid polymer structures (*11*). Ultrasonic consolidation, a sheet lamination process, creates metal components by ultrasonically bonding a sheet of metal foil to a previously deposited sheet. A machining process using an end mill renders the required geometry and follows the bonding. Thus, 2D sheets are essentially stacked together to provide a 3D part fabricated with two processes—an early example of multiprocess 3D printing. Robinson *et al.* interrupted the ultrasonic consolidation process to insert simple circuits through the combination of material extrusion with both thermoplastic and conductive ink (*12*). Using the material extrusion 3D printing technique, Malone *et al.* demonstrated a circuit and clever electromechanical applications by using an open-source fabrication system that dispensed multiple materials, including conductors and dielectrics (*13*). Navarrete *et al.* described enhancements to a vat photopolymerization process that introduced microchannels into the substrate to guide and contain curable conductive fluid, which was microdispensed to leverage the minimum feature size of the laser-curing process (*14*). Conductive trace spacing was thus controlled by the precision of the laser beam, rather than the secondary dispensing process, illustrating the symbiotic benefit of a compound process over either process acting alone.

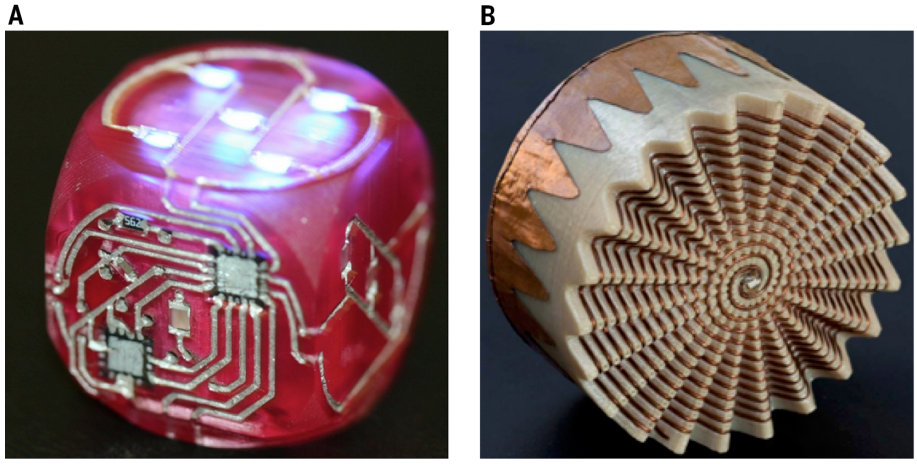

Fig. 2. Examples of multifunctional 3D-printed products only possible with multiprocess 3D printing. (**A**) A gaming die with an embedded processor and accelerometer. [From (*7*)] (**B**) A 3D periodic spiral antenna. [Image courtesy of Draper Labs]

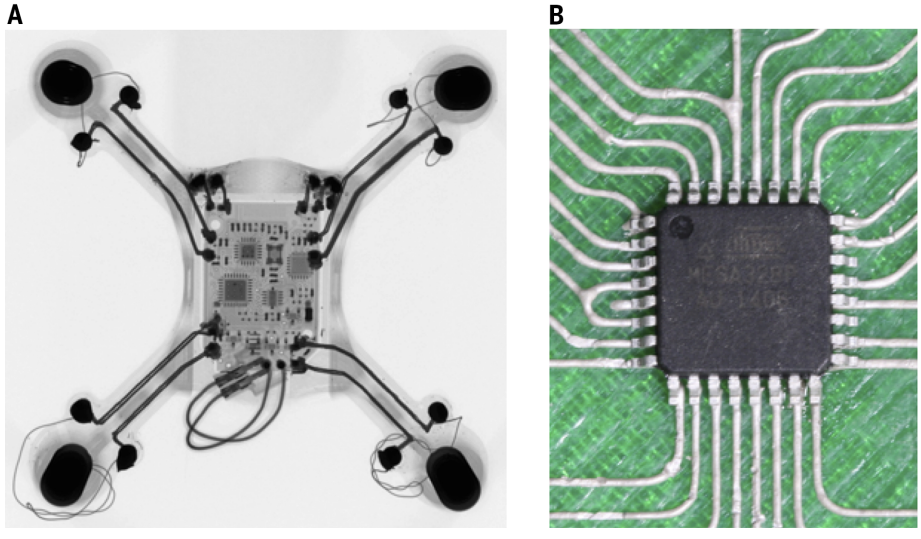

Fig. 3. Examples of printed structures from Voxel8. (**A**) X-ray micrograph of a quad copter drone. (**B**) Printed electrical interconnection. [Photos courtesy of Voxel8]

Multifunctionality in additive manufacturing can be defined broadly as the introduction of any additional functionality beyond rendering a basic shape. Multiple colors and densities can be graded throughout a structure, for example, which qualifies as multifunctionality (albeit minimally), and these structures can be fabricated with various forms of standard commercial 3D printing. In fact, processes capable of multiple colors have been commercially available for years (*15*–*20*). Other examples of multifunctionality with commercial 3D printers include mechanical metamaterials that induce negative stiffness to dampen vibrations and reduce cabin noise (*21*) or that allow pneumatic actuation, as shown in Fig. 1. Related but not identical to multifunctional 3D printing, multiprocess 3D printing—the collaborative use of multiple processes—often but not necessarily results in multifunctional devices. A counter example is a single-material metal structure printed additively and then machined subtractively within a single gantry for the sole purpose of improving

Downloaded from http://science.sciencemag.org/ on October 7, 2016

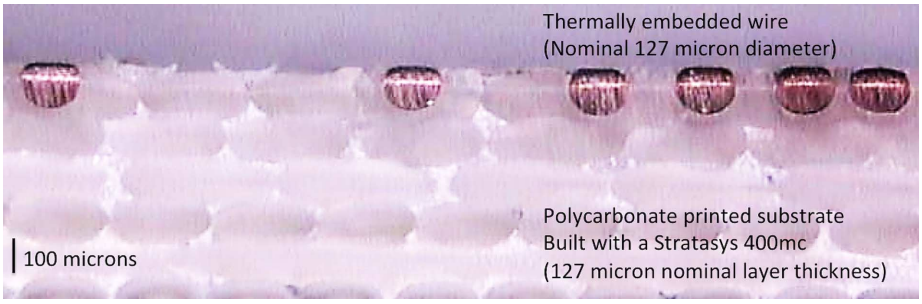

Fig. 4. Cross-sectional view of a 3D-printed polycarbonate substrate with structurally integrated 36-gauge (127-μm-diameter) copper wire.

the surface finish. Although commercially available 3D printers are capable of printing structures with more than one function, this Review specifically focuses on multiprocess 3D printing for multifunctional devices.

The fabrication of most (but not all) multifunctional structures requires processing with multiple integrated technologies, including the combination of 3D printing with other complementary processes to provide or improve spatial control of material, geometry, and functionality. These additional manufacturing capabilities can embed components, wires, batteries, antennas, and other subcomponents. The introduction of electrical and thermal interconnects allows for subsystem communication or the delivery of energy or heat across a structure. Conductive inks and pastes have been used in conjunction with 2D printing, given the manufacturing flexibility of direct writing (e.g., the ability to print conformally, no tooling required), and the combination has been investigated for over a decade with microdispensing (*22*–*25*), ink jetting (*26*–*30*), and aerosol jetting (*31*). Generally, the inks have been dispensed onto external surfaces of finished structures, but only a limited number of examples have involved interrupting and re-initiating a 3D printing process to fully embed interconnect capability. Conductive inks have improved over the past two decades but still suffer from high resistance relative to traditional printed circuit boards created with a bulk copper plating process. Higher resistance conductors result in performance reductions with voltage drops and power loss, and reliability remains an additional concern (*32*). Low-temperature metal alloys have been printed with modified thermoplastic extrusion heads (*33*) and through injection into polymer structures (*34*) to provide interconnection with improved conductivity relative to inks. Although these alloys tend to have higher conductivity relative to conductive particle-loaded inks, interconnection continues to disappoint in comparison with bulk plated copper used in traditional electronics. The use of laser direct structuring to allow for selective plating on 3D printed substrates has been demonstrated, provides bulk properties, and is an exciting development, but it does require an additional chemical bath process (*35*).

A startup company from the Lewis group at Harvard, Voxel8, has announced the first low-cost commercial 3D printer combined with a pneumatic ink dispenser for creating conductive interconnects in 3D printed structures. The ink is printed and cured at room temperature, providing substantial manufacturing benefits and flexibility (*36*). Self-supporting, the ink can bridge internal cavities within structures and is dispensed through a 250-μm nozzle, which is well within the spatial precision required by the majority of traditional electronic components. When a printed trace extends to a pin of a chip, an electrical connection forms without the requirement of high-temperature soldering. An example circuit is shown with an x-ray image of a drone copter in Fig. 3A, along with an example of a modern surface mount chip with connections (0.8-mm pin pitch thin quad flat pack) in Fig. 3B. However, the process involves a higher resistivity of 50×10^{-8} ohm·m (as opposed to bulk copper at 1.68×10^{-8} ohm·m), but it nevertheless provides the first example of an economical desktop 3D printer specifically for electronics (*37*).

The W. M. Keck Center for 3D Innovation at the University of Texas at El Paso has produced 3D-printed electronic circuits since as early as 2004 (*38*) and was recently named a Satellite Center of America Makes, a federal public-private partnership focusing on additive manufacturing and based in Youngstown, Ohio. Recently, the 3D devices produced by the group have featured interconnects that can compete directly with traditional electronics in terms of cost and performance, enabled through the use of structurally embedded wires and foils within 3D-printed thermoplastic structures. Metal filament is selectively heated and in situ submerged flush with the top surface of the thermoplastic structure during a print interruption. Because the embedded wires are available in a wide range of diameters ranging from 80 μm or smaller to virtually any larger size, the fabrication of geometrically elaborate structures can incorporate small intricate routing patterns or large high-power circuits. Once the wires are integrated, the substrate remains planar, and subsequent 3D printing can continue uninhibited. Figure 4 shows 36-gauge (127-μm-diameter) wires embedded in a polycarbonate structure that was printed with a material extrusion printer (Stratasys Fortus 400mc). Movie 1 illustrates the hybrid process as two 3D printers collaboratively create a multimaterial structure in combination with a gantry, which provides complementary processes such as wire embedding or micromachining for fine detail. The blue six-axis robot acts as conveyance to transport the build chamber between manufacturing stations and can be used for postprocess assembly if required. The embedded wires originally intended to afford high-performance electrical interconnection also provide the serendipitous benefit of increased mechanical strength, because they make the structure a reinforced composite (like rebar in concrete). This process can render 3D-printed plastic structures that are stronger than those fabricated with traditional injection molding and helps eliminate the anisotropic strength differences that can compromise 3D-printed structures (e.g., weakness between added layers, so-called *z*-strength weakness in the vertical or *z* direction) (*39*).

Another example of robotic multiprocess additive manufacturing has been integrated with this same wire-embedding technology. The system, called the multirobotic cluster and intended for

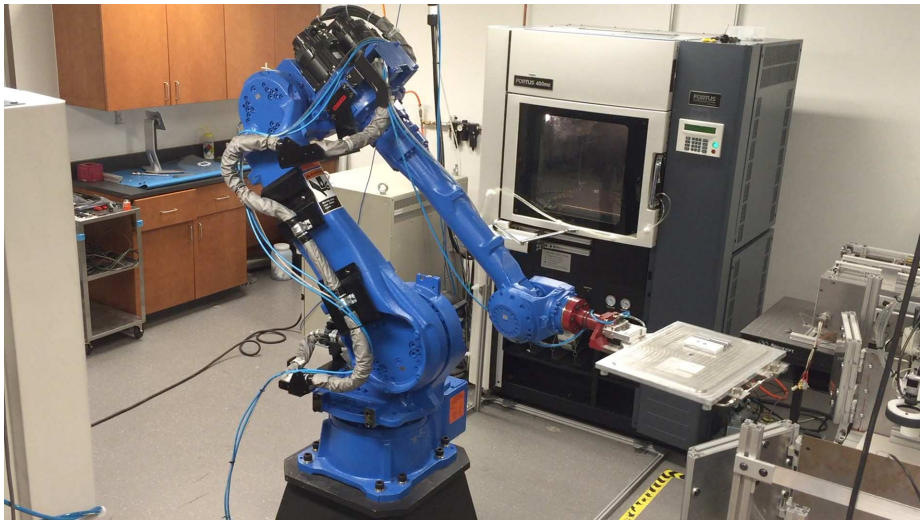

Movie 1. Multiprocess 3D printing.

Downloaded from http://science.sciencemag.org/ on October 7, 2016

large-area manufacturing, includes two six-axis robots to respectively implement additive and subtractive processes (*40*) and is enhanced with a tool exchanger to implement thermal wire embedding during print interruptions. One important contribution of the multirobotic cluster is enabling 3D printing of parts larger than the machine itself, exceeding the size constraint imposed by nearly all 3D printing machines to date, as well as enabling conformal 3D printing.

Comparison with traditional manufacturing

With 3D printing as a foundation, multiprocess additive technologies generally suffer from lower throughput when compared with traditional methods. However, new 3D-printed geometries are now possible, and additive manufacturing has its own advantages; for example, the elimination of tooling allows mass customization through which each production part can be personalized, and the amount of labor required is reduced by the nonassembly methodology. The mechanical performance of the structures produced by some of the additive processes struggles in the area of anisotropic strength; however, more recent technologies, and particularly the powder bed fusion of metals by means of lasers or electron beams, provide many equivalent properties of traditional cast and even wrought materials (*41*), motivating General Electric to use these systems to produce Federal Aviation Administration–approved parts.

Interconnect performance metrics in electronics include routing density, conductivity, dielectric strength, dielectric permittivity, dielectric loss, and general reliability. Ink-based traces on polymer substrates can be fabricated with equivalent routing density relative to traditional printed circuit boards but, at least to date, at the expense of lower conductivity. Routing densities are competitive, with microdispensing of line widths below 10 μm (*22*), ink jetting widths as low as 25 μm (*26*), aerosol jetting traces as small as 10 μm (*31*), laser direct structuring defined by a laser beam width and reported at less than 100 μm (*42*), and structurally embedded wires as thin as 80 μm (*38*). All of these approaches have routing densities at or approaching that of the state-of-the-art printed circuit board, which for comparison is typically around 50 μm. A hypothetical example of conductivity highlights the importance of this parameter to electronics. If an ink-jetted trace is required to deliver a typical 100 mA of electric current to a motor through a printed connection with a width of 250 μm, thickness of 10 μm, and length of 100 mm, the total resistance would accumulate to ~16 ohms for an ink with 40×10^{-8} ohm·m resistivity. The motor would receive a voltage degraded by 1.6 volts, reducing performance. Comparatively, bulk copper (e.g., a similar trace on a printed circuit board, structurally embedded wires, or laser direct structuring) would deliver a resistance less than 1 ohm. Beyond conductivity, the dielectric performance of 3D-printed substrates, particularly polycarbonate and polyetherimide, are close to the levels of traditional electronics (e.g., FR4 laminates), with reasonable permittivity, loss tangent (*43*), and dielectric strength (*44*). Reliability remains relatively unknown for all of these 3D interconnect processes because of the lack of manufacturing history compared with the much older traditional electronics industry.

Printable and embeddable function

For decades, additive processes have been used to achieve complex geometric shapes, which often serve as physical models and prototypes for a range of applications. However, in the past decade, specific features that go beyond simple mechanical functionality have been produced by a growing number of researchers, generally by printing or embedding using multiple processes. Printable functions beyond those provided by basic 3D printing include sensing, transducing, thermal management, electromagnetic, energy storage, and propulsion utility, as described in this section.

Sensors

In terms of embedding sensing into 3D-printed structures, considerable research has focused on either (i) embedding a sensor directly into printed structures during a process interruption or (ii) printing the entire sensor intrinsically into the structure. The integration of sensing into customized complex geometries is beneficial for many applications—examples of which could include patient-specific biomedical devices capable of measuring comfort in prosthetics, optimized control of temperature and pressure in elaborate jet turbines, and motion control in tailor-shaped robotics, to name just a few—and may be useful for many more not yet conceived. Sensing tends to be concentrated into four areas: tactile, motion, vision, and hearing. Of these, tactile sensing is well suited for 3D printing and has dominated research efforts. The other three sensing categories tend to be implemented by integrating traditional commercial off-the-shelf components into 3D-printed structures through robotic or manual insertion. However, in the case of acoustics, Mannoor *et al.* printed a functional microphone in the form and feel of a human ear with biocompatible hydrogels (*45*), and Van Tiem *et al.* printed an angular accelerometer (*46*). Other sensors such as cameras, infrared LEDs (*47*), accelerometers (*7*), pressure sensors, dust sensors, and bioelectrical sensors (*48*) have been inserted directly into designated cavities during fabrication.

Optical sensing of motion has been implemented in structures with material jetting at Disney Research (*47*). Inexpensive infrared diodes can radiate and measure reflections in the translucent 3D-printed walls of an enclosure. Integrating the sensors into the overall structure simplifies sensing and improves volumetric efficiency; however, the proposed optics require a sufficiently transparent structure possible only with liquid-based processes in 3D printing, such as vat photopolymerization or material jetting. Based on photo-curable polymers, these technologies can provide sufficient clarity to serve as light guides but are also constrained by the limitations of photochemistry and the layered fabrication process. The translucence can degrade over time in photo-curable polymers because cross-linking continues after fabrication.

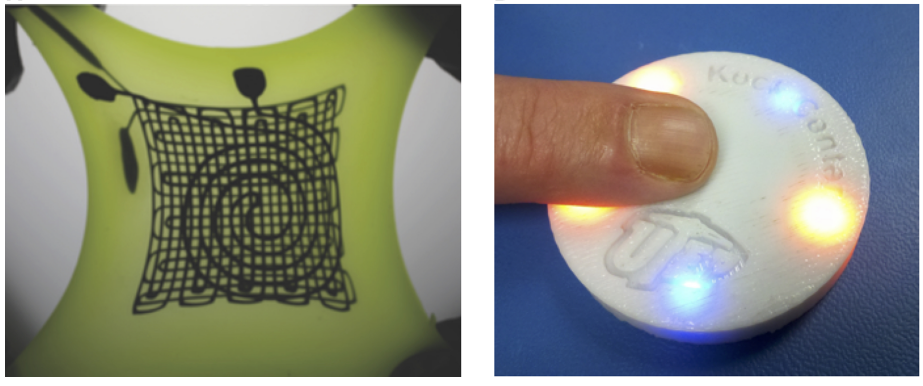

Fig. 5. 3D-printed tactile sensors. (**A**) A stretchable touch sensor. [From (*50*)] (**B**) A capacitive touch sensor. [From (*52*)]

However, a possible alternative is to interrupt the printing process (of virtually any 3D printing technology) and to insert transparent components (glass or optical fiber) into the structure. The work at Disney described many derivative sensing techniques such as (i) displacement with a flexible light guide mounted below the surface of a device, (ii) pressure sensing in which the application of linear force displaces a light guide, (iii) rotation with a screw dial altering a waveguide, and (iv) linear motion with a mechanical slider altering a light reflection path.

Vataini *et al.* presented compliant tactile sensors produced by using a conformal microdispensing system to create a stretchable matrix of piezoresistive traces, the intersections of which provided information about the location of an applied force (*49*). Nanocomposite traces were printed within a skinlike structure that was itself fabricated by 3D printing. The piezoresistive sensing material was created by uniform mixing of multiwalled carbon nanotubes into a polymeric

Downloaded from http://science.sciencemag.org/ on October 7, 2016

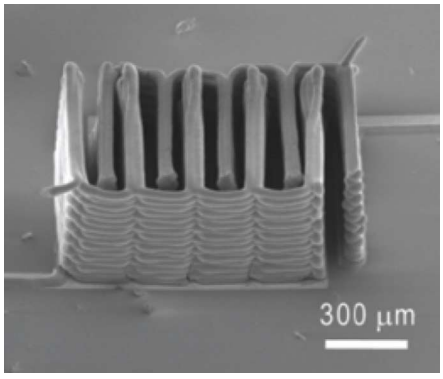

Fig. 6. A 3D-printed Li-ion battery. [From (*70*)]

matrix. Conductive networks were formed inside the polymeric matrix, and external forces deformed the network, increasing contact between nanotubes, and thus the resistance was modulated. Similarly, Muth *et al.* reported creating highly stretchable sensors by 3D printing of a carbon-based ink within an elastomer structure (*50*). The stretchability was well suited for strain gauge measurement. The sensor is shown in Fig. 5A. Hossain *et al.* included high-temperature-tolerant piezoelectric sensors in a metal structure during a pause in the powder bed fusion process, in which the build temperatures are typically above 600°C—a temperature that severely limits the type of components that can survive insertion during fabrication (*51*).

Capacitive touch sensing has been demonstrated by Shemelya *et al.* (*52*). Wire or wire mesh was submerged into 3D-printed thermoplastic structures to act as a single capacitive plate of a touch sensor, in which changes in capacitance could be readily measured indirectly through the frequency of a simple oscillator. A modification in the electric field would indicate the presence of new material in the vicinity (Fig. 5B). The integration of single-sided capacitor plates can be used for custom 3D grip detection, keyboards, and even microfluidic sensors capable of detecting the presence and type of material flowing through structure capillaries.

Actuation

Several forms of mechanical actuation, from simple retraction to fully functional rotational motors, have been demonstrated. Richter and Lipson used vat photopolymerization to create bio-inspired flapping wing insects (*53*). Several groups have created prosthetic hands with embedded external motion (*4*, *54*, *55*). In (*56*), the ability to produce sound with 3D-printed speakers, including for entertainment, was described. By embedding wires coaxially into extruded dielectric filament, Saari *et al.* printed coils as the basis for producing speakers with a tight cylindrical configuration that was coaxially isolated (*57*), providing increased magnetic coupling; however, this isolation limits the applicability for more complex topologies necessary for general interconnection (e.g., multilayered printed circuit boards). Aguilera *et al.* described the fabrication of a high-power (>25 W) electromechanical device (a rotational motor) through a nonassembly additive build sequence based on a material extrusion printer (*58*). With high-performance conductors (solid copper wires) embedded directly into the printed substrate, coiled electromagnets were integrated in an external stator. Two bearings introduced at the top and bottom of a rotor created a mechanical circuit with an internal structure that could rotate freely. The typical requirement for water-soluble support material for internal cavities had to be eliminated because this support is incompatible with embedded electronics, given that water-sensitive circuits would be required to be submerged to remove the support. Consequently, design features were limited to inclines of less than 45° from vertical to minimize overhanging structures and allow the two independent mechanical structures to be constructed without intermediary support. Movie 2 is a time-lapse video of the fabrication of an original proof-of-concept print, and although the intervention was manual, this video highlights a potential application of multiprocess printing providing multifunctionality. In this 5-hour process (shown in time lapse in under 1 min), component and wire embedding were completed by hand to demonstrate the potential of a fully automated fabrication system under development. With the inclusion of an energy source, the possibility exists of fabricating a motorized robot capable of walking or flying out of the 3D printer on completion.

Thermal management

Given the design freedoms afforded by 3D printing, advanced geometrically complex heat exchangers have been explored by researchers for years. Metal 3D printing systems have been used to fabricate complex large-surface-area structures with high thermal conductivity (*59*) for applications such as fluidic heat transfer devices (*60*), 3D-printed plastic injection molds (*61*), and even thermonuclear reactors (*62*). As multiprocess 3D printing advances, thermal management applications will as well, including advanced designs with embedded heat pipes and reservoirs of phase change material, leading to improved thermal management in 3D structures.

Energy storage

At present, contemporary battery manufacturing can provide custom-shaped lithium ion batteries, which are well suited for providing an energy source in an arbitrary shape to improve volumetric efficiencies in assemblies, but these batteries are confined to high-volume production with expensive molds. Research is ongoing to enable the printing of batteries with programmable shapes, but the energy density is orders of magnitude less than that of contemporary commercial batteries, and the long-term reliability is untested. Several groups have printed batteries with roll-to-roll manufacturing (*63*–*66*). The research does not necessarily project to the full 3D geometries; however, sheets may be sufficiently flexible to be rolled or folded. Another option for energy sources in the context of 3D printing is to robotically insert traditional batteries as components during the 3D print, but an obstacle is that many of the printing processes use high-temperature build envelopes. Because most batteries have high energy densities, they have a dangerous sensitivity to temperature, as a result of which they could potentially become unstable (*67*). Consequently, combining component batteries into 3D-printed structures is often not possible unless confined to post-processing assembly steps or low-temperature 3D printing processes, such as binder jetting or vat photopolymerization. MacDonald *et al.* included commercial batteries during postprocessing (*7*). Polymer caps were printed to cover the battery after insertion into the structure, and a low-temperature chemical process welded the plastic cap. A micro–USB (universal serial bus) plug and charging circuit were included to allow for the recharging of a test coupon, which was intended for space flight qualification for a project with the NASA Glenn Research Center. Another option is to embed ultra- or supercapacitors into the structure, which are far less sensitive to temperature in comparison with the chemical storage techniques (*68*).

Malone *et al.* reported a 3D-printed batteries (Zn-air), providing an early example of the combination of 3D-printed structures and energy storage (*69*). 3D-printed Li-ion batteries have been preliminarily demonstrated with high-aspect-ratio interdigitated anodes encapsulated within an electrolyte solution, as shown in Fig. 6 (*70*). The aspect ratios of the patterned microelectrodes were as high as 11 (height to width) for 16-layer electrode walls. The printed array was cured to 600°C to remove binder and sinter the nanoparticles. This temperature would preclude the integration of the process with thermoplastic

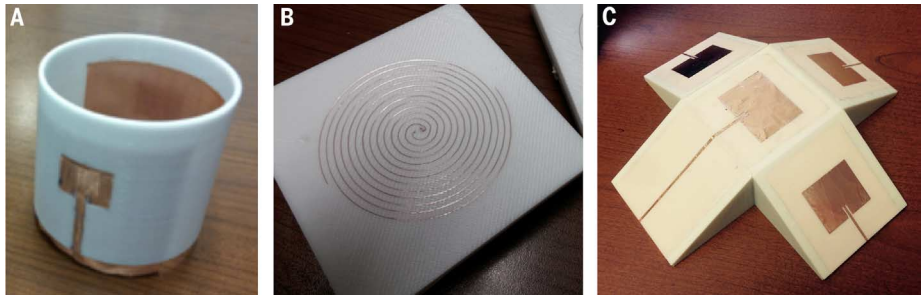

Fig. 7. 3D-printed antenna structures. (**A**) A cylindrical patch antenna, (**B**) an Archimedes antenna, (**C**) and a multiplane patch antenna (*71*).

Downloaded from http://science.sciencemag.org/ on October 7, 2016

3D printing; however, batteries could be printed in custom, arbitrary shapes as a separate process and then inserted within a specific 3D-printed structure after sintering. The most difficult challenge for realization is related to energy density, because at present, printed batteries provide orders of magnitude less energy density than traditional batteries.

Antennas and electromagnetic structures

The rising interest in 3D printing technology is resulting in rethinking of traditional approaches for the design and manufacture of antennas and electromagnetic devices. Several groups have used multiprocess 3D printing technology to embed conductors such as conductive wires, meshes, and metallic foils in order to provide full spatial control of dielectric and conductive structure (*71*–*74*) (Fig. 7). The ability to arbitrarily fabricate structures with a complex network topology of interwoven dielectric components and conductors is enabling a new class of 3D-printed antennas that can provide multiple frequency bands or maintain a small physical footprint while potentially outperforming traditional antennas. The dielectric materials used in these processes can have generally reasonable radio frequency (RF) performances with low loss tangents and, in some cases, can be tailored with the inclusion of high-permittivity additives. Furthermore, these antennas can be integrated seamlessly in the overarching mechanical structure (in the nose cone of a plane, for instance) to save volume, and they provide the serendipitous benefit of improving the mechanical strength of the device by virtue of being a composite structure—demonstrating true multifunctionality. One aspect of 3D printing that has a profound impact on antenna design is the ability to spatially vary the density of a structure with intentional porosity and thus functionally grade the permittivity and permeability. These gradients can enable electromagnetic transitions through material interfaces to minimize reflections or allow for sculpting of RF waves (*75*, *76*). However, one challenge with 3D-printed electromagnetic devices is the reduction in permittivity resulting from the well-known and unintentional porosity inherent in thermoplastic 3D printing processes (*43*).

Propulsion

Interest in 3D printing of space vehicles and satellites has grown in the past decade as a result of NASA's encouragement of the use of 3D printing for structures suitable for space and orbit (*77*–*79*). In addition, the National Academy of Sciences commissioned a committee to study the utility of 3D printing in space (*80*). Propulsion is a specialized case of actuation and is particularly relevant to NASA and motion in space. The use of metal printers to fabricate rocket thrusters for spacecraft was reported in (*81*). Presently, CubeSats are generally free-floating, low-cost satellites used in inexpensive university space science and often constructed with off-the-shelf components. These satellites often are launched parasitically and can use magnetic torque rods or momentum wheels if attitude control is required, but these generally consume a large fraction of precious space in the volume-limited format of CubeSats. Although various electric propulsion concepts are available, micro–pulsed plasma thrusters (μPPTs) offer tight integration, long shelf life, and survivability in the high fabrication temperatures of 3D printing build chambers. Additionally, because 3D-printed polymers provide appropriate dielectric strength and recently available copper wires have sufficiently low resistance, Marshall *et al.* were able to demonstrate this form of propulsion by delivering high voltages (over 1000 V) in 3D-printed test coupons to ignite μPPTs (*82*). This example manifests the utility of multiprocess 3D printing with wire and component placement, substantially benefitting the manufacturing of space components and vehicles. Movie 3 shows a series of ignitions in an evacuated bell jar.

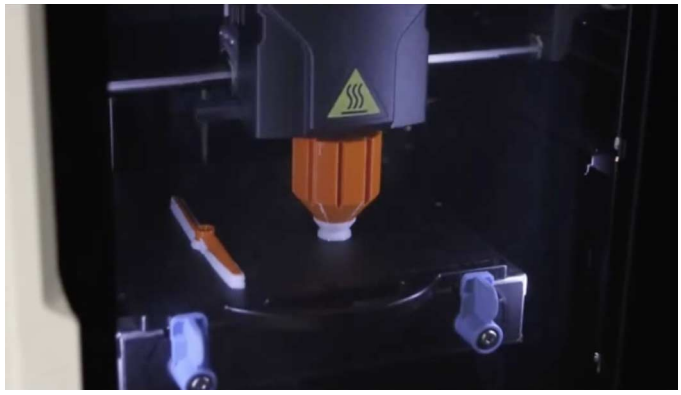

Movie 2. Time-lapse video of the fabrication of a 3D-printed motor.

Movie 3. 3D-printed propulsion. Shown are Busek electro-pulsed plasma thrusters integrated into a 3D-printed structure and ignited by high voltages (*82*).

Conclusions and outlook

Multiprocess (or hybrid) 3D printing, where complementary processes are combined to advance manufacturing by increasing the functionality of fabricated components, has been the focus of this Review. As 3D printing continues to advance, the next generation of printers will fabricate not just dissimilar materials but structures with embedded and interconnected active components to provide functionality that was not possible previously. The progress thus far has illustrated the potential for leveraging multiprocess 3D printing to provide a broad base of capabilities necessary for customized end-use production. For multifunctional additive manufacturing to become an economic reality, however, substantial hurdles must be overcome in a number of areas: (i) material enhancements, including for mechanical performance; (ii) the diversity of materials available in terms of characteristics such as flexibility or thermal and electrical conductivity; (iii) improved material interfacial performance to ensure the reliability of structures composed of multiple materials; (iv) computer-aided design and computer modeling to optimize the complex geometries and performance possible when working with disparate content simultaneously (e.g., mechanical and electrical features fabricated concurrently); (v) process feedback control, which is widely absent in most contemporary printers and will become even more necessary in the context of multiple interacting processes required for fabrication of aerospace-grade or biomedical devices; and (vi) development of the manufacturing hardware and software necessary for a wide range of complementary technologies to collaborate with 3D printers in order to fabricate fully multifunctional devices. The required investment has begun, notably in the federal public-private initiative on manufacturing and the resulting America Makes program, which is focused on many of the challenges facing 3D printing technologies. Similar investment from industry and government will need to grow in order to fully leverage the advantages made possible by this next generation of manufacturing.

REFERENCES AND NOTES

1. H. Smith, "GE aviation to grow better fuel nozzles using 3D printing," *3D Printing News and Trends*, 17 June 2013; http://3dprintingreviews.blogspot.co.uk/2013/06/ge-aviation-to-grow-better-fuel-nozzles.html.
2. I. Gibson, D. W. Rosen, B. Stucker, *Additive Manufacturing Technologies* (Springer, 2010).
3. Wohlers Associates, *Wohlers Report 2014* (Wohlers Associates, 2014).
4. L. J. Love, R. F. Lind, J. F. Jansen, "Mesofluidic actuation for articulated finger and hand prosthetics," in *2009 IEEE/RSJ Conference on Intelligent Robots and Systems* [Institute of Electrical and Electronics Engineers (IEEE), 2009], pp. 2586–2591.

Downloaded from http://science.sciencemag.org/ on October 7, 2016

5. B. P. Conner *et al.*, Making sense of 3-D printing: Creating a map of additive manufacturing products and services. *Addit. Manuf.* **1–4**, 64–76 (2014). doi: 10.1016/j.addma.2014.08.005
6. P. Reeves, C. Tuck, R. Hague, "Additive manufacturing for mass customization," in *Mass Customization: Engineering and Managing Global Operations*, F. S. Fogliatto, G. J. C. da Silveira, Eds. (Springer, 2011), pp. 275–289.
7. E. MacDonald *et al.*, 3D printing for the rapid prototyping of structural electronics. *IEEE Access* **2**, 234–242 (2014). doi: 10.1109/ACCESS.2014.2311810
8. ASTM F42 Committee, *Terminology for Additive Manufacturing Technologies* (ASTM International, 2012).
9. L. E. Weiss *et al.*, Shape deposition manufacturing of heterogeneous structures. *J. Manuf. Syst.* **16**, 239–248 (1997). doi: 10.1016/S0278-6125(97)89095-4
10. A. Kataria, D. W. Rosen, Building around inserts: Methods for fabricating complex devices in stereolithography. *Rapid Prototyping J.* **7**, 253–262 (2001). doi: 10.1108/13552540110410459
11. A. J. Lopes, E. MacDonald, R. B. Wicker, Integrating stereolithography and direct print technologies for 3D structural electronics fabrication. *Rapid Prototyping J.* **18**, 129–143 (2012). doi: 10.1108/13552541211212113
12. C. Robinson, B. E. Stucker, A. J. Lopes, R. Wicker, J. A. Palmer, "Integration of direct-write and ultrasonic consolidation technologies to create advanced structures with embedded electrical circuitry," in *Solid Freeform Fabrication Symposium Proceedings* (University of Texas at Austin, 2006), pp. 60–69.
13. E. Malone, H. Lipson, Fab@Home: The personal desktop fabricator kit. *Rapid Prototyping J.* **13**, 245–255 (2007). doi: 10.1108/13552540710776197
14. M. Navarrete, A. Lopes, J. Acuna, R. Estrada, E. MacDonald, J. Palmer, R. Wicker, "Integrated layered manufacturing of a novel wireless motion sensor system with GPS," in *Solid Freeform Fabrication Symposium Proceedings* (University of Texas at Austin, 2007), pp. 575–585; http://sffsymposium.engr.utexas.edu/Manuscripts/2007/2007-49-Wicker.pdf.
15. S. Scott Crump, "Apparatus and method for creating three-dimensional objects," U.S. Patent 5,121,329 (1992).
16. J. Liu, Z. Bor, "Layered manufacturing of a multi-material or multi-color 3-D object using electrostatic imaging and lamination," U.S. Patent 6,780,368 (2004).
17. D. Qiu, N. A. Langrana, Void eliminating toolpath for extrusion-based multi-material layered manufacturing. *Rapid Prototyping J.* **8**, 38–45 (2002). doi: 10.1108/13552540210413293
18. J. W. Choi, E. MacDonald, R. Wicker, Multi-material microstereolithography. *Int. J. Adv. Manuf. Technol.* **49**, 543–551 (2010). doi: 10.1007/s00170-009-2434-8
19. R. B. Wicker, E. MacDonald, Multi-material, multi-technology stereolithography. *Virtual Phys. Prototyping* **7**, 181–194 (2012). doi: 10.1080/17452759.2012.721119
20. L. W. Ming, I. Gibson, Specification of VRML in color rapid prototyping. *Int. J. CAD/CAM* **1**, 1 (2002).
21. M. R. Haberman, T. D. Klatt, P. S. Wilson, C. Seepersad, Negative stiffness metamaterials and periodic composites. *J. Acoust. Soc. Am.* **131**, 3372 (2012). doi: 10.1121/1.4708717
22. B. Y. Ahn *et al.*, Planar and three-dimensional printing of conductive inks. *J. Vis. Exp.* **58**, e3189 (2011). pmid: 22214978
23. R. O. Kadara, N. Jenkinson, B. Li, K. H. Church, C. E. Banks, Manufacturing electrochemical platforms: Direct-write dispensing versus screen printing. *Electrochem. Commun.* **10**, 1517–1519 (2008). doi: 10.1016/j.elecom.2008.08.002
24. N. S. Kim, K. N. Han, Future direction of direct writing. *J. Appl. Phys.* **108**, 102801 (2010). doi: 10.1063/1.3510359
25. K. B. Perez, C. B. Williams, "Combining additive manufacturing and direct write for integrated electronics—a review," in *Solid Freeform Fabrication Symposium Proceedings* (University of Texas at Austin, 2013), pp. 962–979; http://sffsymposium.engr.utexas.edu/Manuscripts/2013/2013-77-Perez.pdf.
26. J. U. Park *et al.*, High-resolution electrohydrodynamic jet printing. *Nat. Mater.* **6**, 782–789 (2007). doi: 10.1038/nmat1974; pmid: 17676047
27. J. Mei, M. R. Lovell, M. H. Mickle, Formulation and processing of novel conductive solution inks in continuous inkjet printing of 3-D electric circuits. *IEEE Trans. Electron. Packag. Manuf.* **28**, 265–273 (2005).
28. P. J. Smith, D. Y. Shin, J. E. Stringer, B. Derby, N. Reis, Direct ink-jet printing and low temperature conversion of conductive silver patterns. *J. Mater. Sci.* **41**, 4153–4158 (2006). doi: 10.1007/s10853-006-6653-1
29. G. Shaker, S. Safavi-Naeini, N. Sangary, M. M. Tentzeris, Inkjet printing of ultrawideband (UWB) antennas on paper-based substrates. *IEEE Antennas Wireless Propag. Lett.* **10**, 111–114 (2011). doi: 10.1109/LAWP.2011.2106754
30. F. Zhang *et al.*, Inkjet printing of polyimide insulators for the 3D printing of dielectric materials for microelectronic applications. *J. Appl. Polym. Sci.* **133**, 43361 (2016). doi: 10.1002/app.43361
31. M. O'Reilly, J. Leal, Jetting your way to fine-pitch 3D interconnects. *Chip Scale Rev.* **14**, 18–21 (2010).
32. J. L. Zunino III, D. P. Schmidt, A. M. Petrock, B. E. Fuchs, Inkjet printed devices for armament applications. *NSTI-Nanotech* **2**, 542–545 (2010).
33. J. Mireles *et al.*, Development of a fused deposition modeling system for low melting temperature metal alloys. *J. Electron. Packag.* **135**, 011008 (2013). doi: 10.1115/1.4007160
34. J. P. Swensen, L. U. Odhner, B. Araki, A. M. Dollar, Printing three-dimensional electrical traces in additive manufactured parts for injection of low melting temperature metals. *J. Mech. Robotics* **7**, 021004 (2015). doi: 10.1115/1.4029435
35. A. Wild, Integration of functional circuits into FDM parts. *Adv. Mater. Res.* **1038**, 29–33 (2014). doi: 10.4028/www.scientific.net/AMR.1038.29
36. J. A. Lewis, B. Y. Ahn, Device fabrication: Three-dimensional printed electronics. *Nature* **518**, 42–43 (2015). doi: 10.1038/518042a; pmid: 25652992
37. Voxel8, "Materials," www.voxel8.co/materials/.
38. D. Espalin, D. W. Muse, E. MacDonald, R. B. Wicker, 3D printing multi-functionality: Structures with electronics. *Int. J. Adv. Manuf. Technol.* **72**, 963–978 (2014). doi: 10.1007/s00170-014-5717-7
39. D. Espalin, D. Roberson, R. Wicker, "Expanding the impact of polymeric-based 3D printing technologies," *Plastics Trends*, 14 June 2014; www.plasticstrends.net/index.php/component/content/article/1-this-month/370-expanding-the-impact-of-polymeric-based-3d-printing-technologies.
40. C. Newell *et al.*, Out of bounds additive manufacturing. *Adv. Mater. Process.* **171**, 15–19 (2013).
41. L. E. Murr *et al.*, Metal fabrication by additive manufacturing using laser and electron beam melting technologies. *J. Mater. Sci. Technol.* **28**, 1–14 (2012). doi: 10.1016/S1005-0302(12)60016-4
42. J. Franke, Ed., *Three-Dimensional Molded Interconnect Devices (3D-MID): Materials, Manufacturing, Assembly and Applications for Injection Molded Circuit Carriers* (Hanser, 2014).
43. P. I. Deffenbaugh, R. C. Rumpf, K. H. Church, Broadband microwave frequency characterization of 3-D printed materials. *IEEE Trans. Components Packag. Manuf. Technol.* **3**, 2147–2155 (2013). doi: 10.1109/TCPMT.2013.2273306
44. D. M. French, J. P. O'Loughlin, B. Hoff, S. Maestas, D. Lepell, T. Montoya, "Dielectric strength testing of 3D printed plastics and application to a high voltage transformer pulser," in *2015 IEEE Pulsed Power Conference* (IEEE, 2015).
45. M. S. Mannoor *et al.*, 3D printed bionic ears. *Nano Lett.* **13**, 2634–2639 (2013). doi: 10.1021/nl4007744; pmid: 23635097
46. J. Van Tiem, G. Jarno, R. Sanders, G. Krijnen, "3D printed bio-inspired angular acceleration sensor," in *SENSORS, IEEE 2015* (IEEE, 2015), pp. 1430–1433.
47. K. Willis, E. Brockmeyer, S. Hudson, I. Poupyrev, "Printed optics: 3D printing of embedded optical elements for interactive devices," in *UIST '12: Proceedings of the 25th Annual ACM Symposium on User Interface Software and Technology* [Association for Computing Machinery (ACM), 2012], pp. 589–598; http://dl.acm.org/citation.cfm?id=2380190.
48. P. Salvo *et al.*, A 3D printed dry electrode for ECG/EEG recording. *Sens. Actuators A Phys.* **174**, 96–102 (2012). doi: 10.1016/j.sna.2011.12.017
49. M. Vatani, E. D. Engeberg, J. W. Choi, Conformal direct-print of piezoresistive polymer/nanocomposites for compliant multi-layer tactile sensors. *Addit. Manuf.* **7**, 73–82 (2015). doi: 10.1016/j.addma.2014.12.009
50. J. T. Muth *et al.*, Embedded 3D printing of strain sensors within highly stretchable elastomers. *Adv. Mater.* **26**, 6307–6312 (2014). doi: 10.1002/adma.201400334; pmid: 24934143
51. M. S. Hossain *et al.*, Fabrication of smart parts using powder bed fusion additive manufacturing technology. *Addit. Manuf.* **10**, 58–66 (2016). doi: 10.1016/j.addma.2016.01.001
52. C. Shemelya *et al.*, Encapsulated copper wire and copper mesh capacitive sensing for 3-D printing applications. *IEEE Sensors J.* **15**, 1280–1286 (2015). doi: 10.1109/JSEN.2014.2356973
53. C. Richter, H. Lipson, Untethered hovering flapping flight of a 3D-printed mechanical insect. *Artif. Life* **17**, 73–86 (2011). doi: 10.1162/artl_a_00020; pmid: 21370958
54. L. U. Odhner *et al.*, A compliant, underactuated hand for robust manipulation. *Int. J. Robot. Res.* **33**, 736–752 (2014). doi: 10.1177/0278364913514466
55. L. Kelion, "Open Bionics robotic hand for amputees wins Dyson Award," BBC News, 25 August 2015; www.bbc.com/news/technology-34044453.
56. Y. Ishiguro, I. Poupyrev, "3D printed interactive speakers," in *CHI '14: Proceedings of the SIGCHI Conference on Human Factors in Computing Systems* (ACM, 2014), pp. 1733–1742; http://dl.acm.org/citation.cfm?id=2557046.
57. M. Saari, B. Cox, E. Richer, P. S. Krueger, A. L. Cohen, Fiber encapsulation additive manufacturing: An enabling technology for 3D printing of electromechanical devices and robotic components. *3D Print. Addit. Manuf.* **2**, 32–39 (2015).
58. E. Aguilera, J. Ramos, D. Espalin, F. Cedillos, D. Muse, R. Wicker, E. MacDonald, "3D printing of electro mechanical systems," in *Solid Freeform Fabrication Symposium Proceedings* (University of Texas at Austin, 2013), pp. 950–961; http://sffsymposium.engr.utexas.edu/Manuscripts/2013/2013-76-Aguilera.pdf.
59. T. J. Horn, O. L. Harrysson, Overview of current additive manufacturing technologies and selected applications. *Sci. Prog.* **95**, 255–282 (2012). doi: 10.3184/003685012X13420984463047; pmid: 23094325
60. M. Wong, S. Tsopanos, C. J. Sutcliffe, I. Owen, Selective laser melting of heat transfer devices. *Rapid Prototyping J.* **13**, 291–297 (2007). doi: 10.1108/13552540710824797
61. E. Sachs, E. Wylonis, S. Allen, M. Cima, H. Guo, Production of injection molding tooling with conformal cooling channels using the three dimensional printing process. *Polym. Eng. Sci.* **40**, 1232–1247 (2000). doi: 10.1002/pen.11251
62. M. A. García, C. García-Pando, C. Marto, "Conformal cooling in moulds with special geometry," in *Innovative Developments in Virtual and Physical Prototyping* (CRC Press, 2011), pp. 409–412.
63. A. M. Gaikwad, G. L. Whiting, D. A. Steingart, A. C. Arias, Highly flexible, printed alkaline batteries based on mesh-embedded electrodes. *Adv. Mater.* **23**, 3251–3255 (2011). doi: 10.1002/adma.201100894; pmid: 21661062
64. M. Wendler, G. Hübner, I. M. Krebs, Development of printed thin and flexible batteries. *Int. Circ. Graphic Ed. Res.* **4**, 32–41 (2011).
65. M. Hilder, B. Winther-Jensen, N. B. Clark, Paper-based, printed zinc–air battery. *J. Power Sources* **194**, 1135–1141 (2009). doi: 10.1016/j.jpowsour.2009.06.054
66. M. Kaltenbrunner, G. Kettlgruber, C. Siket, R. Schwödiauer, S. Bauer, Arrays of ultracompliant electrochemical dry gel cells for stretchable electronics. *Adv. Mater.* **22**, 2065–2067 (2010). doi: 10.1002/adma.200904068; pmid: 20354974
67. P. G. Balakrishnan, R. Ramesh, T. Prem Kumar, Safety mechanisms in lithium-ion batteries. *J. Power Sources* **155**, 401–414 (2006). doi: 10.1016/j.jpowsour.2005.12.002
68. C. Zhao *et al.*, Three dimensional (3D) printed electrodes for interdigitated supercapacitors. *Electrochem. Commun.* **41**, 20–23 (2014). doi: 10.1016/j.elecom.2014.01.013
69. E. Malone, M. Berry, H. Lipson, Freeform fabrication and characterization of Zn-air batteries. *Rapid Prototyping J.* **14**, 128–140 (2008). doi: 10.1108/13552540810877987
70. K. Sun *et al.*, 3D printing of interdigitated Li-ion microbattery architectures. *Adv. Mater.* **25**, 4539–4543 (2013). doi: 10.1002/adma.201301036; pmid: 23776158
71. M. Liang, C. Shemelya, E. MacDonald, R. Wicker, H. Xin, 3-D printed microwave patch antenna via fused deposition method and ultrasonic wire mesh embedding technique. *IEEE Antennas Wireless Propag. Lett.* **14**, 1346–1349 (2015). doi: 10.1109/LAWP.2015.2405054
72. S. Moscato *et al.*, Infill-dependent 3D-printed material based on NinjaFlex filament for antenna applications. *IEEE Antennas Wireless Propag. Lett.* **15**, 1506–1509 (2016). doi: 10.1109/LAWP.2016.2516101
73. T. P. Ketterl *et al.*, A 2.45 GHz phased array antenna unit cell fabricated using 3-D multi-layer direct digital manufacturing. *IEEE Trans. Microwave Theory Tech.* **63**, 4382–4394 (2015).
74. P. I. Deffenbaugh, T. M. Weller, K. H. Church, Fabrication and microwave characterization of 3-D printed transmission lines. *IEEE Microwave Wireless Components Lett.* **25**, 823–825 (2015). doi: 10.1109/LMWC.2015.2495184
75. M. Liang *et al.*, A 3-D Luneburg lens antenna fabricated by polymer jetting rapid prototyping. *IEEE Trans. Antenna Propag.* **62**, 1799–1807 (2014). doi: 10.1109/TAP.2013.2297165

Downloaded from http://science.sciencemag.org/ on October 7, 2016

76. R. C. Rumpf, J. J. Pazos, J. L. Digaum, S. M. Kuebler, Spatially variant periodic structures in electromagnetics. *Phil. Trans. R. Soc. A* **373**, 20140359 (2015). doi: 10.1098/rsta.2014.0359; pmid: 26217058
77. J. C. Lyke, Plug-and-play satellites. *IEEE Spectr.* **49**, 36–42 (2012). doi: 10.1109/MSPEC.2012.6247560
78. L. Novakova-Marcincinova, I. Kuric, Basic and advanced materials for fused deposition modeling rapid prototyping technology. *Manuf. Ind. Eng.* **11**, 24–27 (2012).
79. C. M. Shemelya *et al*., Mechanical, electromagnetic, and x-ray shielding characterization of a 3D printable tungsten–polycarbonate polymer matrix composite for space-based applications. *J. Electron. Mater.* **44**, 2598–2607 (2015). doi: 10.1007/s11664-015-3687-7
80. Aeronautics and Space Engineering Board, National Materials and Manufacturing Board, Division on Engineering and Physical Sciences, National Research Council, *3D Printing in Space* (National Academies Press, 2014).
81. M. Kramer, "3-D-printed rocket part passes major NASA test," *NBC News*, 18 July 2013; www.nbcnews.com/science/3-d-printed-rocket-part-passes-major-nasa-test-6C10674019.
82. W. M. Marshall, M. Zemba, C. Shemelya, R. Wicker, D. Espalin, E. MacDonald, A. Kwas, "Using additive manufacturing to print a CubeSat propulsion system," *51st AIAA/SAE/ASEE Joint Propulsion Conference* (American Institute of Aeronautics and Astronautics, 2015); http://arc.aiaa.org/doi/pdf/10.2514/6.2015-4184.

ACKNOWLEDGMENTS

We acknowledge NSF, the Department of Defense, the National Institute of Standards and Technology, NASA, the Department of Energy, and the intelligence community for support that enabled much of this broad research. America Makes, a U.S. public-private partnership with member organizations from industry, academia, and government (www.americamakes.us), has provided support and guidance for substantial portions of these developments and has had a profound impact on the authors and their research.

10.1126/science.aaf2093

Downloaded from http://science.sciencemag.org/ on October 7, 2016

RESEARCH ARTICLE SUMMARY

NEURODEGENERATION

Pathological α-synuclein transmission initiated by binding lymphocyte-activation gene 3

Xiaobo Mao, Michael Tianhao Ou, Senthilkumar S. Karuppagounder, Tae-In Kam, Xiling Yin, Yulan Xiong, Preston Ge, George Essien Umanah, Saurav Brahmachari, Joo-Ho Shin, Ho Chul Kang, Jianmin Zhang, Jinchong Xu, Rong Chen, Hyejin Park, Shaida A. Andrabi, Sung Ung Kang, Rafaella Araújo Gonçalves, Yu Liang, Shu Zhang, Chen Qi, Sharon Lam, James A. Keiler, Joel Tyson, Donghoon Kim, Nikhil Panicker, Seung Pil Yun, Creg J. Workman, Dario A. A. Vignali, Valina L. Dawson,* Han Seok Ko,* Ted M. Dawson*

INTRODUCTION: Parkinson's disease (PD) is the second most common neurodegenerative disorder and leads to slowness of movement, tremor, rigidity, and, in the later stages of PD, cognitive impairment. Pathologically, PD is characterized by the accumulation of α-synuclein in Lewy bodies and neurites. There is degeneration of neurons throughout the nervous system, with the degeneration of dopamine neurons in the substantia nigra pars compacta leading to the major symptoms of PD.

RATIONALE: In the brains of PD patients, pathologic α-synuclein seems to spread from cell to cell via self-amplification, propagation, and transmission in a stereotypical and topographical pattern among neighboring cells and/or anatomically connected brain regions. The spread or transmission of pathologic α-synuclein is emerging as a potentially important driver of PD pathogenesis. The underlying mechanisms and molecular entities responsible for the transmission of pathologic α-synuclein from cell to cell are not known, but the entry of pathologic α-synuclein into neurons is thought to occur, in part, through an active clathrin-dependent endocytic process.

RESULTS: Using recombinant α-synuclein preformed fibrils (PFF) as a model system with which to study the transmission of misfolded α-synuclein from neuron to neuron, we screened a library encoding transmembrane proteins for α-synuclein-biotin PFF–binding candidates via detection with streptavidin-AP (alkaline phosphatase) staining. Three positive clones were identified that bind α-synuclein PFF and include lymphocyte-activation gene 3 (LAG3), neurexin 1β, and amyloid β precursor-like protein 1 (APLP1). Of these three transmembrane proteins, LAG3 demonstrated the highest ratio of selectivity for α-synuclein PFF over the α-synuclein monomer. α-Synuclein PFF bind to LAG3 in a saturable manner (dissociation constant = 77 nM), whereas the α-synuclein monomer does not bind to LAG3. Co-immunoprecipitation also suggests that pathological α-synuclein PFF specifically bind to LAG3. Tau PFF, β-amyloid oligomer, and β-amyloid PFF do not bind to LAG3, indicating that LAG3 is specific for α-synuclein PFF. The internalization of α-synuclein PFF involves LAG3 because deletion of LAG3 reduces the endocytosis of α-synuclein PFF. LAG3 colocalizes with the endosomal guanosine triphosphatases Rab5 and Rab7 and coendocytoses with pathologic α-synuclein. Neuron-to-neuron transmission of pathologic α-synuclein and the accompanying pathology and neurotoxicity is substantially attenuated by deletion of LAG3 or by antibodies to LAG3. The lack of LAG3 also substantially delayed α-synuclein PFF–induced loss of dopamine neurons, as well as biochemical and behavioral deficits in vivo.

CONCLUSION: We discovered that pathologic α-synuclein transmission and toxicity is initiated by binding to LAG3 and that neuron-to-neuron transmission of pathological α-synuclein involves the endocytosis of exogenous α-synuclein PFF by the engagement of LAG3 on neurons. Depletion of LAG3 or antibodies to LAG3 substantially reduces the pathology set in motion by the transmission of pathologic α-synuclein. The identification of LAG3 as an α-synuclein PFF–binding protein provides a new target for developing therapeutics designed to slow the progression of PD and related α-synucleinopathies. ■

ON OUR WEBSITE

Read the full article at http://dx.doi.org/10.1126/science.aah3374

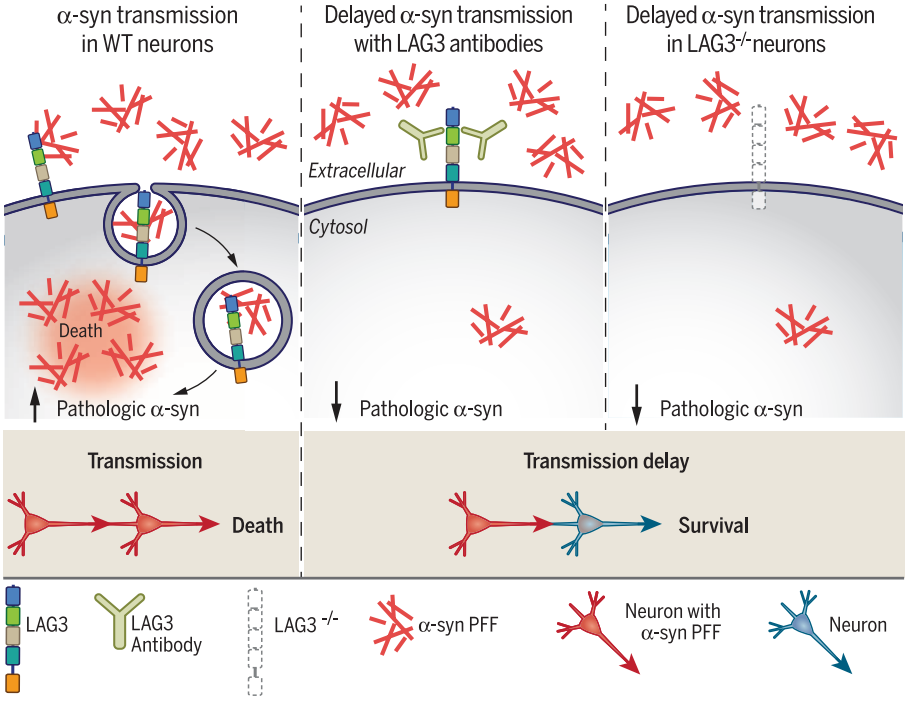

ILLUSTRATION CREDIT: I-HSUN WU

LAG3 deletion or antibodies to LAG3 delay α-synuclein PFF transmission. Compared with wild-type neurons, binding and endocytosis of α-synuclein PFF is dramatically reduced with antibodies to LAG3 or when LAG3 is deleted, resulting in delayed pathologic α-synuclein transmission and toxicity.

The list of author affiliations is available in the full article online.
*Corresponding author. Email: tdawson@jhmi.edu (T.M.D.); hko3@jhmi.edu (H.S.K.); vdawson1@jhmi.edu (V.L.D.)
Cite this article as X. Mao *et al.*, *Science* 353, aah3374 (2016). DOI: 10.1126/science.aah3374

Downloaded from http://science.sciencemag.org/ on October 7, 2016

RESEARCH ARTICLE

NEURODEGENERATION

Pathological α-synuclein transmission initiated by binding lymphocyte-activation gene 3

Xiaobo Mao,[1,2,3] Michael Tianhao Ou,[1,2] Senthilkumar S. Karuppagounder,[1,2,3] Tae-In Kam,[1,2,3] Xiling Yin,[1,2,3] Yulan Xiong,[1,2,3]* Preston Ge,[1,2] George Essien Umanah,[1,2,3] Saurav Brahmachari,[1,2,3] Joo-Ho Shin,[1,2,4] Ho Chul Kang,[1,2,5] Jianmin Zhang,[1,2]† Jinchong Xu,[1,2,3] Rong Chen,[1,2,3] Hyejin Park,[1,2,3] Shaida A. Andrabi,[1,2,3]‡ Sung Ung Kang,[1,2,3] Rafaella Araújo Gonçalves,[1,2]§ Yu Liang,[1,2] Shu Zhang,[1,2] Chen Qi,[1,2,6] Sharon Lam,[1,2] James A. Keiler,[1,2] Joel Tyson,[1,2,7] Donghoon Kim,[1,2] Nikhil Panicker,[1,2,3] Seung Pil Yun,[1,2,3] Creg J. Workman,[8] Dario A. A. Vignali,[8,9] Valina L. Dawson,[1,2,3,10,11]‖ Han Seok Ko,[1,2,3]‖ Ted M. Dawson[1,2,7,11,12]‖

Emerging evidence indicates that the pathogenesis of Parkinson's disease (PD) may be due to cell-to-cell transmission of misfolded preformed fibrils (PFF) of α-synuclein (α-syn). The mechanism by which α-syn PFF spreads from neuron to neuron is not known. Here, we show that LAG3 (lymphocyte-activation gene 3) binds α-syn PFF with high affinity (dissociation constant = 77 nanomolar), whereas the α-syn monomer exhibited minimal binding. α-Syn-biotin PFF binding to LAG3 initiated α-syn PFF endocytosis, transmission, and toxicity. Lack of LAG3 substantially delayed α-syn PFF–induced loss of dopamine neurons, as well as biochemical and behavioral deficits in vivo. The identification of LAG3 as a receptor that binds α-syn PFF provides a target for developing therapeutics designed to slow the progression of PD and related α-synucleinopathies.

Parkinson's disease (PD) is the second most common neurodegenerative disorder and is characterized clinically by motor dysfunction and pathologically by the aggregation and accumulation of α-synuclein (α-syn) (*1*–*3*). Emerging evidence suggests that α-syn spreads from neuron to neuron via self-amplification, propagation, and transmission in the pathogenesis of PD (*4*–*6*). In the brains of PD patients, α-syn aggregates seem to spread in a stereotypical and topographical pattern (*7*, *8*). Postmortem examination of fetal grafts in patients with PD found α-syn–positive Lewy bodies, which is suggestive of spread of α-syn from host to graft (*9*, *10*). Other proteins such as β-amyloid and tau in Alzheimer's disease are also thought to propagate and spread and contribute to the onset and progression of these disorders (*11*, *12*). Pathological α-syn has been shown to spread among neighboring cells and/or anatomically connected brain regions. Recently recombinant α-syn preformed fibrils (PFF) provide a model system that enables the study of the transmission of misfolded α-syn from neuron to neuron both in vitro (*13*) and in vivo (*14*). How pathological α-syn exits cells and transmits to neighboring neurons is not known, but entry into neurons is thought to occur, in part, through an active clathrin-dependent endocytic process (*15*–*17*).

Identification of α-syn PFF-binding proteins

Mouse α-syn was synthesized and conjugated to biotin (α-syn-biotin) and then aggregated over 7 days followed by sonication to form α-syn PFF of relatively uniform size (*18*). We used size exclusion chromatography to separate α-syn PFF from α-syn monomers (fig. S1A). We validated recombinant α-syn-biotin monomers and α-syn PFF with immunoblot analysis (fig. S1B). We examined α-syn-biotin monomers and PFF by means of atomic force microscopy (AFM) and transmission electron microscopy (TEM). α-Syn-biotin monomers exhibited no regular structure, whereas α-syn-biotin PFF exhibited short fibrillar structures (fig. S1, C and D). We then sought to investigate the interaction between extracellular α-syn and neurons. α-Syn-biotin PFF binds to cortical neurons as detected with streptavidin-AP (alkaline phosphatase) staining (*19*–*21*), whereas α-syn-biotin monomers weakly bind nonspecifically to neurons (fig. S2, A to C). α-Syn-biotin PFF binding to neurons is saturable with an apparent dissociation constant (K_d) of 374 nM (fig. S2, A to C), suggesting the existence of receptor(s) or binding site(s) for α-syn PFF. We screened a library of transmembrane proteins for potential α-syn-biotin PFF-binding candidates via detection with streptavidin-AP staining (fig. S3A) (*19*–*21*). A key requirement for expression cloning is the existence of a cell line with low α-syn-biotin PFF background binding. SH-SY5Y cells exhibited <8% of the binding levels of α-syn-biotin PFF as compared with cortical neurons, whereas COS7 and HeLa cells exhibited relatively high binding, and human embryonic kidney (HEK) 293FT cells exhibited mild binding (fig. S3, B and C). Complementary DNAs encoding 352 transmembrane proteins (TMGW10001, GFC-transfection array panel, Origene) were expressed in SH-SY5Y cells and screened for α-syn-biotin PFF–binding candidates. This screening approach is a well-established method with which to identify ligand receptor interactions (*19*, *20*) but will not identify receptors composed of heteromeric subunits. Three positive clones were identified that bind α-syn-biotin PFF and include lymphocyte-activation gene 3 (LAG3), neurexin 1β, and amyloid β precursor-like protein 1 (APLP1) (Fig. 1A). Our screen provides Z-factor coefficients of 0.82, 0.84, and 0.84 through three independent experiments, suggesting that the screen was within the optimal signal window to preclude false positives or negatives.

α-Syn PFF preferentially binds LAG3

The selectivity of LAG3, neurexin 1β, and APLP1 and related transmembrane proteins for α-syn-biotin PFF versus α-syn-biotin monomers was determined via the ratio of K_d values (Fig. 1B). LAG3 exhibited the highest selectivity with a ratio of 38, followed by neurexin 1β with a ratio of 11 and APLP1 with a ratio of 7. The binding of α-syn-biotin PFF to LAG3 was specific because α-syn-biotin PFF does not bind to the CD4 receptor, which has 20% homology to LAG3 (Fig. 1B and fig. S4). In addition to α-syn-biotin PFF binding

[1]Neuroregeneration and Stem Cell Programs, Institute for Cell Engineering, Johns Hopkins University School of Medicine, Baltimore, MD 21205, USA. [2]Department of Neurology, Johns Hopkins University School of Medicine, Baltimore, MD 21205, USA. [3]Adrienne Helis Malvin Medical Research Foundation, New Orleans, LA 70130-2685, USA. [4]Division of Pharmacology, Department of Molecular Cell Biology, Sungkyunkwan University School of Medicine, Samsung Biomedical Research Institute, Suwon 440-746, South Korea. [5]Department of Physiology, Ajou University School of Medicine, Suwon 443–721, South Korea. [6]Department of Neurology, Xin Hua Hospital affiliated to Shanghai Jiaotong University School of Medicine, Shanghai 200092, China. [7]Johns Hopkins Institute for NanoBio Technology, Johns Hopkins University, Baltimore, MD 21218, USA. [8]Department of Immunology, University of Pittsburgh School of Medicine, Pittsburgh, PA 15261, USA. [9]Tumor Microenvironment Center, University of Pittsburgh Cancer Institute, Pittsburgh, PA 15232, USA. [10]Department of Physiology, Johns Hopkins University School of Medicine, Baltimore, MD 21205, USA. [11]Solomon H. Snyder Department of Neuroscience, Johns Hopkins University School of Medicine, Baltimore, MD 21205, USA. [12]Department of Pharmacology and Molecular Sciences, Johns Hopkins University School of Medicine, Baltimore, MD 21205, USA.

*Present address: Department of Anatomy and Physiology, Kansas State University, Manhattan, KS 66506, USA. †Present address: State Key Laboratory of Medical Molecular Biology, Department of Immunology, Institute of Basic Medical Sciences, Chinese Academy of Medical Sciences and School of Basic Medicine, Peking Union Medical College, Beijing 100005, China. ‡Present address: Department of Pharmacology and Toxicology, University of Alabama at Birmingham, Birmingham, AL 35294, USA. §Present address: Institute of Medical Biochemistry Leopoldo de Meis, Federal University of Rio de Janeiro, Rio de Janeiro, RJ, Brazil.
‖Corresponding author. Email: tdawson@jhmi.edu (T.M.D.); hko3@jhmi.edu (H.S.K.); vdawson1@jhmi.edu (V.L.D.)

Downloaded from http://science.sciencemag.org/ on October 7, 2016

to neurexin 1β, it also binds to neurexin 3β and mildly binds to neurexin 1α and neurexin 2β (Fig. 1B). α-Syn-biotin PFF does not bind the amyloid precursor protein (APP) or the amyloid precursor–like protein 2 (APLP2), suggesting that the binding to APLP1 was specific (Fig. 1B). Because LAG3 exhibited the highest selectivity for α-syn-biotin PFF, it was advanced for further study. No LAG3 immunoreactive band was observed in HEK293FT and SH-SY5Y cells, which is consistent with the absence of a streptavidin signal in these cell lines (fig. S5A). Immunoblot analysis with a LAG3 antibody, 410C9, revealed that LAG3 was expressed in wild-type (WT) but not LAG3 knockout ($LAG3^{-/-}$) cortical cultures, confirming the specificity of the antibody to LAG3. LAG3 was primarily expressed in neurons because LAG3 was not detectable in astrocytes or microglia (fig. S5B). α-Syn-biotin PFF binds to LAG3 in a saturable manner, with a K_d of 77 nM (Fig. 1, B and C, and fig. S4). α-Syn-biotin monomers did not demonstrate specific binding to LAG3-expressing SH-SY5Y cells up to 3000 nM (Fig. 1, B and C, and fig. S4). In the absence of cell permeabilization by excluding TX-100, α-syn-biotin PFF still binds with a K_d of 71 nM (Fig. 1, B and C, and fig. S4). WT mouse cortical neurons demonstrated α-syn-biotin PFF–binding, whereas $LAG3^{-/-}$ mouse cortical neurons had reduced α-syn-biotin PFF–binding (Fig. 1D and fig. S6). Specific binding of α-syn-biotin PFF to LAG3 in cortical neurons was determined by subtracting the binding in WT cultures from the binding in $LAG3^{-/-}$ cultures and revealed a K_d of 103 nM (Fig. 1D and fig. S6). These results taken together suggest that α-syn-biotin PFF binds to extracellular LAG3 on neurons.

In vitro co-immunoprecipitation (Co-IP) studies showed that α-syn-biotin PFF, but not α-syn-biotin monomers, pulls down LAG3 (fig. S7A), and conversely, LAG3 pulls down α-syn-biotin PFF but not α-syn-biotin monomers (fig. S7B). Moreover, in vivo Co-IP studies showed that misfolded α-syn from aged transgenic mice pulls down LAG3, but monomeric α-syn from young transgenic mice overexpressing human A53T α-syn mutant protein does not (*22*), nor do α-syn monomers from WT aged or young mice (fig. S7C), which suggests that LAG3 binds specifically to pathological species of α-syn. We further confirmed using an enzyme-linked immunosorbent assay (ELISA) that α-syn-biotin PFF binds to human recombinant LAG3 directly with a K_d of 2.7 nM (fig. S7D).

LAG3 specifically binds to α-syn PFF

To test the specificity of α-syn-biotin PFF binding to LAG3, tau-biotin PFF, β-amyloid-biotin oligomer, and β-amyloid PFF were tested in nontransfected and LAG3-transfected SH-SY5Y cells via the streptavidin-AP staining assay (Fig. 1E and figs. S8 and S9) (*19*, *20*). Tau-biotin PFF binds to

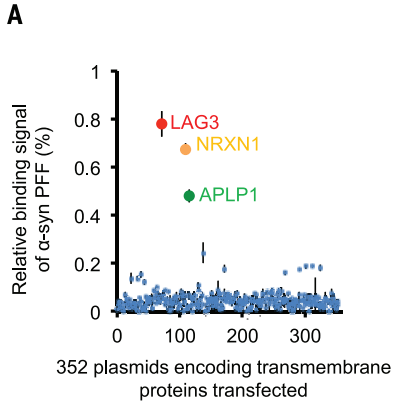

B

α-Syn binding to SH-SY5Y cells expressing the indicated proteins

Surface protein	α-Syn PFF K_d (nM)	α-Syn monomer K_d (nM)	Selectivity
LAG3*	71 ± 8	>3000	>42
LAG3	77 ± 9	>3000	>38
CD4	>3000	>3000	-
NRXN1β	260 ± 44	>3000	>11
NRXN1α	933 ± 657	>3000	>3
NRXN2β	630 ± 437	>3000	>4
NRXN3β	340 ± 45	>3000	>8
APLP1	401 ± 68	>3000	>7
APP	>3000	>3000	-
APLP2	>3000	>3000	-

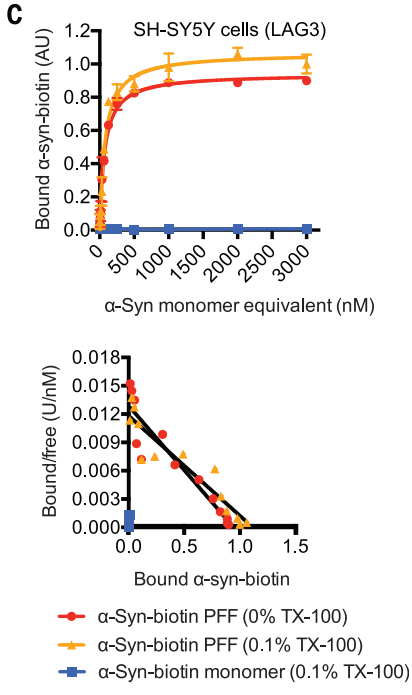

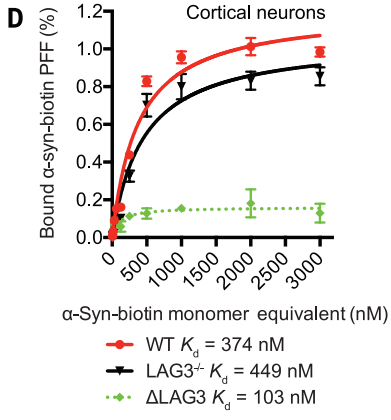

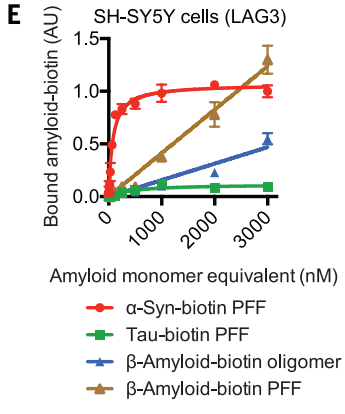

Fig. 1. α-Syn PFF binds to LAG3. (**A**) Individual clones from a library consisting of 352 individual cDNAs encoding transmembrane proteins (GFC-transfection array panel, Origene) were transfected into SH-SY5Y cells, and the relative binding signals of human α-syn PFF to individual transmembrane proteins are shown. Positive candidates are LAG3 (NM_002286), NRNX1 (NM_138735), and APLP1 (NM_005166). (**B**) Mouse α-syn-biotin monomer and α-syn-biotin PFF–binding affinity to SH-SY5Y cells expressing the indicated proteins. LAG3* K_d assessment was performed without Triton X-100 (TX-100). All other experiments were performed with 0.1% TX-100. Transmembrane proteins similar to the candidates were also tested. Quantification of bound α-syn-biotin PFF to the candidates was performed with ImageJ. K_d values are means ± SEM and are based on monomer equivalent concentrations. Selectivity was calculated by dividing K_d (monomer) by K_d (PFF). Binding of α-syn-biotin monomer was detected at a concentration of 3000 nM, but binding was not saturable. (**C**) (Top) α-Syn-biotin monomer or α-syn-biotin PFF binding to LAG3-overexpressing SH-SY5Y cells as a function of total α-syn concentration in 0% TX-100 or 0.1% TX-100 conditions (monomer equivalent for PFF preparations). (Bottom) Scatchard analysis. K_d = 71 nM (0% TX-100) and 77 nM (0.1% TX-100); data are the means ± SEM, n = 3 independent experiments. (**D**) Binding of α-syn-biotin PFF to cultured cortical neurons (21 days in vitro) is reduced by LAG3 knockout ($LAG3^{-/-}$), as assessed by means of alkaline phosphatase assay. α-Syn-biotin PFF WT-K_d = 374 nM, $LAG3^{-/-}$-K_d = 449 nM, estimated K_d for neuronal LAG3 (dotted line, ΔLAG3 = wild type minus $LAG3^{-/-}$) is 103 nM. Data are the means ± SEM, n = 3 independent experiments. *P < 0.05, Student's t test. Power (1 – β error probability) = 1. (**E**) Specificity of LAG3 binding with α-syn-biotin PFF (fig. S4). Tau-biotin PFF (fig. S8), β-amyloid-biotin oligomer, and β-amyloid-biotin PFF (fig. S9) are negative controls.

Downloaded from http://science.sciencemag.org/ on October 7, 2016

nontransfected SH-SY5Y cells in a saturable manner, whereas overexpression of LAG3 fails to increase the binding of tau-biotin PFF (Fig. 1E and fig. S8, A and B). β-amyloid-biotin oligomer and β-amyloid PFF binds to both nontransfected and LAG3-overexpressing SH-SY5Y cells at high concentrations in a nonspecific manner (Fig. 1E and fig. S9, A and B). Taken together, these results indicate that LAG3 specifically binds to α-syn PFF.

Like other immunoglobulin (Ig) superfamily molecules, LAG3 contains an ectodomain composed of four Ig-like domains (D1 to D4) (*23*). To determine the α-syn-biotin PFF–binding domain, we sequentially deleted each Ig-like domain of LAG3 and performed the cell surface–binding assay with overexpression of LAG3 deletion mutants. These experiments revealed that α-syn-biotin PFF preferentially binds to the D1 domain, whereas deletion of the D2, D3, or intracellular domain (ICD) substantially weakens binding, but deletion of the D4 domain does not (fig. S10). Because α-syn-biotin PFF binding to LAG3 is eliminated by deletion of the D1 domain, additional deletions of D1 subdomains (Δdel1-5-D1) were examined. Δdel2(aa 52-80)-D1 and Δdel3(aa 81-109)-D1 significantly reduced α-syn-biotin PFF binding to LAG3, whereas Δdel1(aa23-51)-D1, Δdel4(aa110-138)-D1, and Δdel5(aa139-167)-D1 moderately reduced binding of LAG3 to α-syn-biotin PFF (fig. S10), suggesting that LAG3 residues 52 to 109 in the D1 domain are responsible for the LAG3 interaction with α-syn-biotin PFF.

The endocytosis of α-syn PFF involves LAG3

To determine whether LAG3 is involved in the endocytosis of α-syn PFF, pHrodo red was conjugated to α-syn PFF. pHrodo red is a pH-dependent dye that increases in fluorescence as pH decreases from the neutral cytosolic pH to the acidic pH of the endosome (fig. S11A) (*24*). Conjugation of α-syn PFF with pHrodo red does not appreciably change the properties of the α-syn PFF as assessed with immunoblot and AFM (fig. S11, A and B). α-Syn-pHrodo PFF undergoes endocytosis in WT cortical neuron cultures, whereas LAG3$^{-/-}$ neurons exhibited minimal α-syn-pHrodo PFF endocytosis (Fig. 2, A and B, and fig. S11C). Overexpression of LAG3 in WT cultures enhanced the endocytosis of α-syn-pHrodo PFF, and overexpression of LAG3 in the LAG3$^{-/-}$cortical cultures restored endocytosis of α-syn-pHrodo PFF (Fig. 2, A and B, and fig. S11C). Adeno-associated virus serotype 2 (AAV2) expressing enhanced green fluorescent protein (EGFP) via a synapsin promoter was used to identify neurons and confirmed that α-syn-pHrodo PFF was endocytosed in WT neurons, but much less in LAG3$^{-/-}$ neurons (fig. S11D). Examination of overexpression of the deletion mutants in LAG3$^{-/-}$ cortical cultures showed that the D1 domain deletion mutant failed to restore the endocytosis of α-syn-pHrodo PFF (fig. S11, E and F). However, introduction of LAG3 deletion mutants (D2, D3, or D4) restored the internalization of α-syn-pHrodo PFF (fig. S11, E and F).

The Rab5 guanosine triphosphatase is an early endosomal marker and helps mediate endocytosis (*25*). As such, we sought to confirm the endocytosis of α-syn-biotin PFF into endosomes by measuring the intensity of colocalized α-syn-biotin PFF with Rab5. We found that α-syn-biotin PFF was colocalized with Rab5 in WT cortical neurons (Fig. 2, C and D). In contrast, there was less α-syn-biotin PFF in LAG3$^{-/-}$ cortical neurons (Fig. 2, C and D). Overexpression of LAG3 in WT and LAG3$^{-/-}$ cortical neurons enhanced the intensity of α-syn-biotin PFF colocalizing with Rab5 (Fig. 2, C and D). Rab5 appears to be upregulated after LAG3 overexpression. LAG3 coendocytoses with α-syn PFF as LAG3, Rab5, and α-syn-biotin PFF were colocalized (fig. S12A). α-Syn-biotin PFF also colocalized with Rab5 in dendrites and showed a similar pattern in WT, WT + LAG3, LAG3$^{-/-}$, and LAG3$^{-/-}$ + LAG3 neurons (fig. S12, B and C). The endosome markers

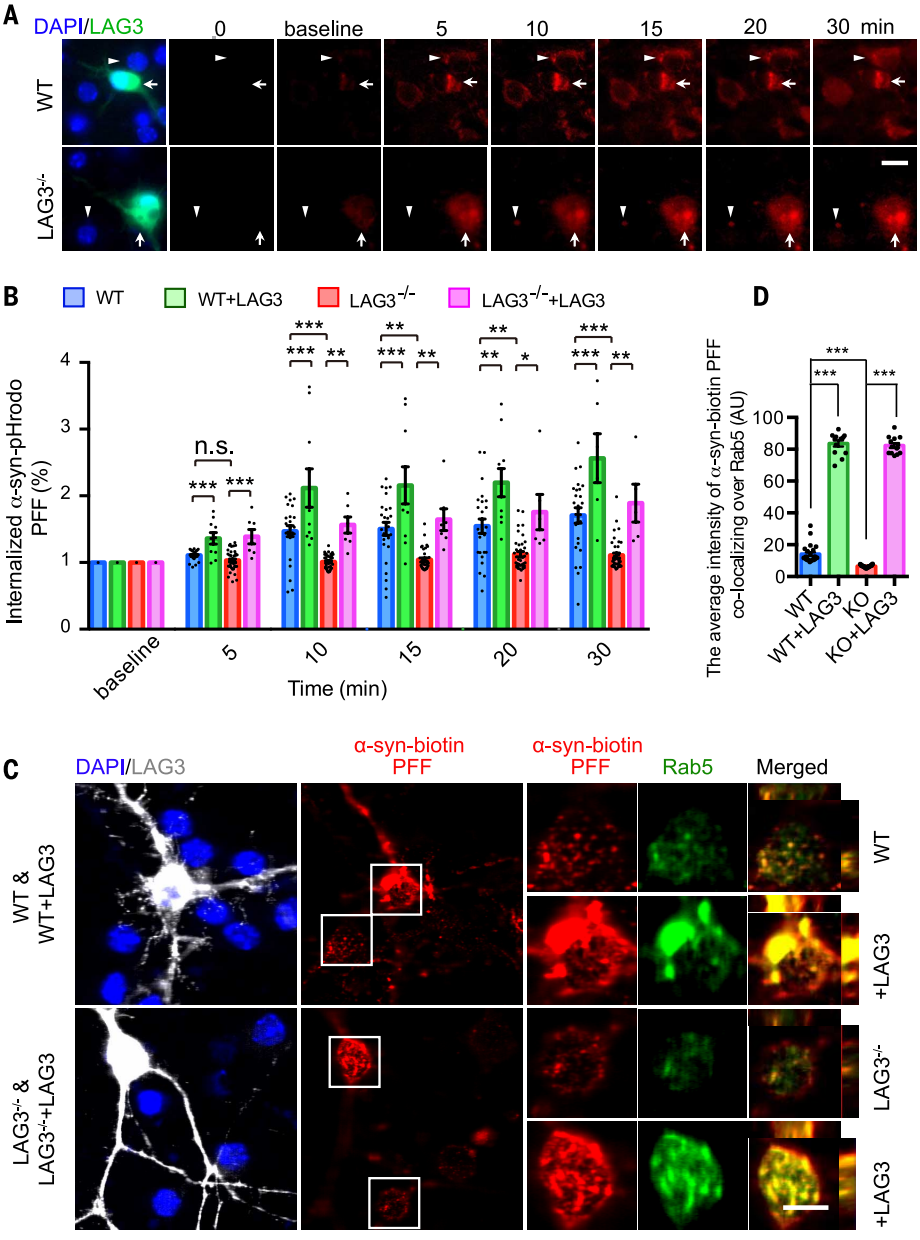

Fig. 2. Endocytosis of α-syn PFF is dependent on LAG3. (**A**) Live image analysis of the endocytosis of α-syn-pHrodo PFF. α-Syn PFF was conjugated with a pH-dependent dye (pHrodo red), in which fluorescence increases as pH decreases from neutral to acidic environments. White arrowheads indicate nontransfected WT or LAG3$^{-/-}$ neurons, and white arrows indicate LAG3-transfected neurons. Scale bar, 10 μm. (**B**) Quantification of (A), cell number (5-46) from $n = 3$ independent experiments. (**C**) Internalized α-syn-biotin PFF colocalizes with Rab5. Colocalization of internalized α-syn-biotin PFF and Rab5 was assessed by means of confocal microscopy. Scale bar, 10 μm. (**D**) Quantification of (C), cell number (13-32) from $n = 4$ independent experiments. One-way analysis of variance (ANOVA) with Tukey's correction. Data in (B) and (D) are as means ± SEM. *$P < 0.05$, **$P < 0.01$, ***$P < 0.001$. Power (1 – β error probability) = 1.

Downloaded from http://science.sciencemag.org/ on October 7, 2016

Rab7 and LAMP1 were also colocalized with α-syn-biotin PFF (fig. S12D).

Examination of overexpression of the deletion mutants in LAG3$^{-/-}$ neuronal cultures showed that the D1 domain deletion mutants failed to increase the colocalization of α-syn-biotin PFF with Rab5 (fig. S13). However, introduction of LAG3 deletion mutants (D2, D3, D4, and the ICD) enhanced the intensity α-syn-biotin PFF colocalizing with Rab5 (fig. S13). Deletions of D1 subdomains [Δdel(1-5)-D1] were also examined for α-syn-biotin PFF colocalization with Rab5. Consistent with our binding assays, Δdel2-D1 and Δdel3-D1 exhibited the greatest effect on reducing the intensity α-syn-biotin PFF colocalizing with Rab5 (fig. S13).

Endosome-enriched fractions were isolated via differential centrifugation (*26*, *27*) from WT and LAG3$^{-/-}$ cultures after treatment with α-syn-biotin PFF (fig. S14A). Both monomeric and higher-molecular-weight forms of α-syn-biotin PFF were found in the endosome-enriched fraction of WT neuron cultures, whereas there was significantly less of both forms in LAG3$^{-/-}$ cultures (fig. S14, B and C). Lentiviral-mediated overexpression of LAG3 in WT cultures enhanced the levels of α-syn-biotin PFF in the endosome-enriched fractions and restored the levels of α-syn-biotin PFF in LAG3$^{-/-}$ culture endosome-enriched fractions (fig. S14, B and C). LAG3 exists in the endosome-enriched fraction (fig. S14D), which is consistent with the data that LAG3, Rab5, and α-syn-biotin PFF are colocalized (fig. S12A). To exclude the possibility that deletion of LAG3 causes a generalized defect in endocytosis, we studied the internalization of latex beads, and there was no difference in the internalization of latex beads between WT and LAG3$^{-/-}$ cultures (fig. S14, E and F). LAG3 also specifically recognized α-syn PFF because tau-biotin PFF as characterized by means of TEM (fig. S15A) were internalized in LAG3$^{-/-}$ neurons and failed to show greater internalization in neurons overexpressing LAG3 (fig. S15B), which is consistent with the observation of the lack of tau-biotin PFF binding to LAG3 (Fig. 1E and fig. S8, A and B). Taken together, these results indicate that LAG3 can mediate the endocytosis of α-syn-biotin PFF into neurons.

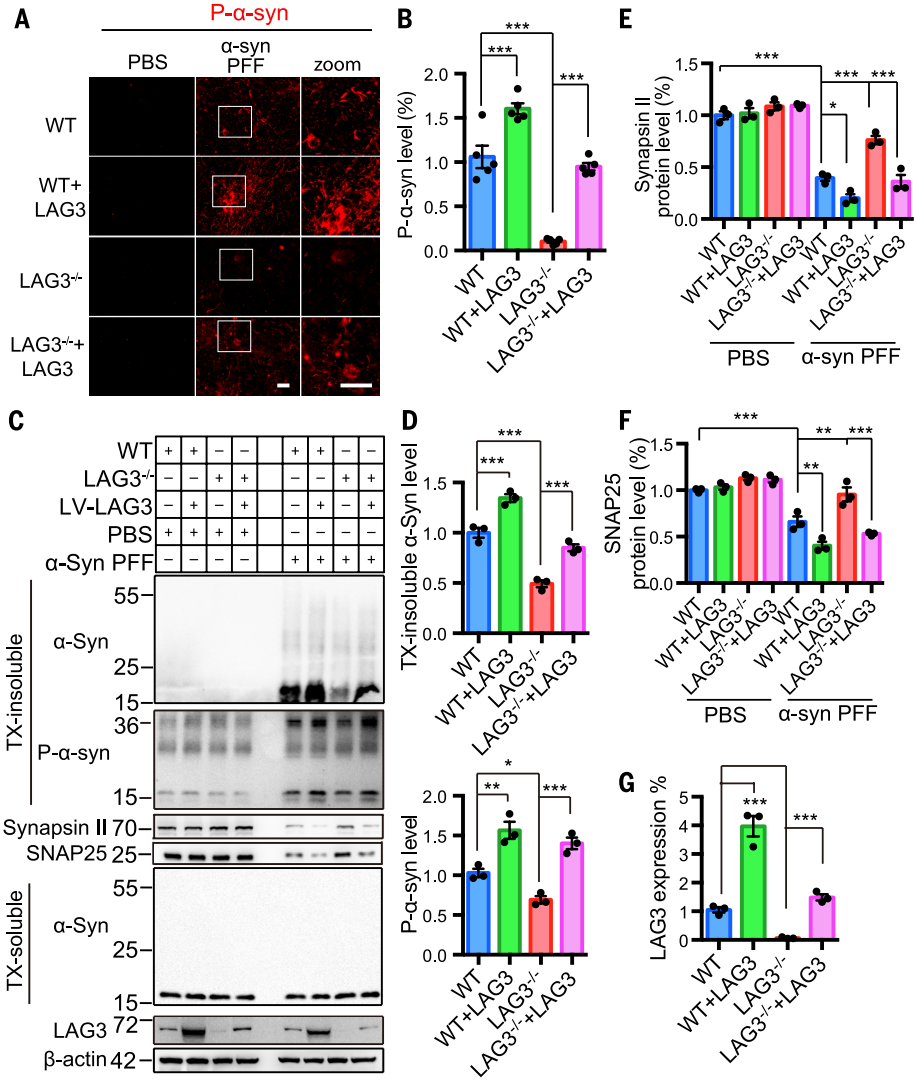

Fig. 3. α-Syn PFF induced pathology is reduced by deletion of LAG3 in vitro. (**A**) WT and LAG3$^{-/-}$ primary cortical neurons at 7 days in vitro were treated with α-syn PFF or PBS. LAG3 was overexpressed via Lentivirus (LV) transduction in WT or LAG3$^{-/-}$ neurons at 4 days in vitro. Three days after transduction, cultures 7 days in vitro were treated with α-syn PFF or PBS. All the cultures were fixed 10 days after treatment in 4% PFA. Neurons were stained with rabbit mAb MJF-R13 (8-8) for P-α-syn. Scale bar, 40 μm. (**B**) Quantification of (A), $n = 5$ independent experiments, each performed in duplicate. Values are given as the means ± SEM. Statistical significance was determined by using one-way ANOVA followed with Tukey's correction; ***$P < 0.001$. Power (1 − β error probability) = 1. (**C**) Immunoblots in WT and LAG3$^{-/-}$ neuron lysates of misfolded α-syn, P-α-syn, synapsin II, SNAP25, and LAG3. β-actin served as a loading control. WT and LAG3$^{-/-}$ neuron lysates were sequentially extracted in 1% TX-100 (TX-soluble) followed by 2% SDS (TX-insoluble) 14 days after α-syn PFF treatment. α-Syn PFF recruited endogenous α-syn into TX-insoluble and hyperphosphorylated aggregates, which was ameliorated by deletion of LAG3. α-Syn PFF caused a reduction in levels of SNAP25 and synapsin II compared with PBS 14 days after treatment. Deletion of LAG3 prevented PFF-induced synaptic protein loss. (**D** to **G**) Quantification of (C). Values are given as means ± SEM, $n = 3$ independent experiments. Statistical significance was determine by using one-way ANOVA followed by Tukey's correction; *$P < 0.05$, **$P < 0.01$, ***$P < 0.001$.

The absence of LAG3 prevents α-syn PFF pathology

We then asked whether knocking out LAG3 prevents the pathology induced by α-syn PFF. Phosphorylation of α-syn at serine 129 (P-α-syn) is associated with pathology in α-synucleinopathies. Its levels increase after treatment of α-syn PFF to neuronal cultures (*13*, *14*). Accordingly, we added α-syn PFF to WT and LAG3$^{-/-}$ cortical cultures at 7 days in vitro. Ten days after α-syn PFF treatment, the levels of P-α-syn were markedly increased in WT cultures, whereas the levels of P-α-syn in LAG3$^{-/-}$ cultures were barely detectable (Fig. 3, A and B). Overexpression of LAG3 enhanced the level of P-α-syn in WT cultures and restored P-α-syn levels in LAG3$^{-/-}$ cultures (Fig. 3, A and B). Furthermore, the accumulation of P-α-syn colocalized with LAG3 (fig. S16A), which is consistent with binding (fig. S16B) and the coendocytosis of LAG3 and α-syn PFF (fig. S14D). Overexpressing the D1 domain deletion mutant in LAG3$^{-/-}$ neuron cultures failed to restore P-α-syn levels (fig. S17). Overexpression of the D2, D3, and D4 domain deletion mutants in LAG3$^{-/-}$ cortical cultures recaptured the α-syn pathology as monitored by P-α-syn (fig. S17).

Two weeks after α-syn PFF treatment of cortical neurons, we examined immunoblots of α-syn and P-α-syn from lysates sequentially extracted in 1% Triton X-100 (TX-soluble) followed by 2% SDS (TX-insoluble). α-Syn PFF led to an accumulation of α-syn and P-α-syn in the TX-insoluble fraction in WT cultures, whereas there was significantly less accumulation in LAG3$^{-/-}$ cultures (Fig. 3, C and D). α-Syn PFF also caused a reduction in SNAP25 and synapsin II levels compared with phosphate-buffered saline (PBS) 14 days after

Downloaded from http://science.sciencemag.org/ on October 7, 2016

treatment, as previously described (*13*). Deletion of LAG3 prevented the α-syn PFF–induced synaptic protein loss (Fig. 3, C to G). Overexpression of LAG3 in WT cultures caused an increase accumulation of α-syn and P-α-syn in the TX-insoluble fraction in WT cultures and a further reduction in SNAP25 and synapsin II levels, whereas it prevented the sparing in LAG3$^{-/-}$ cultures (Fig. 3, C to G).

Cell-to-cell transmission of α-syn PFF is reduced in LAG3$^{-/-}$ neurons

To examine the transmission of α-syn PFF and to establish the role of LAG3 in the interneuron transmission of α-syn, we used a microfluidic neuronal culture device with three chambers connected in tandem by a series of microgrooves separating the chambers (TCND1000, Xona Microfluidics). The medium volume in chamber 1 (C1) is 50 μL lower than the one in chamber 2 (C2) and 100 μL lower than the one in chamber 3 (C3) in order to prevent diffusion of α-syn PFF to adjacent chambers. Cortical neurons were cultured in each chamber. To ensure that α-syn PFF cannot diffuse between chambers, primary WT cortical neurons in C1 were treated with α-syn-biotin PFF. Fourteen days after treatment, the neurons were fixed in 4% paraformaldehyde (PFA) and stained with streptavidin-568 fluorescence dye. Only neurons in C1 exhibited immunofluorescence, indicating that α-syn-biotin PFF cannot transmit from chamber to chamber through diffusion (fig. S18A).

α-Syn transmission from C1 to C3 requires intermediating neurons in C2 because α-syn PFF administration to C1 failed to induce P-α-syn accumulation in C3 when C2 was left empty (Fig. 4, A to C). Using this system, the transmission of α-syn PFF was monitored via P-α-syn levels in WT and LAG3$^{-/-}$ cultures (Fig. 4, D to F, and fig. S18B). The microfluidic neuron culture device was then set up to contain WT cultures in C1 and C3, whereas C2 either contained WT or LAG3$^{-/-}$ cultures. In another set of chambers, LAG3 was overexpressed in the C2 chamber containing either WT or LAG3$^{-/-}$ cultures. Administration of α-syn PFF to C1 led to increased P-α-syn levels (Fig. 4, E and F, and fig. S18B). To assess the propagation of α-syn PFF along dendrites and axons as well as transmission of misfolded α-syn, we monitored the levels of P-α-syn in C2 and C3. When C2 contains WT cultures, P-α-syn was observed in both C2 and C3, and LAG3 overexpression in C2 neurons enhanced the levels of P-α-syn in both chambers (Fig. 4, E and F, and fig. S18B). In contrast, when C2 contains LAG3$^{-/-}$ cultures, P-α-syn levels were significantly reduced in C2 and were absent in C3 (Fig. 4, E and F, and fig. S18B). LAG3 overexpression in C2 neurons restored the propagation of α-syn PFF as assessed by similar levels of P-α-syn compared with that in WT cultures (Fig. 4, E and F, and fig. S18B). These results taken together indicate that LAG3 is required for the propagation and transmission of pathologic α-syn.

α-Syn PFF toxicity is reduced in LAG3$^{-/-}$ neurons

Treatment of WT cortical cultures with α-syn PFF causes neuronal cell death, as previously described (fig. S19) (*13*). α-Syn PFF treatment led to substantial cell death compared with PBS-treated cultures as assessed with propidium iodide staining (fig. S19, A and B). LAG3$^{-/-}$ cultures exhibited significantly less cell death, and overexpression of LAG3 restored the toxicity to α-syn PFF (fig. S19, A and B). We also performed neuronal nuclei (NeuN) antibody staining to assess neuronal number. α-Syn PFF treatment caused a significant loss of NeuN immunoreactivity, and overexpression of LAG3 enhanced neuronal loss (fig. S19, C and D). NeuN immunoreactivity was preserved in LAG3$^{-/-}$ cultures after α-syn PFF treatment, whereas overexpression of LAG3 in LAG3$^{-/-}$ cultures led to a loss of NeuN immunoreactivity (fig. S19, C and D). NeuN immunostaining in LAG3$^{-/-}$ neurons with overexpression of deletion mutants (ΔD1-ΔD4 and ΔICD) indicated that deletion of the D1 domain failed to exhibit cell death, but deletion of D2, D3, D4, or the ICD domains still led to cell death (fig. S19, E and F). Because deletion of the LAG3 ICD domain may reduce α-syn PFF toxicity, signaling through the ICD of LAG3 may contribute to α-syn PFF toxicity. Furthermore, because calcium might be involved in α-syn–induced neurotoxicity (*13*, *28*–*32*), calcium influx was monitored in response to α-syn PFF.

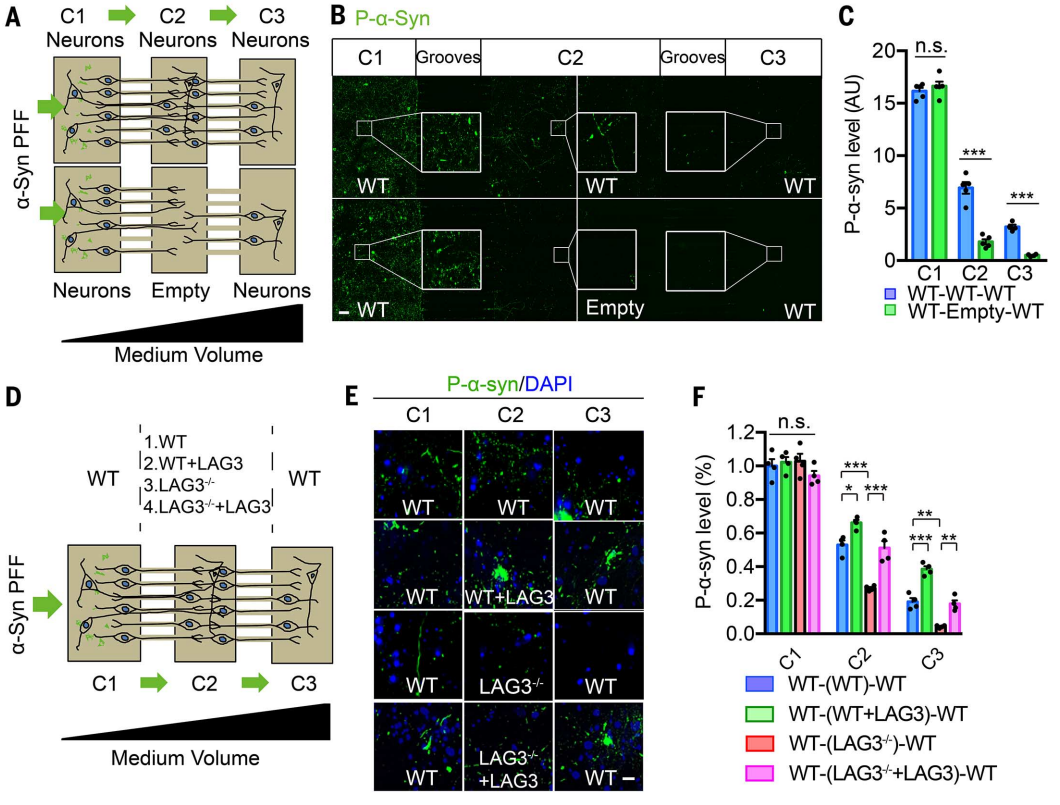

Fig. 4. α-Syn PFF transmission is reduced by deletion of LAG3 in vitro. (**A**) Schematic representation of the three chambers in which neurons were cultured: chamber 1 (C1), chamber 2 (C2), and chamber 3 (C3) (top); or C1 and C3 (bottom). (**B**) α-Syn PFF was added to C1 of the microfluidic device. On day 14, P-α-syn was detected in C2 and C3 when neurons were present in all three chambers. Transmission to C3 is not detectable when neurons are not present in C2. Scale bar, 100 μm. (**C**) Quantification of immunofluorescent images in (B). Data are the means ± SEM, $n = 3$ independent experiments. One-way ANOVA followed by Sidak's correction; ***$P < 0.001$ versus C1. Power (1 – β error probability) = 1. (**D**) Schematic of microfluidic neuron device with three chambers to separate neurons seeded in three chambers. (**E**) Transmission of pathologic P-α-syn from C1 to C2 to C3 14 days after addition of α-syn PFF in C1. The different combinations of neurons tested in C2, listed as C1-(C2)-C3, are WT-(WT)-WT, WT-(WT+LAG3)-WT, WT-(LAG3$^{-/-}$)-WT, WT-(LAG3$^{-/-}$+LAG3)-WT. Scale bar, 10 μm. (**F**) Quantification of (E). Values are given as means ± SEM, $n = 3$ independent experiments. Statistical significance was determine by using one-way ANOVA followed by Tukey's correction; *$P < 0.05$, **$P < 0.01$, ***$P < 0.001$. Power (1-β error probability) = 1.

Downloaded from http://science.sciencemag.org/ on October 7, 2016

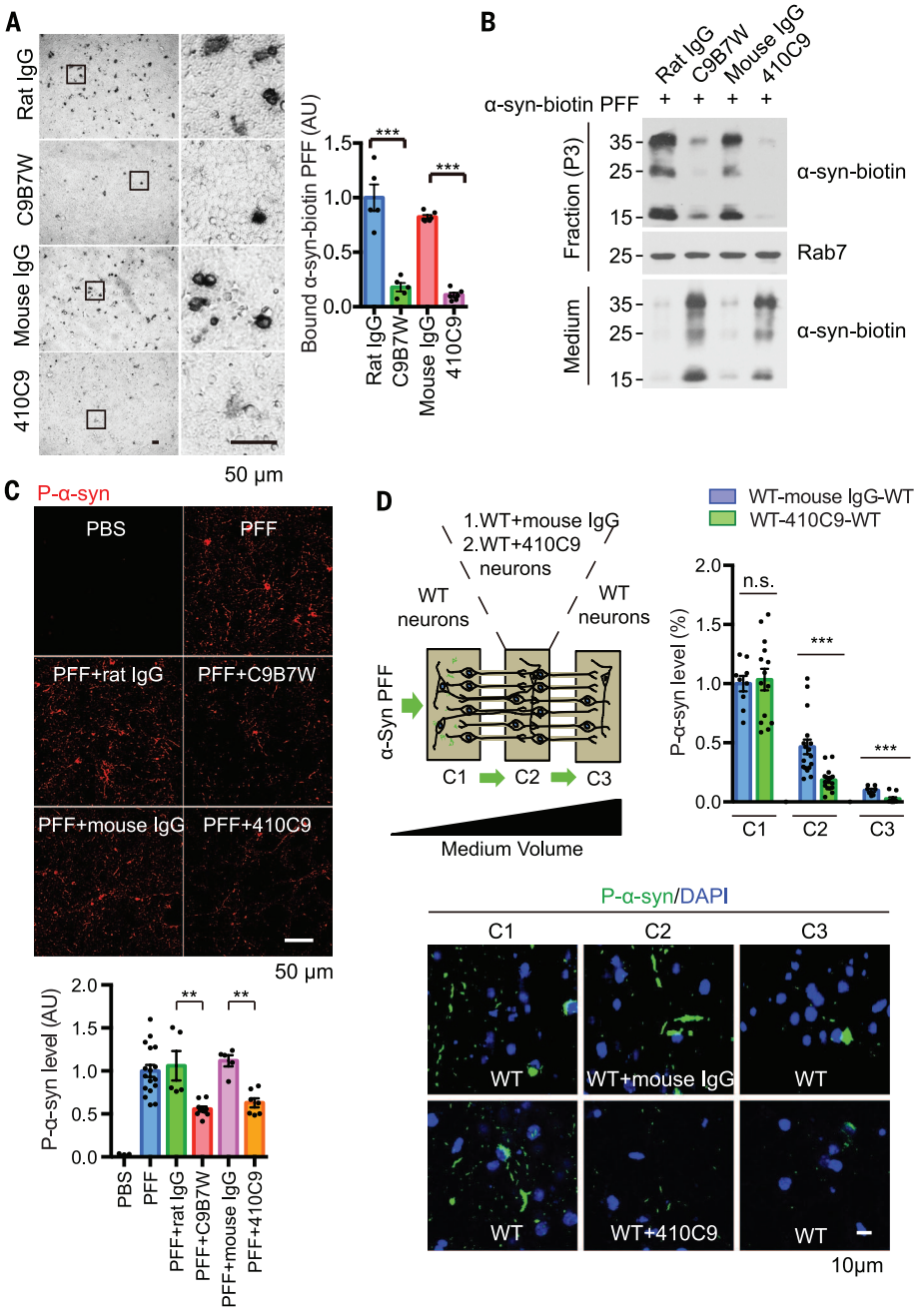

Fig. 5. Antibodies to LAG3 block α-syn PFF binding, endocytosis, pathology, and transmission. (**A**) C9B7W and 410C9 (both 50 μg/mL), antibodies to LAG3, block the binding of α-syn-biotin PFF (500 nM) on SH-SY5Y cells expressing LAG3. Scale bar, 50 μm. (Right) Quantification of images in (A). Data are the means ± SEM, *n* =3 independent experiments, Student's *t* test; ***$P < 0.001$. (**B**) C9B7W and 410C9 (both 50 μg/mL) reduced the endocytosis of α-syn-biotin PFF (1 μM) in primary cortical neurons 12 days in vitro. Rab7 was used to confirm the isolation of endosomes. (**C**) P-α-syn as detected with rabbit mAb MJF-R13 (8-8) was reduced by antibodies to LAG3 in primary cortical neurons. Scale bar, 50 μm. (Bottom) Quantification of images in (C). Data are the means ± SEM, *n* = 3 independent experiments, one-way ANOVA followed by Tukey's correction; **$P < 0.01$. (**D**) 410C9 delays α-syn PFF transmission in neurons. (Top left) A schematic representation of the three microchambers in which neurons were cultured in C1, C2, and C3. α-Syn PFF was added to C1 of the microfluidic device on day 7. Mouse IgG or 410C9 (both 50 μg/mL) was added to C2 on day 7. α-Syn PFF transmission was detected via P-α-syn immunostaining in C2 and C3 on day 21. Scale bar, 10 μm. (Top right) Quantification of images at bottom. Data are the means ± SEM, *n* = 3 independent experiments, one-way ANOVA followed by Tukey's correction. ***$P < 0.001$; n.s., nonsignificant.

Perfusion of α-syn PFF (500 nM) onto WT cortical neurons led to a gradual increase in intracellular calcium levels (fig. S20). Lack of LAG3 caused a significant decrease of α-syn PFF–induced calcium influx, which may account for the reduced toxicity in LAG3$^{-/-}$ cultures (fig. S20).

Antibodies to LAG3 reduce α-syn PFF toxicity and cell-to-cell transmission

Two different antibodies to LAG3, C9B7W (50 μg/mL) (*33*) and 410C9 (50 μg/mL) (*34*), blocked the binding of α-syn-biotin PFF (500 nM) in SH-SY5Y cells expressing LAG3 (Fig. 5A). The antibodies to LAG3 also reduced the enrichment of α-syn-biotin PFF (1 μM) in the endosomal-enriched fraction of primary cortical neurons 12 days in vitro (Fig. 5B), which is consistent with reduced endocytosis in LAG3$^{-/-}$ neuron culture. Both antibodies reduced the subsequent α-syn PFF pathology detected with phosphorylated α-syn Ser^{129} (P-α-syn) (Fig. 5C). Rat or mouse IgG had no effect in these assays. Cell-to-cell transmission of α-syn PFF as detected with P-α-syn was significantly reduced by 410C9, whereas mouse IgG had no effect after 14 days of α-syn PFF treatment (Fig. 5D and fig. S21).

To determine whether LAG3 mediates the pathology induced by human α-syn PFF, we assessed P-α-syn immunoreactivity in cortical cultures from mouse prion promoter transgenic mice overexpressing human A53T mutant α-syn (*22*) in the presence or absence of the 410C9 and in human A53T mutant α-syn cultures lacking LAG3. Human α-syn PFF treatment of A53T α-syn neuron cultures increased P-α-syn, whereas the absence of LAG3 or the antibody to LAG3 significantly reduced P-α-syn immunoreactivity (fig. S22, A and B). Brain homogenates from 10-month-old symptomatic human A53T transgenic mice were used to assess endogenous α-syn aggregates, and we found that they also increased the level of P-α-syn, whereas deletion of LAG3 or treatment with the antibody to LAG3 410C9 reduced the level of P-α-syn induced by A53T transgenic brain homogenates (fig. S22, C and D). Human α-syn PFF induced toxicity in human A53T α-syn transgenic neuronal cultures, whereas deletion of LAG3 or 410C9 significantly reduced the toxicity (fig. S22, E and F). These results, taken together, suggest that LAG3 can mediate the pathology of human α-syn aggregates.

The absence of LAG3 reduces α-syn PFF transmission and toxicity in vivo

To determine whether LAG3 is necessary for α-syn PFF transmission and toxicity in vivo, we stereotactically injected α-syn PFF into the dorsal striatum of WT and LAG3$^{-/-}$ mice (*35*). Representative maps (fig. S23A, red dots) and representative images and quantification (fig. S23, B and C) of the distribution of LB/LN-like pathology of P-α-syn accumulation and the stereotaxic injection site indicated by gray circles in the α-syn PFF–injected hemisphere are shown for mice sacrificed at 30 and 180 days after injection (fig. S23). P-α-syn immunoreactivity was monitored in substantia nigra pars compacta (SNpc) tyrosine hydroxylase (TH)–positive neurons 30 and

Downloaded from http://science.sciencemag.org/ on October 7, 2016

180 days after α-syn PFF injection. We observed substantial P-α-syn staining in WT SNpc TH–positive neurons at 30 and 180 days (Fig. 6A). In LAG3$^{-/-}$ SNpc TH–positive neurons, P-α-syn staining is reduced by >50% at both time points. Accompanying the α-syn pathology, stereologic counting of SNpc TH– and Nissl-positive neurons revealed significant loss of dopamine (DA) neurons in WT mice at 180 days after injection (Fig. 6B). There was a dramatic preservation of DA neurons in α-syn PFF–injected LAG3$^{-/-}$ mice (Fig. 6B). High-performance liquid chromatography (HPLC) analysis demonstrated a significant reduction in DA and its metabolites 3,4-dihydroxyphenylacetic acid (DOPAC), homovanillic acid (HVA), and 3MT in WT mice and a sparing of the reduction in LAG3$^{-/-}$ mice (Fig. 6C and fig. S24, A to C). Immunoblot analysis demonstrated a significant reduction in TH and the DA transporter (DAT) in WT mice and a sparing of the reduction in LAG3$^{-/-}$ mice (fig. S24D). At 180 days after α-syn PFF injection, WT mice exhibited robust clasping behavior when suspended by their tail similar to prior reports (*14*, *36*), whereas LAG3$^{-/-}$ mice demonstrated a response similar to PBS-injected mice (fig. S24E). WT mice injected with α-syn PFF showed significant impairment in the pole test, which is thought to be a sensitive behavioral indicator of dopaminergic function (*37*), with increased time to turn and time to reach the base, whereas LAG3$^{-/-}$ mice injected with α-syn PFF showed no significant impairments (Fig. 6D). Grip strength analysis indicated that WT mice have reduced forelimb and forelimb plus hindlimb strength after α-syn PFF injection, which is similar to prior reports (*14*, *36*), whereas the LAG3$^{-/-}$ mice showed no significant loss in grip strength (Fig. 6E). Therefore, LAG3 is crucial for α-syn PFF–induced neurodegeneration and the development of PD-related motor defects.

Conclusion

The major finding of this paper is that α-syn PFF transmission and toxicity is initiated by binding LAG3. We isolated LAG3 via an unbiased screen for α-syn PFF–binding sites. Although our data indicate that LAG3 is not the sole α-syn PFF–binding site, it plays a major role in α-syn PFF endocytosis and transmission. Moreover, mice lacking LAG3 exhibit delayed α-syn PFF–induced pathology and reduced toxicity.

Consistent with our observations that the absence of LAG3 does not completely reduce α-syn PFF–binding and pathology, we observed that α-syn PFF also binds to APLP1 and neurexins. A recent study also identified neurexin 1α and 2α as α-syn fibril–binding partners (*32*). The Toll-like receptor 2 (TLR2) on microglia was shown to be involved in the activation of microglia because of exposure to oligomeric α-syn from conditioned neuronal media (*38*). Heparan sulfate proteoglycans

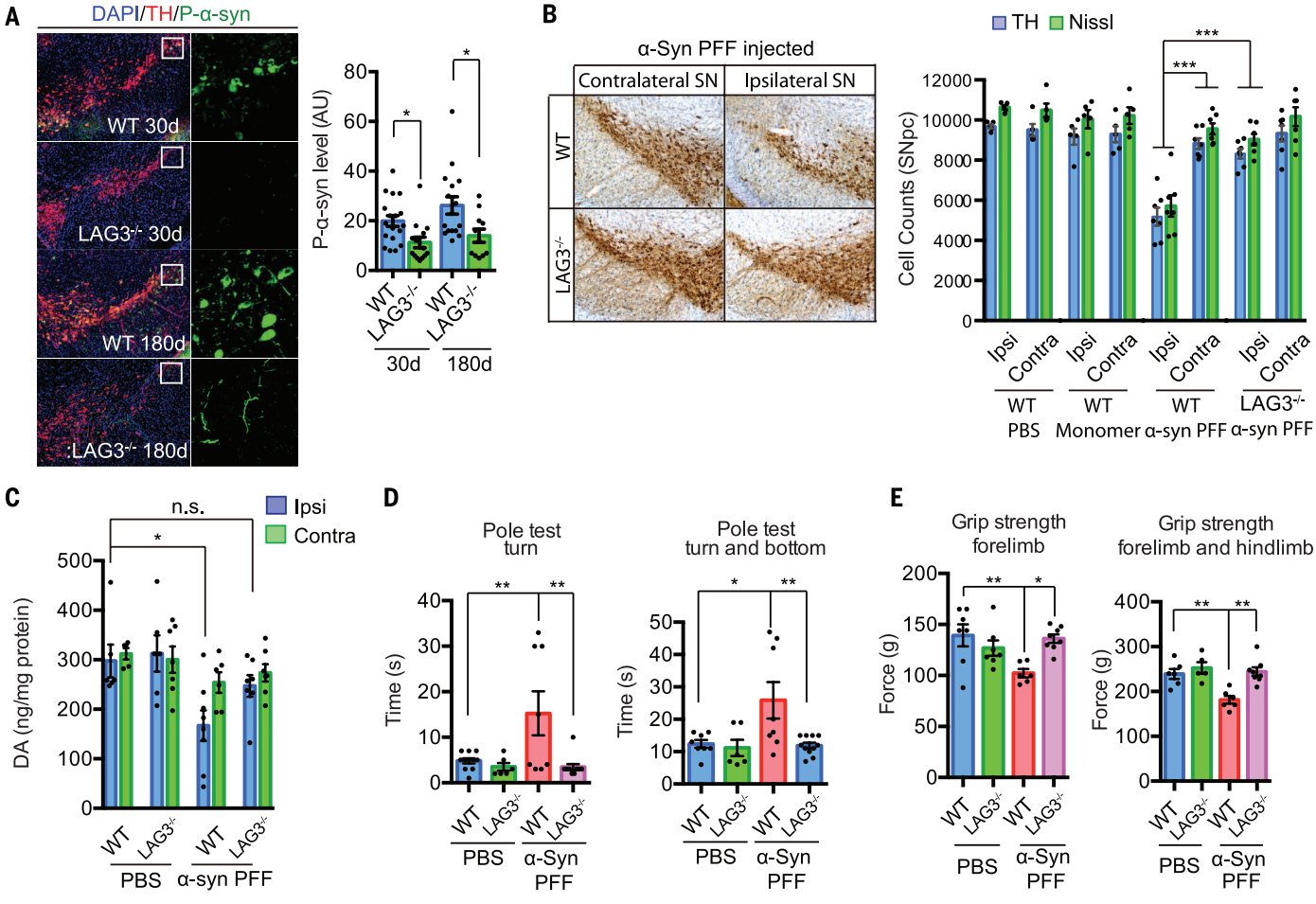

Fig. 6. α-Syn PFF–induced pathology is reduced by deletion of LAG3 in vivo. (**A**) Representative P-α-syn immunostaining and quantification in the substantia nigra par compacta (SNpc) of WT and LAG3$^{-/-}$ mice sacrificed at 30 and 180 days after intrastriatal α-syn PFF injection. Data are the means ± SEM, n = 5 to 9 mice per group, one-way ANOVA with Sidak's correction. (**B**) Stereology counts from TH immunostaining and Nissl staining of SNpc DA neurons of WT and LAG3$^{-/-}$ mice at 180 days after intrastriatal α-syn PFF, α-syn monomer, or PBS injection. Data are the mean number of cells per region ± SEM, n = 5 to 9 mice per group, one-way ANOVA with Dunnett's correction. (**C**) DA concentrations in the striatum of α-syn PFF–injected mice and PBS-treated controls measured at 180 days by means of HPLC. Data are the means ± SEM, n = 5 to 8 mice per group, one-way ANOVA with Tukey's correction. (**D** and **E**) 180 days after α-syn PFF injection, the pole test and grip strength were performed in WT or LAG3$^{-/-}$ mice injected with PBS or α-syn PFF. Behavioral abnormalities in the pole test and grip strength induced by α-syn PFF injection were ameliorated in LAG3$^{-/-}$ mice. Data are the means ± SEM, n = 7 to 9 mice per group for behavioral studies. Statistical significance was determined by using one-way ANOVA with Tukey's correction; *P < 0.05, **P < 0.01, ***P < 0.001; n.s., nonsignificant. Power (1 – β error probability) = 1.

Downloaded from http://science.sciencemag.org/ on October 7, 2016

(HSPGs) can mediate α-syn aggregate uptake and seeding via micropinocytosis (*39*), and the A3-subnit of the Na^+/K^+–adenosine triphosphatase (α3-NKA) binds to α-syn fibrils and oligomers (*32*). Whether these alternative α-syn–binding partners contribute to α-syn transmission and pathogenesis and how they might interact with LAG3 requires further study.

LAG3 is enriched not only in the thymus and spleen, but the brain as well (*33*). Immunoblot analysis indicates that LAG3 is expressed predominantly in neurons, which is consistent with the observation that LAG3 mediates the transmission of misfolded α-syn from neuron to neuron. According to the Allen Brain Atlas, LAG3 is localized to neurons throughout the central nervous system (CNS), including DA neurons. It is becoming increasingly clear that proteins that were thought to function primarily in the immune system also have important roles in the nervous system, including the functional requirement for class I major histocompatibility complex (MHC) in CNS development and plasticity (*40*, *41*). Class II MHC is also expressed in the nervous system (*42*). The function of LAG3 in the CNS is not known, and whether misfolded α-syn activates downstream signaling after engagement of LAG3 requires further study.

We propose a previously unknown mechanism for cell-to-cell transmission of misfolded α-syn that involves the endocytosis of exogenous α-syn PFF by the engagement of LAG3 on neurons.

The interaction between LAG3 and α-syn PFF provides a new target for the development of therapeutics designed to slow the progression of PD and related α-synucleinopathies. This could potentially be quickly translated in PD because many pharmaceutical companies are developing agents that block LAG3 (*43*). The prion-like spread of α-syn PFF and other amyloidogenic proteins is a multistep process involving the uptake, propagation, and release of pathological amyloid proteins. USP19 was recently shown to promote α-syn secretion, suggesting a pathway by which pathologic α-syn exits cells in α-synucleinopathies (*44*). Combined with LAG3 playing a major role in the internalization of pathologic α-syn, we speculate that more mediators will be discovered that are involved in the cell-to-cell transmission of pathologic α-syn.

Materials and methods

α-Syn purification and α-syn PFF preparation

Recombinant α-syn proteins were purified as previously described (*18*). α-Syn PFF were prepared by agitating α-syn in a transparent glass vial with a magnetic stirrer (350 rpm at 37°C). After 7 days of incubation the α-syn aggregates were sonicated for 30 s at 10% amplitude (Branson Digital Sonifier, Danbury, CT, USA) and the α-syn monomer and α-syn PFF were separated by FPLC using a Superose 6 10/300GL column (GE Healthcare, Life Sciences, Wauwatosa, WI, USA) and fractions containing the α-syn monomer and α-syn PFF were kept at -80°C. To characterize α-syn PFF mediators, recombinant α-syn monomer was purified and labeled with sulfo-NHS-LC-Biotin (Thermo Scientific, Grand Island, NY, USA. EZ-link Sulfo-NHS-LC-Biotin, 21435). The molar ratio of biotin to α-syn was 2~3. After conjugation, α-syn-biotin monomer and α-syn-biotin PFF was prepared as mentioned above.

Preparation and characterization of tau fibrils

Recombinant Tau protein was obtained from rPeptide (T-1001-2, Bogart, GA, USA). Tau was labeled with sulfo-NHS-LC-Biotin as described above for α-syn. In vitro fibrillization of full-length Tau (2N4R) was prepared by mixing 50 μM low molecular weight heparin and 2 mM DTT with 300 μM recombinant Tau in 100 mM sodium acetate buffer (pH 7.0) under constant orbital agitation (1,000 rpm) at 37°C for 5-7 days (*45*). Successful fibrillization was confirmed using the thioflavin T fluorescence assay and transmission electron microscopy. The fibrils were mechanically broken down into small fragments by sonication (30 s, 10% amplitude).

Preparation of synthetic β-amyloid$_{1-42}$ oligomers

β-amyloid$_{1-42}$ peptide was purchased from Anaspec (AS-64129-1). The β-amyloid$_{1-42}$ peptide was first dissolved in Hexafluoro-2-propanol (HFIP), evaporated overnight in the fume hood, and then completely dried down for 1 hour using a SpeedVac (Thermo Scientific, USA). The resulting peptide film was dissolved in DMSO at 2.2 mM and diluted in PBS to obtain a 250 μM stock solution. β-amyloid$_{1-42}$ was labeled with sulfo-NHS-LC-Biotin as described above for α-syn. The solution was incubated at 4°C for at least 24 hours to oligomerize the peptides (*46*). The solution was aliquoted after oligomerization and stored at -80°C until use. Before usage, the solution was centrifuged at 12,000 g for 10 min to remove the fibril forms of β-amyloid$_{1-42}$. The supernatant, which contains the dissolved oligomeric β-amyloid$_{1-42}$ was used for experiments.

Preparation of synthetic β-amyloid$_{1-42}$ fibrils and PFF

β-amyloid$_{1-42}$ peptide was purchased from Anaspec (AS-64129-1). After HFIP treatment, β-amyloid$_{1-42}$ monomer was freshly resuspended in DMSO at concentration of 2.2 mM. The stock solution was further dissolved in PBS to a final concentration of 250 μM and labeled with sulfo-NHS-LC-Biotin, then incubated in 37°C for 24 hours. After forming β-amyloid fibrils, the solution was sonicated for 2 min to fragment and form the pre-formed fibrils (PFF) before treatment to neurons.

Atomic force microscopy (AFM) measurements

An atomic force microscope (AFM) (Asylum MFP-3D-BIO™, Santa Barbara, CA, USA) was used to perform AFM experiments. Under ambient condition using Si cantilevers with nominal resonance frequency of 330 kHz and nominal spring constant 20-80 N/m (Veeco, Horsham, PA, USA) AFM was performed in the tapping mode.

Transmission electron microscopy (TEM) measurements

Samples were adsorbed to glow discharged 400 mesh carbon coated copper grids (EMS) for 2 min. The grids were quickly transferred through three drops of Tris-HCl (50 mM pH 7.4) rinse, then floated upon two consecutive drops of 0.75% uranyl formate 30 s each. Stain was either aspirated or blotted off with #1 Whatman filter paper triangles. Grids were allowed to dry before imaging on a Phillips CM 120 TEM operating at 80 kV. Images were captured and digitized with an ER-80 CCD (8 megapixel) by advanced microscopy techniques.

Cell line selection for expression cloning

COS-7, HeLa, HEK293FT and SH-SY5Y cells were screened for α-syn-biotin PFF binding using a similar method that was used to identify binding partners of β-amyloid-biotin oligomer (*21*). Cells were incubated with α-syn-biotin PFF (0 μM, 0.5 μM and 1 μM total α-syn-biotin monomer concentrations) in DMEM media with 10% FBS at room temperature for 2 hours. We removed unbound α-syn-biotin PFF by thoroughly washing (4-6 times, 20 min each) with DMEM media with 10% FBS followed by fixation with 4% paraformaldehyde in PBS. The cells were then washed three times with PBS, blocked for 30 min with 10% horse serum and 0.1% Triton X-100 in PBS. Using alkaline-phosphatase-conjugated streptavidin (final dilution 1:2000) in PBS supplemented with 5% horse serum and 0.05% Triton X-100, the cells were incubated for 16 hours and then bound alkaline phosphatase was visualized by 5-bromo-4-chloro-3-indolyl phosphate/nitro blue tetrazolium reaction (*19*, *20*). α-Syn-biotin PFF binding to mouse cortical neurons was used as a positive control. Quantification of bound α-syn-biotin PFF to cells was performed with ImageJ.

Screening strategy, expression cloning and SH-SY5Y cell surface binding assays

A focused set of experiments to identify α-syn PFF mediator(s) was performed. We transfected a library consisting of 352 individual cDNA clones encoding transmembrane proteins (TMGW10001, GFC-transfection array panel, Origene, Rockville, MD, USA) into SH-SY5Y cells (*21*). Two days after transfection, the cells were incubated for 2 hours with α-syn-biotin PFF (1 μM total α-syn-biotin monomer concentration) in DMEM media with 10% FBS at room temperature. We removed unbound α-syn-biotin PFF by thoroughly washing (4-6 times, 20 min each) with DMEM media with 10% FBS and then fixed with 4% paraformaldehyde in PBS. The cells were then washed three times with PBS, blocked for 30 min with 10% horse serum and 0.1% Triton X-100 in PBS. Using alkaline-phosphatase-conjugated streptavidin (final dilution 1:2000) in PBS supplemented with 5% horse serum and 0.05% Triton X-100, the cells were incubated for 16 hours and then bound alkaline phosphatase was visualized by 5-bromo-4-chloro-3-indolyl phosphate/nitro blue tetrazolium reaction (*19*–*21*). Bound α-syn-biotin PFF to LAG3-transfected SH-SY5Y cells was quantified with ImageJ. The Z-factor was calculated by the value of the positive control (neuron) and the negative control (SH-SY5Y cells expressed GFP) in each plate.

Downloaded from http://science.sciencemag.org/ on October 7, 2016

ImageJ analysis

Threshold was selected under Image/Adjust in order to achieve a desired range of intensity values for each experiment. Once determined, this threshold was applied to all the images in each experiment. The threshold setting was also used to exclude the background. After exclusion of the background, the selected area in the signal intensity range of the threshold was measured using the measurement option under the Analyze/Measure menu. The area values with different concentrations of α-syn-biotin (monomer or PFF) were input into the Prism program to obtain K_d.

Primary neuronal cultures, α-syn PFF transduction and neuron binding assays

CD1 mice were obtained from the Jackson Laboratories (Bar Harbor, ME). Primary cortical neurons were prepared from E15.5 pups and cultured in Neurobasal media supplemented with B-27, 0.5 mM L-glutamine, penicillin and streptomycin (all from Invitrogen, Grand Island, NY, USA) on tissue culture plates coated with poly-L-lysine. The neurons were maintained by changing medium every 3-4 days. α-Syn PFF (final concentration 5 μg/mL) was added at 7 days in vitro (DIV) and α-syn PFF was incubated for 10-21 days followed by biochemical experiments or toxicity assays. Each experiment was performed in duplicate and repeated 3-6 times. Neurons were harvested for indirect immunofluorescence and sequential extraction. To determine the amount of bound α-syn-biotin PFF in WT and LAG3$^{-/-}$ neuronal cultures, α-syn-biotin PFF with different concentrations were used. Quantification of bound α-syn-biotin PFF to WT and LAG3$^{-/-}$ neurons were performed with ImageJ.

Primary microglial and astrocyte culture

Primary microglial and astrocyte cultures were performed as described previously (*47*). Whole brains from mouse pups at postnatal day age 1 (P1) were obtained. After removal of the meninges the brains were washed in DMEM-F12 supplemented with 10% heat-inactivated FBS, 50 U/mL penicillin, 50 μg/mL streptomycin, 2 mM L-glutamine, 100 μM non-essential amino acids, and 2 mM sodium pyruvate (DMEM-F12 complete medium) three times. The brains were transferred to 0.25% Trypsin-EDTA followed by 10 min of gentle agitation. DMEM-F12 complete medium was used to stop the trypsinization. The brains were washed three times in this medium again. A single cell suspension was obtained by trituration. Cell debris and aggregates were removed by passing the single cell suspension through a 100 μm nylon mesh. The final single cell suspension thus achieved was cultured in T-75 flasks for 13 days, with a complete medium change on day 6. The mixed glial cell population was separated into astrocyte rich and microglia rich fractions using the EasySep Mouse CD11b Positive Selection Kit (StemCell). The magnetically separated fraction containing microglia and the pour-off fraction containing astrocytes were cultured separately, and harvested 48 hours after plating by scraping.

Mouse strains

C57BL6 and CD1 mice were obtained from the Jackson Laboratories (Bar Harbor, ME). LAG3$^{-/-}$ mice (*48*) were kindly provided Dr. Charles Drake (Johns Hopkins University) and were maintained on a C57BL6 background. The mice do not develop any autoimmune or inflammatory phenotype. However, they do have a defect in T cell homeostasis and at 3-4 months they have enlarged spleens and lymph nodes (*43*). All housing, breeding, and procedures were performed according to the NIH Guide for the Care and Use of Experimental Animals and approved by the Johns Hopkins University Animal Care and Use Committee.

Human A53T α-synuclein transgenic mice, neuron culture and brain homogenates

LAG3$^{-/-}$ mice were crossbred to G2-3 human A53T α-synuclein transgenic mice to obtain A53T α-synuclein and LAG3$^{-/-}$/A53T α-synuclein neuron cultures. Substantial neurodegeneration is observed in the human A53T α-synuclein transgenic mice including serine 129 phosphorylation and the formation of α-synuclein fibrils (*22*). Brain areas that exhibit neuropathology including the brainstem and cerebellum of the human A53T α-synuclein transgenic mice were dissected and stored at -80°C. The brain tissue was sonicated in sterile PBS (100 mg per 1 ml of buffer) and centrifuged for 5 min (3000 g at 4°C). The resultant supernatant was taken and stored at -80°C until further use.

Enzyme-linked immunosorbent assay (ELISA) analysis

The binding affinity between α-syn-biotin PFF and LAG3 was analyzed using a sandwich ELISA kit (Sigma, St. Louis, MO, USA) according to the manufacturer instructions. The lyophilized human LAG3 protein was added into a human LAG3 antibody-coated ELISA plate and left overnight at 4°C with gentle shaking. Followed by 5 washes, 20 min each. Different concentrations of α-syn-biotin PFF (0.1 nM to 100 nM) were added to each well and were incubated for 2 hours at 22°C with gentle shaking. HRP-streptavidin solution was incubated for 45 min at 22°C with gentle shaking followed by 5 washes, 20 min each. Finally, the ELISA colorimetric TMB (3,3′,5,5′-tetramethylbenzidine) reagent was added and incubated for 10 min at 22°C in the dark with gentle shaking.

Plasmids

Human and mouse LAG3 cDNA clones were kindly obtained from Dr. Charles Drake at the Johns Hopkins University, School of Medicine. pcDNA3.1-APLP1, APP and APLP2 cDNA clone were obtained from Dr. Yasushi Shimoda at Nagaoka University of Technology and Dr. Gopal Thinakaran at The University of Chicago. pCAG-Neurexin cDNA clones were obtained from Dr. Thomas C. Südhof at Stanford University and Dr. Peter Scheiffele at Basel University. The pMX-CD4 plasmid #14614 was obtained from Addgene (Cambridge, MA, USA).

Deletion mutants

LAG3 deletion mutants with a HA tag were constructed by PCR using herculase polymerase (Agilent Technologies, Wilmington, DE, USA) and primers were designed to flank the sequences to be deleted. The DNA was separated on a 1% agarose gel and the appropriate band was excised and isolated using a gel extraction kit (Qiagen, Valencia, CA, USA). 100 ng of DNA was phosphorylated at the 5′ end using T4 polynucleotide kinase (Invitrogen, Grand Island, NY, USA) for 30 min at 37°C and ligated overnight at room temperature using T4 DNA ligase (Invitrogen, Grand Island, NY, USA). Reactions were purified with a PCR purification kit (Qiagen, Valencia, CA, USA) and transformed into competent Stbl3 cells (Invitrogen, Grand Island, NY, USA). Integrity of the constructs was verified by sequencing.

Live images

α-Syn PFF was labeled with pHrodo red (Invitrogen, Grand Island, NY, USA). pHrodo red is weakly fluorescent at neutral pH, but fluorescence increases as the pH drops. α-syn-pHrodo PFF was directly added to LAG3 WT and LAG3$^{-/-}$ neuron groups. For the WT + LAG3 and LAG3$^{-/-}$ + LAG3 groups, neurons were co-transfected with LAG3 and GFP expression vector 2 days prior to the addition of α-syn-pHrodo PFF. Live images were recorded every 0.5~1 min for 20~30 min using Microscope Axio Observer Z1 (Zeiss, Dublin, CA, USA). 1~4 min later after α-syn-pHrodo treatment, the cells were suitable for recording. Treatment with calcein AM (C1430, ThermoFisher Scientific, USA) was used to identify the outline of neurons for quantification. Transduction with AAV2-eSYN-EGFP-WPRE in some experiments (VB4870, Vector Biosystems Inc., USA) was also used to identify neurons. This AAV is a EGFP construct driven by the neuron E/SYN promoter, a hybrid promoter consisting of a 0.4 Kb CMV enhancer (E) and the 0.45 Kb human Synapsin I promoter fragment (SYN). Outlining the neuron via the Zeiss Zen Software and then subtracting the background determined the signal intensity of the α-syn-pHrodo PFF. The baseline was established as the fluorescence intensity of the neuron at 2-3 min after α-syn-pHrodo PFF treatment. The percentage of internalized α-syn-pHrodo PFF signal at each time point was obtained by calculating the ratio to the baseline in each experiment. The live images in Fig. 2A were normalized to reduce background.

Colocalization of Rab5 and α-syn-biotin PFF

The images were obtained using the same exposure time and treated in the same way for analysis. The signal of α-syn-biotin PFF colocalized with Rab5 was measured and quantified by the Zeiss Zen software, by outlining the colocalization and measuring the signal intensity and area of the colocalized signals. The overall signal was determined by multiplying the signal intensity by the area to determine the overall value.

Neuronal internalization of latex beads

Latex beads (Sigma, USA) were applied to 12-14 DIV wild type and LAG3$^{-/-}$ neuron culture (1 μL/mL)

Downloaded from http://science.sciencemag.org/ on October 7, 2016

for 4 hours at 37°C. The numbers of internalized latex beads were quantified by confocal microscopy.

Calcium imaging

Intracellular calcium levels were monitored with the fluorescent calcium indicator, Fluo-4 acetoxymethyl (AM) ester (Thermo Fisher Scientific, Waltham, MA, USA). Primary cortical neurons derived from wild-type and LAG3$^{-/-}$ embryo mouse brains were plated on polyornithine-coated glass coverslips for 18 days, and then were loaded with Fluo-4 AM for 30 min at 1 μM final concentration. After one wash with Hank's balanced salt solution (HBSS) (with 2 mM Calcium chloride), the cells were placed in a 37°C heated adaptor on a confocal microscope (Carl Zeiss, Germany). Live imaging was performed with an excitation wavelength of 485 nm and an emission wavelength of 525 nm. Regions of interest (ROI) were selected in a field having usually more than 10 neurons. PFF (0.5 μM) was added with perfusion when the baseline fluorescent signals had been steady for 5 min, and recordings continued for an additional 70 min. Images were acquired at 30 s intervals, and were analyzed with Zen (Carl Zeiss, Germany) and ImageJ software.

LAG3 antibody blocking experiments

Anti-LAG3 antibodies (C9B7W and 410C9) were administered to cell cultures (50 μg/mL) 30 min before α-syn PFF treatment (*33*, *34*). Rat IgG and mouse IgG were applied as negative controls at the same concentration. SH-SY5Y cells overexpressing LAG3 were used for the binding assay 2 days after transfection of LAG3. Mouse primary cortical neurons (12 DIV) were used for the endocytosis endosome enrichment assay. Neurons (7 DIV) were treated with α-syn PFF for pathology and transmission assays. The antibodies were added to chamber 2 of the microfluidic chambers in the transmission assay.

Endosome enrichment

α-Syn-biotin PFF was administered to neuron (12 DIV) cultures and incubated for 1.5 hours. To remove the bound α-syn-biotin PFF, trypsin was added for 30 s and followed by three brief washes with culture medium. Endosomes were enriched as previously described (*26*, *27*). The neurons were harvested with PBS and prepared with lysis buffer (250 mM sucrose, 50 mM Tris-HCl (pH 7.4), 5 mM $MgCl_2$, 1 mM EDTA, 1 mM EGTA) with a protease inhibitor cocktail (Roche, New York, NY, USA). The suspended cell lysates were pipetted 6 times and passed through a syringe 20 times (1 ml TB Syringe, BD, Franklin Lakes, NJ, USA). The endosomes were harvested in the third pellet followed by three steps of centrifugation 1st(1000 g, 10 min), 2nd (16,000 g, 20 min) 3rd (100,000 g, 1 h) for immunoblot analysis.

Biochemical analysis

Dissected brain regions of interest or culture samples were prepared with sequential lysis buffers. For the soluble fraction, samples were homogenized in the following TX-soluble buffer (50 mM Tris [pH 8.0], 150 mM NaCl, 1% Triton-100) containing protease and phosphatase inhibitors (Roche, New York, NY, USA) and samples were centrifuged and the soluble supernatant was collected. The insoluble pellet was resuspended in TX-insoluble buffer (50 mM Tris [pH 8.0], 150 mM NaCl, 1% Triton X-100, 2% SDS) containing protease and phosphatase inhibitors (Roche, New York, NY, USA). Samples were sonicated and centrifuged at 20,000 g for 20 min. Protein concentrations were determined using the BCA assay (Pierce, Rockford, IL, USA) and samples (10 μg total proteins) were separated on SDS-polyacrylamide gels (13.5%) and transferred onto nitrocellulose membranes. Blots were blocked in 5% non-fat milk or 7.5% BSA in TBS-T (Tris-buffered saline-Tween 20) and probed using various primary antibodies. Target antigens were incubated with appropriate secondary antibodies and were detected using ECL substrate and imaged by ImageQuant LAS 4000mini scanner (GE Healthcare Life Sciences, Wauwatosa, WI, USA) or via film.

Lentiviral vector construction, production and transduction

Lentiviral vectors were generated as previously described (*49*). LAG3 or deletion mutants of LAG3 with HA tag were subcloned into a lentiviral cFugw vector by Age I restriction sites. The human ubiquitin C (hUBC) promoter was used to drive expression. The recombinant cFugw vector was transiently transfected into HEK293FT cells together with three packaging vectors: pLP1, pLP2, and pVSV-G (1.3:1.5:1:1.5) to generate the lentiviruses. 48 hours and 72 hours after transfection, the viral supernatants were collected and concentrated by ultracentrifugation for 3 hours at 50,000 *g*. Viral particles were resuspended into serum free medium and stored at -80°C. At DIV 4 to 5, neurons were infected by lentivirus carrying LAG3, deletion mutants of LAG3, or empty vector as a control [1 × 10^9 transduction units (TU)/ml] for 72 hours.

In vitro co-immunoprecipitation (co-IP)

HEK293FT cells were transfected with cFUGW-LAG3 or cFUGW-GFP by lipofectamine 2000. 2 days later the cultures were treated with α-syn-biotin monomer or α-syn-biotin PFF (final concentration 1 μM) for 2-3 hours. The cells were washed 2 times with PBS and harvested with lysis buffer containing 50 mM Tris [pH 8.0], 150 mM NaCl, 1% Triton X-100, and protease inhibitors (Roche, New York, NY, USA). Samples were frozen and thawed three times, followed by centrifugation at 20627 X g for 20 min. Protein concentrations of the supernatants were determined using the BCA assay (Pierce, Rockford, IL, USA). Aliquots of the samples containing 500 μg of protein were incubated with Dynabeads MyOneTM Streptavidin T1 (Invitrogen, Grand Island, NY, USA) overnight at 4°C for α-syn-biotin co-IP assay. In LAG3 co-IP, aliquots of the samples were pre-cleared with 10 μL of Dynabeads® Protein G (Life Technologies, Grand Island, NY, USA) for 1 hour. Simultaneously, 50 μL of Dynabeads® were incubated for one hour with 4 μL of either mouse 410C9 antibody or mouse IgG (Santa Cruz, Dallas, TX, USA). Pre-cleared samples were incubated with Dynabead®-antibody/IgG overnight at 4°C. The IP complexes were washed 5 times with IP buffer and then denatured by adding 2 x Laemlli Buffer plus β-mercaptoethanol, followed by boiling for 5 min.

In vivo co-immunoprecipitation (co-IP)

Transgenic mice overexpressing human A53T α-synuclein (*22*), and WT littermate controls were euthanized at 4 months and 10 months of age. The brainstem was removed and lysates were prepared with brain lysis buffer containing 50 mM Tris [pH 8.0], 150 mM NaCl, 1% NP-40, and protease inhibitors (Roche, New York, NY, USA). Samples were frozen and thawed three times, followed by centrifugation at 20627 X g for 20 min. Protein concentrations of the supernatants were determined using the BCA assay (Pierce, Rockford, IL, USA). Aliquots of the samples containing 500 μg of protein were pre-cleared with 10 μL of Dynabeads® Protein G (Life Technologies, Grand Island, NY, USA) for one hour. Simultaneously, 50 μL of Dynabeads® were incubated for 1 hour with 4 μL of either rabbit α-synuclein antibody (Cell Signaling, Beverly, MA, USA) or rabbit IgG (Santa Cruz, Dallas, TX, USA). Pre-cleared samples were incubated with Dynabead®-antibody/IgG overnight at 4°C. The immunocomplexes were washed 5 times with IP buffer and then denatured by adding 2 x Laemlli Buffer plus β-mercaptoethanol, followed by boiling for 5 min.

Microfluidic chambers

Triple compartment microfluidic devices (TCND1000) were obtained from Xona Microfluidic, LLC (Temecula, CA, USA). Glass coverslips were prepared and coated as described, before being affixed to the microfluidic device (*13*). Approximately 100,000 neurons were plated per chamber. At 4 DIV, WT and LAG3$^{-/-}$ neurons were transduced with lentivirus LAG3 to create WT + LAG3 and LAG3$^{-/-}$ + LAG3 neurons. At 7 DIV, 0.5 μg α-syn PFF was added into chamber 1. To control for direction of flow, a 50 μL difference in media volume was maintained between chamber 1 and chamber 2 and chamber 2 and chamber 3 according to the manufacturers' instructions. Neurons were fixed on day 14 after α-syn PFF treatment using 4% paraformaldehyde in PBS. The chambers were then processed for immunofluorescence staining.

α-Syn fibril and stereotaxic procedure

Purification of recombinant of α-syn proteins and in vitro fibril generation was performed as published (*14*). Assembly reactions of α-syn were performed by continuous agitation of α-syn for 7 days in an amber glass vial with a magnetic stirrer (350 rpm at 37°C). α-Syn PFF was harvested and evaluated for the quality of the fibrils. To avoid repeated freeze and thaw, the PFF were aliquoted and stored in -80°C. On the day of intrastriatal injections, preparations were diluted in sterile PBS and briefly sonicated in a temperature controlled sonicator water bath. Three month old mice were anesthetized with pentobarbital and PBS, recombinant α-syn PFF (5 μg/2 μL) or recombinant α-syn monomer (5 μg/2 μL) was stereotactically

Downloaded from http://science.sciencemag.org/ on October 7, 2016

delivered into one striatum. The following reference coordinates for the dorsal neostriatum were used: +0.2 mm Medial-lateral (ML); +2.0 mm antero-posterior (AP) and +2.8 mm dorso-ventral (DV) from bregma. Injections were performed using a 2 μL syringe (Hamilton, Reno, NV, USA) at a rate of 0.1 μL per minutes with the needle left in place for ≥ 5 min before slow withdrawal of the needle. After surgery, animals were monitored and post-surgical care was provided. Animal behavior was performed at 30 or 180 days and mice were euthanized for biochemical, neurochemical and histological studies. For biochemical studies, tissues were immediately frozen after removal and stored at -80°C. For histological studies, mice were perfused transcardially with PBS and 4% PFA and brains were removed, followed by overnight fixation in 4% PFA and transfer to 30% sucrose for cryoprotection.

HPLC for DA, DOPAC, HVA, and 3MT

High-performance liquid chromatography with electrochemical detection (HPLC-ECD) was used to measure biogenic amine concentrations. Briefly, mice were sacrificed by decapitation. After rapid removal of the striatum, it was weighed and sonicated in 0.2 ml ice cold 0.01 mM perchloric acid containing 0.01% EDTA. 60 ng 3,4-dihydroxybenzylamine (DHBA) was included as an internal standard. This was followed by centrifugation (15,000 × g, 30 min, 4°C) and passing the supernatant through a 0.2 μm filter. Twenty μl of the supernatant was analyzed in the HPLC column (3 mm × 150 mm, C-18 reverse phase column, Acclaim™ Polar Advantage II, Thermo Scientific, USA) by a dual channel coulochem III electrochemical detector (Model 5300, ESA, Inc. Chelmsford, MA, USA). The BCA protein assay kit (Pierce, Rockford, IL, USA) was used to measure protein concentration of the tissue homogenates. Data were normalized to protein concentrations and expressed in ng/mg protein.

Immunohistochemistry, immunofluorescence and mapping of α-syn pathology

Immunohistochemistry (IHC) and immunofluorescence (IF) was performed on 50 μm thick serial brain sections. Primary antibodies and working dilutions are detailed in Table S1. For histological studies, coronal sections were incubated in primary antibodies for P-α-syn or Tyrosine Hydroxylase followed by incubation with biotin-conjugated anti-mouse or anti-Rabbit antibody respectively (Vector Labs, Burlingame, CA, USA), ABC reagents (Vector Labs, Burlingame, CA, USA), and SigmaFast DAB Peroxidase Substrate (Sigma-Aldrich, St. Louis, MO, USA). Sections were counterstained with Nissl (0.09% thionin). Immunoreactivity in double-labeled sections was labeled using appropriate fluorescent secondary antibodies conjugated to Alexa-fluor 488, 594 or 647 (Invitrogen, Carlsbad, CA, USA). Images (IHC) were captured on AxioCam Mrc camera connected to Observer. Z1 microscope (Zeiss, Oberkochen, Germany). Images (IF) were obtained by confocal scanning microscopy (LSM710, Zeiss, Dublin, CA, USA). Photoshop CS6 (Adobe Systems) was used to assemble montages. Fine mapping of P-α-syn pathology was performed by tracing all visible immunoreactive inclusions/cells and neurites at 10 × magnification from sections at multiple rostrocaudal levels corresponding to coronal sections at approximately +1.92, +0.74, -0.82, and -2.30, and -3.52 mm relative to Bregma.

Animals

All procedures involving animals were approved by and conformed to the guidelines of the Institutional Animal Care Committee of Johns Hopkins University. Animals were housed in a 12 h dark and light cycle with free access to water and food. All mice were acclimatized in the procedure room before starting any animal experiments. We have taken great measure to reduce the number of animal used in these studies and also taken effort to reduce animal suffering from pain and discomfort.

Behavioral analysis

To evaluate α-syn PFF-induced behavioral deficits, control and α-syn PFF injected mice were assessed by the pole test, grip strength, and clasping behavior 1-week prior to sacrifice. The experimenter was blinded to treatment group for all behavioral studies. All tests were performed between 10:00-16:00 in the lights-on cycle.

Pole test

A 9 mm diameter 2.5 foot metal rod wrapped with bandage gauze was used as the pole. Mice were placed on the top of the pole (3 inch from the top of the pole) facing head-up. The time taken to turn and total time taken to reach the base of the pole was recorded. Before the actual test the mice were trained for two consecutive days and each training session consisted of three test trials. The maximum cutoff of time to stop the test was 120 s. Results were expressed in turn and total time (in seconds) (*37*).

Grip strength

Neuromuscular strength was measured by maximum holding force generated by the mice (Biosed, USA). Mice were allowed to grasp a metal grid with either by their fore and/or hind limbs or both. The tail was gently pulled and the maximum holding force recorded by the force transducer when the mice released their grasp on the grid. The peak holding strength was digitally recorded and displayed as force in grams (*50*).

Hindlimb clasping

Hindlimb clasping is a marker of disease progression in neurodegeneration. The procedure was performed by grasping the mouse-tail and hindlimb clasping was monitored for 10 s. Mice with neuropathologic deficits exhibit retracted hindlimbs and grasping of the abdominal area. In addition the mice were observed for a hunchbacked posture (*51*).

REFERENCES AND NOTES

1. M. Goedert, Alpha-synuclein and neurodegenerative diseases. *Nat. Rev. Neurosci.* **2**, 492–501 (2001). doi: 10.1038/35081564; pmid: 11433374
2. M. Goedert, M. G. Spillantini, K. Del Tredici, H. Braak, 100 years of Lewy pathology. *Neurology* **9**, 13–24 (2013). doi: 10.1038/nrneurol.2012.242; pmid: 23183883
3. V. M. Lee, J. Q. Trojanowski, Mechanisms of Parkinson's disease linked to pathological alpha-synuclein: New targets for drug discovery. *Neuron* **52**, 33–38 (2006). doi: 10.1016/j.neuron.2006.09.026; pmid: 17015225
4. B. Dehay, M. Vila, E. Bezard, P. Brundin, J. H. Kordower, Alpha-synuclein propagation: New insights from animal models. *Mov. Disord.* **31**, 161–168 (2016). doi: 10.1002/mds.26370; pmid: 26347034
5. S. J. Lee, P. Desplats, H. J. Lee, B. Spencer, E. Masliah, Cell-to-cell transmission of α-synuclein aggregates. *Methods Mol. Biol.* **849**, 347–359 (2012). doi: 10.1007/978-1-61779-551-0_23; pmid: 22528101
6. T. Tyson, J. A. Steiner, P. Brundin, Sorting out release, uptake and processing of alpha-synuclein during prion-like spread of pathology. *J. Neurochem.* 10.1111/jnc.13449 (2015). doi: 10.1111/jnc.13449; pmid: 26617280
7. H. Braak *et al.*, Staging of brain pathology related to sporadic Parkinson's disease. *Neurobiol. Aging* **24**, 197–211 (2003). doi: 10.1016/S0197-4580(02)00065-9; pmid: 12498954
8. K. Del Tredici, H. Braak, Review: Sporadic Parkinson's disease: development and distribution of α-synuclein pathology. *Neuropathol. Appl. Neurobiol.* **42**, 33–50 (2016). doi: 10.1111/nan.12298; pmid: 26662475
9. J. H. Kordower, Y. Chu, R. A. Hauser, T. B. Freeman, C. W. Olanow, Lewy body-like pathology in long-term embryonic nigral transplants in Parkinson's disease. *Nat. Med.* **14**, 504–506 (2008). doi: 10.1038/nm1747; pmid: 18391962
10. J. Y. Li *et al.*, Lewy bodies in grafted neurons in subjects with Parkinson's disease suggest host-to-graft disease propagation. *Nat. Med.* **14**, 501–503 (2008). doi: 10.1038/nm1746; pmid: 18391963
11. L. C. Walker, M. Jucker, Neurodegenerative diseases: Expanding the prion concept. *Annu. Rev. Neurosci.* **38**, 87–103 (2015). doi: 10.1146/annurev-neuro-071714-033828; pmid: 25840008
12. M. Jucker, L. C. Walker, Self-propagation of pathogenic protein aggregates in neurodegenerative diseases. *Nature* **501**, 45–51 (2013). doi: 10.1038/nature12481; pmid: 24005412
13. L. A. Volpicelli-Daley *et al.*, Exogenous α-synuclein fibrils induce Lewy body pathology leading to synaptic dysfunction and neuron death. *Neuron* **72**, 57–71 (2011). doi: 10.1016/j.neuron.2011.08.033; pmid: 21982369
14. K. C. Luk *et al.*, Pathological α-synuclein transmission initiates Parkinson-like neurodegeneration in nontransgenic mice. *Science* **338**, 949–953 (2012). doi: 10.1126/science.1227157; pmid: 23161999
15. T. Ben Gedalya *et al.*, Alpha-synuclein and polyunsaturated fatty acids promote clathrin-mediated endocytosis and synaptic vesicle recycling. *Traffic* **10**, 218–234 (2009). doi: 10.1111/j.1600-0854.2008.00853.x; pmid: 18980610
16. F. Cheng *et al.*, α-Synuclein promotes clathrin-mediated NMDA receptor endocytosis and attenuates NMDA-induced dopaminergic cell death. *J. Neurochem.* **119**, 815–825 (2011). doi: 10.1111/j.1471-4159.2011.07460.x; pmid: 21883224
17. S. H. Oh *et al.*, Mesenchymal stem cells inhibit transmission of α-synuclein by modulating clathrin-mediated endocytosis in a Parkinsonian model. *Cell Reports* **14**, 835–849 (2016). doi: 10.1016/j.celrep.2015.12.075; pmid: 26776513
18. L. A. Volpicelli-Daley, K. C. Luk, V. M. Lee, Addition of exogenous α-synuclein preformed fibrils to primary neuronal cultures to seed recruitment of endogenous α-synuclein to Lewy body and Lewy neurite-like aggregates. *Nat. Protoc.* **9**, 2135–2146 (2014). doi: 10.1038/nprot.2014.143; pmid: 25122523
19. H. J. Cheng, J. G. Flanagan, Identification and cloning of ELF-1, a developmentally expressed ligand for the Mek4 and Sek receptor tyrosine kinases. *Cell* **79**, 157–168 (1994). doi: 10.1016/0092-8674(94)90408-1; pmid: 7522971
20. H. J. Cheng, J. G. Flanagan, Cloning and characterization of RTK ligands using receptor-alkaline phosphatase fusion proteins. *Methods Mol. Biol.* **124**, 313–334 (2001). pmid: 11100484
21. J. Laurén, D. A. Gimbel, H. B. Nygaard, J. W. Gilbert, S. M. Strittmatter, Cellular prion protein mediates impairment of synaptic plasticity by amyloid-β oligomers. *Nature* **457**, 1128–1132 (2009). doi: 10.1038/nature07761; pmid: 19242475
22. M. K. Lee *et al.*, Human alpha-synuclein-harboring familial Parkinson's disease-linked Ala-53 → Thr mutation causes neurodegenerative disease with alpha-synuclein aggregation in transgenic mice. *Proc. Natl. Acad. Sci. U.S.A.* **99**, 8968–8973 (2002). doi: 10.1073/pnas.132197599; pmid: 12084935

Downloaded from http://science.sciencemag.org/ on October 7, 2016

23. B. Huard *et al*., Characterization of the major histocompatibility complex class II binding site on LAG-3 protein. *Proc. Natl. Acad. Sci. U.S.A.* **94**, 5744–5749 (1997). doi: 10.1073/pnas.94.11.5744; pmid: 9159144
24. J. Han, K. Burgess, Fluorescent indicators for intracellular pH. *Chem. Rev.* **110**, 2709–2728 (2010). doi: 10.1021/cr900249z; pmid: 19831417
25. J. Huotari, A. Helenius, Endosome maturation. *EMBO J.* **30**, 3481–3500 (2011). doi: 10.1038/emboj.2011.286; pmid: 21878991
26. F. T. Mu *et al*., EEA1, an early endosome-associated protein. EEA1 is a conserved α-helical peripheral membrane protein flanked by cysteine "fingers" and contains a calmodulin-binding IQ motif. *J. Biol. Chem.* **270**, 13503–13511 (1995). doi: 10.1074/jbc.270.22.13503; pmid: 7768953
27. M. S. Taha *et al*., Subcellular fractionation and localization studies reveal a direct interaction of the fragile X mental retardation protein (FMRP) with nucleolin. *PLOS ONE* **9**, e91465 (2014). doi: 10.1371/journal.pone.0091465; pmid: 24658146
28. P. R. Angelova *et al*., Ca^{2+} is a key factor in α-synuclein-induced neurotoxicity. *J. Cell Sci.* **129**, 1792–1801 (2016). doi: 10.1242/jcs.180737; pmid: 26989132
29. N. T. Hettiarachchi *et al*., alpha-Synuclein modulation of Ca^{2+} signaling in human neuroblastoma (SH-SY5Y) cells. *J. Neurochem.* **111**, 1192–1201 (2009). doi: 10.1111/j.1471-4159.2009.06411.x; pmid: 19860837
30. K. Melachroinou *et al*., Deregulation of calcium homeostasis mediates secreted α-synuclein-induced neurotoxicity. *Neurobiol. Aging* **34**, 2853–2865 (2013). doi: 10.1016/j.neurobiolaging.2013.06.006; pmid: 23891486
31. S. Nath, J. Goodwin, Y. Engelborghs, D. L. Pountney, Raised calcium promotes α-synuclein aggregate formation. *Mol. Cell. Neurosci.* **46**, 516–526 (2011). doi: 10.1016/j.mcn.2010.12.004; pmid: 21145971
32. A. N. Shrivastava *et al*., α-synuclein assemblies sequester neuronal α3-Na^+/K^+-ATPase and impair Na^+ gradient. *EMBO J.* **34**, 2408–2423 (2015). doi: 10.15252/embj.201591397; pmid: 26323479
33. C. J. Workman, D. S. Rice, K. J. Dugger, C. Kurschner, D. A. Vignali, Phenotypic analysis of the murine CD4-related glycoprotein, CD223 (LAG-3). *Eur. J. Immunol.* **32**, 2255–2263 (2002). doi: 10.1002/1521-4141(200208)32:8<2255::AID-IMMU2255>3.0.CO;2-A; pmid: 12209638
34. S. R. Woo *et al*., Differential subcellular localization of the regulatory T-cell protein LAG-3 and the coreceptor CD4. *Eur. J. Immunol.* **40**, 1768–1777 (2010). doi: 10.1002/eji.200939874; pmid: 20391435
35. T. Miyazaki, A. Dierich, C. Benoist, D. Mathis, Independent modes of natural killing distinguished in mice lacking Lag3. *Science* **272**, 405–408 (1996). doi: 10.1126/science.272.5260.405; pmid: 8602528
36. K. C. Luk *et al*., Intracerebral inoculation of pathological α-synuclein initiates a rapidly progressive neurodegenerative α-synucleinopathy in mice. *J. Exp. Med.* **209**, 975–986 (2012). doi: 10.1084/jem.20112457; pmid: 22508839
37. S. S. Karuppagounder *et al*., The c-Abl inhibitor, nilotinib, protects dopaminergic neurons in a preclinical animal model of Parkinson's disease. *Sci. Rep.* **4**, 4874 (2014). doi: 10.1038/srep04874; pmid: 24786396
38. C. Kim *et al*., Neuron-released oligomeric α-synuclein is an endogenous agonist of TLR2 for paracrine activation of microglia. *Nat. Commun.* **4**, 1562 (2013). doi: 10.1038/ncomms2534; pmid: 23463005
39. B. B. Holmes *et al*., Heparan sulfate proteoglycans mediate internalization and propagation of specific proteopathic seeds. *Proc. Natl. Acad. Sci. U.S.A.* **110**, E3138–E3147 (2013). doi: 10.1073/pnas.1301440110; pmid: 23898162
40. G. S. Huh *et al*., Functional requirement for class I MHC in CNS development and plasticity. *Science* **290**, 2155–2159 (2000). doi: 10.1126/science.290.5499.2155; pmid: 11118151
41. C. J. Shatz, MHC class I: An unexpected role in neuronal plasticity. *Neuron* **64**, 40–45 (2009). doi: 10.1016/j.neuron.2009.09.044; pmid: 19840547
42. H. Neumann, Control of glial immune function by neurons. *Glia* **36**, 191–199 (2001). doi: 10.1002/glia.1108; pmid: 11596127
43. A. C. Anderson, N. Joller, V. K. Kuchroo, Lag-3, Tim-3, and TIGIT: Co-inhibitory receptors with specialized functions in immune regulation. *Immunity* **44**, 989–1004 (2016). doi: 10.1016/j.immuni.2016.05.001; pmid: 27192565
44. J. G. Lee, S. Takahama, G. Zhang, S. I. Tomarev, Y. Ye, Unconventional secretion of misfolded proteins promotes adaptation to proteasome dysfunction in mammalian cells. *Nat. Cell Biol.* **18**, 765–776 (2016). pmid: 27295555
45. J. L. Guo, V. M. Y. Lee, Seeding of normal Tau by pathological Tau conformers drives pathogenesis of Alzheimer-like tangles. *J. Biol. Chem.* **286**, 15317–15331 (2011). doi: 10.1074/jbc.M110.209296; pmid: 21372138
46. T. I. Kam *et al*., FcγRIIb mediates amyloid-β neurotoxicity and memory impairment in Alzheimer's disease. *J. Clin. Invest.* **123**, 2791–2802 (2013). doi: 10.1172/JCI66827; pmid: 23921129
47. N. Panicker *et al*., Fyn kinase regulates microglial neuroinflammatory responses in cell culture and animal models of Parkinson's disease. *J. Neurosci.* **35**, 10058–10077 (2015). doi: 10.1523/JNEUROSCI.0302-15.2015; pmid: 26157004
48. C. J. Workman, D. A. Vignali, The CD4-related molecule, LAG-3 (CD223), regulates the expansion of activated T cells. *Eur. J. Immunol.* **33**, 970–979 (2003). doi: 10.1002/eji.200323382; pmid: 12672063
49. S. A. Andrabi *et al*., Iduna protects the brain from glutamate excitotoxicity and stroke by interfering with poly(ADP-ribose) polymer-induced cell death. *Nat. Med.* **17**, 692–699 (2011). doi: 10.1038/nm.2387; pmid: 21602803
50. H. Y. Park *et al*., Inhibition of adenylyl cyclase type 5 prevents L-DOPA-induced dyskinesia in an animal model of Parkinson's disease. *J. Neurosci.* **34**, 11744–11753 (2014). doi: 10.1523/JNEUROSCI.0864-14.2014; pmid: 25164669
51. T. N. Taylor, J. G. Greene, G. W. Miller, Behavioral phenotyping of mouse models of Parkinson's disease. *Behav. Brain Res.* **211**, 1–10 (2010). doi: 10.1016/j.bbr.2010.03.004; pmid: 20211655

ACKNOWLEDGMENTS

This work was supported by grants from NIH (NS38377) and the JPB Foundation. P.G. was supported by the Summer Student Fellowship PDF-SFW-1572 from the Parkinson's Disease Foundation. Y.X. is supported by NIH/National Institute on Aging grant K01-AG046366 and The William N. & Bernice E. Bumpus Foundation Innovation Awards. H.S.K. is supported by NIH/National Institute of Neurological Disorders and Stroke grant NS082205. C.J.W. and D.A.A.V. are supported by NIH grant PO1-AI108545. T.M.D. is the Leonard and Madlyn Abramson Professor in Neurodegenerative Diseases. The authors acknowledge the joint participation by the Adrienne Helis Malvin Medical Research Foundation through its direct engagement in the continuous active conduct of medical research in conjunction with the Johns Hopkins Hospital and the Johns Hopkins University School of Medicine and the Foundation's Parkinson's Disease Program M-2014. C. Drake from Johns Hopkins University generously provided $LAG3^{-/-}$ mice. I-H. Wu created fig. S3A and fig. S10A. 410C9 hybridoma cell line is available from D.A.A.V. under a materials agreement with the University of Pittsburgh. D.A.A.V. and C.J.W. are inventors on issued patents [U.S. (8,551,481), Europe (1897548), Australia (2004217526), and Hong Kong (1114339)] held by St. Jude Children's Research Hospital and Johns Hopkins University that cover LAG3. Additional applications are pending. X.M., V.L.D., H.S.K., C.J.W., D.A.A.V., and T.M.D. are inventors on a patent application submitted by Johns Hopkins University that covers the use of inhibitors of LAG3 to treat Parkinson's disease. The supplementary materials contain additional data.

SUPPLEMENTARY MATERIALS

www.sciencemag.org/content/353/6307/aah3374/suppl/DC1
Figs. S1 to S24
Tables S1 and S2
References

12 June 2016; accepted 24 August 2016
10.1126/science.aah3374

Downloaded from http://science.sciencemag.org/ on October 7, 2016

RESEARCH ARTICLE SUMMARY

CANCER

The linker histone H1.0 generates epigenetic and functional intratumor heterogeneity

Cristina Morales Torres,* Alva Biran,* Matthew J. Burney, Harshil Patel, Tristan Henser-Brownhill, Ayelet-Hashahar Shapira Cohen, Yilong Li, Rotem Ben-Hamo, Emma Nye, Bradley Spencer-Dene, Probir Chakravarty, Sol Efroni, Nik Matthews, Tom Misteli, Eran Meshorer, Paola Scaffidi†

INTRODUCTION: Cancer arises from clonal expansion of a single cell. Yet, most human cancers are characterized by extensive intratumor heterogeneity and comprise various subpopulations of cells with distinct phenotypes and biological properties. Intratumor heterogeneity poses major challenges in understanding cancers, managing patients, and designing effective treatment strategies. Functional heterogeneity within individual tumors is partly due to the presence of genetically distinct subclonal cell populations. Furthermore, interactions between cancer cells and the tumor microenvironment can alter the phenotype of cancer cells via nongenetic mechanisms. The combination of cell-intrinsic and cell-extrinsic changes occurring during tumor growth generates functionally distinct subsets of cells that differentially contribute to tumor maintenance.

RATIONALE: In many cancers, phenotypic and functional heterogeneity can be mapped to distinct differentiation states, suggesting that cellular hierarchies established during tumor growth may affect the long-term proliferative potential of cancer cells. To shed light on the mechanisms responsible for the generation of these hierarchies, we searched for epigenetic mechanisms that determine which cancer cells can preserve unlimited proliferative potential, and thus the ability to drive long-term tumor growth, and which cells lose this ability through a differentiation process.

RESULTS: We found that, in several cancer types, individual tumors exhibit high heterogeneity of the major chromatin protein linker histone H1.0, showing strongly reduced H1.0 levels in cells characterized by long-term self-renewal ability and tumorigenic potential and higher levels in nontumorigenic cells. Combined analysis of pan-cancer patient data sets and experimental alteration of the *H1F0* locus in tumor cells revealed that heterogeneous H1.0 expression patterns are partly due to differential methylation of an enhancer region that dynamically modulates H1.0 expression within tumors. Using a controlled system to model functional intratumor heterogeneity, we showed that maintenance of cell tumorigenic potential required silencing of H1.0 to avoid loss of unlimited proliferative capacity through differentiation. Mechanistically, absence of H1.0 led to destabilization of nucleosome-DNA interactions in AT-rich genomic regions and coordinated derepression of large sets of neighboring genes, resulting in activation of transcriptional programs that support cancer cell self-renewal. Gene expression changes induced by H1.0 loss were reversible, and epigenetic states restricting cell proliferative potential were reestablished upon H1.0 reexpression. In multiple cancer types, in agreement with the observed inhibition of cancer cell self-renewal by H1.0, patients expressing overall strongly reduced levels of H1.0 showed a significantly worse outcome than patients expressing higher H1.0 levels.

ON OUR WEBSITE

Read the full article at http://dx.doi.org/10.1126/science.aaf1644

CONCLUSION: Intratumor heterogeneity has emerged as a general feature of cancer, but the molecular features underlying functionally diverse cellular phenotypes have been elusive. Our results uncover epigenetic determinants of tumor-maintaining cells and identify an integral component of chromatin as an important regulator of cell differentiation states within tumors. We propose that only cells insensitive to extracellular differentiation cues, capable of permanently silencing H1.0, can act as self-renewing tumor-maintaining cells and that such a mechanism supports maintenance of several types of cancer. Our results suggest that intervention aimed at restoring high levels of H1.0 in all cancer cells may enhance the differentiation process that naturally occurs during tumor growth and may be beneficial for therapeutic purposes. ■

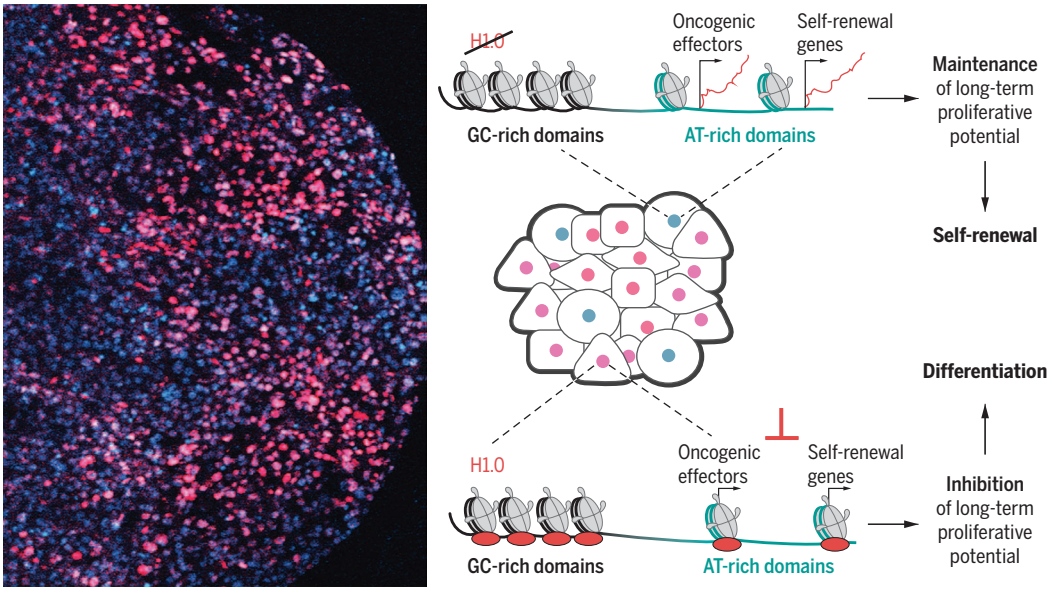

Epigenetic heterogeneity within tumors. In many cancer types, self-renewing and differentiated epigenetic states coexist in individual tumors. (**Left**) Image of a breast cancer section showing heterogeneous levels of the linker histone H1.0 (red). (**Right**) Schematic depiction of the chromatin status of cancer cells in which H1.0 is down-regulated (blue) or expressed at high levels (red).

The list of author affiliations is available in the full article online.
*These authors contributed equally to this work.
†Corresponding author. Email: paola.scaffidi@crick.ac.uk
Cite this article as C. Morales Torres *et al.*, *Science* 353, aaf1644 (2016). DOI: 10.1126/science.aaf1644

Downloaded from http://science.sciencemag.org/ on October 7, 2016

RESEARCH ARTICLE

CANCER

The linker histone H1.0 generates epigenetic and functional intratumor heterogeneity

Cristina Morales Torres,[1]* Alva Biran,[2]* Matthew J. Burney,[1] Harshil Patel,[3] Tristan Henser-Brownhill,[1] Ayelet-Hashahar Shapira Cohen,[2] Yilong Li,[4] Rotem Ben-Hamo,[5] Emma Nye,[6] Bradley Spencer-Dene,[6] Probir Chakravarty,[3] Sol Efroni,[5] Nik Matthews,[7] Tom Misteli,[8] Eran Meshorer,[2] Paola Scaffidi[1,9]†

Tumors comprise functionally diverse subpopulations of cells with distinct proliferative potential. Here, we show that dynamic epigenetic states defined by the linker histone H1.0 determine which cells within a tumor can sustain the long-term cancer growth. Numerous cancer types exhibit high inter- and intratumor heterogeneity of H1.0, with H1.0 levels correlating with tumor differentiation status, patient survival, and, at the single-cell level, cancer stem cell markers. Silencing of H1.0 promotes maintenance of self-renewing cells by inducing derepression of megabase-sized gene domains harboring downstream effectors of oncogenic pathways. Self-renewing epigenetic states are not stable, and reexpression of H1.0 in subsets of tumor cells establishes transcriptional programs that restrict cancer cells' long-term proliferative potential and drive their differentiation. Our results uncover epigenetic determinants of tumor-maintaining cells.

Cancer is a clonal disease originating from a single cell. Yet, most human cancers are characterized by extensive intratumor heterogeneity and comprise various subpopulations of cells with distinct phenotypes and biological properties (*1*, *2*). Intratumor heterogeneity poses major challenges in understanding cancers, managing patients, and designing effective treatment strategies. Functional heterogeneity within individual tumors is partly due to intercellular genetic variation, which results in the generation of genetically distinct subclonal cell populations (*3*, *4*). Furthermore, tumors have complex architecture, differing regionally in vessel content, stroma, host infiltrates, and other features that can alter the phenotype of genetically identical cells (*5*).

In many cancers, phenotypic and functional heterogeneity can be mapped to distinct differentiation states (*5*–*7*), suggesting that epigenetic changes occurring during tumor growth may establish cellular hierarchies within the neoplastic mass, thereby affecting the long-term proliferative potential of cancer cells. In line with this notion, individual tumors have been shown to contain distinct subpopulations of undifferentiated, self-renewing cells and more differentiated cells, which only have limited proliferative ability (*8*, *9*). Regardless of their cell of origin, cancer cells endowed with unlimited proliferative potential can be identified by their ability to propagate the disease when transplanted into immunocompromised mice and are referred to as tumor-propagating cells (TPCs) or cancer stem cells (CSCs) (*9*). The mechanisms through which epigenetic changes occurring during tumor growth establish differentiation hierarchies and contribute to functional heterogeneity within individual tumors are largely unknown.

We have previously shown that hierarchically organized human primary tumors containing functionally distinct subsets of cancer cells can be generated in a controlled manner using de novo transformed cells. Expression of human telomerase (hTERT) and oncogenic $HRAS^{V12}$ and concomitant inhibition of p53 and pRB by SV40 T antigens confer tumorigenic potential to various cell types (*10*–*12*). We have shown that, upon experimental transformation of primary dermal fibroblasts, a subpopulation of cells marked by the CSC marker SSEA1 (*13*, *14*) acquire uncontrolled long-term proliferative potential and multipotency (*15*). Thus, when injected into mice, $SSEA1^+$ cells form hierarchically organized tumors in which a small subset of self-renewing $SSEA1^+$ cells maintain tumor growth while generating $SSEA1^-$ differentiated progeny with only limited proliferative capacity (*15*). The functional differences that distinguish $SSEA1^+$ and $SSEA1^-$ tumor cells—undifferentiated phenotype, long-term self-renewal ability, and high tumorigenic potential versus differentiated phenotype, limited proliferative potential, and low tumorigenicity—are general features associated with differentiation hierarchies in many cancer types, regardless of the tissue of origin.

Taking advantage of our ability to generate hierarchically organized human tumors in a controlled manner, here we identify an epigenetic mechanism that establishes intratumor functional heterogeneity. We report that reversible silencing of the linker histone H1.0 (*16*) affects the differentiation state of cancer cells and contributes to defining which cells within a tumor can maintain long-term self-renewal potential and drive tumor growth. H1.0 is one of multiple H1 variants. Unlike replication-dependent H1 variants, which are mainly expressed in proliferating cells, H1.0 is expressed in both dividing and nondividing cells (*16*). H1.0 levels are low in pluripotent cells but accumulate in somatic cells, replacing replication-dependent H1 variants (*17*). Here, we demonstrate a critical role for histone H1.0 in inhibiting tumor maintenance.

Results

Heterogeneous levels of H1.0 in individual tumors

We have previously used an engineered system to model functional intratumor heterogeneity of human tumors (see above) (*15*). In this system, we have shown by gene expression analysis that self-renewing tumor cells, which are marked by the surface antigen SSEA1 ($SSEA1^+$ cells), are molecularly distinct from their $SSEA1^-$ differentiated progeny (fig. S1A) (*15*). Among the differentially expressed genes, *H1F0*, which encodes histone H1.0, showed consistent down-regulation in $SSEA1^+$ cells compared with $SSEA1^-$ cells in multiple tumors (Fig. 1A and fig. S1B). Other H1 variants were either expressed at very low levels in all tumor cells (*HIST1H1A*, *HIST1H1B*, *HIST1H1C*, *HIST1H1D*, *HIST1H1T*, *H1F00*, *H1FNT*, and *H1FX*) or expressed at comparable levels in $SSEA1^+$ and $SSEA1^-$ cells (*HIST1H1E*) (fig. S1B). Analysis of protein levels by quantitative immunofluorescence microscopy of sorted tumor cells and tumor sections confirmed low levels of H1.0 in self-renewing $SSEA1^+$ cells (Fig. 1, B and C, and fig. S1C). In contrast, $SSEA1^-$ cells expressed heterogeneous, but overall higher, levels of H1.0 (Fig. 1, B and C, and fig. S1C), similarly to hTERT-immortalized, nontransformed fibroblasts, from which $SSEA1^+$ cells were originally derived (Fig. 1, B and C). As a control, comparable levels of H1.4 (*HIST1H1E* gene product) were detected in $SSEA1^+$ and $SSEA1^-$ cells (Fig. 1B and fig. S1D). Low abundance of H1.0 in $SSEA1^+$ cells was further confirmed in unsorted tumor cells by imaging flow cytometry, which showed a mutually exclusive

[1]Cancer Epigenetics Laboratory, The Francis Crick Institute, Lincoln's Inn Fields Laboratory, London WC2A 3LY, UK. [2]Department of Genetics, The Institute of Life Sciences, and The Edmond and Lily Safra Center for Brain Sciences (ELSC), The Hebrew University of Jerusalem, Edmond J. Safra Campus, Givat Ram, Jerusalem 91904, Israel. [3]Bioinformatics, The Francis Crick Institute, Lincoln's Inn Fields Laboratory, London WC2A 3LY, UK. [4]Cancer Genome Project, Wellcome Trust Sanger Institute, Wellcome Trust Genome Campus, Hinxton CB101SA, UK. [5]The Mina and Everard Goodman Faculty of Life Science, Bar Ilan University, Ramat-Gan 52900, Israel. [6]Experimental Histopathology, The Francis Crick Institute, Lincoln's Inn Fields Laboratory, London WC2A 3LY, UK. [7]Advanced Sequencing, The Francis Crick Institute, Lincoln's Inn Fields Laboratory, London WC2A 3LY, UK. [8]National Cancer Institute, National Institutes of Health, Bethesda, MD 20892, USA. [9]UCL Cancer Institute, University College London, London WC1E 6DD, UK.
*These authors contributed equally to this work. †Corresponding author. Email: paola.scaffidi@crick.ac.uk

Downloaded from http://science.sciencemag.org/ on October 7, 2016

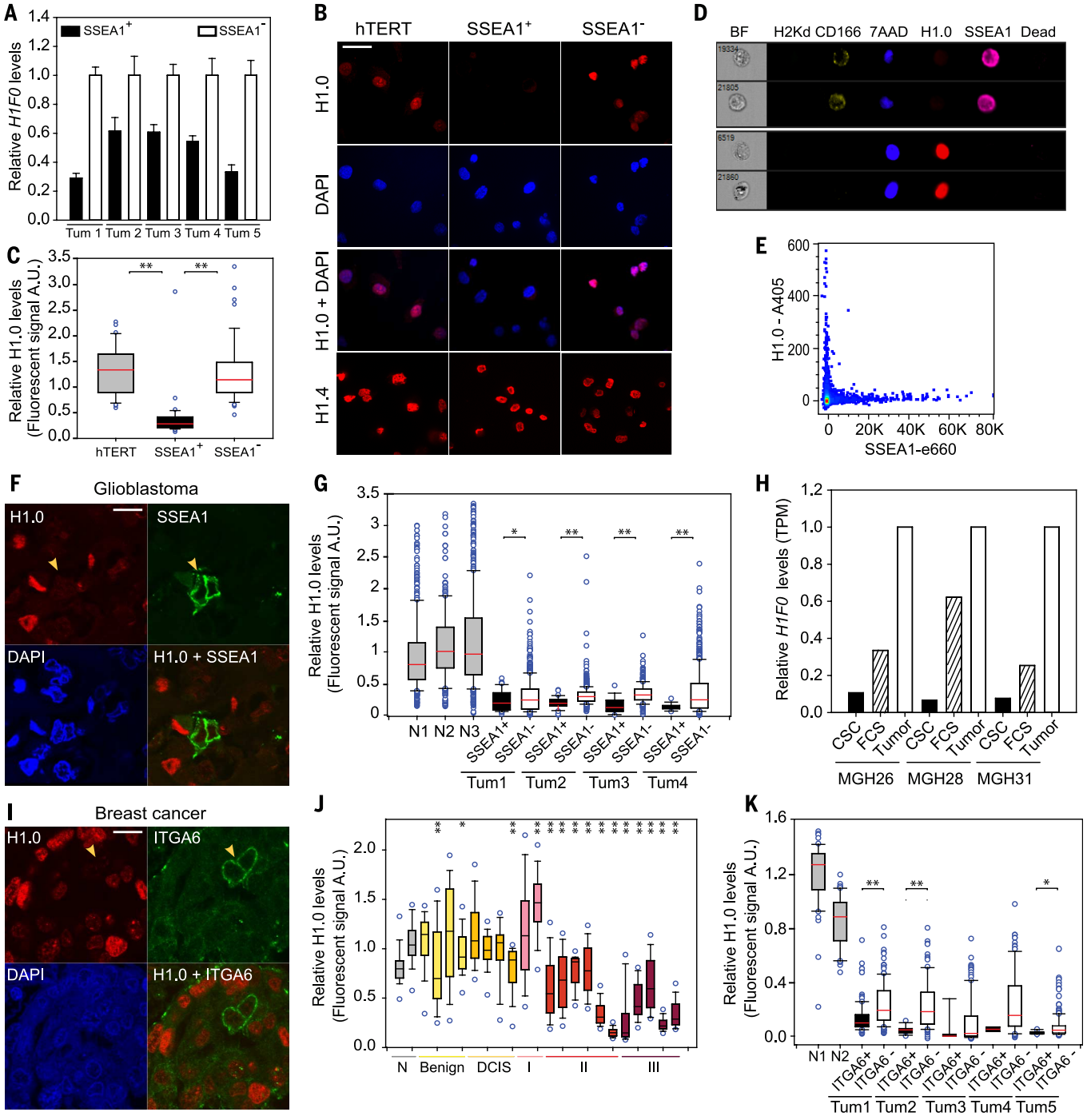

Fig. 1. Intratumor heterogeneity of H1.0 levels. (**A**) qRT-PCR analysis of *H1F0* mRNA levels in SSEA1$^+$ and SSEA1$^-$ cells isolated from five tumors induced by in vitro–transformed fibroblasts (*15*). Values indicate average ± SEM of three technical replicates. (**B** and **C**) Quantitative immunodetection of H1.0 and H1.4 (red) by immunofluorescence microscopy in the indicated sorted tumor cells and telomerase-immortalized parental cells (hTERT). Scale bar, 20 μm. $^{**}P < 0.01$ (Student's *t* test). $37 < N < 60$. (**D** and **E**) Quantitative immunodetection of H1.0 by imaging flow cytometry in unsorted tumor cells. SSEA1$^+$, self-renewing cells; CD166^{low}, highly differentiated cells; 7′AAD, nuclei; live/dead$^+$, dead cells; H2Kd$^+$, host mouse cells excluded from analysis. Scale bar, 10 μm. (E) Scatter plot of H1.0 and SSEA1 levels in individual cells. (**F** and **G**) Quantitative immunodetection of H1.0 and SSEA1 in GBM samples by immunofluorescence microscopy. Scale bar, 10 μm. (G) Quantification of H1.0 levels in three normal (N1 to N3) and four tumor (Tum1 to Tum4) samples. $^*P < 0.05$; $^{**}P < 0.01$ (Student's *t* test). $15 < N < 910$. (**H**) Quantification of *H1F0* mRNA levels in cells from three GBM samples by RNA-seq. CSC, cells grown as neurospheres; FCS, cells differentiated in vitro by FCS addition; Tumor, whole tumor population. (**I** to **K**) Quantitative immunodetection of H1.0 and ITGA6 in breast cancer samples by immunofluorescence microscopy. Scale bar, 10 μm. Quantification of H1.0 levels in two normal breast tissues (N) and tumor samples of different histological grade. $^*P < 0.05$; $^{**}P < 0.01$, compared with N2 (Student's *t* test). (J) $38 < N < 134$. (K) Quantification of H1.0 levels in two normal breast tissues (N1 and N2) and five tumor samples (Tum 1 to 5). $^*P < 0.05$; $^{**}P < 0.01$ (Student's *t* test). $7 < N < 131$, except ITGA6+ Tum 4, for which $N = 2$.

Downloaded from http://science.sciencemag.org/ on October 7, 2016

relationship between H1.0 and SSEA1 (Fig. 1, D and E). H1.0 levels negatively correlated with the presence of the mitotic marker phopho-H3S28 in tumors, confirming an association between H1.0 levels and cell proliferative potential (fig. S2).

We next examined H1.0 levels in clinical samples from cancer patients. Glioblastoma multiforme (GBM) is an aggressive brain cancer characterized by highly undifferentiated cells. SSEA1 is an established GBM stem cell marker that enriches for tumor-propagating cells (*13*, *14*). Single-cell analysis of normal brain and GBM tissue sections by quantitative immunofluorescence microscopy showed overall reduced levels of H1.0, but not H1.4, in cancer samples (Fig. 1, F and G, and fig. S3A). However, whereas the SSEA1$^-$ cell population was heterogeneous and included cells expressing H1.0 at comparable levels as normal brain cells (*H1F0*^{high} cells), SSEA1$^+$ cells consistently exhibited low levels of the protein (*H1F0*^{low} cells) ($P < 0.01$) (Fig. 1, F and G, and fig. S3A). Analysis of single-cell RNA-sequencing (RNA-seq) data sets from primary GBMs (*2*) confirmed these results, because self-renewing GBM cells isolated from multiple tumors (CSCs) showed ~10 times lower average levels of *H1F0* compared with the whole tumor cell population and ~4 times lower levels compared with cells cultured under differentiating conditions (FCS) (Fig. 1H). Although the average *H1F0* levels were variable across GBM samples, the range of *H1F0* levels in individual cells was similar in all analyzed tumors (fig. S3B), indicating that bulk measurements of the heterogeneous GBM populations mainly reflected the relative abundance of *H1F0*^{high} and *H1F0*^{low} cells within each population. Furthermore, analysis of gene expression data sets from The Cancer Genome Atlas (TCGA) showed significantly higher bulk levels of *H1F0* in lower-grade glioma (LGG) compared with grade 4 GBM ($P < 0.001$) (fig. S3C), suggesting that more aggressive brain tumors contain more *H1F0*^{low} cells than well- and moderately differentiated tumors.

Intratumor heterogeneity of H1.0 levels was also observed in other types of cancer. In breast cancer (BRCA), the abundance of H1.0^{low} cells correlated with histopathological grade, being lower in well-differentiated cancers (grade I) and higher in moderately (grade II) and poorly (grade III) differentiated tumors (Fig. 1J and fig. S3D). Levels of H1.0 were particularly low ($P < 0.01$) in cells expressing ITGA6, a surface antigen marking breast CSCs (*18*), which has been shown to have prognostic value as a single parameter (*19*) (Fig. 1,

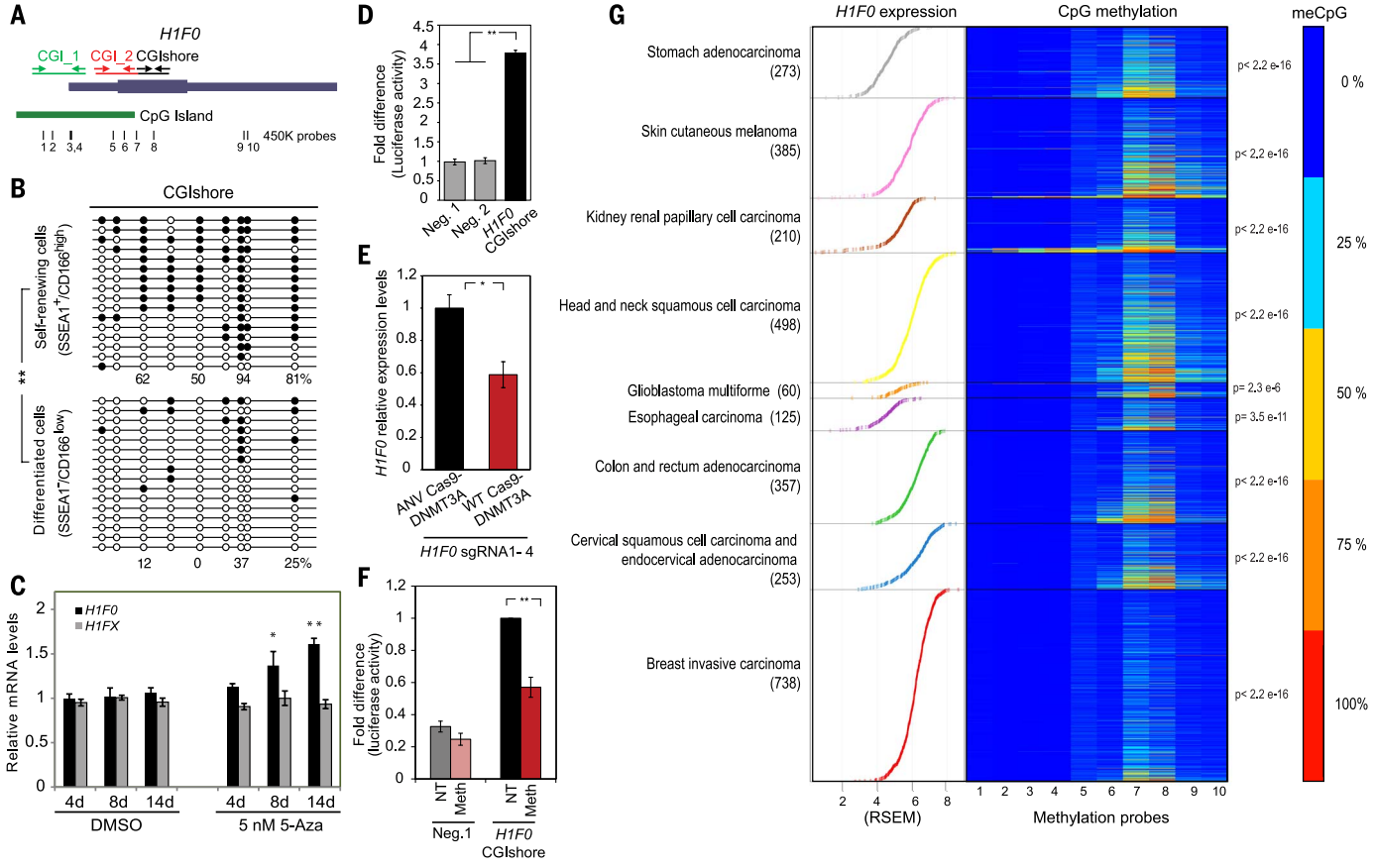

Fig. 2. Dynamic methylation of an enhancer element regulates *H1F0* expression in cancer. (**A**) Representation of the *H1F0* regions probed by bisulfite sequencing analysis (arrows indicate PCR-amplified regions) and 450 K Infinium arrays. (**B**) Bisulfite sequencing analysis comparing the *H1F0* CGI shore methylation status in the indicated subsets of sorted tumor cells. Lines represent individual sequenced molecules. White and black circles represent unmethylated and methylated CpGs, respectively. The percentage of methylation of selected CpGs is indicated. $^{**}P < 0.001$ [two-way analysis of variance (ANOVA)]. (**C**) qRT-PCR of SSEA1$^+$ tumor cells treated with 5-Aza-2′-deoxycytidine (5-Aza) or with dimethyl sulfoxide (DMSO) as a control. Values represent average ± SEM from three technical replicates. Two independent experiments gave similar results. $^*P < 0.05$ $^{**}P < 0.01$, compared with DMSO (one-way ANOVA and Tukey Kramer test). (**D**) Luciferase reporter assay. Normalized luciferase activity comparing the transactivation potential of two negative control DNA fragments (Neg. 1 and 2) (*21*, *43*) and the *H1F0* CGI shore. Values are average ± SEM from three experiments. $^{**}P < 0.01$ (Student's *t* test). (**E**) qRT-PCR comparing *H1F0* expression levels in cells expressing *H1F0*-targeting sgRNAs and Cas9 fused to either wild-type (WT) or a catalytically dead (ANV) DNMT3A. Values are average ± SEM from three biological replicates. $^*P < 0.05$ (Student's *t* test). (**F**) Normalized luciferase activity comparing the transactivation potential of untreated (NT) or in vitro methylated (Meth) *H1F0* CGI shore and a negative control fragment (Neg. 1). Values are average ± SEM from five biological replicates. $^{**}P < 0.01$ (Student's *t* test). (**G**) Analysis of *H1F0* methylation in TCGA samples. Patients are sorted based on *H1F0* expression levels (RSEM), and the corresponding DNA methylation levels are visualized as a heat map. Each row corresponds to a patient, and the number of patients for each cohort is indicated. *P* values of the Spearman's rank correlation between *H1F0* mRNA levels and methylation of CpG 7 and 8 are indicated (see fig. S6). Expression levels are normalized across tissues.

Downloaded from http://science.sciencemag.org/ on October 7, 2016

I and K). As a control, H1.4 was not affected in BRCA samples (fig. S3D). Similarly, analysis of samples from patients affected by stomach, prostate, uterus, and ovary cancer revealed heterogeneous H1.0 levels in tumor sections, whereas homogeneous high levels were detected in the corresponding normal tissues (fig. S4A). A panel of 20 cell lines from 10 cancer types also showed overall reduced levels of H1.0 (fig. S4, B and C). In culture, H1.0 levels were sensitive to extracellular signaling, as assessed by treatment of cells with various ligands previously implicated in mediating interactions between cancer cells and the tumor microenvironment. Out of 16 proteins tested, including cytokines, activators or inhibitors of stem cell–related pathways, and growth factors, 9 increased H1.0 levels whereas 2 further lowered them ($P < 0.05$) (fig. S4D). This observation suggests that heterogeneous H1.0 expression patterns within tumors may be the result of differential exposure of cancer cells to extracellular cues.

Taken together, these results indicate that several cancer types exhibit highly heterogeneous expression patterns of H1.0 within individual tumors and that cells characterized by an undifferentiated phenotype and expressing functionally validated CSC markers contain particularly low levels of H1.0.

Dynamic H1F0 methylation in tumors

Aberrant DNA-methylation patterns contribute to gene down-regulation in cancer (*8*). *H1F0* is unmethylated and highly expressed in most adult tissues (figs. S3, A and D, and S4A) (*17*) (Fig. 2A and fig. S5A). To assess whether DNA methylation affects *H1F0* levels within tumors, we performed bisulfite sequencing analysis of the *H1F0* locus, comparing self-renewing SSEA1$^+$ cells with the most differentiated tumor cells, characterized by the absence of SSEA1 and reduced levels of the surface antigen CD166 (SSEA1$^-$/CD166^{low}) (*15*) (see Fig. 3D). We examined a region spanning ~1.1 Kb around the transcriptional start site (TSS) (from −263 to +858), including a CpG island (CGI) (Fig. 2A). The CGI in the *H1F0* promoter was not methylated in either subset (fig. S5B), but a differentially methylated region was identified in the adjacent CGI shore (*20*) (Fig. 2A). SSEA1$^+$/CD166^{high} cells showed considerable methylation in multiple consecutive CpGs (26 to 94%; average, 50%), whereas significantly reduced methylation (0 to 37%; average, 18%) was detected in differentiated SSEA1$^-$/CD166^{low} cells (P <0.001) (Fig. 2B). Treatment of isolated SSEA1$^+$ tumor cells with the DNA methyltransferase inhibitor 5-Aza-2′-deoxycytidine resulted in demethylation of the CGI shore and a progressive increase of *H1F0* mRNA with similar kinetics, whereas *H1FX*, as a control, remained constant (Fig. 2C and fig. S5, C and D; also see methods). Chromatin immunoprecipitation (ChIP) revealed high levels of H3K27ac in the CGI shore, suggesting the presence of an enhancer element (*21*) (fig. S5, E and F). In agreement, the *H1F0* CGI shore showed transactivating potential in reporter assays (Fig. 2D), and its deletion by clustered regularly interspaced short palindromic repeats (CRISPR)–Cas9–mediated genome editing resulted in decreased levels of endogenous *H1F0* mRNA (fig. S5, G and H). Furthermore, targeted methylation of the enhancer region by CRISPR-Cas9-DNMT3A (*22*) (~65% methylation) induced a ~45% reduction in *H1F0* mRNA levels (Fig. 2E and fig. S5I), and in vitro–methylated reporter constructs showed a similar reduction in luciferase assays (Fig. 2F and fig. S5J). We conclude that differential methylation of an enhancer controlling *H1F0* expression induces *H1F0* silencing in self-renewing tumor cells.

We then analyzed expression and methylation data sets from various cancer types generated by TCGA. For each cancer type, correlation between *H1F0* mRNA levels measured by RNA-seq and *H1F0* methylation assessed by 450 K Infinium microarrays was examined. Similar to what we observed in tumors induced by in vitro–transformed cells, the *H1F0* promoter (450 K probes 1 to 4) was not methylated in most patients (Fig. 2, A and G, and fig. S6), whereas a downstream region centered on the CGI shore (450 K probes 5 to 10) showed variable degrees of methylation, which inversely correlated with *H1F0* mRNA levels (Fig. 2, A and G, and fig. S6). Out of the 27 analyzed types of cancer, 26 showed a significant inverse correlation between *H1F0* mRNA levels and DNA methylation (*P*-value range: $P < 2.2 \times 10^{-16}$ to $P = 0.009$) (Fig. 2G and fig. S6). Remarkably, the location of the methylated region within *H1F0* was the same in all cancers, with the CGI shore (probes 7 and 8) showing the highest correlation with expression levels. In several cohorts, patients characterized by high *H1F0* methylation showed a significantly higher proportion of aggressive tumors, such as triple-negative breast cancers and high-grade glioma, kidney cancer, and stomach adenocarcinoma (*P*-value range: $P < 0.0001$ to $P = 0.016$) (table S1). Bisulfite sequencing analysis of multiple cell lines from various cancer types confirmed methylation of the *H1F0* CGI shore in clinically derived samples expressing low H1.0 levels (figs. S5K and S4, B and C). We conclude that methylation of the *H1F0* CGI shore is associated with silencing of *H1F0* in a large variety of cancers.

Chromatin-mediated inhibition of cancer cell self-renewal

To investigate whether changes in H1.0 levels play a functional role in generating functional heterogeneity within tumors, we assessed whether restoring high levels of H1.0 in self-renewing SSEA1$^+$ cells during tumor growth or, conversely, inhibiting reexpression of the protein in their differentiated progeny affects tumor organization and cancer cell long-term proliferative potential. To do so, we introduced into in vitro–transformed cells lentiviral constructs expressing either H1.0 cDNA or short-hairpin RNAs (shRNAs) targeting *H1F0* (shH1.0) under a doxycycline (Dox)–inducible promoter. Induction of H1.0 cDNA in vitro resulted in a ~4-fold increase in *H1F0* mRNA (fig. S7A), whereas expression of two distinct shRNAs reduced mRNA levels by ~80% (fig. S7, B to E), leaving other H1 variants unaffected (fig. S7, F and G). Cell lines expressing H1.4 cDNA or an H1.4-targeting shRNA were also generated as controls (fig. S7, A and B). Neither forced expression nor knockdown of H1.0 or H1.4 affected cell viability, but cells expressing exogenous H1.0 showed decreased proliferation rates in vitro (fig. S8, A and B). Although the overall population of H1.0-expressing cells did not undergo immediate cell-cycle arrest and most cells were positive for the proliferation marker Ki67 early upon H1.0 expression, the fraction of Ki67-negative cells increased over time ($P = 0.014$) (fig. S8, C and D), similarly to what is observed upon cell differentiation (*23*, *24*), suggesting that constitutive expression of H1.0 impairs cell long-term proliferative potential. In agreement, cells expressing high levels of exogenous H1.0 were negatively selected over time in favor of those expressing lower levels (fig. S8E). Progressive negative selection of Ki67$^-$/H1.0^{high} cells over passages hindered detection of complete arrest of the whole-cell population.

To determine whether changes in H1.0 levels within established tumors affect tumor organization, cells containing, but not expressing, inducible H1.0 cDNA or H1.0-targeting shRNAs were injected into *NOD.Cg-Prkdc^{scid}Il2rg^{tm1Wjl}/SzJ* (NSG) mice to induce tumor formation. About 4 weeks after injection, when palpable tumors appear, constitutive expression or knockdown of H1.0 was induced and sustained for ~4 weeks while tumors grew (Fig. 3A). Although analysis of control tumors expressing enhanced green fluorescent protein (EGFP) showed efficient in vivo induction of the Dox-responsive construct (five out of five fluorescent tumors) (fig. S8F), when H1.0 was expressed, only 4 out of 11 induced tumors showed higher *H1F0* mRNA levels compared with the uninduced tumors (Fig. 3, B and C). This was not due to inefficient Dox delivery to the tumors, because dissociated tumor cells also failed to induce H1.0 in vitro (fig. S8, G and H), and suggested that cells expressing constitutively high levels of H1.0 were negatively selected during tumor growth, similarly to what we observed in vitro. As a control, treatment of tumors with Dox for only 3 days resulted in detectable expression of exogenous H1.0 in four out of four tumors (Fig. 3B and supplementary text). In contrast, when H1.0 knockdown was induced, no negative selection was observed and all Dox-treated tumors contained high percentages of cells expressing H1.0-targeting shRNAs (9/9) (fig. S8I). Thus, constitutively high levels of H1.0 appear to inhibit the long-term proliferative potential of cells within tumors.

To directly assess whether modulation of H1.0 levels affects tumor organization, we first measured the relative abundance of cells expressing markers of an undifferentiated (SSEA1$^+$/CD166^{high}) or a differentiated (SSEA1$^-$/CD166^{low}) phenotype (*15*) in uninduced and induced tumors (Fig. 3D). Constitutive expression of H1.0 resulted in a significant decrease in the fraction of undifferentiated tumor cells ($P = 0.039$) and a concomitant increase in differentiated cells ($P = 0.005$) in the tumors showing increased *H1F0* levels (Fig. 3E). Furthermore, the percentage of self-renewing tumor cells, as measured by clonogenic assays in vitro, was ~2-fold lower in induced tumors ($P = 0.045$) (Fig.

Downloaded from http://science.sciencemag.org/ on October 7, 2016

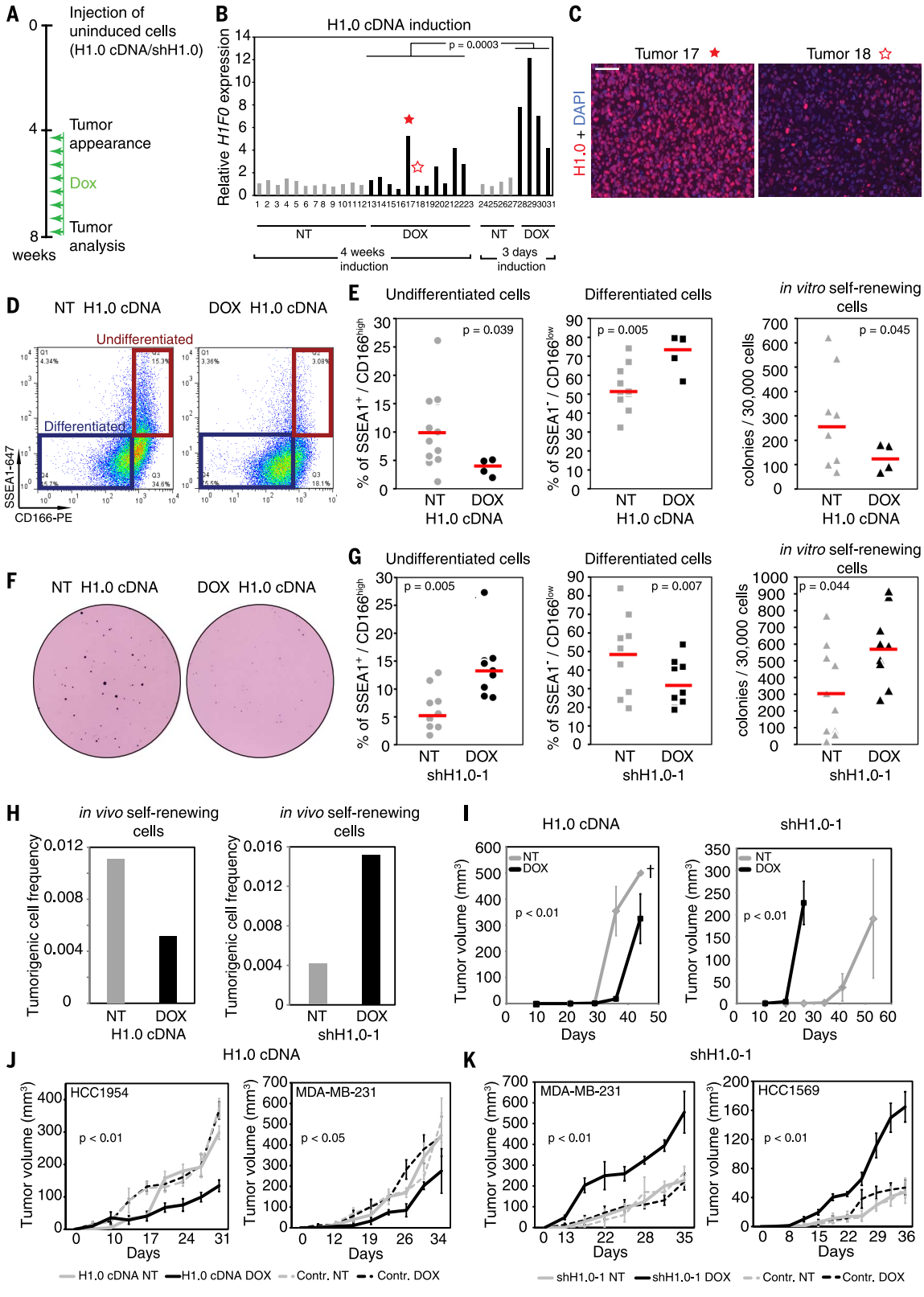

Fig. 3. H1.0 inhibits cancer cell self-renewal and drives differentiation. (**A**) Protocol used to modulate H1.0 levels in established tumors. (**B**) Quantification of in vivo induction efficiency of H1.0 cDNA by qRT-PCR. Every number indicates a tumor, either uninduced (NT) or induced (DOX) for either 4 weeks or 3 days. Tumors shown in (C) are marked by stars. *P* value from Student's *t* test (**C**). Immunodetection of H1.0 in the indicated tumors analyzed by qRT-PCR in (B) (stars). Scale bar, 50 μm. (**D**) Flow cytometry analysis of one uninduced and one induced tumor generated by cells containing Dox-responsive H1.0 cDNA constructs. The gates used to measure the fraction of undifferentiated (SSEA1^{+}/CD166^{high}) or differentiated (SSEA1^{-}/CD166^{low}) cells are indicated. (**E** and **G**) Quantification of the indicated subsets of cells by fluorescence-activated cell sorting (undifferentiated and differentiated cells) or by soft agar assay (in vitro self-renewing cells) in tumors generated by cells containing the indicated constructs. Red line, mean value. *P* value from Student's *t* test. (**F**) Representative images of clonogenic soft agar assay. (**H**) Limiting dilution transplantation assay for secondary tumor formation using cells from uninduced or induced primary tumors containing the indicated constructs. See also table S2 and supplementary text. (**I**) Growth of secondary tumors induced by 5000 cells from uninduced or induced primary tumors containing the indicated constructs. Tumor volume values represent mean ± SEM from four tumors each. The value indicated by a dagger corresponds to two tumors, due to earlier culling of other animals bearing large tumors. *P* value from Student's *t* test based on the last time point. (**J** and **K**) Growth of secondary tumors induced by 1 million (K) or 2 million (J) cells from the indicated breast cancer cell lines containing the indicated constructs. Tumor volume values represent mean ± SEM from five tumors. Significance of the differences between uninduced and induced H1.0 cDNA or shH1.0 at the last time point is indicated (Student's *t* test). Differences between induced and uninduced control tumors (contr.), which express TurboRFP and the mir30 cassette from empty pTRIPZ, are not significant.

Downloaded from http://science.sciencemag.org/ on October 7, 2016

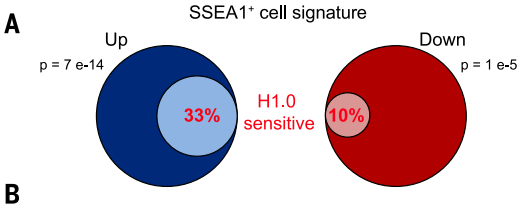

B

ENRICHED GENE SIGNATURES (Upregulated Genes)	SIZE	shH1.0 -1			shH1.0 -2		
		NES	NOM p-val	FDR q-val	NES	NOM p-val	FDR q-val
RPS14_DN.V1_UP	178	1.90	0.000	0.002	1.90	0.000	0.000
PIGF_UP.V1_UP	171	1.87	0.000	0.001	1.87	0.000	0.000
KRAS.KIDNEY_UP.V1_UP	129	1.76	0.000	0.002	1.76	0.000	0.002
PRC2_EZH2_UP.V1_DN	177	1.66	0.000	0.004	1.63	0.000	0.007
KRAS.600_UP.V1_UP	254	1.65	0.000	0.004	1.65	0.000	0.006
EGFR_UP.V1_UP	177	1.63	0.000	0.005	1.60	0.000	0.006
KRAS.300_UP.V1_UP	132	1.62	0.000	0.006	1.65	0.000	0.006
PRC2_EDD_UP.V1_DN	170	1.62	0.000	0.005	1.63	0.000	0.007
SIRNA_EIF4GI_DN	85	1.61	0.000	0.005	1.61	0.000	0.006
MEL18_DN.V1_DN	137	1.59	0.000	0.006	1.62	0.003	0.006
KRAS.LUNG.BREAST_UP.V1_UP	134	1.58	0.000	0.007	1.56	0.000	0.008
RAF_UP.V1_UP	176	1.55	0.000	0.009	1.52	0.000	0.012
BCAT_GDS748_UP	48	1.54	0.008	0.010	1.59	0.010	0.007
KRAS.LUNG_UP.V1_UP	128	1.51	0.003	0.012	1.50	0.000	0.014
PTEN_DN.V2_UP	129	1.50	0.000	0.014	1.50	0.003	0.014
KRAS.600.LUNG.BREAST_UP.V1_UP	258	1.50	0.000	0.013	1.52	0.000	0.011
KRAS.BREAST_UP.V1_UP	130	1.50	0.003	0.013	1.48	0.000	0.015
BMI1_DN.V1_DN	132	1.42	0.003	0.026	1.40	0.011	0.028
KRAS.50_UP.V1_UP	45	1.40	0.048	0.028	1.39	0.043	0.030
TBK1.DF_UP	269	1.40	0.000	0.028	1.41	0.000	0.027
KRAS.DF.V1_UP	174	1.39	0.003	0.029	1.39	0.003	0.030
BMI1_DN_MEL18_DN.V1_DN	134	1.37	0.009	0.036	1.37	0.009	0.037
BCAT.100_UP.V1_UP	45	1.33	0.067	0.050	1.32	0.063	0.052
PRC2_SUZ12_UP.V1_DN	166	1.33	0.010	0.049	1.33	0.018	0.052
NOTCH_DN.V1_DN	171	1.23	0.059	0.107	1.24	0.020	0.095
PTEN_DN.V1_UP	171	1.21	0.056	0.121	1.21	0.043	0.121

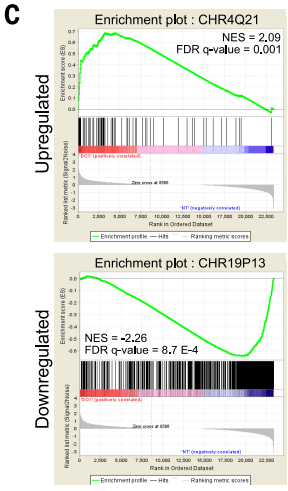

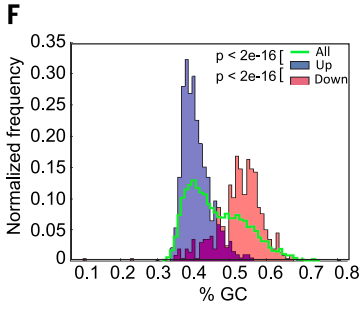

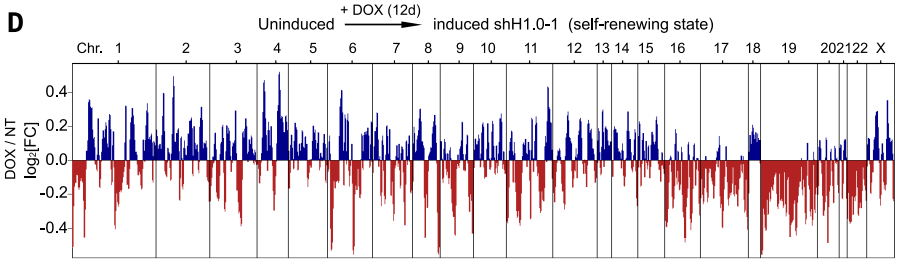

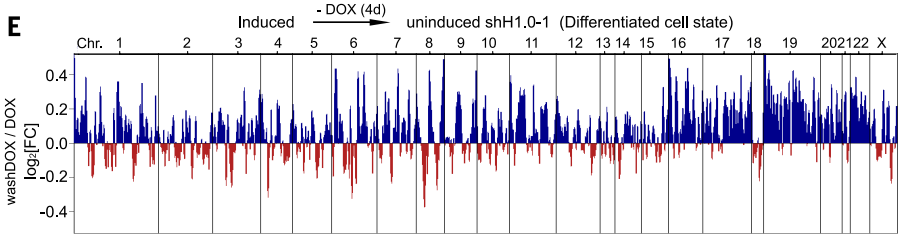

Fig. 4. Activation of transcriptional programs supporting oncogenic self-renewal via up-regulation of large gene domains. (**A**) Venn diagrams showing the percentage of genes up-regulated (Up) or down-regulated (Down) in SSEA1$^+$ cells compared with SSEA1$^-$ cells that are affected by H1.0 knockdown (see also table S4). The significance of the overlap is indicated (hypergeometric test). (**B**) Oncogenic gene signatures positively correlating with DOX samples. NES, normalized enrichment score; NOM *P*-val, nominal *P* value. Blue, stem cell–related gene signatures. (**C**) GSEA plots of positional gene sets positively (CHR4Q21) or negatively (CHR19P13) correlating with DOX samples. (**D** and **E**) Smoothed $\log_2$ fold change of gene expression between DOX and NT (D) or washDOX and DOX samples (E) (shH1.0-1) along the human genome. Similar plots were obtained with shH1.0-2. Numbers indicate the chromosomes delimited with vertical lines. Only expressed genes (TPM > 0) are plotted. Blue, up-regulated domains; red, down-regulated domains. (**F**) Distribution of GC content in RefSeq genes (all) and in the subsets of up-regulated (Up) or down-regulated (Down) DEGs. *P* value from Student's *t* test.

3, E and F). As a control, expression of H1.4 had no significant effect on tumor organization (fig. S9A). Conversely, when knockdown of H1.0 was induced to prevent its accumulation in differentiated cells, the percentage of undifferentiated tumor cells significantly increased (P = 0.005), the fraction of differentiated cells decreased (P = 0.007), and tumors contained ~2-fold more self-renewing cells (P = 0.044) (Fig. 3G fig. S9D, and supplementary text). In agreement, tumors expressing constitutive H1.0 showed a lower fraction of mitotic cells, whereas tumors in which H1.0 had been knocked down had a higher mitotic index (fig. S9, B and C). Limiting dilution transplantation assays for secondary tumor formation confirmed the altered self-renewal ability of cancer cells in vivo, showing a lower frequency of tumorigenic cells in primary tumors constitutively expressing H1.0 and a higher frequency in tumors where H1.0 had been knocked down (Fig. 3H, supplementary text, and table S2). In line with the notion that even moderate changes in the fraction of self-renewing cancer cells strongly affect long-term tumor growth (*18*, *25*, *26*) (supplementary text), transplantation of cells from primary tumors constitutively expressing H1.0 resulted in significantly delayed appearance of secondary tumors compared with control tumors (P < 0.01), whereas faster growth was observed upon transplantation of shH1.0-expressing cells (P < 0.01) (Fig. 3I). Orthotropic transplantation assays using multiple breast cancer cell lines confirmed these results. Forced expression of H1.0 cDNA in MDA-MB-231 or HCC1954 cells specifically impaired tumor growth, whereas knockdown of the endogenous protein in MDA-MB-231 or HCC-1569 cells resulted in more aggressive tumors (Fig. 3, J and K). Furthermore, analysis of Dox-induced tumors showed partial negative selection of H10^{high} cells, confirming the negative impact of H1.0 on cell long-term proliferative potential (fig. S8, J and K). We conclude that H1.0 silencing is required for the ability of cancer cells to self-renew and that its reexpression in subsets of cells during tumor growth contributes to driving their differentiation and restricting their proliferative potential.

Derepression of adenine-thymine (AT)–rich genes sustains cancer cell self-renewal

To understand how H1.0 affects cancer cell self-renewal, we employed two inducible shRNAs to knock down H1.0 in transformed cultured cells and compared the transcriptional profiles of three cellular states by RNA-seq: uninduced cells expressing H1.0 (NT); cells induced with Dox for 14 days, which down-regulated H1.0 similarly to self-renewing SSEA1$^+$ tumor cells (DOX); and cells washed out of Dox for 4 days, which began to reexpress H1.0 and mimicked differentiated SSEA1$^-$ tumor cells (washDOX). Comparison between NT and DOX samples detected 860 differentially expressed genes (DEGs) [false discovery rate (FDR) < 0.05] upon H1.0 knockdown by both shRNAs (475 up-regulated and 385 down-regulated) (table S3 and fig. S10, A to C). The extent of gene expression changes was moderate, with only 25 genes

Downloaded from http://science.sciencemag.org/ on October 7, 2016

showing >2-fold changes (table S3), but differences were highly consistent and reversible upon H1.0 reexpression (fig. S10, C and D). Quantitative reverse transcription polymerase chain reaction (qRT-PCR) analysis confirmed differential expression of genes detected by RNA-seq and showed that H1.0-sensitive genes did not respond to H1.4 knockdown (fig. S10E).

To identify H1.0-sensitive genes important for cancer cell self-renewal, we compared the identified DEGs with a gene signature (132 genes) defined by comparing self-renewing SSEA1$^+$ and differentiated SSEA1$^-$ cells from multiple tumors (table S4) (*15*). About 30% of genes expressed at higher levels in SSEA1$^+$ cells underwent up-regulation upon H1.0 knockdown ($P < 10 \times 10^{-14}$), whereas 10% of genes down-regulated in SSEA1$^+$ cells showed lower levels in cells lacking H1.0 ($P = 1.5 \times 10^{-5}$), indicating that a significant fraction of genes defining the subset of self-renewing tumor cells, particularly those up-regulated, are regulated by H1.0 (Fig. 4A). Gene set enrichment analysis (GSEA) confirmed that genes up-regulated upon H1.0 knockdown were particularly relevant for cancer cell self-renewal ability (Fig. 4B). Several oncogenic gene signatures were enriched in the subset of up-regulated genes, including signatures related to the activation of the oncoproteins KRAS, EGFR, and RAF1 or to the inactivation of the tumor suppressor PTEN (Fig. 4B). Furthermore, gene signatures important for stem cell maintenance, such as those related to the Polycomb complex components EZH2, EED, BMI1, and SUZ12 (*27*), were also enriched among up-regulated genes (Fig. 4B). Based on GSEA, down-regulated genes did not seem to substantially contribute to the self-renewing phenotype. Thus, loss of H1.0 results in activation of downstream effectors of multiple oncogenic and self-renewal cellular pathways. Interestingly, these genes are not randomly distributed in the genome but are enriched in AT-rich regions (fig. S11A).

GSEA also revealed linear proximity of H1.0-sensitive genes along chromosomes. Of 296 positional gene sets, corresponding to genes located in individual chromosomal cytogenetic subbands, 75 were enriched in DOX samples, using either H1.0-targeting shRNA, indicating overall up-regulation of genes located in those bands upon H1.0 knockdown. Conversely, 37 bands negatively correlated with the DOX samples, indicating overall gene down-regulation (Fig. 4C; fig. S11, B and C; and table S5). In agreement, analysis of the distribution of gene expression fold changes between NT and DOX samples (see methods) showed that domains

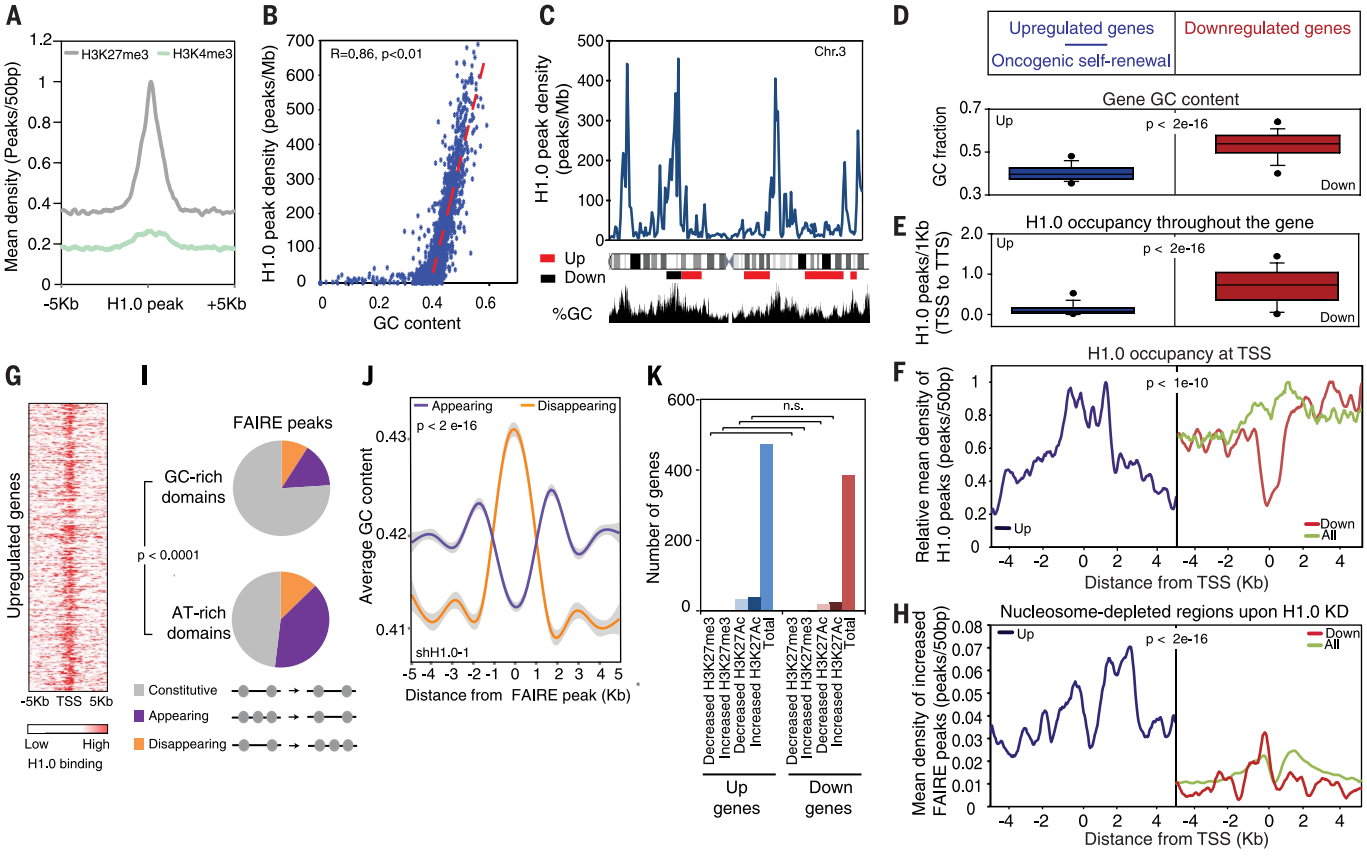

Fig. 5. Destabilization of nucleosome-DNA interactions in AT-rich regions in the absence of H1.0. (**A**) Average peak density profiles of H3K4me3 and H3K27me3 centered on H1.0 binding sites. (**B**) Correlation between H1.0 peak density and DNA GC content. The best-fit line of the experimental values for GC content > 0.4, the correlation coefficient *R*, and statistical accuracy of the fit are indicated. (**C**) H1.0 peak density along chromosome 3. The approximate location of cytogenetic bands, up-regulated (Up) or down-regulated (Down) positional gene sets identified by GSEA, and the corresponding DNA GC content are shown. (**D** to **F** and **H**) Comparison between genes up-regulated (Up) or down-regulated (Down) in response to H1.0 knockdown, with respect to the indicated features. Smoothed average density profile of H1.0 peaks (F) and FAIRE peaks (H) show enrichment of H1.0 and increased FAIRE signal (decreased nucleosome occupancy) upon H1.0 knockdown around the TSS of up-regulated genes. RefSeq genes (All) are shown as reference. *P* value from paired *t* test, with Benjamini-Hochberg adjustment for (F) and (H). (**G**) Heat map showing tag density of H1.0 ChIP-seq around the TSS of genes up-regulated upon H1.0 knockdown. Each line represents a gene. (**I**) Relative abundance of the indicated types of FAIRE peaks in GC-rich and AT-rich domains. Nucleosome occupancy corresponding to the different types of FAIRE peaks is schematized next to the legend. Black line, DNA; gray circles, nucleosomes. Results from shH1.0-1 are shown. Similar results were obtained with shH1.0-2. *P* value from Fisher's exact test for constitutive peaks. (**J**) Average DNA GC content centered on FAIRE peaks that appear or disappear upon H1.0 knockdown. See also fig. S14D. *P* value from paired *t* test with Benjamini-Hochberg adjustment. Gray area, 95% confidence interval of the best fit after smoothing. (**K**) Number of up-regulated or down-regulated H1.0-sensitive genes showing altered acetylated or methylated H3K27 at TSS upon H1.0 knockdown. Differences are not significant (n.s., Fisher's exact test).

Downloaded from http://science.sciencemag.org/ on October 7, 2016

of up-regulated genes alternated with down-regulated regions along chromosomes (Fig. 4D). The differentially expressed domains contained up to 365 genes over several megabases (average genes per domain = 30) (fig. S11E). A similar profile was observed 24 hours after Dox induction, when H1.0 levels began to decrease, indicating that transcriptional changes occur rapidly upon H1.0 loss (fig. S11, F and G). Reexpression of H1.0 in washDOX samples, mimicking what happens in differentiated tumor cells, restored transcriptional profiles similar to those detected in uninduced NT samples (Fig. 4E and fig. S11, F and G), indicating that gene expression changes induced by H1.0 silencing are reversible.

Up-regulated domains were enriched in AT-rich chromosomes, such as chromosome 4 (chr.4), chr.5, and chr.18 [average guanine-cytosine (GC) content <0.40], whereas down-regulated domains mainly localized in GC-rich chromosomes such as chr.17, chr.19, and chr.22 (average GC content >0.45) (*28*) (Fig. 4D). In agreement, individual up-regulated genes had significantly lower GC content compared with all Reference Sequence (RefSeq) genes (median %GC: 0.40 versus 0.45, $P < 10 \times 10^{-16}$) or down-regulated genes (median %GC: 0.40 versus 0.53, $P < 10 \times 10^{-16}$) (Fig. 4F), even though the two groups of H1.0-sensitive genes contained a similar proportion of CGI-containing genes (fig. S11D). We conclude that cells lacking H1.0 undergo genome-wide changes in gene expression, affecting large gene domains in a coordinated manner. In particular, up-regulation of sets of neighboring AT-rich genes mediating oncogenic cellular responses and stem cell maintenance contributes to the activation and maintenance of transcriptional programs that support uncontrolled self-renewal. These effects are reversible, and reexpression of H1.0 reestablishes gene expression profiles that restrict cell tumorigenic potential.

Destabilized nucleosome-DNA interactions in self-renewing cancer cells

To map genomic regions bound by H1.0 before its down-regulation in self-renewing tumor cells, we performed ChIP-seq analysis of transformed cultured cells. About 120,000 H1.0 peaks were consistently detected in two biological replicates (fig. S12, A to C, and table S6), using an H1.0-specific antibody (fig. S7, C to E). ChIP-qPCR confirmed accurate detection of H1.0 peaks (fig. S12E). H1.0 binding sites positively correlated with the histone mark H3K27me3 (Fig. 5A and fig. S12, B and D). No significant correlation was observed between H1.0 binding profiles and maps of topological associating domains (TADs) (*29*) (fig. S12D). H1.0 binding sites were enriched in GC-rich chromosomes and at GC-rich genes (fig. S12, F and G), and H1.0 peak density showed a tight linear relationship with GC content in regions with >40% GC ($R = 0.86$) (Fig. 5B), indicating that GC content is a major determinant of H1.0 binding sites. Megabase-scale density plots of H1.0 binding sites along chromosomes allowed visualization of the correlation between H1.0 occupancy, GC content, and cytogenetic bands (Fig. 5C and fig. S13A). In line with the notion that nucleosomes are overall enriched in GC-rich genomic regions, H1.0 occupancy also correlated with nucleosome density (*30*, *31*) (fig. S12H). We conclude that large-scale H1.0 binding profiles are mainly determined by DNA sequence, which affects the broad distribution of nucleosomes. Of note, AT-rich regions characterized by low H1.0 peak density contain the self-renewal–related genes up-regulated upon H1.0 knockdown (Fig. 5C and fig. S13A).

To gain insights into how H1.0 loss results in up-regulation of AT-rich self-renewal–related genes, we examined H1.0 occupancy around their TSSs. Although up-regulated genes were bound by H1.0 at overall low density (Fig. 5, D and E), similar to the pattern observed at other AT-rich regions, H1.0 binding sites were highly enriched around the TSS (Fig. 5, F and G and fig. S12, J to L). In contrast, all RefSeq genes and genes down-regulated upon H1.0 knockdown showed an average depletion of H1.0 binding sites around the TSS (Fig. 5F and fig. S12, J to L). Similar patterns, with enhanced differences, were observed when analyzing the positional gene sets identified as up-regulated by GSEA (fig. S13, B to D). Together with the notion that AT-rich regions may be thermodynamically unstable when wrapped around nucleosomes (*32*, *33*), this observation suggests that H1.0 may repress the AT-rich, self-renewal–related genes by stabilizing nucleosomes at their promoters. To test this possibility, we assessed changes in genome-wide nucleosome occupancy induced by H1.0 loss by formaldehyde-assisted isolation of regulatory elements-sequencing (FAIRE-seq) (*34*), which allows detection of nucleosome-depleted regions irrespectively of DNA GC content (*35*, *36*) (fig. S14A). Up-regulated genes specifically showed increased FAIRE signal around the TSS upon H1.0 knockdown using two independent H1.0-targeting shRNAs, indicating decreased nucleosome occupancy (Fig. 5H and figs. S13E and S14, B and C). Similar patterns were observed at distal regulatory regions of H1.0-sensitive genes, identified by comparing an H3K27ac map with an atlas of human enhancers (*21*) (see methods and fig. S14, F and G). As a control, knockdown of H1.4, which was depleted at H1.0-sensitive genes (fig. S12I), only induced minimal changes in promoter nucleosome occupancy (fig. S14H), which did not translate into changes in gene expression (fig. S10E). Nucleosome remodeling in the absence of H1.0 did not correlate with increased occupancy of other nucleosome-binding architectural proteins, such as HMGA1, HMGN2, and PARP1 (fig. S15).

In agreement with H1.0 distribution, genome-wide analysis of differential FAIRE peaks indicated that altered nucleosome occupancy in the absence of H1.0 depends on GC content, both at a global and local scale. In GC-rich domains [average GC content per 500 base pairs (bp) >0.45], most detected nucleosome-depleted regions were stable and unaffected by H1.0 knockdown (constitutive FAIRE peaks, table S6), and only ~25% either appeared or disappeared as a consequence of altered nucleosome occupancy (Fig. 5I). In contrast, in AT-rich domains (average GC content per 500 bp <0.45), ~50% of detected nucleosome-depleted regions showed altered nucleosome occupancy, indicating that nucleosome-DNA interactions in AT-rich regions become particularly unstable in the absence of H1.0 (Fig. 5I). Furthermore, nucleosome-depleted regions appeared in DNA regions with local minimal GC content, whereas they disappeared from regions of local maximal GC content, suggesting that nucleosomes forced to occupy regions with higher AT content, in the absence of H1.0 moved to locations with higher GC content (Fig. 5J and fig. S14D).

Mapping of H3K27ac and H3K27me3 by ChIP-seq indicated that altered nucleosome occupancy induced by H1.0 loss was uncoupled from changes in histone modifications. Most appearing or disappearing FAIRE peaks were located within non-acetylated chromatin (fig. S14E), suggesting that alterations in nucleosome occupancy were not a consequence of transcription. Furthermore, up-regulated self-renewal–related genes did not show significant differences in H3K27ac and H3K27me3 at their promoters upon H1.0 knockdown compared with down-regulated genes ($P > 0.05$) (Fig. 5K), indicating that changes in gene expression were a direct consequence of altered nucleosome occupancy. Taken together, these results suggest that loss of H1.0 destabilizes nucleosome-DNA interactions in AT-rich genomic regions and increases accessibility to regulatory elements important for cellular self-renewal.

Low *H1F0* levels predict negative patient outcome in multiple cancer types

To assess the clinical relevance of H1.0 alterations, we examined whether *H1F0* levels stratify cancer patients. Kaplan-Meier and multivariate analysis of three GBM data sets showed a significant correlation between low *H1F0* levels and negative patient outcome ($P < 0.05$) (Fig. 6A and fig. S16C), revealing a prognostic value for *H1F0*. Low *H1F0* levels also predicted poor patient prognosis in three BRCA data sets (Fig. 6B). Importantly, *H1F0* correlated with BRCA patient survival independently of estrogen receptor (ER), progesterone receptor (PR), erb-b2 receptor tyrosine kinase 2 (Her2) and lymph node status and effectively stratified patients typically associated with negative outcome (ER- or PR-negative and lymph node–positive patients) ($P < 0.05$) (fig. S16, A and C). Furthermore, *H1F0* expression showed no significant association with breast cancer subtype, which strongly affects patient outcome (fig. S16B). Analysis of 17 other types of cancers using TCGA data sets showed a significant correlation between low *H1F0* levels and poor patient prognosis also in melanoma (SKMC), liver cancer (LIHC), kidney cancer (KIRP), and low-grade glioma (LGG), independently of other clinically relevant features (Fig. 6C and fig. S16C). As controls, other H1 variants either did not stratify patients or correlated with patient survival in an opposite manner compared with *H1F0* (fig. S17). Thus, alterations in H1.0 levels are clinically relevant in multiple cancer types.

Discussion

Heterogeneity among cancer cells within individual tumors has emerged as a general feature of cancer,

Downloaded from http://science.sciencemag.org/ on October 7, 2016

with critical implications for cancer diagnosis and treatment (*4*, *9*). Increasing evidence points to the existence of both genetic and nongenetic sources of intratumor heterogeneity (*4*, *5*, *14*, *37*, *38*), but the molecular features underlying functionally diverse cellular phenotypes have been elusive. Cell-to-cell signaling pathways, such as Wnt, Tgfβ, and Notch pathways, have been shown to play critical roles in driving functional heterogeneity within tumors (*38*), but very little is known about the downstream, cell-intrinsic mechanisms that translate signaling into differential cell function. Here, we show that distinct epigenetic states, determined by an integral component of chromatin, define cellular subpopulations that differentially contribute to tumor maintenance. The observation that experimental modulation of epigenetic states affects the balance between self-renewing and differentiated cancer cells demonstrates that chromatin-based mechanisms mediating differentiation programs play a key role in specifying tumor organization and affecting tumor maintenance. In line with the notion that epigenetic mechanisms acting during tumor growth may be dominant over genetic alterations that initiate the disease (*37*, *39*), we show that subsets of cells that stably silence H1.0 preserve their ability to proliferate indefinitely, whereas cells that reexpress the protein and, as a consequence, repress oncogenic gene networks acquire a differentiated phenotype characterized by limited proliferative potential. Reversible changes in H1.0 levels may be due to interactions of cancer cells with the tumor microenvironment (*38*). In line with this notion, H1.0 expression responds to a variety of extracellular cues, many of which are associated with cellular differentiation (*40*, *41*) (fig. S4D). It is likely that, at least in the early stages of tumor development, cancer cells may be exposed to differentiation stimuli that support normal tissue homeostasis, and subsets of cells may respond to such stimuli, changing their epigenetic landscape, partly through H1.0 and losing self-renewal potential. Thus, H1.0 may act as a downstream effector of extracellular signaling inhibiting cancer cell self-renewal.

Our results suggest that numerous cancer types may share similar epigenetic heterogeneity. Numerous solid tumors show heterogeneity of H1.0, and a regulatory region within the *H1F0* gene shows variable degrees of DNA methylation in 26 types of cancers, correlating with *H1F0* expression levels. Furthermore, low *H1F0* levels are independent predictors of poor patient outcome in six prevalent cancer types. Importantly, the molecular mechanism through which H1.0 restricts cell proliferative potential is largely dependent on DNA sequence and GC content, suggesting that changes in H1.0 levels may have similar consequences in various cell types. We show that silencing of *H1F0* supports cancer cell self-renewal by inducing simultaneous derepression of downstream effectors of oncogenic and stem cell–related pathways located in AT-rich genomic regions. AT-rich regions are known to poorly incorporate into nucleosomes, partly because of their inherent relative rigidity and difficulty to bend around the core histone particle (*30*–*33*). Thus, it is conceivable that AT-rich regions may be particularly dependent on the linker histone to stabilize nucleosome positioning at unfavorable sequences, especially when nucleosomes are forced to occupy promoters of genes that must be repressed. Indeed, we find lower nucleosome occupancy at AT-rich gene promoters in the absence of H1.0, correlating with enhanced transcription.

In conclusion, our results uncover epigenetic determinants of tumor-maintaining cells and identify an integral component of chromatin as an important regulator of cell differentiation states within tumors. We propose that only cells insensitive to extracellular differentiation cues, capable of permanently silencing H1.0, can act as self-renewing tumor-maintaining cells and that such a mechanism supports maintenance of several types of cancer. Our results suggest that intervention aimed at restoring high levels of H1.0 in all cancer cells may enhance the differentiation process that naturally occurs during tumor growth and may be beneficial for therapeutic purposes.

Materials and methods summary

Cell lines and constructs

Growth conditions of all cell lines used in the study are listed in table S7. Inducible cell lines were generated by introducing lentiviral constructs (original or modified pTRIPZ, Open Biosystems) expressing specific cDNAs or shRNAs, or control

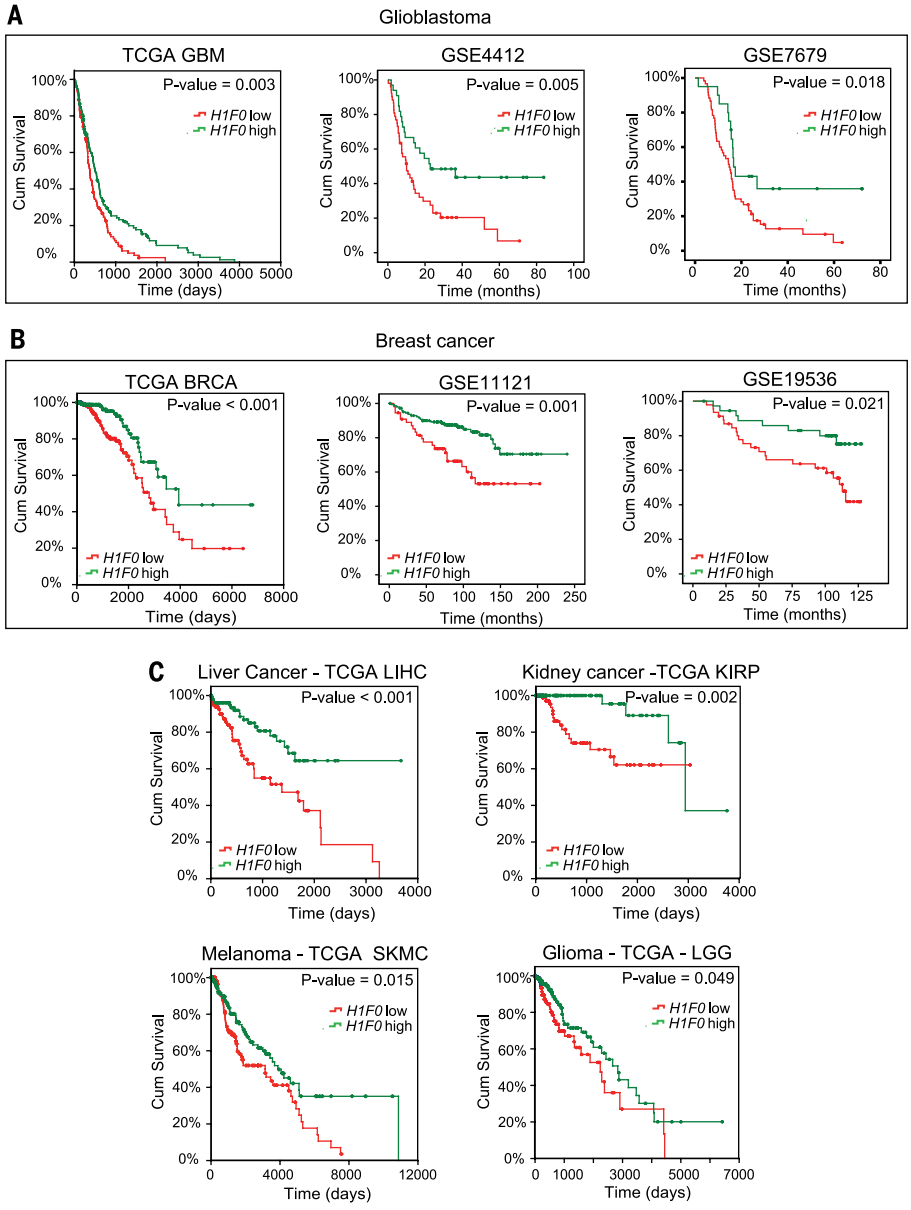

Fig. 6. Low *H1F0* levels correlate with low patient survival in multiple cancer types. (**A** to **C**) Kaplan-Meier analysis of the indicated data sets showing significant correlation between *H1F0* levels and patient survival. *P* value from log-rank test. Multivariate analysis is shown in fig. S16.

Downloaded from http://science.sciencemag.org/ on October 7, 2016

plasmids into in vitro–transformed fibroblasts (*15*) or breast cancer cells lines. All cancer cell lines were sourced from the Crick Institute common repository, authenticated by STR profiling, and tested for mycoplasma. Cell proliferation rate was measured using the 96 Aqueous One Solution kit (Promega). For details on cell lines generation, see the supplementary materials (SM).

Patient samples

Normal brain and GBM (grade 4 astrocytoma) tissue sections were obtained from the Whittington tissue bank (UCL license number: 12055, three normal and four tumors) and from US Biomax (tissue microarray GL806b). All other tissue sections were obtained from US Biomax (tissue microarrays: BR1053b, BCN962). Single-cell RNA-seq data of GMB tumors was downloaded from GEO series GSE57872 (*2*). DNA methylation and survival analysis were performed using TCGA data sets. For details on patients used in the study, see SM.

Protein immunodetection

Western blot analysis, flow cytometric analysis, cell sorting, and immunofluorescence microscopy of cultured or sorted tumor cells were performed as previously described (*15*) using anti-H1.0 (Millipore, raised in mouse, clone 3H9, 1:300, originally produced in M. Bustin's laboratory) (*42*) and other antibodies detailed in SM. Recombinant proteins were purchased from Peprotech. Quantification of the fluorescent signal was performed using Metamorph software or with HCS Studio Cell Analysis Software. For details about staining procedures, see SM.

Tumorigenicity assays

Tumor formation in NSG mice, tumor dissociation, limiting dilution transplantation assays, soft agar assays and proliferation assays were performed as previously described (*15*). For experiments requiring in vivo modulation of H1 variants in established tumors, cells infected with inducible constructs were injected intradermally into NSG mice (2000 transformed cells and 100,000 hTERT-fibroblasts as carrier cells) in the uninduced state to induce tumor formation (10 injections per condition). When tumors first became palpable, typically after 4 weeks, doxycycline treatment (2μg/ml Dox in drinking water supplemented with 1% sucrose, changed every 2 to 3 days) was started and sustained for about a month until tumors were collected and analyzed as detailed in SM. Animal studies were conducted in agreement with the approved NCI animal protocol LRBGE-007 and the Crick project license PPL 70/8167.

DNA methylation analysis

For bisulfite sequencing analysis, genomic DNA was treated for bisulfite conversion using EZ DNA Methylation-Direct Kit (Zymo research) according to the manufacturer's instructions. Three regions of *H1F0* (CGI_1, CGI_2, and CGIshore) were amplified by PCR (primer sequences in table S8) from bisulfite-treated DNA and cloned into pCR 2.1 Topo vector. 15 to 20 colonies were sequenced for each region. For 5-Aza-2′-deoxycytidine (5-Aza) treatment, SSEA1^{+} cells isolated from a tumor were treated with 5nM 5-Aza (Sigma) or DMSO as a control (Fisher Chemical) for up to 14 days. Higher concentrations of 5-Aza were toxic to the SSEA1+ cells. For analysis of TCGA samples, gene expression (Illumina HiSeq RNA-seq) and DNA methylation (Illumina 450K Infinium analysis) data sets from individual cancers downloaded from the UCSC Cancer browser https://genome-cancer.ucsc.edu were analyzed as detailed in SM.

CGI shore functional assays

Luciferase assays were performed using the Nano-Glo Dual-Luciferase reporter assay system (Promega) comparing the *H1F0* CGI shore and two previously published DNA fragments showing no transactivation potential (*21*, *43*). Deletion of the endogenous *H1F0* CGI shore was carried out by CRISPR-Cas9–mediated genome editing using two sgRNAs flanking the CGI shore (table S8). Clones with homozygous deletions of the *H1F0* CGI shore were analyzed by qRT-PCR using primers located downstream of the deletion. For heterozygous clones, allele-specific primers probing either the deleted or the full-length mRNA were used (table S8). To induce targeted methylation of the endogenous *H1F0* CGI shore, cells were transiently transfected with plasmids encoding either WT or ANV mutant Cas9-DNMT3A (*22*) and a pool of four sgRNAs targeting *H1F0* CGI shore (table S8). For details on luciferase assays and CRISPR-mediated alterations of the *H1F0* CGI shore, see SM.

RNA-seq analysis and GSEA

RNA libraries prepared using TruSeq Stranded Total RNA-Seq Library Prep (Illumina) were sequenced on a HiSEq. 2500 sequencer (table S6). Differentially expressed genes were defined as those showing statistically significant differences (FDR <0.05) using both H1.0-targeting shRNAs. Genome-wide expression plots were generated using similar methods to those described in (*44*). Deviation from random distribution was calculated on raw, unsmoothed data by performing a Monte Carlo simulation in which genes where randomly shuffled along chromosomes (1000 iterations). GSEA was performed using GSEA software (version 2.1.0, Broad Institute). FPKM values for NT and DOX samples were provided to the algorithm and tested for enrichment of oncogenic signatures from the MSigDB or custom-made positional gene sets generated based on RefSeq genes and cytogenetic sub-bands coordinates downloaded from the UCSC genome browser. For details on RNA-seq analysis, GSEA, and validation by qRT-PCR, see SM.

ChIP-seq analysis

ChIP was performed on in vitro-transformed fibroblasts using an anti-H1.0 antibody (Millipore, 05-629, originally generated in M. Bustin's laboratory) (*42*), and other antibodies detailed in SM. Multiplexed libraries were sequenced on a HiSEq. 2500 using either 50-bp single end or 101-bp paired-read runs (table S6). Peak detection for H1.0 was performed with a custom-made algorithm as detailed in SM.

FAIRE-seq analysis

Cells were processed and analyzed as previously described (*45*). FAIRE peaks were called using MACS-2.0.10 in paired-end mode using broad settings with a bandwidth of 300 bp, normalizing each sample to its own background as described (*45*). The top 100,000 peaks (based on adjusted *P* value) were selected for each replicate, and those common to both (with a 20% reciprocal overlap) were selected for downstream analysis. Differential FAIRE peaks analysis was performed using DiffReps (*46*). For details on FAIRE-seq analysis, see SM.

Survival analysis

Survival analysis was performed on all TCGA data sets containing more than 200 patients. Patients were ranked based on *H1F0* expression, and the top and bottom tertile were compared with respect to vital status by Kaplan-Meier analysis. Log-rank test was used to assess statistical significance of the differences between patient groups. Additional data sets for GBM and BRCA were analyzed as validation. Multivariate analysis and chi-square tests were performed to assess the relationship between H1.0 and other clinically relevant features. For details on the survival analysis, see SM.

Statistical analysis

Unless otherwise stated in figure legends, data are presented either as individual samples or as mean ± standard error of the mean (SEM) of multiple replicates, with *N* indicated in the figure legend. In box plots, the boundary of the box closest to zero indicates the 25th percentile, a line within the box marks the median, and the boundary of the box farthest from zero indicates the 75th percentile. Whiskers (error bars) above and below the box indicate the 95th and 5th percentiles. Outliers are plotted as dots. The statistical test used for each comparison, whether adjustment for multiple corrections was performed, and the *P* value are indicated in the corresponding figure legends.

Downloaded from http://science.sciencemag.org/ on October 7, 2016

REFERENCES AND NOTES

1. G. H. Heppner, Tumor heterogeneity. *Cancer Res.* **44**, 2259–2265 (1984). pmid: 6372991
2. A. P. Patel *et al.*, Single-cell RNA-seq highlights intratumoral heterogeneity in primary glioblastoma. *Science* **344**, 1396–1401 (2014). doi: 10.1126/science.1254257; pmid: 24925914
3. P. C. Nowell, The clonal evolution of tumor cell populations. *Science* **194**, 23–28 (1976). doi: 10.1126/science.959840; pmid: 959840
4. R. A. Burrell, N. McGranahan, J. Bartek, C. Swanton, The causes and consequences of genetic heterogeneity in cancer evolution. *Nature* **501**, 338–345 (2013). doi: 10.1038/nature12625; pmid: 24048066
5. A. Marusyk, V. Almendro, K. Polyak, Intra-tumour heterogeneity: A looking glass for cancer? *Nat. Rev. Cancer* **12**, 323–334 (2012). doi: 10.1038/nrc3261; pmid: 22513401
6. K. Illmensee, B. Mintz, Totipotency and normal differentiation of single teratocarcinoma cells cloned by injection into blastocysts. *Proc. Natl. Acad. Sci. U.S.A.* **73**, 549–553 (1976). doi: 10.1073/pnas.73.2.549; pmid: 1061157

7. F. Barabé, J. A. Kennedy, K. J. Hope, J. E. Dick, Modeling the initiation and progression of human acute leukemia in mice. *Science* **316**, 600–604 (2007). doi: 10.1126/science.1139851; pmid: 17463288
8. H. Easwaran, H. C. Tsai, S. B. Baylin, Cancer epigenetics: Tumor heterogeneity, plasticity of stem-like states, and drug resistance. *Mol. Cell* **54**, 716–727 (2014). doi: 10.1016/j.molcel.2014.05.015; pmid: 24905005
9. A. Kreso, J. E. Dick, Evolution of the cancer stem cell model. *Cell Stem Cell* **14**, 275–291 (2014). doi: 10.1016/j.stem.2014.02.006; pmid: 24607403
10. W. C. Hahn *et al*., Creation of human tumour cells with defined genetic elements. *Nature* **400**, 464–468 (1999). doi: 10.1038/22780; pmid: 10440377
11. B. Elenbaas *et al*., Human breast cancer cells generated by oncogenic transformation of primary mammary epithelial cells. *Genes Dev.* **15**, 50–65 (2001). doi: 10.1101/gad.828901; pmid: 11156605
12. J. N. Rich *et al*., A genetically tractable model of human glioma formation. *Cancer Res.* **61**, 3556–3560 (2001). pmid: 11325817
13. M. J. Son, K. Woolard, D. H. Nam, J. Lee, H. A. Fine, SSEA-1 is an enrichment marker for tumor-initiating cells in human glioblastoma. *Cell Stem Cell* **4**, 440–452 (2009). doi: 10.1016/j.stem.2009.03.003; pmid: 19427293
14. M. L. Suvà *et al*., Reconstructing and reprogramming the tumor-propagating potential of glioblastoma stem-like cells. *Cell* **157**, 580–594 (2014). doi: 10.1016/j.cell.2014.02.030; pmid: 24726434
15. P. Scaffidi, T. Misteli, In vitro generation of human cells with cancer stem cell properties. *Nat. Cell Biol.* **13**, 1051–1061 (2011). doi: 10.1038/ncb2308; pmid: 21857669
16. A. Izzo, K. Kamieniarz, R. Schneider, The histone H1 family: Specific members, specific functions? *Biol. Chem.* **389**, 333–343 (2008). doi: 10.1515/BC.2008.037; pmid: 18208346
17. D. Doenecke, A. Alonso, Organization and expression of the developmentally regulated H1(o) histone gene in vertebrates. *Int. J. Dev. Biol.* **40**, 395–401 (1996). pmid: 8735954
18. S. Pece *et al*., Biological and molecular heterogeneity of breast cancers correlates with their cancer stem cell content. *Cell* **140**, 62–73 (2010). doi: 10.1016/j.cell.2009.12.007; pmid: 20074520
19. H. R. Ali *et al*., Cancer stem cell markers in breast cancer: Pathological, clinical and prognostic significance. *BCR* **13**, R118 (2011). doi: 10.1186/bcr3061; pmid: 22112299
20. R. A. Irizarry *et al*., The human colon cancer methylome shows similar hypo- and hypermethylation at conserved tissue-specific CpG island shores. *Nat. Genet.* **41**, 178–186 (2009). doi: 10.1038/ng.298; pmid: 19151715
21. R. Andersson *et al*.FANTOM Consortium, An atlas of active enhancers across human cell types and tissues. *Nature* **507**, 455–461 (2014). doi: 10.1038/nature12787; pmid: 24670763
22. A. Vojta *et al*., Repurposing the CRISPR-Cas9 system for targeted DNA methylation. *Nucleic Acids Res.* **44**, 5615–5628 (2016). doi: 10.1093/nar/gkw159; pmid: 26969735
23. E. Järvinen, A. Angers-Loustau, A. M. Osiceanu, K. Wartiovaara, Timing of the cell cycle exit of differentiating hippocampal neural stem cells. *Int. J. Stem Cells* **3**, 46–53 (2010). doi: 10.15283/ijsc.2010.3.1.46; pmid: 24855540
24. M. Snir *et al*., Assessment of the ultrastructural and proliferative properties of human embryonic stem cell-derived cardiomyocytes. *Am. J. Physiol. Heart Circ. Physiol.* **285**, H2355–H2363 (2003). doi: 10.1152/ajpheart.00020.2003; pmid: 14613910
25. S. Prost *et al*., Erosion of the chronic myeloid leukaemia stem cell pool by PPARγ agonists. *Nature* **525**, 380–383 (2015). doi: 10.1038/nature15248; pmid: 26331539
26. Y. Wang *et al*., The long noncoding RNA lncTCF7 promotes self-renewal of human liver cancer stem cells through activation of Wnt signaling. *Cell Stem Cell* **16**, 413–425 (2015). doi: 10.1016/j.stem.2015.03.003; pmid: 25842979
27. L. Aloia, B. Di Stefano, L. Di Croce, Polycomb complexes in stem cells and embryonic development. *Development* **140**, 2525–2534 (2013). doi: 10.1242/dev.091553; pmid: 23715546
28. M. Costantini, O. Clay, F. Auletta, G. Bernardi, An isochore map of human chromosomes. *Genome Res.* **16**, 536–541 (2006). doi: 10.1101/gr.4910606; pmid: 16597586
29. J. R. Dixon *et al*., Topological domains in mammalian genomes identified by analysis of chromatin interactions. *Nature* **485**, 376–380 (2012). doi: 10.1038/nature11082; pmid: 22495300
30. A. Valouev *et al*., Determinants of nucleosome organization in primary human cells. *Nature* **474**, 516–520 (2011). doi: 10.1038/nature10002; pmid: 21602827
31. D. Tillo, T. R. Hughes, G+C content dominates intrinsic nucleosome occupancy. *BMC Bioinformatics* **10**, 442 (2009). doi: 10.1186/1471-2105-10-442; pmid: 20028554
32. J. D. Anderson, J. Widom, Poly(dA-dT) promoter elements increase the equilibrium accessibility of nucleosomal DNA target sites. *Mol. Cell. Biol.* **21**, 3830–3839 (2001). doi: 10.1128/MCB.21.11.3830-3839.2001; pmid: 11340174
33. A. E. Vinogradov, Bendable genes of warm-blooded vertebrates. *Mol. Biol. Evol.* **18**, 2195–2200 (2001). doi: 10.1093/oxfordjournals.molbev.a003766; pmid: 11719569
34. G. J. Hogan, C. K. Lee, J. D. Lieb, Cell cycle-specified fluctuation of nucleosome occupancy at gene promoters. *PLOS Genet.* **2**, e158 (2006). doi: 10.1371/journal.pgen.0020158; pmid: 17002501
35. H. Koohy, T. A. Down, T. J. Hubbard, Chromatin accessibility data sets show bias due to sequence specificity of the DNase I enzyme. *PLOS ONE* **8**, e69853 (2013). doi: 10.1371/journal.pone.0069853; pmid: 23922824
36. C. Dingwall, G. P. Lomonossoff, R. A. Laskey, High sequence specificity of micrococcal nuclease. *Nucleic Acids Res.* **9**, 2659–2674 (1981). doi: 10.1093/nar/9.12.2659; pmid: 6269057
37. P. Dalerba *et al*., Single-cell dissection of transcriptional heterogeneity in human colon tumors. *Nat. Biotechnol.* **29**, 1120–1127 (2011). doi: 10.1038/nbt.2038; pmid: 22081019
38. K. Kise, Y. Kinugasa-Katayama, N. Takakura, Tumor microenvironment for cancer stem cells. *Adv. Drug Deliv. Rev.* **99** (Pt B), 197–205 (2016). doi: 10.1016/j.addr.2015.08.005; pmid: 26362921
39. M. Shipitsin *et al*., Molecular definition of breast tumor heterogeneity. *Cancer Cell* **11**, 259–273 (2007). doi: 10.1016/j.ccr.2007.01.013; pmid: 17349583
40. A. Alonso, B. Breuer, H. Bouterfa, D. Doenecke, Early increase in histone H1(0) mRNA during differentiation of F9 cells to parietal endoderm. *EMBO J.* **7**, 3003–3008 (1988). pmid: 2846273
41. J. M. Terme *et al*., Histone H1 variants are differentially expressed and incorporated into chromatin during differentiation and reprogramming to pluripotency. *J. Biol. Chem.* **286**, 35347–35357 (2011). doi: 10.1074/jbc.M111.281923; pmid: 21852237
42. E. Mendelson, M. Bustin, Monoclonal antibodies against distinct determinants of histone H5 bind to chromatin. *Biochemistry* **23**, 3459–3466 (1984). doi: 10.1021/bi00310a012; pmid: 6205690
43. A. Rada-Iglesias *et al*., A unique chromatin signature uncovers early developmental enhancers in humans. *Nature* **470**, 279–283 (2011). doi: 10.1038/nature09692; pmid: 21160473
44. A. Letourneau *et al*., Domains of genome-wide gene expression dysregulation in Down's syndrome. *Nature* **508**, 345–350 (2014). doi: 10.1038/nature13200; pmid: 24740065
45. J. M. Simon, P. G. Giresi, I. J. Davis, J. D. Lieb, Using formaldehyde-assisted isolation of regulatory elements (FAIRE) to isolate active regulatory DNA. *Nat. Protoc.* **7**, 256–267 (2012). doi: 10.1038/nprot.2011.444; pmid: 22262007
46. L. Shen *et al*., diffReps: Detecting differential chromatin modification sites from ChIP-seq data with biological replicates. *PLOS ONE* **8**, e65598 (2013). doi: 10.1371/journal.pone.0065598; pmid: 23762400

ACKNOWLEDGMENTS

We thank M. Salton and D. Donato for assistance; D. Bonnet and M. Bustin for sharing mice and reagents; I. Malanchi for help with transplantation assays; M. Becker, P. Van Loo, and I. Varela for useful discussions; and the Crick core facilities for technical support. pdCas9-DNMT3A-EGFP and pdCas9-DNMT3A-EGFP (ANV) plasmids are available from Addgene under a material transfer agreement with V. Zoldos. The results published here are in part based upon data generated by The Cancer Genome Atlas pilot project established by the National Cancer Institute and the National Human Genome Research Institute. This work was supported by the Francis Crick Institute, which receives its core funding from Cancer Research UK (FC001152), the UK Medical Research Council (FC001152), and the Wellcome Trust (FC001152), the Intramural Research Program of the NIH, NCI, Center for Cancer Research, the Israel Science Foundation (ISF 1252/12, 657/12), and the European Research Council (ERC-281781). Accompanying data sets are available through GEO (GSE65520, GSE66169, GSE73600, and GSE73580). Author contributions are in the supplementary text.

SUPPLEMENTARY MATERIALS

www.sciencemag.org/content/353/6307/aaf1644/suppl/DC1
Materials and Methods
Supplementary Text
Figs. S1 to S17
Tables S1 to S8
References (*47*–*50*)

28 December 2015; accepted 30 August 2016
10.1126/science.aaf1644

Downloaded from http://science.sciencemag.org/ on October 7, 2016

REPORTS

GEOPHYSICS

High-resolution lithosphere viscosity and dynamics revealed by magnetotelluric imaging

Lijun Liu[1]* and Derrick Hasterok[2]

An accurate viscosity structure is critical to truthfully modeling lithosphere dynamics. Here, we report an attempt to infer the effective lithospheric viscosity from a high-resolution magnetotelluric (MT) survey across the western United States. The high sensitivity of MT fields to the presence of electrically conductive fluids makes it a promising proxy for determining mechanical strength variations throughout the lithosphere. We demonstrate how a viscosity structure, approximated from electrical resistivity, results in a geodynamic model that successfully predicts short-wavelength surface topography, lithospheric deformation, and mantle upwelling beneath recent volcanism. We further show that this viscosity is physically consistent with and better constrained than that derived from laboratory-based rheology. We conclude that MT imaging provides a practical observational constraint for quantifying the dynamic evolution of the continental lithosphere.

During the last decade, progress in both seismic imaging (*1*, *2*) and geodynamic modeling (*3*, *4*) produced many useful insights into the large-scale dynamics of the continental lithosphere. However, the driving forces for fine-scale (<200-km) tectonic processes, such as those within the western United States, remain heavily debated (*5*–*10*). Large-scale deformation generally results from mantle convection-induced sublithospheric stress, such as dynamic topography and mantle traction (*3*, *4*, *7*, *10*–*12*). Consequently, the existing debate on the fine-scale tectonic deformation is largely due to the uncertain lithospheric buoyancy and viscosity structures. Fortunately, recent geophysical measurements constrain the density distribution of the crust and mantle lithosphere very well (*13*, *14*). However, the detailed viscosity structure of the lithosphere still remains poorly understood.

Taking the western United States as an example, its lithospheric density structure could be derived from multiple geophysical observations, including seismic velocity and heat flow measurements (*13*), as well as the geometry of lithospheric discontinuities (*14*). In contrast, the spatial pattern of lithospheric viscosity is more difficult to infer observationally because of the intimate involvement of time. Previous attempts included matching geodetic deformations with gravitational potential energy (GPE), by assuming either isostatic equilibrium (*9*) or considering large-scale mantle convection (*10*), and fitting the postseismic relaxation of earthquakes (*15*). However, considerable discrepancies still exist among these inferred lithosphere viscosity structures.

Magnetotelluric (MT) imaging represents a promising and independent approach to inferring a detailed lithospheric viscosity structure. This approach builds on direct geophysical and geological observations, requiring no a priori assumptions about lithospheric dynamics. Changes in the physical state that alter electrical conductivity generally affect viscosity as well, which allows us to use MT sounding to investigate the spatial distribution of viscosity. In reality, the viscosity depends on temperature, strain rate, grain size, and composition (*16*–*21*). Among these, compositional effects, specifically trace amounts of water and melt, are the most difficult to determine, but play a crucial role in the reduction of strength (*17*). Fluids, including melts, accumulate in regions of strong deformation (*17*). The presence of melts greatly reduces rock strength while enhancing electrical conductivity (*18*). Hydration of nominally anhydrous minerals also increases electrical conductivity [(*22*) and references therein]. Likewise, laboratory experiments on major minerals (e.g., olivine, pyroxene, and garnet) indicate weakening in the presence of water (*19*–*21*).

We established a theoretical framework between electrical conductivity and viscosity based on their similar controlling factors. Effective viscosity is the ratio of stress to strain rate, $\eta = \sigma\dot{\epsilon}^{-1}$, where σ is stress and $\dot{\epsilon}$ is the strain rate. A general form of this relation is

$$\eta = \sigma\dot{\epsilon}^{-1} = \left\{ A d^{-m} C_{OH}^{r} \sigma^{n-1} \exp\left(-\frac{E^* + PV^*}{RT} \right) \right\}^{-1} \quad (1)$$

where d is grain size; C_{OH}, water fugacity; E^* and V^*, activation energy and activation volume, respectively; P and T, pressure and temperature, respectively; R, the ideal gas constant; and A, m, n, and r, all laboratory-derived parameters (*23*). The electrical resistivity model takes a similar form

$$\rho = \left\{ A_e C_w^{r_e} \exp\left(-\frac{E_e^* + PV_e^*}{RT} \right) \right\}^{-1} \quad (2)$$

where the parameters are also like those in Eq. 1 (*24*).

Using Eq. 1, one could first estimate stress (σ), independent of viscosity, from local buoyancy variations (*3*–*8*) and/or far field mechanical conditions (*9*, *10*, *15*). One could then numerically calculate the accurate stress, including that induced by lithosphere deformation for a given viscosity structure. In contrast to the viscosity formulation, the omission of grain size in the formulation for resistivity (Eq. 2) could likely be naturally restored in the structural information of MT sounding (Fig. 1), as demonstrated below. Consequently, we suggest, using the similarity between Eqs. 1 and 2, that electrical resistivity is positively correlated with effective viscosity ($\rho \propto \eta$). Previous conceptual models of rifting that highlight variations in strain appear to mimic patterns seen in the midcrustal electrical conductivity under similar circumstances (*25*). We propose that these high-conductivity patterns (Fig. 1, A and B) also represent low-viscosity regions owing to consequences of past deformation of the continental lithosphere.

We think that the above theory and observations support using MT images as a proxy for mechanical strength throughout the lithosphere. However, we recognize several difficulties limiting the direct application of the above relations in accurately estimating viscosity. First, large uncertainties in laboratory models result in large uncertainties in viscosity. Second, developing a rigorous model is restricted by additional uncertain factors, such as composition and grain size. Third, MT models do not yield precise estimates of the absolute conductivity, as they are sensitive to conductance (the product of conductivity and thickness) and are insensitive to the resistivity of resistors. Furthermore, the spatial sensitivity of magnetotellurics to electrical conductivity variations with depth and the smoothing effect due to inversion cannot capture the true scale of viscosity variations. With these uncertainties in mind, we processed the MT image in a way similar to that in which seismic tomography is converted into density anomalies (*2*, *3*). We converted the resistivity structure into a viscosity profile using an empirical relation,

$$\frac{\eta}{\eta_0} = C_0 \cdot \left(\frac{\rho}{\rho_0} \right)^{C_1} \quad (3)$$

where η is effective viscosity; η_0, reference viscosity (10^{20} Pa·s); ρ, apparent resistivity; ρ_0, reference resistivity (10^2 Ω m); and C_0 and C_1, numerical coefficients. Because of the unknown values of C_0 and C_1, both the regional average and maximum contrast of the viscosity structure, controlled by these two respective coefficients, are uncertain. Subsequently, we updated these

[1]Department of Geology, University of Illinois at Urbana-Champaign, Champaign, IL 61820, USA. [2]Department of Earth Sciences, University of Adelaide, Adelaide, South Australia 5005, Australia.
*Corresponding author. Email: ljliu@illinois.edu

Downloaded from http://science.sciencemag.org/ on October 7, 2016

coefficients and, thus, viscosity properties using observational constraints, including surface topography and intraplate deformation. Overall, we looked for an effective lithospheric viscosity structure resembling the spatial pattern of the MT image that satisfies the available constraints. For simplicity and to show the effectiveness of the technique, we limited ourselves to a two-variable problem where C_0 and C_1 are constant over space.

We used a recent high-resolution MT inversion for the tectonically active western United States (*25*) and estimated the lithospheric buoyancy by considering thermal and compositional effects. The thermal structure was estimated from surface heat flow by solving for a two-dimensional (2D) steady-state thermal diffusion problem with the observed heat flow as the upper boundary condition (Fig. 2 and fig. S1). We assumed that the 1350°C isotherm approximately follows the 100 Ω m contour of the apparent resistivity (Fig. 1B) (*26*). The compositional buoyancy of the continental crust was approximated using the recent estimate on Moho depth (*14*), highlighting thicker crust beneath the Colorado Plateau (CP) than the Eastern Great Basin (EGB) and the Transition Zone (TZ) (Fig. 2). A uniform crustal density of 2850 kg·m^{-3} was adopted for the study region (*27*).

We verified the resulting lithospheric density structure with both analytical and numerical solutions (Fig. 2B). By assuming a simple viscosity profile with only depth-dependence, similar to traditional geodynamic models (*2*–*4*), we found that the topography contribution owing to crustal buoyancy (orange line in Fig. 2B) is a mirror image of the Moho (magenta line in Fig. 2C), consistent with Airy compensation. The resulting topographic relief owing to thermal buoyancy (blue line in Fig. 2B) also resembled that from a recent global geodynamic model (*4*), a resemblance that validated our calculation. More important, the predicted total topography also matched a smoothed version of the observed topography. We note that the regional model used here could not properly reproduce the baseline topography of the region because of the undefined sea level.

This model (Fig. 2), although it satisfied the smooth profile of surface topography, failed to reproduce the westward block motion (3 mm/year) of the EGB relative to the CP (Fig. 2A), as revealed geodetically (*28*) (fig. S2). If we assume an average lithospheric viscosity of 10^{22} Pa·s over a lithospheric thickness of 50 km, as suggested by earlier studies (*9*), the model predicts negligible lithospheric deformation (Fig. 2A). A weaker lithosphere (with a viscosity of 10^{21} Pa·s) leads to larger intraplate deformation, but the resulting velocity profile differs from that observed, with most deformation occurring inside the CP. Physically, the deformation mechanism here is similar to earlier GPE models, so that the mismatch suggests that either some far-field tectonic stress is needed (*9*, *10*) or the viscosity structure is inappropriate or possibly both. Furthermore, these models predict limited magnitudes of mantle upwelling flow beneath the region, inconsistent with the recent volcanic activities within the TZ.

Adopting a spatially variable viscosity structure, converted from the MT image using Eq. 3 (Fig. 3), greatly improved the prediction of surface topography and lithosphere deformation. To show the validity of this approach on inferring viscosity by matching tectonic observables, we performed a parameter test by systematically changing the values of C_0 and C_1, which control the lithosphere's average strength and spatial viscosity variation, respectively. Among the five models showing different amounts of spatial viscosity contrast (Fig. 3A and fig. S3), the smallest amount (10×) of viscosity variation generated surface predictions similar to those in the 1D viscosity model (Figs. 2 and 3), with strong lithospheric deformation inside the CP and the TZ. The deformation localized more toward the EGB and TZ with increasing viscosity variations. In addition, a perfect step-profile of intraplate velocity emerged as the viscosity contrast increases to 10^7, similar to the observed lithospheric deformation (*28*). A larger viscosity contrast (10^9) produced progressively decreasing surface velocity from the EGB to the east, which was inconsistent with observations.

Besides intraplate deformation, the predicted surface topography also showed clear improvements relative to the 1D viscosity model. The MT-based viscosity structures predicted large variations of surface topography on length scales as small as ~20 km (fig. S3). We further corrected the flexural effect on these raw topography signals (*26*) while considering the spatially varying lithospheric elastic thickness (*29*) (fig. S4). In general, predicted topography smooths with the degree of viscosity homogeneity (Fig. 3B). A 10-fold lateral variation in viscosity results in topography that (blue line in Fig. 3B) largely resembled the 1D viscosity model (pink line in Fig. 3B), but a

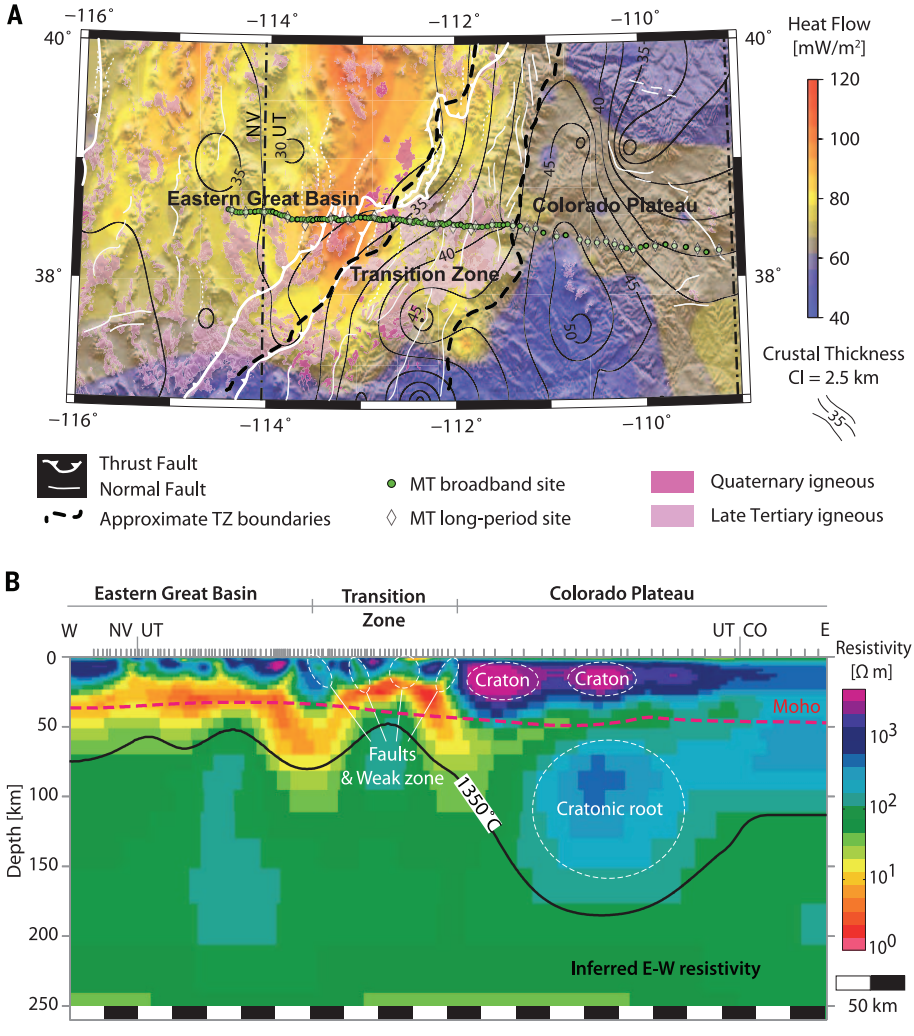

Fig. 1. Geophysical characteristics of the Basin and Range and Colorado Plateau. (**A**) Shaded topography, surface heat flow interpolated from the global heat flow database (*13*), crustal thickness estimated by seismic receiver functions (*14*), MT station locations, and late Cenozoic volcanism. (**B**) Inverted resistivity model from (*25*), along the 2D profile shown in (A). The vertical gray bars at the surface represent MT stations. Note the correlation of faults and weak zones with low resistivity and that of cratonic lithosphere with high resistivity.

Downloaded from http://science.sciencemag.org/ on October 7, 2016

clear difference was that the former predicted more uplift (subsidence) in the TZ (CP) because of a larger contribution from subsurface convection (Fig. 3C). This topographic difference became more pronounced with increasing viscosity contrast, as shown by the increasing amplitude of topographic roughness. We suggest that the short-wavelength topography reflects shear displacement of crustal blocks along the resolved faults, driven by lithospheric strain variation resulting from flow at greater depths. This relation can be seen from the striking correlation of localized elevation peaks (Fig. 3, B and E) with the strong crustal blocks right below (Fig. 3, C and F), as well as the independence of topography on local lithospheric density structure (fig. S5). The model that best matched lithosphere deformation (Fig. 3A, with viscosity variations of 10^5 to 10^7) also well predicted the fine-scale topography, with remarkable similarity in both wavelength and amplitude (Fig. 3B).

Similar tests on the average (or net) lithospheric viscosity by varying the parameter C_0 demonstrated an almost linear correlation with the magnitude of intraplate deformation (Fig. 3D) and topography variation (Fig. 3E and fig. S6) (*26*), which implied a strong constraint. Collectively, we found that intraplate deformation and surface topography represented sufficient and complementary constraints on the average strength and spatial variation of lithosphere viscosity structure (Fig. 3). The model that best matched all observations had a spatial viscosity variation between 3×10^{23} Pa·s and 3×10^{17} Pa·s (Fig. 4A).

Another robust prediction from our models was a region with vigorous mantle upwelling at the lower-crust and uppermost mantle depths beneath the TZ, where the peak ascending velocity exceeded 5 cm/year (Figs. 3 and 4). The locally reduced viscosity and the large lateral gradient of buoyancy in this region facilitated the mantle upwelling responsible for late Cenozoic volcanism, high surface heat flow (Fig. 1), and rough TZ topography (Figs. 3 and 4). The apparent eastward encroachment of flow beneath the western edge of the CP was consistent with the volcanic history (*5*) and the proposed destabilization of the plateau's cratonic root (*8*).

In our best-fitting model (Fig. 4A), the dramatic lithospheric viscosity reduction to the west of the CP led to a sharp change of lithospheric deformation rate, where almost nonexistent internal deformation inside the CP increased rapidly to ~3 mm/year westward within a short distance of <100 km, which was close to that observed (*28*). Toward the western end of the MT survey line, the predicted deformation rate dropped slightly to ~2.5 mm/year. This decrease was likely related to an apparent lithospheric strengthening because of the limited resolution of the MT image toward the edge of the inversion domain. The overpredicted topography within the western CP may reflect surface erosion attributable to the local river system (Fig. 4A). Alternatively, this may be due to a lithosphere density anomaly not considered in our simple buoyancy structure or local inaccuracy of the MT-image in representing lithosphere viscosity.

We further investigated the physical consistency of the MT-converted viscosity with that forwardly derived from laboratory-based rheologies (*23*). By solving the mantle flow using the power-law rheology with other factors in Eq. 1 assumed uniform (*26*) (fig. S7), we obtained a viscosity structure that resembled the MT image at large scales, but the model failed to predict both fine-scale topography and lithosphere deformation (fig. S7). Inclusion of pseudo-plasticity in the model improved the fit in both viscosity and lithosphere deformation (Fig. 4B). However, deformation within the CP was overpredicted, likely related to the artificial return flow close to the eastern boundary of the model; this model also lacked localized crustal weak zones and, thus, the short-wavelength topography within the EGB and TZ. These mismatches should reflect the missing effects of compositional variation and grain size in the viscosity calculation.

The general consistency between the forward [using rheological laws (Fig. 4B and fig. S7)] and their inverse [using MT (Fig. 4A)] viscosity calculations showed that the latter properly captured the effects of strain-rate dependence and plastic deformation. The fact that the MT-converted viscosity best matched observations implied that the MT image also captured the effects of other viscosity-influencing factors like composition and grain size, which are difficult to infer using a forward approach. We suggest that future research including MT as a quantitative constraint will better unearth the physics of lithospheric rheology. Consideration of mineral physics and geochemical and geological data in high-fidelity geodynamic models will help to push this research frontier forward. Application of the MT-based modeling approach to other tectonic regions (*30*) should help to better understand the detailed dynamic evolution of continents including topography, deformation, and volcanic history.

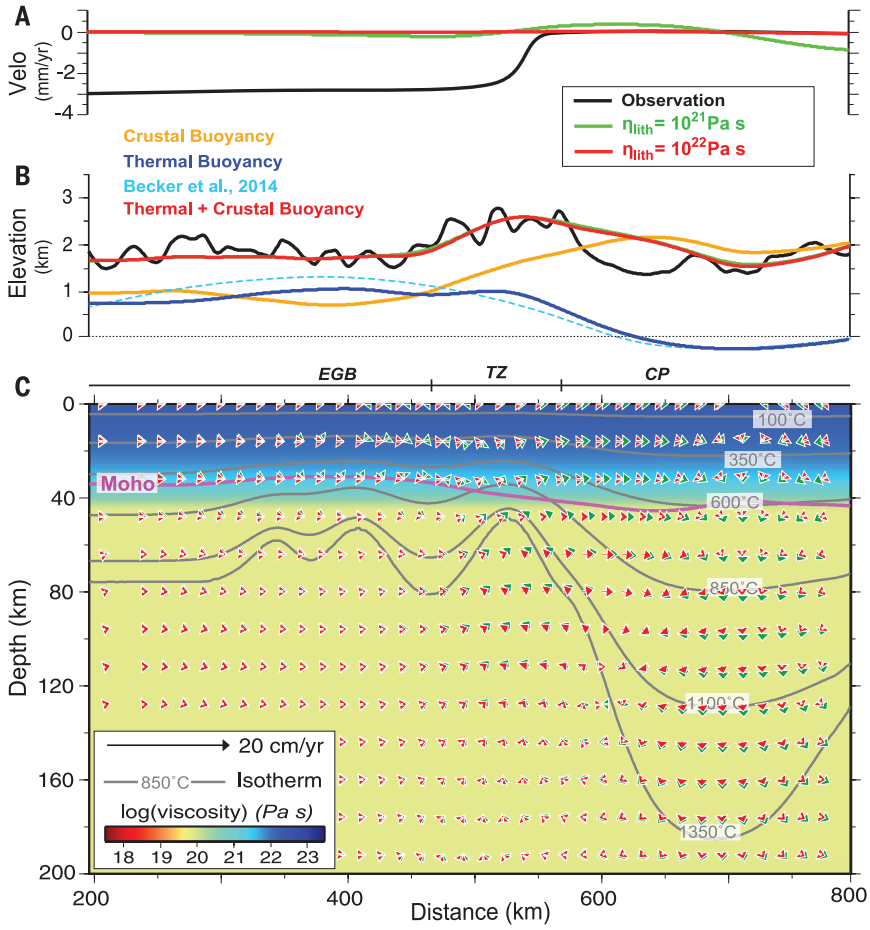

Fig. 2. Models with a 1D viscosity profile predicting intraplate deformation, surface topography, and mantle flow. (**A** and **B**) Intraplate deformation and surface topography. The black curves in (A) and (B) represent the observed Basin and Range extension rate and surface topography, respectively. The green and red colors represent results from a weak and strong lithosphere, respectively. (B) The corresponding contributions to topography from crustal buoyancy (orange), thermal buoyancy (blue), and their combined effects (red) are shown. (**C**) Mantle flow. The background viscosity is for the strong lithosphere model, but the mantle flow from both the weak (green) and strong (red) lithosphere models are shown. Gray lines represent the geotherms, and magenta line marks the Moho.

Downloaded from http://science.sciencemag.org/ on October 7, 2016

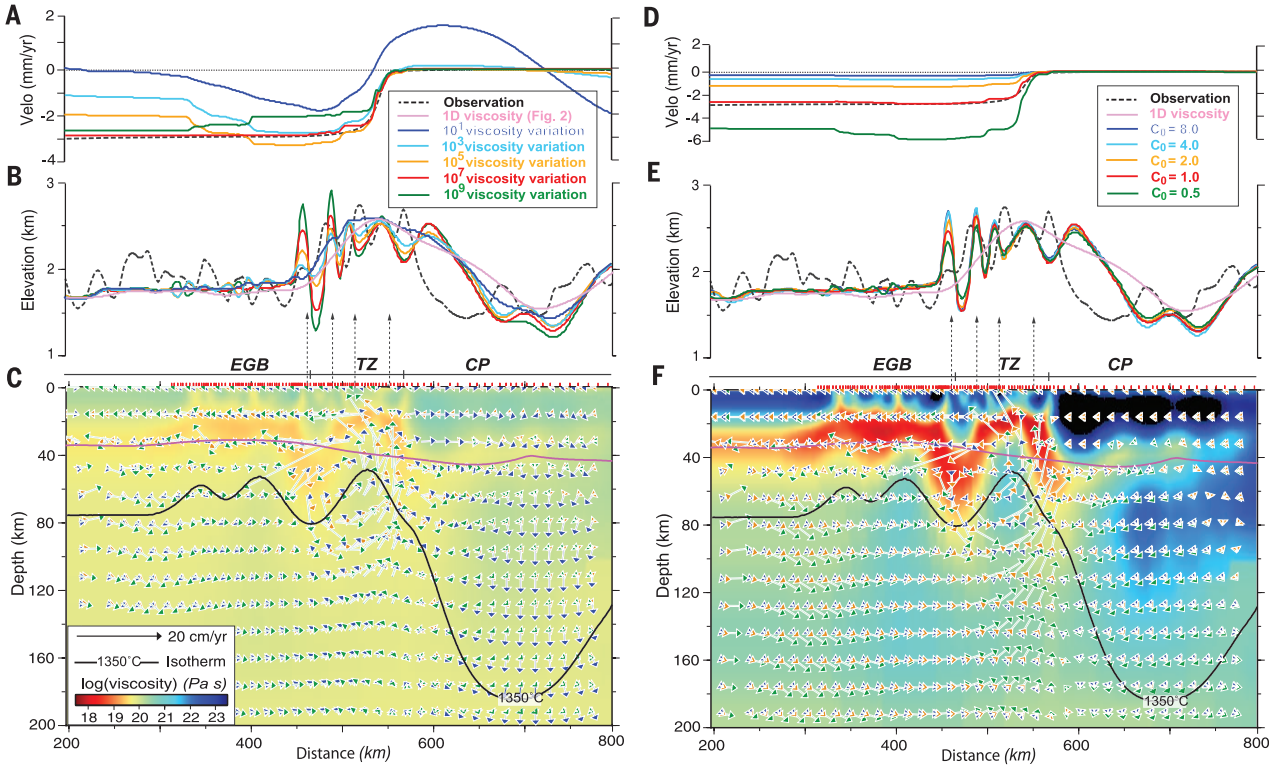

Fig. 3. Sensitivity of tectonic constraints on the MT-converted lithosphere viscosity. (**A** and **B**) Dependence of (A) intraplate deformation rate and (B) surface topography on the amount of spatial variation of lithosphere viscosity. (**C**) The background color shows the viscosity with a 10-fold spatial variation, and the three mantle flow fields correspond to cases with 10 (blue), 10^5 (orange), and 10^9 (green) of viscosity variations, respectively. (**D** and **E**) Dependence of tectonic constraints on the average (or net) viscosity of the lithosphere. (**F**) Background color represents viscosity of the strongest (C_0 = 8.0) lithosphere case, and the three flow fields are from cases with C_0 of 8.0 (blue), 2.0 (orange), and 0.5 (green), respectively. The red bars on the surface mark the MT stations.

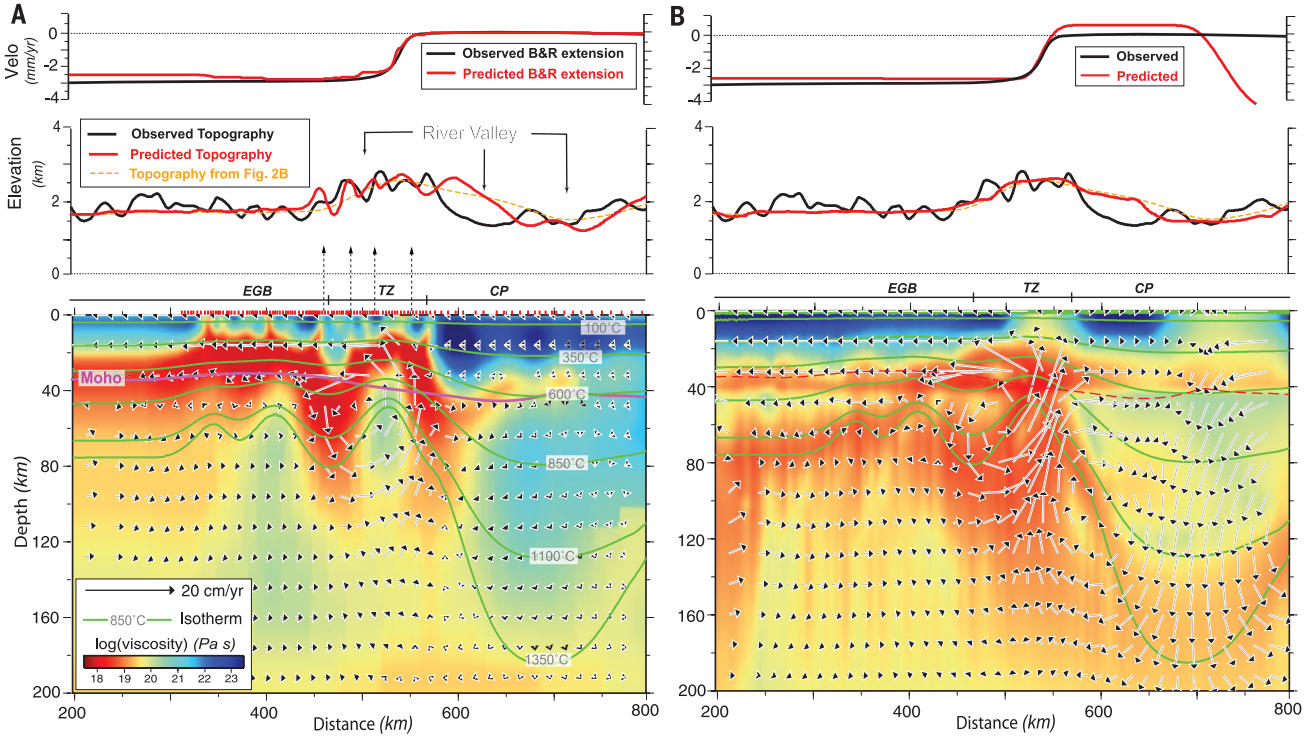

Fig. 4. Effective viscosity structures derived from the MT image and laboratory-based rheologies. (**A**) Best-fitting model with an MT-converted viscosity structure, including six orders of magnitude of viscosity variations. (**B**) Viscosity structure and model predictions using a power-law rheology (n = 3 in Eq. 1 and other parameters listed in supplementary materials) and pseudoplasticity (yield stresses of 40,150 MPa for above and below 40 km in depth, respectively). The general similarity between the two viscosity structures and model predictions confirms the physical validity of the MT-converted viscosity.

Downloaded from http://science.sciencemag.org/ on October 7, 2016

REFERENCES AND NOTES

1. S. P. Grand, *Philos. Trans. A Math. Phys. Eng. Sci.* **360**, 2475–2491 (2002).
2. N. A. Simmons, A. M. Forte, S. P. Grand, *Geophys. J. Int.* **177**, 1284–1304 (2009).
3. L. Liu, S. Spasojević, M. Gurnis, *Science* **322**, 934–938 (2008).
4. T. W. Becker, C. Faccenna, E. D. Humphreys, A. R. Lowry, M. S. Miller, *Earth Planet. Sci. Lett.* **402**, 234–246 (2014).
5. M. Roy, T. H. Jordan, J. Pederson, *Nature* **459**, 978–982 (2009).
6. J. W. van Wijk *et al.*, *Geology* **38**, 611–614 (2010).
7. L. Liu, M. Gurnis, *Geology* **38**, 663–666 (2010).
8. A. Levander *et al.*, *Nature* **472**, 461–465 (2011).
9. L. M. Flesch, W. E. Holt, A. J. Haines, B. Shen-Tu, *Science* **287**, 834–836 (2000).
10. A. Ghosh, W. E. Holt, *Science* **335**, 838–843 (2012).
11. N. Flament, M. Gurnis, R. D. Müller, *Lithosphere* **5**, 189–210 (2013).
12. L. Liu, *Rev. Geophys.* **53**, 1022–1049 (2015).
13. D. Hasterok, D. S. Chapman, *Earth Planet. Sci. Lett.* **307**, 59–70 (2011).
14. Incorporated Research Institutions in Seismology Data Management Center, Data Services Products: EARS EarthScope Automated Receiver Survey (IRIS, 2010); http://ds.iris.edu/ds/products/ears/.
15. R. E. M. Riva, R. Govers, *Geophys. J. Int.* **176**, 614–624 (2009).
16. M. I. Billen, *Annu. Rev. Earth Planet. Sci.* **36**, 325–356 (2008).
17. D. L. Kohlstedt, B. K. Holtzman, *Annu. Rev. Earth Planet. Sci.* **37**, 561–593 (2009).
18. A. Pommier *et al.*, *Geochem. Geophys. Geosyst.* **14**, 1685–1692 (2013).
19. S. Mei, W. Bai, T. Hiraga, D. L. Kohlstedt, *Earth Planet. Sci. Lett.* **201**, 491–507 (2002).
20. S. Chen, T. Hiraga, D. L. Kohlstedt, *J. Geophys. Res.* **111** (B8), B08203 (2006).
21. L. Xu *et al.*, *Earth Planet. Sci. Lett.* **379**, 158–165 (2013).
22. E. Gardés, F. Gaillard, P. Tarits, *Geochem. Geophys. Geosyst.* **15**, 4984–5000 (2014).
23. S. Karato, H. Jung, *Philos. Mag.* **83**, 401–414 (2003).
24. D. Wang, M. Mookherjee, Y. Xu, S. Karato, *Nature* **443**, 977–980 (2006).
25. P. E. Wannamaker *et al.*, *Geochem. Geophys. Geosyst.* **9**, Q05019 (2008).
26. Methods and data processing techniques are available in the supplementary materials on *Science* Online.
27. D. Hasterok, D. S. Chapman, *J. Geophys. Res.* **112**, B06415 (2007).
28. W. C. Hammond, W. Thatcher, *J. Geophys. Res.* **109** (B8), B08403 (2004).
29. A. R. Lowry, R. B. Smith, *J. Geophys. Res.* **99** (B10), 20123–20140 (1994).
30. N. M. Meqbel, G. D. Egbert, P. E. Wannamaker, A. Kelbert, A. Schultz, *Earth Planet. Sci. Lett.* **402**, 290–304 (2014).

ACKNOWLEDGMENTS

The authors thank J. Hu for helping with the non-Newtonian rheology. L.L. is supported by NSF grants EAR-1554554 and ACI-1516586. Collection of MT data and support for D.H. are provided by NSF grants to P. E. Wannamaker EAR81-16602, 84-17765, and 02-30027. L.L. conceived the project and performed the geodynamic calculations. D.H. provided expertise on MT-sounding and lithosphere buoyancy. Both authors contributed to manuscript preparation. MT data are available in reference (*25*). Additional information on the geodynamic modeling is available in the supplementary materials.

SUPPLEMENTARY MATERIALS

www.sciencemag.org/content/353/6307/1515/suppl/DC1
Materials and Methods
Supplementary Text
Figs. S1 to S7
References (*31*–*34*)

9 March 2016; accepted 24 August 2016
10.1126/science.aaf6542

PROTOPLANETARY DISKS

Spiral density waves in a young protoplanetary disk

Laura M. Pérez,[1]* John M. Carpenter,[2] Sean M. Andrews,[3] Luca Ricci,[3] Andrea Isella,[4] Hendrik Linz,[5] Anneila I. Sargent,[6] David J. Wilner,[3] Thomas Henning,[5] Adam T. Deller,[7] Claire J. Chandler,[8] Cornelis P. Dullemond,[9] Joseph Lazio,[10] Karl M. Menten,[1] Stuartt A. Corder,[2] Shaye Storm,[3] Leonardo Testi,[11,12] Marco Tazzari,[11] Woojin Kwon,[13,14] Nuria Calvet,[15] Jane S. Greaves,[16] Robert J. Harris,[17] Lee G. Mundy[18]

Gravitational forces are expected to excite spiral density waves in protoplanetary disks, disks of gas and dust orbiting young stars. However, previous observations that showed spiral structure were not able to probe disk midplanes, where most of the mass is concentrated and where planet formation takes place. Using the Atacama Large Millimeter/submillimeter Array, we detected a pair of trailing symmetric spiral arms in the protoplanetary disk surrounding the young star Elias 2-27. The arms extend to the disk outer regions and can be traced down to the midplane. These millimeter-wave observations also reveal an emission gap closer to the star than the spiral arms. We argue that the observed spirals trace shocks of spiral density waves in the midplane of this young disk.

Spiral density waves are expected to be excited in the midplane of protoplanetary disks by the action of gravitational forces, generated by, for example, planet-disk interactions (*1*) or gravitational instabilities (*2*). These waves give rise to a spiral structure whose observable characteristics—the number and location of arms and their amplitudes and pitch angles—depend on the driving mechanism and the disk physical properties (*1*, *3*–*5*). Theoretical predictions agree that these spiral features can be very prominent and thus more easily observable than the putative embedded planets or instabilities driving such waves (*6*, *7*). Spiral-like patterns have been observed in evolved protoplanetary disks with depleted inner regions, in optical scattered light (*8*–*13*) or gas spectral lines (*14*, *15*). However, at the wavelength of such observations the emission is optically thick, and scattered light only traces the tenuous surface layers of these disks rather than their midplane densities. This makes it impossible to disentangle between minute perturbations near the disk surface and true density enhancements over the disk column attributable to spiral density waves (*5*, *16*). To probe the disk density structure, particularly the disk midplane that contains most of the mass and where planets form, observations of optically thin emission are necessary.

We used the Atacama Large Millimeter/submillimeter Array (ALMA) to observe the protoplanetary disk around the young star Elias 2-27 at a wavelength of 1.3 mm. Our spatially resolved image (Fig. 1) shows two symmetric spiral arms extending from an elliptical emission ring. To emphasize the spirals and the dark ring of attenuated emission seen at ≈70-astronomical-unit (AU) radial distance from the star, we applied an unsharp masking filter (*17*) to increase substantially the image contrast (Fig. 1B).

The young star Elias 2-27 (*18*) is a member of the ρ-Ophiuchus star-forming complex at a distance of 139 pc (*19*) and is classified as a class II young stellar object from analysis of its spectral energy distribution (SED) (*20*, *21*). Although the star is only 50 to 60% of the Sun's mass ($M_{\odot}$) (*20*, *22*), it is known to harbor an unusually massive [0.04 to 0.14 $M_{\odot}$ (*20*, *23*, *24*)] protoplanetary disk. The star, obscured by 15 magnitudes of extinction at optical wavelengths by the

[1]Max-Planck-Institut für Radioastronomie, Auf dem Hügel 69, 53121 Bonn, Germany. [2]Joint Atacama Large Millimeter/submillimeter Array (ALMA) Observatory, Avenida Alonso de Córdova 3107, Vitacura, Santiago, Chile. [3]Harvard-Smithsonian Center for Astrophysics, 60 Garden Street, Cambridge, MA 02138, USA. [4]Rice University, 6100 Main Street, Houston, TX 77005, USA. [5]Max-Planck-Institut für Astronomie, Königstuhl 17, 69117 Heidelberg, Germany. [6]California Institute of Technology, 1200 East California Boulevard, Pasadena, CA 91125, USA. [7]Netherlands Institute for Radio Astronomy (ASTRON), 7990-AA Dwingeloo, Netherlands. [8]National Radio Astronomy Observatory, Post Office Box O, Socorro, NM 87801, USA. [9]Heidelberg University, Center for Astronomy, Albert Ueberle Strasse 2, Heidelberg, Germany. [10]Jet Propulsion Laboratory, California Institute of Technology, 4800 Oak Grove Drive, Pasadena, CA 91106, USA. [11]European Southern Observatory, Karl Schwarzschild Strasse. 2, 85748 Garching, Germany. [12]Istituto Nazionale di Astrofisica (INAF)–Osservatorio Astrofisico di Arcetri, Largo E. Fermi 5, 50125 Firenze, Italy. [13]Korea Astronomy and Space Science Institute, 776 Daedeokdae-ro, Yuseong-gu, Daejeon 34055, Republic of Korea. [14]Korea University of Science and Technology, 217 Gajeong-ro, Yuseong-gu, Daejeon 34113, Republic of Korea. [15]University of Michigan, 830 Dennison Building, 500 Church Street, Ann Arbor, MI 48109, USA. [16]Cardiff University, School of Physics and Astronomy, 4 The Parade, Cardiff CF24 3AA, UK. [17]University of Illinois, 1002 West Green Street, Urbana, IL 61801, USA. [18]Department of Astronomy, University of Maryland, College Park, MD 20742, USA.
*Corresponding author. Email: lperez@mpifr-bonn.mpg.de

Downloaded from http://science.sciencemag.org/ on October 7, 2016

parent molecular cloud (*22*), accretes material from its surrounding disk with a mass accretion rate of 8×10^{-8} $M_{\odot}$ year^{-1} (*25*). Previous observations at 0.6″ to 1.1″ angular resolution were well described by a smooth and axisymmetric distribution of material in the disk that extends near the stellar photosphere and decreases monotonically with distance from the star (*20*, *23*).

To estimate the optical depth of the observed dust continuum emission, we performed radiative transfer calculations using RADMC-3D (*26*) at 1.3 mm (*17*), using the previous surface density constraint found for the Elias 2-27 disk (*20*). This model reproduces the azimuthally averaged radial profile of the observed ALMA 1.3-mm continuum emission (fig. S1) (*17*). At a radial distance from the star (hereafter referred to as radius and denoted by R) larger than $R \approx 10$ AU, the emission is optically thin and thus traces the density of solid material down to the midplane of the disk. At the location of the spiral structures (from R = 100 to 300 AU), the azimuthally averaged optical depth τ of the dust continuum emission is $\tau = 0.1$ at R = 100 AU, decreasing to $\tau = 0.02$ at R = 300 AU (fig. S1B), which is consistent with the measured peak brightness temperature on the spirals of 1.2 K at R = 150 AU.

The spiral structures are even more evident in Fig. 2A, in which the data has been projected into a polar coordinate grid that accounts for the viewing geometry of the disk. In polar coordinates, a ring with zero eccentricity would have a constant radius for all polar angles. However, shown in Fig. 2A are two bright structures that grow in radius from ~100 to 300 AU as the polar angle increases. The brightest of these two structures lies northwest of the star, labeled "NW"; the spiral structure southeast of the star is labeled "SE." In Fig. 2B, we present the surface brightness contrast of the NW and SE arms, defined as the ratio between the peak of emission at the arm and the background surface brightness (*17*). We found that both arms have similar contrasts ranging between values of 1.3 and 2.5. The spiral arms reach their highest contrast at R = 150 AU, coinciding with the location in the disk where gravity has the most influence over thermal pressure and shear forces, that is, where the Toomre Q parameter is lowest (fig. S2) (*17*). However, even at its minimum value Toomre Q is well inside the stable regime (*17*). If the spirals arms suffer from beam dilution (if their physical size is smaller than the angular resolution of our observation), a higher optical depth than our previous estimate could be possible, implying an even higher density contrast in the arms. Thus, the contrast values measured for NW and SE are lower limits.

We determined the local maxima and minima of emission in the dust continuum observations at evenly spaced azimuthal angles, after subtracting a smooth monotonically decreasing intensity profile that best fit the intensity radial profile of the disk (fig. S3) (*17*). As demonstrated in Fig. 3, the emission local maxima (Fig. 3, crosses) describe two spiral structures, whereas the emission local minima (Fig. 3, circles) describe an ellipse. We

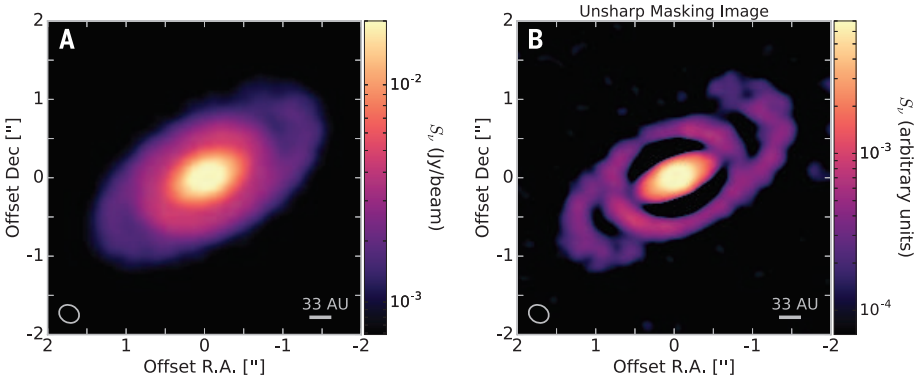

Fig. 1. Thermal dust emission from the protoplanetary disk surrounding Elias 2-27. The disk was imaged at a wavelength of 1.3 mm, with ALMA reaching an angular resolution of 0.26″ by 0.22″ (indicated by the ellipse in the bottom left corner), which corresponds to 36 by 31 AU at the distance of the star. The field-of-view center (at 0, 0) corresponds to the disk emission peak located at right ascension (J2000) = 16 hours 26 min 45.024 s, declination (J2000) = −24 degrees 23 min 08.250 s, and coincidental with the position of the star Elias 2-27. (**A**) 1.3-mm dust continuum image from the Elias 2-27 protoplanetary disk over a 4″ by 4″ area. The color scale represents flux density measured in units of Jansky per beam (1 Jy = 10^{-26} W m^{-2} Hz^{-1}). (**B**) Increased contrast image from processing the original ALMA observations shown in (A) with an unsharp masking filter (*17*).

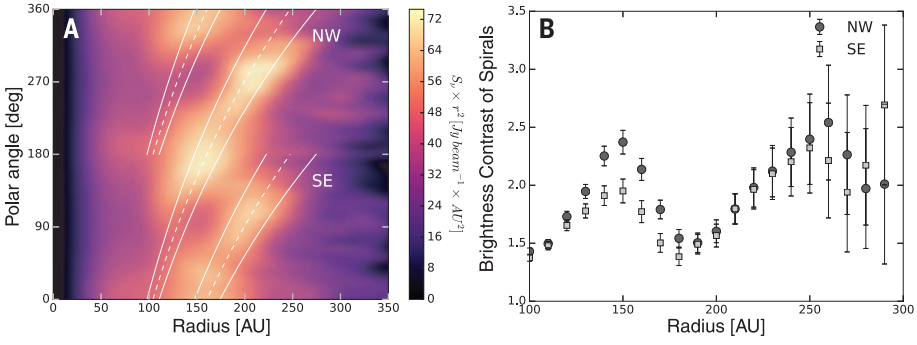

Fig. 2. Polar projection of disk emission and measured contrast over the spirals in the Elias 2-27 protoplanetary disk. (**A**) Projection onto polar coordinates (polar angle θ versus deprojected radial distance to the central star R) of the dust continuum observations from the Elias 2-27 disk. The emission has been scaled by R^2 in order to aid visualization, and the polar angle is defined as θ = 0° (north) increasing toward east. Curves correspond to the best-fit model spirals for the NW and SE arms (dashed lines) and their constraint at the 3σ level (solid lines). (**B**) Surface brightness contrast of the continuum emission along each spiral arm, defined as the ratio between the peak of emission and the background surface brightness (*17*), which is computed at increasing radial distance from the star.

constrained the geometry of these structures by modeling their location in polar coordinates (where R is the distance from the star located at the origin and θ is the angle from the x axis), taking into account that these structures have been inclined and rotated with respect to our line of sight by their inclination (i) and position angle (PA). The emission local minima were fitted with a circular ring ($R = a_0$, where a_0 is the radius at which the gap is located), whereas the emission local maxima were fitted with two symmetric logarithmic spirals ($R = R_0\, e^{b\theta}$, where R_0 is the spiral radius at θ = 0°, and b is the rate at which the spirals increase their distance from the origin). The best-fit parameters for the symmetric spirals that describe the local maxima are R_0 = 84 ± 4 AU and b = 0.138 ± 0.007 (which corresponds to a pitch angle of ϕ= 7.9° ± 0.4°), whereas the circular ring that describes the local minima has a radius of a_0 = 71 ± 2 AU. The geometry of the spiral arms and dark ring can all be described with a single inclination angle of i = 55.8° ± 0.9° and position angle PA = 117.3° ± 0.9°. The best-fit model and constraints at the 3σ level are shown in Fig. 3 for the spiral arms and dark ring.

Spatially resolved molecular line observations of CO and two isotopologues, simultaneous to the continuum observations discussed here, suggest that the southwest side of the disk is tilted toward Earth while the disk rotates in a clockwise direction in a Keplerian velocity pattern (figs. S4 to S7) (*17*). It is most likely that the observed NW and SE spirals point away from the direction of rotation—that these are trailing spiral arms.

Downloaded from http://science.sciencemag.org/ on October 7, 2016

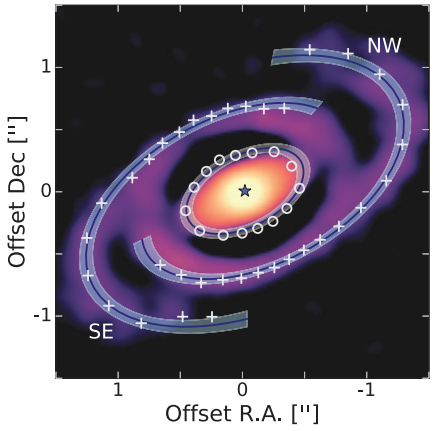

Fig. 3. Model of symmetric spirals and dark ring for the Elias 2-27 protoplanetary disk. The local maxima (crosses) and local minima (circles) in the continuum emission of Elias 2-27 are indicated. The maxima trace the NW and SE spirals, and the minima trace a ring. A model with symmetric spirals that shares the same geometry (inclination and position angle) with the inner dark ring was able to reproduce the location of the local maxima and minima of emission, as illustrated by the best-fit model (solid curve) and 3σ constraints (shaded regions). The blue star denotes the position of Elias 2-27. To illustrate the location of these features in the image, we overlaid these results over the unsharp masked image from Fig. 1B; however, this image was not used for the calculations.

Simulations indicate that planet–companion-disk interactions (PDIs) alone are capable of opening a gap creating density and temperature contrasts along spiral arms that are consistent with the observed values in NW and SE (*1*, *6*). However, the observed gap at 70 AU is of low contrast, which is indicative of a narrow or partially opened gap as predicted from PDIs with low-mass planets. Such planets will have a harder time exciting spiral density waves of the observed contrast in Elias 2-27 (*27*). Grain growth could in principle create such a low-contrast gap at 70 AU, but we see no evidence of this process in our 9 mm observations from the Karl G. Jansky Very Large Array (fig. S8) (*17*). Additionally, PDI simulations generally predict spiral arms with different contrasts to each other, unlike the similar contrast of NW and SE. Those models often struggle to produce the symmetric spiral pattern observed in the Elias 2-27 disk (*27*, *28*), unless the planet-induced density waves are driven by a massive companion at large disk radii exterior to the spirals (*6*), of which we see no evidence in the Elias 2-27 system.

Alternatively, gravitational instabilities (GIs) can also excite spiral density waves with contrasts in density and temperature that are similar to the observed contrasts in NW and SE. A high mass accretion rate, on the order of 10^{-6} to $10^{-7}\,M_{\odot}$ year^{-1} (*29*), coupled with a large disk-to-star mass ratio of at least $M_{\rm disk}/M_{\rm star} \approx 0.5$ (*3*) are required to induce the "grand design" symmetric spiral arms observed in Elias 2-27. Although the mass accretion rate of the star is high (*25*), even in the most optimistic case the disk-to-star mass ratio is $M_{\rm disk}/M_{\rm star} \approx 0.3$, limiting the possibility of GI acting alone. Additionally, simulations of disks undergoing GI generally cannot maintain spiral arms at radii larger than 100 AU because the disk begins to fragment at large radii (*2*, *3*, *29*–*31*). A possibility to avoid fragmentation in the GI scenario is that the Elias 2-27 disk is in a marginally unstable state (*32*)—for example, supported by external irradiation or sustained by an envelope that is feeding mass to the outer disk. However, no evidence for a massive envelope is found in the infrared SED of this object (*20*, *21*), making the possibility of a marginally unstable disk unlikely.

A combination of PDI and GI mechanisms acting together (*5*) could be another alternative to explain the high degree of symmetry of the arms in both contrast and location, the presence of both arms out to large disk radii, together with the gap in the disk located at 70 AU. However, this scenario also requires a high-mass planet (*5*), whose effect in the disk structure should be discernable as a larger and deeper gap than the one constrained in this work.

The observed structure in Fig. 1 delineates two symmetric trailing spiral arms, NW and SE, whose low optical depth enables material to be traced in the disk midplane. Together with the measured contrast values of at least 1.3 to 2.5 in the spiral arms, these results imply that NW and SE are tracing density and/or temperature enhancements at the disk midplane, which are arranged into two "grand design" symmetric spiral arms. Given the disk differential rotation (similar to the case of spiral galaxies), if the observed spirals were material arms rotating at the disk Keplerian velocity, then the inner part of the spiral (at 100 AU) would rotate five times faster than the outer part of the arm (at 300 AU). Thus, in a time scale much shorter than the lifetime of the disk (only a few orbital periods of roughly 1000 years) these spiral arms would wind up and disappear. We conclude that instead of tracing material arms, the NW and SE spiral structures trace density and temperature enhancements owing to spiral density waves in the midplane of the Elias 2-27 disk.

Unlike the spiral features from scattered-light observations, the spiral arms detected with our millimeter-wave imaging trace structures at the midplane of the disk—where planet formation takes place—allowing us to discern the location, shape, contrast, and size of these spiral density waves at the disk midplane. These results provide a distinct benchmark for numerical simulations of spiral structure in protoplanetary disks, particularly because fragmentation of such spirals remains the only plausible formation mechanism for planets and companions at large disk radii, where core-accretion becomes inefficient (*33*). Thus, the detection of spiral features in Elias 2-27 is a first step to determine what is the dominant mechanism of planet formation at different locations in the disk.

REFERENCES AND NOTES

1. Z. Zhu, R. Dong, J. M. Stone, R. R. Rafikov, *Astrophys. J.* **813**, 88 (2015).
2. K. M. Kratter, G. Lodato, http://arxiv.org/abs/1603.01280 (2016).
3. R. Dong, C. Hall, K. Rice, E. Chiang, *Astrophys. J.* **812**, L32 (2015).
4. M. Flock *et al.*, *Astron. Astrophys.* **574**, A68 (2015).
5. A. Pohl *et al.*, *Mon. Not. R. Astron. Soc.* **453**, 1768–1778 (2015).
6. R. Dong, Z. Zhu, R. R. Rafikov, J. M. Stone, *Astrophys. J.* **809**, L5 (2015).
7. G. Dipierro, G. Lodato, L. Testi, I. de Gregorio Monsalvo, *Mon. Not. R. Astron. Soc.* **444**, 1919–1929 (2014).
8. M. Fukagawa *et al.*, *Astrophys. J.* **636**, L153–L156 (2006).
9. J. Hashimoto *et al.*, *Astrophys. J.* **729**, L17 (2011).
10. S. P. Quanz *et al.*, *Astrophys. J.* **738**, 23 (2011).
11. T. Muto *et al.*, *Astrophys. J.* **748**, L22 (2012).
12. C. A. Grady *et al.*, *Astrophys. J.* **762**, 48 (2013).
13. M. Benisty *et al.*, *Astron. Astrophys.* **578**, L6 (2015).
14. V. Christiaens, S. Casassus, S. Perez, G. van der Plas, F. Ménard, *Astrophys. J.* **785**, L12 (2014).
15. Y. W. Tang *et al.*, *Astron. Astrophys.* **547**, A84 (2012).
16. A. Juhász *et al.*, *Mon. Not. R. Astron. Soc.* **451**, 1147–1157 (2015).
17. Materials and methods are available as supplementary materials on *Science* Online.
18. The star is also known as GSS 39, VSSG 28, GY116, and/or BKLT J162645.242309.
19. E. E. Mamajek, *Astron. Nachr.* **329**, 10–14 (2008).
20. S. M. Andrews, D. J. Wilner, A. M. Hughes, C. Qi, C. P. Dullemond, *Astrophys. J.* **700**, 1502–1523 (2009).
21. N. J. Evans II *et al.*, *Astrophys. J. Suppl. Ser.* **181**, 321–350 (2009).
22. A. Natta, L. Testi, S. Randich, *Astron. Astrophys.* **452**, 245–252 (2006).
23. A. Isella, J. M. Carpenter, A. I. Sargent, *Astrophys. J.* **701**, 260–282 (2009).
24. L. Ricci, L. Testi, A. Natta, K. J. Brooks, *Astron. Astrophys.* **521**, A66 (2010).
25. J. R. Najita, S. M. Andrews, J. Muzerolle, *Mon. Not. R. Astron. Soc.* **450**, 3559–3567 (2015).
26. C. P. Dullemond, RADMC-3D: A multi-purpose radiative transfer tool. *Astrophysics Source Code Library*, record ascl:1202.015 (2012).
27. J. Fung, R. Dong, *Astrophys. J.* **815**, L21 (2015).
28. J. Bae, Z. Zhu, L. Hartmann, *Astrophys. J.* **819**, 134 (2016).
29. C. Hall *et al.*, *Mon. Not. R. Astron. Soc.* **458**, 306–318 (2016).
30. C. J. Clarke, *Mon. Not. R. Astron. Soc.* **396**, 1066–1074 (2009).
31. P. Cossins, G. Lodato, L. Testi, *Mon. Not. R. Astron. Soc.* **407**, 181–188 (2010).
32. G. Bertin, G. Lodato, *Astron. Astrophys.* **350**, 694–704 (1999).
33. K. Rice, *Publ. Astron. Soc. Aust.* **33**, e012 (2016).

ACKNOWLEDGMENTS

We thank L. Loinard for useful discussions. L.M.P. acknowledges support from the Alexander von Humboldt Foundation. A.I. acknowledges support from NSF award AST-1109334/1535809 and from the NASA Origins of Solar Systems program through award NNX14AD26G. A.I.S. is partially supported by NSF grant AST 1140063. The National Radio Astronomy Observatory (NRAO) is a facility of the National Science Foundation (NSF) operated under cooperative agreement by Associated Universities Inc. (AUI). This paper makes use of the following ALMA data: ADS/JAO.ALMA#2013.1.00498.S, which can be obtained from the ALMA Science Data Archive, https://almascience.nrao.edu/alma-data (raw format) and from https://safe.nrao.edu/evla/disks/elias2-27 in the calibrated fits format used for analysis here. ALMA is a partnership of the European Southern Observatory (ESO) (representing its member states), NSF (USA) and the National Institute of Natural Sciences (Japan), together with the National Research Council (Canada), National Science Council and Academia Sinica's Institute of Astronomy and Astrophysics (Taiwan), and the Korea Astronomy and Space Science Institute (Republic of Korea), in cooperation with the Republic of Chile. The Joint ALMA Observatory is operated by ESO, AUI/NRAO, and the National Astronomical Observatory of Japan. Part of this research was carried out at the Jet Propulsion Laboratory, California Institute of Technology, under a contract with NASA.

SUPPLEMENTARY MATERIALS

www.sciencemag.org/content/353/6307/1519/suppl/DC1
Materials and Methods
Figs. S1 to S8
References (*34*–*49*)

6 April 2016; accepted 5 September 2016
10.1126/science.aaf8296

Downloaded from http://science.sciencemag.org/ on October 7, 2016

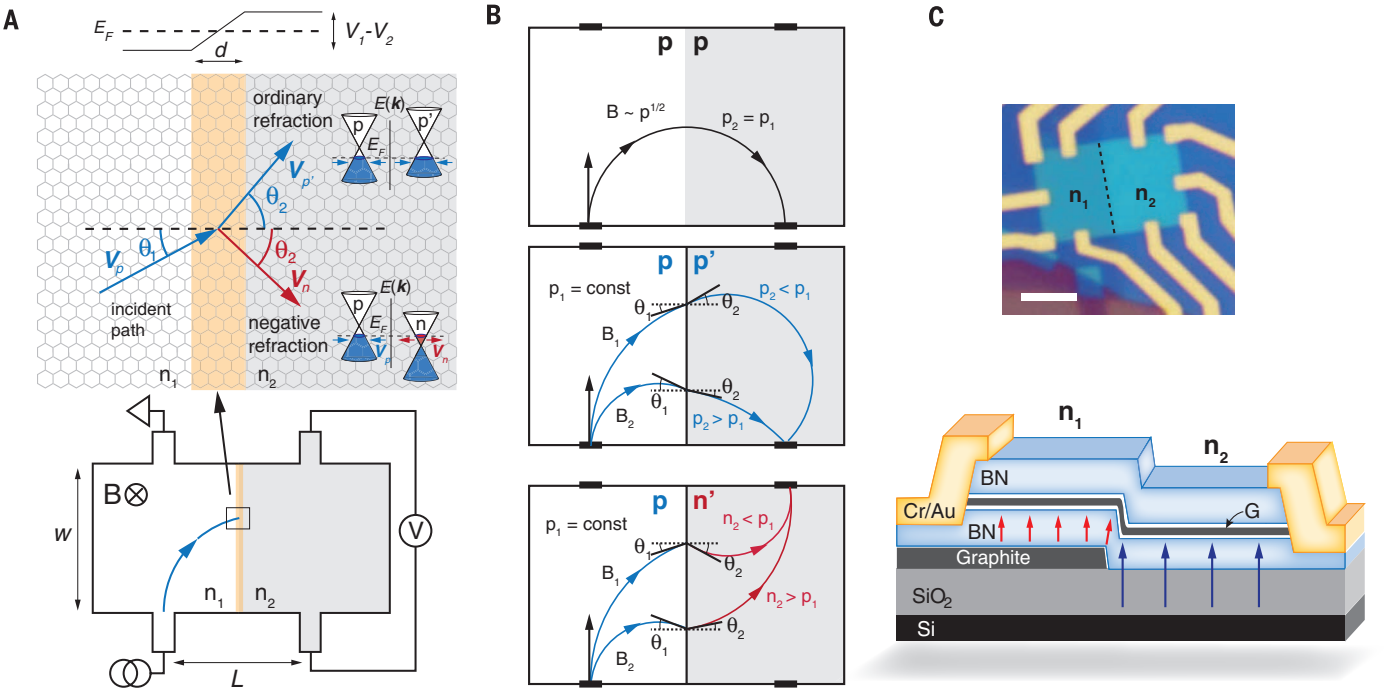

Fig. 1. Electron refraction. (**A**) A transverse magnetic field is used to focus electrons onto a split-gate junction at variable incident angles. The cyclotron radius, determined by the magnetic field and Fermi momentum (or related carrier density), determines the incidence angle. The density difference across the boundary, induced by the two gate voltages, determines the refraction angle. (**B**) A resonant path is shown for three example scenarios corresponding to p-p (equal hole density), p-p′ (unequal hole density), and p-n′ (unequal hole-electron densities). In our measurement scheme, density n_1 is fixed, whereas B and n_2 are varied. (**C**) Optical image (top) anmd cartoon schematic (bottom) of split-gate device. A naturally cleaved graphite edge is used to define an atomically smooth electrostatic boundary. Scale bar, 5 μm.

both the fundamental resonance and multiple higher-order resonant peaks appear. The resonance paths can not be fit to a simple $B \sim \sqrt{n}$ dependence (fig. S4), with the most notable deviation a pronounced kink in the second-order resonance. For positive Si gate values (p-n′ configuration), only the lowest-order resonance mode is observed, with all higher orders apparently suppressed. The resonance peak is opposite in sign compared with the p-p′ case. This is a direct signature of carrier focusing to the upper voltage terminal.

A detailed simulation of electron trajectories using a semiclassical Billiard model (*34*, *35*) was performed and compared to experiment (*32*). In this model, electrons are injected from the source at randomly distributed angles, weighted by a normal distribution of standard deviation $\sigma_{inj} = \pi/15$. By following their cyclotron trajectories across the junction (junction roughness is not included in the model), the probabilities of reaching the voltage probes are calculated. Transmission across the junction is modeled assuming the electronic Snell's law and momentum filtering (*20*, *25*). Figure 2B shows the difference in probability between the two voltage leads from our simulation using identical conditions as the experiment data in Fig. 2A. The simulation matches well with the general features of our experimental data for both p-p′ and p-n′ cases, reproducing the trajectory of all higher-order resonances in the p-p′ condition, as well as the existence of only a single mode, with opposite sign for the p-n′ case. Simulation reveals that the kink in the p-p′ case results from electrons hitting the edge of device at the junction (fig. S9). For p-n′, only the lowest order is observed as the number of electrons reaching the upper electrode reduces exponentially owing to a filtering effect every time electrons cross the p-n junction (*18*, *27*). There is some discrepancy in the higher-order p-p′ resonances between experiment (Fig. 2A) and simulation (Fig. 2B). We believe that this is caused by the uncertainty in the fabricated device geometry (~50 nm), finite contact width (~300 nm), and edge roughness (fig. S11), all of which become increasingly important as the cyclotron radius approaches a similar length scale.

In both the experimental and simulated data sets, the trajectory of the lowest-order resonance is well captured by our geometric model (dashed lines in Fig. 2, A and B). In Fig. 2D, the peak position is shown as a function of B and n_2 for both p-p′ (red circles) and p-n′ (blue circles). Also plotted are similar data points acquired by synchronizing the gates to maintain matched carrier density, giving the trajectory of the p-p (green circles) and n-n (yellow circles) response (see fig. S5) for the magnetic focusing in the matched density regime). The theoretical resonant peak positions calculated from the geometric model are shown as solid and dashed lines. Excellent agreement is found between the peak positions and the theoretical curves for all four cases. In generating the theoretical curves, we use as inputs only the sample geometry (length $L = 4.05$ μm and width $W = 3.95$ μm) and the gate efficiencies as extracted from Hall effect measurements (*32*), so that effectively there are no free parameters. We have repeated this measurement with three devices of varying sizes and with various gate configurations, all giving similar results (fig. S6). For any combination of B, n_1, and n_2, the device geometry dictates the intersection of the electron trajectory with the junction. For each point along the first-order resonant peak in Fig. 2A, we can therefore deduce the angle between the charge-carrier trajectory and the boundary normal in each region. In Fig. 2E, the corresponding values of $k_i \sin(\theta_i)$ for each region are plotted. The data show a linear relation with unity slope, confirming the expected Snell's law relation for electrons. For the case of opposite carrier type, the relation shows a negative unity slope, unambiguously confirming negative refraction.

Because the points along the resonance mode can be correlated with the incidence angle, comparing the peak intensity at each point provides a measure of the angular-dependent transmission coefficient across the junction. The transmission probability across a p-n junction is theoretically determined by a chiral tunneling process between

Downloaded from http://science.sciencemag.org/ on October 7, 2016

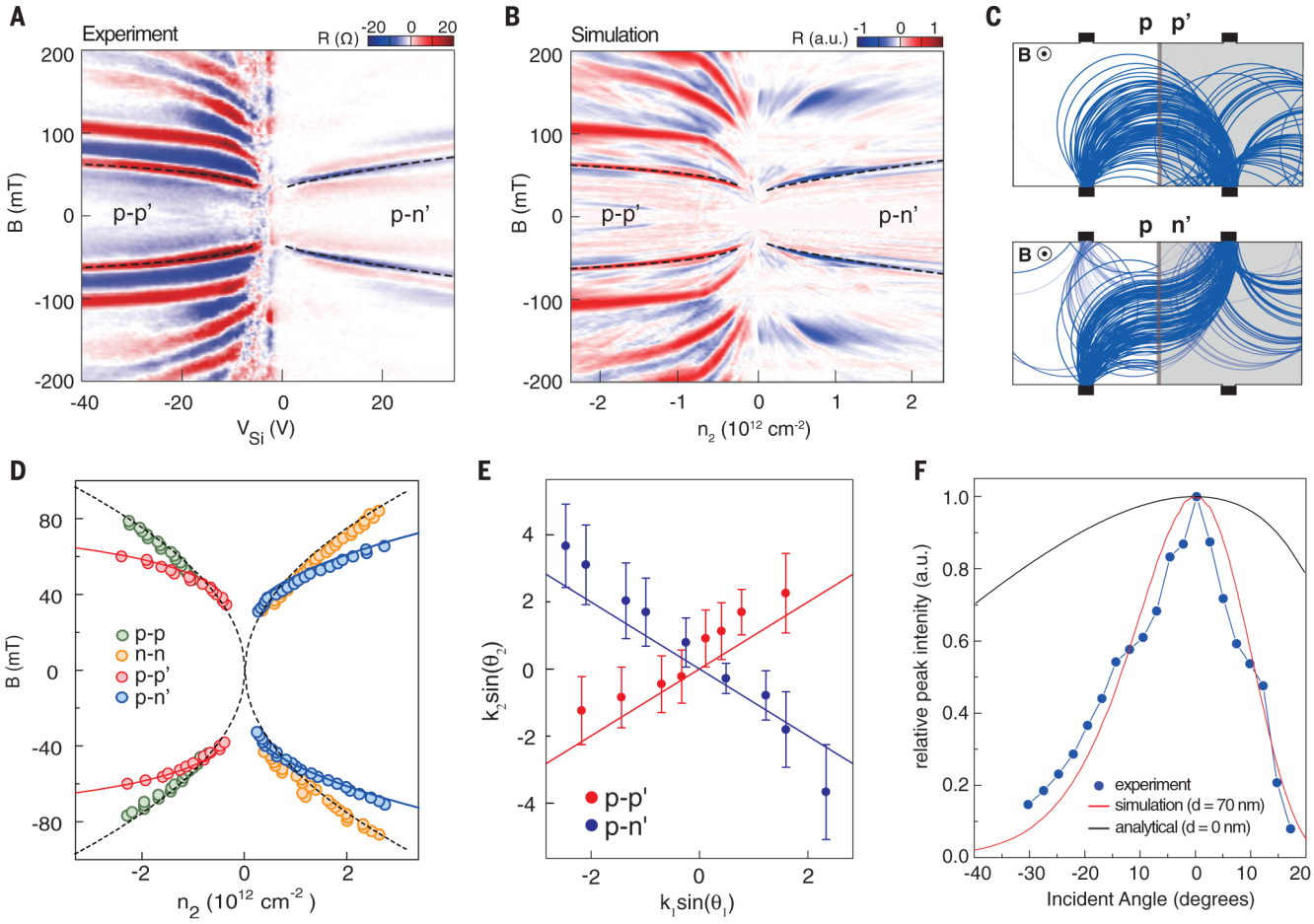

Fig. 2. Snell's law for electrons. (**A**) Resistance parallel to the junction at 1.7 K (corresponding to the measurement configuration shown in Fig. 1B) versus magnetic field and silicon gate V_{Si}. The graphite gate region is fixed to constant p-type carrier density (V_G = –1 V). (**B**) Simulation of the experimental data in (A), from ray tracing paths. The horizontal axis in (A) and (B) span the same range in carrier density. Representative resonant electron trajectories are shown in (**C**) for a p-p′ (top) and p-n′ (bottom) junction. (**D**) Position of the peak plotted as B versus n_2 from the lowest-order resonance modes. p-p′ and p-n′ data points are taken from (A). p-p and n-n data points are determined from a similar map in which the gates are synchronized to maintain a matched density (fig. S5). Dashed line represents the theoretical resonance condition for graphene with matched density (i.e., no junction). Solid red line and blue lines are the theoretical curves deduced from our geometric model, including refraction, for p-p′ and p-n′ junctions, respectively. (**E**) Snell's law parameters calculated from the peak points. (**F**) Transmission intensity versus incident angle. Blue circles correspond to the normalized peak resistance values extracted from (A). Red line is the normalized intensity from simulation for a device with a graded junction of width 70 nm. Black line is the theoretical angle dependence for an abrupt (d = 0 nm) junction.

the bands and depends strongly on both the incidence angle and effective junction width (*20*, *25*, *36*). For a symmetrically biased junction, the transmission probability is given by (*20*)

$$T \sim e^{-\pi k_F d \sin^2\theta} \quad (1)$$

where θ is the incident and refracted angle, k_F is the graphene Fermi wave vector on two sides, and d is the junction width. In Fig. 2F, the normalized peak intensity for the p-n′ resonance curve is plotted versus incident angle, with the blue circles and solid red line deduced from the experimental and simulated data sets, respectively. In our simulation, the transmission probability for each electron trajectory at the boundary was calculated using a more generalized form of Eq. 1 that allows for asymmetric bias (*25*) [for more detail, see section 1.2 in (*32*)]. We compared experimental results with simulated responses for varying junction widths (fig. S13A), finding excellent agreement for d = 70 nm (Fig. 2F). This is consistent with our device geometry, where we anticipate a junction width on the order of 60 nm by electrostatic modeling (fig. S14). Various σ_{inj} were also tested in our simulation, but no dependence was found (fig. S15). Our results provide strong experimental support for an angle-dependent transmission coefficient given by Eq. 1, which can be viewed as the electron equivalent of the Fresnel equations in optics, relating the transmitted and reflected probability intensities. Our findings further demonstrate that wide junctions result in selective collimation (*17*, *20*, *23*, *26*) of the electron beam compared with abrupt junctions with zero width (solid black line in Fig. 2F).

A striking consequence of negative refraction in graphene is Veselago lensing, in which a planar p-n′ junction focuses diverging electrons (*5*). Recent transport measurements suggest evidence of this effect (*37*), but the response is weak, appearing in the signal derivative. Good agreement between our simulation and measurement for magnetic focusing allows us to use the same model to revisit zero-field focusing across p-n′ junctions. In Fig. 3, the transmission coefficient for our device is calculated from simulation for varying junction widths d. We find that, owing to the strong reflection of non-normally incident electrons, the transmission decays rapidly with increasing d, and, indeed, to realize transmission of 50% compared with an abrupt junction requires the d to be less than 5 nm. This experimental constraint provides one explanation for why Veselago-type lensing has been difficult to achieve in previous devices and suggests that scaling the p-n′ junction width to the few-nm limit is an important criteria for realizing electron optics based on negative refraction in graphene.

Downloaded from http://science.sciencemag.org/ on October 7, 2016

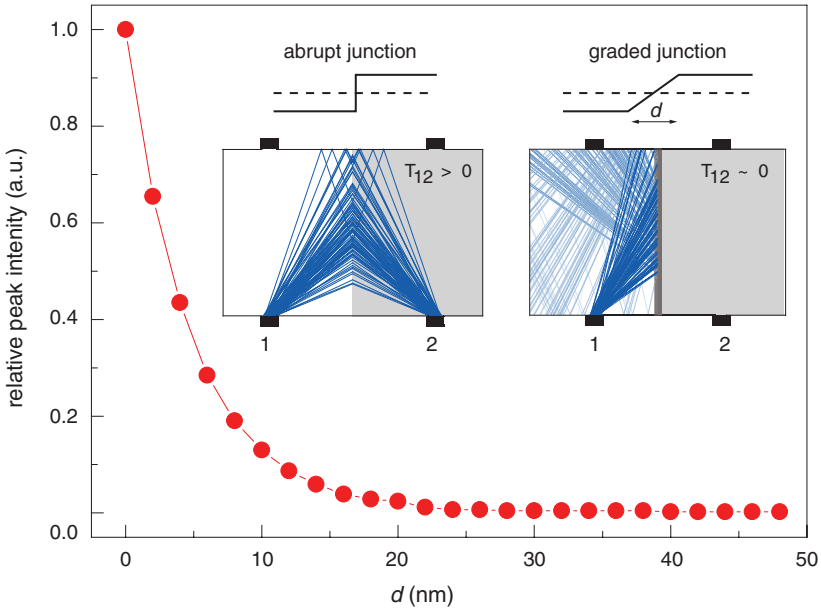

Fig. 3. Simulation of Veselago lensing. Transmission coefficient for electrons focused across a p-n junction. Main panel shows the variation in transmission probability versus junction width *d*, determined from simulation. Diverging electrons across a p-n junction theoretically converge to an equidistant point owing to negative refraction. For a graded junction the majority of the electrons are reflected, explaining why Veselago focusing is not observed. Inset shows representative simulated electron trajectories for an abrupt (left) and graded (right) junction.

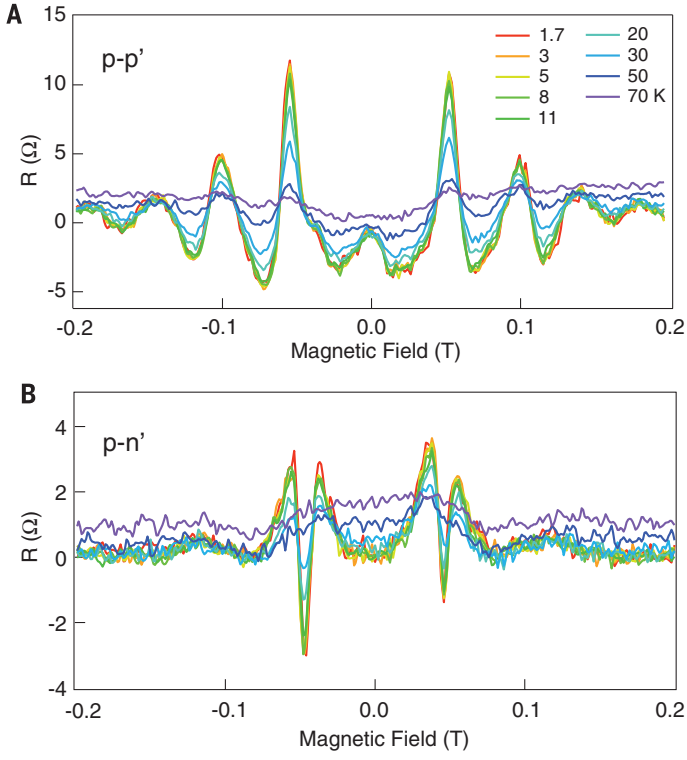

Fig. 4. Temperature dependence. (**A**) and (**B**) show the temperature dependence of p-p′ and p-n′ resonance peaks. Data correspond to a cut through Fig. 2A along a fixed value of V_{Si}.

Finally, owing to the interest in electron focusing for technological applications, we consider temperature-dependent effects. Figure 4, A and B, shows the height of the resonant peaks as a function of magnetic field at various temperatures for p-p′ and p-n′ cases, respectively. It is observed that the peak signal vanishes at around 70 K, coinciding with the temperature at which the graphene mean free path becomes comparable to the resonant path length (~7 μm) in our devices (*33*). At room temperature, graphene remains ballistic over length scales in excess of 1 μm (*33*), making it feasible to realize electron optics-based devices that operate under ambient conditions.

REFERENCES AND NOTES

1. H. van Houten, C. Beenakker, *Confined Electrons and Photons* (Springer, 1995), pp. 269–303.
2. D. Dragoman, M. Dragoman, *Prog. Quantum Electron.* **23**, 131–188 (1999).
3. J. Spector, H. L. Stormer, K. W. Baldwin, L. N. Pfeiffer, K. W. West, *Appl. Phys. Lett.* **56**, 1290 (1990).
4. U. Sivan, M. Heiblum, C. P. Umbach, H. Shtrikman, *Phys. Rev. B* **41**, 7937–7940 (1990).
5. V. V. Cheianov, V. Fal'ko, B. L. Altshuler, *Science* **315**, 1252–1255 (2007).
6. C.-H. Park, Y.-W. Son, L. Yang, M. L. Cohen, S. G. Louie, *Nano Lett.* **8**, 2920–2924 (2008).
7. M. S. Jang, H. Kim, Y.-W. Son, H. A. Atwater, W. A. Goddard 3rd, *Proc. Natl. Acad. Sci. U.S.A.* **110**, 8786–8789 (2013).
8. Q. Wilmart *et al.*, *2D Materials* **1**, 011006 (2014).
9. P. Rickhaus, P. Makk, M.-H. Liu, K. Richter, C. Schönenberger, *Appl. Phys. Lett.* **107**, 251901 (2015).
10. V. G. Veselago, *Sov. Phys. Usp.* **10**, 509–514 (1968).
11. V. M. Shalaev, *Nat. Photonics* **1**, 41–48 (2007).
12. J. B. Pendry, *Phys. Rev. Lett.* **85**, 3966–3969 (2000).
13. R. A. Shelby, D. R. Smith, S. Schultz, *Science* **292**, 77–79 (2001).
14. N. Fang, H. Lee, C. Sun, X. Zhang, *Science* **308**, 534–537 (2005).
15. D. Schurig *et al.*, *Science* **314**, 977–980 (2006).
16. J. R. Williams, T. Low, M. S. Lundstrom, C. M. Marcus, *Nat. Nanotechnol.* **6**, 222–225 (2011).
17. P. Rickhaus *et al.*, *Nat. Commun.* **4**, 2342 (2013).
18. T. Taychatanapat *et al.*, *Nat. Commun.* **6**, 6093 (2015).
19. C. R. Dean *et al.*, *Nat. Nanotechnol.* **5**, 722–726 (2010).
20. V. V. Cheianov, V. I. Fal'ko, *Phys. Rev. B* **74**, 041403 (2006).
21. B. Huard *et al.*, *Phys. Rev. Lett.* **98**, 236803 (2007).
22. R. V. Gorbachev, A. S. Mayorov, A. K. Savchenko, D. W. Horsell, F. Guinea, *Nano Lett.* **8**, 1995–1999 (2008).
23. A. F. Young, P. Kim, *Nat. Phys.* **5**, 222–226 (2009).
24. N. Stander, B. Huard, D. Goldhaber-Gordon, *Phys. Rev. Lett.* **102**, 026807 (2009).
25. R. N. Sajjad, S. Sutar, J. U. Lee, A. W. Ghosh, *Phys. Rev. B* **86**, 155412 (2012).
26. A. L. Grushina, D.-K. Ki, A. F. Morpurgo, *Appl. Phys. Lett.* **102**, 223102 (2013).
27. P. Rickhaus *et al.*, *Nat. Commun.* **6**, 6470 (2015).
28. M. A. Topinka *et al.*, *Nature* **410**, 183–186 (2001).
29. K. E. Aidala *et al.*, *Nat. Phys.* **3**, 464–468 (2007).
30. J. Baringhaus, A. Stöhr, S. Forti, U. Starke, C. Tegenkamp, *Sci. Rep.* **5**, 9955 (2015).
31. T. Taychatanapat, K. Watanabe, T. Taniguchi, P. Jarillo-Herrero, *Nat. Phys.* **9**, 225–229 (2013).
32. Supplementary materials are available on *Science* Online.
33. L. Wang *et al.*, *Science* **342**, 614–617 (2013).
34. C. W. J. Beenakker, H. van Houten, *Phys. Rev. Lett.* **63**, 1857–1860 (1989).
35. S. P. Milovanović, M. Ramezani Masir, F. M. Peeters, *J. Appl. Phys.* **115**, 043719 (2014).
36. J. Cayssol, B. Huard, D. Goldhaber-Gordon, *Phys. Rev. B* **79**, 075428 (2009).
37. G.-H. Lee, G.-H. Park, H.-J. Lee, *Nat. Phys.* **11**, 925–929 (2015).

ACKNOWLEDGMENTS

We thank P. Kim, A. Pasupathy, and J.-D. Pillet for helpful discussion, and R. Ribeiro for fabrication assistance. This work is supported by the Semiconductor Research Corporation's NRI Center for Institute for Nanoelectronics Discovery and Exploration (INDEX).

SUPPLEMENTARY MATERIALS

www.sciencemag.org/content/353/6307/1522/suppl/DC1
Materials and Methods
Figs. S1 to S16
References

25 February 2016; accepted 6 September 2016
10.1126/science.aaf5481

Downloaded from http://science.sciencemag.org/ on October 7, 2016

GRAPHENE

Ballistic miniband conduction in a graphene superlattice

Menyoung Lee,[1] John R. Wallbank,[2] Patrick Gallagher,[1] Kenji Watanabe,[3] Takashi Taniguchi,[3] Vladimir I. Fal'ko,[2,4] David Goldhaber-Gordon[1]*

Rational design of long-period artificial lattices yields effects unavailable in simple solids. The moiré pattern in highly aligned graphene/hexagonal boron nitride (h-BN) heterostructures is a lateral superlattice with high electron mobility and an unusual electronic dispersion whose miniband edges and saddle points can be reached by electrostatic gating. We investigated the dynamics of electrons in moiré minibands by measuring ballistic transport between adjacent local contacts in a magnetic field, known as the transverse electron focusing effect. At low temperatures, we observed caustics of skipping orbits extending over hundreds of superlattice periods, reversals of the cyclotron revolution for successive minibands, and breakdown of cyclotron motion near van Hove singularities. At high temperatures, electron-electron collisions suppress focusing. Probing such miniband conduction properties is a necessity for engineering novel transport behaviors in superlattice devices.

In solids, the quantum nature of electrons generates band structure, which controls conduction and optical properties. Similarly, longer-period superlattices generate minibands that disperse at a finer energy scale over a reduced Brillouin zone, enabling phenomena such as negative differential conductance and Bloch oscillations (*1*–*3*). However, fabricating long-range periodic patterns that strongly modulate the potential to form well-separated minibands without undermining the material quality and electron coherence remains challenging. Most experiments on laterally patterned semiconductor heterostructures have revealed classical commensurability effects (*4*–*6*), which do not require well-formed and separated minibands. Despite evidence for Fermi surface reconstruction in a patterned superlattice, details of Fermi surfaces were obscured by poor separation between minibands and consequent magnetic breakdown across weakly avoided crossings (*7*).

The arrival of high-quality graphene/h-BN van der Waals heterostructures with misalignment angle below 1° (*8*, *9*) has drastically changed the situation. In such systems, the periodic potential for electrons in graphene is imposed by the hexagonal moiré pattern generated by the incommensurability and misalignment between the two crystals (*10*–*12*). Formation of minibands for Dirac electrons has been demonstrated by scanning tunneling (*13*), capacitance (*14*), and optical (*15*) spectroscopies, as well as magnetotransport (*16*–*19*). These studies have elucidated the electronic structure known as the Hofstadter butterfly, which emerges in a quantizing magnetic field (*20*). By contrast, a small magnetic field may be treated semiclassically. Then the connection between the miniband dispersion $\varepsilon(\mathbf{k})$ and transport properties is established by the equations of motion for an electron in an out-of-plane magnetic field $\mathbf{B} = B\hat{z}$,

$$\hbar\mathbf{v} = \frac{\partial\varepsilon}{\partial\mathbf{k}}, \hbar\dot{\mathbf{k}} = -e\mathbf{E} + eB\hat{z}\times\mathbf{v} \qquad (1)$$

where e is the charge on the electron, $\hbar$ is the Planck constant divided by 2π, and the relation between carrier velocity $\mathbf{v}$ and momentum $\hbar\mathbf{k}$ is approximately $\mathbf{v} = v\mathbf{k}/k$ ($v \approx 10^6$ m/s) close to the Dirac point of graphene's spectrum (*10*, *11*, *13*, *14*).

The shape of the cyclotron orbit in a two-dimensional (2D) metal is a 90° rotation of the shape of the Fermi surface, and the carrier revolves along it clockwise or counterclockwise. Electron trajectories near the boundary of a metal open into skipping orbits (*21*), which drift in the direction determined by the effective charge of the carrier. These skipping orbits bunch along caustics (*22*–*27*), leading to the transverse electron focusing (TEF) effect (*22*, *23*). Experimentally, TEF takes place when the magnetic field is tuned such that caustics of skipping orbits, emanating from an emitter E, end up at a collector C, located at position $x = L$ along the boundary. Then a voltage V_C is induced at C, proportional to the current I_E injected into E. Figure 1B illustrates skipping orbits and caustics in a material with an isotropic Fermi surface, such as unperturbed graphene near the Dirac point, where TEF occurs for $B = B_j \equiv 2j\hbar k_F/\pm eL$ (for j = 1, 2, …). An equidistant series of peaks (oscillations) appears in the focusing "spectrum"—the nonlocal magnetoresistance $V_C/I_E(B)$ (Fig. 1C, lower trace), from which the Fermi momentum $\hbar k_F$ and the sign of effective charge $\pm e$ can be inferred. TEF was initially used to study the Fermi surfaces of bulk metals (*22*, *28*) and was later extended to 2D systems (*23*), including graphene (*29*).

Here, we report the observation of TEF in a moiré superlattice at the interface between graphene and h-BN in a van der Waals heterostructure (from top to bottom) h-BN/graphene/h-BN/bilayer graphene assembled on an SiO_2 substrate. One of the h-BN layers (we do not know which) is aligned with graphene to better than 1°, forming a moiré pattern with a period of 14 nm (*30*). We use the bilayer graphene as an electrostatic gate, tuning electron density in the superlattice by applying voltage V_g to it. The device (Fig. 1A) has three etched local contacts along the linear sample boundary. Two other ohmic contacts are grounded and act as absorbers. We measure the multiterminal, nonlocal resistance $(V_M - V_R)/I_L$ at our base temperature $T = T_{base} = 1.55$ K. Figure 2B is the resulting map of $(V_M - V_R)/I_L$ as a function of B and V_g, exhibiting TEF spectra and their evolution as a function of electron density n. When the Fermi level in graphene is close to the Dirac point at $V_g = -0.4$ V, the superlattice spectrum is almost isotropic, and $k_F = \sqrt{\pi|n|}$. Hence, the TEF spectra show TEF oscillations with peaks at $B_j = (2j\hbar/\pm eL)\sqrt{\pi|n|}$ (dashed curves in Fig. 2B) as in unperturbed graphene (*29*). The observation of TEF confirms that electrons travel ballistically from the emitter to the collector. The visibility of as many as eight focusing peaks (Figs. 1C and 2B) shows that carrier reflection at the boundary is mostly specular: Each peak is lower than the last by a factor of the probability of diffuse scattering (*22*). Quantum effects are suppressed because the thermal length $\hbar w_F/kT$ is shorter than the emitter-collector separation L.

At higher densities approaching four electrons (or holes) per moiré unit cell, the Fermi level is near the first minibands' outer edges, and TEF spectra reflect the modification of electronic states by the superlattice potential. A candidate miniband structure from the model family proposed in (*12*) is shown in Fig. 2A with relevant minibands labeled. Carrier dynamics in the form of skipping orbits and caustics are represented using ensembles of simulated electron trajectories in Fig. 3. The map of measured TEF spectra (Fig. 2B) matches the theoretically simulated spectra (Fig. 2C) obtained by applying Eq. 1 to the electrons emitted into the minibands of Fig. 2A from a local emitter at the sample edge (*30*).

In addition to TEF of electrons in C1 and holes in V1, both theory and experiment show focusing of holes in C2 and electrons in V2: The carrier charge is reversed relative to the corresponding (conduction or valence) band of graphene. For $V_g > V_c^3$, where V_c^3 is the lower band edge of C3, the electron-like pocket of C3 overlaps in energy with the holelike pocket of C2, leading to TEF oscillations for both signs of B. TEF oscillations abruptly terminate at gate voltage values V_v^1, V_c^1, V_v^2, and V_c^2, which coincide with the passing of the Fermi level across the saddle-point van Hove singularities (VHSs) at which the constant energy contour of the miniband dispersion percolates across all repeated

[1]Department of Physics and Geballe Laboratory for Advanced Materials, Stanford University, Stanford, CA 94305, USA. [2]National Graphene Institute, University of Manchester, Manchester M13 9PL, UK. [3]National Institute for Materials Science, 1-1 Namiki, Tsukuba 305-0044, Japan. [4]School of Physics and Astronomy, University of Manchester, Manchester M13 9PL, UK.
*Corresponding author. Email: goldhaber-gordon@stanford.edu

Downloaded from http://science.sciencemag.org/ on October 7, 2016

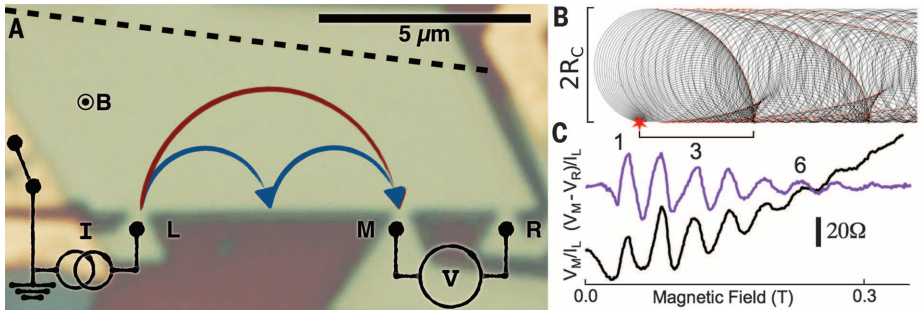

Fig. 1. Experimental concept. (**A**) Schematic of the experiment overlaid on a photo of the device. The h-BN/graphene/h-BN/bilayer graphene heterostructure is shown in green, the SiO_2 substrate is in purple, and the dashed line denotes the upper boundary of the graphene flake. In the electrical measurement configuration applied to obtain the data in Fig. 2B, the two leftmost contacts are grounded to act as absorbers. We inject current into the left local contact *L* and measure the voltage difference between two local contacts, *M* and *R*. Arrows depict skipping orbits a hole would take if injected at normal incidence with $B = B_1 \equiv 2\hbar k_F/eL$ (red) or $B_2 \equiv 4\hbar k_F/eL$ (blue). (**B**) Ensemble of simulated skipping orbits emanating from an emitter (red star). Electron trajectories bunch along caustics (red dashed curves) and focus onto an equidistant array of points at the boundary. Scale markers show the cyclotron diameter $2R_C = 2\hbar k_F/eB$. (**C**) Transverse electron focusing (TEF) spectra collected at a single voltage probe *M* [$V_M/I_L(B)$, lower trace] and differentially between voltage probes *M* and *R* [$(V_M - V_R)/I_L(B)$, upper trace], with $n = -1.1 \times 10^{12}$ cm^{-2} and $T = 1.55$ K. The first, third, and sixth focusing peaks are labeled. Taking the differential measurement of the spectrum does not shift peak positions, because the device geometry partially shields *R* from being reached by skipping orbits from *L*, such that oscillations of V_R are much weaker.

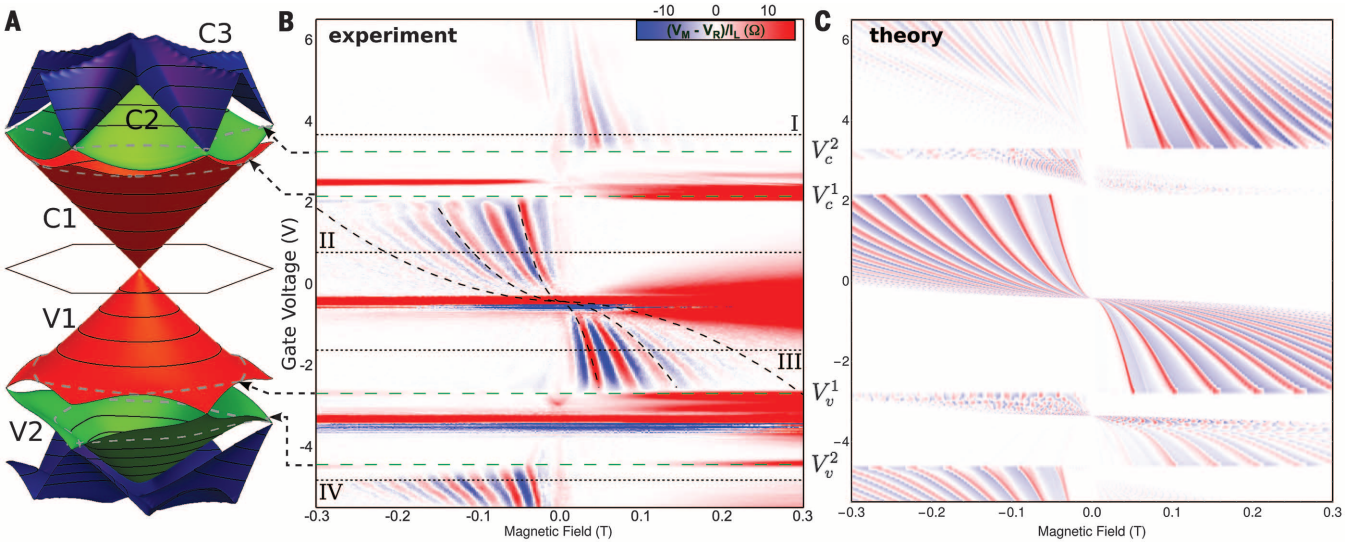

Fig. 2. TEF spectra at base temperature. (**A**) Miniband structure of the graphene/h-BN superlattice, calculated as in (*12*, *30*). Each miniband for which we observe TEF is labeled. This dispersion results from a symmetric moiré perturbation: $\varepsilon^+ = 17$ meV and $\varepsilon^- = 0$ meV; this choice gives the best match between experiment (B) and theory (C) (*30*). Equipotential contours are shown; the dashed contours are at the energy levels of saddle-point VHSs. (**B**) TEF spectra as a function of gate voltage V_g. $T = 1.55$ K. The plotted ratio $(V_M - V_R)/I_L$ is measured as depicted in Fig. 1A. Black dashed curves indicate B_1, B_3, and B_6, which are some of the peak positions expected when the Fermi level is close to the Dirac point. Green dashed lines indicate the abrupt termination of TEF caused by the breakdown of cyclotron motion at each VHS. Dashed arrows from (B) to (A) point to the energy levels (dashed contours) of the corresponding VHS; voltage values are labeled by the miniband in which the breakdown occurs (e.g., V_c^1 for the breakdown of cyclotron motion in C1). Dotted lines show selected densities (I, II, III, and IV) that place the Fermi level in minibands C2, C1, V1, and V2, respectively. (**C**) TEF spectra as a function of V_g, calculated from the dispersion in (A) and Eq. 1 (*30*).

Brillouin minizones. At these saddle points, cyclotron orbits experience an extreme variant of magnetic breakdown termed orbital switching (*31*), opening up into runaway trajectories such that electrons do not follow skipping orbits. In the ranges $V_v^2 < V_g < V_v^1$ and $V_c^1 < V_g < V_c^2$, the Fermi surface consists of small and highly anisotropic pockets just above or below the secondary Dirac points. Thus, even the theoretically calculated pattern in Fig. 2C is both weak and dense; experimental observation of these pockets is obscured because of smearing by finite emitter and collector widths and suppression by partial diffusivity of reflection from the edge.

The positions of saddle points V_v^1, V_c^1, V_v^2, and V_c^2 can be directly compared to miniband models. We tested the observed ratios $(V_v^1 - V_v^2)/(V_c^1 - V_v^1)$ and $(V_c^2 - V_c^1)/(V_c^1 - V_v^1)$ against predictions from a family of moiré superlattice models parameterized by strengths of inversion-symmetric (ε^+) and antisymmetric (ε^-) interlayer coupling between graphene carbons and the boron and nitrogen sites of h-BN (*30*, *32*). The best match to experimental data corresponds to an inversion-symmetric moiré perturbation with $\varepsilon^+ \approx 17$ meV, $\varepsilon^- \approx 0$ (fig. S2), which we used to calculate the miniband structure, electron dynamics, and TEF maps in Figs. 2 and 3. This value for ε^+ is similar to previous estimates from optical spectroscopy (*15*).

We can learn more about carrier dynamics, in particular the effect of their scattering, by examining the temperature dependence of TEF oscillations (*28*). Throughout the probed temperatures and densities, the suppression of TEF upon heating (Fig. 4A) is faster than what could be expected from merely thermal broadening of injected electron momenta, as $|k - k_F| \sim k_B T/\hbar v_F << k_F$. For quantitative analysis, we determine the area A_1 under the first ($j = 1$) focusing peak and interpret the ratio $A_1(T)/A_1(T_{base})$ as the fraction of electrons $\exp(-\pi L/2v_F\tau)$ that propagated ballistically from the emitter to the collector, along the semicircular cyclotron trajectory of length $\pi L/2$ that touches the caustic near the collector, even though the electrons scatter with a characteristic rate τ^{-1}. Figure 4B shows the temperature dependence of this effective scattering rate, extracted from the data according to the

Downloaded from http://science.sciencemag.org/ on October 7, 2016

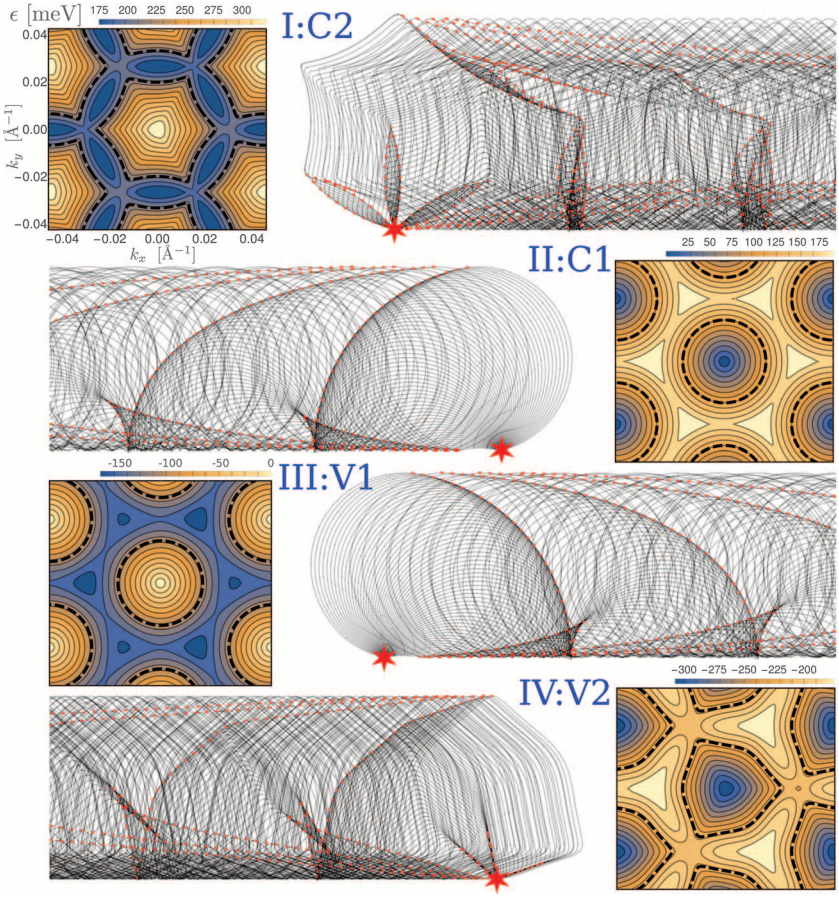

Fig. 3. Simulated skipping orbits. Representative ensembles of simulated skipping orbits emanating from an emitter (red star) at the boundary of the graphene/h-BN superlattice possessing the miniband dispersion of Fig. 2A, for selected electron densities I, II, III, and IV marked in Fig. 2B. The corresponding Fermi surfaces are in minibands C2, C1, V1, and V2, respectively, and each is drawn as a thick, dashed constant-energy contour on the color map of the dispersion. The magnetic field points out of the page, so electron-like carriers turn counterclockwise and their skipping orbits drift left, and holelike carriers do the opposite. Red dashed curves mark caustics.

formula $\tau(T)^{-1} = -2v_F/\pi L \log[A_1(T)/A_1(T_{base})]$. The experimentally observed dependence $\tau(T)^{-1} \propto T^2$ points toward an electron-electron (*e-e*) scattering mechanism for the suppression of TEF oscillations upon heating, the same mechanism responsible for the evolution of electronic transport from the ballistic to the viscous regime (*33*–*35*). Theoretical analysis of spreading of a narrow beam of electrons due to low-angle scattering processes, governed by the Thomas-Fermi–screened *e-e* interaction, shows that for $T \lesssim T_*$ (where $k_B T_* = 2v_F\sqrt{k_F/\pi L}$), the decay of TEF signal can be described by a scattering rate

$$\tau_{e-e}^{-1} \approx \frac{(k_B T)^2}{2\hbar v_F k_F} \log\left(\frac{3.6L}{w}\right) \quad (2)$$

where w is the width of the emitting and collecting contacts (*30*). Figure 4B shows the theoretical values [calculated without free parameters (*30*)] of τ_{e-e}^{-1}, including the theoretically predicted crossover to a slower scattering rate for $T > T_*$. The rate of scattering by phonons, τ_{ph}^{-1}, can be inferred from temperature-dependent sheet resistivity of similar encapsulated graphene/h-BN heterostructures (*35*, *36*) (Fig. 4B). This inferred τ_{ph}^{-1} is much lower than both the experimentally measured value of $\tau(T)^{-1}$ and the calculated value of τ_{e-e}^{-1}, so it appears that low-angle *e-e* scattering is the dominant mechanism for suppression of TEF.

The direct observation and manipulation of ballistic transport is a powerful probe of the low-energy physics of an electron system. Here, the quasiparticles propagate freely from the emitter to the collector through ballistic trajectories as long as $\pi L/2 = 10$ μm, which is 700 in dimensionless units of the superlattice period. Ballistic motion of ultracold atoms has been seen in homogeneous optical lattices as large

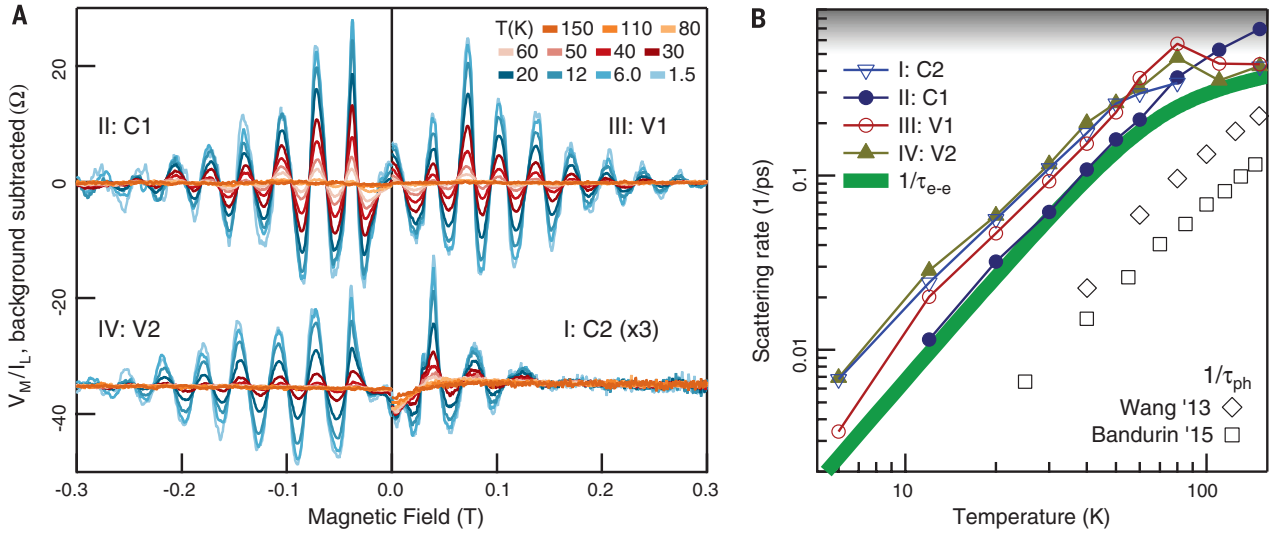

Fig. 4. Temperature dependence of TEF spectra. (**A**) $V_M/I_L(B)$ minus a smooth background (*30*), for the electron densities I, II, III, and IV (marked in Fig. 2B) and temperatures up to 150 K. Increasing the temperature suppresses TEF. (**B**) Circles and triangles denote effective scattering rates $\tau(T)^{-1}$ extracted from the amplitude of TEF oscillations in (A). The heavy green curve shows the theoretical scattering rate τ_{e-e}^{-1} related to the electron-electron interaction. Square and diamond symbols denote the rate of scattering by phonons τ_{ph}^{-1} inferred from temperature-dependent sheet resistivity reported in Bandurin *et al*. (*35*) and Wang *et al*. (*36*). The detection limit set by noise is shaded.

Downloaded from http://science.sciencemag.org/ on October 7, 2016

as 100 unit cells (*37*), but in the solid state, the mean free path of electrons in semiconductor 1D superlattices has been limited to 10 unit cells (*38*). Our experiment elucidates the key features of miniband electron dynamics in a moiré superlattice and points toward further explorations of novel transport effects. For instance, the saddle-point VHS could host exotic effects caused by enhanced electron-electron interactions (*19*, *39*), and valley-contrasting physics could be accessed by taking advantage of the severe trigonal warping of minibands (*40*). For technology, such a clear validation of the miniband conduction properties suggests that graphene/h-BN (and perhaps other moiré superlattices) may be a practical platform for devices based on miniband physics. Efficient photocurrent generation at the edge of a graphene superlattice in a magnetic field (*41*) may be caused by the skipping orbits we have observed; furthermore, THz devices such as the Bloch oscillator can benefit from the much longer scattering times in this system.

REFERENCES AND NOTES

1. L. Esaki, R. Tsu, *IBM J. Res. Develop.* **14**, 61–65 (1970).
2. L. Esaki, L. L. Chang, *Phys. Rev. Lett.* **33**, 495–498 (1974).
3. C. Waschke *et al.*, *Phys. Rev. Lett.* **70**, 3319–3322 (1993).
4. D. Weiss, K. V. Klitzing, K. Ploog, G. Weimann, *Europhys. Lett.* **8**, 179–184 (1989).
5. H. A. Carmona *et al.*, *Phys. Rev. Lett.* **74**, 3009–3012 (1995).
6. A. Sandner *et al.*, *Nano Lett.* **15**, 8402–8406 (2015).
7. C. Albrecht *et al.*, *Phys. Rev. Lett.* **83**, 2234–2237 (1999).
8. J. Xue *et al.*, *Nat. Mater.* **10**, 282–285 (2011).
9. R. Decker *et al.*, *Nano Lett.* **11**, 2291–2295 (2011).
10. C. Ortix, L. Yang, J. van den Brink, *Phys. Rev. B* **86**, 081405 (2012).
11. M. Kindermann, B. Uchoa, D. L. Miller, *Phys. Rev. B* **86**, 115415 (2012).
12. J. R. Wallbank, A. A. Patel, M. Mucha-Kruczynski, A. K. Geim, V. I. Fal'ko, *Phys. Rev. B* **87**, 245408 (2013).
13. M. Yankowitz *et al.*, *Nat. Phys.* **8**, 382–386 (2012).
14. G. L. Yu *et al.*, *Nat. Phys.* **10**, 525–529 (2014).
15. Z. Shi, P. V. Lin, T. Sasagawa, V. Dobrosavljević, D. Popović, *Nat. Phys.* **10**, 437–443 (2014).
16. L. A. Ponomarenko *et al.*, *Nature* **497**, 594–597 (2013).
17. C. R. Dean *et al.*, *Nature* **497**, 598–602 (2013).
18. B. Hunt *et al.*, *Science* **340**, 1427–1430 (2013).
19. W. Yang *et al.*, *Nano Lett.* **16**, 2387–2392 (2016).
20. D. R. Hofstadter, *Phys. Rev. B* **14**, 2239–2249 (1976).
21. N. Bohr, *Niels Bohr Collected Works* (Elsevier, 1972), vol. 1, p. 276.
22. V. S. Tsoi, *J. Exp. Theor. Phys. Lett.* **19**, 70 (1974).
23. C. W. J. Beenakker, H. van Houten, B. J. van Wees, *Europhys. Lett.* **7**, 359–364 (1988).
24. L. Oroszlány, P. Rakyta, A. Kormányos, C. J. Lambert, J. Cserti, *Phys. Rev. B* **77**, 081403 (2008).
25. T. K. Ghosh, A. De Martino, W. Häusler, L. Dell'Anna, R. Egger, *Phys. Rev. B* **77**, 081404 (2008).
26. N. Davies *et al.*, *Phys. Rev. B* **85**, 155433 (2012).
27. A. A. Patel, N. Davies, V. Cheianov, V. I. Fal'ko, *Phys. Rev. B* **86**, 081413 (2012).
28. P. C. van Son, H. van Kempen, P. Wyder, *Phys. Rev. Lett.* **58**, 1567–1570 (1987).
29. T. Taychatanapat, K. Watanabe, T. Taniguchi, P. Jarillo-Herrero, *Nat. Phys.* **9**, 225–229 (2013).
30. See supplementary materials on *Science* Online.
31. R. S. Markiewicz, *J. Phys. Condens. Matter* **6**, 3059–3072 (1994).
32. X. Chen *et al.*, *Phys. Rev. B* **89**, 075401 (2014).
33. I. Torre, A. Tomadin, A. K. Geim, M. Polini, *Phys. Rev. B* **92**, 165433 (2015).
34. A. Principi, G. Vignale, M. Carrega, M. Polini, *Phys. Rev. B* **93**, 125410 (2016).
35. D. A. Bandurin *et al.*, *Science* **351**, 1055–1058 (2016).
36. L. Wang *et al.*, *Science* **342**, 614–617 (2013).
37. U. Schneider *et al.*, *Nat. Phys.* **8**, 213–218 (2012).
38. C. Rauch, G. Strasser, M. Kast, E. Gornik, *Superlattices Microstruct.* **25**, 47–51 (1999).
39. R. Nandkishore, L. S. Levitov, A. V. Chubukov, *Nat. Phys.* **8**, 158–163 (2012).
40. J. L. Garcia-Pomar, A. Cortijo, M. Nieto-Vesperinas, *Phys. Rev. Lett.* **100**, 236801 (2008).
41. S. Wu *et al.*, *Sci. Adv.* **2**, e1600002 (2016).

ACKNOWLEDGMENTS

We thank A. L. Sharpe and G. Pan for technical assistance and W. A. Goddard, M. S. Jang, H. Kim, A. Maharaj, S. Goswami, E. J. Heller, L. S. Levitov, J. C. W. Song, and A. Benyamini for discussions. Supported by a Stanford graduate fellowship and a Samsung scholarship (M.L.) and by ERC Synergy grant Hetero2D, the EU Graphene Flagship Project, and a Lloyd Register Foundation nanotechnology grant (J.R.W. and V.I.F.). Work done at Stanford was funded in part by Air Force Office of Scientific Research award FA9550-16-1-0126 and by Gordon and Betty Moore Foundation grant GBMF3429 and was performed in part in the Stanford Nano Shared Facilities.

SUPPLEMENTARY MATERIALS

www.sciencemag.org/content/353/6307/1526/suppl/DC1
Materials and Methods
Supplementary Text
Figs. S1 to S6
References (*42*–*53*)

26 February 2016; accepted 26 August 2016
10.1126/science.aaf1095

COGNITION

Unexpected rewards induce dopamine-dependent positive emotion–like state changes in bumblebees

Clint J. Perry,* Luigi Baciadonna, Lars Chittka

Whether invertebrates exhibit positive emotion–like states and what mechanisms underlie such states remain poorly understood. We demonstrate that bumblebees exhibit dopamine-dependent positive emotion–like states across behavioral contexts. After training with one rewarding and one unrewarding cue, bees that received pretest sucrose responded in a positive manner toward ambiguous cues. In a second experiment, pretest consumption of sucrose solution resulted in a shorter time to reinitiate foraging after a simulated predator attack. These behavioral changes were abolished with topical application of the dopamine antagonist fluphenazine. Further experiments established that pretest sucrose does not simply cause bees to become more exploratory. Our findings present a new opportunity for understanding the fundamental neural elements of emotions and may alter the view of how emotion states affect decision-making in animals.

Emotions are transient subjective states, underpinned by physiological, behavioral, and cognitive phenomena, triggered by appraisal of environmental situations (*1*–*3*). Our conceptual understanding of emotions is largely based on human subjective experiences—what we "feel"—assessed directly through verbal reports. In animals, similar emotion-like states can be inferred through observable, quantifiable parameters. To ensure that the criteria of emotion-like states are met and to distinguish these from other forms of environmentally induced states, perhaps driven by learning, we must quantify the range of physiological, behavioral, and cognitive phenomena that occur in response to environmental factors, similar to those studied in humans (*4*).

The majority of work on animal emotions focuses on mammals and almost exclusively on negative emotions (*5*). The idea that invertebrates may exhibit basic forms of emotion is increasingly accepted (*6*–*8*), and given the assumed adaptive function of emotions [to coordinate the individual's cognitive and behavioral resources toward fitness-relevant priorities (*1*, *2*, *9*)], we might expect that a diversity of emotion-like states, including positive ones, exist across phyla, albeit not necessarily consciously so (*9*–*11*).

In humans, consumption of sweet snacks can induce positive emotions (*12*–*14*). Here we examine whether consuming a small amount of sucrose solution before performing a test causes bumblebees (*Bombus terrestris*) to behave in a way that is indicative of an induced positive emotion–like state.

In experiment 1.1, we used the well-established judgment bias paradigm, in which subjects associate one cue with a positive event and another cue with a negative event (*15*). Subjects in a positive emotion state tend to respond to ambiguous (intermediate) stimuli as though predicting the positive event (*4*).

We trained bees in a go/no-go task. On some trials, bees learned to enter a cylinder beneath a colored (e.g., blue) placard on one side of an arena, where they would find a 30% sucrose solution

Department of Biological and Experimental Psychology, School of Biological and Chemical Sciences, Queen Mary University of London, London E1 4NS, UK.
*Corresponding author. Email: clint.perry@qmul.ac.uk

Downloaded from http://science.sciencemag.org/ on October 7, 2016

(Fig. 1, A and B). On alternate trials, bees learned not to enter a cylinder at the opposite side of the arena under a placard of different color (e.g., green), where they would find no reward (water only). The latency from the time that bees entered the arena to the time that they entered the presented cylinder was recorded.

We then examined bees' response to ("judgment" of) ambiguous information (intermediate placard color and position; Fig. 1C). Half of the trained bees, randomly selected, received for the first time a 5-µl droplet (equivalent to <5% of stomach capacity) of 60% sucrose solution in the tunnel leading to the arena; the other half received no pretest reward. Bees that consumed sucrose solution before making a decision took less time to enter the chamber of the middle ambiguous stimulus (Fig. 1D, tables S1 and S2, and supplementary materials).

Could it be that when bees consumed the small pretest reward, rather than experiencing a positive emotion–like state, a higher expectation of subsequent reward resulted in greater exploration of novel stimuli? Previous work indicates that honeybees' foraging choices are controlled by short-term memories initiated by recently experienced rewards (*16*, *17*). However, in our study, bees tested with stimuli that were not intermediate to the trained stimuli (novel in terms of color, position, and number; experiment 1.2; Fig. 1E) exhibited no difference in choice time (Fig. 1F and table S3) or number of choices (Fig. 1G and table S4) between the two groups, indicating that pre-decision sucrose consumption did not cause a general increase in expectation of reward.

We considered whether the consumption of sucrose solution may simply make bees more excited or active, resulting in faster decisions in response to ambiguous stimuli. Thorax temperature increased after consumption of 5 µl of 60% sucrose solution (n = 72, t_{70} = 6.78, $P = 3.12 \times 10^{-9}$; experiment 2.1; fig. S1, A and B, and supplemental materials), denoting increased metabolic rate. But this did not translate to increased activity. Sucrose-receiving and control bees (n = 12 per group) showed no difference in flight time (t_{22} = 0.666, P = 0.512) or speed (t_{22} = 0.241, P = 0.812) to reach a feeder (experiment 2.2; fig. S1, C and D, and supplemental materials), and when the feeder was removed, speed during a 120-s flight also did not differ between groups (n = 24, t_{22} = −0.403, P = 0.691; experiment 2.3; fig. S1E), suggesting that unexpected rewards did not affect bees' overall activity level.

It has been argued that one characteristic of emotions across species is generalization, a property whereby an induced emotion state operates across behavioral contexts (*9*). To examine whether these behavioral results were similar across contexts, we tested whether an unanticipated reward would change bees' reaction to later aversive stimuli (experiment 3). We trained bees to forage at a feeder containing 30% sucrose solution. After training and on their next foraging trip, bees were held temporarily in the tunnel connecting the hive and arena. Bees either received an unanticipated 5-µl droplet of 60% sucrose solution or nothing (control). After a 10-s delay, a predator attack was simulated. In nature, bees are sometimes ambushed at flowers by sit-and-wait predators such as crab spiders; bees often escape after a brief struggle, allowing them to modify their subsequent behavior to cope with such threats (*18*). Mimicking such an attack, each bee was captured by a trapping mechanism, in which constant pressure was applied for 3 s by a stamp-shaped device softened with a sponge and connected to

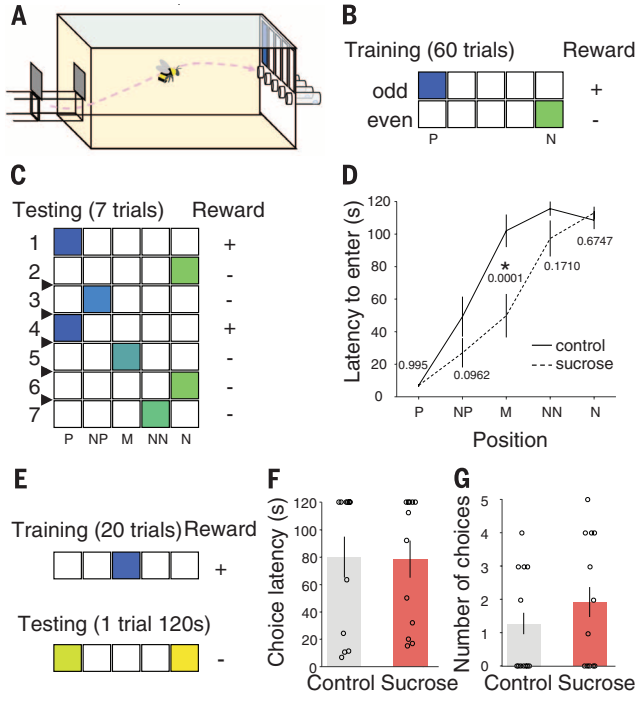

Fig. 1. Judgment bias in response to ambiguous stimuli. (**A**) Set up for experiment 1.1. (**B** and **C**) Each row shows a "bee's-eye view" of placards within the arena. Training stimuli for one of four counterbalanced orientations are shown in (B) (N, negative stimulus position, P, positive stimulus position; fig. S2). Bees (n = 24) were trained find sucrose solution in a cylinder under one placard and to avoid another. Only one cylinder was accessible in any one trial; odd trials were rewarded and even trials unrewarded. The testing procedure is shown in (C) (NP, near the positive stimulus position; M, middle position; NN, near the negative stimulus position). Half of the bees received pretest sucrose (arrowheads). After two "reminder" trials, bees were tested with three ambiguous stimuli that alternated between the trained stimuli. The order was counterbalanced (fig. S3). (**D**) Results of experiment 1.1. The sucrose-receiving group took less time to enter the middle position (M) than the control group. Numbers shown are P values (the asterisk indicates significance). (**E**) Training procedure for experiment 1.2 [the view is as in (B) and (C)]. Bees (n = 24) were trained to find a reward under a blue placard and subsequently tested with two novel stimuli. (**F** and **G**) Results of experiment 1.2. Latency time to the feeder (F) and the number of choices (G) did not differ between groups. Here and elsewhere, bars indicate means, open circles represent individual bees, and error bars denote standard error. Generalized linear modeling analyses are reported in tables S1 to S4.

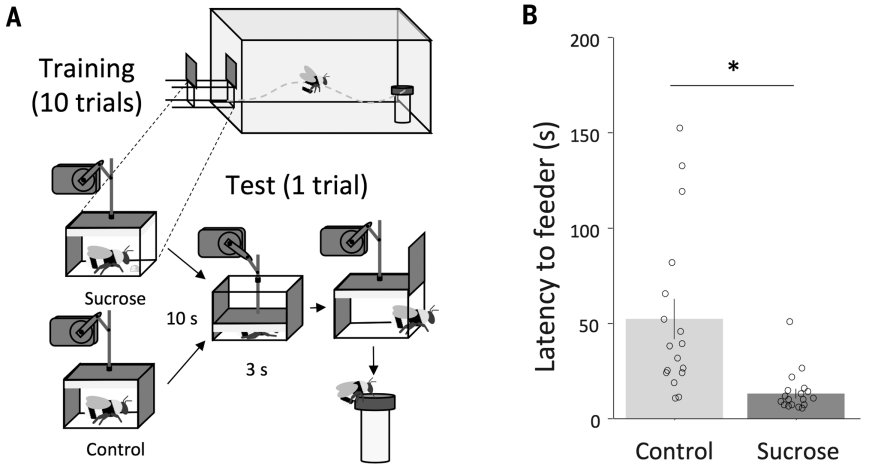

Fig. 2. Attenuation of response to aversive stimuli. (**A**) Training and test procedure for experiment 3. Bees (n = 35) were trained to feed at a 30% sucrose solution feeder. Subsequently, bees received or did not receive 5 µl of 60% sucrose solution before a simulated predator attack. (**B**) Results of experiment 3. Sucrose-receiving bees took less time to resume foraging behavior than the control group (t_{33} = −3.70, *$P = 7.87 \times 10^{-4}$).

Downloaded from http://science.sciencemag.org/ on October 7, 2016

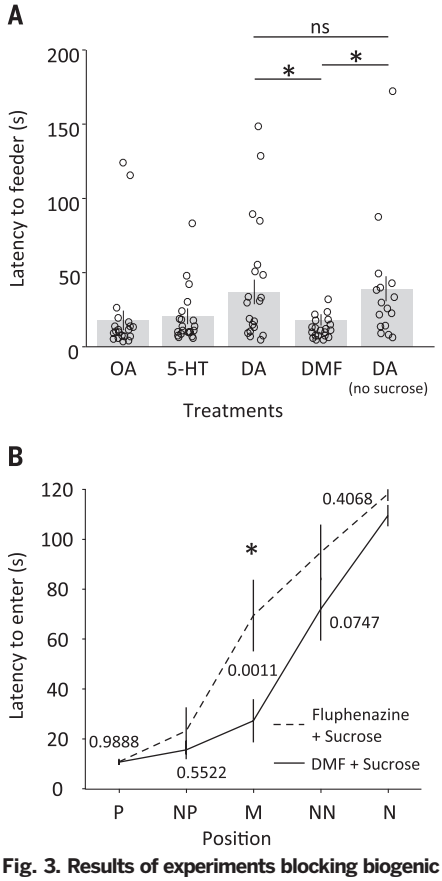

Fig. 3. Results of experiments blocking biogenic amines. All bees received 5 µl of 60% sucrose solution before testing, except as indicated in the rightmost column of (A). (**A**) Results of experiment 4.1. Dopamine (DA) antagonist–treated bees—but not octopamine (OA) antagonist–treated bees, serotonin (5-HT) antagonist–treated bees, or DA antagonist–treated bees that did not receive pretest sucrose—took more time to resume foraging behavior than DMF-treated bees after a simulated predator attack (asterisks denote significance; ns, not significant). (**B**) Results of experiment 4.2. Fluphenazine (DA antagonist)–treated bees took more time to enter the middle position (M) than DMF-treated bees, indicating that drug treatment inhibited the judgment bias caused by pretest sucrose in the control group. Numbers shown are *P* values (the asterisk indicates significance). Generalized linear modeling analyses are reported in tables S5 to S6.

a micro-servo (Fig. 2A) (*18*). The bee was subsequently released, and the time it took to commence foraging was recorded.

Sweet food can increase positive emotions and improve negative mood in human adults, and reduce crying and grimacing of newborns in response to aversive stimuli (*12*–*14*). If drinking an unexpected sucrose solution caused a positive emotion–like state in bees, we predicted that, after consumption, bees' aversive reaction to the "predator" would be attenuated. Indeed, bees that consumed sucrose solution before the "attack" took less time to reinitiate foraging ($n = 35$, $t_{33} = -3.70$, $P = 7.87 \times 10^{-4}$; Fig. 2B).

The insect reward system parallels that of mammals in several aspects, including some of the neurochemicals involved (*19*). In mammals, several neurotransmitters play key roles in both reward processing and emotions. We asked whether the biogenic amines linked to reward processing in the insect brain might be involved in the behaviors suggestive of emotion-like states that we observed. We topically treated bees (*20*, *21*) with antagonists of the biogenic amines octopamine (OA; antagonist, mianserin; $n = 20$), dopamine (DA; antagonist, fluphenazine; $n = 20$), and serotonin (5-HT; antagonist, yohimbine; $n = 20$) and determined their effect on the behavior induced by pretest sucrose. Bees were trained as in experiment 3. Fifteen minutes after application of an antagonist or vehicle control (*N*,*N*′-dimethylformamide, DMF; $n = 20$), bees received, for the first time, a 5-µl droplet of 60% sucrose solution. After this, bees were subjected to a simulated predator attack, and the time taken to return to foraging was recorded (experiment 4.1). Only bees treated with the DA antagonist took longer to begin foraging than control bees (analysis of variance, $n = 96$, $F_{4,90} = 3.48$, $P = 0.011$; Tukey post hoc test, $P = 0.039$; Fig. 3A). We speculate that this is a consequence of brain DA signals responding to an unexpected reward (*22*–*25*). To ensure that the DA antagonist was not simply interacting with pathways mediating normal response to the aversive stimulus, bees were topically treated with DA antagonist without receiving pretest sucrose. The time to begin foraging for these bees was similar to both that of bees treated with DA antagonist and given pretest sucrose and that of control bees given no pretest sucrose [$n = 16$; Figs. 3A (DA antagonist and pretest sucrose) and 2B (control)].

We explored whether blocking DA had similar effects on the observed cognitive consequences of pre-decision reward in the judgment bias paradigm. Bees were trained as in experiment 1.1 and then treated with either DA antagonist or DMF 15 min before consuming an unexpected 5 µl of 60% sucrose solution and entering the test arena. Compared with control bees, DA antagonist–treated bees took longer to enter the middle ambiguous stimulus chamber (experiment 4.2; Fig. 3B and tables S5 and S6).

Recent evidence suggests clear roles for DA in reward-related processes in invertebrates (*23*), including motivation for reward (*25*), nutritional valuation of reward (*22*), and arousal (*26*). Our results corroborate DA's role in the neuronal processes mediating reward signals in bees. An intriguing prospect for research would be whether similar circuits controlling wanting, hunger, nutritional valuation, and/or arousal underpin the emotion-like states in bees indicated by our results.

The behaviors displayed by bumblebees in response to a small amount of pre-decision sucrose conform to the criteria commonly applied to mammals for the interaction of internal emotion-like states with decision-making—namely, positive judgment bias in response to ambiguous stimuli and attenuated response to negative stimuli. Whether common neural processing features evolved independently or an ancient role of biogenic amines evolved to serve similar functions, new findings (including ours) support the hypothesis that the fundamental elements of emotion exist in many species (*9*).

Our results lend support to the notion that invertebrates have states that fit the criteria defining emotion (*1*, *9*). The adaptive function of emotions is thought to be the integration of information about the environment and body to modulate decisions and behavior (*9*). Understanding and investigating the basic features of emotion states will bring us a step closer to determining the brain mechanisms underlying emotion across taxa.

REFERENCES AND NOTES

1. D. Nettle, M. Bateson, *Curr. Biol.* **22**, R712–R721 (2012).
2. J. LeDoux, *Neuron* **73**, 653–676 (2012).
3. M. Mendl, O. H. P. Burman, E. S. Paul, *Proc. R. Soc. London B* **277**, 2895–2904 (2010).
4. E. S. Paul, E. J. Harding, M. Mendl, *Neurosci. Biobehav. Rev.* **29**, 469–491 (2005).
5. B. L. Fredrickson, *Rev. Gen. Psychol.* **2**, 300–319 (1998).
6. W. T. Gibson *et al.*, *Curr. Biol.* **25**, 1401–1415 (2015).
7. P. Fossat, J. Bacqué-Cazenave, P. De Deurwaerdère, J. P. Delbecque, D. Cattaert, *Science* **344**, 1293–1297 (2014).
8. M. Bateson, S. Desire, S. E. Gartside, G. A. Wright, *Curr. Biol.* **21**, 1070–1073 (2011).
9. D. J. Anderson, R. Adolphs, *Cell* **157**, 187–200 (2014).
10. J. Panksepp, *Affective Neuroscience: The Foundations of Human and Animal Emotions* (Oxford Univ. Press, 1998).
11. P. Winkielman, K. C. Berridge, *Curr. Dir. Psychol. Sci.* **13**, 120–123 (2004).
12. P. M. A. Desmet, H. N. J. Schifferstein, *Appetite* **50**, 290–301 (2008).
13. M. Fernandez *et al.*, *J. Dev. Behav. Pediatr.* **24**, 261–266 (2003).
14. M. Macht, J. Mueller, *Appetite* **49**, 667–674 (2007).
15. E. J. Harding, E. S. Paul, M. Mendl, *Nature* **427**, 312–312 (2004).
16. U. Greggers, R. Menzel, *Behav. Ecol. Sociobiol.* **32**, 17–29 (1993).
17. L. C. Nigel, E. Raine, *Entomol. Gen.* **29**, 179–199 (2007).
18. T. C. Ings, L. Chittka, *Curr. Biol.* **18**, 1520–1524 (2008).
19. C. J. Perry, A. B. Barron, *Annu. Rev. Entomol.* **58**, 543–562 (2013).
20. A. B. Barron, J. Maleszka, R. K. Vander Meer, G. E. Robinson, R. Maleszka, *J. Insect Physiol.* **53**, 187–194 (2007).
21. N. DiRienzo, D. R. McDermott, J. N. Pruitt, *Ethology* **121**, 801–812 (2015).
22. W. Huetteroth *et al.*, *Curr. Biol.* **25**, 751–758 (2015).
23. A. B. Barron, E. Søvik, J. L. Cornish, *Front. Behav. Neurosci.* **4**, 163 (2010).
24. E. Søvik, C. J. Perry, A. B. Barron, in *Genomics, Physiology and Behaviour of Social Insects*, A. Zayed, C. F. Kent, Eds., vol. 48 of *Advances in Insect Physiology*, R. Jurenka, Ed. (Academic Press, 2015), pp. 189–226.
25. M. J. Krashes *et al.*, *Cell* **139**, 416–427 (2009).
26. R. Andretic, B. van Swinderen, R. J. Greenspan, *Curr. Biol.* **15**, 1165–1175 (2005).

ACKNOWLEDGMENTS

We thank E. Søvik, M. Osman, J. Zeil, C. Nawroth, A. McElligott, and A. Barron for comments on earlier drafts and two anonymous reviewers for their helpful critical feedback. We also thank E. Søvik for help with statistical analyses. C.J.P. was funded by a Marie Curie Postdoctoral Fellowship. L.B. was funded by a Queen Mary University of London Departmental Studentship. L.C. was supported by a European Research Council Advanced Grant and a Royal Society Wolfson Research Merit Award. Data are available in the supplementary materials. L.B. conceived the study. C.J.P., L.B., and L.C. designed the experiments. C.J.P. and L.B. conducted the experiments and carried out behavioral data analysis. The manuscript was written by C.J.P., L.B., and L.C.

SUPPLEMENTARY MATERIALS

www.sciencemag.org/content/353/6307/1529/suppl/DC1
Materials and Methods
Figs. S1 to S5
Tables S1 to S6
Reference (*27*)
Database S1

9 February 2016; resubmitted 30 May 2016
Accepted 5 August 2016
10.1126/science.aaf4454

Downloaded from http://science.sciencemag.org/ on October 7, 2016

BIODIVERSITY

An Anthropocene map of genetic diversity

Andreia Miraldo,[1]* Sen Li,[1] Michael K. Borregaard,[1] Alexander Flórez-Rodríguez,[1] Shyam Gopalakrishnan,[2] Mirnesa Rizvanovic,[1] Zhiheng Wang,[1,3] Carsten Rahbek,[1,4] Katharine A. Marske,[1] David Nogués-Bravo[1]*

The Anthropocene is witnessing a loss of biodiversity, with well-documented declines in the diversity of ecosystems and species. For intraspecific genetic diversity, however, we lack even basic knowledge on its global distribution. We georeferenced 92,801 mitochondrial sequences for >4500 species of terrestrial mammals and amphibians, and found that genetic diversity is 27% higher in the tropics than in nontropical regions. Overall, habitats that are more affected by humans hold less genetic diversity than wilder regions, although results for mammals are sensitive to choice of genetic locus. Our study associates geographic coordinates with publicly available genetic sequences at a massive scale, yielding an opportunity to investigate both the drivers of this component of biodiversity and the genetic consequences of the anthropogenic modification of nature.

Intraspecific genetic diversity, or the amount of genetic variation among individuals within a species, provides the critical basis for evolutionary change (*1*, *2*), such as adaptation to new environmental conditions. Because it both reflects and influences processes at the population (*3*, *4*), species (*5*, *6*), community (*7*), and ecosystem levels (*8*, *9*), genetic diversity is often considered the most fundamental dimension of biodiversity (*10*). Although the global distribution of species and ecosystems and their responses to global change have been extensively investigated in recent decades (*11*–*14*), the global distribution of intraspecific genetic diversity is still largely unknown (*15*). Genetic diversity has already diminished for many species as a result of abrupt climatic fluctuations and human activity across the Late Quaternary (*16*), and this trend may be accelerating today. Knowledge of the global distribution of genetic diversity is therefore of critical importance if we want to fully understand the long-term impacts of human-induced global changes in climate and land use on genetic diversity, evaluate the potential of species to adapt to global change in the Anthropocene, and ultimately to succeed in halting biodiversity loss. Indeed, genetic diversity has recently been identified as an essential biodiversity variable (*17*) required to monitor biosphere integrity, one of the nine environmental planetary boundaries within which humanity can safely operate (*18*).

[1]Center for Macroecology, Evolution, and Climate, Natural History Museum of Denmark, University of Copenhagen, DK-2100 Copenhagen Ø, Denmark. [2]Centre for GeoGenetics, Natural History Museum of Denmark, University of Copenhagen, DK-2100 Copenhagen Ø, Denmark. [3]Department of Ecology and Key Laboratory for Earth Surface Processes of the Ministry of Education, College of Urban and Environmental Sciences, Peking University, Beijing 100871, China. [4]Imperial College London, Silwood Park Campus, Ascot, Berkshire SL5 7PY, UK.
*Corresponding author. Email: andreia.miraldo@snm.ku.dk (A.M.); dnogues@snm.ku.dk (D.N.-B.)

Most of the current knowledge about the spatial distribution of intraspecific genetic diversity comes from the wealth of phylogeographic studies accumulated over the past 25 years. Although these studies have reported some emergent spatial patterns of genetic diversity at regional scales (*16*, *19*), few regions have been studied as intensively as temperate Europe and North America (*20*), and truly global patterns thus remain to be identified. However, millions of genetic sequences from a diverse array of studies have been deposited in public repositories during this same period (>180 million in GenBank alone), constituting an exceptional source of primary genetic data that could be used to explore global geographical patterns. While impressive in number, the majority of these sequences are not accompanied by geographic coordinates (>85% of all sequences in GenBank), and their integration with other biodiversity information would require manually reviewing the thousands of individual papers in which they are published.

Here, we took advantage of sequences publicly available in the GenBank and BOLD repositories and devised bioinformatic tools to map the global distribution of genetic diversity (*21*). We have attached geographic coordinates to a total of 92,801 mitochondrial sequences (31,029 for amphibians and 61,772 for terrestrial mammals), representing 38% and 27% of available sequences for amphibians and mammals, respectively. Using 86,406 *cytochrome b* (*cytb*) sequences, we performed species-specific sequence alignments for 4675 species and calculated nucleotide diversity per site for each species through pairwise comparisons of georeferenced aligned sequences (24,479 *cytb* sequences from 1992 species). To map the average number of genetic mutations globally (Fig. 1), we estimated the genetic diversity of each equal area grid cell (~150,000 km^2) by averaging nucleotide diversity per site across all species present (*21*).

The global map of genetic diversity for mammals and amphibians together (Fig. 1A) shows that the tropical Andes and Amazonia harbor some of the highest levels of genetic diversity (90th percentile: >0.023; fig. S16). Other regions with high genetic diversity include the subtropical parts of South Africa for mammals (80th percentile: >0.013) and eastern parts of the Sino-Japanese region for amphibians (80th percentile: >0.022; fig. S16). Within the temperate regions of the planet, western North America also contains high levels of genetic diversity, coinciding with the high mammalian species richness there (*22*), whereas eastern North America harbors high levels of genetic diversity in a region that is the global center of speciation and species richness for salamanders (*23*). These patterns are robust to spatial variation in sampling intensity, as demonstrated by rarefaction analyses (*21*), but the high variability of genetic diversity across grid cells with low sample size requires a cautious interpretation of local patterns. The same analysis based on an alternative gene for mammals, *cytochrome oxidase subunit I* (22,762 sequences across 966 species), shows that although genetic diversity values between loci are not correlated for individual grid cells (r = 0.094, P = 0.151; fig. S1), they are highly congruent across latitudinal bands (r = 0.79, P = 0.001; fig. S4).

Sequence availability and taxonomic coverage vary greatly across the globe. The maps of ignorance (Fig. 2 and fig. S10) illustrate the spatial distribution of key gaps in both types of coverage. Unsurprisingly, the majority of knowledge comes from western Europe, North America, and far East Asia, plus individual regions that have recently been the focus of much biogeographic and phylogeographic research, such as Madagascar. Interestingly, western Europe supports some of the lowest levels of genetic diversity (20th percentile: <0.0015) for amphibians (Fig. 1C and fig. S16), although this is one of the best-sampled regions in terms of both sequence availability and taxonomic coverage (Fig. 2C and fig. S10C). This result suggests that our estimates of genetic diversity are robust to the observed geographical bias in data availability, a conclusion that is corroborated by our sensitivity analyses (figs. S7 and S8).

Despite the lower density of data in tropical regions relative to temperate regions of the Northern Hemisphere, we nonetheless identify a pattern of higher genetic diversity in the tropics with a decrease toward the poles, which broadly mirrors the latitudinal gradient of species richness (mammals: pseudo-r^2 = 0.80, quadratic P = 0.001; amphibians: pseudo-r^2 = 0.73, quadratic P = 0.001) (Fig. 3, A and C). It has long been speculated that higher temperatures in the tropics may result in increased evolutionary rates and that this may be the driver for the latitudinal species richness gradient (*24*). Our results are in accordance with the expectation of the proposed mechanism of the evolutionary speed hypothesis, which links biodiversity to temperature through its direct effect on mutation rates and generation time, which in turn may increase the rates of population genetic divergence and speciation (*24*). Mittelbach *et al.*

Downloaded from http://science.sciencemag.org/ on October 7, 2016

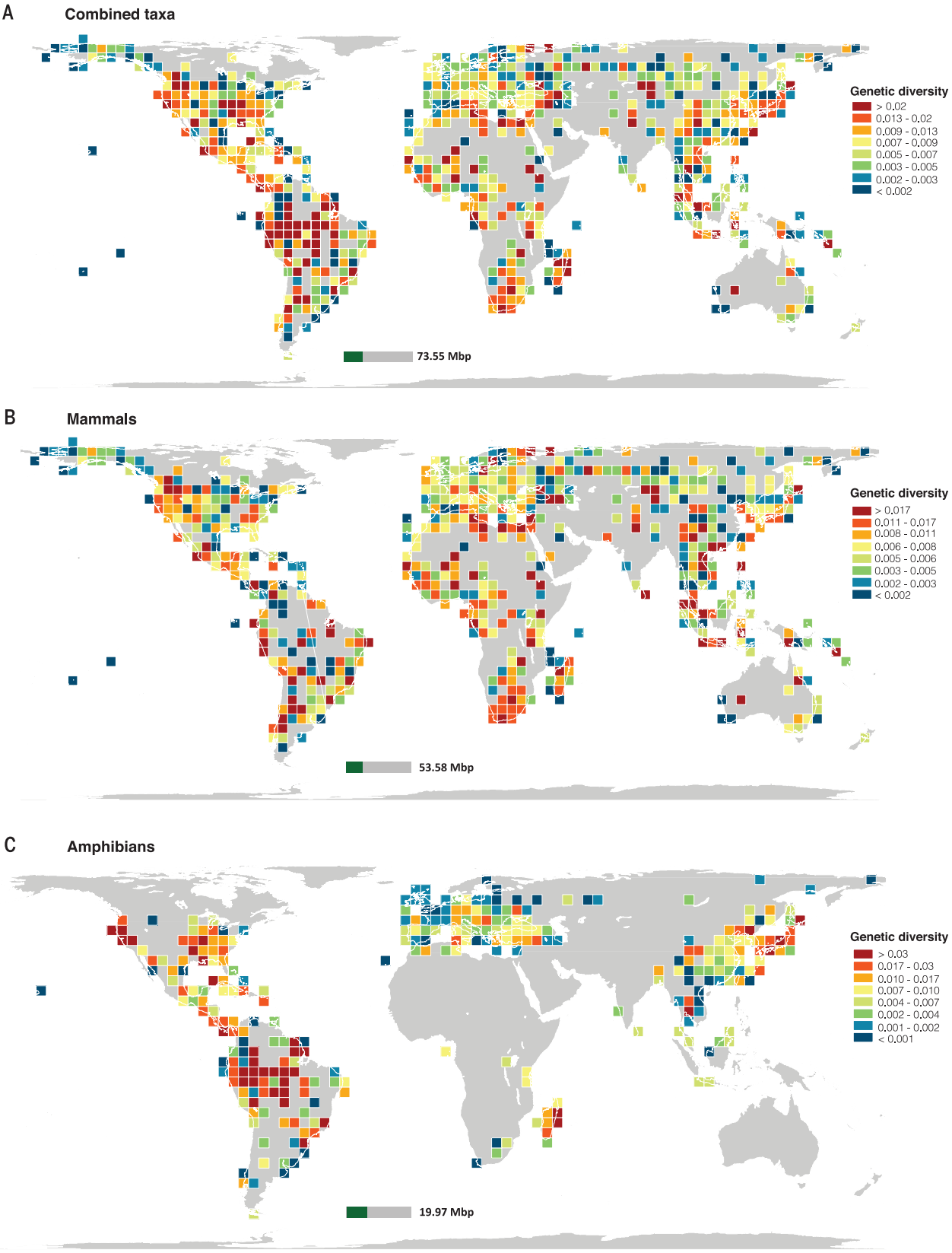

Fig. 1. Global distribution of genetic diversity. (**A** to **C**) Average number of mutations per base pair for *cytb* across species of terrestrial mammals and amphibians together (A), terrestrial mammals alone (B), and amphibians alone (C). Different colors represent eight quantiles. The gray bar below each map represents the total number of *cytb* base pairs retrieved from GenBank and BOLD; the green bar shows the number of georeferenced base pairs used to estimate the global distribution of genetic diversity.

Downloaded from http://science.sciencemag.org/ on October 7, 2016

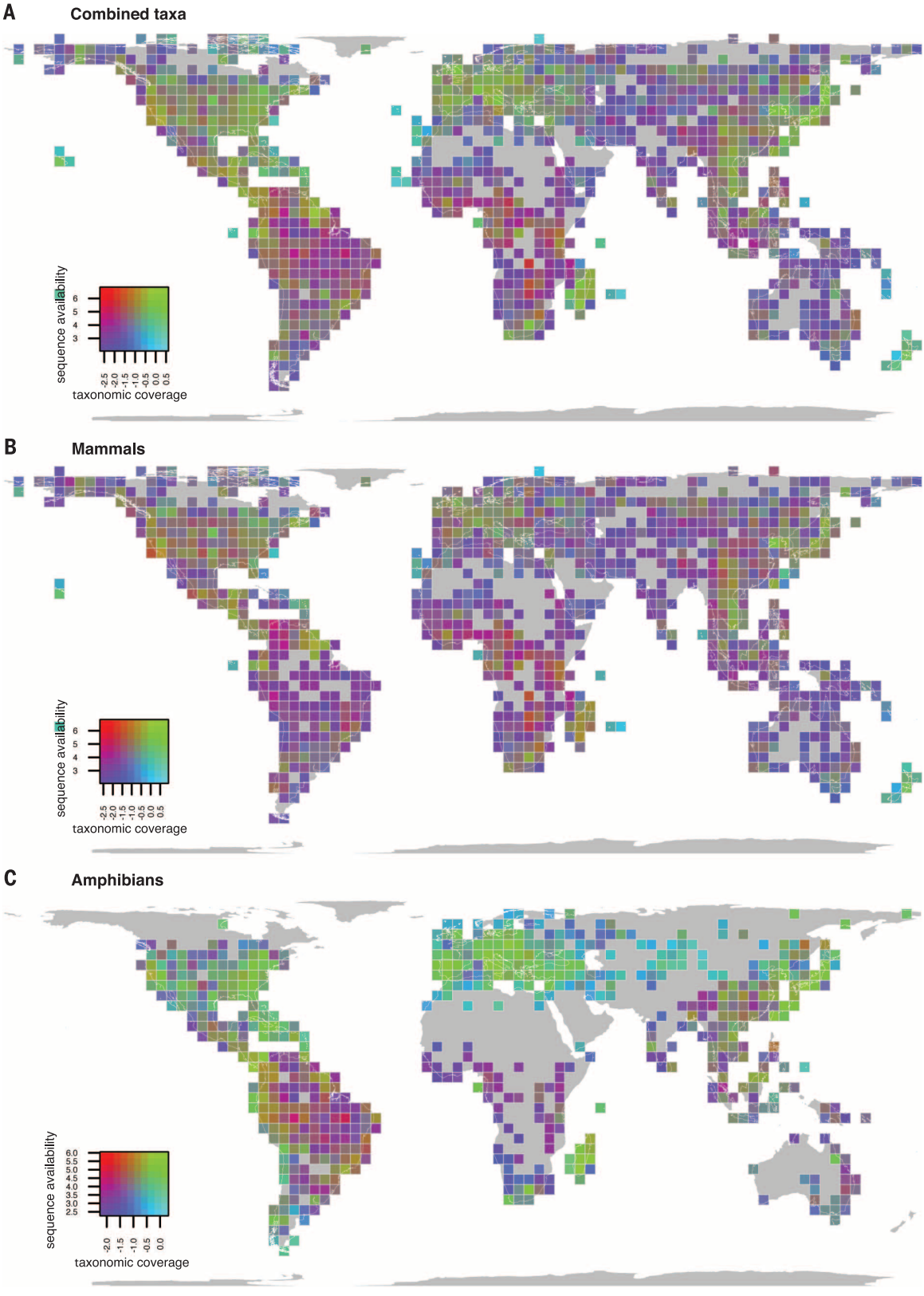

Fig. 2. Global distribution of knowledge and ignorance. (**A** to **C**) Distribution using all mitochondrial data for mammals and amphibians together (A), mammals alone (B), and amphibians alone (C). In the color scale (lower left corner of each map), the *x* axis indicates the taxonomic coverage, defined by the percentage (log scale) of species known to inhabit each grid cell for which at least one georeferenced mitochondrial sequence is available for that cell. The *y* axis indicates sequence availability [i.e., the total number of georeferenced mitochondrial base pairs (log scale) within each grid cell]. In each map, violet colors indicate regions of low taxonomic coverage and relatively few geo referenced base pairs; green colors indicate higher taxonomic coverage and higher numbers of base pairs; light blue colors indicate high taxonomic coverage and few base pairs; red colors indicate low taxonomic coverage and high numbers of base pairs.

(*25*) observed that "several formidable challenges to the evolutionary speed hypothesis remain," including the lack of appropriate data at a scale from which generalities may be inferred and tested. The data presented here open the door to testing this and other potential mechanisms driving biological diversity in the tropics, such as climatic stability or the complex relationship among geographical area, water-energy dynamics, and evolutionary time (*26*).

There is a growing consensus that humans have transformed habitats and have affected ecosystems

Downloaded from http://science.sciencemag.org/ on October 7, 2016

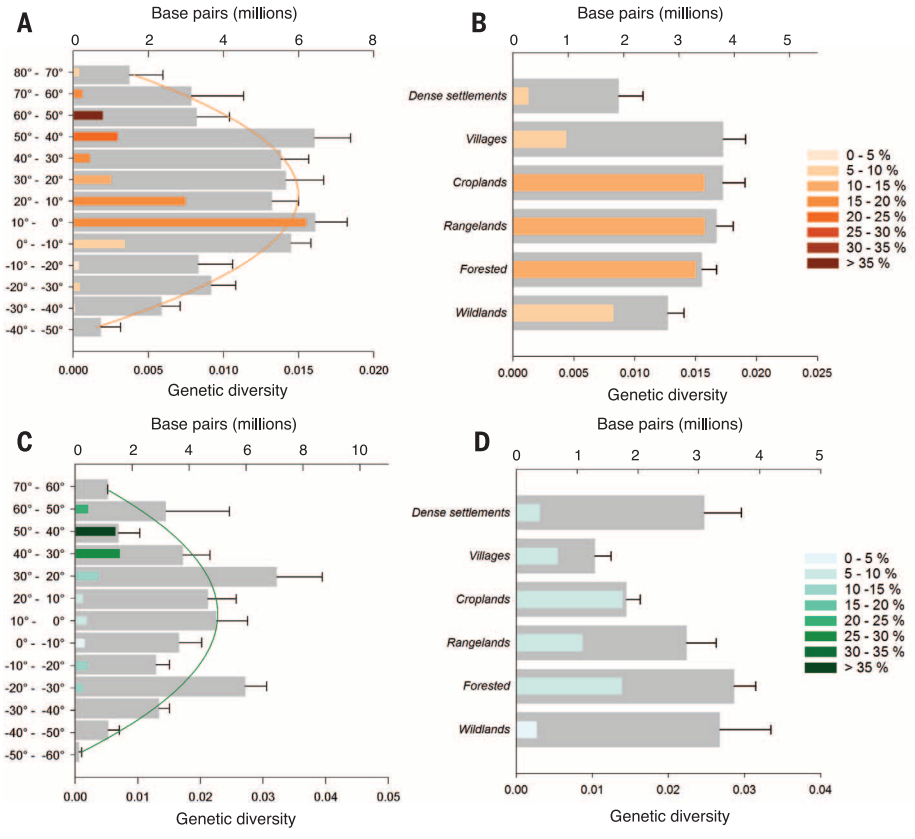

Fig. 3. Distribution of genetic diversity across latitudes and anthromes for mitochondrial *cytb*. (**A** to **D**) Gray bars (lower *x* axis) indicate the average number of mutations per base pair for *cytb* (means ± SD) across species of terrestrial mammals [(A) and (B)] and amphibians [(C) and (D)] in each latitudinal band [(A) and (C)] and anthrome [(B) and (D)]. The length of colored bars (upper *x* axis) indicates the number of *cytb* base pairs used in the calculation of genetic diversity (GD); the depth of color shading denotes the percentage of species used in the calculation of GD relative to species richness of each category. Quadratic polynomial models indicate a peak of GD in the tropics (mammals, pseudo-r^2 = 0.80; amphibians, pseudo-r^2 = 0.73). Error bars represent SD from the mean of the bootstrapping analysis.

across most of the terrestrial biosphere (*27*, *28*). This transformation has been recently mapped on the basis of human population density and land use, leading to a classification of the terrestrial world into anthropogenic ecosystems, or anthromes (*29*). This classification allows exploration of potential anthropogenic impacts on the distribution of genetic diversity, independently for amphibians and mammals. For amphibians, we find an increase in genetic diversity as we move from anthromes more heavily transformed by humans—dense settlements, villages, and croplands—toward those less affected by human pressure, including rangelands, forested ecosystems and wildlands (Jonckheere-Terpstra test, JT statistic = 55,006.5, P = 0.004, increasing trend; Fig. 3D and S14A). For mammals, we detect the same pattern of increasing genetic diversity toward anthromes less affected by human pressure for the *co1* gene (Jonckheere-Terpstra test, JT statistic = 352,761, P = 0.025, increasing trend; figs. S4B and S14B); however, differences in genetic diversity across anthromes are not statistically significant for the *cytb* gene (Kruskal-Wallis test, χ^2 = 9.696, df = 5, P = 0.084; Fig. 3B and fig. S14C).

This study does not intend to explain the processes responsible for the higher levels of genetic diversity in the tropics, nor its relationship with human impacts in the Anthropocene. However, it reveals the very limited knowledge of the global distribution of biological diversity at its most fundamental dimension, the genetic diversity level. As Fig. 2 shows, the regions of least knowledge are also those that harbor some of the highest numbers of species on Earth. Consequently, there is a need to develop data-mining algorithms to georeference the millions of sequences already available in public repositories, as well as better strategies to curate future phylogeographic data. Moreover, it is important to hasten the collection of new genetic data in the field to cover undersampled regions. To encourage such efforts, we make the coordinates of the georeferenced sequences—representing 30% of the sequences available in public repositories for these taxa and genetic loci—freely available at the iMapGenes website (*30*), along with the analytical tools to estimate spatial patterns of intraspecific diversity.

REFERENCES AND NOTES

1. R. Lewontin, *The Genetic Basis of Evolutionary Change* (Columbia Univ. Press, 1974).
2. R. A. Fischer, *The Genetical Theory of Natural Selection* (Oxford Univ. Press, 1930).
3. R. Frankham, *Conserv. Biol.* **9**, 792–799 (1995).
4. I. Saccheri *et al.*, *Nature* **392**, 491–494 (1998).
5. D. Newman, D. Pilson, *Evolution* **51**, 354–362 (1997).
6. D. Spielman, B. W. Brook, R. Frankham, *Proc. Natl. Acad. Sci. U.S.A.* **101**, 15261–15264 (2004).
7. M. Vellend, *Ecology* **87**, 304–311 (2006).
8. G. M. Crutsinger *et al.*, *Science* **313**, 966–968 (2006).
9. J. K. Bailey *et al.*, *Philos. Trans. R. Soc. London Ser. B* **364**, 1607–1616 (2009).
10. R. M. May, J. Godfrey, *Philos. Trans. R. Soc. London Ser. B* **343**, 105–111 (1994).
11. M. C. Urban, *Science* **348**, 571–573 (2015).
12. O. Hoegh-Guldberg, J. F. Bruno, *Science* **328**, 1523–1528 (2010).
13. C. Moritz, R. Agudo, *Science* **341**, 504–508 (2013).
14. R. Menéndez *et al.*, *Proc. R. Soc. London Ser. B* **273**, 1465–1470 (2006).
15. H. M. Pereira, L. M. Navarro, I. S. Martins, *Annu. Rev. Environ. Resour.* **37**, 25–50 (2012).
16. G. Hewitt, *Nature* **405**, 907–913 (2000).
17. W. Steffen *et al.*, *Science* **347**, 1259855 (2015).
18. H. M. Pereira *et al.*, *Science* **339**, 277–278 (2013).
19. G. M. Hewitt, *Front. Zool.* **1**, 4 (2004).
20. L. B. Beheregaray, *Mol. Ecol.* **17**, 3754–3774 (2008).
21. See supplementary materials on *Science* Online.
22. D. R. Vieites, M.-S. Min, D. B. Wake, *Proc. Natl. Acad. Sci. U.S.A.* **104**, 19903–19907 (2007).
23. R. Grenyer *et al.*, *Nature* **444**, 93–96 (2006).
24. K. Rohde, *Oikos* **65**, 514–527 (1992).
25. G. G. Mittelbach *et al.*, *Ecol. Lett.* **10**, 315–331 (2007).
26. P. V. A. Fine, *Annu. Rev. Ecol. Evol. Syst.* **46**, 369–392 (2015).
27. R. Dirzo *et al.*, *Science* **345**, 401–406 (2014).
28. C. N. Waters *et al.*, *Science* **351**, aad2622 (2016).
29. E. C. Ellis, K. K. Goldewijk, S. Siebert, D. Lightman, N. Ramankutty, *Glob. Ecol. Biogeogr.* **19**, 589–606 (2010).
30. Data available at http://macroecology.ku.dk/resources/imapgenes.

ACKNOWLEDGMENTS

Supported by the FrieForskningsrads Sapere Aude Forskerkarriereprogram (A.M., S.L., A.F.-R., and D.N.-B.), Villum Foundation Young Investigators Programme grant VKR023120 (K.A.M. and S.L.), Carlsberg Foundation grants CF14-1069 (M.K.B.) and CF14-0995 (S.G.), National Natural Science Foundation of China grant 31522012 (Z.W.), and Danish National Research Foundation grant DNRF96 to the Center for Macroecology, Evolution, and Climate, Natural History Museum of Denmark (A.M., S.L., M.K.B., A.F.-R., M.R., Z.W., C.R., K.A.M., and D.N.-B.). We thank R. S. Larsen, B. Holt, F. Vieira, R. Pereira, R. Whittaker, R. Colwell, and T. Gilbert for discussion and comment on this manuscript. Data are archived at http://macroecology.ku.dk/resources/imapgenes.

SUPPLEMENTARY MATERIALS

www.sciencemag.org/content/353/6307/1532/suppl/DC1
Materials and Methods
Figs. S1 to S19
Tables S1 to S5
References (*31*–*53*)
Data files S1 and S2

10 February 2016; accepted 26 August 2016
10.1126/science.aaf4381

Downloaded from http://science.sciencemag.org/ on October 7, 2016

SOCIAL MEMORY

Ventral CA1 neurons store social memory

Teruhiro Okuyama,[1] Takashi Kitamura,[1] Dheeraj S. Roy,[1] Shigeyoshi Itohara,[2] Susumu Tonegawa[1,2,3]*

The medial temporal lobe, including the hippocampus, has been implicated in social memory. However, it remains unknown which parts of these brain regions and their circuits hold social memory. Here, we show that ventral hippocampal CA1 (vCA1) neurons of a mouse and their projections to nucleus accumbens (NAc) shell play a necessary and sufficient role in social memory. Both the proportion of activated vCA1 cells and the strength and stability of the responding cells are greater in response to a familiar mouse than to a previously unencountered mouse. Optogenetic reactivation of vCA1 neurons that respond to the familiar mouse enabled memory retrieval and the association of these neurons with unconditioned stimuli. Thus, vCA1 neurons and their NAc shell projections are a component of the storage site of social memory.

The ability to recognize and memorize familiar conspecifics (social memory) is crucial for animals that exhibit social interactions (*1*, *2*). Lesion and recording studies in humans and monkeys have suggested that the medial temporal lobe or the hippocampus plays an essential role in social memory (*3*–*6*). In mice, most early lesion or recording studies concluded that the hippocampus is dispensable for recognizing a familiar conspecific (*7*–*9*), whereas a few recent studies suggested the contrary (*10*–*12*). Although these human and animal studies identified brain areas important for social memory, the precise cellular populations storing this type of memory and their essential circuits are unknown.

The intrinsic pattern of connectivity in the hippocampus is fairly invariable along the longitudinal axis (*13*) across many species (*14*). However, the afferent and efferent connectivity along this axis changes from one end to the other, suggesting that dorsal and ventral hippocampus of rodents (corresponding to posterior and anterior hippocampus, respectively, of primates) may have distinct functions (*14*, *15*). It is well established that the rodent dorsal hippocampus (dHPC) plays an essential role in episodic memory (*15*). In contrast, the memory function of the ventral hippocampus (vHPC) is poorly known. In this study, we generated a transgenic mouse line, transient receptor potential channel 4–Cre (Trpc4-Cre), to investigate the potential role and physiological characteristics of the pyramidal neurons in the CA1 subfield of the ventral hippocampus (vCA1) in social memory.

Mice naturally spend more time interacting with a previously unencountered ("novel") mouse than a familiar one (*16*); social memory can be quantified by measuring the relative interaction durations with a novel and a familiar mouse under free-choice conditions (social discrimination test or SDT) (Fig. 1, A and B). This ability to socially discriminate between the novel and familiar mice persisted for 30 min after a familiarization session, but disappeared by 24 hours (Fig. 1C). To investigate the potential role of vHPC and dHPC in social memory, we targeted bilateral injections of adeno-associated virus 8 (AAV8)–calcium/calmodulin-dependent protein kinase II (CaMKII):eArchT–enhanced yellow fluorescent protein (EYFP) and optic fiber implants to vCA1 or dorsal CA1 (dCA1) of wild-type mice (Fig. 1D). Expression of eArchT-EYFP was abundant in vCA1 or dCA1, although it was also observed to a lesser extent in CA3 and the dentate gyrus (DG) (Fig. 1, E and F). Optogenetic cell body inhibition of vHPC but not dHPC resulted in a deficit in the SDT (Fig. 1, G, H, O, and P). In the resident-intruder test (Fig. 1I and fig. S1), optogenetic inhibition of vHPC but not dHPC increased the sniffing duration toward a familiar intruder with no effect when a novel intruder was used (Fig. 1, J and K).

To identify downstream brain region(s) involved in social memory, we injected AAV9–tetracycline response element (TRE):channelrhodopsin-2 (ChR2)–EYFP into vCA1 of c-fos:tetracycline transactivator (tTA) mice to label neurons activated by social interaction (*17*, *18*). NAc shell, olfactory bulb (OB), and basolateral amygdala (BLA) were the major targets of the social interaction–specific vCA1 neuronal projections (fig. S2). Moreover, retrograde tracer cholera toxin subunit B (CTB)–Alexa555 injection into NAc, OB, or BLA labeled vCA1 but not dCA1 neurons (fig. S3). We then examined whether any of these projections are necessary for social memory by bilaterally injecting AAV8-CaMKII:eArchT-EYFP into vHPC and then optogenetically inhibiting axonal terminals of the vCA1 neurons in the respective target areas while the mice went through the SDT (Fig. 1, L to N, Q to S, and fig. S4). vHPC-NAc projections, but not vHPC-OB or vHPC-BLA, were essential for social discrimination behavior.

To more rigorously establish the functional role of the vCA1-NAc connection, we generated a CA1 pyramidal cell–specific Cre mouse line, Trpc4-Cre, that covers both vCA1 and dCA1 (fig. S5 and Methods). Using Trpc4-Cre mice, we selectively targeted vCA1 excitatory pyramidal neurons by injecting AAV9–human synapsin (hsyn): double-floxed inverse open reading frame (DIO)–eArchT-EYFP into vCA1 (Fig. 2, A and B, and fig. S6). We confirmed that the vCA1 neurons specifically project to the NAc shell but not to the NAc core, as identified by tyrosine hydroxylase (TH) staining (Fig. 2C). Further, CTB injection into NAc labeled the Trpc4-expressing deep layer (vCA1d), but not the superficial layer (vCA1s), pyramidal cells in vCA1 (Fig. 2B). Bilateral injections of AAV9-hsyn:DIO-eArchT-EYFP into the vCA1 of Trpc4-Cre mice and optogenetic inhibition of vCA1 cell body (Fig. 2, D and H) or its axonal terminals in NAc (Fig. 2, F, G, and J) resulted in a SDT deficit similar to that observed by vHPC-NAc inhibition (compare Fig. 2G with Fig. 1L). Optogenetic inhibition of vCA1 cell body during the familiarization period also led to a similar SDT defect (fig. S8). The possibility that these deficits are due to inhibition of dorsal CA2 (dCA2) activity is excluded because dCA2 is unlabeled with eArchT-EYFP in these mice (fig. S6C). dCA1 cell body inhibition was carried out using Wfs1-Cre mouse line expressing Cre in dCA1 but not in vCA1 or dCA2 (fig. S9) (*19*), which showed no deficit in a SDT (Fig. 2, E and I).

Inhibition of vCA1-NAc shell projections in Trpc4-Cre mice only during the interaction with a novel mouse did not affect the SDT (Fig. 2K, middle, and fig. S7A), whereas inhibition only during interaction with a familiar mouse disrupted social discrimination between the two mice (Fig. 2K, right, and fig. S7A). In contrast, when a pair of novel mice (Fig. 2L and fig. S7B), novel and familiar objects (fig. S10A), or novel and familiar contexts (fig. S10B) were used, there was no effect of vCA1-NAc shell inhibition.

We performed a SDT using Trpc4-Cre mice expressing AAV9–elongation factor 1α (EF1α):DIO-ChR2-EYFP in vCA1 while stimulating vCA1-NAc shell projections (Fig. 2, M and N, and fig. S7). Optogenetic activation of vCA1-NAc shell terminals during social interaction with a novel mouse disrupted the SDT (Fig. 2M, middle, and fig. S7C). With a pair of novel mice as the targets, stimulating vCA1-NAc shell projections during interactions with one of the novel mice greatly reduced the sniffing duration of that mouse compared to the other novel mouse (Fig. 2N and fig. S7D). Optogenetic activation of vCA1-NAc shell terminal during interaction with a familiar mouse had no effect in the SDT (Fig. 2M, right, and fig. S7C). Light activation did not affect the SDT in the EYFP control groups (fig. S11, A and B). With novel objects in place of mice, interactions of the test mouse were not affected by activation of the vCA1-NAc shell projections (fig. S11C).

[1]RIKEN–MIT Center for Neural Circuit Genetics at the Picower Institute for Learning and Memory, Department of Biology and Department of Brain and Cognitive Sciences, Massachusetts Institute of Technology (MIT), Cambridge, MA 02139, USA. [2]Brain Science Institute, RIKEN, Saitama, 351-0198, Japan. [3]Howard Hughes Medical Institute at MIT, Cambridge, MA 02139, USA.
*Corresponding author. Email: tonegawa@mit.edu

Downloaded from http://science.sciencemag.org/ on October 7, 2016

These results suggest that increased activation of the vCA1-NAc shell projections while the test mouse was in the novel-mouse domain disrupted the discriminatory social behavior by making the test mouse perceive the novel mouse as familiar.

To monitor the activity of vCA1 cells before and after the familiarization of a conspecific mouse, we injected AAV5-hsyn:DIO-GCaMP6f into the vCA1 of Trpc4-Cre mice and implanted a microprism grin lens targeting the pyramidal cell layer in vCA1 (Fig. 3, A and B; see Methods) (*20*, *21*). Ca^{2+} events in vCA1 neurons (Fig. 3, D and E) were recorded during exposure to two novel mice (A and B) in two consecutive 5-min sessions with mouse A and mouse B in counterbalanced positions, followed by a 5-min control session with no mice (Before group). The test mice were subjected to 3-day-long or 2-hour-long familiarization with mouse A, and the recording sequence was repeated after 30 min or 24 hours' separation (After-1 group) (Fig. 3F). For each neuron, we calculated a "preference score" based on the head position of the test mouse during each recorded Ca^{2+} event and identified vCA1 cells that exhibited selective activation by mouse A or mouse B (Fig. 3G and fig. S12). There was a significant increase in the proportion of mouse-A neurons after 3 days' or 2 hours' familiarization to mouse A (Fig. 3H). In contrast, there was no effect of familiarization on the proportion of cells active around mouse sampling locations in control sessions (No mouse). Similarly, familiarization had no effect on the proportion of mouse-A neurons in dCA1 of Wfs1-Cre transgenic mice (Fig. 3, C and H).

We determined the preference score of mouse-A neurons in Before group and After-1 group, as well as After-2 group that had a second 3-day familiarization. The preference scores of individual mouse-A neurons were not correlated between Before group and After-1 group, whereas these scores were correlated between After-1 group and After-2 group (Fig. 3, I to L). In addition, mouse-A neurons of After-1 group showed an increase in Ca^{2+} event probability around the mouse-A sniffing area, whereas mouse-A neurons did not show such an increase in Ca^{2+} probability in the mouse B sniffing area (Fig. 3M). Although the individual mouse-A neurons were still significantly activated by mouse A (Fig. 3, N

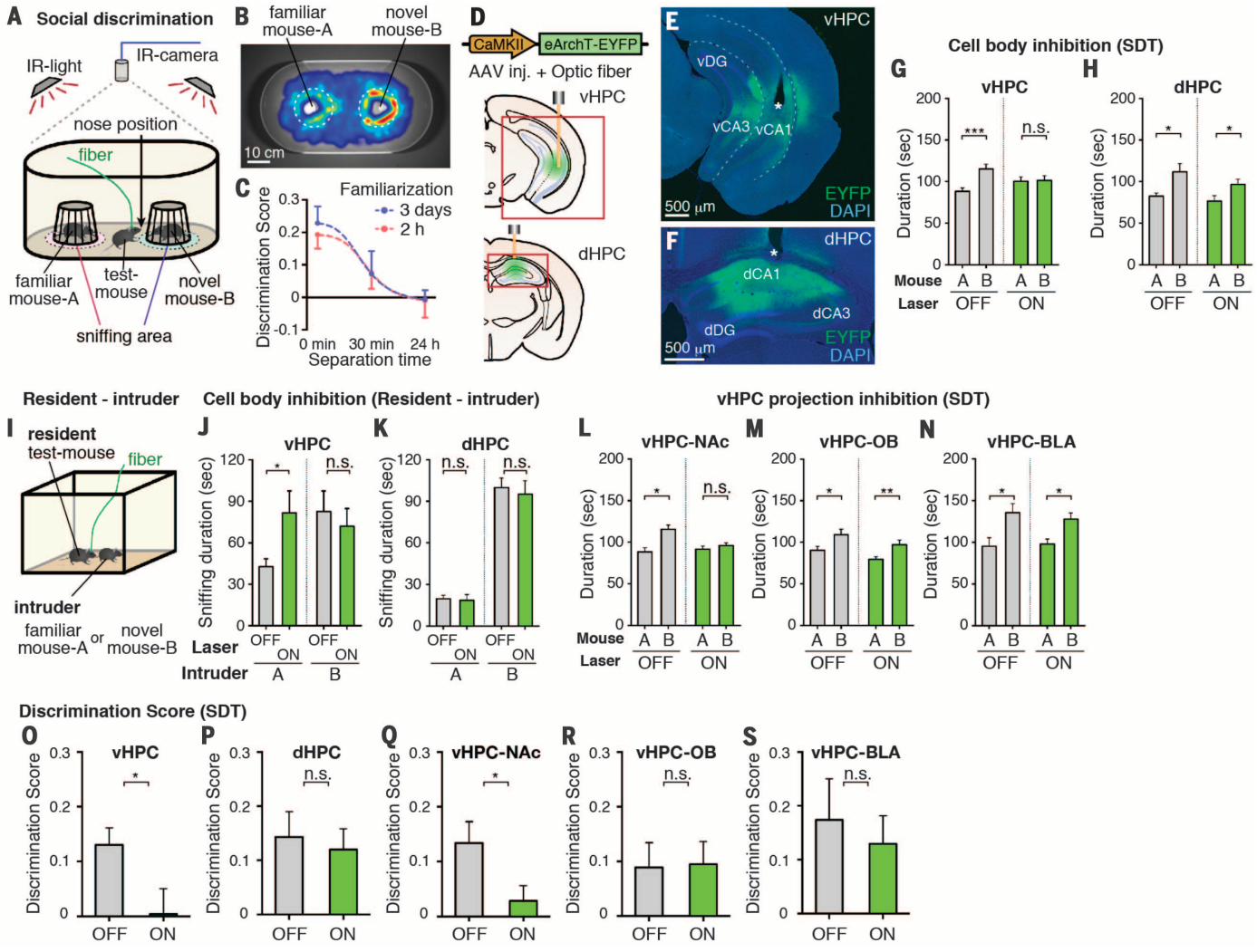

Fig. 1. vHPC in social memory. (**A**) Social discrimination test (SDT). (**B**) Representative heat map of test-mouse position during the SDT. (**C**) Kinetics of the SDT (see Methods). (**D** to **F**) Expression of AAV8-CaMKII:eArchT-EYFP (green) in vHPC or dHPC of wild-type mice. Asterisk indicates optic fiber tip. (**G** and **H**) Total duration in the sniffing area of familiar mouse A or novel mouse B during a SDT with inhibition of vHPC [(G) and (O), $n = 17$ mice] or dHPC [(H) and (P), $n = 14$ mice]. (**I**) Resident-intruder test. (**J** and **K**) Total sniffing duration by the resident to intruder [(J), vHPC inhibition; (K), dHPC inhibition] in familiar-intruder group (left) and novel-intruder group (right) ($n = 7$ mice, each group). (**L** to **N**) Total duration in sniffing area during a SDT observed in wild-type mice bilaterally injected with AAV8-CaMKII:eArchT-EYFP into vHPC and implanted with optical fibers targeting NAc [(L) and (Q), $n = 23$ mice], OB [(M) and (R), $n = 16$ mice], or BLA [(N) and (S), $n = 13$ mice]. (**O** to **S**) Comparison of discrimination scores. Green bars, laser on; gray bars, laser off. Significance for multiple comparisons: paired t test, $^{*}P < 0.05$; $^{**}P < 0.01$; $^{***}P < 0.001$, n.s., not significant. Data presented as mean ± SEM.

Downloaded from http://science.sciencemag.org/ on October 7, 2016

and O), Ca^{2+} event probability of these neurons in mouse-A area was reduced when the recordings were conducted after 24 hours' separation following familiarization (Fig. 3P).

The c-fos:tTA/TRE system permits labeling and manipulations of memory engram cells (*17*, *22*). We used this technology to characterize mouse-A neurons. First, we injected AAV9-TRE:fluorescent timer (FT)–Slow into the vCA1 of c-fos:tTA mice and induced expression of FT-Slow in neurons activated by social interaction (Fig. 4A). The fluorescence of FT-Slow changes naturally over time (*23*), from blue (pseudo-green), 12 hours after induction, to red, 72 hours after induction (Fig. 4, A and B, and fig. S13). Test mice interacted with mouse A twice, or with mouse A and then mouse B, with a 72-hour separation (Fig. 4, C and D). The proportions of reactivated cells with an overlap of red and blue signal was significantly higher in test mice exposed to the same mouse A twice, versus those exposed to mouse A followed by mouse B (Fig. 4E and fig. S13). A similar quantitative analysis of vCA1 reactivation using H2B-EGFP [nuclear localized EGFP (enhanced green fluorescent protein)] and c-Fos expression showed comparable results (fig. S14).

Second, we targeted injection of AAV9-TRE:ChR2-EYFP and optic fibers to vCA1 of c-fos:tTA mice and labeled vCA1 cells that were activated by 2 hours of exposure to a mouse A with ChR2 while the c-fos:tTA mouse was off doxycycline (OFF-Dox) (Fig. 4, F and G, and fig. S2). As expected, social memory was absent in the SDT conducted after 24 hours' separation (Fig. 4H, left), but was present when blue light was shone to the whole test box (Fig. 4H, right). Control experiments conducted with no ChR2 mice (Fig. 4I) or a pair of novel mice during the SDT (fig. S15A) did not show social memory. Restricting blue light to mouse-A area but not mouse-B area also caused the restoration of social memory (Fig. 4J). These results suggest that even after social memory cannot be retrieved by natural cues, the memory engram cells for the familiar mouse are sufficiently retained and can be reactivated optogenetically for memory retrieval (*17*, *24*). Indeed, the proportion of mouse-A neurons reactivated by blue light is much greater than that reactivated by natural cues (i.e., mouse A) after a 3-day separation (compare fig. S16G and Fig. 4E). We further investigated the parameters that affect social memory, including the postfamiliarization separation periods, the proportion of reactivated familiar mouse-A neurons, the nature of recall cues (natural versus optogenetic), and the strength of the reactivation methods (figs. S14 and S16). The data indicate that optogenetic stimulation is more effective than natural stimulation in reactivating memory engram cells and that a certain minimum threshold level of reactivation of mouse-A neurons will have to be reached for social memory to be expressed in the SDT paradigm.

Third, we used the memory inception protocol (Fig. 4K) (*22*). After 24 hours' separation, ChR2-labeled mouse-A neurons were light-activated simultaneously with foot-shock delivery [i.e., negative unconditioned stimulus (US)] or cocaine administration (i.e., positive US). The test mouse exhibited avoidance or approach behavior toward mouse A, respectively, in a SDT conducted the next day (Fig. 4, K to N). Negative control groups with no ChR2 (i.e., AAV9-TRE:EYFP alone) (Fig. 4, O and P) or no US (fig. S15B) did not show any behavioral alterations. No avoidance or approaching behavior was observed when two novel mice (B and B') were used as the target mice during the test (fig. S15, C and D). AAV9-TRE:ChR2-EYFP injection into dCA1 of c-fos:tTA mice did not lead to memory inception (fig. S17).

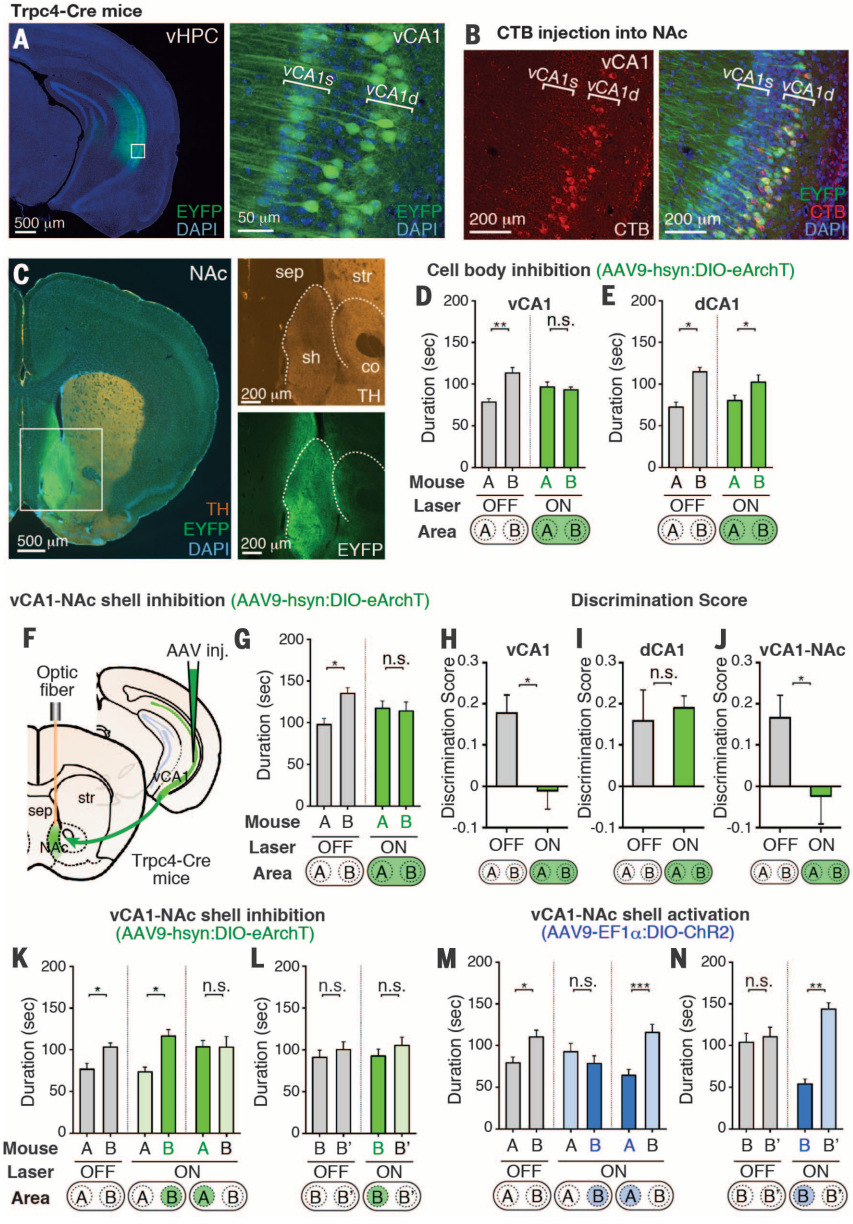

Fig. 2. vCA1-NAc circuit in a SDT. (**A**) Coronal vHPC sections of a Trpc4-Cre mouse injected with AAV9-hsyn:DIO-eArchT-EYFP into vCA1, stained with anti-GFP (green) and DAPI (4′,6-diamidino-2-phenylindole, blue). (**B**) CTB-Alexa555 (red) injection into NAc and stained with anti-GFP (green) and DAPI (blue). (**C**) Coronal NAc sections of a Trpc4-Cre mouse injected with AAV9-hsyn:DIO-eArchT-EYFP into vCA1, stained with anti-GFP (green), anti-TH (orange), and DAPI (blue). NAc shell (sh); NAc core (co); septum (sep); striatum (str). Boxed areas in (A) and (C) are magnified. (**D** and **E**) Cell body inhibition of vCA1 and dCA1 during a SDT in Trpc4-Cre and Wfs1-Cre mice, respectively. (**F**) Manipulation of vCA1-NAc shell projections. (**G** and **K** to **N**) SDT in Trpc4-Cre mice during vCA1-NAc manipulation. vCA1 injections of AAV9-hsyn:DIO-eArchT-EYFP [(G), n =14 mice; (K) and (L), each n = 12 mice] and AAV9-EF1α:DIO-ChR2-EYFP [(M) and (N), each n = 14 mice]. (**H** to **J**) Comparison of discrimination scores. Bottom, targeting area for the laser stimulation. Mouse A, familiar mouse; mouse B and -B', novel mouse. Green bars, green laser on; blue bars, blue laser on; gray bars, laser off. Significance for multiple comparisons: paired t test, $^*P < 0.05$; $^{**}P < 0.01$; n.s., not significant. Data presented as mean ± SEM.

Downloaded from http://science.sciencemag.org/ on October 7, 2016

The possibility that the observed optogenetic recall or memory inception is due to memory held in adjacent dCA2 is excluded because no labeling of dCA2 cells with ChR2 could be observed under our experimental conditions (fig. S17, D to F).

We have established that vCA1 and its projections to NAc shell play a necessary and sufficient role in social memory in the mouse. Furthermore, we have provided evidence that vCA1 pyramidal cells hold the memory of a familiar mouse; a population of vCA1 pyramidal cells are activated by exposure to a familiar mouse, a large fraction of these cells are reactivated by reexposure to the same mouse, and optogenetic reactivation of the vCA1 cells previously activated by exposure to a familiar mouse elicited recall of the specific social memory as

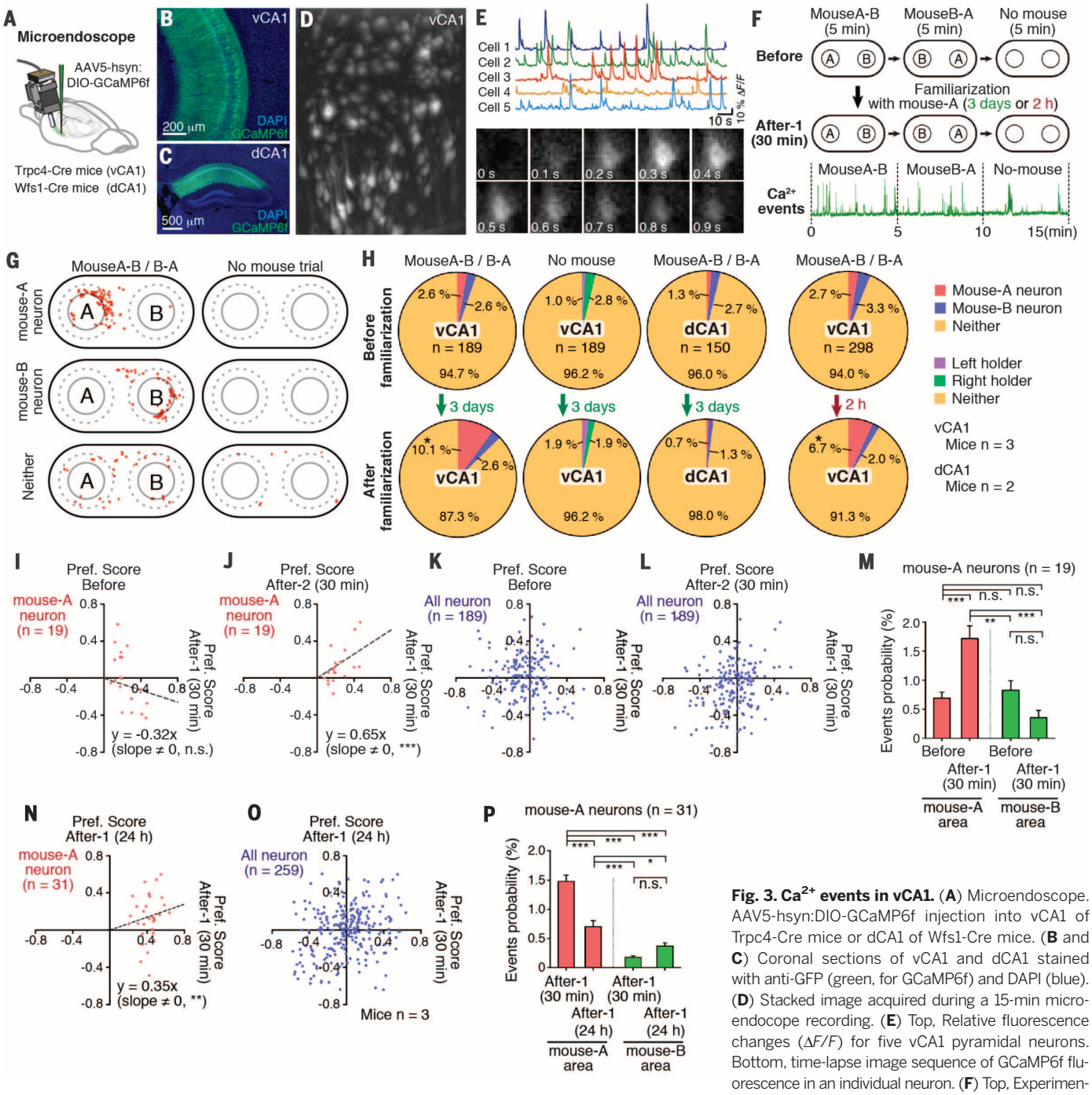

Fig. 3. Ca^{2+} events in vCA1. (**A**) Microendoscope. AAV5-hsyn:DIO-GCaMP6f injection into vCA1 of Trpc4-Cre mice or dCA1 of Wfs1-Cre mice. (**B** and **C**) Coronal sections of vCA1 and dCA1 stained with anti-GFP (green, for GCaMP6f) and DAPI (blue). (**D**) Stacked image acquired during a 15-min microendocope recording. (**E**) Top, Relative fluorescence changes ($\Delta F/F$) for five vCA1 pyramidal neurons. Bottom, time-lapse image sequence of GCaMP6f fluorescence in an individual neuron. (**F**) Top, Experimental protocol for microendoscope recording. Bottom, relative fluorescence changes during 15-min recording. (**G**) Representative mouse-A neuron, mouse-B neuron, and neither neuron. Head position at each Ca^{2+} event (red dots). (**H**) Proportion of mouse-A, mouse-B, or neither neurons in vCA1 and dCA1, before and after familiarization (3 days or 2 hours) (chi-square test, $^{*}P < 0.05$). (**I** to **L** and **N** to **O**) Comparison of the preference scores of mouse-A neurons [(I), (J), and (N), red dots) and all recorded neurons [(K), (L), and (O), blue dots] between After-1 (30 min) and Before sessions [(I) and (K); linear regression, $P = 0.208$], between After-1 (30 min) and After-2 (30 min) [(J) and (L), linear regression, $P = 0.0002$; Spearman rank correlation test, $r = 0.65$), and between After-1 (30 min) and After-1 (24 hours) [(N) and (O), linear regression, $P = 0.0019$; Spearman rank correlation test, $r = 0.23$). (**M** and **P**) Comparison of Ca^{2+} event probabilities of mouse-A neurons [analysis of variance (ANOVA); post-hoc, Scheffe, $^{***}P < 0.001$, $^{**}P < 0.01$). Data presented as mean ± SEM.

Downloaded from http://science.sciencemag.org/ on October 7, 2016

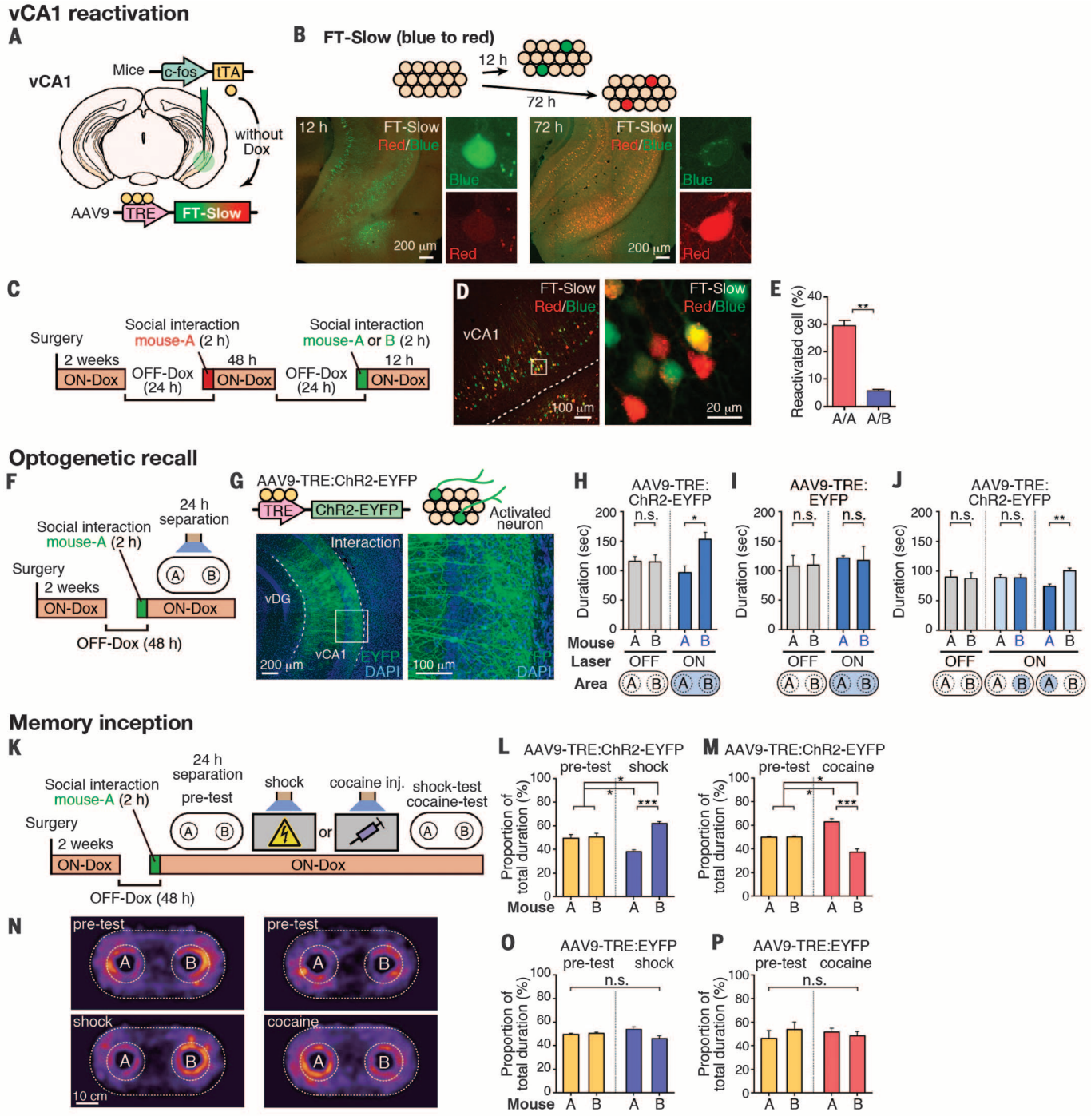

Fig. 4. Social-memory engrams. (**A**) Activity-dependent labeling method. (**B**) Injection of AAV9-TRE:FT-Slow into vCA1 of c-fos:tTA mice. Top, fluorescent color alteration of FT-Slow. Bottom, coronal vCA1 sections 12 hours (left) and 72 hours (right) after induction. Representative images of a blue-form (pseudo-green color)– or red-form (red)–expressing cell. (**C**) Protocol for visualizing two activated neuronal populations. (**D**) FT-Slow blue form–, red form–, and double (yellow)–positive cells in vCA1 (left) with magnified image (right). (**E**) Percentage of reactivated cells when the test mouse was exposed to the same mouse A twice (A/A) or mouse A and then mouse B (A/B) (n = 3 mice, each group). (**F**) Protocol for optogenetic recall of social-memory engram. (**G**) vCA1 section of c-fos:tTA mice injected with AAV9-TRE:ChR2-EYFP showing ChR2-labeling by social interaction. (**H** to **J**) SDT with or without activation of engram cells. Blue bars, blue laser on; gray bars, laser off. Bottom, targeting area for the laser stimulation. (**K**) Protocol for memory inception. (**L**, **M**, **O**, and **P**) Proportion of total duration in the sniffing area of mouse A or mouse B (yellow bars, pretest; blue bars, shock test; red bars, cocaine test). c-fos:tTA mice injected with AAV9-TRE:ChR2-EYFP [(H), (J), (L), and (M)] or AAV9-TRE:EYFP [(I), (O), and (P)]. (**N**) Heat map representing nose position of test mice. (H), n = 10 mice; (I), n = 6 mice; (J), n = 10 mice, (L), n = 10 mice; (M), n = 14 mice; (O), n = 7 mice; (P), n = 7 mice; significance for multiple comparisons: paired t test [(H) to (I)] and ANOVA, post-hoc, Scheffe [(L), M), (O), and (P)], $^{*}P < 0.05$; $^{**}P < 0.01$; n.s., not significant. Data presented as mean ± SEM.

Downloaded from http://science.sciencemag.org/ on October 7, 2016

monitored by a social discrimination test. Thus, the vCA1 cells activated by the exposure to a familiar mouse satisfy the criteria to be met by engram cells for a specific memory (*25*). It is interesting that this recall of the social memory by light can occur even after the mice have fallen into an amnesic state. This indicates that the specific social memory information is retained in the specific vCA1 cell population during at least 1 day after encoding but that natural recall cues are not strong enough to reactivate these cells for memory recall; in contrast, the 20-Hz blue light is stronger and reactivates the engram cells above the threshold necessary for recall. This interpretation of light-mediated recall of the social memory is supported by the inception experiment; the social memory is retained in the amnesic mice, and the light-reactivated engram serves as a CS and becomes associated with a high-valence US (footshocks or cocaine) to evoke avoidance or preference behavior.

The present study helps to resolve the controversy (*7*–*9*) regarding the necessity of mouse hippocampus for social memory and corroborates previous observations made in primates (*4*–*6*). In macaques, a large population of neurons in the anterior hippocampus responded to socially relevant cues such as faces and voices of individuals (*6*). In human medial temporal lobe, including the anterior hippocampus, there are cells that respond more to famous or personally relevant people than to unfamiliar people (*4*, *5*). The overall results suggest evolutionary conservation of the role of the hippocampal areas as the sites of social memory.

Recent studies have shown that dCA2 is critical for sociocognitive memory processing (*10*, *11*, *26*). dCA2 neurons have longitudinal rostro-caudal projections to vCA1 (fig. S18) (*27*, *28*) and connect with the deep layer of CA1 more strongly than with the superficial layer (*28*). It is thus possible that the dCA2-vCA1d-NAc circuit composes the engram cell ensemble pathway for social memory (*25*). However, it is also possible that the role of dCA2 in social memory is to convey to vCA1d appropriately processed and socially relevant cues, rather than holding memory information per se.

Compared to other forms of episodic memory, social memory lasts no more than a few hours (Fig. 1C) under laboratory conditions (*29*, *30*), although it can be prolonged to a week by vasopressin release, or to 24 hours by group housing (*12*, *29*, *31*). We have demonstrated by optogenetics that the engram cells for social memory formed in a laboratory environment can be retained in vCA1 for at least 2 days. Thus, the relatively short duration of social memory is apparently due to inefficient retrieval rather than failed retention of the memory. It would be interesting to test the hypothesis that increased vasopressin and/or group housing prolongs social memory duration by promoting the retrieval process.

Overall, our study establishes vCA1 and its NAc projections as a site of social memory and provides insights and clues to the neuronal mechanisms underlying this important form of memory (fig. S19).

REFERENCES AND NOTES

1. L. A. McGraw, L. J. Young, *Trends Neurosci.* **33**, 103–109 (2010).
2. T. Okuyama *et al.*, *Science* **343**, 91–94 (2014).
3. C. N. Smith *et al.*, *Proc. Natl. Acad. Sci. U.S.A.* **111**, 9935–9940 (2014).
4. R. Q. Quiroga, L. Reddy, G. Kreiman, C. Koch, I. Fried, *Nature* **435**, 1102–1107 (2005).
5. I. V. Viskontas, R. Q. Quiroga, I. Fried, *Proc. Natl. Acad. Sci. U.S. A.* **106**, 21329–21334 (2009).
6. J. Sliwa, A. Planté, J. R. Duhamel, S. Wirth, *Cereb. Cortex* **26**, 950–966 (2016).
7. M. von Heimendahl, R. P. Rao, M. Brecht, *J. Neurosci.* **32**, 2129–2141 (2012).
8. A. S. Squires, R. Peddle, S. J. Milway, C. W. Harley, *Neurobiol. Learn. Mem.* **85**, 95–101 (2006).
9. D. M. Bannerman, M. Lemaire, S. Beggs, J. N. Rawlins, S. D. Iversen, *Exp. Brain Res.* **138**, 100–109 (2001).
10. F. L. Hitti, S. A. Siegelbaum, *Nature* **508**, 88–92 (2014).
11. E. L. Stevenson, H. K. Caldwell, *Eur. J. Neurosci.* **40**, 3294–3301 (2014).
12. J. H. Kogan, P. W. Frankland, A. J. Silva, *Hippocampus* **10**, 47–56 (2000).
13. P. Andersen, T. V. Bliss, K. K. Skrede, *Exp. Brain Res.* **13**, 222–238 (1971).
14. B. A. Strange, M. P. Witter, E. S. Lein, E. I. Moser, *Nat. Rev. Neurosci.* **15**, 655–669 (2014).
15. M. S. Fanselow, H. W. Dong, *Neuron* **65**, 7–19 (2010).
16. J. Camats Perna, M. Engelmann, in *Current Opinion in Behavioral Neurosciences*, M. Geyer, B. Ellenbrook, C. Marsden, Eds. (Springer, 2015), pp. 1–21.
17. X. Liu *et al.*, *Nature* **484**, 381–385 (2012).
18. L. G. Reijmers, B. L. Perkins, N. Matsuo, M. Mayford, *Science* **317**, 1230–1233 (2007).
19. T. Kitamura *et al.*, *Science* **343**, 896–901 (2014).
20. Y. Ziv *et al.*, *Nat. Neurosci.* **16**, 264–266 (2013).
21. T. W. Chen *et al.*, *Nature* **499**, 295–300 (2013).
22. S. Ramirez *et al.*, *Science* **341**, 387–391 (2013).
23. F. V. Subach *et al.*, *Nat. Chem. Biol.* **5**, 118–126 (2009).
24. T. J. Ryan, D. S. Roy, M. Pignatelli, A. Arons, S. Tonegawa, *Science* **348**, 1007–1013 (2015).
25. S. Tonegawa, X. Liu, S. Ramirez, R. Redondo, *Neuron* **87**, 918–931 (2015).
26. D. A. Caruana, G. M. Alexander, S. M. Dudek, *Learn. Mem.* **19**, 391–400 (2012).
27. N. Tamamaki, K. Abe, Y. Nojyo, *Brain Res.* **452**, 255–272 (1988).
28. K. Kohara *et al.*, *Nat. Neurosci.* **17**, 269–279 (2014).
29. R. M. Bluthé, G. Gheusi, R. Dantzer, *Psychoneuroendocrinology* **18**, 323–335 (1993).
30. D. H. Thor, W. R. Holloway, *J. Comp. Physiol. Psychol.* **96**, 1000–1006 (1982).
31. A. S. Smith, S. K. Williams Avram, A. Cymerblit-Sabba, J. Song, W. S. Young, *Mol. Psychiatry* **21**, 1137–1144 (2016).

ACKNOWLEDGMENTS

We thank C. Sun, X. Liu, S. LeBlanc, J. Derwin, W. Yu, F. Bushard, S. Huang, G. Das, T. O'Connor, J. Young, and L. Brenner for their help. Supported by the RIKEN Brain Science Institute, Howard Hughes Medical Institute, the JPB Foundation (to S.T.), and Japan Society for the Promotion of Science Grant-in-Aid (to T.O.). All data and computer codes necessary to understand and assess the conclusions of this research are available in the supplementary materials. AAV9-hSyn:DIO-eArchT3.0-EYFP, AAV9-TRE:FT-Slow, AAV9-TRE:ChR2-EYFP, and AAV9-TRE:EYFP were developed at MIT by the group of S.T.; virus plasmids are available through a material transfer agreement. The Trpc4-Cre transgenic mouse line was developed at RIKEN BSI by the group of S.I. and is available through a material transfer agreement.

SUPPLEMENTARY MATERIALS

www.sciencemag.org/content/353/6307/1536/suppl/DC1
Materials and Methods
Figs. S1 to S19
References (*32*–*35*)

16 March 2016; accepted 29 July 2016
10.1126/science.aaf7003

VIROLOGY

MAVS-dependent host species range and pathogenicity of human hepatitis A virus

Asuka Hirai-Yuki,[1,2] Lucinda Hensley,[1,2] David R. McGivern,[1,3] Olga González-López,[1,2] Anshuman Das,[1,2] Hui Feng,[1,2] Lu Sun,[1,2] Justin E. Wilson,[1,2,4] Fengyu Hu,[1,2] Zongdi Feng,[1,2]* William Lovell,[1] Ichiro Misumi,[1,2,4] Jenny P.-Y. Ting,[1,2,4] Stephanie Montgomery,[1,5] John Cullen,[6] Jason K. Whitmire,[1,2,4] Stanley M. Lemon[1,2,3]†

Hepatotropic viruses are important causes of human disease, but the intrahepatic immune response to hepatitis viruses is poorly understood because of a lack of tractable small-animal models. We describe a murine model of hepatitis A virus (HAV) infection that recapitulates critical features of type A hepatitis in humans. We demonstrate that the capacity of HAV to evade MAVS-mediated type I interferon responses defines its host species range. HAV-induced liver injury was associated with interferon-independent intrinsic hepatocellular apoptosis and hepatic inflammation that unexpectedly resulted from MAVS and IRF3/7 signaling. This murine model thus reveals a previously undefined link between innate immune responses to virus infection and acute liver injury, providing a new paradigm for viral pathogenesis in the liver.

Although viral hepatitis is an important cause of human morbidity worldwide, there are no small-animal models that accurately recapitulate liver disease caused by any of the five responsible viruses (*1*, *2*). Previous studies have relied heavily on nonhuman primates, especially chimpanzees (*3*, *4*), to investigate pathogenesis and immune responses to hepatitis viruses. This has handicapped efforts to understand host responses within the unique immunologic environment of the liver (*5*, *6*). Recent NIH policies effectively eliminate the use of chimpanzees

Downloaded from http://science.sciencemag.org/ on October 7, 2016

in such studies (*7*), intensifying the need for alternative models. Here, we report a murine model that recapitulates many features of human infection with hepatitis A virus (HAV), a hepatotropic picornavirus (genus *Hepatovirus*) that circulates in blood as quasi-enveloped, membrane-cloaked virions and is shed in feces as naked, nonenveloped particles (*8*).

Like hepatitis B (HBV) and hepatitis C (HCV) viruses, the host range of HAV is considered restricted to humans and nonhuman primates (*2*, *9*). However, successful adaptation to growth in murine and guinea pig cells suggests a broader host range (*10*, *11*). Closely related viruses have also been discovered recently in bats, rodents, shrews, and hedgehogs, with phylogenetic evidence suggesting past shifts among host species (*12*). HAV replication is strongly suppressed by type I interferon (IFN) (*13*), but HAV—like HCV—blunts IFN responses in human cells by expressing proteinases that degrade MAVS and TRIF, adaptor molecules involved in the induction of IFN (*13*, *14*). As a result, infected chimpanzees demonstrate limited type I IFN responses (*4*). Because the sequences targeted in human MAVS and TRIF are not conserved in small mammals (fig. S1A), the inability of HAV to infect these species could stem from a failure to disrupt IFN responses.

To test this hypothesis, we intravenously inoculated *Ifnar1*$^{-/-}$*Ifngr1*$^{-/-}$ double knockout (DKO) mice, which lack receptors for both type I and type II IFN, with wild-type human HAV (*15*). These mice proved highly permissive for infection, developing multiple features of acute hepatitis A in humans (*4*, *16*): fecal HAV shedding, low-grade viremia, and elevated serum alanine aminotransferase (ALT) activity (Fig. 1A). Multifocal inflammatory cell infiltrates, often surrounding necrotic or apoptotic hepatocytes, were present in liver at 37 to 41 days post-inoculation (dpi) together with HAV RNA (Fig. 1B and fig. S2A). Fecal shedding of infectious virus was confirmed by three subsequent passages in DKO mice, each leading to intrahepatic HAV RNA, fecal virus shedding, and elevated ALT (Fig. 1C and fig. S2B). Antibodies to HAV were detectable at 28 dpi (fig. S3A). A fifth serial passage used fourth-passage liver extract as inoculum. Unlike nonenveloped virions present in feces (density ~1.23 g/cm^3) (*8*), ~65% of liver-derived virus was membrane-associated (~1.11 g/cm^3) (fig. S4). This inoculum rapidly induced ALT elevation with impressive fecal shedding and intrahepatic HAV RNA abundance (Fig. 1, C and D).

Like DKO mice, *Ifnar1*$^{-/-}$ animals shed virus and developed ALT elevation when challenged with liver-derived virus, whereas type II IFN receptor *Ifngr1*$^{-/-}$ knockouts and wild-type mice showed no evidence of infection (Fig. 1, D and E). The rapid induction of disease in this experiment, compared with slower onset in early DKO passages (Fig. 1A), resulted from a higher inoculum titer rather than viral adaptation to mice. Only a single nonsynonymous nucleotide substitution occurred in the viral sequence over four mouse passages (table S1). Infection persisted in *Ifnar1*$^{-/-}$ and DKO mice for more than 3 months (Fig. 1D). Declining serum ALT and fecal virus shedding over this period of time suggested slow immune control in both types of mice, but histopathologic lesions persisted throughout (fig. S2C). As in chimpanzees (*4*), HAV RNA copy numbers remained high in liver after fecal virus shedding had terminated (Fig. 1, E and F).

These data suggest that the capacity of HAV to evade type I IFN responses defines its host range. However, DKO mice were resistant to

[1]Lineberger Comprehensive Cancer Center, University of North Carolina, Chapel Hill, NC 27517, USA. [2]Department of Microbiology and Immunology, University of North Carolina, Chapel Hill, NC 27517, USA. [3]Department of Medicine, University of North Carolina, Chapel Hill, NC 27517, USA. [4]Department of Genetics, University of North Carolina, Chapel Hill, NC 27517, USA. [5]Department of Pathology and Laboratory Medicine, University of North Carolina, Chapel Hill, NC 27517, USA. [6]Department of Population Health and Pathobiology, North Carolina State University College of Veterinary Medicine, Raleigh, NC 27607, USA.
*Present address: Center for Vaccines and Immunity, The Research Institute at Nationwide Children's Hospital, Columbus, OH, USA. †Corresponding author. Email: smlemon@med.unc.edu

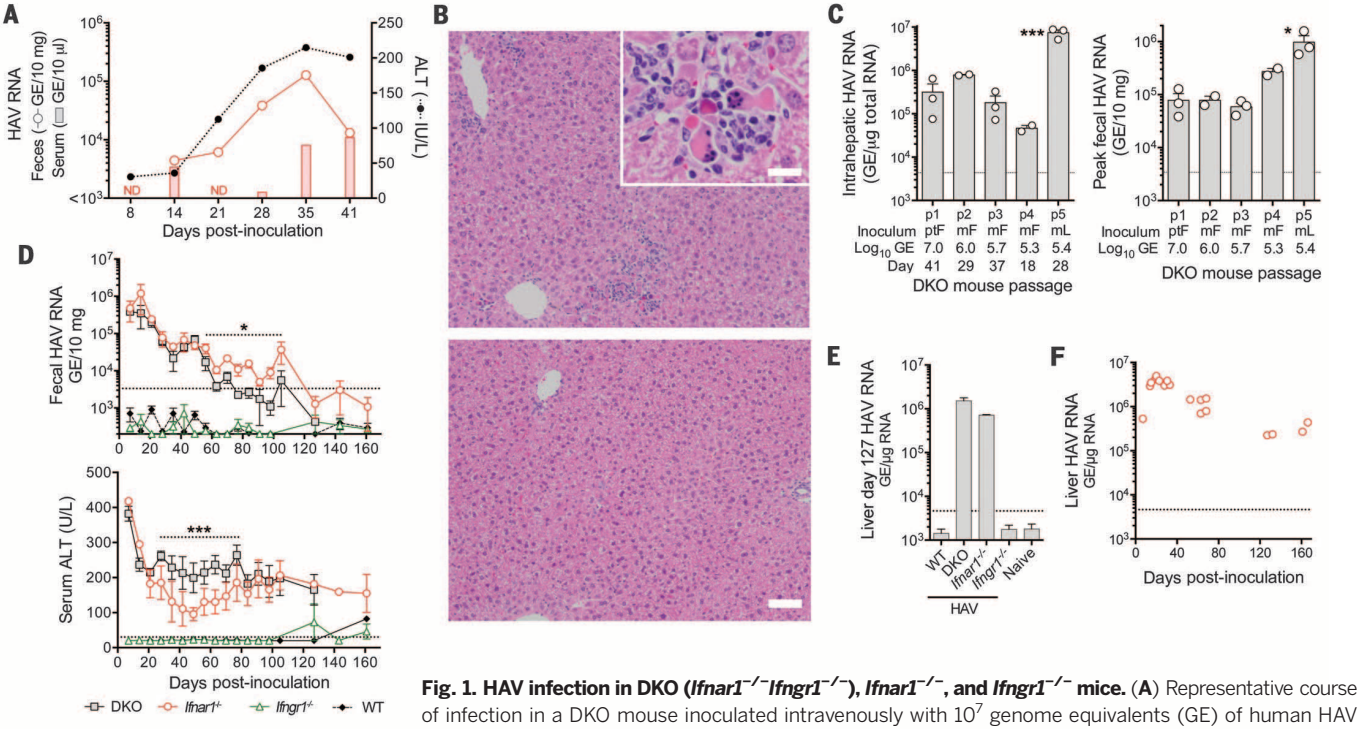

Fig. 1. HAV infection in DKO (*Ifnar1*$^{-/-}$*Ifngr1*$^{-/-}$), *Ifnar1*$^{-/-}$, and *Ifngr1*$^{-/-}$ mice. (**A**) Representative course of infection in a DKO mouse inoculated intravenously with 10^7 genome equivalents (GE) of human HAV (chimpanzee fecal extract). (**B**) Hematoxylin and eosin–stained liver from representative infected (top) and control (bottom) DKO mice at 41 dpi showing inflammatory infiltrates; scale bar, 50 μm. Inset shows apoptotic hepatocytes; scale bar, 12.5 μm. (**C**) Summary of serial passage of HAV in DKO mice showing intrahepatic HAV RNA (left) and fecal HAV RNA (right), source and magnitude of HAV inocula (ptF, chimpanzee feces; mF, DKO mouse feces; mL, DKO mouse liver), and day of harvest. Data are means ± SEM or range; $n = 2$ or 3 animals (shown by open circles in each bar). *$P < 0.05$, ***$P < 0.001$ for p1 versus p5 [one-way analysis of variance (ANOVA)]. (**D**) Fecal HAV RNA (top) and serum ALT (bottom) in DKO, *Ifnar1*$^{-/-}$, *Ifngr1*$^{-/-}$, and wild-type (WT) BL6 mice challenged with fourth-passage DKO liver extract (2.6×10^8 GE). Data are means ± SEM; $n = 4$. *$P < 0.05$, ***$P < 0.001$ for *Ifnar1*$^{-/-}$ versus DKO (ANOVA). (**E**) Intrahepatic HAV RNA in WT, DKO, *Ifnar1*$^{-/-}$, and *Ifngr1*$^{-/-}$ mice at 127 dpi (mean ± range, $n = 2$). (**F**) Intrahepatic HAV RNA in *Ifnar1*$^{-/-}$ mice infected with fourth-passage liver extract. Symbols represent individual mice. Dotted horizontal lines in panels indicate level of detection (RNA) or upper limit of normal (ALT).

Downloaded from http://science.sciencemag.org/ on October 7, 2016

challenge with either fecal or liver-derived virus administered by oral gavage, possibly reflecting a greater role for type III IFN in the gut (*17*, *18*) or absence of an essential receptor. *Rag1*$^{-/-}$ and NSG mice lacking adaptive immunity were resistant to intravenous virus challenge (Fig. 2A and fig. S5A), further highlighting the importance of innate immunity in control of HAV. Because HAV-encoded proteinases disrupt IFN responses by degrading human MAVS and TRIF (*13*, *14*), we challenged *Mavs*$^{-/-}$ and *Trif*$^{-/-}$ mice to ascertain whether signaling through these adaptor molecules restricts replication. *Mavs*$^{-/-}$ mice were highly permissive for HAV, shedding 10 times as much virus as DKO or *Ifnar1*$^{-/-}$ mice (Fig. 2A), whereas *Trif*$^{-/-}$ mice were nonpermissive (Fig. 2A and fig. S5, B and C). Thus, MAVS-mediated type I IFN responses block HAV replication in wild-type mice. Consistent with this finding, HAV 3ABC, a proteinase that degrades MAVS in human cells (*13*), did not cleave murine MAVS (fig. S1B).

Intrahepatic HAV RNA copy numbers were higher in *Mavs*$^{-/-}$ mice than in *Ifnar1*$^{-/-}$ mice by a factor of 10 (Fig. 2B), with the majority of *Mavs*$^{-/-}$ hepatocytes containing HAV RNA (fig. S5, D and E, and table S2). Nonetheless, *Mavs*$^{-/-}$ mice developed neither ALT elevation (Fig. 2C) nor hepatic inflammation (Fig. 2D). Immunohistochemical staining for activated caspase 3 (Fig. 2D) and terminal deoxynucleotidyl transferase–mediated deoxyuridine triphosphate nick end labeling (TUNEL) assays (fig. S6A) revealed numerous apoptotic hepatocytes in infected *Ifnar1*$^{-/-}$ liver, but none in *Mavs*$^{-/-}$ tissue. Apoptotic cells in *Ifnar1*$^{-/-}$ and DKO mice were surrounded by inflammatory infiltrates in proximity to cells containing HAV RNA (Fig. 2D and fig. S6B). The activities of caspases 8 and 9 (and of caspase 3) were slightly increased in infected DKO and *Ifnar1*$^{-/-}$ liver (fig. S6C), but cleaved caspase was not detected in immunoblots; only ~1% of hepatocytes were apoptotic (fig. S6D). These data show that apoptosis and inflammation result from a MAVS-dependent but IFN-independent mechanism. MAVS-mediated apoptosis has been recognized previously, but its role in vivo is uncertain (*19*, *20*).

Virus was largely restricted to the liver in *Mavs*$^{-/-}$ mice: HAV genomes were less abundant in spleen by a factor of 400 and were less abundant in lung by three orders of magnitude (Fig. 2E). Viral RNA was more abundant in spleens of *Ifnar1*$^{-/-}$ mice, possibly reflecting sequestration of virus released from damaged hepatocytes. Little virus was present in ileum or colon of either knockout, indicating that fecal shedding originates in the liver, as in primates (*21*, *22*). Thus, HAV is highly hepatotropic in mice. Viral shedding persisted unabated for 56 days in *Mavs*$^{-/-}$ mice with only minimal ALT increases (Fig. 2F and fig. S6E). Rare, isolated apoptotic hepatocytes were observed in only two of five mice at 63 dpi. The appearance of antibodies to HAV was delayed in *Mavs*$^{-/-}$ mice (fig. S3B), but virus-neutralizing activities were comparable to *Ifnar1*$^{-/-}$ mice at 63 dpi.

Irf3$^{-/-}$ and *Irf7*$^{-/-}$ mice lack transcription factors downstream of MAVS that drive type I IFN expression (*23*). These mice supported only limited HAV replication, whereas *Irf3*$^{-/-}$*Irf7*$^{-/-}$ double knockouts shed virus and accumulated intrahepatic HAV RNA levels equivalent to those of *Mavs*$^{-/-}$ or *Ifnar1*$^{-/-}$ mice (Fig. 2A, fig. S5A, and table S2). This is consistent with redundant roles for IRF3 and IRF7 in the control of flaviviruses (*24*, *25*). Serum ALT elevations were minimal in infected *Irf3*$^{-/-}$, *Irf7*$^{-/-}$, and *Irf3*$^{-/-}$*Irf7*$^{-/-}$ mice (Fig. 2C and fig. S7A). *Irf7*$^{-/-}$ and *Irf3*$^{-/-}$*Irf7*$^{-/-}$ livers contained rare apoptotic hepatocytes (fig. S7B), possibly reflecting activation of IRF5 (*25*). However, a general lack of pathology in infected *Irf3*$^{-/-}$*Irf7*$^{-/-}$ animals mirrored the absence of disease in *Mavs*$^{-/-}$ mice.

Hepatocyte apoptosis is known to drive inflammation within the liver (*26*). The livers of *Ifnar1*$^{-/-}$ mice at 7 dpi showed a factor of 55 increase in F4/80^{+}CD11b^{+} macrophages and a factor of 13 increase in NK1.1^{+} natural killer (NK) cells, whereas CD4^{+} and CD8^{+} T cells were increased by factors of only 3 to 5 (Fig. 3A). Increases in CD3^{+}CD4^{-}CD8^{-} and γ/δ T cells did not achieve statistical significance. Immunohistochemistry confirmed a mixed cellular infiltrate (Fig. 3B). Luminex assays showed increased hepatic CCL3 (MIP-1α), CCL5 (RANTES), and CXCL10 (IP-10) protein, but not IFN-γ, tumor necrosis factor–α (TNF-α), or interleukin (IL)–1β, IL-2, or IL-6 (Fig. 3C). Similarly, serum IFN-β was markedly elevated (>10 ng/ml) in infected DKO and *Ifnar1*$^{-/-}$ mice (Fig. 3D), but enzyme-linked immunosorbent assays (ELISAs) for IFN-γ, TNF-α, IL-1β, and IL-6 were negative. Nonetheless, reverse transcription polymerase chain reaction demonstrated HAV-induced intrahepatic transcripts for multiple cytokines and chemokines in DKO and *Ifnar1*$^{-/-}$ mice, but not in *Mavs*$^{-/-}$ mice (Fig. 3E

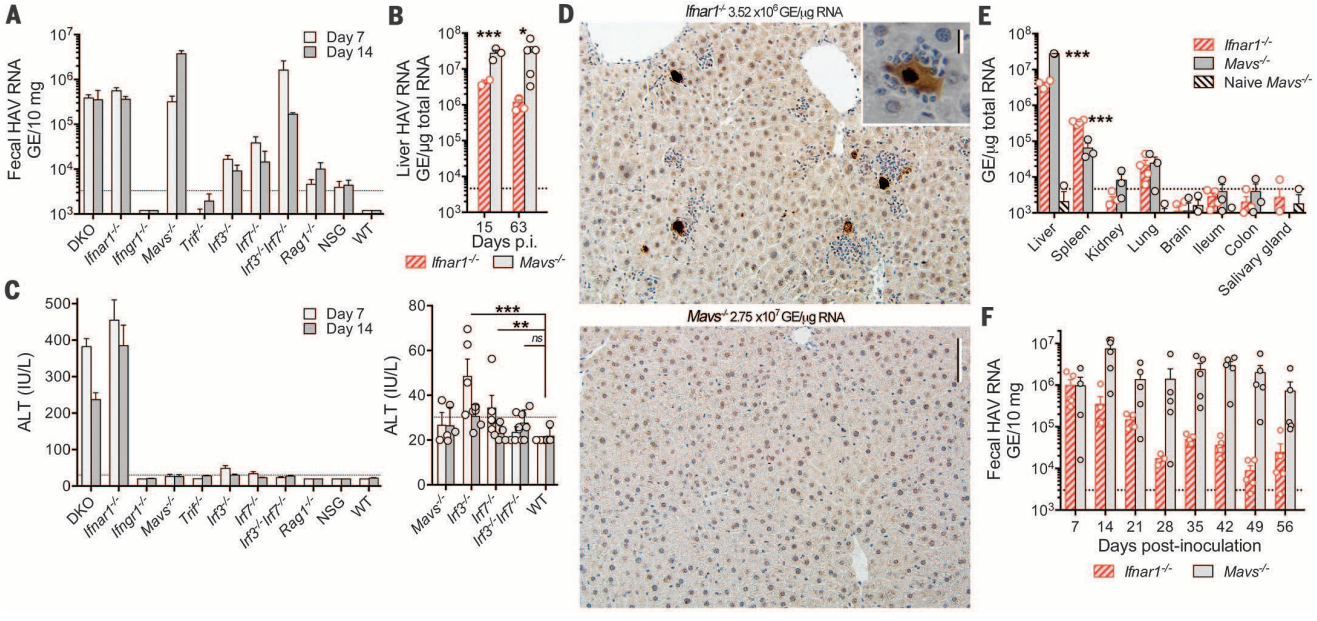

Fig. 2. HAV infection in *Ifnar1*$^{-/-}$ and *Mavs*$^{-/-}$ mice. (**A**) Fecal HAV RNA on day 7 and day 14 after intravenous challenge of different genetically deficient mice. Data are means ± SEM; n = 3 to 5. (**B**) Viral RNA in livers of *Ifnar1*$^{-/-}$ and *Mavs*$^{-/-}$ mice at 15 and 63 dpi. Data are means ± SEM; n = 2 to 5 as shown. *P < 0.05, ***P < 0.001 (two-sided t test). (**C**) Serum ALT at 7 and 14 dpi in genetically deficient mice, with expanded low ALT range at right. Data are means ± SEM; n = 5. **P < 0.01, ***P < 0.001 for combined day 7 and day 15 data (two-sided Mann-Whitney test); ns, not significant. (**D**) Immunohistochemical staining of cleaved caspase 3 in liver from representative (top) *Ifnar1*$^{-/-}$ versus (bottom) *Mavs*$^{-/-}$ mice at 15 dpi; scale bar, 100 μm. Inset shows an apoptotic hepatocyte; scale bar, 12.5 μm. (**E**) Tissue distribution of HAV RNA in infected *Ifnar1*$^{-/-}$ and *Mavs*$^{-/-}$ mice. Data are means ± SEM; n = 3 or 4. ***P < 0.001 (multiple t test with false discovery rate of 1%). (**F**) Fecal virus shedding in infected *Ifnar1*$^{-/-}$ or *Mavs*$^{-/-}$ mice over 56 days of infection. Data are means ± SEM; n = 3 to 5.

Downloaded from http://science.sciencemag.org/ on October 7, 2016

and fig. S8A). CCL2 (MCP-1) and CCL5 mRNA responses were maximal at 7 dpi, whereas CCL3, IFN-γ, and TNF-α mRNAs peaked at 15 dpi (Fig. 3E) despite the absence of detectable protein in serum or liver. Diminishing chemokine and cytokine responses at 28 dpi (Fig. 3E) correlated temporally with a decline in fecal virus shedding by two orders of magnitude. NLRP3 inflammasome-related transcripts were not increased (fig. S8B).

IFN-β transcription is coordinately regulated by IRF3/7 and nuclear factor (NF)–κB (*27*). Phosphorylation of IRF3 confirmed IRF3 activation in infected *Ifnar1*$^{-/-}$ mice (Fig. 3F), and IFN-stimulated genes (ISGs) such as ISG15, IFIT1, and CXCL10 that are directly regulated by IRF3 (*28*) were induced (Fig. 3, C, G, and H). IRF3 similarly regulates CCL5 transcription (*29*), explaining prominent and early CCL5 expression by HAV-infected hepatocytes in *Ifnar1*$^{-/-}$ but not *Mavs*$^{-/-}$ mice (Fig. 3, C and E, and fig. S8C). The phospho-p65 component of NF-κB was not measurably increased (fig. S8D).

Several possible mechanisms could account for apoptosis induced through a MAVS-IRF3/7 pathway (fig. S8E). First, CCL5 expression could recruit cytotoxic lymphocytes to the liver, resulting in death receptor–mediated apoptosis (*30*, *31*). However, depletion of CD4$^+$ or CD8$^+$ T cells had no impact on acute (7 dpi) disease in *Ifnar1*$^{-/-}$ mice (fig. S9). Moreover, virus-specific T cell responses were minimal in *Ifnar1*$^{-/-}$ and *Mavs*$^{-/-}$ mice (fig. S10). Depletion of NK1.1$^+$ NK cells similarly failed to reduce liver injury (fig. S11). This argues against primary death receptor–mediated apoptosis. Clodronate depletion of macrophages prior to infection also had no effect on viral replication or inflammation (fig. S12).

Alternatively, apoptosis could be induced by ISGs that are directly regulated by IRF3 (*28*). The functions of these proteins are only partly understood, but IFIT2 (an ISG that is transcriptionally regulated by IRF3) is known to trigger mitochondrial apoptosis in human cells (*28*, *32*). IRF3 similarly regulates PMAIP1, a proapoptotic BH3-only protein (*33*). Both *Ifit2* and *Pmaip1* transcripts were induced early, and this induction was more extensive in *Ifnar1*$^{-/-}$ mice than in *Mavs*$^{-/-}$ mice (fig. S13). IRF3 can also induce apoptosis through a transcription-independent mechanism involving a direct interaction with mitochondrial Bax (*34*). However, this would not explain the rare apoptotic hepatocytes observed in *Irf3*-deficient mice (fig. S7B).

Although many details remain to be resolved, our data show that *Ifnar1*$^{-/-}$ mice provide a useful model that recapitulates many aspects of type A hepatitis in humans. Despite heroic efforts, such a model has proved elusive for HBV or HCV infection (*2*). Our results suggest that HAV host species range is dictated largely by its capacity to evade MAVS-mediated type I IFN responses, and reveal an unexpected role for MAVS signaling in virus-mediated liver injury. Such signaling leads to IRF3/7-dependent, but IFN-α/β– and IFN-γ–independent, hepatocellular apoptosis with a secondary inflammatory response (fig. S8E). This may explain why HAV and HCV have evolved independently to target MAVS for degradation. Disrupting innate immune signaling upstream of IRF3/7 not only limits IFN-mediated antiviral responses, but also restricts inflammation within the liver, delays antiviral antibody responses, and slows viral clearance (Fig. 2, D and E, and figs. S3B and S6E). IRF3, activated through STING as a result of endoplasmic reticulum stress, has been implicated recently in acute ethanol-induced hepatitis (*35*), suggesting a common final pathway for toxin- and virus-induced liver injury. Our findings establish the critical importance of innate

Downloaded from http://science.sciencemag.org/ on October 7, 2016

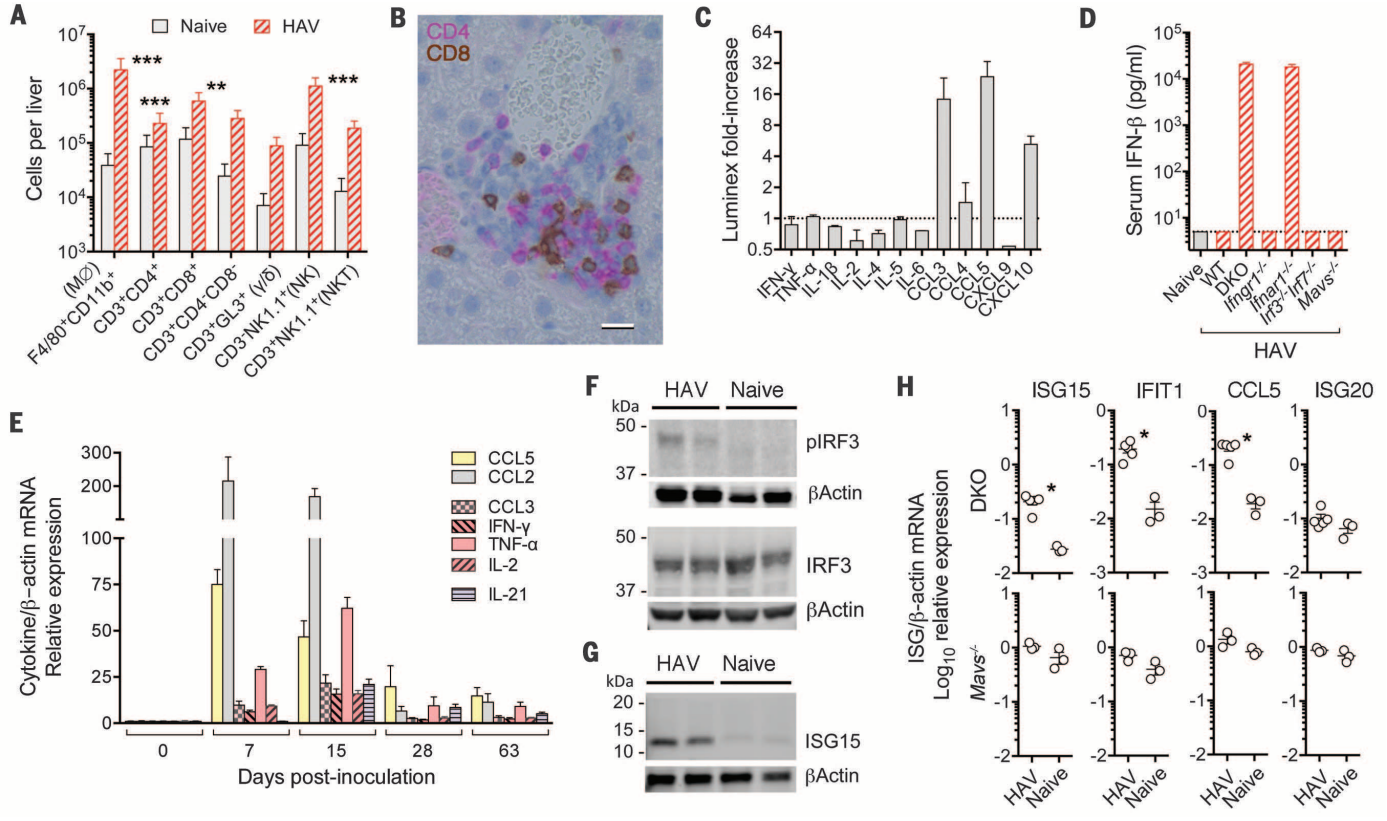

Fig. 3. Cellular and cytokine response to HAV infection in DKO and *Ifnar1*$^{-/-}$ mice. (**A**) Estimated intrahepatic leukocyte numbers in naïve and infected *Ifnar1*$^{-/-}$ mice at 7 dpi. Data are means ± SD; $n = 5$ (mean ALT = 372 IU/liter). $^{**}P < 0.01$, $^{***}P < 0.001$ (two-way ANOVA with Tukey multiple comparison test). (**B**) Dual immunohistochemical staining of infected *Ifnar1*$^{-/-}$ liver for CD4 (magenta) and CD8 (brown) showing a mixed cellular infiltrate at 14 dpi. Scale bar, 10 μm. (**C**) Relative increase in liver cytokine levels in HAV-infected DKO mice (Luminex assay) with ALT >200 IU/liter. Data are means ± range; $n = 2$. (**D**) Serum IFN-β measured by ELISA at 7 dpi. Data are means ± SD; $n = 4$. (**E**) Relative increase in intrahepatic cytokine and chemokine mRNA abundance in *Ifnar1*$^{-/-}$ mice. Data are means ± SEM; $n = 4$ or 5. (**F** and **G**) Immunoblots of phospho-Ser^{396} and total IRF3 (F) and ISG15 (G) in livers from HAV-infected and naïve DKO mice; β-actin was included as a loading control. (**H**) Intrahepatic transcripts of IRF3-regulated ISGs, ISG15, IFIT1 (ISG56), CCL5 (RANTES), and ISG20 (not directly regulated by IRF3) in HAV-infected DKO ($n = 4$) and *Mavs*$^{-/-}$ ($n = 3$) mice and naïve animals at 18 to 28 dpi. $^{*}P < 0.05$ (*t* test).

immune responses in control of viral infection in the liver, and provide a paradigm for HAV pathogenesis that is likely relevant to other hepatotropic human viruses.

REFERENCES AND NOTES

1. C. Dembek, U. Protzer, *Med. Microbiol. Immunol.* **204**, 95–102 (2015).
2. B. Y. Winer, Q. Ding, J. M. Gaska, A. Ploss, *FEBS Lett.* **590**, 1987–1999 (2016).
3. R. E. Lanford, S. M. Lemon, C. Walker, in *Hepatitis C Antiviral Drug Discovery & Development*, Y. He, T. Tan, Eds. (Horizon Scientific, Norwich, UK, 2011), pp. 99–132.
4. R. E. Lanford *et al.*, *Proc. Natl. Acad. Sci. U.S.A.* **108**, 11223–11228 (2011).
5. U. Protzer, M. K. Maini, P. A. Knolle, *Nat. Rev. Immunol.* **12**, 201–213 (2012).
6. I. N. Crispe, *Annu. Rev. Immunol.* **27**, 147–163 (2009).
7. J. Kaiser, *Science* **350**, 1013 (2015).
8. Z. Feng *et al.*, *Nature* **496**, 367–371 (2013).
9. F. Deinhardt, J. B. Deinhardt, in *Hepatitis A*, R. J. Gerety, Ed. (Academic Press, 1984), pp. 185–204.
10. B. Hornei *et al.*, *J. Med. Virol.* **64**, 402–409 (2001).
11. D. A. Feigelstock, P. Thompson, G. G. Kaplan, *J. Virol.* **79**, 2950–2955 (2005).
12. J. F. Drexler *et al.*, *Proc. Natl. Acad. Sci. U.S.A.* **112**, 15190–15195 (2015).
13. Y. Yang *et al.*, *Proc. Natl. Acad. Sci. U.S.A.* **104**, 7253–7258 (2007).
14. L. Qu *et al.*, *PLOS Pathog.* **7**, e1002169 (2011).
15. See supplementary materials on *Science* Online.
16. S. M. Lemon, *N. Engl. J. Med.* **313**, 1059–1067 (1985).
17. J. Pott *et al.*, *Proc. Natl. Acad. Sci. U.S.A.* **108**, 7944–7949 (2011).
18. T. J. Nice *et al.*, *Science* **347**, 269–273 (2015).
19. Y. Lei *et al.*, *PLOS ONE* **4**, e5466 (2009).
20. K. Guan *et al.*, *Mol. Cell. Biol.* **33**, 3137–3149 (2013).
21. A. N. Schulman *et al.*, *J. Infect. Dis.* **134**, 80–84 (1976).
22. C. M. Walker, Z. Feng, S. M. Lemon, *Curr. Opin. Virol.* **11**, 7–13 (2015).
23. H. Ikushima, H. Negishi, T. Taniguchi, *Cold Spring Harb. Symp. Quant. Biol.* **78**, 105–116 (2013).
24. H. W. Chen *et al.*, *J. Immunol.* **191**, 4194–4201 (2013).
25. H. M. Lazear *et al.*, *PLOS Pathog.* **9**, e1003118 (2013).
26. S. Faouzi *et al.*, *J. Biol. Chem.* **276**, 49077–49082 (2001).
27. M. G. Wathelet *et al.*, *Mol. Cell* **1**, 507–518 (1998).
28. N. Grandvaux *et al.*, *J. Virol.* **76**, 5532–5539 (2002).
29. R. Lin, C. Heylbroeck, P. Genin, P. M. Pitha, J. Hiscott, *Mol. Cell. Biol.* **19**, 959–966 (1999).
30. B. Rehermann, *Cell. Mol. Gastroenterol. Hepatol.* **1**, 578–588 (2015).
31. F. Marra, F. Tacke, *Gastroenterology* **147**, 577–594.e1 (2014).
32. N. C. Reich, *J. Interferon Cytokine Res.* **33**, 199–205 (2013).
33. R. Besch *et al.*, *J. Clin. Invest.* **119**, 2399–2411 (2009).
34. S. Chattopadhyay, T. Kuzmanovic, Y. Zhang, J. L. Wetzel, G. C. Sen, *Immunity* **44**, 1151–1161 (2016).
35. J. Petrasek *et al.*, *Proc. Natl. Acad. Sci. U.S.A.* **110**, 16544–16549 (2013).

ACKNOWLEDGMENTS

We thank D. Yamane, K. McKnight, T. Benzine, L. Wai, D. Hilliard, and M. Chua for helpful discussions and technical assistance; R. Lanford (Texas Biomedical Research Institute) for chimpanzee-passaged HAV; and C. Walker (Research Institute of Nationwide Children's Hospital) for the generous gift of HAV peptides. The data presented in this manuscript are tabulated in the main paper and in the supplementary materials. DNA sequences are deposited in GenBank with accession numbers KX343014, KX343015, KX343016, KX343017, and KX343018. *Irf3*$^{-/-}$, *Irf7*$^{-/-}$, and *Irf3*$^{-/-}$*Irf7*$^{-/-}$ mice were provided under a materials transfer agreement from Tokyo University; *Mavs*$^{-/-}$ mice were provided under a materials transfer agreement from the University of Washington. Supported by NIH grants R01-AI103083 and U19-AI109965 (S.M.L.), NIH grants R01-AI074862, R21-AI117575, and R56-AI110682 (J.K.W.), and NCI Center Core Support Grant P30-CA016086 to the Lineberger Comprehensive Cancer Center.

SUPPLEMENTARY MATERIALS

www.sciencemag.org/content/353/6307/1541/suppl/DC1
Materials and Methods
Figs. S1 to S13
Tables S1 and S2
References (*36*–*52*)

6 April 2016; accepted 2 September 2016
Published online 15 September 2016
10.1126/science.aaf8325

ENHANCER FUNCTION

High-resolution interrogation of functional elements in the noncoding genome

Neville E. Sanjana,[1,2]*†‡ Jason Wright,[1,2]† Kaijie Zheng,[1,2] Ophir Shalem,[1,2] Pierre Fontanillas,[1] Julia Joung,[1,2] Christine Cheng,[1,3] Aviv Regev,[1,3] Feng Zhang[1,2]*

The noncoding genome affects gene regulation and disease, yet we lack tools for rapid identification and manipulation of noncoding elements. We developed a CRISPR screen using ~18,000 single guide RNAs targeting >700 kilobases surrounding the genes *NF1*, *NF2*, and *CUL3*, which are involved in BRAF inhibitor resistance in melanoma. We find that noncoding locations that modulate drug resistance also harbor predictive hallmarks of noncoding function. With a subset of regions at the *CUL3* locus, we demonstrate that engineered mutations alter transcription factor occupancy and long-range and local epigenetic environments, implicating these sites in gene regulation and chemotherapeutic resistance. Through our expansion of the potential of pooled CRISPR screens, we provide tools for genomic discovery and for elucidating biologically relevant mechanisms of gene regulation.

More than 98% of the human genome does not code for proteins; however, unlike for the coding genome, there exists no overarching framework to translate the noncoding genomic sequence into functional elements (*1*, *2*). Evidence from genome-wide association studies suggests that many noncoding regions are critical for human health (*3*, *4*). The implications of these associations, however, have been difficult to assess, in part because we lack the tools to determine which variants alter functional elements. Molecular hallmarks, such as epigenetic state, chromatin accessibility, transcription factor binding, and evolutionary conservation, correlate with putative functional elements in the noncoding genome and can predict regulatory function (*2*, *5*). However, these predictions largely bypass regions lacking hallmarks, and it is difficult to ascertain which hallmarks play a correlative or truly causal role in function or phenotype (*6*, *7*). Efforts to determine causality have used preselected DNA fragments, with expression serving as a proxy for function (*8*), but these methods lack the local chromatin context and broader regulatory interactions. Thus, there is a need for systematic approaches to sift through noncoding variants and determine whether and how they affect phenotypes in a native biological context.

For this purpose, we designed a high-throughput method that uses pooled CRISPR (clustered regularly interspaced short palindromic repeat)–Cas9 single guide RNA (sgRNA) libraries to screen noncoding genomic loci in order to identify functional regions related to phenotype and gene regulation. Previous applications of CRISPR screens to the noncoding genome have focused on specific functional elements (e.g., microRNAs and transcription factor binding sites) or required fluorescent reporters (*9*–*12*). In this work, we comprehensively assayed a total of 715 kilobases (kb) of sequence surrounding three different genes by performing unbiased mutagenesis to identify functional elements relevant to cancer drug resistance.

Vemurafenib inhibits BRAF proteins carrying the V600E mutation, which are found in 50 to 70% of melanomas (*13*). Resistance to vemurafenib arises within months in almost all melanoma patients (*14*), and surviving tumor cells display increased malignancy that rapidly leads to lethality (*15*). A genome-scale CRISPR screen found that loss-of-function mutations in *NF1*, *NF2*, and *CUL3* result in vemurafenib resistance (*16*). To explore whether mutations in the noncoding regions around these three genes could similarly affect drug resistance, we designed three sgRNA libraries tiling across 100-kb regions 5′ and 3′ of each gene's major isoforms (Fig. 1A). For each library, we synthesized the sgRNAs as a pool (6682 for *NF1*, 6934 for *NF2*, and 4699 for *CUL3*; 18,315 sgRNAs in total) and cloned them into a lentiviral vector (fig. S1). We transduced A375 human melanoma cells, which carry the BRAF mutation, with the sgRNA libraries at a low multiplicity of infection and cultured them in 2 uM vemurafenib or control (dimethyl sulfoxide, DMSO) for 14 days. Using deep sequencing, we counted the representation of sgRNAs in both conditions (Fig. 1, B to D) and identified vemurafenib-enriched sgRNAs as those enriched by >4 standard deviations from the control distribution (fig. S2).

[1]Broad Institute of MIT and Harvard, 7 Cambridge Center, Cambridge, MA 02142, USA. [2]McGovern Institute for Brain Research, Department of Brain and Cognitive Sciences, Department of Biological Engineering, Massachusetts Institute of Technology, Cambridge, MA 02139, USA. [3]Howard Hughes Medical Institute, David H. Koch Institute of Integrative Cancer Biology, Department of Biology, Massachusetts Institute of Technology, Cambridge, MA 02142, USA.
***Corresponding author. Email: nsanjana@nygenome.org (N.E.S.); zhang@broadinstitute.org (F.Z.)** †These authors contributed equally to this work. ‡Present address: New York Genome Center and Department of Biology, New York University, New York, NY 10012, USA.

Downloaded from http://science.sciencemag.org/ on October 7, 2016

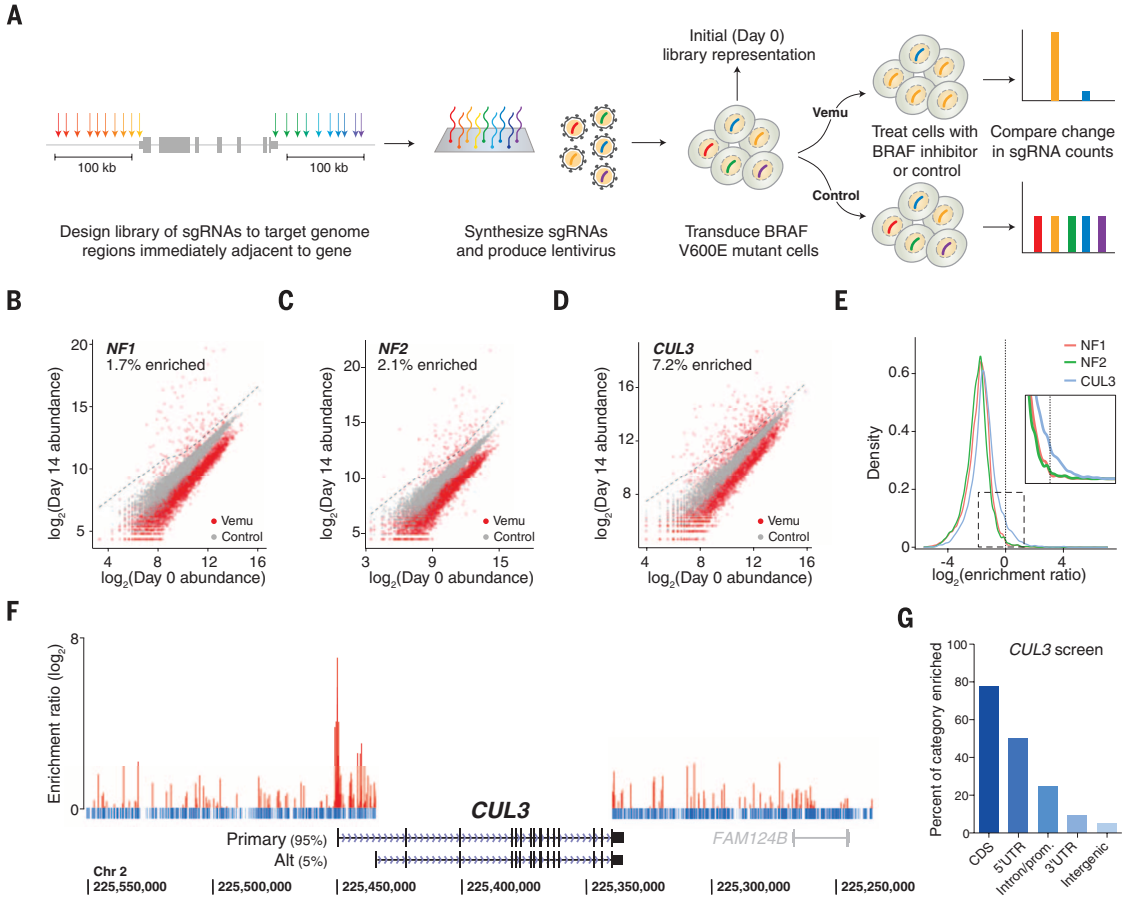

Fig. 1. CRISPR mutagenesis of noncoding regions flanking three genes involved in BRAF inhibitor resistance. (**A**) Design of sgRNA libraries targeting 100 kb 5′ and 100 kb 3′ of a gene. The sgRNAs are array-synthesized and cloned into a lentiviral vector. BRAF mutant cells are transduced with the pooled lentivirus and treated with vemurafenib (vemu) or DMSO (control). A deep sequencing readout identifies sgRNAs enriched after treatment with vemurafenib. (**B**) Scatterplot of normalized read counts (average of the two infection replicates) for *NF1*, (**C**) *NF2*, and (**D**) *CUL3* sgRNAs at days 0 (*x* axes) and 14 (*y* axes). Read counts from control (gray) and vemurafenib-treated cells (red) are shown relative to 4 standard deviations of the control cell distribution (dotted line). The percentage of sgRNAs enriched after vemurafenib treatment (>4 standard deviations) is indicated. (**E**) Distribution of the $\log_2$ ratio of the normalized read count for each sgRNA in vemurafenib to its normalized read count in control (minimum of the two infection replicates). (**F**) All *CUL3* sgRNAs, plotted by human reference genome hg19 coordinates, and the percent expression of the two most highly expressed *CUL3* isoforms [primary and alternate (alt)]. For vemurafenib-enriched sgRNAs, the $\log_2$ enrichment relative to control sgRNAs (minimum value of two replicate screens) is plotted (red); nonenriched sgRNAs are indicated in blue. (**G**) Percent of enriched sgRNAs in each genomic category. CDS, coding sequence; UTR, untranslated region; prom., promoter.

Overall, most sgRNAs were depleted after treatment with vemurafenib, which is expected because vemurafenib targets the oncogene addiction that drives A375 growth (Fig. 1E). However, in all three libraries, we found a small group of sgRNAs that were enriched after vemurafenib treatment ($\log_2$ ratio of vemurafenib to control > 0), with the *CUL3* library having the largest percentage of enriched sgRNAs. We also included a small number of sgRNAs targeting the coding region of each gene, and most of these (70 to 80%) were enriched, as expected (fig. S3A). However, among the sgRNAs targeting noncoding regions, about fourfold more were enriched in the *CUL3* library than in the *NF1* or *NF2* libraries (7.2% in *CUL3*, 1.7% in *NF1*, and 2.1% in *NF2*), suggesting the presence of more gene regulatory elements in the noncoding regions flanking the gene (fig. S3A). To determine whether this increase in putative gene regulatory elements in the 200-kb region surrounding *CUL3* is also reflected in human gene expression and genotyping data, we queried the Genotype-Tissue Expression (GTEx) database (7051 tissue samples from 449 donors). We found that *CUL3* had the largest number of cis-expression quantitative trait loci (eQTL) (n = 161 eQTLs, mean effect size = −0.21), and the region targeted by the sgRNA library overlapped with a large number of these eQTLs (fig. S3B) (*17*). We thus chose to focus our downstream analysis and validation efforts on *CUL3*.

We visualized the enriched sgRNAs in a genome browser–style view (Fig. 1F and fig. S4, A and B). We found that a higher percentage of sgRNAs targeting gene-proximal elements were enriched compared with other noncoding regions (Fig. 1G), and we found greater enrichment for sgRNAs targeting noncoding elements on the 5′ side of the gene than for those on the 3′ side (fig. S4C).

To test whether regions targeted by enriched sgRNAs from the screen physically interact with the *CUL3* promoter through chromatin looping (*18*), we created three independent chromosome conformation capture (3C) libraries (Fig. 2A) (*19*). We quantified the interaction frequency for each site across the ~200-kb region (supplementary methods) and found that regions on the 5′ side of *CUL3* tend to interact more strongly with the promoter. Regions with higher 3C interaction contained, on average, more vemurafenib-enriched sgRNAs (Fig. 2B).

Because chromatin accessibility can identify regulatory regions (*20*, *21*), we performed ATAC-seq (assay for transposase-accessible chromatin with sequencing) in A375 melanoma, MCF7 breast adenocarcinoma, and U87 glioblastoma cells (Fig. 2C). Overall, we found higher sgRNA enrichment near A375-specific ATAC peaks than near those from other cell types, and this finding was replicated with deoxyribonuclease (DNase) I hypersensitivity data (Fig. 2, D and E, and fig. S5). Enrichment in these regions suggests the presence of cell type–specific enhancers (*22*, *23*). Even though the accessible peaks overlapped with enriched sgRNA sites, the chromatin accessibility data by themselves only predict a small fraction of the total number of enriched sgRNA sites (table S1).

Given that evolutionary conservation varies widely across the noncoding genome, we sought to test whether regions exhibiting higher levels of conservation harbor more enriched sgRNAs. We examined phastCons conservation scores over the

Downloaded from http://science.sciencemag.org/ on October 7, 2016

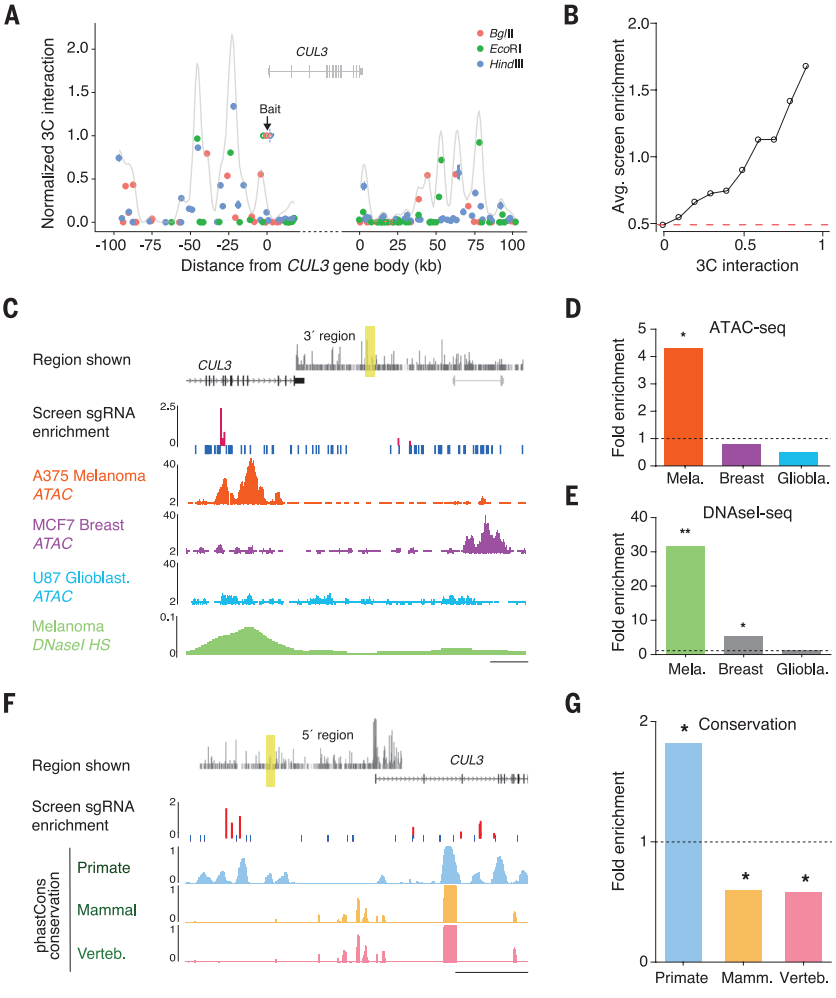

Fig. 2. Characteristics of functional noncoding elements at the *CUL3* locus. (**A**) Plot of the normalized 3C interactions with the *CUL3* promoter in A375 cells. Data points represent independent libraries generated with BglII, EcoRI, and HindIII restriction enzymes. The gray curve shows a smoothed estimate of interaction frequency. Table S3 provides the genomic coordinates of baits and probes. (**B**) Average window enrichment of sgRNAs (log_2 ratio of vemurafenib to DMSO reads) near 3C sites with the specified minimum normalized 3C interaction with the *CUL3* promoter (supplementary methods). The red dashed line indicates average window enrichment for all 3C sites in (A). (**C**) An example of enriched sgRNAs (red) that overlap with a melanoma-specific region of open chromatin. Read counts are shown from ATAC-seq in A375 melanoma (orange), MCF7 breast cancer (purple), and U87 glioblastoma (blue) cells and from melanoma DNase I hypersensitivity (HS) sequencing (green; ENCODE/Colo-829 cell line). Loci investigated with respect to *CUL3* are shown at the top (yellow). Scale bar, 500 bases. (**D**) Fold enrichment of enriched sgRNAs near ATAC-seq open chromatin peaks in melanoma, breast cancer, and glioblastoma cell lines. (**E**) Same as (D), but for DNAse I hypersensitivity sequencing. (**F**) An example of enriched sgRNAs (red) that coincide with regions that show greater primate-specific conservation than placental mammal and vertebrate conservation. Loci investigated with respect to *CUL3* are shown at the top (yellow). Scale bar, 200 bases. (**G**) Fold enrichment of enriched sgRNAs near phastCons peaks in primates, placental mammals, and vertebrates. $^{**}P < 0.01$; $^{*}P < 0.05$.

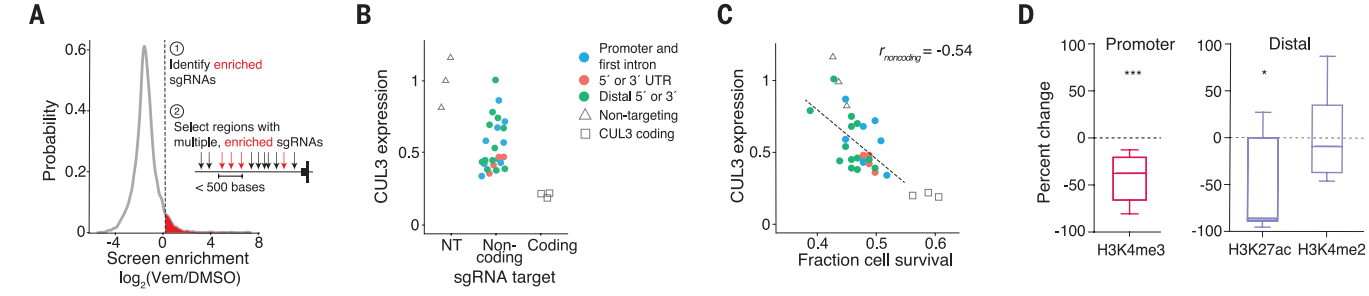

Fig. 3. Noncoding mutations affect *CUL3* expression and histone modifications. (**A**) Criteria for selecting 25 sgRNAs targeting noncoding regions for validation. (**B**) *CUL3* RNA expression (normalized to nontargeting sgRNAs) after transduction with lentivirus expressing nontargeting (triangles), noncoding region–targeting (colored circles), and coding region–targeting (squares) sgRNAs. (**C**) Relationship between *CUL3* expression and cell survival after vemurafenib treatment. The linear fit is to noncoding sgRNAs only ($r_{noncoding}$ = −0.54, P = 0.005) and does not include coding region–targeting or nontargeting sgRNAs. (**D**) Percent change in (left) average H3K4me3 ChIP for all validation sgRNAs within 1 kb of the transcription start site of *CUL3* and (right) average H3K27ac and average H3K4me2 ChIP for all validation sgRNAs >1 kb from the transcriptions start site of *CUL3*. $^{***}P < 0.001$; $^{*}P < 0.05$.

CUL3 locus among primates, placental mammals, and vertebrates (Fig. 2F) (*24*). Overall, enriched sgRNAs were ~1.8-fold more likely to be found near peaks of primate conservation and ~1.7-fold less likely to be found near conservation peaks among mammals and vertebrates (Fig. 2G and fig. S5). In contrast, the genomic sites of sgRNAs targeting coding regions of *CUL3* did not demonstrate differential conservation (phastCons probability of ~0.95 in primates, mammals, and vertebrates). This observation supports recent findings that enhancers evolve rapidly in a lineage- or species-specific manner and that conserved enhancers between mammals tend to be rare (*25*).

To confirm that mutations in these specific noncoding regions were mediated by *CUL3* and lead to altered drug resistance, we transduced cells with individual sgRNAs that have at least one other enriched sgRNA within 500 bases (Fig. 3A). We validated that the sgRNAs created mutations at the intended target sites (fig. S6) and found that 24 of the 25 sgRNAs resulted in decreased *CUL3* expression relative to nontargeting sgRNAs (Fig. 3B). As expected, there was a negative correlation between *CUL3* gene expression and vemurafenib resistance (correlation coefficient r = −0.54, P = 0.005) (Fig. 3C), and increased vemurafenib

Downloaded from http://science.sciencemag.org/ on October 7, 2016

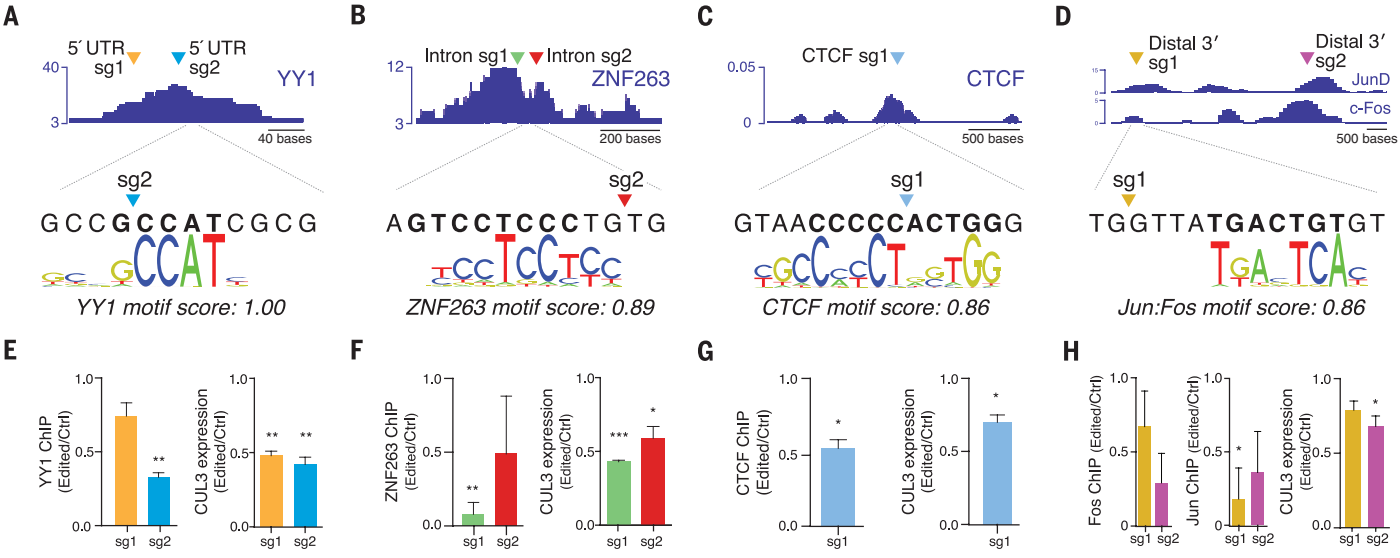

Fig. 4. Cas9 mutagenesis disrupts predicted transcription factors and DNA binding proteins at target sites of vemurafenib-enriched sgRNAs. (**A** to **D**) sgRNA target locations in relation to predicted binding sites. Table S4 gives sgRNA sequences and target locations. (**E** to **H**) Change in transcription factor or DNA binding protein occupancy around cleavage sites and change in *CUL3* expression. Both measurements are normalized to cells transduced with non-targeting sgRNAs. ***$P < 0.001$; **$P < 0.01$; *$P < 0.05$.

resistance could be reversed by restoring *CUL3* expression (fig. S7).

Next, we surveyed changes in posttranslational histone modifications at each target site (fig. S8A). For target sites near the promoter, we found a 56% average decrease in H3K4me3 after editing ($P = 7 \times 10^{-4}$, $n = 9$ sites) (Fig. 3D), which is consistent with the reduced gene expression. At distal sites, we found a 41% average decrease in H3K27ac ($P = 0.02$, $n = 7$ sites) after editing and no significant change in H3K4me2 ($P = 0.82$, $n = 7$ sites) (Fig. 3D), although a subset of H3K4me2 levels decreased after editing (fig. S8B). We also found that mutagenesis of a ~22-kb distal histone acetyltransferase (p300) binding site that has a strong 3C promoter interaction resulted in a 75% decline of promoter H3K27ac and a 50% decrease in *CUL3* expression (fig. S9 and supplementary text).

By examining regions targeted by enriched sgRNAs, we found individual loci containing the canonical transcription factor binding motifs for yin yang 1 (YY1), zinc finger protein 263 (ZNF263), CCCTC-binding factor (CTCF), and activation protein 1 (AP-1) complex, which were disrupted after editing (Fig. 4, A to D, and fig. S10). We found that mutations within these binding sites abrogated transcription factor recruitment, leading to loss of *CUL3* expression (Fig. 4, E to H). For example, specific sgRNAs that target loci near a YY1 chromatin immunoprecipitation (ChIP) peak (Fig. 4A) disrupted the YY1 motif (fig. S11), and vemurafenib treatment selected for mutations that were more deleterious to the binding site (fig. S12). Although both of the sgRNAs targeting loci near the site decreased YY1 binding, the sgRNA whose cut site overlaps the motif disrupted YY1 binding more efficiently (67 versus 26%) (Fig. 4E). In addition, mutagenesis by either sgRNA significantly decreased *CUL3* expression. Similarly, two sgRNAs in the first intron of *CUL3*, spaced 30 bases apart, overlap a ZNF263 ChIP sequencing peak (Fig. 4B). Both resulted in a significant decrease in ZNF263 occupancy and in *CUL3* expression (Fig. 4F).

Although we observed a bias in the presence of regulatory elements 5′ of the transcription start site, we did find several enriched sgRNAs downstream of *CUL3* (Fig. 4, C and D, and supplementary text). One sgRNA cuts inside the core motif of CTCF (Fig. 4C). After editing, CTCF occupancy was decreased by 45%, with a concurrent 30% decrease in *CUL3* expression (Fig. 4G). For AP-1, a heterodimer of FOS and JUN, editing at either of two nearby sites decreased FOS and JUN binding compared with binding in control cells and decreased *CUL3* expression by ~25% (Fig. 4H). Overall, as in the pooled screen, mutagenesis at transcription factor binding sites located on the 3′ side exhibited weaker effects on gene expression than those located on the 5′ side.

Thus, we show how a Cas9-mediated systematic dissection of noncoding loci can identify functional elements involved in gene regulation and cancer drug resistance. In combination with other genome-wide assays, we demonstrate high-throughput identification of regions where changes in chromatin context and transcription factor binding are causally linked to loss of gene expression and a disease-relevant phenotype. This approach is generalizable, and we anticipate that the extension of pooled CRISPR screens into the noncoding genome will provide further insights and methods for unbiased interrogation of the genome.

REFERENCES AND NOTES

1. A. Visel, E. M. Rubin, L. A. Pennacchio, *Nature* **461**, 199–205 (2009).
2. ENCODE Project Consortium, *Nature* **489**, 57–74 (2012).
3. L. A. Hindorff *et al.*, *Proc. Natl. Acad. Sci. U.S.A.* **106**, 9362–9367 (2009).
4. M. T. Maurano *et al.*, *Science* **337**, 1190–1195 (2012).
5. Roadmap Epigenomics Consortium *et al.*, *Nature* **518**, 317–330 (2015).
6. J. C. Kwasnieski, C. Fiore, H. G. Chaudhari, B. A. Cohen, *Genome Res.* **24**, 1595–1602 (2014).
7. R. Mundade, H. G. Ozer, H. Wei, L. Prabhu, T. Lu, *Cell Cycle* **13**, 2847–2852 (2014).
8. A. Melnikov *et al.*, *Nat. Biotechnol.* **30**, 271–277 (2012).
9. S. Chen *et al.*, *Cell* **160**, 1246–1260 (2015).
10. M. C. Canver *et al.*, *Nature* **527**, 192–197 (2015).
11. G. Korkmaz *et al.*, *Nat. Biotechnol.* **34**, 192–198 (2016).
12. N. Rajagopal *et al.*, *Nat. Biotechnol.* **34**, 167–174 (2016).
13. Cancer Genome Atlas Network, *Cell* **161**, 1681–1696 (2015).
14. J. A. Sosman *et al.*, *N. Engl. J. Med.* **366**, 707–714 (2012).
15. I. Zubrilov *et al.*, *Cancer Lett.* **361**, 86–96 (2015).
16. O. Shalem *et al.*, *Science* **343**, 84–87 (2014).
17. GTEx Consortium, *Science* **348**, 648–660 (2015).
18. E. Lieberman-Aiden *et al.*, *Science* **326**, 289–293 (2009).
19. J. Dekker, K. Rippe, M. Dekker, N. Kleckner, *Science* **295**, 1306–1311 (2002).
20. G. E. Crawford *et al.*, *Proc. Natl. Acad. Sci. U.S.A.* **101**, 992–997 (2004).
21. J. D. Buenrostro, P. G. Giresi, L. C. Zaba, H. Y. Chang, W. J. Greenleaf, *Nat. Methods* **10**, 1213–1218 (2013).
22. N. D. Heintzman *et al.*, *Nat. Genet.* **39**, 311–318 (2007).
23. N. C. Sheffield *et al.*, *Genome Res.* **23**, 777–788 (2013).
24. J. Felsenstein, G. A. Churchill, *Mol. Biol. Evol.* **13**, 93–104 (1996).
25. D. Villar *et al.*, *Cell* **160**, 554–566 (2015).

ACKNOWLEDGMENTS

We thank R. Macrae, D. Scott, and the entire Zhang laboratory. N.E.S. is supported by the NIH through a Pathway to Independence Award (R00-HG008171) from the National Human Genome Research Institute and a postdoctoral fellowship from the Simons Center for the Social Brain at the Massachusetts Institute of Technology. J.W. is supported by the NIH through a Ruth L. Kirschstein National Research Service Award (F32-DK096822). O.S. is a Klarman Fellow of the Broad-Israel Partnership. F.Z. is a New York Stem Cell Foundation–Robertson Investigator and is supported by the NIH through the National Institute of Mental Health (grants 5DP1-MH100706 and 1R01-MH110049); the NSF; the New York Stem Cell, Simons,

Downloaded from http://science.sciencemag.org/ on October 7, 2016

Paul G. Allen Family, and Vallee Foundations; and J. and P. Poitras, R. Metcalfe, and D. Cheng. A.R. is on the scientific advisory board for Syros Pharmaceuticals and Thermo Fisher and is a consultant for Driver Group. N.E.S., J.W., O.S., and F.Z. are listed as inventors on a related patent application. Plasmids are available from Addgene, subject to a material transfer agreement. Deep sequencing data are available at Sequence Read Archive under BioProject accession number PRJNA324504, and software tools are available on GitHub (https://github.com/nsanjana/BashRegion).

SUPPLEMENTARY MATERIALS

www.sciencemag.org/content/353/6307/1545/suppl/DC1
Materials and Methods
Supplementary Text
Figs. S1 to S13
Tables S1 to S7
References (*26*–*42*)

25 March 2016; accepted 16 August 2016
10.1126/science.aaf7613

GENE REGULATION

Cyclin A2 is an RNA binding protein that controls *Mre11* mRNA translation

Arun Kanakkanthara,[1] Karthik B. Jeganathan,[1] Jazeel F. Limzerwala,[2] Darren J. Baker,[1] Masakazu Hamada,[1] Hyun-Ja Nam,[1] Willemijn H. van Deursen,[1] Naomi Hamada,[1] Ryan M. Naylor,[2] Nicole A. Becker,[2] Brian A. Davies,[2] Janine H. van Ree,[1] Georges Mer,[2] Virginia S. Shapiro,[3] L. James Maher III,[2] David J. Katzmann,[2] Jan M. van Deursen[1,2]*

Cyclin A2 activates the cyclin-dependent kinases Cdk1 and Cdk2 and is expressed at elevated levels from S phase until early mitosis. We found that mutant mice that cannot elevate cyclin A2 are chromosomally unstable and tumor-prone. Underlying the chromosomal instability is a failure to up-regulate the meiotic recombination 11 (Mre11) nuclease in S phase, which leads to impaired resolution of stalled replication forks, insufficient repair of double-stranded DNA breaks, and improper segregation of sister chromosomes. Unexpectedly, cyclin A2 controlled Mre11 abundance through a C-terminal RNA binding domain that selectively and directly binds *Mre11* transcripts to mediate polysome loading and translation. These data reveal cyclin A2 as a mechanistically diverse regulator of DNA replication combining multifaceted kinase-dependent functions with a kinase-independent, RNA binding–dependent role that ensures adequate repair of common replication errors.

Cyclin A2 is a core cell cycle regulator that activates Cdk1 and Cdk2. Cyclin A2 levels increase upon S phase entry and remain high until its proteasome-dependent destruction in prometaphase (*1*). Cyclin A2–Cdk complexes that assemble at the onset of S phase drive chromosome duplication through phosphorylation of key DNA replication factors. Subsequently, cyclin A2–Cdk activity initiates mitosis by phosphorylating and inactivating the protein kinase Wee1, resulting in activation and nuclear localization of cyclin B1–Cdk1. During early mitosis, cyclin A2 is implicated in mitotic spindle anchoring (*2*) and correction of aberrant kinetochore-microtubule attachments (*3*). Furthermore, in a Cdk-independent manner, cyclin A2 regulates RhoA and RhoC, two guanosine triphosphatases implicated in cell morphogenesis, adhesion, and migration (*4*).

In mice, cyclin A2 is essential for early embryogenesis, limiting investigations of its biological functions (*5*). Studies of conditional knockout mice revealed that cyclin A2 is essential for cell cycle progression of certain cell types, including pluripotent and hematopoietic stem cells and select neuronal progenitors, yet is dispensable in fibroblasts because of redundancy with cyclin E in this cell type (*6*). To uncover novel biological processes that critically depend on a full complement of cyclin A2, we used a combination of knockout (*Ccna2*$^{-}$) and hypomorphic (*Ccna2*^{H}) alleles to markedly down-regulate cyclin A2 expression in mice without overtly affecting embryogenesis or postnatal development. *Ccna2*^{H} was created by targeted insertion of a neomycin resistance cassette into *Ccna2* intron 2; *Ccna2*$^{-}$ was created by gene trap mutagenesis (fig. S1, A to D). *Ccna2*$^{-/H}$ mice showed markedly reduced levels of cyclin A2 protein in tissues with a high mitotic index, including small intestine, bone marrow, and spleen (Fig. 1A). In contrast, cyclin A2 levels appeared normal in tissues with few cycling cells, such as brain, liver, and lung. However, actively cycling cultured lung epithelial cells from *Ccna2*$^{-/H}$ mice had lower amounts of cyclin A2 relative to the wild type (Fig. 1A). Analysis of mouse embryonic fibroblasts (MEFs) confirmed this, with *Ccna2*$^{-/H}$ MEFs expressing only ~25% of normal cyclin A2 levels (Fig. 1A and fig. S1E). In *Ccna2*$^{+/+}$ MEFs, cyclin A2 expression typically started to increase during G_1 and peaked from G_2 until prophase (fig. S2). Cyclin A2 levels remained low in *Ccna2*$^{-/H}$ MEFs throughout the cell cycle, resulting in markedly reduced Cdk activity during S and G_2 phase (fig. S3). Despite these abnormalities, *Ccna2*$^{-/H}$ MEFs showed a normal cell cycle profile (fig. S4).

Both cyclin A2 deficiency and overabundance have been observed in human tumors and predict poor clinical outcome (*7*), but whether and how cyclin A2 deregulation drives malignant growth is unknown. To determine whether reduced cyclin A2 expression contributes to tumorigenesis, we treated *Ccna2*$^{+/+}$ and *Ccna2*$^{-/H}$ mice with 7,12-dimethylbenz(a)anthracene (DMBA), a carcinogen that predisposes mice to lung adenomas and skin papillomas (*8*). *Ccna2*$^{-/H}$ mice showed a marked increase in tumor incidence and multiplicity in both lung and skin (Fig. 1B). Furthermore, lung adenomas of *Ccna2*$^{-/H}$ mice were larger in size. *Ccna2*$^{-/H}$ mice were also more susceptible to spontaneous tumors, particularly lung adenomas (Fig. 1C). Collectively, these data establish that cyclin A2 insufficiency promotes neoplastic transformation.

To identify the underlying defects, we screened for chromosomal instability, a hallmark of human malignancies. Splenocytes and MEFs of *Ccna2*$^{-/H}$ mice had increased aneuploidy (fig. S5A). *Ccna2*$^{-/H}$ MEFs showed predisposition to two types of chromosome segregation errors: chromatin bridges and lagging chromosomes (Fig. 2A). The latter are the result of merotelic attachment, a microtubule-kinetochore malattachment caused by spindle defects, including defects in attachment error correction, microtubule dynamics, mitotic timing, centrosome disjunction, and centrosome movement (*9*). We systematically screened *Ccna2*$^{-/H}$ MEFs for lagging chromosomes, and by measuring the separation between centrosomes in G_2 and prophase, we found that the movement of sister centrosomes to opposite poles was impaired (Fig. 2B and fig. S5, B to F). Cells with delayed centrosome separation form asymmetrical spindles and lagging chromosomes at increased rates (*10*). Consistent with this, spindle geometry defects occurred at high frequency in *Ccna2*$^{-/H}$ MEFs (Fig. 2C). Furthermore, lagging chromosomes were more prevalent in *Ccna2*$^{-/H}$ MEFs with asymmetrical as opposed to symmetrical spindles (fig. S5, G and H).

The motor protein Eg5 accumulates at centrosomes in prophase to drive centrosome movement (*11*). Loading of Eg5 was markedly reduced in *Ccna2*$^{-/H}$ MEFs, as was centrosomal accumulation of cyclin A2 (Fig. 2D and fig. S5I). Centrosome targeting of Eg5 is dependent on Cdk-mediated phosphorylation of Thr^{926} (T926) (*11*). T926 phosphorylation was reduced in *Ccna2*$^{-/H}$ MEFs despite normal expression of Eg5 and alternative Cdk1 and Cdk2 partners, including cyclins B and E (Fig. 2E and fig. S5J). Restoration of cyclin A2 expression in *Ccna2*$^{-/H}$ MEFs normalized T926 phosphorylation and corrected centrosomal loading of Eg5, centrosome movement, and spindle geometry (fig. S5, K to N). Collectively, these results uncover a nonredundant catalytic role of cyclin A2–Cdk in targeting Eg5 to centrosomal

[1]Department of Pediatric and Adolescent Medicine, Mayo Clinic, Rochester, MN, USA. [2]Department of Biochemistry and Molecular Biology, Mayo Clinic, Rochester, MN, USA. [3]Department of Immunology, Mayo Clinic, Rochester, MN, USA.
***Corresponding author. Email: vandeursen.jan@mayo.edu**

Downloaded from http://science.sciencemag.org/ on October 7, 2016

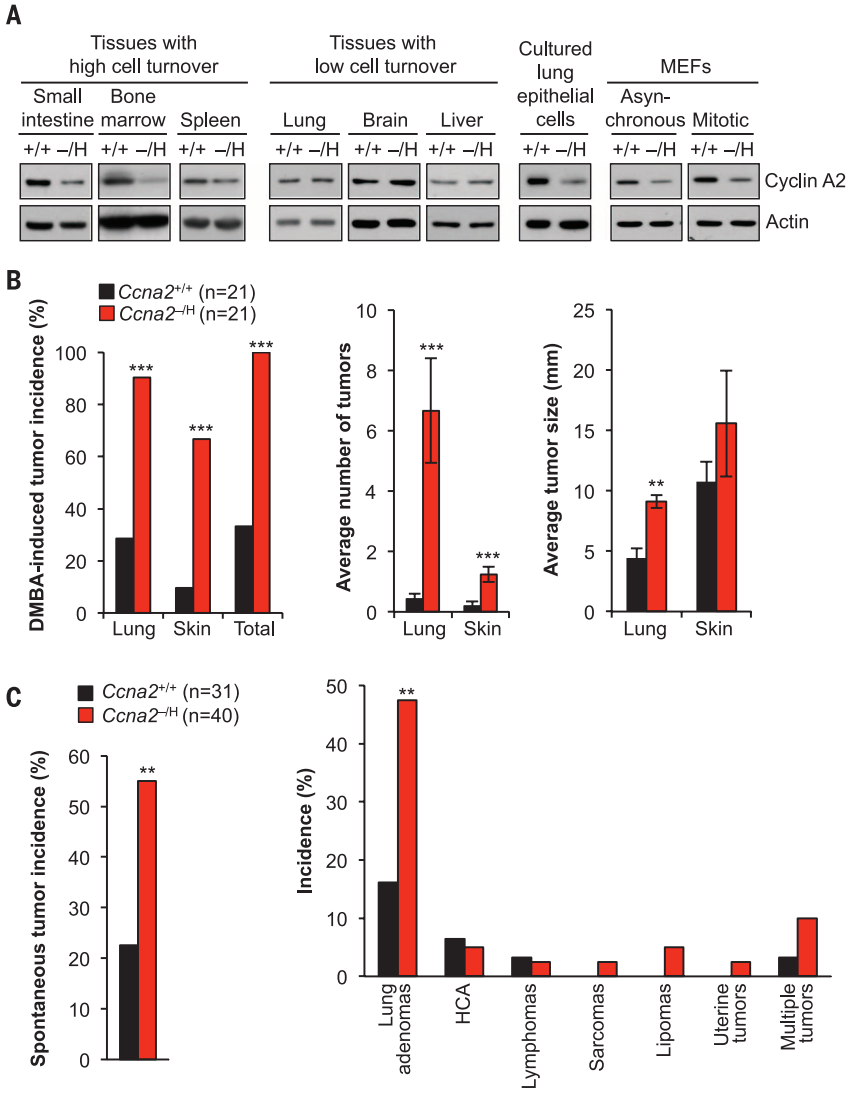

Fig. 1. Cyclin A2 insufficiency drives tumorigenesis. (**A**) Immunoblot analysis of cyclin A2 in tissues and cultured primary cells of *Ccna2*$^{+/+}$ (+/+) and *Ccna2*$^{-/H}$ (−/H) mice. Actin was used as a loading control. (**B**) Incidence, multiplicity, and size of DMBA-induced tumors in 5-month-old mice. (**C**) Overall and tissue-specific incidences of spontaneous tumors in 16-month-old mice. HCA, hepatocellular adenomas. $^{**}P < 0.01$, $^{***}P < 0.001$.

microtubules for proper centrosome movement and spindle formation.

Chromatin bridges, the other chromosome segregation defect observed in *Ccna2*$^{-/H}$ MEFs, can be caused by defects in DNA replication, DNA decatenation, or cohesin cleavage (*12*, *13*). *Ccna2*$^{-/H}$ MEFs properly targeted topoisomerase IIα to inner centromeric regions early in mitosis and had normal separase activity (fig. S6, A and B), which suggests that bridge formation was unlikely to result from decatenation or cohesin cleavage defects. In DNA fiber assays, replication forks of *Ccna2*$^{-/H}$ cells progressed at reduced rates and stalled more frequently than did *Ccna2*$^{+/+}$ cells (Fig. 3A and fig. S6, C to G). Phosphorylation of checkpoint kinase 1 (Chk1) at Ser^{345} (S345), a marker of replication stress (*14*), was elevated in *Ccna2*$^{-/H}$ MEFs (Fig. 3B). Furthermore, the efficiency with which hydroxyurea-stalled replication forks of *Ccna2*$^{-/H}$ MEFs restarted was markedly reduced (fig. S6H). Unreplicated single-stranded DNA (ssDNA) at stalled replication forks is vulnerable to breakage (*14*). Visualization of DNA damage repair foci by staining for the presence of the DNA repair proteins γH2AX and 53BP1 demonstrated that *Ccna2*$^{-/H}$ cells accumulate more double-stranded DNA breaks (DSBs; fig. S7, A to F). Furthermore, radiation-induced DSBs were repaired with reduced efficiency in *Ccna2*$^{-/H}$ MEFs (fig. S7, G and H). Rad51, a key component of DSB repair (*15*), failed to accumulate at radiation-induced DSBs in a large proportion of *Ccna2*$^{-/H}$ MEFs (fig. S7, I to L). Rad51 accumulation at DSBs is dependent on end resection, a key step in the repair process that is measured by staining for RPA2, a repair protein that stabilizes ssDNA intermediates (*15*). Analysis of RPA2 and γH2AX at 8 hours after γ-irradiation revealed that RPA2 localization at DSBs was markedly reduced in *Ccna2*$^{-/H}$ MEFs (fig. S7, M and N).

The MRN complex, composed of Mre11, Rad50, and Nbs1, plays a central role in both replication fork restart and DSB repair (*15*). Western blot analysis revealed that levels of Mre11 and Rad50 protein, but not Nbs1 protein, were consistently reduced in both irradiated and nonirradiated *Ccna2*$^{-/H}$ MEFs (Fig. 3C). Levels of Mre11 and Rad50 were also low in *Ccna2*$^{-/H}$ tumors, although Cdk2 activity appeared normal (fig. S8). Analysis of cell cycle–dependent expression showed that both Mre11 and Rad50 levels peaked in *Ccna2*$^{+/+}$ MEFs during S and G_2 phase, similar to cyclin A2 expression (figs. S9 and S10). Expression of Mre11 and Rad50 in S and G_2 phases was substantially lower in *Ccna2*$^{-/H}$ MEFs. Ectopic expression of cyclin A2 restored both Mre11 and Rad50 protein levels (Fig. 3D). *Mre11* and *Rad50* mRNA levels and ratios of nuclear to cytoplasmic distribution in *Ccna2*$^{-/H}$ MEFs were similar to those of *Ccna2*$^{+/+}$ MEFs (fig. S11, A to C), indicating that reduced expression of Mre11 and Rad50 was not due to altered transcription or defective nuclear export. Furthermore, proteasome degradation was not responsible, as treatment of *Ccna2*$^{-/H}$ MEFs with the proteasome inhibitor MG132 did not alter Mre11 and Rad50 levels (fig. S11D).

However, *Mre11* and *Rad50* mRNA abundance in polysomes was reduced in *Ccna2*$^{-/H}$ MEFs, suggesting reduced translation (Fig. 3E and fig. S12, A to C). To determine whether this was a direct effect, we immunoprecipitated cyclin A2 and analyzed it for the presence of *Mre11*, *Rad50* transcripts, and several control transcripts by quantitative reverse transcription polymerase chain reaction (RT-qPCR). Intriguingly, cyclin A2 selectively precipitated *Mre11* transcripts in *Ccna2*$^{+/+}$ MEFs (Fig. 3F). Similar results were obtained using human primary fibroblasts and HeLa cells (fig. S12D). Cyclin A2 knockdown in these cells resulted in reduced MRE11 and RAD50 protein levels, consistent with results in *Ccna2*$^{-/H}$ MEFs (fig. S12E). Cyclin A1 had no Mre11 RNA binding ability (fig. S12, F and G). Two observations suggested that cyclin A2 regulation of Mre11 and Rad50 was Cdk-independent: Neither Cdk2 nor Cdk1 immunoprecipitation enriched *Mre11* transcripts comparably to cyclin A2 immunoprecipitation (fig. S12H), and inhibition of Cdk2 activity in wild-type MEFs by roscovitine had no impact on Mre11 levels (fig. S12I). Mre11 knockdown resulted in low Rad50 protein levels, but Rad50 depletion did not affect Mre11, indicating that Rad50 abundance is Mre11-dependent (fig. S13, A and B). Ectopic expression of Mre11 in *Ccna2*$^{-/H}$ MEFs normalized both Mre11 and Rad50 protein levels but had no impact on cyclin A2 levels (Fig. 3G). Coincidentally, polysome association of *Rad50* mRNA was restored (fig. S13C), reinforcing the idea that Rad50 translation is Mre11-dependent, although Mre11 immunoprecipitates did not contain *Rad50* transcripts (fig. S13D). Ectopic expression of Mre11 in *Ccna2*$^{-/H}$ cells rescued DSBs and chromatin bridges, indicating that Mre11 deficiency is the driver of these chromosomal phenotypes (fig. S13, E and F). Expression of CtIP, a binding partner of the MRN

Downloaded from http://science.sciencemag.org/ on October 7, 2016

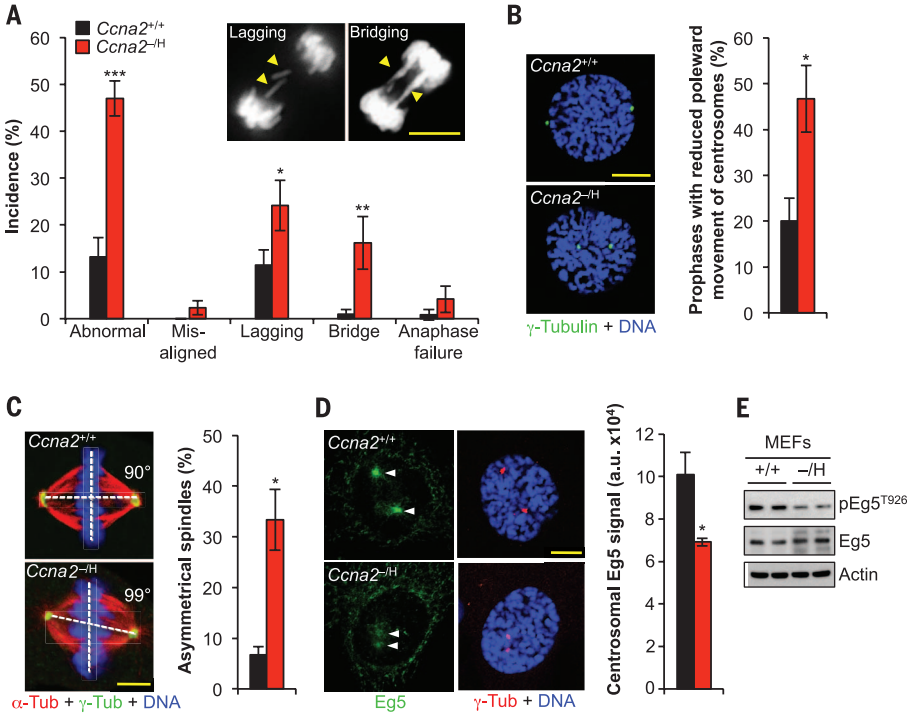

Fig. 2. Cyclin A2–Cdk1 regulates spindle pole movement by targeting Eg5 to centrosomes. (**A**) Live-cell imaging analysis of chromosome mis-segregations in MEFs expressing histone H2B tagged with a monomeric form of red fluorescent protein (H2B-mRFP). Inset shows examples of *Ccna2*$^{-/H}$ MEFs with chromosome lagging or bridging. (**B**) Left: Images of MEFs in prophase stained for γ-tubulin and DNA. Right: Incidence of prophases with delayed centrosome movement. (**C**) Left: Maximum-intensity projection images of immunostained metaphases. Right: Incidence of cells with abnormal spindle geometry. (**D**) Left: Images of prophase MEFs immunostained for Eg5 and γ-tubulin. Right: Quantification of Eg5 signal at centrosomes in prophase. (**E**) Immunoblot analysis of phosphorylated Eg5^{T926} and total Eg5 in asynchronously cultured MEFs. Actin was used as loading control. DNA in (B) to (D) was visualized with Hoechst. Scale bars, 10 μm. Data are means ± SEM [N = 6 independent MEF lines per genotype in (A), and N = 3 in (B) to (D); 10 cells per line were analyzed in (B) to (D)]. *P < 0.05, **P < 0.01, ***P < 0.001 (unpaired t test).

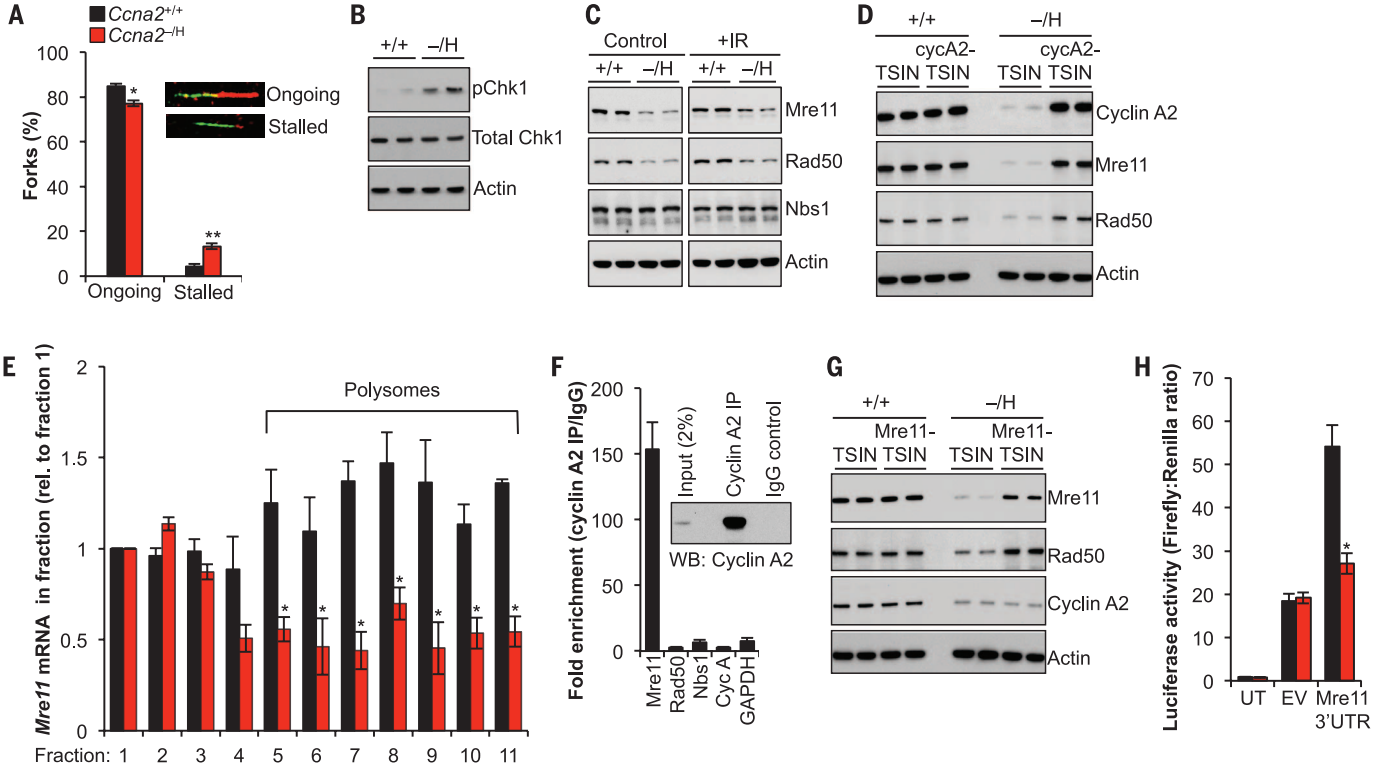

Fig. 3. Cyclin A2 interacts with *Mre11* mRNA to regulate its translation. (**A**) Percentages and examples of ongoing and stalled replication forks in MEFs. Inset shows examples of fibers. (**B**) Immunoblot analysis for Chk1 phosphorylation at S345. (**C**) Immunoblots of control and γ-irradiated (IR) MEF lysates probed for the indicated proteins. (**D**) Immunoblot analysis of asynchronously cultured MEFs transduced with control (TSIN) or *Ccna2*-containing (cycA2-TSIN) lentiviruses. (**E**) Quantification of *Mre11* mRNA in polysome fractions of MEFs. (**F**) Cyclin A2 RNA immunoprecipitation (IP) in MEFs followed by RT-qPCR analysis for the indicated genes. IgG, immunoglobulin G; WB, Western blot. (**G**) As (D) but using control (TSIN) and *Mre11*-containing lentivirus. (**H**) Luciferase activity in cells transfected with 3′UTR of *Mre11* mRNA. UT, untransfected; EV, empty vector. Actin was used as loading control in (B), (C), (D), and (G). Data in (A), (E), (F), and (H) are means ± SEM (N = 3 independent MEF lines per genotype). *P < 0.05, **P < 0.01 (unpaired t test).

Downloaded from http://science.sciencemag.org/ on October 7, 2016

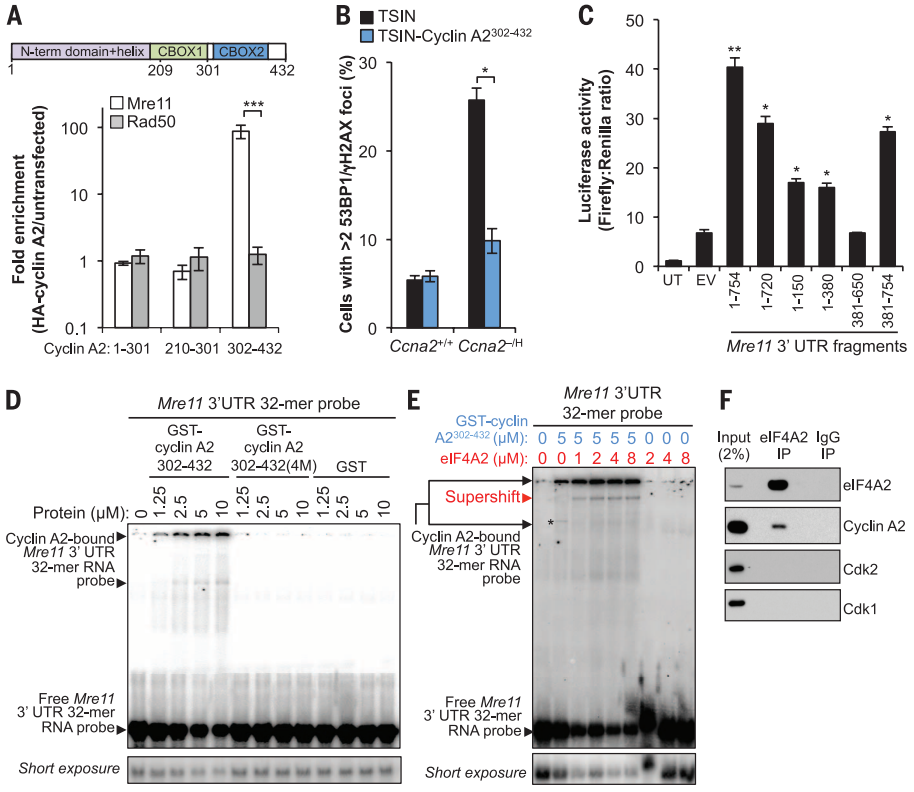

Fig. 4. The cyclin A2 C terminus directly binds to a conserved sequence in the *Mre11* 3′UTR. (**A**) RNA immunoprecipitation in wild-type MEFs expressing the indicated HA-tagged cyclin A2 deletion mutants. RNAs coprecipitating with HA–cyclin A2 mutants were analyzed by RT-qPCR. (**B**) Quantification of cyclin $A2^{302-432}$–expressing cells with two or more γH2AX- and 53BP1-colocalized foci. (**C**) Luciferase activity in MEFs transfected with different regions of the *Mre11* 3′UTR. (**D**) Representative native gel shifts showing a specific interaction between recombinant cyclin $A2^{302-432}$ and the *Mre11* 3′UTR conserved sequence. (**E**) Same as (D) but in the presence of recombinant human eIF4A2. (**F**) Western blot analysis of eIF4A2-coprecipitating proteins in wild-type MEFs. Data in (A) to (C) are means ± SEM ($N = 3$ independent MEF lines per genotype). $^*P < 0.05$, $^{**}P < 0.01$, $^{***}P < 0.001$ (unpaired t test).

complex implicated in end resection, was subnormal in $Ccna2^{-/H}$ MEFs through a Cdk2-dependent, Mre11-independent mechanism and therefore is unlikely to contribute to the chromosomal phenotype of $Ccna2^{-/H}$ cells (fig. S14).

RNA sequencing analysis of cyclin A2, E2, and B1 immunoprecipitates demonstrated that cyclin A2 exclusively binds *Mre11* transcripts and that cyclins E2 and B1 have no RNA binding ability (tables S1 to S3). Mre11 RNA sequence reads exclusively mapped to the 3′ untranslated region (3′UTR), indicating that this region contains the cyclin A2 binding site (fig. S15A). When introduced downstream of a luciferase reporter, the *Mre11* 3′UTR enhanced luciferase activity in $Ccna2^{+/+}$ MEFs but not in $Ccna2^{-/H}$ MEFs (Fig. 3H). Ectopic expression of cyclin A2 in $Ccna2^{-/H}$ MEFs corrected this deficiency (fig. S15B).

Expression of hemagglutinin (HA)–tagged cyclin A2 deletion mutants in MEFs revealed that residues 302 to 432 are necessary and sufficient for *Mre11* transcript binding (Fig. 4A). This fragment, which lacks Cdk-binding ability, restored Mre11 and Rad50 expression and prevented DSB formation in $Ccna2^{-/H}$ MEFs (Fig. 4B and fig. S16A) but did not correct Cdk-dependent phenotypes such as Eg5 loading, centrosome movement, spindle geometry, and chromosome lagging (fig. S16, B to F). Conversely, expression of amino acids 1 to 301, a fragment that binds to Cdk, corrected the latter defects but failed to restore Mre11 and Rad50 expression and DSB repair (fig. S16, G to K). Using deletion mutagenesis, we identified two subregions within the *Mre11* 3′UTR, a 150-nucleotide (nt) segment at the 5′ end and a 34-nt segment at the 3′ end, as potential cyclin A2 binding sites (Fig. 4C). Recombinant glutathione *S*-transferase (GST)–cyclin $A2^{302-432}$ directly bound a radiolabeled RNA probe spanning the last 32 nt of the *Mre11* 3′UTR in an electrophoretic mobility shift assay, but not a scrambled 32-nt oligomer (32-mer) (Fig. 4D and fig. S17, A and B). Neither GST–cyclin $A2^{1-209}$ nor GST–cyclin $A2^{302-432(4M)}$, which carries mutations in four putative ribonucleic acid contact sites required for restoration of Mre11 and Rad50 expression in $Ccna2^{-/H}$ MEFs by ectopic expression of cyclin A2 (fig. S17, B to E), was able to bind the *Mre11* RNA probe (Fig. 4D).

Translation initiation factor eIF4A2, a previously documented putative cyclin A2 interactor (*16*), supershifted GST–cyclin $A2^{302-432}$–bound *Mre11* RNA complexes but did not bind the probe in the absence of cyclin A2 (Fig. 4E). eIF4A2, but not Cdk1 or Cdk2, coimmunoprecipitated cyclin A2 under physiological conditions, indicating that cyclin A2 bound to *Mre11* mRNA is free of Cdk binding partners (Fig. 4F). Cyclin A2 interacted with eIF4A2 and *Mre11* RNA through a common domain (fig. S17F). Finally, using the CRISPR/Cas9 technique, we generated mice homozygously lacking the last 47 nt of the *Mre11* 3′UTR (designated $Mre11^{\Delta A2/\Delta A2}$ MEFs), which were viable and overtly normal (fig. S18). $Mre11^{\Delta A2/\Delta A2}$ MEFs had normal amounts of *Mre11* mRNA, but the transcripts showed markedly reduced polysome association, resulting in low Mre11 protein levels (fig. S19, A to D). $Mre11^{\Delta A2/\Delta A2}$ MEFs entirely phenocopied $Ccna2^{-/H}$ MEFs, except for phenotypes related to phosphorylation of Eg5 mediated by cyclin A2–Cdk (fig. S19, E to K, and fig. S20).

Our work exposed two novel cyclin A2 functions. First, we identified a role for the cyclin A2 N terminus in the formation of bipolar mitotic spindles by regulating Eg5 loading onto centrosomes through phosphorylation of T926. Second, the C terminus of cyclin A2, which has low sequence conservation among cyclin family members, directly binds to a conserved region in the 3′UTR of *Mre11* transcripts to promote their translation, presumably through an interaction with eIF4A2. In doing so, cyclin A2 coordinates its well-established Cdk-dependent functions in the initiation and progression of DNA synthesis (*16*) while simultaneously reinforcing stabilization of the key machinery responsible for repairing DNA lesions caused by replication errors. Cyclins have hitherto not been implicated in RNA binding. The observation that cyclin A2 seemingly interacts with just a single transcript, *Mre11* mRNA, was unexpected and appears to be a unique feature among RNA binding proteins.

REFERENCES AND NOTES

1. H. Hochegger, S. Takeda, T. Hunt, *Nat. Rev. Mol. Cell Biol.* **9**, 910–916 (2008).
2. H. Beamish *et al.*, *J. Biol. Chem.* **284**, 29015–29023 (2009).
3. L. Kabeche, D. A. Compton, *Nature* **502**, 110–113 (2013).
4. N. Arsic *et al.*, *J. Cell Biol.* **196**, 147–162 (2012).
5. M. Murphy *et al.*, *Nat. Genet.* **15**, 83–86 (1997).
6. I. Kalaszczynska *et al.*, *Cell* **138**, 352–365 (2009).
7. C. H. Yam, T. K. Fung, R. Y. Poon, *Cell. Mol. Life Sci.* **59**, 1317–1326 (2002).
8. M. Serrano *et al.*, *Cell* **85**, 27–37 (1996).
9. R. M. Naylor, K. B. Jeganathan, X. Cao, J. M. van Deursen, *J. Clin. Invest.* **126**, 543–559 (2016).
10. J. H. van Ree, H. J. Nam, K. B. Jeganathan, A. Kanakkanthara, J. M. van Deursen, *Nat. Cell Biol.* **18**, 814–821 (2016).
11. A. Slangy *et al.*, *Cell* **83**, 1159–1169 (1995).
12. H. J. Nam, J. M. van Deursen, *Nat. Cell Biol.* **16**, 538–549 (2014).
13. R. A. Burrell *et al.*, *Nature* **494**, 492–496 (2013).
14. M. K. Zeman, K. A. Cimprich, *Nat. Cell Biol.* **16**, 2–9 (2014).
15. T. H. Stracker, J. H. Petrini, *Nat. Rev. Mol. Cell Biol.* **12**, 90–103 (2011).
16. F. W. Pagliuca *et al.*, *Mol. Cell* **43**, 406–417 (2011).

ACKNOWLEDGMENTS

We thank W. Zhou, M. Li, F. Jin, and X. Wang for assistance and D. Compton for providing photoactivatable GFP-tagged α-tubulin. Supported by NIH grants CA126828 and CA168709 (J.M.v.D.) and CA166025 (L.J.M.).

SUPPLEMENTARY MATERIALS

www.sciencemag.org/content/353/6307/1549/suppl/DC1
Materials and Methods
Figs. S1 to S20
Tables S1 to S4
References (*17*–*38*)

24 March 2016; accepted 29 August 2016
10.1126/science.aaf7463

Downloaded from http://science.sciencemag.org/ on October 7, 2016

SIGNALING

Drosophila insulin release is triggered by adipose Stunted ligand to brain Methuselah receptor

Renald Delanoue,[1]‡ Eleonora Meschi,[1]† Neha Agrawal,[1]*† Alessandra Mauri,[1] Yonit Tsatskis,[2] Helen McNeill,[2] Pierre Léopold[1]‡

Animals adapt their growth rate and body size to available nutrients by a general modulation of insulin–insulin-like growth factor signaling. In *Drosophila*, dietary amino acids promote the release in the hemolymph of brain insulin-like peptides (Dilps), which in turn activate systemic organ growth. Dilp secretion by insulin-producing cells involves a relay through unknown cytokines produced by fat cells. Here, we identify Methuselah (Mth) as a secretin-incretin receptor subfamily member required in the insulin-producing cells for proper nutrient coupling. We further show, using genetic and ex vivo organ culture experiments, that the Mth ligand Stunted (Sun) is a circulating insulinotropic peptide produced by fat cells. Therefore, Sun and Mth define a new cross-organ circuitry that modulates physiological insulin levels in response to nutrients.

Environmental cues, such as dietary products, alter animal physiology by acting on developmental and metabolic parameters like growth, longevity, feeding, and energy storage or expenditure (*1*). The systemic action of this control suggests that intermediate sensor tissues evaluate dietary nutrients and trigger hormonal responses. Previous work in *Drosophila melanogaster* established that a specific organ called the fat body translates nutritional information into systemic growth-promoting signals (*2*–*4*). The leptinlike Janus kinase–signal transducers and activators of transcription (JAK-STAT) ligand unpaired 2 and the CCHamid2 peptide are produced by fat cells in response to both sugar and fat and trigger a metabolic response (*5*, *6*). Dietary amino acids activate TORC1 signaling in fat cells and induce the production of relay signals that promote the release of insulin-like peptides (Dilps) by brain insulin-producing cells (IPCs) (*3*, *7*). Two fat-derived peptides (GBP1 and GBP2) activate insulin secretion in response to a protein diet, although their receptor and neural targets remain uncharacterized (*8*). To identify critical components of this organ crosstalk, we conducted a genetic screen in *Drosophila* larvae (fig. S1A). The gene *methuselah* (*mth*), which encodes a heterotrimeric GTP-binding protein (G protein)–coupled receptor belonging to the subfamily of the secretin-incretin receptor subfamily (*9*–*12*) came out as a strong hit. Impairing *mth* function in the IPCs reduces larval body growth (Fig. 1A), whereas silencing *mth* in a distinct set of neurons or in the larval fat body had no impact on pupal volume (fig. S1B). Larvae in which expression of the *mth* gene is reduced by RNA interference (RNAi), specifically in the IPCs (hereafter, *dilp2>mth-Ri*), present an accumulation of Dilp2 (Fig. 1B) and Dilp5 (fig. S1G) in the IPCs, whereas *dilp2* gene expression remains unchanged (fig. S1H), a phenotype previously described as impaired Dilp secretion (*13*). Indeed, forced depolarization of the IPCs rescues pupal volume and Dilp2 accumulation upon IPC-specific *mth* depletion (knockdown) (fig. S1, J and K). Therefore, Mth is required for Dilps secretion and larval body growth.

Two peptides encoded by the *stunted* (*sun*) gene, SunA and SunB, serve as bona fide ligands for Mth and activate a Mth-dependent intracellular calcium response (*14*, *15*) (see fig. S3E for peptide map). Silencing *sun* in fat cells, but no other larval tissue, of well-fed larvae mimics the *mth* loss-of-function phenotype (Fig. 1, C and D, and fig. S1I) with no effect on the developmental timing (fig. S1L). Conversely, overexpression of *sun* in the larval fat body (*lpp>sun*) partially rescues the systemic growth inhibition observed upon feeding larvae a diet low in amino acids (Fig. 1E and fig. S1M) or upon "genetic starvation" [silencing of the *slimfast* (*slif*) gene in fat cells (*3*)] (fig. S1N). This growth rescue is abolished in mth^1 homozygous mutants (Fig. 1F). This shows that Sun requires Mth to control growth. However, *sun* overexpression has no effect in animals fed a normal diet (Fig. 1E). A modification of *sun* expression does not prevent fat body cells from responding to amino acid deprivation as seen by the level of TORC1 signaling, general morphology, and lipid droplet accumulation (fig. S2, A and B) but affects the ability of larvae to resist to starvation (fig. S2C).

Dilp2-containing secretion granules accumulate in the IPCs following starvation and are rapidly released upon refeeding (*7*) (fig. S3A). Mth is required in the IPCs to promote Dilp secretion after refeeding (Fig. 2A and fig. S3B), and forced membrane depolarization of IPCs using a bacterial sodium channel (*dilp2>NaChBac*) is dominant over the blockade of Dilp2 secretion in *dilp2>mth-Ri* animals (Fig. 2A). This dominance indicates that Mth acts upstream of the secretion machinery. In addition, Dilp2 secretion after refeeding is abrogated in *lpp>sun-Ri* animals (Fig. 2B), and overexpression of *sun* in fat cells prevents Dilp2 accumulation upon starvation (Fig. 2B). Altogether, these findings indicate that Mth and its ligand Sun are two components of the systemic nutrient response controlling Dilp secretion.

Hemolymph from fed animals triggers Dilp2 secretion when applied to brains dissected from starved larvae (*7*) (Fig. 3A). This insulinotropic activity requires the function of Mth in the IPCs (Fig. 3A and fig. S3C) and the production of Sun by fat body cells (Fig. 3B). Conversely, overexpressing *sun* in the fat body (*lpp>sun*) is sufficient to restore insulinotropic activity to the hemolymph of starved larvae (fig. S3D). A 2-hour incubation with a synthetic peptide corresponding to the Sun isoform A (Sun-A) is also sufficient to induce Dilp secretion from starved brains (Fig. 3C). A similar effect is observed with an N-terminal fragment of Sun (N-SUN) that contains the Mth-binding domain (*14*, *15*) but not with a C-terminal fragment (C-SUN) that does not bind Mth (fig. S3, E and F). The insulinotropic effect of N-SUN is no longer observed in brains from larvae of the *mth* allele, mth^1 (fig. S3F). This absence of effect indicates that N-SUN action requires Mth in the brain. In addition, preincubation of control hemolymph with antiserum containing Sun antibodies specifically suppresses its insulinotropic function (Fig. 3D). These results indicate that Sun is both sufficient and necessary for insulinotropic activity in the hemolymph of protein-fed animals.

To directly quantify the amount of circulating Sun protein, we performed Western blot experiments on hemolymph using antibodies against Sun. A 6-kD band was detected in hemolymph collected from fed larvae (Fig. 4A), and size was confirmed using Schneider 2 (S2) cell extracts (Fig. 4C). The band intensity was reduced upon *sun* knockdown in fat body cells but not in gut cells (Fig. 4C). Therefore, circulating Sun peptide appears to be mostly contributed by fat cells, as suggested by functional experiments (see Fig. 1C). The levels of circulating Sun are strongly reduced upon starvation (Fig. 4A). In line with this, *sun* transcripts are drastically reduced after 4 hours of protein starvation and start increasing after 1 hour of refeeding (Fig. 4B), whereas expression of the *sun* homolog *CG31477* is not modified (fig. S4A). *sun* transcription is not affected by blocking TORC1, the main sensor for amino acids in fat body cells (*3*) (*lpp>TSC1/2* in fig. S4B). However, adipose-specific TORC1 inhibition induces a dramatic reduction of circulating Sun (Fig. 4C), indicating that TORC1 signaling controls

[1]Université Côte d'Azur, CNRS, INSERM, Institute of Biology Valrose (iBV), 06100 Nice, France. [2]Lunenfeld Tanenbaum Research Institute, Mount Sinai Hospital, Toronto, Ontario M5G 1X5, Canada
*Present address: The Gurdon Institute and Department of Physiology, Development and Neuroscience, University of Cambridge, Tennis Court Road, Cambridge CB2 1QN, UK.
†These authors contributed equally to this work.
‡Corresponding author. Email: delanoue@unice.fr (R.D.); leopold@unice.fr (P.L.)

Downloaded from http://science.sciencemag.org/ on October 7, 2016

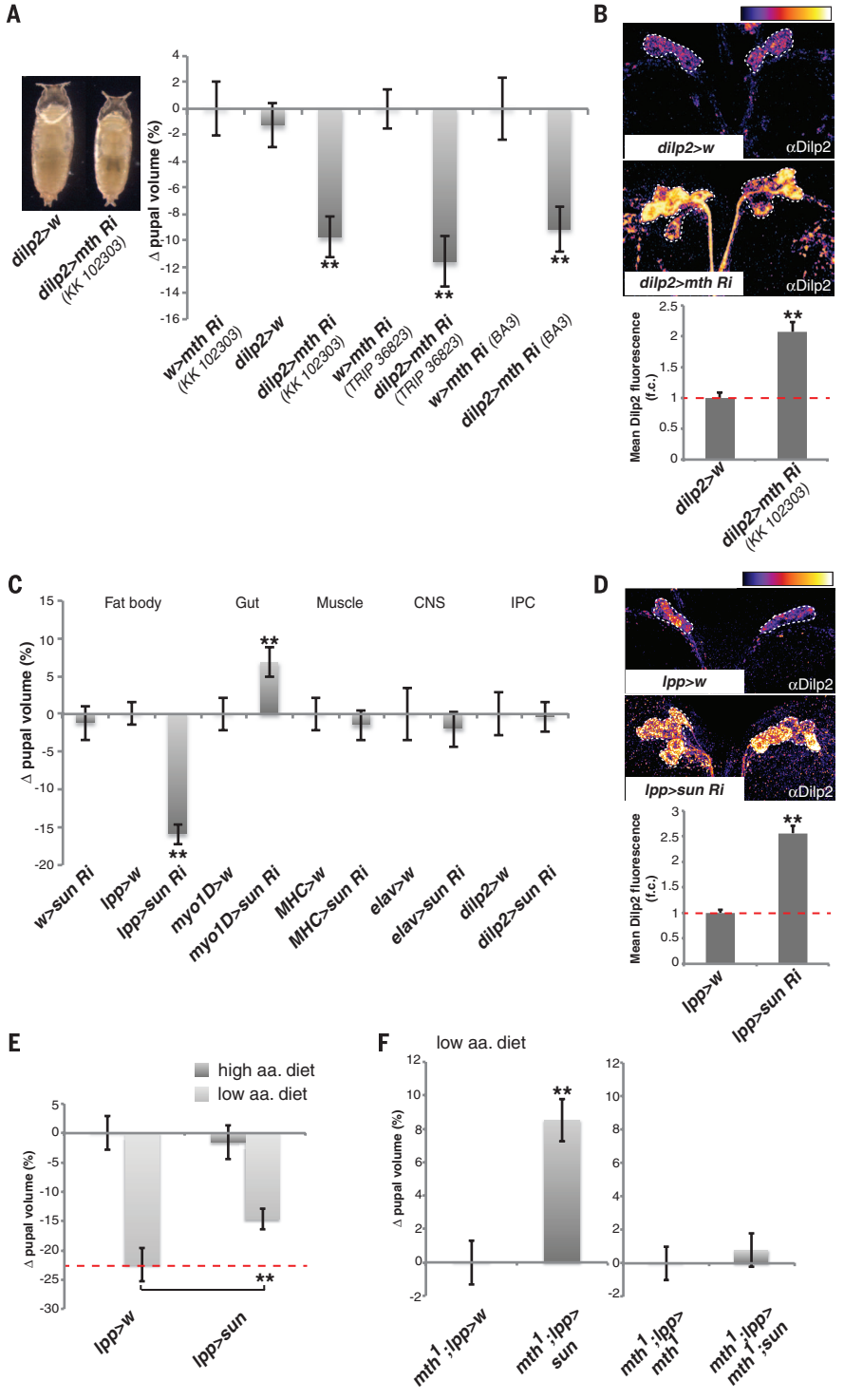

Fig. 1. Mth and Sun are required for systemic growth. (**A**) Three different *mth* RNAi constructs (*KK 102303*, *TRIP 36823*, and *BA3*) decrease pupal size when driven in the IPC (*dilp2>*) ($n > 20$). (**B**) Silencing *mth* in the IPC induces accumulation of Dilp2 ($n > 20$). Fluorescence intensity measured as fold change (f.c.). (**C**) Silencing *sun* in the fat body (*lpp-Gal4>sun-Ri*) reduces pupal volume. No defect is observed when silencing in other tissues (*myo1d-Gal4*, gut; *MHC-Gal4*, muscle; *elav-Gal4*, CNS; or *dilp2-Gal4*, IPC). (**D**) *sun* silencing in the fat body causes Dilp2 accumulation in the IPC ($n > 60$). (**E**) *sun* overexpression in the fat body partially rescues the pupal size reduction observed in larvae fed a low-protein diet compared with those fed a high-protein diet ($n > 20$). Amino acid, aa. Red dashed line here and below shows the level of controls. (**F**) Overgrowth observed upon forced fat body expression of *sun* in larvae fed a low–amino acid diet is observed in $mth^{1/+}$ but not in $mth^{1/1}$ homozygous flies ($n > 40$). In graphs, means are shown, and error bars represent ±SEM; $^{**}P < 0.01$.

Sun peptide translation or secretion from fat cells. PGC1-Spargel is a transcription activator, the expression of which relies on nutritional input (fig. S4D) (*16*). We find that *PGC1* is required for *sun* transcription (Fig. 4D) and that fat body silencing of *PGC1* and *sun* induce identical larval phenotypes (Fig. 4E and fig. S4C). Although *PGC1* expression is strongly suppressed upon starvation, blocking TORC1 activity in fat cells does not reduce *PGC1* expression (fig. S4E). Conversely, knocking down PGC1 does not inhibit TORC1 activity (fig. S4F). This finding suggests that PGC1 and TORC1 act in parallel. Therefore, Sun production by fat cells in response to nutrition is controlled at two distinct levels by PGC1 and TORC1.

The Sun peptide is identical to the ε subunit of the mitochondrial F_1F_0-adenosine triphosphatase (F_1F_0-ATPase) synthase (complex V) (*14*, *17*). Indeed, both endogenous Sun and Sun labeled with a hemagglutinin tag (Sun-HA) (fig. S5A) colocalize with mitochondrial markers in fat cells (fig. S5B), and the Sun peptide cofractionates with mitochondrial complex V in blue native polyacrylamide gel electrophoresis (fig. S5C). In addition, silencing *sun* in fat cells decreases mitochondrial Sun staining (fig. S5B) and the amounts of adenosine triphosphate (ATP) (fig. S5D). However, recent evidence indicates that an ectopic (ecto) form of the F_1F_0-ATP synthase is found associated with the plasma membrane in mammalian and insect cells (*18*–*21*). In addition, coupling factor 6, a subunit of complex V, is found in the plasma (*22*). Therefore, Stunted could participate in two separate functions carried by distinct molecular pools. To address this possibility, we used a modified form of Stunted carrying a green fluorescent protein (GFP) tag at its N terminus (GFP-Sun), next to the mitochondria-targeting signal (MTS) (fig. S5A). When expressed in fat cells, GFP-Sun does not localize to the mitochondria (fig. S6A), contrarily to a Sun peptide tagged at its C-terminal end (Sun-GFP) (fig. S6C). This suggests that addition of the N-terminal tag interferes with the MTS and prevents mitochondrial transport of Sun. However, both GFP-Sun and Sun-GFP are found in the hemolymph (fig. S6B) and rescue pupal size and Dilp2 accumulation in larvae fed a low–amino acid diet as efficiently as wild-type Sun (*wt*-Sun) (Figs. 4F and 1E and fig. S6E) and do so in a *mth*-dependent manner (fig. S6D). This indicates that the growth-promoting function of Sun requires its secretion but not its mitochondrial localization and suggests the existence of one pool of Sun peptide located in the mitochondria devoted to F_1F_0-ATP synthase activity and ATP production and another pool released in the hemolymph for coupling nutrient and growth control. In this line, although fat body levels of Sun are decreased upon starvation (fig. S6F), its mitochondrial localization is not reduced (fig. S6G). This finding indicates that starvation affects a nonmitochondrial pool of Sun. In support of this, starved fat bodies contain normal levels of ATP and lactate (fig. S6, H and I), indicating that mitochondrial oxidative

Downloaded from http://science.sciencemag.org/ on October 7, 2016

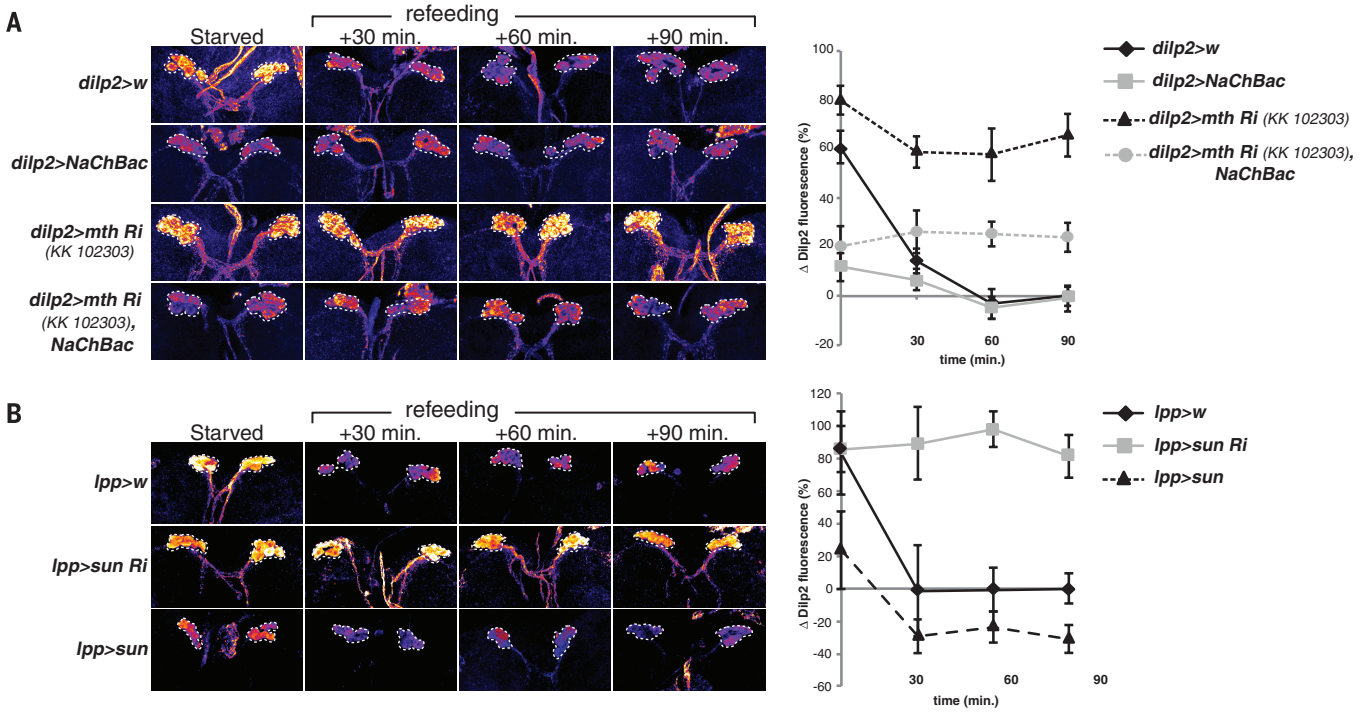

Fig. 2. Mth and Sun control Dilp2 secretion from brain IPCs. (**A**) Representative pictures of Dilp2 staining in IPCs (dashed outline) showing the kinetics of Dilp2 accumulation upon refeeding after prolonged starvation. Genotypes are as indicated. (**B**) *sun* silencing (*lpp>sun-Ri*) in the fat body prevents Dilp2 secretion upon refeeding, whereas *sun* overexpression (*lpp>sun OE*) reduces Dilp2 accumulation upon starvation. Graphs represent quantifications of ΔDilp2 fluorescence relative to *lpp>w* control after 90 min of feeding (means ± SEM; $n > 20$).

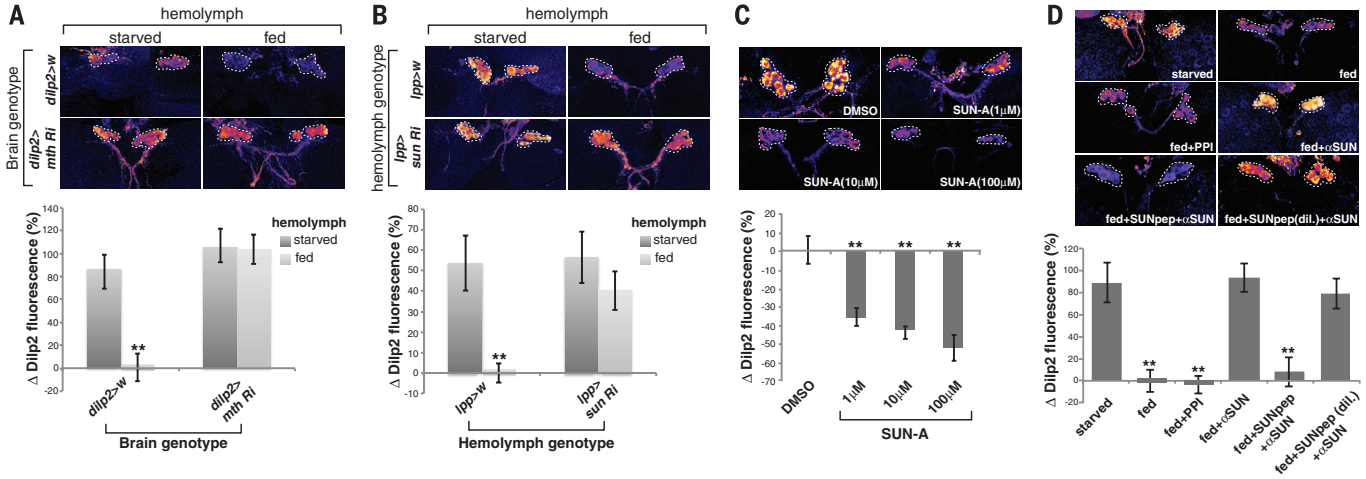

Fig. 3. Sun is a fat body–derived insulinotropic signal. (**A**) Hemolymph collected from fed, but not starved, larvae activates Dilp2 secretion when incubated on dissected brains from starved control (*dilp2>w*), but not *mth*-deficient (*dilp2>mth-Ri*), larvae. (**B**) Hemolymph from fed larvae deficient for adipose *sun* (*lpp>sun-Ri*) does not induce Dilp2 secretion. (**C**) Incubation of brains from starved larvae with various concentrations of SUN-A stimulates Dilp2 secretion. DMSO, dimethyl sulfoxide. (**D**) Hemolymph collected from fed larvae preincubated with preimmune serum (fed+PPI), but not from larvae treated with antibodies against SUN (αSUN), induces Dilp2 secretion. Titration of αSUN with blocking peptides allows reactivation of Dilp2 secretion. Diluted (dil.) blocking peptides do not block αSun action [fed+SUNpep(dil.) + αSUN]. Graphs represent quantifications of ΔDilp2 fluorescence relative to control brains (brains from starved larvae incubated with hemolymph, from fed larvae, or with DMSO) (means ± SEM; $n > 20$); $^{**}P < 0.01$.

phosphorylation is preserved in fat cells in poor nutrient conditions. Last, other subunits from complex V (ATP5a) or complex I (NdufS3) were not detected in circulating hemolymph (fig. S6J). Therefore, the release of Sun in the hemolymph relies on a specific mechanism.

In conclusion, we provide evidence for a molecular cross-talk between fat cells and brain IPCs involving the ligand Stunted and its receptor

Downloaded from http://science.sciencemag.org/ on October 7, 2016

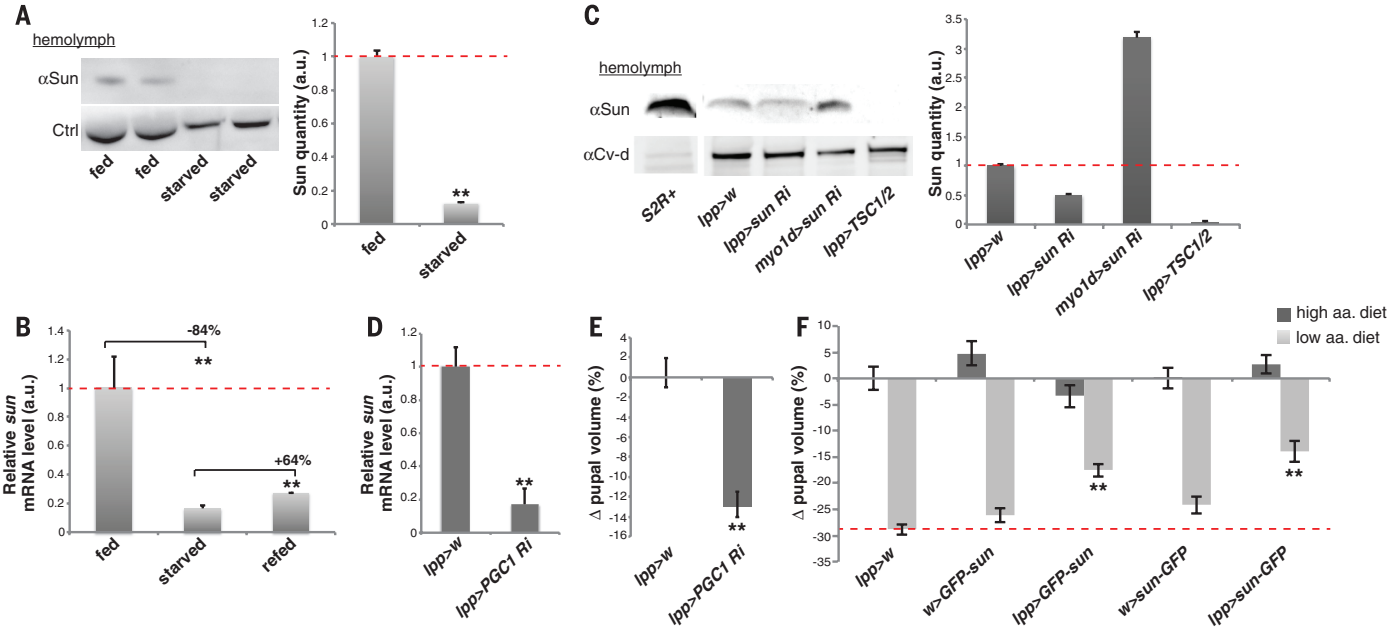

Fig. 4. The level of circulating Sun relies on TOR and PGC1 in fed animals. (**A**) Circulating Sun peptide is detected by Western blotting of hemolymph from fed larvae (lanes 1 and 2) but not starved larvae (lanes 3 and 4). Antibodies against Crossveinless d lipoprotein (αCv-d) are used as a loading control. Quantification in arbitrary units (a.u.) of the normalized circulating Sun detected in the hemolymph according to nutritional conditions (means ± SEM; $n = 4$); $^{**}P < 0.01$. (**B**) The *sun* transcript levels in the fat body decrease upon starvation and increase upon refeeding (measured by quantitative reverse transcription polymerase chain reaction) (means ± SEM; $n = 4$); $^{**}P < 0.01$. (**C**) Circulating Sun levels decrease upon *sun* silencing in fat body cells (*lpp>sun-Ri*) but not in gut cells (*myo1d>sun-Ri*). Blocking TORC1 in fat cells (*lpp>TSC1/2*) strongly decreases circulating Sun. Quantification of normalized circulating Sun. (**D**) *sun* expression is severely reduced when *PGC1* is silenced in fat body cells (means ± SEM; $n = 3$); $^{**}P < 0.01$. (**E**) Silencing *PGC1* in the fat body (*lpp>PGC1-Ri*) decreases pupal size (means ± SEM; $n > 40$); $^{**}P < 0.01$. (**F**) Forced fat body expression of GFP-Sun (*lpp>GFP-Sun*) or Sun-GFP (*lpp>Sun-GFP*) rescues pupal size reduction observed from larvae fed the low–amino acid diet (means ± SEM; $n > 40$); $^{**}P < 0.01$.

Methuselah. Stunted is a moonlighting peptide present both in the mitochondria as part of the F_1F_0-ATP synthase complex and as an insulinotropic ligand circulating in the hemolymph. The mechanism of Stunted release remains to be clarified. The beta subunit of the ectopic form of F_1F_0-ATP synthase is a receptor for lipoproteins (*18*–*21*), which serve as cargos for proteins and peptides. In addition, *Drosophila* lipid transfer particle–containing lipoproteins were shown to act on the larval brain to control systemic insulin signaling in response to nutrition (*23*). This suggests that Sun could be loaded on lipoproteins for its transport. Given the role of insulin–insulin-like growth factor (IGF) signaling in aging, our findings could help in understanding the role of Sun/Mth in aging adult flies (*9*–*11*, *13*, *14*).

The same genetic screen previously identified the fly tumor necrosis factor α Eiger (Egr) as an adipokine necessary for long-term adaptation to protein starvation (*24*), and recent work pointed to other adipose factors (*5*, *6*, *8*), illustrating the key role of the larval fat body in orchestrating nutrient response. The multiplicity of adipose factors and their possible redundancy could explain the relatively mild starvation-like phenotype obtained after removal of only one of them. Overall, these findings suggest a model whereby partially redundant fat-derived signals account for differential response to positive and negative valence of various diet components, as well as acute versus long-term adaptive responses.

REFERENCES AND NOTES

1. D. S. Andersen, J. Colombani, P. Léopold, *Trends Cell Biol.* **23**, 336–344 (2013).
2. J. S. Britton, B. A. Edgar, *Development* **125**, 2149–2158 (1998).
3. J. Colombani *et al.*, *Cell* **114**, 739–749 (2003).
4. J. F. Martin, E. Hersperger, A. Simcox, A. Shearn, *Mech. Dev.* **92**, 155–167 (2000).
5. A. Rajan, N. Perrimon, *Cell* **151**, 123–137 (2012).
6. H. Sano *et al.*, *PLOS Genet.* **11**, e1005209 (2015).
7. C. Géminard, E. J. Rulifson, P. Léopold, *Cell Metab.* **10**, 199–207 (2009).
8. T. Koyama, C. K. Mirth, *PLOS Biol.* **14**, e1002392 (2016).
9. A. R. Araújo *et al.*, *PLOS ONE* **8**, e63747 (2013).
10. Y. J. Lin, L. Seroude, S. Benzer, *Science* **282**, 943–946 (1998).
11. W. Song *et al.*, *Neuron* **36**, 105–119 (2002).
12. A. P. West Jr., L. L. Llamas, P. M. Snow, S. Benzer, P. J. Bjorkman, *Proc. Natl. Acad. Sci. U.S.A.* **98**, 3744–3749 (2001).
13. L. E. Gimenez *et al.*, *Aging Cell* **12**, 121–129 (2013).
14. S. Cvejic, Z. Zhu, S. J. Felice, Y. Berman, X. Y. Huang, *Nat. Cell Biol.* **6**, 540–546 (2004).
15. W. W. Ja, G. B. Carvalho, M. Madrigal, R. W. Roberts, S. Benzer, *Protein Sci.* **18**, 2203–2208 (2009).
16. B. Gershman *et al.*, *Physiol. Genomics* **29**, 24–34 (2007).
17. T. Kidd *et al.*, *Genetics* **170**, 697–708 (2005).
18. L. L. Fruttero, D. R. Demartini, E. R. Rubiolo, C. R. Carlini, L. E. Canavoso, *Insect Biochem. Mol. Biol.* **52**, 1–12 (2014).
19. L. Giot *et al.*, *Science* **302**, 1727–1736 (2003).
20. L. O. Martinez *et al.*, *Nature* **421**, 75–79 (2003).
21. M. Zalewska *et al.*, *Biochim. Biophys. Acta* **1788**, 1695–1705 (2009).
22. T. Osanai *et al.*, *Circulation* **104**, 3132–3136 (2001).
23. M. Brankatschk, S. Dunst, L. Nemetschke, S. Eaton, *eLife* **3**, e02862 (2014).
24. N. Agrawal *et al.*, *Cell Metab.* **23**, 675–684 (2016).

ACKNOWLEDGMENTS

We thank G. Jarretou for technical assistance and L. Martinez and laboratory members for discussions and comments on the manuscript. We thank B. Ja, the Vienna *Drosophila* RNAi Centers, the *Drosophila* Genetics Resource Center, and the Bloomington stock center for providing *Drosophila* lines. This work was supported by the CNRS; INSERM; European Research Council (advanced grant 268813); the French Foundation for Cancer Research, ARC (grant PGA120150202355); and the Labex SIGNALIFE program (grant ANR-11-LABX-0028-01). Funding for H.M. was provided by a Canadian Institutes of Health Research (CIHR) Foundation Grant. H.M. is a Tier 1 Canada Research Chair.

SUPPLEMENTARY MATERIALS

www.sciencemag.org/content/353/6307/1553/suppl/DC1
Materials and Methods
Fig. S1 to S6
References (*25*–*30*)

8 April 2016; accepted 24 August 2016
10.1126/science.aaf8430

Downloaded from http://science.sciencemag.org/ on October 7, 2016

HIV-1 VACCINES

Priming HIV-1 broadly neutralizing antibody precursors in human Ig loci transgenic mice

Devin Sok,[1,2,3]* Bryan Briney,[1,2,3]* Joseph G. Jardine,[1,2,3]* Daniel W. Kulp,[1,2,3]* Sergey Menis,[1,2,3] Matthias Pauthner,[1,2,3] Andrew Wood,[4] E-Chiang Lee,[4] Khoa M. Le,[1,2,3] Meaghan Jones,[1,2,3] Alejandra Ramos,[1,2,3] Oleksandr Kalyuzhniy,[1,2,3] Yumiko Adachi,[1,2,3] Michael Kubitz,[1,2,3] Skye MacPherson,[1,2,3] Allan Bradley,[4,5] Glenn A. Friedrich,[4] William R. Schief,[1,2,3,6]† Dennis R. Burton[1,2,3,6]†

A major obstacle to a broadly neutralizing antibody (bnAb)–based HIV vaccine is the activation of appropriate B cell precursors. Germline-targeting immunogens must be capable of priming rare bnAb precursors in the physiological setting. We tested the ability of the VRC01-class bnAb germline-targeting immunogen eOD-GT8 60mer (60-subunit self-assembling nanoparticle) to activate appropriate precursors in mice transgenic for human immunoglobulin (Ig) loci. Despite an average frequency of, at most, about one VRC01-class precursor per mouse, we found that at least 29% of singly immunized mice produced a VRC01-class memory response, suggesting that priming generally succeeded when at least one precursor was present. The results demonstrate the feasibility of using germline targeting to prime specific and exceedingly rare bnAb-precursor B cells within a humanlike repertoire.

It is widely thought that vaccine elicitation of sustained levels of potent broadly neutralizing antibodies (bnAbs) may protect humans against HIV (*1*, *2*). HIV bnAbs from natural infection show extensive somatic mutation (*1*–*9*), and this maturation is required for cross-reactivity to diverse isolates: bnAb inferred-germline variants typically show detectable affinity for few if any HIV envelope protein (Env) antigens tested (*3*–*5*, *7*, *10*–*21*). Most wild-type Env proteins are therefore poor immunogens to prime bnAb responses (*3*–*5*, *17*, *22*, *23*). Reliable vaccine initiation of bnAb responses will likely require design or discovery of "germline-targeting" priming immunogens with appreciable affinity for bnAb germline precursors (*3*–*5*, *10*, *11*, *17*, *22*–*29*). Furthermore, consistent bnAb priming may only be possible for bnAb precursors present at reasonable frequency in all or most vaccine recipients (*27*).

Proof of principle that a germline-targeting immunogen can prime relatively rare bnAb-precursor B cells was shown with the eOD-GT8 60-subunit self-assembling nanoparticle (60mer) that targets precursors of CD4–binding- site–directed VRC01-class bnAbs (*26*). VRC01-class precursors are defined by their use of a heavy-chain V_H1-2*02 (or *03 or *04) gene and light chains with unusually short complementarity-determining region 3 (CDR3) loops of five amino acids (*5*, *30*–*32*). In a transgenic mouse model expressing the germline-reverted VRC01 heavy chain paired with wild-type mouse light chains (VRC01 gH mouse), in which the frequency of VRC01-class precursor B cells was estimated to be higher than in humans by a factor of as little as ~5, a single immunization with eOD-GT8 60mer activated VRC01-class precursors and generated VRC01-class memory responses in nearly all immunized mice, whereas control immunogens presenting a native CD4 binding site failed to activate such precursors (*26*). The eOD-GT8 60mer activated target precursors less robustly in a different VRC01-class inferred-germline heavy-chain transgenic mouse (*25*). Several properties of both mouse models lowered the bar for germline targeting compared to the challenges confronted in a human: elevated bnAb precursor frequency, reduced competition from other B cell specificities, limited diversity of bnAb precursors owing to their uniform recombined heavy chains, and an affinity advantage conferred on bnAb precursors due to their mature H-CDR3s.

To better model the conditions for initiation of a VRC01-class bnAb response in humans, we investigated immunization with eOD-GT8 60mer in Kymab mice transgenic for the complete unrearranged human antibody germline gene repertoire (*33*). Kymab mice contain human heavy chains paired with either human kappa light chains (HK mice) or human lambda light chains (HL mice), or both (HKL mice). To determine the level of difficulty for VRC01-class bnAb priming in Kymab mice, we first measured the frequency

[1]Department of Immunology and Microbial Science, The Scripps Research Institute, La Jolla, CA 92037, USA. [2]International AIDS Vaccine Initiative (IAVI) Neutralizing Antibody Center, The Scripps Research Institute, La Jolla, CA 92037, USA. [3]Center for HIV/AIDS Vaccine Immunology and Immunogen Discovery, The Scripps Research Institute, La Jolla, CA 92037, USA. [4]Kymab Ltd, The Bennet Building (B930), Babraham Research Campus, Cambridge CB22 3AT, UK. [5]Wellcome Trust Sanger Institute, Hinxton, Cambridge CB10 1SA, UK. [6]Ragon Institute of Massachusetts General Hospital (MGH), MIT, and Harvard, Cambridge, MA 02129, USA.

*These authors contributed equally to this work. **†Corresponding author. Email: burton@scripps.edu (D.R.B.); schief@scripps.edu (W.R.S.)**

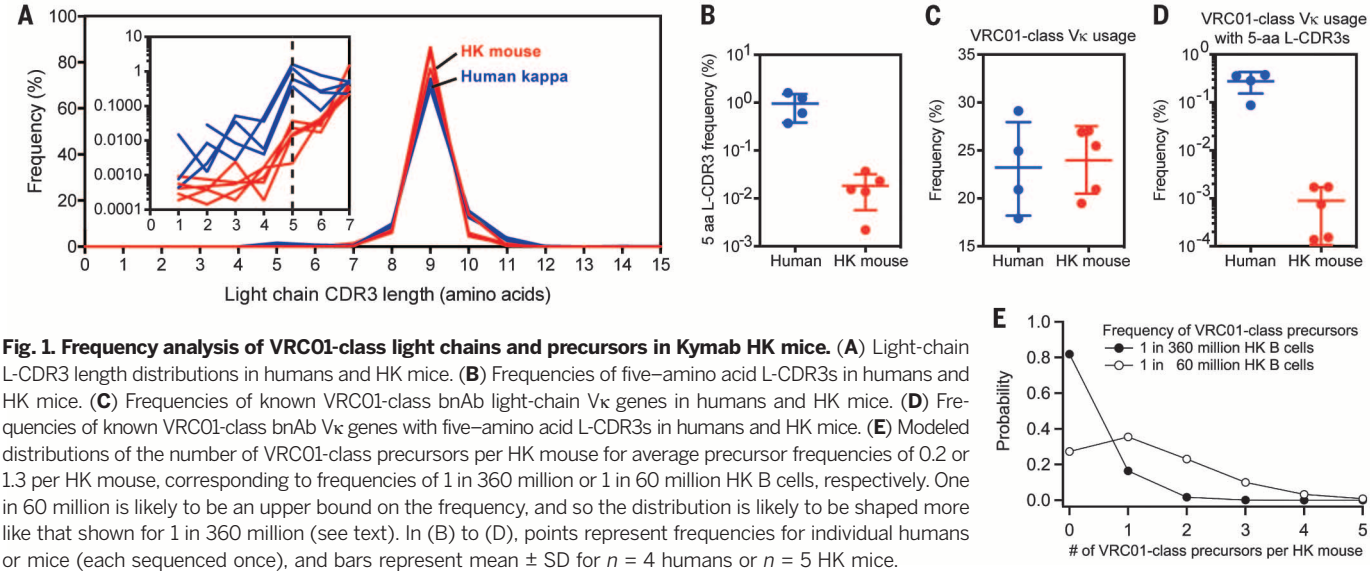

Fig. 1. Frequency analysis of VRC01-class light chains and precursors in Kymab HK mice. (**A**) Light-chain L-CDR3 length distributions in humans and HK mice. (**B**) Frequencies of five–amino acid L-CDR3s in humans and HK mice. (**C**) Frequencies of known VRC01-class bnAb light-chain Vκ genes in humans and HK mice. (**D**) Frequencies of known VRC01-class bnAb Vκ genes with five–amino acid L-CDR3s in humans and HK mice. (**E**) Modeled distributions of the number of VRC01-class precursors per HK mouse for average precursor frequencies of 0.2 or 1.3 per HK mouse, corresponding to frequencies of 1 in 360 million or 1 in 60 million HK B cells, respectively. One in 60 million is likely to be an upper bound on the frequency, and so the distribution is likely to be shaped more like that shown for 1 in 360 million (see text). In (B) to (D), points represent frequencies for individual humans or mice (each sequenced once), and bars represent mean ± SD for n = 4 humans or n = 5 HK mice.

Downloaded from http://science.sciencemag.org/ on October 7, 2016

of VRC01-class precursors in the above mouse strains. Using B cell sorting methods, we previously detected eOD-GT8–specific VRC01-class precursors at a frequency of 1 in 2.4 million among human naïve B cells expressing kappa light chains (*27*). Using similar methods to probe a total of ~300 million naïve B cells from the spleens and lymph nodes of unimmunized HK and HL mice (n = 3 each), we were unable to isolate any VRC01-class B cells, suggesting that the frequency of such B cells was considerably lower than in humans. The frequency of the V_H1-2*02, *03, or *04 alleles among HK B cells was previously measured as 0.9% (*33*, *34*), lower than the frequency in humans (2.9 ± 1.3%) (fig. S1) (*35*, *36*) by a factor of only ~3. Therefore, to explain the reduced frequency of VRC01-class B cells in Kymab mice, we analyzed the light-chain variable gene (V_L) usage and CDR3 length distributions from immunoglobulin M–positive (IgM^+) or IgG^+ B cells for five HK mice and four healthy humans by next-generation sequencing (NGS) (*37*). The kappa light chain–CDR3 (L-CDR3) length distributions were broadly similar in HK mice and humans (Fig. 1A), but the frequency of five–amino acid L-CDR3s was lower in HK mice (0.018 ± 0.013%) than in humans (0.95 ± 0.57%) by a factor of ~50 (Fig. 1B). The cumulative frequency of Vκ genes used by known VRC01-class bnAbs [IGVK3-20, IGVK1-33, and IGVK3-15 (*32*, *38*)] was 24.0 ± 3.5% in HK mice, similar to the 23.2 ± 4.9% that we measured in humans (Fig. 1C). However, the frequency of five–amino acid L-CDR3s associated with known VRC01-class kappa chains was reduced by a factor of ~300 in HK mice (0.00089 ± 0.00079%) compared to humans (0.27 ± 0.13%) (Fig. 1D). Restricting the analysis to light chains with five or fewer V_L nucleotide mutations produced similar conclusions (fig. S2). Whatever the cause, our data indicate that VRC01-class precursors are less frequent in HK mice than in humans by a factor of 150 to 900.

Although we previously detected eOD-GT8–specific VRC01-class precursors at a frequency of 1 in 2.4 million naïve human kappa light-chain B cells, by correcting for cell sorter and polymerase chain reaction (PCR) losses, we estimated the true frequency as 1 in 400,000 (*27*). Based on this number and the calculations above, we conclude that the frequency of VRC01-class precursors in HK mice is unlikely to be higher than 1 in 60 million (=150 × 400,000) B cells and might be as low as 1 in 360 million (=900 × 400,000) B cells. The spleens of HK and HL mice (7 to 18 weeks of age) contain 50 million $B220^+$ B cells, of which ~60% are mature B cells (*33*) that are thought prepared to respond to antigen. By also accounting for the lymph nodes and periphery, we estimate that each mouse contains ~75 million B cells, of which 45 million are mature. Thus, we expect a very low average frequency of 0.2 (≈75/360) to 1.3 (≈75/60) eOD-GT8–specific VRC01-class precursors per HK mouse at any given time. Modeling the number of precursors per mouse with Poisson distributions predicts that 27 to 82% of HK mice will have zero precursors and the remainder one to four precursors (Fig. 1E). Thus, priming VRC01-class responses in HK mice appears substantially more difficult than in humans, as the precursor frequency is lower (by a factor of 150 to 900) and the number of precursors per individual is lower [by 3000 to 30,000 precursors (*27*)]. Frequency analysis in one HL mouse and two HKL mice reached similar conclusions that were only slightly more favorable for VRC01-class priming (table S1).

We conducted immunization experiments to determine if eOD-GT8 60mer could prime rare VRC01-class precursors in Kymab mice. Our first experiment (Fig. 2A), in both HK and HL mice (28 mice each), evaluated differences in antigen dose (20 versus 4 μg), adjuvant formulation, and route (Iscomatrix/subcutaneous versus Sigma Adjuvant system, also known as "Ribi"/intraperitoneal), and time point of analysis (14 days versus 42 days after immunization). Unimmunized mice (three HK and three HL) and mice immunized with 20 μg of non–germline-targeting eOD-17 60mer in Iscomatrix were controls. Serum enzyme-linked immunosorbent assay showed robust responses to eOD-GT8 [endpoint titers of (1 to 5) × 10^{-5} and half-maximal inhibitory concentrations of (5 to 13) × 10^{-4} at day 42] and lower responses to eOD-GT8 KO (fig. S3), a mutant with reduced binding to VRC01-class antibodies (*26*), indicating epitope-specific responses (fig. S4) (*37*). Spleens and lymph nodes from culled mice were processed, stained, and single-cell sorted for IgM^-/IgD^- memory B cells that bound to eOD-GT8 tetramers but not to eOD-GT8 KO tetramers (*27*, *37*). Only eOD-GT8 60mer-immunized mice showed evidence of epitope-specific ($eOD\text{-}GT8^+/eOD\text{-}GT8\ KO^-$) memory B cells (Fig. 2B). A control sort of eOD-17 60mer-immunized samples with eOD-17/eOD-17-KO probes identified memory B cells reactive with eOD-17 but not eOD-GT8.

We performed a second experiment (Fig. 2A), in HK and HKL mice, with eOD-GT8 60mer, eOD-17 60mer, the native-like trimer BG505 SOSIP (*39*–*44*), and eOD-GT8 d41m3 60mer, a variant of eOD-GT8 60mer with disulfide stabilization and modification of the underlying nanoparticle (fig. S5). The results for eOD-GT8 d41m3 60mer are combined with those of eOD-GT8 60mer, as the two were indistinguishable (fig. S6). Although epitope-specific memory B cell frequencies were slightly (factor of ~3) lower in the second experiment, potentially because of sorting with a different eOD-GT8 KO bait [eOD-GT8 KO2 (fig. S3)], comparison of frequencies between groups (Fig. 2C) supported the findings from the first experiment (Fig. 2B).

To determine whether or not the epitope-specific memory B cells generated by eOD-GT8

A

Experiment	Immunogen	Amount (μg)	Adjuvant/ route	Number of mice HK	HL	HKL	Timeline d0	d14	d28	d42
1	eOD-GT8 60mer	20	Isco/SC	5	5	0	- immunize - bleed	- cull 2/gp - bleed	bleed all	cull 3/gp
	eOD-GT8 60mer	4	Isco/SC	5	5	0				
	eOD-GT8 60mer	20	Ribi/IP	5	5	0				
	eOD-GT8 60mer	4	Ribi/IP	5	5	0				
	eOD-17 60mer	20	Isco/SC	5	5	0				
2	eOD-GT8 60mer	20	Isco/SC	10	0	10	- immunize - bleed	--	--	cull all
	eOD-17 60mer	20	Isco/SC	5	0	5				
	BG505 SOSIP	20	Isco/SC	5	0	5				

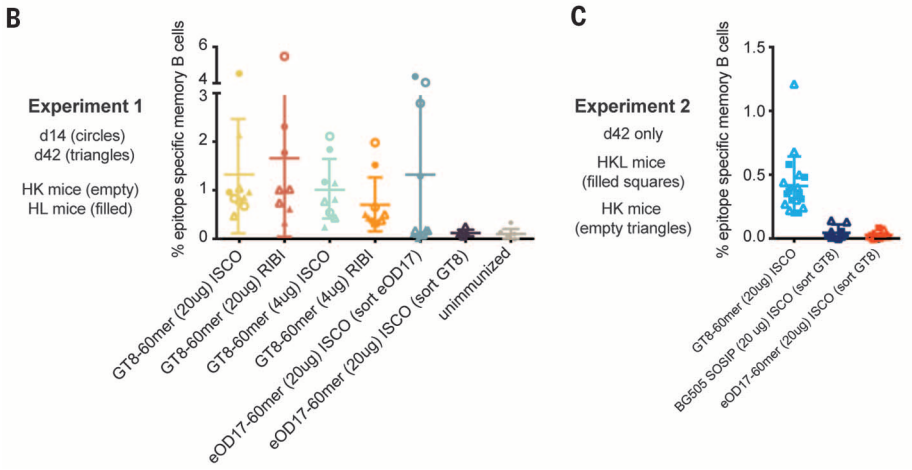

Fig. 2. B cell sorting analysis reveals reproducible epitope-specific responses to eOD-GT8 60mer prime. (**A**) Overview of two immunization experiments in Kymab mice. (**B**) Frequencies of epitope-specific memory B cells at days 14 or 42 after priming in experiment 1. (**C**) Same type of data as in (B) but for experiment 2, in which analysis was carried out at day 42 only. In (B) and (C), points represent frequencies measured for a single mouse, each measured once, and bars represent mean ± SD for all data in each column of the graph.

Downloaded from http://science.sciencemag.org/ on October 7, 2016

A

	HCs	LCs	Pairs	V_H1-2 HCs	5 aa L-CDR3 LCs	V_H1-2 pairs	5 aa L-CDR3 pairs	VRC01-class pairs
GT8	4043	4286	2526	192	62	136	32	28
BG505 SOSIP	209	388	136	4	0	2	0	0
eOD-17	721	931	401	17	0	3	0	0
unimmunized	136	102	59	7	0	2	0	0
TOTAL	5109	5707	3122	220	62	143	32	28

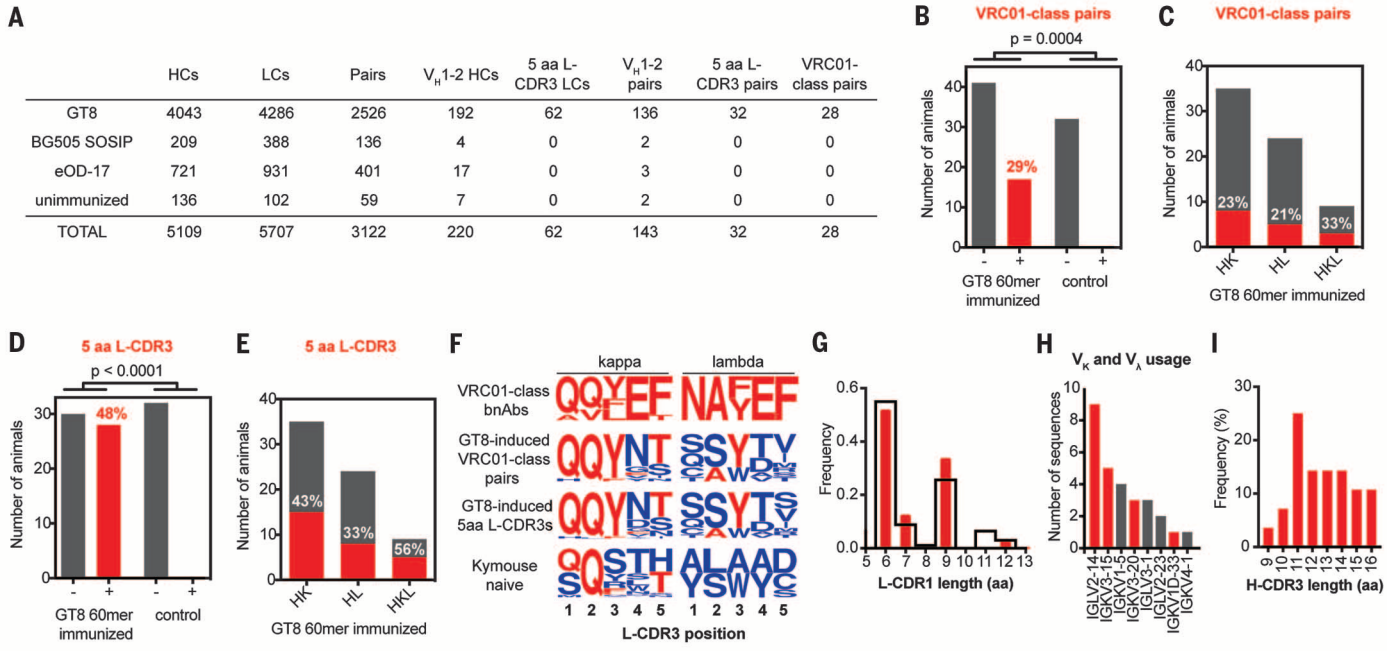

Fig. 3. Analysis of antibody sequences from epitope-specific memory B cells. (**A**) Summary of all sequence information obtained from experiments 1 and 2. Of the 33 VRC01-class pairs, 28 were identified as unique in nucleotide sequence. (**B**) Number of eOD-GT8 60mer-immunized or control mice from which at least one VRC01-class pair was isolated by B cell sorting (+) or no VRC01-class pairs were isolated (-). Data are aggregated from all animals and conditions in experiments 1 and 2, with a total of 90 mice. The *P* value was calculated by using Fisher's exact test. (**C**) Number of eOD-GT8 60mer-immunized HK, HL, or HKL mice for which at least one VRC01-class pair was isolated (red, with percentages listed in white) or no VRC01-class pairs were isolated (gray). In (**D**) and (**E**), the same analysis was performed as in (B) and (C), respectively, but with five–amino acid L-CDR3 light chains instead of VRC01-class pairs. (**F**) L-CDR3 sequence logos for VRC01-class bnAbs (top row), eOD-GT8 60mer-induced VRC01-class paired antibodies (second row), eOD-GT8 60mer-induced five–amino acid L-CDR3s (third row), and naïve Kymab mice (bottom row), shown separately for kappa light chains (left column) and lambda light chains (right column). (**G**) L-CDR1 length distribution for eOD-GT8 60mer-induced VRC01-class antibodies (red) and all LCs in (A) (black). (**H**) Light chain Vκ and Vλ gene usage for eOD-GT8 60mer-induced VRC01-class antibodies. Red bars denote genes used by, or highly similar to those used by, known VRC01-class antibodies. (**I**) H-CDR3 length distribution for eOD-GT8 60mer-induced VRC01-class antibodies.

60mer immunization contained VRC01-class memory B cells, RNA from single eOD-GT8$^+$/eOD-GT8 KO$^-$ sorted memory B cells was reverse transcribed and IgG variable genes were amplified and sequenced by NGS (*37*). The two experiments yielded a total of 10,816 wells from which unique heavy- and/or light-chain nucleotide sequences could be determined, and of these, 3122 wells contained a heavy- and light-chain pair (2526 pairs for eOD-GT8 60mer-immunized mice, 537 pairs for control-immunized mice, and 59 pairs for unimmunized mice) (Fig. 3A and tables S2 to S4). From these sequences, we identified 28 nucleotide-unique (26 amino acid–unique) VRC01-class heavy-light paired memory responses among 29% (17 of 58) of eOD-GT8 60mer-immunized mice (aggregating across different doses, adjuvants, time points, types of mice, and the two experiments) (Fig. 3B, fig. S7, and table S5). In contrast, we detected no VRC01-class responses from 32 control mice. eOD-GT8 60mer–induced VRC01-class responses were found at approximately similar frequencies in HK, HL, and HKL mice (Fig. 3C).

Whereas only 21% (28/136) of paired sequences with V_H1-2*04 heavy chains had L-CDR3s of five amino acids, 88% (28/32) of paired sequences with a five–amino acid L-CDR3 included a V_H1-2*04 heavy chain (Fig. 3A), suggesting that five–amino acid L-CDR3s in memory B cells may serve as a proxy for VRC01-like responses. Therefore, we examined the frequency of five–amino acid L-CDR3s among all paired and unpaired light-chain sequences. We identified 62 light chains with 5-amino acid L-CDR3s from 48% (28 out of 58) of eOD-GT8 60mer-immunized mice, whereas we found no five–amino acid L-CDR3s among control mice (Fig. 3, A and D). eOD-GT8 60mer induced memory B cells with five–amino acid L-CDR3s at substantial frequencies in all three types of mice (Fig. 3E). All combinations of dose, adjuvant, and time point produced VRC01-class responses and five–amino acid L-CDR3 responses (fig. S8). Given the very low frequency of VRC01-class precursors, these results indicate that VRC01-class priming by eOD-GT8 60mer was highly efficient and may have succeeded in all or most mice in which at least one precursor was present.

The VRC01-class antibodies induced by eOD-GT8 60mer shared other characteristic features of VRC01-class bnAbs in addition to the V_H1-2 alleles and five–amino acid L-CDR3. The L-CDR3 is a key site of affinity maturation in VRC01-class bnAbs (*32*), and the 28 VRC01-class antibodies showed clear signs of selection toward bnAb sequences in both kappa and lambda L-CDR3 (Fig. 3F). In addition, 21 of 28 VRC01-class pairs had L-CDR1 lengths matching those of the germline V_L genes of known VRC01-class bnAbs (Fig. 3G) (*32*). Further, 18 of these 28 antibodies used known VRC01-class V_L genes (Fig. 3H), and the H-CDR3 lengths among the VRC01-class pairs (9 to 16 amino acids) were similar to those of known VRC01-class bnAbs (12 to 18 amino acids) (Fig. 3I).

Consistent with a VRC01-class binding mode, all 20 VRC01-class antibodies that we expressed bound to eOD-GT8 but had no detectable affinity for either eOD-GT8 mutant, eOD-GT8 KO, or eOD-GT8 KO2 (fig. S9). These VRC01-class antibodies had geometric mean (GM) affinity for eOD-GT8 of 134 nM [geometric standard deviation (GSD), 9.4], a factor of 25 higher than the geometric mean eOD-GT8 affinities of VRC01-class antibodies isolated from naïve human B cells (3.4 μM; GSD, 5.6) (*27*), possibly due to maturation of the immunogen-induced antibodies (mean ± SD mutation levels were 0.8 ± 1.1% in V_H and 1.5 ± 1.1% in V_L). eOD-GT8 60mer-induced VRC01-class antibodies in the VRC01 gH mouse had similar mutation levels (V_H: 1.3 ± 3.2%; V_L:2.1 ± 1.9%) but higher GM affinity for eOD-GT8 by a factor of 22 (GM, 6.0 nM; GSD, 38.7) (*26*), probably due at least in part to the

Downloaded from http://science.sciencemag.org/ on October 7, 2016

engineering of eOD-GT8 for ultrahigh affinity (9 pM) to germline-reverted VRC01 (*27*). Thus, the Kymab antibody affinities are likely better predictors of the affinities of human responses to a single immunization of eOD-GT8 60mer.

Ultimate elicitation of bnAbs will probably require sequential boosting with more native-like epitope variants to select sufficient bnAb-like mutations (*1*, *4*, *5*, *10*, *16*, *17*, *22*, *23*, *25*, *26*). Consistent with this expectation and with results of eOD-GT8 60mer priming experiments in knock-in mice (*25*, *26*), the primed VRC01-class antibodies in this study showed no affinity for the native-like trimer BG505 SOSIP (fig. S10) and no neutralizing activity against the VRC01-sensitive HXB2 HIV strain from which eOD-GT8 was derived (fig. S11). That only ~1% (28/2526) of epitope-specific antibodies were VRC01-class (Fig. 3A) suggests that immunofocusing strategies may be needed to suppress competing responses during boosting (*1*, *45*)—though in humans, the higher VRC01-class precursor frequency may mitigate this challenge.

Germline targeting is a promising vaccine strategy, but developing suitable model systems to evaluate targeting of human germline B cells is difficult. Kymab human immunoglobulin loci transgenic mice offer a more stringent and human-like model compared to most knock-in mice. Although Kymab mice underrepresent the frequency of VRC01-class precursor B cells compared to humans and possess an average of at most 1.3 such precursors per mouse, the eOD-GT8 60mer still proved capable of priming. The seemingly high targeting efficiency of eOD-GT8 60mer in this mouse model encourages human testing wherein the VRC01-class precursor frequency among B cells and the number of precursors per individual are more favorable for bnAb priming. The results of this study should also encourage germline targeting for other bnAbs with lower human precursor frequencies.

REFERENCES AND NOTES

1. J. R. Mascola, B. F. Haynes, *Immunol. Rev.* **254**, 225–244 (2013).
2. D. R. Burton, L. Hangartner, *Annu. Rev. Immunol.* **34**, 635–659 (2016).
3. X. Xiao *et al.*, *Biochem. Biophys. Res. Commun.* **390**, 404–409 (2009).
4. D. S. Dimitrov, *MAbs* **2**, 347–356 (2010).
5. T. Zhou *et al.*, *Science* **329**, 811–817 (2010).
6. X. Wu *et al.*, *Science* **333**, 1593–1602 (2011).
7. J. F. Scheid *et al.*, *Science* **333**, 1633–1637 (2011).
8. L. M. Walker *et al.*, *Nature* **477**, 466–470 (2011).
9. M. Bonsignori *et al.*, *J. Virol.* **85**, 9998–10009 (2011).
10. M. Pancera *et al.*, *J. Virol.* **84**, 8098–8110 (2010).
11. B. J. Ma *et al.*, *PLOS Pathog.* **7**, e1002200 (2011).
12. T. Ota *et al.*, *J. Immunol.* **189**, 4816–4824 (2012).
13. H. Mouquet *et al.*, *Proc. Natl. Acad. Sci. U.S.A.* **109**, E3268–E3277 (2012).
14. S. Hoot *et al.*, *PLOS Pathog.* **9**, e1003106 (2013).
15. F. Klein *et al.*, *Cell* **153**, 126–138 (2013).
16. H. X. Liao *et al.*, *Nature* **496**, 469–476 (2013).
17. J. Jardine *et al.*, *Science* **340**, 711–716 (2013).
18. D. Sok *et al.*, *PLOS Pathog.* **9**, e1003754 (2013).
19. N. A. Doria-Rose *et al.*, *Nature* **509**, 55–62 (2014).
20. R. Andrabi *et al.*, *Immunity* **43**, 959–973 (2015).
21. J. Gorman *et al.*, *Nat. Struct. Mol. Biol.* **23**, 81–90 (2016).
22. B. F. Haynes, G. Kelsoe, S. C. Harrison, T. B. Kepler, *Nat. Biotechnol.* **30**, 423–433 (2012).
23. A. T. McGuire *et al.*, *J. Exp. Med.* **210**, 655–663 (2013).
24. A. T. McGuire *et al.*, *Science* **346**, 1380–1383 (2014).
25. P. Dosenovic *et al.*, *Cell* **161**, 1505–1515 (2015).
26. J. G. Jardine *et al.*, *Science* **349**, 156–161 (2015).
27. J. G. Jardine *et al.*, *Science* **351**, 1458–1463 (2016).
28. A. T. McGuire *et al.*, *Nat. Commun.* **7**, 10618 (2016).
29. J. G. Jardine *et al.*, *PLOS Pathog.* **12**, e1005815 (2016).
30. X. Wu *et al.*, *Science* **329**, 856–861 (2010).
31. A. P. West Jr., R. Diskin, M. C. Nussenzweig, P. J. Bjorkman, *Proc. Natl. Acad. Sci. U.S.A.* **109**, E2083–E2090 (2012).
32. T. Zhou *et al.*, *Immunity* **39**, 245–258 (2013).
33. E. C. Lee *et al.*, *Nat. Biotechnol.* **32**, 356–363 (2014).
34. Among human V_H1-2 alleles, Kymab mice only contain V_H1-2*04. This was misreported as *02 in (*33*).
35. R. Arnaout *et al.*, *PLOS ONE* **6**, e22365 (2011).
36. B. J. DeKosky *et al.*, *Nat. Med.* **21**, 86–91 (2015).
37. See supplementary materials on *Science* Online.
38. I. S. Georgiev *et al.*, *Science* **340**, 751–756 (2013).
39. R. W. Sanders *et al.*, *PLOS Pathog.* **9**, e1003618 (2013).
40. J. P. Julien *et al.*, *Science* **342**, 1477–1483 (2013).
41. D. Lyumkis *et al.*, *Science* **342**, 1484–1490 (2013).
42. M. Pancera *et al.*, *Nature* **514**, 455–461 (2014).
43. Y. D. Kwon *et al.*, *Nat. Struct. Mol. Biol.* **22**, 522–531 (2015).
44. R. W. Sanders *et al.*, *Science* **349**, aac4223 (2015).
45. L. Kong, Q. J. Sattentau, *J. AIDS Clin. Res.* **S8**, 3 (2012).

ACKNOWLEDGMENTS

We thank P. Kellam for comments on the manuscript. This work was partially funded by IAVI with the generous support of the U.S. Agency for International Development, Ministry of Foreign Affairs of the Netherlands, and the Bill & Melinda Gates Foundation; a full list of IAVI donors is available at www.iavi.org (W.R.S., D.R.B). This work was also supported by the Bill and Melinda Gates Foundation (G.A.F., A.B.); the Ragon Institute of MGH, MIT, and Harvard (D.R.B. and W.R.S.); the Helen Hay Whitney Foundation (J.G.J.); and National Institute of Allergy and Infectious Diseases grants P01 AI094419 (W.R.S.) and CHAVI-ID 1UM1AI100663 (W.R.S., D.R.B.). The data presented in this manuscript are tabulated in the main paper and in the supplementary materials. All mice were maintained, and all procedures carried out, under United Kingdom Home Office License 70/8718 and with the approval of the Sanger Institute Animal Welfare and Ethical Review Body. The VRC01-class paired sequences described in this study were deposited in GenBank under accession numbers KX814864 to KX814919. Materials and information concerning the immunogens are available by material transfer agreement from the Scripps Research Institute. IAVI and the Scripps Research Institute have filed a patent (U.S. PCT Application no. PCT/US2016/038162) relating to the eOD-GT8 immunogens in this manuscript, which included inventors J.G.J., D.W.K., S.M., and W.R.S. W.R.S. is a cofounder and stockholder in Compuvax Inc., which has programs in non-HIV vaccine design that might benefit indirectly from this research. D.R.B. is a paid consultant of IAVI, which may benefit from this research. The Kymab mouse strains described are corporate assets protected by multiple patents; access to these mice is available through licensing. A.W., E-C. L., A.B., and G.F. hold equity in Kymab, Ltd., and Kymab, Ltd., holds patents and patent applications related to the Kymouse technology and the use of that technology in vaccine characterization. A.B. and G.F. are officers of Kymab, Ltd., which may benefit from this research.

SUPPLEMENTARY MATERIALS

www.sciencemag.org/content/353/6307/1557/suppl/DC1
Materials and Methods
Fig. S1 to S11
Tables S1 to S6
References (*46*–*50*)

20 June 2016; accepted 1 September 2016
Published online 8 September 2016
10.1126/science.aah3945

Downloaded from http://science.sciencemag.org/ on October 7, 2016

Microbial Protein Kit

The NoviPure Microbial Protein Kit is designed to isolate total cellular proteins from microbial cultures in a quick and user-friendly spin filter format. An optimized bead-beating method enables efficient lysis and solubilization of total proteins from a large diversity of microbial species including fungi and gram-negative and gram-positive bacteria. The use of silica spin filters to achieve reversible immobilization of protein—a patent-pending technical advance in protein extraction—greatly simplifies the isolation process by removing traditionally cumbersome, bias-inducing precipitation steps. Isolated proteins are suitable for many downstream applications such as 1D and 2D sodium dodecyl sulfate polyacrylamide gel electrophoresis (SDS PAGE) as well as mass spectrometry. The novel spin filter-based method enables protein extraction in just 22 minutes without the need for precipitation.

MO BIO Laboratories
For info: 800-606-6246
https://mobio.com

Laboratory Blender

With proven reliability and durability over 40 years, Seward Stomacher blenders are used to prepare over 8 million food samples in more than 150 countries. The new Seward Stomacher 400 EVO combines these gold-standard attributes with improved features that make it even easier to use, easier to clean, and quieter than previous models. The unique, one-touch bag-loading system means that operators just need to place the bag in the loading slot and push the start button, which seals the bag so blending can begin. The Seward Stomacher 400 EVO's rubber base, combined with a host of design and engineering developments, eliminates bench movements and ensures almost silent operation, which reduces stress and disruptions to other lab work. A removable drip tray means that spillages can be quickly cleaned, and for thorough cleaning, the paddle chamber can be easily opened and the paddles removed, making the entire chamber accessible.

Seward
For info: +44-(0)-1903-823077
www.seward.co.uk

Cell Culture Analyzer

BioProfile FLEX 2's innovative design provides comprehensive analysis of 16 key cell culture chemistries including glucose, lactate, glutamine, glutamate, ammonium, sodium, potassium, calcium, pH, pCO_2, pO_2, osmolality by freezing point depression, total and viable cell density, and viability by trypan blue dye exclusion method. The full panel of tests can be run in under 4 minutes with just 265 µL of sample, and users can select from manual sampling or two modes for batch sampling: 96-well plates or the built-in 24-position tray. BioProfile FLEX 2's maintenance-free technology comprises two credit card-sized MicroSensor cards, each with a minimum 14-day use life and capacity for more than 500 samples. BioProfile FLEX 2's reagent cartridges combined with maintenance-free MicroSensor Card technology reduce maintenance to just minutes per week. BioProfile FLEX 2 will help to meet the sizable need for automated cell culture analysis for small-volume culture systems like the Sartorius ambr microbioreactor systems.

Nova Biomedical
For info: 781-894-0800
www.novabiomedical.com

Cell-Free DNA Isolation from Urine

The NextPrep-Mag Urine Cell-Free DNA (cfDNA) Isolation Kit is an automation-friendly kit designed to extract cell-free DNA from urine using a magnetic bead format. The rapid procedure can be completed in only 30 minutes and does not require a vacuum manifold. Using the kit, sufficient cfDNA is recovered from urine sample volume—ranging from less than 1 mL to more than 20 mL—to allow robust construction of libraries for targeted- or whole-genome sequencing. The cfDNA isolated with this kit can be used for applications including circulating fetal DNA studies and cancer diagnostic-related liquid biopsy studies.

Bioo Scientific
For info: 888-208-2246
www.biooscientific.com

Biomarker Assays

Aushon BioSystems introduces new Ciraplex ULTRA Ultrasensitive Assays, combining the power of multiplexing with ultrasensitivity, in conjunction with Pacific Biomarkers' Comparative Platform Study. Featuring femtogram/mL levels of detection, these assays address multiple biomarkers in a wide range of therapeutic areas. They offer enhanced sensitivity and an extended dynamic range providing quantification below standard detection limits. This new high-performing assay product line yields consistent discrimination at the lower levels of detection required for clinical studies and patient stratification. In addition, intuitive Cira software streamlines the data management process, offering exceptional data control. Through its unique combination of proprietary microarray printing, extensive biomarker content, and ease of use, the Cira immunoassay platform is serving leading pharmaceutical companies, contract research organizations, and clinical reference laboratories worldwide. Ciraplex assays are used for applications in preclinical and clinical biomarker research, accelerating the evaluation of potential drug candidates and advancing the use of biomarker profiles in diagnostics.

Aushon BioSystems
For info: 978-436-6400
www.aushon.com

Electronically submit your new product description or product literature information! Go to www.sciencemag.org/about/new-products-section for more information.

Newly offered instrumentation, apparatus, and laboratory materials of interest to researchers in all disciplines in academic, industrial, and governmental organizations are featured in this space. Emphasis is given to purpose, chief characteristics, and availability of products and materials. Endorsement by *Science* or AAAS of any products or materials mentioned is not implied. Additional information may be obtained from the manufacturer or supplier.

Downloaded from http://science.sciencemag.org/ on October 7, 2016

AMERICAN ASSOCIATION FOR THE ADVANCEMENT OF SCIENCE

BE THE CORE MIND SPIRIT FACE HEART REACH CENTER VOICE OF SCIENCE.

AAAS members harness the power of scientific thinking to help tackle complex, global challenges.

Join the community of scientists, engineers, and educators whose work impacts millions.

How will YOU make your mark in science?

Join AAAS today.
www.aaas.org/join

AAAS

2016 Laureate for Science
Myungshik Kim
Professor, Imperial College London

2016 Laureate for Engineering
Jun Ho Oh
Professor, KAIST

2016 Laureate for Medicine
Larry W. Kwak
Vice-President, City of Hope National Medical Center

The Ho-Am Prize ignites the passion and innovative spirit for scientific discovery

We welcome your recommendations for the 2017 Ho-Am Prize candidates.

-Award categories are Science, Engineering, and Medicine.
-Researchers of Korean heritage are eligible for the Prize.
-Deadline for submission is Oct. 31, 2016.
*Learn more about candidate recommendation at **www.hoamprize.org**

To continue Samsung Founder 'Ho-Am' Byung-Chull Lee's (1910-1987) efforts to maximize both human potential and public interest, Chairman Kun-Hee Lee of Samsung established the Prize in 1990. The Prize is awarded annually to outstanding researchers of Korean heritage around the world who have made important contributions to the advancement of science.

THE HO-AM PRIZE

HOAM
THE HO-AM FOUNDATION

SAMSUNG

三水 SANSHUI

The name of Sanshui has been given because the three rivers of Xijiang River, Beijiang River and Suijiang River converge here,and the Pearl River Delta began from here.

三水之名，得于西、北、绥三江汇流于此，珠江三角洲肇始于斯。

Here, ever possess the earliest custom in China, the first railway station and railway in Guangdong.

Here, with picturesque scenery, people live and enjoy the peaceful and prosperous environment as well as the wonderful and leisurely moment.

Here, has got the breeze, drizzle and canoes on the river form the wonderful scenery of three rivers in the misty rain.

Here, becomes affluent and prosperous due to water. As a watery city in the south and a green core among Guangzhou, Foshan and Zhaoqing, it is the exclusive characteristic in Foshan.

Not only an ecopolis but also a longevity county

The southern scenery is coquettish and graceful. As a part of the south, Sanshui owns not a few tourist attrac-tions, such as, one of the new eight sceneries in Foshan—Lotus World, more than 466 hectare lake region keeping abreast with the West Lake—the lake area of Yundonghai, Sanshui Forest Park, the first batch agricultural tourism demonstration plot in China—Zoology Kingold Park, the famous historical and cultural village in China—Daqitou Village and Changqi Village, the "Southern Wudang" in China—Lubao Ancestral Temple, and the "The first drift in Foshan" —Jiudaogu Rafting and so on. More importantly, the people in Sanshui are beatific and macrobiotic because of the livable geographic and climatic conditions, natural and harmonious village ecology, simple and placid attitude toward life, and thorough and complete public service. Therefore, Sanshui has become the "The longevity county in China", which is the fourth city granted this title in China and the first in Guangdong. Moreover, it has become the first opulent "The longevity county" in China.

ADVERTISEMENT

About Sanshui

Sanshui, one of the five districts under the jurisdiction of Foshan in Guangdong, is named after the confluence of Xijiang River, Beijiang River and Suijiang River, and has a total area of 827 square kilometers with a population of about 620 thousand. On the one hand, it is the demonstration base for food safety in China and the only opulent longevity county. On the other hand, it is also the largest wetland and "Green Lung" in the urban agglomeration of Pearl River delta. In 2015, the GDP of Sanshui has reached 100.9 billion yuan, and the gross value of industrial output has exceeded 300 billion yuan. Therefore, it has become the fourth district stepping into the economy of county with over 100 billion achievement in Foshan. The Comprehensive Index of Social and Economic Development in Sanshui ranks No. 21 in the "Top 100 Counties in China", and ranks No. 10 in the "Top 100 Most Potential Small and Medium-Sized Cities for Investment in China". With a favorable investment environment, Sanshui ranked No. 4 in "World Expo City Star—the 2010 Top 100 Most Potential Counties (Districts) for Investment in China".

Vying with numerous rivals in a changeable environment

It is inevitable for nature to nurture all living things on the earth. In an unpredictable environment, one has to vie with numerous rivals for development. Gone through the baptism of 500 years, Sanshui has developed from "Country of Miraculous Water in China" to "City of Food and Beverage in China", from "Advanced Agricultural County" to "Modern Industrial Zone", from "Top 100 county" to "Top 100 Most Potential Counties (Districts) for Investment" etc. Sanshui, has been standing in the forefront of reform and opening up in China, of which the huge driving power has promoted the development of the city constantly.

Standing on the Sixianjiao Waterway, overlooking the magnificent scenery of three rivers converging, and looking up and down the world, we could find that Sanshui, as time went by, in the integration and collision of old tradition and modern civilization , has combined its historical sediment with the industrial new town to create the seven leading industries competitive worldwide, which are advanced equipment, food and beverage, automobile and components, new energy ,new material, electronic information, and modern service industry.

The advantage of location occupies the commanding heights of economy.

Sanshui, located in the core zone called "advanced manufacturing base" in the Pearl River Delta, is the junction of Guangzhou-Foshan-Zhaoqing economic circle. With the geographic advantages, it has been the vital region since ancient times, where leads Guangzhou to Southwest China and Southeast Asia. Nowadays, for the convergence of capital and logistics in all directions, it even possesses multi-dimensional transportation network, of which railway, highway, shipping and air transportation radiate in all directions.

The distance from Sanshui to Hong Kong is 230 kilometers, to Macau is 190 kilometers, to the capital of Guangdong—Guangzhou is only 35 kilometers, and to the center of Foshan is 30 kilometers. Besides, it takes no more than two hours to every big city in the Pearl River Delta, such as, Shenzhen, Dongguan, Zhuhai, Zhongshan and so on. Located in the "Guangzhou-Foshan One Hour Economic and Living Circle", it is the cutting-edge deeply affected by Hong Kong, Macau, Taiwan, and the core area in the Pearl River Delta.

From 2012 to 2015, Sanshui has attracted more than 350 projects, which have introduced 80 billion yuan of investment. Moreover, with satisfactory development status, it has become the new engine for economic growth in Foshan. At present, there are about 50 global (China) Top 500 enterprises in the district, including ABInbev, Heinz, Red Bull, Coca Cola, Haier, Foton and so on.

ADVERTISEMENT

创智禅城

创智禅城

创造之城 智慧集聚

CHUANGZHI CHANCHENG

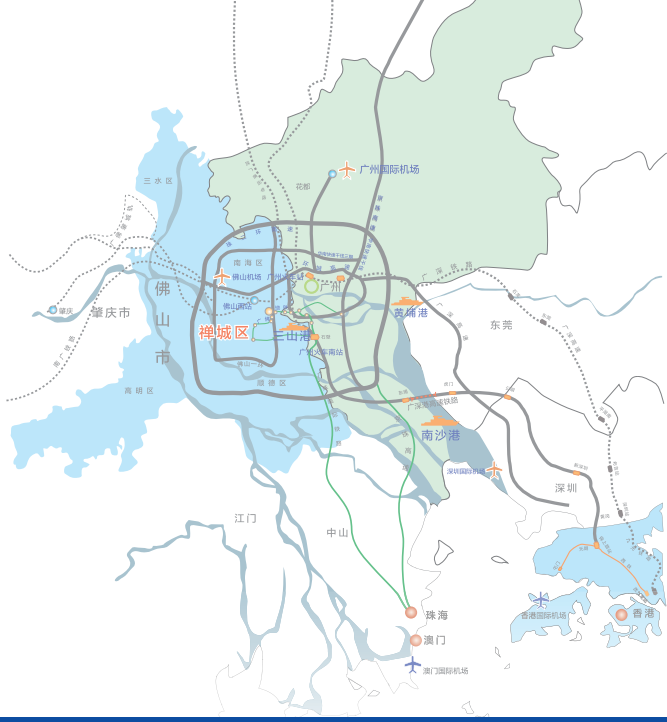

About Chancheng

Foshan, with Guangzhou to the east and Hong Kong and Macau to the south, is strategically located at the core of the Guangzhou-Foshan Metropolis Circle and the Pearl River Delta. The overall competitiveness of Foshan stays at the head of other municipal cities and ranked top 12th on the national level.Chancheng District is the central district of Foshan city. It is also the center of politics, finance, culture, transportation, and information of Foshan, with an area of 154.68 square kilometers and a population of 1.12 million. The GDP output of Chancheng in 2015 is RMB146.9 billion, with the GDP per capita more than RMB130 thousand.

ADVERTISEMENT

A Well–known Cultural City and Transportation Hub

With a long history and profound culture, Chancheng was recognized as one of the "Four Reputed Towns" in the Song Dynasty and was crowned as one of the "Four Largest Clusters" in the Ming and Qing Dynasty. Chancheng is a national historical city, with a series of titles and reputations including hometown of martial arts, hometown of Canton opera and hometown of ceramics,and a significant cradle of Cantonese cuisine and Chinese patent medicine.What' s more, it is one of the Top 10 Happiest Cities in China, and awarded the title of Excellent Model City in Human Settlement by United Nations.

As a transportation hub with developed logistics network, it' s only about half hour to the core city in Southern China Guangzhou, one hour to cities in the Pearl River Delta like Shenzhen, Zhuhai, and Zhongshan, and two hours to Hong Kong and Macau. In the meanwhile, Foshan Airport has inaugurated some flights to large and medium-sized cities like Beijing, Shanghai, Hangzhou, and Changzhou.

Converging Industries and Creating a New Level of Innovation and Technology

Made in Foshan is known to the world. Also, Foshan is the most potential city for investment with its total industrial output value ranking in the top 10 in China. Meanwhile the comprehensive strength of Chancheng ranks No.21 in China in 2014. Chancheng possesses a solid foundation of traditional industries, such as ceramic, knitwear, stainless steel, seasoning and so on. In addition, new industries like IT, intelligent manufacturing, big health, environmental protection and energy saving are growing rapidly. Moreover, high-end service industries like culture and creativity, science technology and finance, commercial logistics are developing prosperously.

Supporting by powerful industrial strength and excellent urban quality, Chancheng creates a one-door administrative service with wisdom elaborately, dedicates to develop the cluster for international industries in Southern China, and builds the manufacturing center, service centers for international culture, tourism and business.

ADVERTISEMENT

DOES YOUR LAB SEEK TO UNDERSTAND MECHANISMS OF DRUG RESISTANCE OR DISEASE PATHOLOGY?

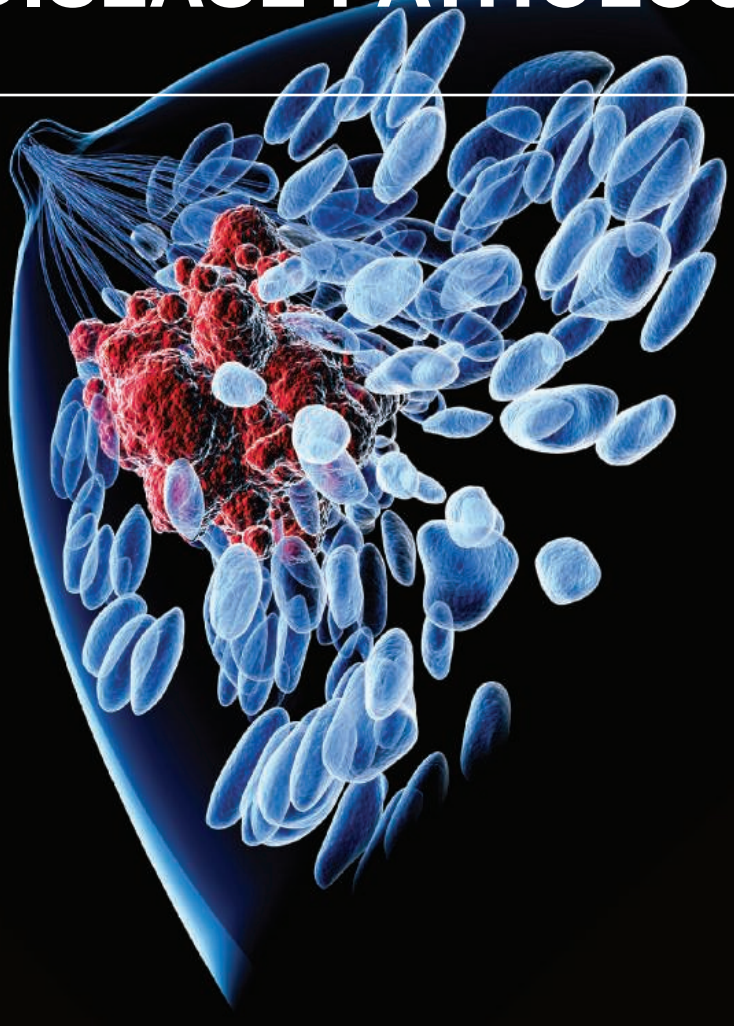

Leslie K. Ferrarelli, "Focus Issue: Refining the War on Cancer", *Sci. Signal.* 7, 318eg2 (2014). Image: Raycat/iStockphoto

Science Signaling | AAAS

CELL SIGNALING IN PHYSIOLOGY AND DISEASE

Find out more about the scope of the journal and submit your research today!
ScienceSignaling.org

eppendorf

Eppendorf Consumables –
it´s your sample

Impress Yourself

Eppendorf Cell Culture Consumables
Proven Eppendorf quality brought to a new level. Premium in all aspects: Product, Performance and Packaging according to highest Eppendorf standards.

Find more information about our outstanding quality as a result of experience and constant development on www.eppendorf.com/ccc

www.eppendorf.com/consumables

Watch Video!

Eppendorf® and the Eppendorf logo are registered trademarks of Eppendorf AG, Germany.
All rights reserved, including graphics and images. Copyright © 2016 by Eppendorf AG.

MERCK'S POSTDOCTORAL RESEARCH FELLOW PROGRAM

Connect with us on Facebook, Twitter and LinkedIn.

merck careers

merckbewell

merckcareers1

merck

For more than a century, a special passion has driven us at Merck.* Our goal is to discover and develop medicines, vaccines and animal health innovations that will help improve the lives of millions. Still, we know that there is much more to be done. And we're doing it, with a long-standing commitment to research and development.

Developing Talent, Harnessing Innovation, Building for the Future

Our Postdoctoral Research Fellow Program builds on our legacy of scientific excellence and innovation.

If you join us, you'll be a part of a team of motivated scientists working to discover and develop medicines and vaccines that help meet the world's unmet medical needs. You will work alongside outstanding researchers and collaborators as part of Merck's industry-leading research and development organization. Our postdocs:

- Work in unique laboratory environments with top capabilities, equipment, expertise and knowledge
- Obtain experience in drug discovery and development
- Generate innovative science resulting in high-quality external publications
- Participate in seminars, lectures and meetings, and have the opportunity to interact with the local scientific community
- Become positioned for choice careers in pharma, biotechnology or academia

As a postdoc, you will receive a competitive salary and access to the full benefits programs offered by Merck.

At Merck, our passion is improving health. This is what keeps us at the forefront of scientific discovery and innovation. We invite you to apply.

To learn more about the Merck Research Laboratories (MRL) Postdoctoral Research Fellow Program, visit www.merck.com/research/fellow/home.html.

To apply for a position, visit www.merck.com/careers.

*Merck & Co., Inc., Kenilworth, NJ, USA, is known as MSD outside the United States and Canada.

Postdoctoral Research Fellow Program

125 YEARS SINCE 1891

life science EXPERT and e-commerce leader

The life science leaders of
EMD Millipore + Sigma-Aldrich
have joined together and, with our agile e-commerce and global distribution, we can help to simplify your world.
So you can focus with confidence on tackling life science's biggest challenges.

MilliporeSigma now offers:

- **An extended global network** across more than 66 countries
- **A world-class e-commerce platform** to simplify transactions
- **A vast portfolio** that has grown to over 300,000 products

Our combined strengths will deliver the **knowledge, know-how, and best-in-class resources.**

Learn more at **milliporesigma.com**

The life science business of Merck KGaA, Darmstadt, Germany operates as MilliporeSigma in the U.S. and Canada.

EMD Millipore, MilliporeSigma and the vibrant M are trademarks of Merck KGaA, Darmstadt, Germany and its affiliates.
Sigma-Aldrich is a trademark of Sigma-Aldrich Co. LLC and its affiliates.
Copyright © 2016 EMD Millipore Corporation. All Rights Reserved.

MilliporeSigma

Science Careers Advertising

For full advertising details, go to ScienceCareers.org and click For Employers, or call one of our representatives.

Tracy Holmes
Worldwide Associate Director
Science Careers
Phone: +44 (0) 1223 326525

THE AMERICAS

E-mail: advertise@sciencecareers.org
Fax: +1 (202) 289 6742

Tina Burks
Phone: +1 (202) 326 6577

Nancy Toema
Phone: +1 (202) 326 6578

Online Job Posting Questions
Phone: +1 (202) 312 6375

EUROPE / INDIA / AUSTRALIA / NEW ZEALAND / REST OF WORLD

E-mail: ads@science-int.co.uk
Fax: +44 (0) 1223 326532

Sarah Lelarge
Phone: +44 (0) 1223 326527

Kelly Grace
Phone: +44 (0) 1223 326528

Online Job Posting Questions
Phone: +44 (0) 1223 326528

JAPAN

Katsuyoshi Fukamizu (Tokyo)
E-mail: kfukamizu@aaas.org
Phone: +81 3 3219 5777

Hiroyuki Mashiki (Kyoto)
E-mail: hmashiki@aaas.org
Phone: +81 75 823 1109

CHINA / KOREA / SINGAPORE / TAIWAN / THAILAND

Danny Zhao
E-mail: dzhao@aaas.org
Phone: +86 131 4114 0012

All ads submitted for publication must comply with applicable U.S. and non-U.S. laws. *Science* reserves the right to refuse any advertisement at its sole discretion for any reason, including without limitation for offensive language or inappropriate content, and all advertising is subject to publisher approval. *Science* encourages our readers to alert us to any ads that they feel may be discriminatory or offensive.

ScienceCareers
FROM THE JOURNAL SCIENCE AAAS

ScienceCareers.org

SCHOOL OF MEDICINE
CASE WESTERN RESERVE UNIVERSITY

Tenure Track Faculty Position
Department of Physiology and Biophysics

The Department of Physiology and Biophysics at Case Western Reserve University School of Medicine seeks a faculty member at the rank of Assistant, Associate or Full Professor engaged in kidney research. Applicants must have a Ph.D., M.D. or equivalent degree, and demonstrated academic excellence appropriate for career stage. Individuals seeking appointment at the Assistant Professor level must have at least 3 years of postdoctoral experience, a strong record of scholarly activity and evidence of academic potential. Candidates for Associate Professor should have a considerable publication record, evidence of an international reputation and a demonstrated ability to renew funding. For appointment at the Professor level substantial evidence of leadership in the applicant's academic field, outstanding productivity and a sustained funding history are required. Rank will be commensurate with experience.

The successful applicant will be expected to develop and/or continue a robust extramurally-funded research program that compliments current programs within the Department. All areas will be considered; however, areas of particular interest are: (1) mechanisms of ion/water transport; (2) regulation of transport; and (3) renal control of blood pressure.

The Department of Physiology and Biophysics includes 18 primary and 32 secondary faculty members. The Department has a strong record of renal research.

Interested candidates should send an electronic application that includes a cover letter, complete curriculum vitae including funding history, a one-page summary of research interests and the names and contact information for three references to: **RenalSearch@case.edu**. Review of applications will begin **November 1, 2016**.

In employment, as in education, Case Western Reserve University is committed to Equal Opportunity and Diversity. Women, veterans, members of underrepresented minority groups, and individuals with disabilities are encouraged to apply.

Case Western Reserve University provides reasonable accommodations to applicants with disabilities. Applicants requiring a reasonable accommodation for any part of the application and hiring process should contact the Office of Inclusion, Diversity and Equal Opportunity at 216-368-8877 to request a reasonable accommodation. Determinations as to granting reasonable accommodations for any applicant will be made on a case-by-case basis.

SCHOOL OF MEDICINE
CASE WESTERN RESERVE UNIVERSITY

Tenure Track Faculty Position
Department of Physiology and Biophysics

The Department of Physiology and Biophysics at Case Western Reserve University School of Medicine seeks a faculty member at the rank of Assistant, Associate or Full Professor engaged in any area of cardiac research. Applicants must have a Ph.D., M.D. or equivalent degree and demonstrated academic excellence appropriate for career stage. Individuals seeking appointment at the Assistant Professor level must have at least 3 years of postdoctoral experience, a strong record of scholarly activity and evidence of academic potential are required. Candidates for Associate Professor should have a considerable publication record, evidence of an international reputation and a demonstrated ability to renew funding. For appointment at the Professor level substantial evidence of leadership in the applicant's academic field, outstanding productivity and a sustained funding history are required. Rank will be commensurate with experience.

The successful applicant will be expected to develop or continue a robust extramurally-funded research program that compliments current strengths within the Department. Any area of cardiac biology will be considered, however, we particularly encourage applicants with expertise in the areas of cellular and molecular mechanisms of cardiac muscle contraction, genetics of cardiovascular disease, cardiac electrophysiology and arrhythmias, cardiac regeneration and heart failure.

Interested candidates should send an electronic application that includes a cover letter, complete curriculum vitae, a two-page summary of current and future research plans, and the names and contact information for four references to: **CardiacSearch@case.edu**. Review of applications will begin **November 1, 2016**.

In employment, as in education, Case Western Reserve University is committed to Equal Opportunity and Diversity. Women, veterans, members of underrepresented minority groups, and individuals with disabilities are encouraged to apply.

Case Western Reserve University provides reasonable accommodations to applicants with disabilities. Applicants requiring a reasonable accommodation for any part of the application and hiring process should contact the Office of Inclusion, Diversity and Equal Opportunity at 216-368-8877 to request a reasonable accommodation. Determinations as to granting reasonable accommodations for any applicant will be made on a case-by-case basis.

GAIN THE STRENGTH OF A MARKET LEADER — AND THE ENERGY OF A START-UP.

Are you a leader in proteostasis?

AbbVie has made a commitment to finding new therapies for Alzheimer's Disease and other neurodegenerative diseases by opening the Foundational Neuroscience Center (FNC) in Cambridge, Boston.

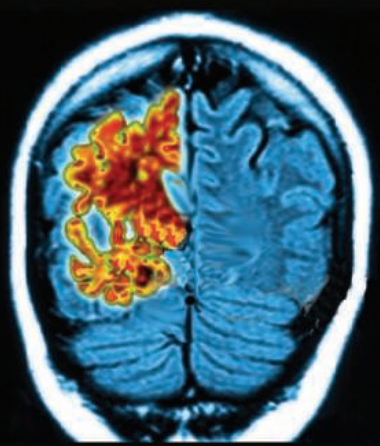

We seek a proteostasis expert to lead a team of 10 scientists. As a member of the FNC leadership team, the ideal candidate will have a strong publication record with a vibrant international network. Prior experience in biotech is advantageous – a desire to see novel discoveries translate into patient benefit is essential.

We seek scientists at all levels for research groups investigating neuroinflammation and tau pathobiology.

Visit abbviecareers.com and reference job ID 1600000118

PEOPLE. PASSION.
POSSIBILITIES.

abbvie

California State Polytechnic University, Pomona
Biological Sciences Department

TENURE-TRACK FACULTY POSITION
POPULATION GENETICIST

The Biological Sciences Department at California State Polytechnic University, Pomona (Cal Poly Pomona) invites applications for a tenure-track, ASSISTANT PROFESSOR position in Population Genetics, beginning September 2017. The area of specialty is open, but candidates who study vertebrates, in such aspects as conservation of wild populations, evaluation of endangered species, and impact of invasive species, are encouraged to apply. Utilization of next generation data analysis and/or quantitative genetics is desirable. A Ph.D. in biology or a related field is required. Post-doctoral experience and previous teaching experience are preferred. The successful candidate will have the potential for excellence in undergraduate teaching, and for developing an externally-funded research program that will involve undergraduate and Master's students. Teaching responsibilities will include Population Genetics, and specialty courses in the candidate's area of expertise. Ability to teach a course in mammalogy is preferred. Teaching responsibilities may also include introductory biology, genetics, evolution, bioinformatics, and/or biostatistics. Cal Poly Pomona is a comprehensive Master's university with a diverse student body. The successful candidate will be expected to contribute to the diversity and excellence of the academic community through research, teaching and/or service, and be committed to teaching and working in a multicultural environment.

Applicants should forward: (1) a cover letter that briefly describes the candidate's training, experience, and teaching and research interests; (2) *curriculum vitae*; (3) statement of teaching philosophy that includes a statement regarding how your teaching or other experiences, successes, and challenges will impact the success of a diverse student population; (4) proposed plan of research; (5) representative publication reprints; and (6) the names and contact information of five references to: **Chair, Population-Geneticist Search Committee, Biological Sciences Department, California State Polytechnic University, 3801 West Temple Avenue, Pomona, CA 91768**. Electronic submission of application materials as a single PDF file is preferred (**popgen_search@cpp.edu**). Review of applications begins on **November 28, 2016**. Official transcripts and three letters of reference will be required of all semifinalists. For further information, visit the Department web site at: **http://www.cpp.edu/~biology**.

California State Polytechnic University, Pomona is an Equal Opportunity, Affirmative Action Employer.

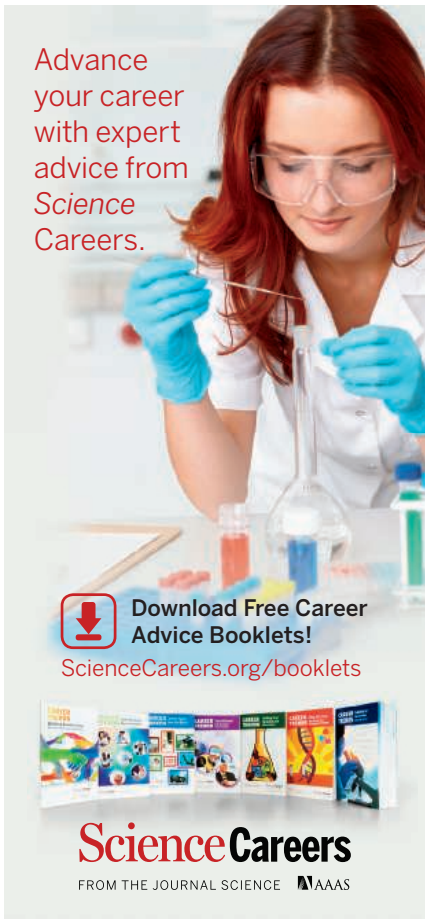

University of Minnesota
Driven to Discover℠

Faculty Position in Cardiovascular Immunology

The Department of Integrative Biology and Physiology and the Center for Immunology at the University of Minnesota Medical School invite applications for a faculty position to be filled at the tenure-track Assistant Professor level.

We seek an outstanding scientist who will establish a competitive extramurally funded research program that focuses on the innate or adaptive immunology of cardiovascular function or disease. The position offers exceptional startup support, a dynamic intellectual environment, state-of-the-art facilities, a competitive salary, and quality research space within the Center for Immunology (http://www.immunology.umn.edu). Additional information about the Department of Integrative Biology and Physiology, affiliated institutes and centers, and the graduate training program, can be found at https://www.physiology.umn.edu and http://www.micab.umn.edu.

Minimum qualifications: Ph.D., M.D., or equivalent in a relevant field of study, plus applicable postdoctoral or faculty experience. To apply, please upload a curriculum vitae and concise summary of current and planned research in response to job number **#301596**, under '**anytime**' at **http://www1.umn.edu/ohr/employment**. Please also arrange to have 3 letters of recommendation sent to **jotto@umn.edu** or **Cardiovascular Immunology Search Committee, Department of Integrative Biology and Physiology, 6-125 Jackson Hall, 321 Church Street S.E., Minneapolis, MN 55455**. Review of applications will begin **October 15, 2016** and continue until the position is filled.

The University of Minnesota provides equal access to and opportunity in its programs, facilities, and employment without regard to race, color, creed, religion, national origin, gender, age, marital status, disability, public assistance status, veteran status, sexual orientation, gender identity, or gender expression. To learn more about diversity at the U http://diversity.umn.edu.

UF UNIVERSITY of FLORIDA
The Foundation for The Gator Nation

Department of Medicinal Chemistry

The Department of Medicinal Chemistry, College of Pharmacy (http://pharmacy.ufl.edu/), University of Florida, invites applications for a **tenure-track faculty position at the assistant or associate professor level**. Candidates should have a record of a strong independent research program in drug discovery and development or demonstrate outstanding potential to build such a program. Faculty hires will also participate in professional and graduate instructional efforts of the college. Area of specialization within medicinal chemistry is open, but should complement the interests of the department and the Center for Natural Products, Drug Discovery and Development and agree with institutional strategies adopted by the University of Florida to foster interdisciplinary research in cancer, infectious diseases, neuroscience and diabetes. The department is located within the UF Health Science Center complex (http://www.health.ufl.edu/). This unique research environment offers excellent opportunities for synergistic collaborations.

Applicants should submit a cover letter, CV with names and contact information of referees, and summary of research program through GatorJobs (**https://jobs.ufl.edu/** and search postings for Requisition Number **493599**). Junior candidates should additionally submit three letters of references to HR Deputy Chief Administrator Lila Robertson (**lrobertson@cop.ufl.edu**). To ensure full consideration, materials should be submitted by **October 15, 2016**; however, applications will be reviewed on a rolling basis. Materials received after this date may be considered at the discretion of the committee and/or hiring authority.

The University of Florida is an Equal Opportunity Institution and encourages applications from qualified minority and female applicants.

FRANCIS CRICK INSTITUTE LONDON
RESEARCH GROUP LEADER RECRUITMENT

The Francis Crick Institute is a new discovery biomedical research institute in central London. We are core-funded by Cancer Research UK, the UK Medical Research Council, and the Wellcome Trust and partnered by Imperial College, King's College and University College London.

The Crick is diverse, open and international, with staff from over 70 nationalities. We support creative and ambitious research that addresses important biomedical questions. Our research programme encourages collaborative and multi-disciplinary approaches, encompassing biological, clinical and physical sciences. For details visit **https://www.crick.ac.uk/strategy/**.

Early Career Group Leaders in Biomedicine

We are recruiting enthusiastic and motivated early career researchers who wish to set up their first independent research programme at the Crick. In addition to all areas of biomedicine, applicants proposing relevant programmes in areas such as bioengineering, ecology, evolution, microfabrication, and synthetic biology will be considered. We also welcome applications from those who wish to work on a flexible and/or part-time basis.

Successful candidates will be offered a competitive salary with a 6-year contract, renewable once for a total of 12 years. The institute will provide fully equipped laboratory space and access to core-funded state-of-the-art technology facilities. Salaries and consumables for around five people, including graduate students, will be provided. Research groups will have the opportunity to expand further based on external grants.

The Crick will provide mentoring and support to ensure its early career Group Leaders make the most of their time at the institute and develop a world-class research programme. Towards the end of the 12-year period we will support them to find leadership positions elsewhere, with potential for a transition start-up package for those remaining in the UK.

Applications from candidates with a PhD and postdoctoral experience should be submitted online at: **https://academicrecruitment.crick.ac.uk**
(Applicants will have to register for an account before submitting an application: complete CV; publications; current and proposed work; long term research vision; referee details)

Informal enquiries about the institute or the application procedure can be made through **Group-leader-recruitment@crick.ac.uk**

Closing date: **midnight on 10th November 2016**

ScienceCareers online @sciencecareers.org

Join the "Double Tops" Program

CHINA
聚焦"双一流"

Over the years, the terms "985" and "211" have always been synonymous with high-level Chinese universities. In the past decade after setting up Project 211 and Project 985, more than 110 universities supported by the two projects have achieved worldwide recognition. However, the quality and prestige of these universities vary considerably, and thousands of other Chinese universities without such support are still struggling to upgrade the quality of their teaching and research.

Last year, the State Council of China released a document entitled, "the Scheme of Promoting the Construction of World-class Universities and First-class Disciplines." Recently the Ministry of Education of China announced that Project 211 and Project 985 have been incorporated into this scheme, making the "Double Tops" program an extension and upgrade of Project 211 and Project 985. With the concept of "Top Discipline" being put forward, colleges and universities with a number of high quality disciplines will have a chance to be supported by the project to further build their advantage in these fields and promote their overall development.

Several Chinese provinces, including Sichuan, Hunan, Hebei, and Shandong, have launched their own provincial plans for developing high-level universities. The list of selected universities and disciplines has already been released in Hebei, with detailed information about the general plan and schedule. To seize the opportunity, many universities in China are making strategic plans. At the core of these strategic plans is an effort to attract and retain top talent.

"Four Iconic Statuses and Achievements of a First-class Professor"

Zhimin Li
Director of Center for Science and Technology Development
Ministry of Education, People's Republic of China

First-class professors and leading scholars will be the core of the "Double Tops" program. Over time, excellent scientists/scholars develop into first-class scientific researchers who possess a solid foundation of professional knowledge, keen inspiration and imagination, strong analytical ability, and excellent communication skills. A first-class professor should have been recognized by the international academic community in his/her field of research, such as being invited to deliver keynote talks at academic conferences; serving as an editorial board member, an editor-in-chief, or an editorial board director for a high impact journal; holding the post of chairman or director of an international academic organization; or being the principle investigator behind an international science and technology award. Dr. Li stresses that first-rate teaching and research rely on teams of topnotch scholars. Building a pool of talented scientists and encouraging independent innovation are key goals within the current talent development policy.

As Dr. Zhimin Li points out, master professors are at the core of the construction of a world-class university and first-class disciplines, and are the foundation of knowledge and the hub of creative ideas. High-level overseas talent bring a global perspective, creativity to "think outside the box" and exceptional networking advantages. They play a critical role in developing a faculty team, upgrading the level of scientific research, cultivating the best and most innovative talent, and promoting international exchange and collaboration—they are the indispensable force behind the construction of "Double Tops". In the post Project 985 and Project 211 era, the consensus of the presidents of Chinese universities is that "gain talent, gain the world."

Eastern China

Universities in the east of China continue enjoying their regional advantage in attracting talents. Eastern China is the most dynamic economic region, and universities in this region are also the most active in talent recruitment, a major focus of "Double Tops".

Zhaohui Wu

President of Zhejiang University

"Double Tops" is an ambitious plan to rejuvenate Chinese higher education and build world leading universities. Focusing on this plan and attracting world-renowned talents, Zhejiang University strives to develop a world-class comprehensive innovative research university.

Guangjun Zhang

President of Southeast University

The national "Double Tops" strategic plan in China provides an opportunity as well as a challenge for our university to greatly raise of capabilities in innovations, in fostering first-rate talents, in yielding first-rate achievements in all research fields, at the same time to make it a first-rate university in the world. The Southeast University will continue the principles of "aiming at the foremost developments, following the strategy, depending on both bodies of teachers and students, placing priorities on the outstanding people", maintain the theme of strengthening the status of the university by using capable people,so our goal of making the Southeast University a first rate university in the world will be achieved soon.

Chuangbing Zhou

President of Nanchang University

Higher education works as the junction of the first productivity of science and technology, the first initiative of innovation and the first resource of talents. With the leadership of Jiangxi' s higher education, Nanchang University is exploring earnestly the way to high-level university by implementing talent programs. It commits itself wholeheartedly to the employment of talents without overstressing qualifications. It is our strong hope that talents from all over the world can join us in the development of Nanchang University.

Lianxiang Ma

President of Qingdao University of Science and Technology

At QUST, teachers teach and research in the free academic atmosphere; students acquire knowledge and develop themselves in the rich learning environment. Qingdao University of Science and Technology is striding on the way of realizing the Dream of Ecological University.

Beijiu Cheng

President of Anhui Agricultural University

The construction of "Double Tops" is the crucial and necessary choice for the development of Chinese universities. It is also the basic and intrinsic requirement to help Chinese universities to march on the forefront of world stage of higher education. Adhering to its development orientation, Anhui Agricultural University will seize the opportunity to develop top-level discipline by reform and innovation, sticking to the strategy of developing comparative advantages in a number of disciplines, and continuously creating new prospects of development path.

Science Careers online @sciencecareers.org

ScienceCareers online @sciencecareers.org

Southern China

In August this year, a group of famous universities, including Peking University and Tsinghua University, set up branch campuses in Shenzhen, which has brought about heated public discussion. There are a number of cities similar to Shenzhen in Southern China that have great growth potential and will surely become critical players in the "Double Tops" program. The presidents of universities in Southern China are offering an olive branch to overseas talent.

Xiaohong Li

President of Wuhan University

Wuhan University is a venerable institution devoted to fully supporting talents with top priority in the new and critical chapter of "Double Tops" strategy in Chinese higher education. We sincerely invite your partnership in pursuit of excellence at our university where remarkable talents are highly valued and appreciated.

Jun Hu

President of Jinan University

Currently, our school (JNU) in various disciplines such as life sciences, medicine, chemical, pharmaceutical, environmental science and information science are in a leading position in the region. We sincerely invite you to join us and for your dedication to providing quality research environment and facility. Let us work together to create a better future.

Jianbao Li

President of Hainan University

Hainan University (HNU) is committed to strengthening the academic influence of the faculty and the social competitiveness of the students so as to further contribute to the implementation of the national strategy for the South China Sea and the local socio-economic development.

Western China

In the past, less prosperity and lower salaries for faculty members in Western China compared to other regions were critical factors that added to the brain drain. Now, universities in the region are strengthening their offerings with support from the Ministry of Education, which is encouraging the movement of talent from east to west under the national framework of the "One Belt, One Road" strategy. These policies bring unique opportunities for the development of universities in the region.

Xuhong Zhou

President of Chongqing University

Chongqing University warmly invites global talents to broaden the development prospect in Chongqing, a national Central City with the fastest GDP growth in 2015 in China, and to join Chongqing University to conduct rigorous research, cultivate talents, enlighten masses, guide the revitalization of the society.

Jinhui Peng

President of Kunming University of Science and Technology

The "Double Tops" is a major national strategy to shape China into a higher education giant. Kunming University of Science and Technology will take this great opportunity to develop toward an internationally recognized and nationally first-rate research-oriented university with distinctive characteristics, where students will be able to shine on campus and in their future career.

Han Lei

President of Chongqing Medical University

As the base of "HOME Program" of CAST and Chongqing's innovation and entrepreneurial base for high-level overseas talents, Chongqing Medical University committed to accumulating first-class academic talents and building high-level medical university.

Northern China

Compared with other Chinese universities, universities in Beijing have the geographic and environmental advantage for attracting and retaining talent. The universities in the Northeast region will keep pace with the plan of "Overall Revitalization of Northeast China" and will be ready to unleash the power of talent development teams. With the guidance of the "Coordinated Development of Beijing-Tianjin-Hebei Region" document, the integration of education in these regions has been progressing rapidly. Coordinated development of the Beijing-Tianjin-Hebei region cannot work without the support of talent. The presidents of universities in northern China are putting in place plans for recruiting talent.

Haiyan Hu

President of Beijing Institute of Technology

To cherish talents has always been the deeply-rooted creed and the fountainhead of Beijing Institute of Technology (BIT) . The faculty of high quality, endowing our resilience for core competitiveness and sustainable development, is the major drive for BIT to become a foremost university of science and technology in the world. Over the past decade, BIT has fully addressed the strategy of "Creating an elite faculty for the university's prosperity". A faculty system forging interdisciplinary platforms, especially for young excellent juniors has been constantly propelled and pursued with great efforts with a vision for both the present and the future generations.

Huibin Xu

President of Beihang University

The "Double Tops" plan is the guideline for the reform and development of China' s higher education and will remain its priority for a certain period. Serving the national strategic needs while exploring the international academic frontiers as an organic unity persistently, Beihang University (BUAA) will accelerate the development of the world-class university rooted in China.

Yu Zhou

President of Harbin Institute of Technology

The spirit of the "Double Tops" philosophy cannot survive without a support of the first-class scholars' teams. A large number of the first class scholars will spring up in this process. Our door is going to stay open to world leading scholars who can lead the academic frontiers. At the same time, our attention is also given to young scholars who have bigger dreams. We provide world level career stage, continuing resources input and adequate trust to support talents to achieve academic goals and at the same time to contribute to the goals of the "Double Tops" philosophy of HIT.

Bin Ning

President of Beijing Jiaotong University

Building "Double Tops" has provided Beijing Jiaotong University a rare opportunity for its development. Building a world-class university with world-class disciplines cannot be achieved without first-class teaching staff, top-ranking discipline leaders and first-rate innovative teams. Beijing Jiaotong University warmly invites talents from all over the world to join us and create a promising future together.

Yu Yao

President of Harbin Engineering University

To foster a distinguished university with the highest academic discipline is the key strategic policy the Chinese government is promoting to reform higher education. HEU will create four high-ranking academic discipline groups and propel their systematical construction and distinctive running characteristics in the fields of ship industry, ocean equipment and exploration, and nuclear application. HEU will also collaborate with distinctive experts and scholars from both home and abroad to cooperatively build up this high-ranking research-oriented university with distinctive characteristics.

Science Careers online @sciencecareers.org

ScienceCareers online @sciencecareers.org

Chuanping Yang

President of Northeast Forestry University

The Northeast Forestry University is aiming to build the World-class forestry university, and making great effort to construct currently 3 state key disciplines as Forestry, Forestry Engineering and Ecology into First-class disciplines. We warmly welcome all top talents in these fields to join us, and I believe that you will not be disappointed in my university.

Qingxin Yang

President of Tianjin Polytechnic University

As a higher education institution with a history of more than 100 years and significant characteristics, TJPU is striving to achieve its goal of a comprehensive university with the world-class textile discipline. In that sense, outstanding academic human resources are the important driving force for the goal realization and sustainable development of TJPU, renowned researchers and professors in relevant fields are welcome to joining us, and we will work together to achieve common academic dreams.

Fuping Lu

Vice-President of Tianjin University of Science and Technology

The launching of Double First-class Universities (DFU) would change the unfair and deep-rooted university status caused by the 211 and 985 project, leading in a new path for self-development and adjustments for all Chinese universities. Tianjin University of Science and Technology, a typical municipal-run institute, will seize the opportunity of DFU, highlight its premium disciplines and strive for excellence.

Tiemao Shi

President of Shenyang Jianzhu University

The development of "Double Tops" needs to gather first-class faculty team. Shenyang Jianzhu University has been making great efforts to attract domestic and overseas outstanding talents. At the same time, it also strengthens the self-development and internationalization of the faculty team. He has emphasized the supportive and guiding role of the high-level talents to the academic development, and will strive to build an industry-leading innovative architecture university with distinctive characteristics.

It can be predicted that along with the advancement of "Double Tops" program, top overseas researchers will find a stage in China on which they can fully realize their academic dreams–this is the best time to join!

To help China' s top-ranked universities attract high-level talent from overseas, CERNET has partnered with Science to launch a print and online media campaign. Many of China' s top universities are recognized as world-class and are doing first-class research but the aim is to build on this and establish worldwide acclaim for all of China's top universities in both institute and discipline rankings.

Researchers, interested in working in China, are invited to consider applying for jobs published in the following special section "Opportunities in China" and online at http://jobs.sciencecareeres.org/

Further information can also be located at www.edu.cn/syl

Faculty Positions

At Harbin Institute of Technology, China

Positions: Harbin Institute of Technology (HIT) invites applications for tenure-track or tenured faculty positions at the ranks of Assistant, Associate, and Full Professor in the fields of Engineering, Materials Science, Information, Mathematics, Physics, Chemistry, Life Sciences, Economics and Management, Art, Social Sciences etc. Successful candidates will be committed to excellence in supervising students and teaching at both undergraduate and graduate levels. The successful candidates will have opportunity to work in Harbin, Weihai or Shenzhen campuses. Senior faculty are expected to establish and lead a research team and guide development of selected research subjects. The junior faculty will be encouraged to join an interdisciplinary team, undertaking nationally significant research projects. It is expected the junior faculty to develop an independent research program, becoming leading scholars in their filed.

What we offer: We offer internationally competitive salaries, turnover apartment and settling-in allowance which would be sufficient to afford a commodity flat near the Harbin or Weihai HIT campuses. We provide an ample start-up funding and other necessary resources to ensure the successful candidates to keep their mind unhindered, and focus on teaching and research works. Qualified candidates for the "Thousand Talent Program" or any other governmental talent programs will receive additional support. In Shenzhen campus, qualified candidates will have the opportunity to apply for the start-up funding (ranging from 2,000,000 RMB to 5,000,000 RMB) and living allowance (from 1,600,000 RMB to 3,000,000 RMB respectively) from Shenzhen municipal government. Besides these benefits, HIT offers a number of world class research initiatives, such as the "Major National Science and Technology Infrastructure" program, the "Collaborative Innovation Center" (the "2011 plan"), etc. These programs will offer a strong support and will enable a superiority for the scholars in different fields to display their talents and fulfill their ambitions.

Requirements: Each candidate must have a PhD degree and should have credentials to qualify for a tenure-track or tenured faculty position at the Harbin Institute of Technology. All candidates are expected to propose a research plan and to state academic goals. The ability to fulfill the established goals must be manifested.

How to Apply: Applicants should submit electronic copies of the following documents to talents@hit.edu.cn. (1)The curriculum vitae, including list of publications; (2)Teaching statement, including teaching interests, experiences and a describing of teaching approach and philosophy; (3)Future research plan, including research interests, expected research accomplishments and goals; (4)The set of copies of three representative publications; (5) Three reference letters, including the names and contact information of references. For complete details about this job posting please visit: www.hit.edu.cn.

International Young Scholar forum:

During December 24-25, 2016, HIT will organize the International Young Scholar Forum. At that occasion, international, outstanding young talents in different areas will be invited to come to Harbin to exchange experiences and ideas. Travel and accommodation costs will be covered by the forum. HIT warmly welcomes applicants to visit Harbin during the forum. The applicants should visit the HIT website at: http://talents.edu.cn to register and view more details about the forum.

About Us:

Harbin Institute of Technology was founded in 1920. From its beginning, HIT has received preferential support from the central government. After nearly 100 years of existence, we have developed into a renowned multi-disciplinary university with science, engineering and research as its core. HIT ranks among the top 7 in US NEWS Best Global Universities for Engineering 2016. Eight disciplines, such as engineering and materials are in the top 1% or the top 1‰ of ESI. Especially in the field of aerospace, HIT has established an irreplaceable position in China's aerospace industrial development. Now, we are converging talents from all around the world，and striving to achieve our main goal, HIT to continue to be a world class university.

哈爾濱工業大學
HARBIN INSTITUTE OF TECHNOLOGY

Contact Information:
Add：92 West Dazhi Street , Nan Gang District, Harbin Post Code: 150001
Contacts：Mr. Wang, Miss. Zhang
Tel: +86-451-86418762
Email: talents@hit.edu.cn

ScienceCareers online @sciencecareers.org
OPPORTUNITIES IN CHINA

ScienceCareers online @sciencecareers.org
OPPORTUNITIES IN CHINA

"JINAN DOUBLE HUNDRED TALENTS PLAN"

Recruiting Members (Candidates) Of the "Thousand Young Talents Program"

暨南大學 JINAN UNIVERSITY

About Jinan University

Jinan University is one of China's "One Hundred Key Universities of 21st Century"(the "211 Project") and is operated under the leadership of the Overseas Chinese Affairs Office of State Council. As the first university established by the State for overseas Chinese students, JNU currently has the largest number of overseas and foreign students and is honored as the "top university for overseas Chinese". Abiding by the motto of "loyalty, sincerity, integrity and respect", the university is committed to cultivating talents with the excellent traditional Chinese moralities and culture. In June 2015, JNU was selected into the "High-level University Construction Program" by Guangdong provincial government. The University has 27 colleges, comprising 62 departments, 188 research institutions, 77 laboratories and offering 89 undergraduate majors, 189 master degree programs in 38 Level-I and 5 Level-II disciplines as well as 74 doctoral degree programs in 15 Level-I and 4 Level-II disciplines. Besides, we have 4 national key disciplines (industrial economics, aquatic biology, finance and literary theory) , 8 key disciplines at the level of the Overseas Chinese Affairs Office of the State Council, 20 provincial Level-I key disciplines, and 4 provincial Level-II key disciplines. The University has the following teaching and research bases: a key research base of national humanity & social sciences, a teaching & research base for Chinese language & literature of the Education Ministry, a base for national university cultural quality education, a national base for teaching Chinese as a foreign language, an educational base for overseas Chinese education of the Overseas Chinese Affairs Office of the State Council and a key research base of humanity & social science of Guangdong Province. It also has one national engineering center, 14 ministerial and provincial engineering centers and 13 key ministerial and provincial laboratories.

To achieve the goal of building a high-level university, JNU continues to implement the strategy of "strengthening universities with more talented people" in order to greatly enhance the core competitiveness of talent and sustainable development capacity and to further strengthen the support for the introduction and training of outstanding personnel. For this purpose, the university is now recruiting members or candidates of the "High-level Overseas Young Talents Program" (referred to as the Thousand Young Talents Program) from home and abroad.

Disciplines Open for Recruitment

Optical engineering, information and communication engineering, electronic science and technology, science of Chinese pharmacology, pharmacy, biology, biomedical engineering, ecology, environmental science and engineering, basic medicine, clinical medicine, integration of traditional Chinese and western medicine, traditional Chinese medicine, oral medicine, public health and preventive medicine, nursing, mechanics, cyberspace security, computer science and technology, software engineering, mathematics, chemistry, materials science and engineering, food science and engineering and physics.

Basic Requirements

1. Members of the "Thousand Young Talents Program".
2. Candidates of the "Thousand Young Talents Program" (candidates of the discipline of finance not included). Applicants should meet the following requirements:

(1) Applicants should consciously adhere to China's laws and regulations, and have good academic ethics;

(2) Applicants whose research fields are in natural science and engineering technology should be under 40 years old (up to June.1, 2016, the same below);

(3) Applicants should have acquired a doctoral degree, and have over three years' overseas research and working experience (not including working experience abroad with employment relations remained in China). Applicants who received a doctoral degree in China should not exceed the age limit of 40. Applicants who have received a doctoral degree abroad may be waived from the age limit of 40 if they have outstanding research performance and other great achievements. In such cases, a waiver letter with explanation and proofs is required.

(4) Applicants should have a permanent teaching or research position in overseas universities, research institutions and enterprises of high prestige.

(5) Generally, applicants should not have a full-time position in China at the time of application. However, if applicants are already holding a position in China, it should be less than one year that they returned from abroad.

(6) Applicants should work full time in China once employed.

(7) Applicants should be the top performers among their peers in the same research field and have potentials to become the leading persons of their field.

Package of Salary & Benefits

JNU will provide recruited members and candidates of "Thousand Young Talents Program" with a competitive package of salary and benefits based on the job position.

1. **For members of "Thousand Young Talents Program":**

(1) Salary: no less than ￥500,000 per year(pre-tax).

(2) Supporting funds for research: ￥1,000,000-3,000,000.

(3) Housing/settling allowance: no less than ￥2,000,000(pre-tax).

(4) Recruited members will be directly employed as a senior professional.

(5) Recruited members will have the priority to recruit PhD students, post-doctors and research assistants.

(6) The university will provide applicants assistance in their children's entry into kindergarten, primary school and middle school in Guangzhou.

(7) Members will enjoy the one-stop service for high-level talents.

(8) The university will give priority to solve the job transfer of spouse of members.

(9) Each new recruit is entitled to a central finance subsidy of ￥500,000and a research fund ranging from ￥1,000,000 to ￥3,000,000, which, once ratified, will be allocated according to schedule. The Guangdong provincial finance will also grant the recruit a living allowance of ￥250,000 and a supportive fund of ￥500, 000.

2. **Candidates having successfully passed the university review process can sign an employment contract of intent, and apply for the "Thousand Young Talents Program" membership in the name of Jinan University. Candidates who have entered into the defense session are entitled to the following salary and benefits:**

(1) Salary: no less than ￥400,000 per year(pre-tax).

(2) Supporting funds for research: no less than ￥1,000,000.

(3) Housing/settling allowance: no less than ￥1,000,000(pre-tax).

(4) Recruited members will have the priority to recruit PhD students and research assistants.

(5) The university will provide applicants assistance in their children's entry into kindergarten, primary school and middle school in Guangzhou.

(6) Recruited members will enjoy the one-stop service for high-level talents.

(7) If recruited members are enrolled into the "Thousand Talents Program", they are entitled to all the pay and benefits offered by the university to members of this program.

This advertisement is valid permanently. Electronic copies of your related materials are also required when applying. Please send them to the official email: otalents@jnu.edu.cn.

Contact Information

Home page of Personnel Department, Jinan University
(http://personal.jnu.edu.cn/)
Tel: 0086-20-85227283 (fax available), 0086-20-85223525
Contacts: Mr. Tong, Mr. Liu
Email: otalents@jnu.edu.cn
Address: No. 601, Huangpu Avenue West, Guangzhou, Guangdong, PRC
Post Code: 510632

Faculty Recruitment of Overseas Talents - Beijing Institute of Technology

Beijing Institute of Technology (BIT) announces recruitment for talented applicants for full-time tenured faculty positions in the broad areas of sciences and engineering, including but not limited to: aerospace engineering, mechanical engineering, optoelectronics, electronics and informatics, automation, computer science and technology, material science and engineering, chemistry and chemical engineering, life science and bio-engineering, mathematics and statistics, physics, management and economics. Successful candidates are expected to establish research labs in the corresponding academic schools and to interact with diverse faculty across disciplines. This hiring initiative is a part of the National "Thousand Talents Program", "Outstanding Young Faculty Program", and BIT's tenure tracked faculty program. These programs intend to attract international candidates addressing important research issues and contributing to the signature research areas of the university.

BIT, founded in 1940, has always been a leading institution of science and technology in China. In 2016, BIT was ranked among the Top 70 in QS Asian Universities Ranking and Top 400 in QS World Universities Ranking, as well as the 15th among the Chinese universities in the above rankings. The fundamental research on engineering, material science, chemistry, physics and mathematics in BIT is among the top 1% in ESI ranking

I. Requirements for Positions of National"Thousand Talents Program"

1. Positions Supported by the National "Young Thousand Talents Program"

(1)The applicants are required to hold a Ph. D. and have at least three years overseas research experience in world-class universities, research institutes, or top-ranking overseas companies. Applicants with overseas experience and who are now working in China for less than one year will also be considered.

(2)Exceptional candidates under the age of 40 who have made outstanding research discoveries will be considered as individual cases.

2. Other Positions Supported by the National"Thousand Talents Program"

The candidates are required to hold a professor position or equivalent position at world-class universities or research institutions. Applicants who are under the age of 55 must have held positions supported by the Innovative Talents Project, or under the age of 65, positions supported by the Overseas Experts Project.

II. Requirements for Positions at Tenure-tracked Program

1. The applicants are required to hold a Ph. D. and have more than 2 years experience at world-class universities or research institutions, under the age of 35 for associate professor and 32 for assistant professor.

2. The applicants are required to have expertise about the latest development in the research area with highly recognized research achievements, show potential for being future academic leaders to develop new research directions, and be supported by high-level papers as the first author or corresponding author.

III. Payment and Benefits

1. Recipients of the National "Young Thousand Talents Program"will receive:

(1)Professorship and Ph. D. supervisor, with special enrollment quotas for graduate students

(2)A subsidy of 500,000 RMB from the government, and 1-3million RMB for research funding, matching research funding at an equal ratio to the national standard, office, and laboratory space provided by BIT.

(3)Annual salary from 350,000 to 420,000 RMB (insurance and accumulation fund paid by BIT not included) and housing subsidy of 500,000 RMB provided by BIT.

(4)Opportunity of buying a new flat of one sitting room and two bedrooms with a discount of 1 million RMB compared to the market price. Assistance of housing during the transition period will be provided.

(5)Assistance in the placement of children and spouse for educational and job opportunities.

(6)International travel expenses will be covered for the interview, with recommendations to other positions if not recruited.

2. Other projects in National "Thousand Talents Program"

BIT supports various projects on the basis of payment from the government, appoints entrants as professors and Ph. D. supervisors, provides adequate research start-up funds, competitive salary and other material benefits, helps to arrange assistants, office and laboratories, and supports the entrant to establish research teams.

3. Tenure-tracked Program

Recipients of the Associate Professorship will receive:

(1) Professorship and Ph. D. supervisor, with special enrollment quotas for graduate students.

(2) Annual salary from 300,000-360,000 RMB (Insurance and accumulation fund paid by BIT not included).

(3) Research start-up funds of 600,000 RMB.

(4) Assistance in the placement of children's educational opportunities.

Recipients of the Assistant Professorship will receive:

(1) Associate-professorship and supervisor of master's degree students, with special enrollment quotas for graduate students, and will qualify to apply for Ph. D. supervisor.

(2) Annual salary from 200,000-240,000 RMB (Insurance and accumulation fund paid by BIT not included).

(3) Research start-up funds of 400,000 RMB.

(4) Assistance in the placement of children's educational opportunities.

IV. Application Instructions

Applicants for the National "Thousand Talents Program" should send their CVs and the complete representative published works to the BIT HR Office. Applicants for the Outstanding Young Faculty Program should send their CVs and 5 representative published works, quotations and comments by others, and future working plans to the BIT HR Office. Please state the position being applied for in the subject line of the email.

For any issues related to the "Thousand Talents Program" and the "Outstanding Young Faculty Program", please contact Mr. Gan Zhenkun or Mrs. Yu Xiaotian.

Tel.: +86-10-68918577 **Email:** bitrcb@bit.edu.cn

For more information about the "Thousand Talents Program" and the "Outstanding Young Teachers Program", please visit: http://renshichu.bit.edu.cn/

ScienceCareers online @sciencecareers.org
OPPORTUNITIES IN CHINA

ScienceCareers online @sciencecareers.org
OPPORTUNITIES IN CHINA

QINGDAO UNIVERSITY OF SCIENCE AND TECHNOLOGY RECRUITS GLOBAL TALENTS

Qingdao University of Science & Technology (QUST) is a key university of Shandong Province. It is a multi-disciplinary university which focuses on engineering, coordinately develops with science, engineering, art, economic, management, medicine and law, and distinguishes itself by material science, chemical engineering, applied chemistry, mechanical engineering, automation, and information technology and computer science.

In order to develop itself into a high level university of teaching and research with balanced development of the disciplines and distinctive features, QUST now is recruiting global talents to implement the strategy "School Powered by Talented Professionals".

Disciplines

For more details, please refer to Global Talents Recruitment Notice of Qingdao University of Science and Technology (two-dimensional code).

Levels and Requirements of the Talents

1 The first level:

Academicians of Chinese Academy of Sciences or Chinese Academy of Engineering, or overseas talents of the same level.

2 The second level:

Those who meets one of the following requirements:

a) Member of the "Thousand Talents Program" by the Organization Department of the Central Committee of the CPC (Innovate Class), Professor of "Chang Jiang Scholars Program" National Natural Science Funds for Distinguished Young Scholar or expert of the same level.

b) Chief scientist of National 973 program, National 863 program, The National Key Technology R&D Program, National Natural Science Foundation of China.

c) Top 2 of the first prize winners from National Natural Science Award, National Technology Advancement Award, State Technological Innovation Award and the first place of the second prize from National Natural Science Award, National Technology Advancement Award, State Technological Innovation Award. Other award of the same level.

d) At least two articles in Science, Nature or Cell as the first author or the sole correspondent author in the past 5 years.

3 The third level:

Those who meets one of the following requirements:

a) Member of the "New Century National Hundred, Thousand and Ten Thousand Talent Project" by Ministry of Human Resources and Social Security, young or middle aged experts with National outstanding contributions, Member of the "Thousand Talents Program" by the Organization Department of the Central Committee of the CPC (Entrepreneurial Class), and other expert of the same level.

b) Published a number of high quality articles in the Major International Academic Journals in the past 5 years.

Benefits

The first level:

Benefits to be negotiated for every single task and special policy to be enjoyed in respect of salary, housing and research funds.

The second level:

a) 2 million CNY for housing allowance and 1 million CNY for settlement fee.

b) 5 million CNY research funds for Natural Science field and 0.5 million CNY research funds for humanities and social science field.

c) post allowance of 0.6-0.8 million CNY per year for full-time employees in addition to salary and welfare benefits.

The third level:

a) 1 million CNY for housing allowance and 0.5 million CNY for settlement fee.

b) 2 million CNY research funds for Natural Science field and 0.3 million CNY research funds for humanities and social science field.

c) post allowance of 0.3-0.4 million CNY per year for full-time employees in addition to salary and welfare benefits.

Contact

Mr. Li
Add: No. 99, Songling Rd., Qingdao, Shandong
Qingdao University of Science and Technology
Mailbox 368#
Zip: 266061
Tele: +86-532-88959097
Email: qustrc@163.com

ScienceCareers online @sciencecareers.org
OPPORTUNITIES IN CHINA

Beijing Jiaotong University
"Hundred Excellent Talents Project " Invites Talents

Beijing Jiaotong University (BJTU) is a national key university under the direct administration of the Ministry of Education and now is jointly supported by the Ministry of Education, the China Railway Corporation and Beijing Municipal Government. BJTU is one of the first universities selected into the "National 211 Project" and the "985 Strength Discipline Innovation Platform" project, one of the first institutions authorized to confer master's and doctoral degrees. BJTU, as the leading organization, has established the Collaborative Innovation Center for Rail Transit Safety, which is one of the first 14 collaborative centers approved by the Chinese government to enter the "National 2011 Projects". BJTU has been selected into top 100 in "QS brics countries university rankings" for three consecutive years and six disciplines selected into top 400 in "QS world university discipline ranking".

BJTU is located in Beijing, the capital city of China with east and west campuses in Haidian District. It covers a total area of almost 1,000 mu, and its building area is 910 thousand square meters. The university has also established a new Weihai campus and put it into use in September 2015. With beautiful campus environment, each campus has been equipped with advanced teaching and scientific research facilities.

Aiming at " Distinctive World-class University ", and actively serving the national " Belt and Road " initiatives and " going global " strategy of high-speed railway, Beijing Jiaotong University is vigorously implementing the strategy of "strengthening school with talent", gathering distinguished talents from home and abroad, diligently improving the influence of disciplines, and promoting science and technology innovation to pursue a brilliant future. We cordially welcome talents with ideals and abilities to join us and promote development of BJTU.

●Recruitment of subjects

Systematic Science, Communication and Transportation Engineering, Information and Communication Engineering, Civil Engineering, Applied Economics, Statistics, Mechanical Engineering, Computer Science and Technology, Electrical Engineering or related disciplines.

●Recruitment Requirements

1.Hundred Excellent Talents Project

Qualifications Required

1). First-level talents should reach the level of academicians of Chinese Academy of Sciences and Chinese Academy of Engineering or National Thousand Talents Project Specialty Professors.

2). Second-level talents should reach the level of Changjiang Scholarship Specialty Professors or the winners of National Outstanding Youth Funds.

3). Third-level talents should reach the level of National Thousand Young Talents .

4). Fourth-level talents should achieve outstanding academic accomplishments and have the ability to win National Outstanding Youth Funds within 3 to 5 years.

Salaries and Supporting Conditions

BJTU will provide competitive package of salary and benefits for winners and support housing for experiments and administration, housing or rental subsidies. Salaries and research funds are listed as follows:

Salaries for first-level talents will be decided through mutual negotiation.

Salary for second level talent is 600,000 RMB, and research funds 600,000-5,000,000 RMB.

Salary for third level talent is 450,000 RMB, and research funds 400,000-3,000,000 RMB.

Salary for fourth level talent is 300,000 RMB, and research funds 200,000-1,000,000 RMB.

2.Young Excellent Talents

Young excellent talents who have obtained doctoral degree in well-known universities (institutions) or have research experience over two years with great potential are welcomed . BJTU offers scientific research allowance of 100,000-200,000 RMB for science and engineering , and 50,000-100,000 RMB for arts and humanities, setting in allowance 30,000-50,000 RMB, rent allowance 3,500-4,500 RMB per month for 3 years. Those who have remarkable research achievements could join BJTU's "Young Talents Cultivation Plan" through selections and enjoy corresponding 3,000-5,000 RMB per month subsidies and other supporting policies. The period for the cultivation is 3 years.

●How to Apply

Please send one copy of CV (including basic information, educational background, research experience, academic achievements) to rczp@bjtu.edu.cn, and indicate the discipline and the position you are applying for.

●Contact Information

Website: http://www.bjtu.edu.cn/

Address: Beijing Jiaotong University, No.3shangyuancun, Haidian District, Beijing Zip Code:100044

Contact Person: Ms. Zhang Yi Telephone:+86-10-51683432 Fax:+86-10-51684704 Email: rczp@bjtu.edu.cn

CHONGQING UNIVERSITY CALLS FOR GLOBAL TALENTS

Chongqing University Profiles

Chongqing University, founded in 1929, is a national "Project 985" and "Project 211" comprehensive key university directly governed by the Ministry of Education, China. Located in Chongqing, the significant Central City with the fastest GDP growth, Chongqing University aims to contribute to the national strategic research, municipal social and economic growth. Chongqing University has highly academic reputation, cultural richness and history deposits, known for advanced disciplines of Mechanical Engineering, Power Engineering, Material Science and Engineering, Information Science, Biology, and Economics and Business Administration, and the high-level disciplines of Architecture, Civil Engineering, and Resources and Environmental Science. The university consists of 6 faculties, namely, Faculty of Arts and Humanities, Faculty of Social Science, Faculty of Science, Faculty of Engineering, Faculty of Built Environment, Faculty of Information Science, and 34 colleges. As the best university in the western China, Chongqing University warmly invites global talents to broaden the development prospect here!

Brief Introduction to Tenure Track Recruitment System

Chongqing University carries out the tenure track recruitment system with reference to international recruitment system of foreign universities and the academic evaluation of peer review, strives for providing the guarantees of talents team building, converses the outstanding talents home and abroad, promotes the sustainable development for school construction, and is featured as full implementation, independent system, and international academic standard.

What We Offer

According to the educational background and working experience, successful candidates will be employed as the Full Professor, Associate Professor or Assistant Professor by the university with preferential treatments as follows:

- Appointed as the doctoral advisor and master's advisor;
- Incentive high salary;
- Competitive settling-in allowance;
- Sufficient research start-up fund;
- Purchasable talent apartment with less-than-market price.

How to Apply

Qualified applicants are strongly suggested to submit application materials electronically on http://121.43.192.253:8086/login/login.html?id=59 or email to cqurczp@cqu.edu.cn with a comprehensive CV, certificates of academic degrees, 5 samples of major publications and 3 references.

Contact Information

Home Page of Personnel Department: http://rsc.cqu.edu.cn
Tel: 0086-23-65112823
Email: cqurczp@cqu.edu.cn
Address: No. 174, Shazheng Street, Chongqing, PRC

This Job Advertisement Is Long-term Effective.

KUNMING UNIVERSITY OF SCIENCE AND TECHNOLOGY CALLS FOR GLOBAL TALENTS

Brief Introduction

Kunming University of Science and Technology (KUST) is situated in Kunming, the capital city of Yunnan Province in southwest China, which is well known as the "City of Eternal Spring" for its mild weather and beautiful mountainous scenery. Founded in 1954, KUST is one of the top 100 universities in China and the largest and the only technology university across Yunnan province. KUST has been ranked within the top 1% worldwide by the international ranking of Essential Science Indicators (ESI) for its Engineering and Material Science programs.

KUST's research funding accounts for more than 2/3 of the total amount allocated to the 73 higher education institutions in Yunnan province. In 2015, KUST's research funding reached 828 million RMB. Over the past decade, KUST has accomplished many milestone achievements including 5 national and 34 provincial awards for teaching, 10 national and 278 provincial awards for research and technological invention.

KUST is committed to taking its teaching and research to the next level by providing an excellent environment for its faculty and students. We look forward to a bright future where your academic talent and contribution to KUST will be recognized and rewarded.

Qualifications & Requirements

1) High-Level Talents

Academicians of the Chinese Academy of Engineering or Sciences, selectees of "the Thousand Talents Plan", winners of the National Science Fund for Distinguished Young Scholars, Distinguished Professors under the Yangtze River Scholar Award Plan, and other High-level talents meeting the requirements of KUST.

2) Required Disciplines

Electronic Information, Biology, Food, Medicine, Materials, Electromechanical Integration, Chemical Engineering, New Energy, Environmental Protection Technology, Urban Planning, Architecture, and Transportation.

Salary & Benefits

1) Housing subsidy: 300 thousand RMB to 5 million RMB;

2) Research group start-up funding: 800 thousand RMB to 10 million RMB (80 thousand RMB to 1 million RMB for the Philosophy and Social Science field);

3) Annual salary: 120 thousand RMB to 1 million RMB;

4) Laboratories and assistants provided (Some High-Level Talents).

For more information about Salary & Benefits, please visit: http://ryzp.kmust.edu.cn/enroll/.

Contact Us

Contact Person: Mr. Liu, Ms. Xiao
Phone: +86-0871-65916661
E-mail: kmustrsc@kmust.edu.cn
Address: No.727 South Jingming Rd., Chenggong District, Kunming, Yunnan 650500,China

ScienceCareers online @sciencecareers.org
OPPORTUNITIES IN CHINA

OPPORTUNITIES IN CHINA
Science Careers online @sciencecareers.org

宁波大学
NINGBO UNIVERSITY

Faculty Positions Available in Ningbo University

◆ Seeking bright minds

Located in the historical port city of Ningbo in eastern China, Ningbo University is a burgeoning comprehensive university co-established by the Chinese Ministry of Education, Zhejiang provincial government and Ningbo municipal government. It is among the first five provincially governed key universities designated by the Zhejiang provincial government. Young and dynamic, Ningbo University is already ranked among the top 100 universities in China.

Ningbo University is actively seeking talented researchers to strengthen its faculty team.

Openings for academic leaders

Requirements:

- A doctoral degree from an overseas institution is expected, along with at least three years of work experience conducting research overseas; for those who have obtained their doctoral degree from a domestic institution, at least three years of overseas teaching or research experience is a must
- Experience working as a tenured professor or equivalent in a well-known university or research institution overseas (associate professor experience is fine for young candidates from top universities or institutions); generally, candidates should qualify for the national Thousand Talents Program
- A proven track record of achievements in a specialized research field, with the potential to become an academic or technical leader in the field
- Ability to work full-time on site, and preferably under 50 years old

Openings for top young scientists

Requirements:

- A doctoral degree from an overseas institution is preferred, along with at least three years post-graduate research experience overseas; those with doctoral degrees from domestic institutions must have at least three years of experience conducting research or teaching overseas
- Experience working full-time in a well-known university or research institution overseas, conducting research or teaching; generally, candidates should qualify for the national Thousand Young Talents Program or the provincial Thousand Talents Program
- Ability to work full-time on site, and preferably under 45 years old

Openings for excellent doctoral researchers

Requirements:

- A doctoral degree from an overseas institution is preferred, along with at least three years of work experience conducting research overseas; those with doctoral degrees from domestic institutions should have at least three years of experience conducting research or teaching overseas
- A track record of publication experience, with at least one paper published in Social Sciences Citation Index or Arts & Humanities Citation Index journals for candidates in humanities and social sciences fields; two or more papers published in Science Citation Index-listed journals or at least one publication in a top journal for candidates in natural sciences fields
- Ability to work full-time at the university

◆ Compensation

Generous compensation packages will be available. For excellent doctoral researchers, the successful candidate will receive a settling-in allowance of 600,000 (180,000+420,000) RMB. Those with four or more publications in top journals are eligible to be hired as associate professors, and will receive a settling-in allowance of 800,000 (600,000+200,000) RMB.

◆ Application procedure

Please submit a completed application form, a curriculum vitae and a cover letter, along with other relevant supporting materials via e-mail to: **rsc@nbu.edu.cn**.

For additional information regarding the application, such as the number of openings, please visit: **http://www.nbu.edu.cn/shizi**.

中国安徽高校招聘

Recruitment for Anhui Universities of China

长江三角洲城市群

The Yangtze River Delta City Group

Positions in engineering, science, literature, agriculture, management, law, economics, art, etc. are provided for all the talents interested in working at Anhui, China.

Looking for more positions?

Please send your CV to consultant2@acabridge.edu.cn

or call the direct line: +86 13810344600 (WeChat: wbh917)

www.ustc.edu.cn 中国科学技术大学

www.hfut.edu.cn 合肥工业大学

www.ahu.edu.cn 安徽大学

www.ahau.edu.cn 安徽农业大学

www.ahmu.edu.cn 安徽医科大学

www.aust.edu.cn 安徽理工大学

www.ahut.edu.cn 安徽工业大学

www.ahjzu.edu.cn 安徽建筑大学

www.edu.cn/ahzp

ScienceCareers online @sciencecareers.org
OPPORTUNITIES IN CHINA

Chuangbing ZHOU President of Nanchang University

Higher education works as the junction of the first productivity of science and technology, the first initiative of innovation and the first resource of talents. With the leadership of Jiangxi's higher education, Nanchang University is exploring earnestly the way to high-level university by implementing talent programs. It commits itself wholeheartedly to the employment of talents without overstressing qualifications. It is our strong hope that talents from all over the world can join us in the development of Nanchang University.

Guoping MEI President of Jiangxi Normal University

Jiangxi Normal University endeavors to establish a top rank Chinese university with distinct features. We warmly welcome overseas talent of various academic backgrounds, in particular, Material Science, Organic Chemistry, Fundamental Mathematics, Regional Bionomics, Computer Science and Management Science, to join us. Let's start a pleasant journey of chasing and realizing our dreams together.

Qiao WANG President of Jiangxi University of Finance and Economics

It is a pleasure for decent men to get gifted people to educate. Adhereing to principles of Quality Guaranteeing Survival, Characteristics Contributing to development, Talents Creating Strong University, Law and Morality for Management, JUFE sincerely invites ambitious and talented people to join us to cultivate talents with innovation, entrepreneurship, and qualities of Fidelity, Excellence, Integrity, and Dedication, to establish a high-level university of finance and economics with distinctive characteristics, to fulfill the JUFE dream of a Reputed Century-old University.

Shenglian LUO President of Nanchang Hangkong University

Nanchang Hangkong University endeavors to establish a top rank Chinese university with distinct aviation and engineering science features. We warmly welcome overseas talents of various academic backgrounds, in particular, Aerospace Science and Technology, Environment Science and Engineering, Mechanical Engineering, Instrument Science and Technology, Optical Engineering, Computer Science to join us in the development.

南昌大学
www.ncu.edu.cn

江西师范大学
www.jxnu.edu.cn

江西财经大学
www.jxufe.edu.cn

南昌航空大学
www.nchu.edu.cn

Please send your CV to consultant2@acabridge.edu.cn

or call the direct line: +86 13810344600 (WeChat: wbh917)

www.edu.cn/jxzp

哈爾濱工程大學
HARBIN ENGINEERING UNIVERSITY

Harbin Engineering University Sincerely Invites talents to Apply for "The Recruitment Program for Professionals"

Basic Qualifications

1. Applicants engaged in scientific researches or Engineering technology and below the age of 40.
2.Have obtained a doctorate degree and have no less than three years of overseas working experience.
3. With formal teaching and researching positions in overseas prestigious universities, institutions or enterprises.
4. The applicants should be the top-notch talents in their research fields, and have the potential to become future leaders in relevant areas.
5.The applicants will be able to work full time in China. For those who have worked in China, they should be no more than one year. Outstanding PHD students can be recruited in exceptional cases.

Preferential Policies and Treatments

What we offer for entrants of "The Recruitment Program for Professionals":
1. Employed as professor or doctoral tutor
2.Support to form academic team
3. A lump sum of 500,000 RMB shall be granted by the central budget
4.Research subsidies, varying from 1 million to 3 million RMB, shall be allocated in batches throughout the process of the program according to the level and quality of the program.
5.Provide no less than 400,000 RMB annual salary and 300,000 RMB setting-in allowance.
6.Provide an apartment no less than 80 square meters or 1 million to 1.5 million RMB housing benefit.
7.Offer job opportunities to spouses, and children will have guaranteed admission to schools.
If interested in applying for "The Recruitment Program for Professionals", please send your resume to rencai@hrbeu.edu.cn.
For more information, please contact :
Contact Persons: Gao shan, Bai yun.
Tel:+86-451-82518061
E-mail:rencai@hrbeu.edu.cn

西南交通大學
Southwest Jiaotong University

Southwest Jiaotong University, Chengdu, China Invites Applications for the Academic Positions

Southwest Jiaotong University (SWJTU), founded in 1896 and located in Chengdu, the capital of Sichuan province--China's dynamically growing West. SWJTU is an elite university with national key multidisciplinary "211" and "985 Feature" projects directly managed by the Ministry of Education.SWJTU is currently on the strategic "Developing and Strengthening the University by Introducing and Cultivating talents" campaign. Thus, you are cordially invited to apply for the following academic positions. More information is available at http://www.swjtu.edu.cn/

Positions and Requirements

A. High-level Talented Leaders: Candidates should be qualified to be listed in national top talents programs such as Program of Global Experts, Top Talents of National Special Support Program, "Chang Jiang Scholars", China National Funds for Distinguished Young Scientists and National Award for Distinguished Teacher.

B. Young Leading Scholars: Candidates are preferable to be listed or qualified for the following programs: National Thousand Young Talents Program,The Top Young Talents of National Special Support Program (Program for Supporting Top Young Talents), Science Foundation for the Excellent Youth Scholars.

C. Excellent Young Academic Backbones

D. Excellent Doctors and Post Doctoral Fellows

Please contact Mr. Yu Wang, Ms. Ye Zeng,Ms.Qing Ya Wang
Telephone number: +86-28-66367238/ 66366202
Email: talent@swjtu.edu.cn
Address: Human Resources Department, SWJTU, Western Park of High-Tech Zone, Chengdu, Sichuan, China, 611756

High-level Global Talents Online Job Fair

Job Vacancies in China's Universities and Research Institutes

Holding Date: 9:00-16:00 (GMT+8), October 26th, 2016
Recruitment requirements: Overseas Scholars, Doctors and Post-doctors
Participating Universities:
Shanghai University Of Engineering Science
Shanghai Normal University
Zhengzhou University
Guangdong University of Foreign Studies
Southwest University
Jiangxi University of Finance and Economics
Shanghai University of Electric Power
Guangdong Ocean University
Shanghai Lixin University of Account and Finance
Shanghai Maritime University
Southeast University
Zhengzhou University of Light Industry
Hunan University of Commerce
Shaanxi Normal University
Xi`an Jiaotong University
Southwest University of Science and Technology
Northeast Forestry University
Harbin Engineering University
Shanghai Dianji University
Southwest Jiaotong University
Third Military Medical University

Participation Approaches:
1. Please send your CV to consultant@acabridge.edu.cn
2. For more information, please visit http://www.edu.cn/cv

Want to recommend talents or consult more information?
Please contact consultant@acabridge.edu.cn

ScienceCareers online @sciencecareers.org

For recruitment in science, there's only one *Science*.

Special Job Focus:

Neuroscience

Issue date: November 4

Book ad by October 18 to guarantee space

Ads accepted until October 28 if space allows

What makes *Science* the best choice?

- Read and respected by 400,00 readers around the globe
- 75% of readers read *Science* more often than any other journal
- Your ad dollars support AAAS and its programs, which strengthens the global scientific community.

Why choose this job focus for your advertisement?

- Relevant ads lead off the career section with special neuroscience banner
- Bonus distribution to Society for Neuroscience, November 12–16, San Diego, CA.

Expand your exposure. Post your print ad online to benefit from:

- Link on the job board homepage directly to neuroscience jobs
- Dedicated landing page for jobs in neuroscience
- Additional marketing driving relevant job seekers to the job board.

Deliver your message to a global audience of targeted, qualified scientists.

129,574
subscribers in print every week

49,518
unique active job seekers searching for **neuroscience** positions in 2015

34,780
applications submitted for **neuroscience** positions in 2015

Produced by the *Science*/AAAS Custom Publishing Office.

SCIENCECAREERS.ORG

ScienceCareers
FROM THE JOURNAL SCIENCE AAAS

To book your ad: **advertise@sciencecareers.org**

The Americas
+202 326 6582
Japan
+81 3 3219 5777

Europe/RoW
+44(0)1223 326500
China/Korea/Singapore/Taiwan
+86 186 0082 9345

Programm zur Förderung der Rückkehr des hochqualifizierten Forschungsnachwuchses aus dem Ausland

Ministerium für Innovation, Wissenschaft und Forschung des Landes Nordrhein-Westfalen

Sie stehen am Anfang Ihrer wissenschaftlichen Karriere und möchten mit Ihrer Forschungstätigkeit zur Bewältigung der großen gesellschaftlichen Herausforderungen unserer Zeit beitragen? Der Wissenschaftsstandort Nordrhein-Westfalen bietet Ihnen die Chance zum Aufbau und zur Leitung einer selbstständigen Nachwuchsgruppe an einer hiesigen Hochschule Ihrer Wahl.

Im Falle einer erfolgreichen Bewerbung sind dafür über einen Zeitraum von fünf Jahren bis zu 1,25 Mio. EUR vorgesehen. Die Leitungsposition ist mit Entgeltgruppe 15 TVL – vergleichbar W2 – dotiert. Sie erhalten eine personengebundene Finanzierungszusage und etablieren Ihre Nachwuchsgruppe an einer Hochschule Ihrer Wahl in Nordrhein-Westfalen, welche Ihnen die beste Zukunftsperspektive und eventuell auch Tenure-Track bietet.

Der Beginn dieser Förderung ist bis Ende 2017 vorgesehen.

Ausgehend von den Zielen der Forschungsstrategie Fortschritt NRW werden erneut Nachwuchsforschertalente aus allen Fachgebieten gesucht, die mit ihren herausragenden Ideen zur Bewältigung der großen gesellschaftlichen Herausforderungen unserer Zeit beitragen können. Besonders erwünscht sind dabei in diesem Jahr Anträge aus den Wirtschafts- sowie den Geistes- und Gesellschaftswissenschaften.

Sie forschen derzeit außerhalb Deutschlands und haben Ihre Promotion vor wenigstens zwei, höchsten sechs Jahren (im Fachgebiet Medizin vor höchstens neun Jahren) erworben? Ihr Lebensmittelpunkt lag vor Ihrem Auslandsaufenthalt in Deutschland? Wenigstens die letzten 12 Monate Ihrer mehr als zwei Jahre währenden wissenschaftlichen Forschungstätigkeit haben Sie im Ausland verbracht?

Wenn dies alles auf Sie zutrifft, freuen wir uns auf Ihre Bewerbung! Nähere Informationen zum Bewerbungsverfahren sowie eine ausführliche Beschreibung des Programms finden Sie unter

www.rueckkehrprogramm.nrw.de.

Bewerbungsschluss der diesjährigen Ausschreibung ist der **4. Dezember 2016.**

Das Land Nordrhein-Westfalen fördert die berufliche Entwicklung von Frauen. Bewerbungen von Frauen werden daher besonders begrüßt. Bewerbungen geeigneter schwerbehinderter Menschen sind erwünscht.

WISSEN SCHAFFT CHANCEN.NRW

www.wissenschaft.nrw.de

Georgia Institute of Technology

Tenure Track Faculty Position
Georgia Institute of Technology
School of Chemistry and Biochemistry
Atlanta, GA 30332-0400

THE **GEORGIA INSTITUTE OF TECHNOLOGY, SCHOOL OF CHEMISTRY AND BIOCHEMISTRY** seeks to fill a tenure-track faculty position in the development of any aspect of chemistry or biochemistry related to feedstocks from renewable and sustainable sources. Research areas of interest include, but are not limited to, functional biomaterials, catalysis, energy harvesting and storage, efficient syntheses and processes, and plant bioengineering and synthetic biology. Opportunities for significant interaction with and support from the Renewable Bioproducts Institute at Georgia Tech (www.bioproducts.gatech.edu) will be available. Candidates with interdisciplinary research programs may be considered for joint appointments with other campus units.

Exceptional candidates at **all levels** are encouraged to apply. Assistant Professor candidates should submit a cover letter, curriculum vitae, description of research plans, description of teaching interests and philosophy, and arrange for the submission of three letters of recommendation. Candidates at advanced levels should submit a cover letter, curriculum vitae, and the names and contact information of three references. All materials and requests for information should be submitted electronically, as per the instructions found at:

https://academicjobsonline.org/ajo/jobs/8094

The application deadline is **November 15, 2016**, with application review continuing until the position is filled.

Georgia Tech is an Equal Education/Employment Opportunity Institution.

John Innes Centre
Unlocking Nature's Diversity

Independent Research Fellowships

The John Innes Centre (JIC), Norwich, UK is a world leading centre of excellence in plant and microbial sciences based on the Norwich Research Park. We are inviting applications from outstanding researchers who either hold, or wish to apply for Independent Research Fellowships [such as a BBSRC David Phillips Fellowship (**http://www.bbsrc.ac.uk/funding/fellowships/david-phillips.aspx**), or a Royal Society University Research Fellowship (**https://royalsociety.org/grants-schemes-awards**)], to attend a Conference at the JIC on **30 January, 2017**. At the meeting you will be able to present a talk about your proposed area of research and to discuss your proposals, the development of your group and your future career plans in depth with senior JIC Scientists.

After the Conference we will select and mentor outstanding candidates in writing Fellowship applications and/or offer the opportunity to move existing Fellowships to the JIC. Considerable additional resources will be provided to Fellows by the Centre. We may also offer an independently-funded Fellowship to a suitable candidate.

Further details and particulars can be found at http://www.jic.ac.uk/training-careers/training/fellowships/independent-research-fellows-conference/

Please e-mail a 2-page summary of your research plan, a copy of your CV and arrange for three letters of recommendation to be emailed to wendy.forsdick@jic.ac.uk by Wednesday 30 November 2016.

The John Innes Centre is a registered charity (No223852) grant-aided by the Biotechnology and Biological Sciences Research Council and is an Equal Opportunities Employer and supports flexible working.

POSITIONS OPEN

California State University Northridge

Department of Biology
Assistant/Associate Professorships
(Two positions, effective August 2017)

California State University, Northridge, invites applications for TWO, research-focused, tenure-track positions in the Department of Biology. Applicants must hold a Ph.D. and have post-doctoral experience. The successful candidate shall develop a vigorous research program built on extramural funding, involve undergraduate and Master's students in research, and demonstrate teaching excellence.

Marine Biologists/Ecologists: We seek candidates to complement existing skills in a program focused on organismic biology and population/community ecology with a strong emphasis on fieldwork in temperate and tropical locations. We are particularly interested in building strengths in ecological modeling, conservation biology, and understanding the capacities of organisms and systems to respond to multiple stressors associated with climate change. The successful candidates will demonstrate a proven capacity to develop an externally-funded research program that actively involves graduate and undergraduate students. Teaching options include a course in the candidates specialty, marine biology/ecology, experimental design and analysis, analyses of big ecological data, and introductory biology.

Applicants should submit a cover letter, curriculum vitae, three letters of recommendation, summary of teaching experience, statements of teaching philosophy and research interests, and three publications to e-mail: **marinebio@csun.edu**

Electronic applications as a single file (excepting letters of recommendation) are strongly preferred. Materials may also be mailed to: **Marine Biology Search Committee, Department of Biology, California State University, 18111 Nordhoff Street, Northridge, California 91330-8303, USA.**

For more information visit website: **http://www.csun.edu/science-mathematics/biology/jobs** Screening will begin on **November 17, 2016**.

ASSISTANT PROFESSOR
of FISHERIES ECOPHYSIOLOGY
Montana State University

The Ecology Department at Montana State University invites applications for a tenure-track Assistant Professor of Fisheries Ecophysiology. We seek candidates with research interests and skills that complement our current faculty and who utilize laboratory and field experiments to address important contemporary issues in freshwater fisheries science and management, including but not limited to such areas as climate change, invasive species, angling, hydrological alteration, bioenergetics, contaminants/disease, and fish passage. We are particularly interested in candidates that can integrate research across these disciplines. A major strength of the department is bridging basic and applied science research to address questions that are both regionally important and relevant to society. Because increasing the diversity of the profession is one of our strategic priorities, women and underrepresented minorities in ecological sciences or natural resource management are particularly encouraged to apply.

For more information and application instructions see website: **http://jobs.montana.edu/postings/6028.**

Screening of applications will begin on **November 1, 2016**; however, applications will continue to be accepted until an adequate applicant pool has been established.

MSU is an Equal Opportunity Employer, Veterans/Disabled.

POSITIONS OPEN

California State University Northridge

Department of Biology
Assistant Professorship
/Tenure Track position

California State University, Northridge invites applications for tenure-track Assistant Professor positions in Cellular or Molecular Biology in the Department of Biology to begin August 2017. Applicants must hold a Ph.D. and have post-doctoral experience.

Candidates whose research answers fundamental questions pertaining to plant physiology, plant pathology, plant cell biology or whose research examines cell biology questions using plant-microbe-insect interkingdom interactions are encouraged to apply. Candidates should use proteomics, systems, computational, or molecular approaches to answer their research questions. The successful candidate is expected to develop and maintain a vigorous research program with extramural funding, train undergraduate and graduate (M.S.) students in research, provide effective instruction to students of diverse backgrounds.

For more information and application procedure visit website: **http://www.csun.edu/science-mathematics/biology/jobs**

Screening application will begin on **October 31, 2016**.

California State University, Northridge is an Equal Opportunity Employer committed to excellence through diversity.

Two Position Openings: Assistant/Associate Professors in Chemistry & Biochemistry

As part of a multi-year hiring plan, the Department of Chemistry and Biochemistry at Northern Illinois University anticipates hiring two tenure-track faculty members for the 2017-18 academic year. Hiring is intended at the rank of **ASSISTANT PROFESSOR**, but consideration may be given to appointment at the rank of associate professor. Applications in any sub-discipline of chemistry are encouraged and the ability to teach analytical chemistry is preferred. All applicants must have a PhD or equivalent degree and postdoctoral experience is preferred. Junior applicants should have the potential to develop and senior applicants should have: (1) a nationally/internationally recognized, externally funded research program, (2) proficiency teaching and mentoring students from a range of cultural backgrounds, and (3) experience serving a collegial, student-centered department. Preference will be given to applicants able to work effectively in a multicultural team and to develop synergies with Argonne National Laboratory and/or regional industry. Candidates should provide a letter of application, curriculum vitae, a description of research plans including start-up requests, a teaching philosophy, and the names and contact information for three references to the chair of the search committee (Professor Elizabeth Gaillard, e-mail **CHEMSearch@niu.edu**). Application review begins on **October 31, 2016** and will continue until the positions are filled. *Northern Illinois University actively encourages applications from women, minorities, and individuals of any sexual orientation in keeping with its policy of promoting diversity throughout the institution. Persons who require accommodation(s) in the application process under the Americans with Disabilities Act should notify the search chair. State mandated pre-employed background check is required.*

Post Your Jobs
1.4 million candidates*
235,000 job applications*
Reach Scientists. Fill Positions.
ScienceCareers
employers.sciencecareers.org
*Jan–Dec 2015

POSITIONS OPEN

WISCONSIN
UNIVERSITY OF WISCONSIN-MADISON

The Department of Chemical and Biological Engineering, University of Wisconsin-Madison invites applications for a **TENURE-TRACK FACULTY POSITION** at the assistant, associate or full professor level. Successful candidates are expected to maintain world-class graduate research programs, teach undergraduate and graduate courses and engage in university service. Candidates with a Ph.D. in chemical or biological engineering or a related field and truly outstanding accomplishments in any area of research of importance to chemical and biological engineering will be considered.

For more information, please see website: **http://goo.gl/448XFS**. Enter 87650, 87352 or 87384 in search field and follow the instructions there on how to apply. Applications received by web-specified respective deadlines will receive full consideration. *Women and candidates from groups traditionally under-represented in engineering are strongly encouraged to apply.*

Post your jobs
Fast and Easy

ScienceCareers
employers.sciencecareers.org

2016 Annual Top Employers in Biotech & Pharma

Special Career Feature: October 28, 2016

Reserve your ad by October 11 to guarantee space.
Ads accepted until October 21 if space is still available.

For recruitment in science, there's only one **Science**

WHO IS NO. 1 THIS YEAR?

Science publishes the results of its 15th annual Top Employers Survey on October 28. *Science* has a long history of providing a forum for scientists to express their opinions about the biotech and pharma industry. For 2016, we gathered the responses from 5,984 scientists who had plenty to say about the industry.

Over **48,000** *Science* print readers work in industry—reach these passive job seekers!*

Recruit or brand your organization and reach both ACTIVE and PASSIVE job seekers. Here's how:

1. Scientists in the biotech/pharma community eagerly anticipate the results of this survey every year. By announcing your openings in this special feature, your reach goes beyond active job seekers to those involved in the field, targeting elusive passive job seekers at the same time.

Special online options available. Ask your rep.

2. Your association with this issue tells prospective recruits that you are among the best. You have a unique opportunity to brand your company as a leader. Reach the scientists that your competitors are reaching and promote your advantages.

Start building your pipeline today with *Science*.

* Publisher's Own Data, August 2015.
Produced by the *Science*/AAAS Custom Publishing Office.

SCIENCECAREERS.ORG

Science Careers
FROM THE JOURNAL SCIENCE AAAS

To book your ad: **advertise@sciencecareers.org**

The Americas
202-326-6577

Europe/RoW
+44 (0) 1223-326500

Japan
202-326-6578

China/Korea/Singapore/Taiwan
+86-186-0082-9345

Science Careers online @sciencecareers.org

By **Edward J. Smith**

Doing science while black

When I was 11 years old, my older brother left our village in Sierra Leone to study physics in the West. After completing his degree, he returned home to contribute to development. I followed his lead, though I studied genetics—and I never returned to live in Africa. Instead, I established a career in research and research education in the United States. Being an academic scientist in this country with my skin color and accent has not been easy, but I hope that my resilience amid significant challenges offers a path for younger minority scientists.

I experienced my first brush with bias in the virology lab where I started my Ph.D. Every time I left the photography room, the principal investigator (PI) was there to check on my results. He didn't do this for other students; it was clear that he didn't trust me to do the procedure correctly. At lab meetings, the PI called on every other group member for a progress report. But in my case, he asked the senior Ph.D. student I was working with to speak for me. I felt frustrated and humiliated, but I wouldn't let these experiences derail my plans for a research career. I left that lab after 4 months and completed my doctoral studies in a less flashy lab, in animal sciences, with an extremely supportive adviser.

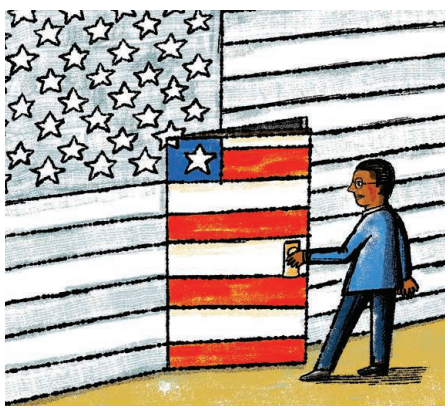

"Being an academic scientist in this country ... has not been easy."

The first place in the United States that really felt like home was Tuskegee University, a historically black institution in Alabama where I had my first faculty position. (I didn't consider returning home because Sierra Leone was in the middle of a brutal civil war at the time.) It was easy to be productive in a place where no one questioned my right to be in the lab or my ability to mentor students.

But my experiences with the larger scientific community still made me feel like I didn't belong. A few years after becoming a professor, for example, I went to a social event at a society meeting with an international, multiracial group of colleagues. I was the only black researcher among them. When we walked into the room, the crowd fell completely silent, apparently uncomfortable with my presence. I considered myself a scientist with great potential, but that experience made me feel that, to others, my skin color was more important than the quality of my work. The next year, as I was starting a sabbatical in a lab at another institution, I asked one of the researchers in the group whether the PI was in. "Are you delivering a package?" he asked. "I can pass it on to him." These and other encounters imply that, no matter how productive my research is or how professionally I present myself, I and other black scientists do not belong in academia's hallowed halls.

In contrast, when I have visited Kenya, Tanzania, and Zambia, I have always received an enthusiastic welcome from the scientists there, who are excited to hear from a black scientist with an accent like theirs who developed a successful research career in the United States. I am happy to be able to share my experiences with my colleagues in Africa. But the differences between my experiences on the two continents also serve as a depressing reminder that a U.S. Ph.D. and passport do not shield me from the realities of being a black scientist in a white world, where I rely on one-liners such as "doing science while black" or "leading while black" to communicate the complexities of my circumstances.

Despite the hostility, both blatant and subtle, that I have experienced in the corridors of science, and still encounter, I'm glad that I stayed here. I believe that the career I have carved out for myself will help pave the way for future generations of underrepresented minority (URM) scientists to thrive, and for all members of the scientific community to be more culturally sensitive than those who came before them. I have spent much of my professional life focused on training URM scientists, and I am as proud of these researchers as anything else in my life. As all of us strive to increase the critical mass of URM scientists, encounters with black scientists will become more commonplace until, hopefully, none of us is ever mistaken for a delivery person. ■

Edward J. Smith is a professor of comparative genomics at Virginia Polytechnic Institute and State University in Blacksburg. Send your story to SciCareerEditor@aaas.org.

ILLUSTRATION: ROBERT NEUBECKER

Downloaded from http://science.sciencemag.org/ on October 7, 2016

Published by AAAS